AERONOMY

PART B

P. M. Banks
Department of Applied Physics
and Information Science
University of California
San Diego, California

G. Kockarts
Institut d'Aéronomie Spatiale
de Belgique
Bruxelles, Belgium



ACADEMIC PRESS New York and London 1973

A Subsidiary of Harcourt Brace Jovanovich, Publishers

COPYRIGHT © 1973, BY ACADEMIC PRESS, INC.
ALL RIGHTS RESERVED.
NO PART OF THIS PUBLICATION MAY BE REPRODUCED OR TRANSMITTED IN ANY FORM OR BY ANY MEANS, ELECTRONIC OR MECHANICAL, INCLUDING PHOTOCOPY, RECORDING, OR ANY INFORMATION STORAGE AND RETRIEVAL SYSTEM, WITHOUT PERMISSION IN WRITING FROM THE PUBLISHER.

ACADEMIC PRESS, INC.
111 Fifth Avenue, New York, New York 10003

United Kingdom Edition published by
ACADEMIC PRESS, INC. (LONDON) LTD.
24/28 Oval Road, London NW1

LIBRARY OF CONGRESS CATALOG CARD NUMBER: 72-88332

PRINTED IN THE UNITED STATES OF AMERICA

Preface

Aeronomy is the scientific discipline devoted to the study of the composition, movement, and thermal balance of planetary atmospheres. The need for such an area of specialization has developed during the past twenty years as sophisticated experiments have revealed the complexities of the upper atmospheres of the earth and other planets.

As a field of research, aeronomy demands an understanding of the basic concepts of both chemistry and physics as applied to a highly rarefied medium composed of neutral and charged particles. The first major accomplishments of aeronomy were associated with attempts to understand basic photochemical processes in the earth's upper atmosphere. Additional studies emphasized the importance of molecular diffusion and its effect in producing the transition from homogeneous molecular gases of the lower atmosphere to the hetrogeneous atomic and molecular gases of the upper atmosphere. As might be expected, progress in aeronomy has frequently been linked with advances in laboratory measurements or the development of new concepts in allied scientific specialities.

In this text we have attempted to make a comprehensive exposition of the basic processes involved in the aeronomy of the earth's upper atmosphere. Accordingly, it has been necessary to reach a balance between generalized descriptions of different phenomena in terms of various models and the actual observed behavior. It has been our goal to emphasize the fundamental character of the upper atmosphere and ionosphere without detailed descriptions of global morphology. Consequently, considerable discussion has been given to chemical and ionic reactions and to the different collisional interactions involving particles and radiation. The data presented have then been used to provide quantitative reaction rates, cross sections, and interaction coefficients of aeronomical interest which reflect current best values and possible ranges consistent with present knowledge.

Owing to the interrelatedness of many aeronomical problems the question of self-consistency of the different atmospheric parameters is always important; i.e., when certain processes are examined it is necessary to question their relationship to the overall atmospheric structure. To avoid as much as possible an inconsistent choice of densities, temperatures, and similar parameters, the calculations given in Part A of this text are largely based upon the sets of atmospheric models described in Chapter 3, while those in Part B are based on Chapter 14 and Appendix B. Such an approach is somewhat unique and reflects the large number of calculations which have gone into the preparation of the text material and figures. This approach is consistent with our desire to present descriptions of basic processes rather than predictions of absolute values.

The material of this text has been divided into two volumes. The first volume is principally concerned with the characteristics of the atmosphere as a whole and a presentation of the outstanding problems of chemical aeronomy. To assist later discussion, the topics of photoabsorption, solar radiation, photodissociation, collision processes and aeronomic reactions are introduced. Next, the chemistry of the atmospheric regions below 100 km is discussed with emphasis on oxygen, ozone, nitrogen compounds, and the effects of hydrogen compounds.

The second volume is concerned with phenomena which occur, for the most part, above 100 km in the heterosphere. The first topics are concerned with the neutral atmosphere and include the behavior of the thermosphere, the derivation of atmospheric models, and the formation of the exosphere. With regard to charged particles, subsequent chapters are devoted to the formation of the ionosphere, the basic ideas of plasma transport and the plasma thermal balance.

Acknowledgments

Portions of the present text are based on manuscripts prepared by Professor M. Nicolet between 1952 and 1965 and by the present authors and Professor Nicolet in the period 1967 to 1971. The development of topics in the first chapters parallels those originally given in the earlier manuscripts. The majority of the material, however, supercedes the earlier versions and represents work through March, 1972. In recognition of Professor Nicolet's long interest in this text, and considering his role in the development of the field, it was felt that the title "Aeronomy," taken from the original manuscript, would be appropriate.

A work such as this cannot be prepared without extensive assistance. Our indebtedness to Professor Nicolet for his years of assistance and association is gratefully acknowledged. In addition, Dr. Eldon Ferguson provided valuable advice and data for Chapter 10 and subsequent calculations. Dr. J. R. Doupnik and Professor A. F. Nagy gave considerable time to reading and criticizing the manuscript in various stages of development. Dr. C. Y. Johnson and others provided many of the experimental data appropriately acknowledged in the various chapters.

The assistance provided by Miss Linda Simpson, Mrs. Carole Gonzales, and Mrs. Lynn Love at the University of California, San Diego was invaluable and helped to ease an otherwise impossible burden. In Belgium, Mrs. Marie-Thérèse Werpin and Miss Marguerite De Clercq typed the first versions of the older manuscripts. The numerous figures were carefully drawn by Arthus Simon and Jacques Schmitz while Maurice Jaumin prepared and checked the references cited in the text. Emile Falise, Jean-Claude Crop, and Marcel Rosseeuw wrote several computer programs necessary for the preparation of the tables and graphs. To the many others who helped in various ways we wish to express our sincere gratitude. In addition, we note

that the responsibility for errors and omissions in the text must remain with us.

To our wives and children we must apologize for the long periods of time spent in preparation of the manuscript. Their understanding of our goals and needs provided us with the strength to continue a difficult task.

Contents of Part A

General Introduction
The Composition of the Homosphere
Physical Conditions of the Homosphere
The Transition from the Homosphere to the Heterosphere
Temperature Gradient in the Thermosphere
Photoabsorption
Solar Radiation and Photoionization
Photodissociation
Collision Processes
Aeronomic Reactions
Oxygen and Ozone
Nitrogen and Nitrogen Oxides
Hydrogen Compounds and Their Effects in the Chemosphere
Appendix A: A Guide to Reactions and Reaction Rate Coefficients

CHAPTER 14

Thermal Structure of the Heterosphere

14.1 Introduction

Knowledge of all the physical parameters involved in the structure of the upper atmosphere can be considered as a major goal of aeronomy. This implies the need for atmospheric models which represent as accurately as possible actual physical phenomena. Using an ideal model, it would be possible to predict real physical properties as a logical consequence of the model. This final stage of development is far from being reached at the present time.

A fundamental parameter for the physical description of the upper atmosphere is the temperature. Actually, several temperatures should be considered, since the neutral particles, the ions, and the electrons do not react in the same way to the heat sources and sinks which can affect the thermal structure of the heterosphere. In this chapter, the behavior of the neutral species will be discussed in relation to the fundamental conservation equations for the mass, the momentum, and the energy. Since the complete solution of these equations has not yet been obtained, a compromise is adopted which leads to the working models used in later chapters. These models should and will be improved, but in their present form they can be used as guides for the discussion of physical phenomena occurring in the terrestrial heterosphere.

14.2 Conservation Equations

14.2.1 Basic Equations

From the Boltzmann equation it is possible to deduce general conservation equations [1, 2] for the concentration, momentum, and energy of a gas mixture. First, however, it is necessary to define certain velocities which are involved in these equations.

When the linear velocity of a particle i is $\mathbf{v}_i$, the *average velocity* $\bar{\mathbf{v}}_i$ is defined by

$$\bar{\mathbf{v}}_i = (1/n_i) \int \mathbf{v}_i f_i(\mathbf{v}, \mathbf{r}, t)\, d\mathbf{v} \tag{14.1}$$

where n_i is the concentration of the particles i and $f_i(\mathbf{v}, \mathbf{r}, t)$ is the velocity distribution function, which eventually depends on the position $\mathbf{r}$ of the particle at a time t.

The *mass average velocity* $\mathbf{v}_0$ is defined by

$$\mathbf{v}_0 = (1/\varrho) \sum_i n_i m_i \bar{\mathbf{v}}_i \tag{14.2}$$

where $\varrho = \sum_i n_i m_i$ is the total density of the particles. The mass average velocity $\mathbf{v}_0$ is not the mean velocity of the molecules, but a weighted mean, giving to each molecule a weight proportional to its mass. If every molecule moved with the velocity $\mathbf{v}_0$, the momentum of the gas per unit volume would be the same as in the real situation.

The *peculiar velocity* $\mathbf{V}_i$ of a particle i in a gas mixture is defined by

$$\mathbf{V}_i = \mathbf{v}_i - \mathbf{v}_0 \tag{14.3}$$

and the *diffusion velocity* $\bar{\mathbf{V}}_i$ for the i particles is simply the average value of the peculiar velocity. Using (14.3), the diffusion velocity $\bar{\mathbf{V}}_i$ is given by

$$\bar{\mathbf{V}}_i = \bar{\mathbf{v}}_i - \mathbf{v}_0. \tag{14.4}$$

From the definition (14.2) of the mass average velocity, it is immediately seen that in a gas mixture

$$\sum_i n_i m_i \bar{\mathbf{V}}_i = 0. \tag{14.5}$$

The continuity equation for the concentration n_i can now be written

$$(\partial n_i/\partial t) + \nabla \cdot [n_i(\mathbf{v}_0 + \bar{\mathbf{V}}_i)] = 0. \tag{14.6}$$

This equation ignores possible production or loss processes for the i-type particles by photoionization, by photodissociation, or by chemical reactions. Summing Eq. (14.6) for all the types of particles, one obtains for the total concentration n

$$(\partial n/\partial t) + \nabla \cdot (n\mathbf{v}_0) + \nabla \cdot \left(\sum_i n_i \bar{\mathbf{V}}_i\right) = 0. \tag{14.7}$$

When Eq. (14.6) is multiplied by the mass m_i, the same procedure leads to the expression

$$(\partial \varrho/\partial t) + \nabla \cdot (\varrho \mathbf{v}_0) = 0 \tag{14.8}$$

for the total density ϱ where Eq. (14.5) has been used to eliminate the diffusion velocity $\bar{\mathbf{V}}_i$. This equation is also valid if production and loss terms had been introduced in (14.6), since the total mass of the system is conserved. However, Eq. (14.8) cannot be applied to a single constituent unless its diffusion velocity is zero.

In a viscous fluid, the general form of the momentum and energy equations is rather complicated [1–3] since the pressure is considered as a tensor in which a nondivergent symmetrical part of the mass average velocity-gradient tensor is involved. When the viscosity μ is considered as constant and when the gradient of $\nabla \cdot \mathbf{v}_0$ is neglected, the momentum equation for a gas mixture can be written

$$\frac{D\mathbf{v}_0}{Dt} + \frac{1}{\varrho}\nabla p - \frac{\mu}{\varrho}\nabla^2 \mathbf{v}_0 - \frac{1}{\varrho}\sum_i n_i \mathbf{X}_i = 0 \tag{14.9}$$

where p is the total hydrostatic pressure and $\mathbf{X}_i$ is any external force acting on the i-type particles. The total derivative operator D/Dt is simply $(\partial/\partial t) + \mathbf{v}_0 \cdot \nabla$.

Neglecting the energy dissipated by viscosity, the energy conservation equation is given by

$$\partial n\mathscr{E}/\partial t + \nabla \cdot (n\mathscr{E}\mathbf{v}_0) + \nabla \cdot \mathbf{E} + p\,\nabla \cdot \mathbf{v}_0 - \sum_i n_i \mathbf{X}_i \bar{\mathbf{V}}_i = P - L \tag{14.10}$$

where $\mathbf{E}$ is the heat flux vector and $\mathscr{E}$ is the total translational energy per particle in a coordinate system moving with a velocity $\mathbf{v}_0$. The production P and loss L terms will be discussed in Section 14.4.

The translational energy is given by

$$\mathscr{E} = \tfrac{1}{2}NkT \tag{14.11}$$

where k is the Boltzmann constant, T the temperature, and N the number of degrees of freedom of the particles. For a monoatomic gas, $N = 3$ and for other gases $N > 3$: In the case of N_2 and O_2, $N = 5$. With Eq. (14.11), the energy conservation equation (14.10) can now be transformed into

$$\frac{Nk}{2}\frac{\partial nT}{\partial t} + \frac{Nk}{2}\nabla \cdot (nT\mathbf{v}_0) + \nabla \cdot \mathbf{E} + p\nabla \cdot \mathbf{v}_0 - \sum_i n_i \mathbf{X}_i \bar{\mathbf{V}}_i = P - L. \tag{14.12}$$

The heat flow vector $\mathbf{E}$ is given by

$$\mathbf{E} = -\lambda \nabla T + T\sum_i c_{p_i} \varrho_i \bar{\mathbf{V}}_i \tag{14.13}$$

where λ is the thermal conductivity coefficient which is discussed in Section 14.3 and c_{p_i} is the specific heat at constant pressure. The specific heats c_{v_i} and c_{p_i} at constant volume and at constant pressure are given respectively by

$$c_{v_i} = Nk/2m_i \tag{14.14}$$

and

$$c_{p_i} = (k/m_i)[1 + (N/2)] \tag{14.15}$$

where m_i is the molecular mass of the i-type particles. In a gas mixture, the specific heats c_v and c_p will be defined formally by expressions similar to (14.14) and (14.15) with the mean molecular mass $m = \sum \varrho_i / \sum n_i$, instead of m_i. The first term in (14.13) is the usual heat flow resulting from temperature inequalities. The second term results from the energy carried by the molecular flow $\sum_i n_i \bar{\mathbf{V}}_i$. This term disappears when the heat flow is measured relative to the mean velocity of the molecules instead of relative to the average mass velocity $\mathbf{v}_0$. A third term, proportional to the thermal diffusion factor α_T (see Section 15.3) should appear in (14.13); it is, however, neglected in all atmospheric studies since thermal diffusion is not important for the major constituents. When the second term in (14.13) is equal to zero, $\sum_i n_i m_i \bar{\mathbf{V}}_i$ is generally different from zero. This last term has then to be introduced in the density continuity equation (14.8), whereas $\sum_i n_i \bar{\mathbf{V}}_i$ is removed from the concentration continuity equation (14.7). A similar modification appears also in the energy equation (14.12). It should be noted that only the translational energy has been considered in (14.12) and (14.13). When an exchange occurs between the translational energy $\mathscr{E}$ and the internal energy, Eq. (14.10) is of the same form for the sum of these energies.

Introducing the specific heat $c_v = Nk/2m$ and using the density continuity equation (14.8), it is possible to write the energy equation (14.12) in the form

$$\varrho(D/Dt)(c_vT) + p\,\nabla \cdot \mathbf{v}_0 + \nabla \cdot \mathbf{E} - \sum_i n_i \mathbf{X}_i \bar{\mathbf{V}}_i = P - L. \quad (14.16)$$

The last term in the left member of (14.16) disappears only when the external accelerations $\mathbf{X}_i/m_i$ are independent of the index i; i.e., of the nature of the particles. This is, for example, the case when gravity is the only external force. Finally, it should be noted that the Eqs. (14.9) and (14.16) are not valid for a single constituent since a nonzero collision term is involved for each species in the Boltzmann equation [1, 2].

To build a complete and detailed atmospheric model is a formidable task which requires the simultaneous solution of the three-dimensional time-dependent conservation equations (14.8), (14.9), and (14.16) coupled with the diffusion equations leading to the velocities $\bar{\mathbf{V}}_i$. This problem is insoluble at the present time without simplifying assumptions and without more experimental information on the physical processes responsible for the thermal structure [4]. In the most complete attempt to date [5] it has been pointed out that from a mathematical point of view it remains to be proved that there exists a unique solution for this system of integropartial differential equations. The results of this same three-dimensional computation [5] show, unfortunately, that above 200 km the temperature peaks earlier than the density. This is in contradiction with the drag data analysis [6, 7] which indicate a density maximum around 14 hr local time, whereas incoherent scatter observations [8–11] show a temperature maximum around 17 hr local time.

Several analyses [12–18] have been made for steady state conditions. A one-dimensional time-dependent calculation [19, 20] required the introduction of a hypothetical heat source in order to explain the satellite drag data. In another time-dependent calculation [21], the second heat source was not introduced and the diurnal maximum of the density occurred around 17 hr local time. Coriolis forces and ion drag terms have been introduced [22] in the hydrodynamic equations in order to analyze the effects of horizontal movements. But in a two-dimensional model the equations become so complicated that important simplifications were necessary, Finally, a completely different approach to the thermal structure of the upper atmosphere has been made in terms of atmospheric waves [23–25]. This model takes into account vertical and horizontal mass and energy transport. The conservation equations are linearized to a set of complex

differential equations which require boundary values which are not well known at the present time.

From the foregoing discussion it is clear that the computation of models describing the structure of the upper atmosphere is far from being complete. All the present models are based on several simplifying assumptions which make the conservation equations more tractable. Some of these assumptions will now be discussed starting from the basic equations.

14.2.2 Simplifying Hypotheses

The general conservation equations have never been solved for a planetary upper atmosphere. Several forms, implying different assumptions, have, however, been treated. Before describing these simplification, it is necessary to specify the nature of the external forces $\mathbf{X}_i$ acting on the atmospheric constituents. Among all possible forces, one should consider the gravitational attraction, the Coriolis force, and several frictional forces resulting from the relative movement between the neutral gas and the ionic species. The gravitational and the Coriolis accelerations are independent of the nature of the neutral particles. Therefore, the term $\sum n_i \mathbf{X}_i \bar{\mathbf{V}}_i$ disappears for these forces, according to (14.5). This is, however, not the case for the frictional forces or ion-drag terms which depend on the relative velocities and on the collision frequencies between the particles. These forces will now be represented by $\mathbf{F}_i$.

The gravitational force for each particle with mass m_i is $m_i\mathbf{g}$, $\mathbf{g}$ being the gravity acceleration vector. When $\boldsymbol{\omega}$ is the constant angular velocity vector of the earth, the Coriolis force at a geocentric position vector $\mathbf{r}$ is $m_i[2\boldsymbol{\omega}\times\mathbf{v}_0 + \boldsymbol{\omega}\times(\boldsymbol{\omega}\times\mathbf{r})]$. With these definitions, the conservation equations (14.8), (14.9), and (14.16) can now be written

$$(\partial\varrho/\partial t) + \nabla\cdot(\varrho\mathbf{v}_0) = 0, \tag{14.17}$$

$$\frac{D\mathbf{v}_0}{Dt} + \frac{1}{\varrho}\nabla p - \frac{\mu}{\varrho}\nabla^2\mathbf{v}_0 - \mathbf{g} - 2\boldsymbol{\omega}\times\mathbf{v}_0 - \boldsymbol{\omega}\times(\boldsymbol{\omega}\times\mathbf{r}) - \frac{1}{\varrho}\sum_i n_i\mathbf{F}_i = 0, \tag{14.18}$$

and

$$\varrho(D/Dt)(c_vT) + p\nabla\cdot\mathbf{v}_0 + \nabla\cdot\mathbf{E} - \sum_i n_i\mathbf{F}_i\bar{\mathbf{V}}_i = P - L. \tag{14.19}$$

All the external forces appear in the momentum equation, whereas only the friction forces $\mathbf{F}_i$ are present in the energy equation. Using atmospheric models, the momentum equation (14.18) has been applied extensively in horizontal wind calculations [26, 27]. These computations require, how-

ever, a knowledge of the vertical thermal structure, which should be deduced from the energy equation (14.19).

A major simplification can be made by assuming that the diffusion velocities $\bar{\mathbf{V}}_i$ are equal to zero. The density continuity equation (14.17) and the momentum equation (14.18) are not affected by this hypothesis. But, the concentration continuity equation (14.7) becomes now

$$(\partial n/\partial t) + \nabla \cdot (n\mathbf{v}_0) = 0. \tag{14.20}$$

Using the definition of the specific heat c_v and Eqs. (14.17) and (14.20), the energy equation (14.19) is written

$$\varrho c_v(D/Dt)(T) + p\,\nabla \cdot \mathbf{v}_0 + \nabla \cdot \mathbf{E} = P - L \tag{14.21}$$

where the heat flow is simply

$$\mathbf{E} = -\lambda \nabla T \tag{14.22}$$

instead of the expression (14.13).

When one assumes that no net diffusion flow occurs in the atmosphere ($\sum_i n_i \bar{\mathbf{V}}_i = 0$), it is necessary to introduce the contribution from the terms $\sum_i n_i \mathbf{F}_i \bar{\mathbf{V}}_i$ in the energy equation (14.19), whereas the other conservation equations are not modified. The only way to avoid the complications arising from diffusion transport is to assume $\bar{\mathbf{V}}_i = 0$ for every constituent. This means that the atmosphere should always be in diffusive equilibrium when the temperature changes. Such an assumption is actually questionable since it implies that the time necessary to reach diffusive equilibrium is negligible compared to the heat conduction time. This simplification has, however, been introduced by several authors [19–22] in order to estimate dynamical effects in the upper atmosphere.

Since several analyses of the atmospheric thermal structure are based on Eq. (14.21), the forms taken by (14.21) for different assumptions regarding the mass average velocity $\mathbf{v}_0$ will now be shown. First of all, when $\mathbf{v}_0$ is neglected the energy equation takes the rather simple form

$$\varrho c_v(\partial T/\partial t) + \nabla \cdot \mathbf{E} = P - L. \tag{14.23}$$

With a diffusive equilibrium distribution for the atmospheric constituents, it is possible to solve the one-dimensional form of (14.23) using an implicit numerical technique. The mass average velocity can, however, be taken into account by noting that, from Eqs. (14.17) and (14.20),

$$\nabla \cdot \mathbf{v}_0 = -\frac{1}{\varrho}\frac{D\varrho}{Dt} = -\frac{1}{n}\frac{Dn}{Dt}. \tag{14.24}$$

This relation implies that $Dm/Dt = 0$, i.e., the mean molecular mass m should not vary with height under steady state conditions. Such an effect is a direct consequence of the previous assumption $\bar{\mathbf{V}}_i = 0$. The energy equation (14.21) is now written

$$\varrho c_v \frac{DT}{Dt} - \frac{p}{n}\frac{Dn}{Dt} + \nabla \cdot \mathbf{E} = P - L. \tag{14.25}$$

Using the perfect gas law $p = nkT$ and an expression similar to (14.15) for the specific heat c_p at constant pressure, Eq. (14.25) becomes

$$\varrho c_p \frac{DT}{Dt} - \frac{Dp}{Dt} + \nabla \cdot \mathbf{E} = P - L. \tag{14.26}$$

This equation shows that the specific heat at constant pressure is indirectly introduced through the term $p\nabla \cdot \mathbf{v}_0$. The same equation is also obtained when the second term in (14.25) is $(p/\varrho)(D\varrho/Dt)$.

Heat production and loss processes are balanced by the three terms on the left-hand side of Eq. (14.25). These terms respectively correspond to the rate of change of internal energy following the motion of a fluid cell, to the adiabatic warming or cooling, and to the downward heat transport by conduction. The system of partial differential equations (14.17), (14.18), and (14.26) can in principle be solved for the dependent variables $\mathbf{v}_0$, ϱ, p, T.

Up to now the energy equation (14.26) has been numerically integrated for a one-dimensional case [19, 21]. Further simplifications are, however, made for the mass average velocity. In the one-dimensional case it has been assumed [19] that $Dp/Dt = 0$. This condition leads to the following expression for the vertical component w_0 of the velocity $\mathbf{v}_0$:

$$w_0 = T \int_{z_0}^{z} \frac{1}{T^2}\frac{\partial T}{\partial t}\, dz \tag{14.27}$$

where z_0 is the altitude of the lower boundary. When the horizontal flow effect on the vertical pressure gradient is neglected, i.e., when $\partial p/\partial z = -\varrho g$, the condition $Dp/Dt = 0$ leads to

$$w_0 = -H\frac{\partial}{\partial t}\int_{z_0}^{z} \frac{dz}{H} \tag{14.28}$$

where $H = kT/mg$ is the atmospheric scale height. For a constant mean molecular mass, $Dm/Dt = 0$, this expression is equivalent to (14.27), since

(14.28) can also be written

$$w_0 = H \int_{z_0}^{z} \frac{1}{H^2} \frac{\partial H}{\partial t} dz. \tag{14.29}$$

Such an expression has also been used in a study [28] of the dynamical response of the atmosphere to short-period heating through approximate analytical solutions of the heat conduction equation. Actually, it can be shown that (14.27) or (14.29) is an approximate solution of the vertical component of the continuity equation (14.24).

When horizontal movements are taken into account, the vertical velocity is not given by (14.29), since a contribution to the vertical movement arises from a lateral net inflow [29]. Such a horizontal mass divergence, characterized by a velocity of the order of 1 m sec^{-1}, can lead to an adiabatic warming comparable to the solar ultraviolet heating. As a consequence, atmospheric movements should be taken into account in the heat balance equation. The ideal situation would be, of course, a three-dimensional solution of the conservation equations leading simultaneously to the composition parameters and to a wind system.

14.3 Viscosity and Heat Conductivity

Practical applications of the conservation equations to the terrestrial atmosphere require a knowledge of the transport coefficients for the atmospheric components. The diffusion coefficients will be discussed in the next chapter. In the earth's upper atmosphere, atomic oxygen, molecular oxygen, and molecular nitrogen are the major neutral components responsible for the thermal and dynamical structure. Since helium and hydrogen become important constituents above 500 km altitude, their viscosity and heat conductivity are also analyzed in this section.

Theoretical expressions for the viscosity μ and the heat conductivity λ depend on the adopted interaction potential between the atoms and molecules [1, 2]. For smooth rigid elastic spherical molecules of diameter d_i, the viscosity μ_i is given by [1]

$$\mu_i = (5/16d_i^2)(km_iT/\pi)^{1/2} \tag{14.30}$$

where m_i is the molecular mass. This expression shows that the viscosity for a single gas is independent of the concentration. Experimental results [30] indicate, however, that the temperature dependence of the viscosity

is not exactly given by (14.30). For aeronomical applications, it is useful to represent the viscosity by an expression like

$$\mu_i = A_i T^s. \tag{14.31}$$

Several theoretical and semiempirical formulas have been developed for gaseous mixtures [31–33]. An accurate formula for the viscosity μ of a mixture of n constituents is [31]

$$\mu = \sum_{i=1}^{n} \frac{\mu_i}{(1/n_i) \sum_{j=1}^{n} n_j \phi_{ij}} \tag{14.32}$$

where μ_i is the viscosity of the single gas i with concentration n_i. A simple expression for ϕ_{ij} is

$$\phi_{ij} = \frac{[1 + (\mu_i/\mu_j)^{1/2}(m_j/m_i)^{1/4}]^2}{2\sqrt{2}\,[1 + (m_i/m_j)]^{1/2}}. \tag{14.33}$$

It should be noted that the viscosity of a mixture depends on the viscosities μ_i of the different species and of the relative abundances of these constituents. From the expression (14.33), it is seen that ϕ_{ij} is independent of the temperature when the different viscosities μ_i are characterized by the same temperature dependence. It is therefore worthwhile to attempt a fitting of the individual experimental data by expressions similar to (14.31) with a common temperature dependence.

Numerous measurements of N_2 and O_2 viscosity have been made and analyzed for different interaction potentials [34]. Between 200° and 2000°K, these data can be approximated by

$$\mu(O_2) = 4.03 \times 10^{-6} T^{0.69} \quad \text{gm cm}^{-1} \text{ sec}^{-1} \tag{14.34}$$

and

$$\mu(N_2) = 3.43 \times 10^{-6} T^{0.69} \quad \text{gm cm}^{-1} \text{ sec}^{-1} \tag{14.35}$$

with an accuracy better than 5%. From a measurement [35] of the O–O_2 diffusion coefficient, the viscosity of atomic oxygen is estimated by the following expression [36]:

$$\mu(O) = 3.90 \times 10^{-6} T^{0.69} \quad \text{gm cm}^{-1} \text{ sec}^{-1}. \tag{14.36}$$

This expression is in good agreement with the formula $3.44 \times 10^{-6} T^{0.71}$ obtained from theoretical computations [37] of the effective viscosity cross section of atomic oxygen.

The experimental results for helium [30] can be approximated by

$$\mu(\mathrm{He}) = 3.84 \times 10^{-6} T^{0.69} \quad \mathrm{gm\ cm^{-1}\ sec^{-1}} \tag{14.37}$$

between 200° and 2000°K. From theory [38, 39] it is possible to express the atomic hydrogen viscosity by

$$\mu(\mathrm{H}) = 1.22 \times 10^{-6} T^{0.69} \quad \mathrm{gm\ cm^{-1}\ sec^{-1}}. \tag{14.38}$$

between 200° and 2000°K.

Since the individual viscosities (14.34)–(14.38) have the same temperature dependence, it is clear that the expressions ϕ_{ij} given by (14.33) reduce to values independent of the temperature distribution in an atmospheric model. *Figure 14.1* gives the vertical distribution of the atmospheric viscosity computed with expression (14.32). The temperature distributions correspond respectively to the 750°K and to the 2000°K models given in Appendix B. The atmospheric viscosity does not vary to a great extent above 200 km altitude. The effect of atomic hydrogen can be seen above 500 km in the 750°K model and the decrease of μ above this altitude is due to the smaller numerical coefficient in (14.38).

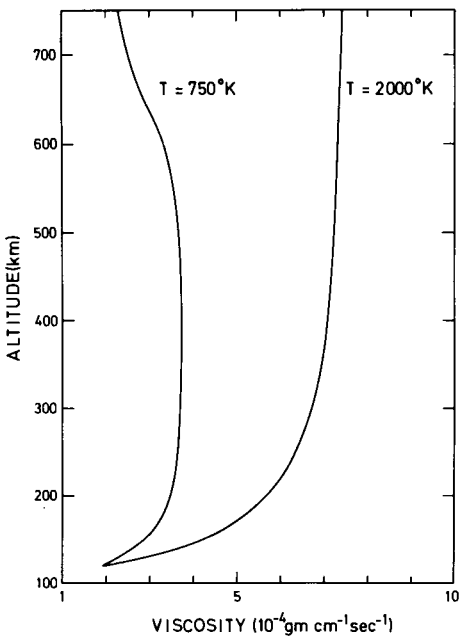


Fig. 14.1 Atmospheric viscosity coefficient for two models with 750°K and 2000°K thermopause temperature.

Instead of expression (14.32) it is possible to use a more simple formula, namely

$$\mu = AT^{0.69} \tag{14.39}$$

with

$$A = \sum A_i n_i / \sum n_i. \tag{14.40}$$

The coefficients A_i are given by the numerical factors of (14.34)–(14.38). The difference between the viscosity obtained from (14.32) and from (14.39) is less than 1% for the adopted atmospheric models.

The thermal conductivity coefficient λ_i of a gas i is connected with the viscosity coefficient μ_i by the relation

$$\lambda_i = f \mu_i c_{v_i} \tag{14.41}$$

where f is a number depending on the interaction potential. For monoatomic gases f is approximately equal to 2.5. With this value and a specific heat $c_{v_i} = 3k/2m_i$, the thermal conductivity becomes

$$\lambda_i = (15/4)(k/m_i)\mu_i. \tag{14.42}$$

Since this relation is valid for monoatomic gases, one obtains between 200° and 2000°K

$$\lambda(\mathrm{H}) = 379T^{0.69} \quad \text{erg cm}^{-1}\,\text{sec}^{-1}\,{}^{\circ}\text{K}^{-1}, \tag{14.43}$$

$$\lambda(\mathrm{He}) = 299T^{0.69} \quad \text{erg cm}^{-1}\,\text{sec}^{-1}\,{}^{\circ}\text{K}^{-1}, \tag{14.44}$$

and

$$\lambda(\mathrm{O}) = 75.9T^{0.69} \quad \text{erg cm}^{-1}\,\text{sec}^{-1}\,{}^{\circ}\text{K}^{-1}. \tag{14.45}$$

The diatomic molecules N_2 and O_2 are, however, also characterized by an internal energy which can affect the usual translational energy. Different expressions of f have been established [1, 2] to take the internal energy into account and an interaction between the translational and the internal energy is not excluded [38]. An analysis [36] of the experimental data [34, 39] leads to the conclusion that for O_2 and N_2 the thermal conductivity can be expressed by

$$\lambda(\mathrm{O_2}) = 39.3T^{0.69} + 2.55T - 92.7 \quad \text{erg cm}^{-1}\,\text{sec}^{-1}\,{}^{\circ}\text{K}^{-1} \tag{14.46}$$

and

$$\lambda(\mathrm{N_2}) = 38.2T^{0.69} + 1.90T + 51.4 \quad \text{erg cm}^{-1}\,\text{sec}^{-1}\,{}^{\circ}\text{K}^{-1}. \tag{14.47}$$

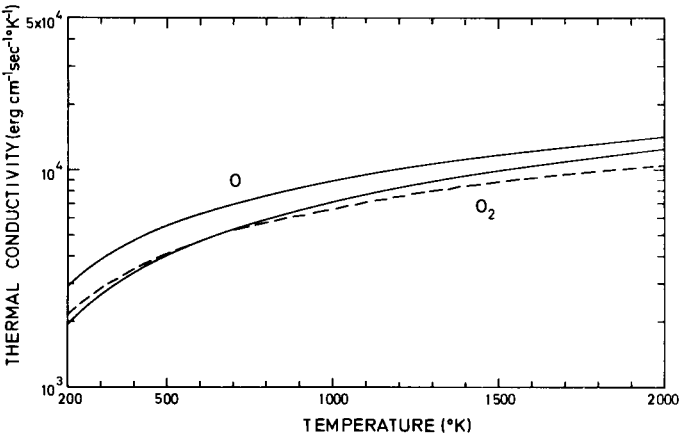


Fig. 14.2 Thermal conductivity of O and O_2 as a function of temperature. The dashed curve corresponds to the simplified expression for O_2 and N_2 (see Fig. 14.3); i.e., $\lambda(O_2) = 56T^{0.69}$.

This first term in (14.46) and (14.47) represents a pure translational effect, whereas the last two terms represent the transport due to internal energy. The thermal conductivities of O, O_2, N_2, H, and He are shown in *Figs. 14.2* and *14.3*. In order to have an expression of the same type for O_2 and

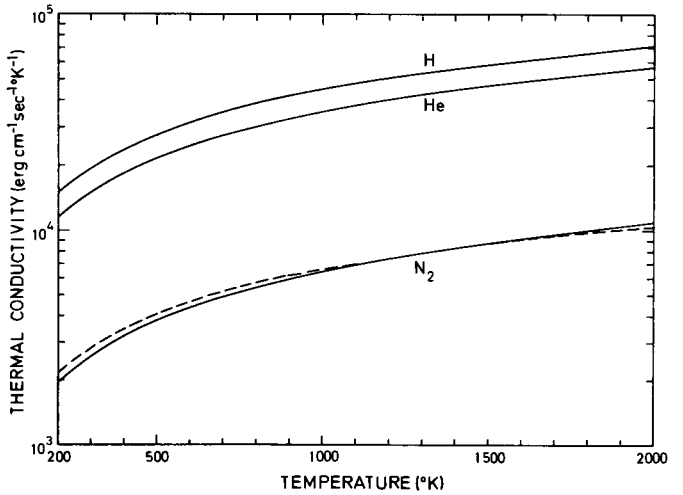


Fig. 14.3 Thermal conductivity of H, He, and N_2 as a function of temperature. The dashed curve corresponds to the simplified expression for N_2 and O_2 (see Fig. 14.2); i.e., $\lambda(N_2) = 56T^{0.69}$.

N_2 as for O, He, and H, the relation

$$\lambda(O_2, N_2) = 56T^{0.69} \quad \text{erg cm}^{-1}\,\text{sec}^{-1}\,{}^{\circ}\text{K}^{-1} \tag{14.48}$$

is represented by the dashed line on Figs. 14.2 and 14.3. It is clear that this approximation is sufficiently accurate for atmospheric applications.

The determination of the thermal conductivity of the atmospheric mixture is similar to that for the viscosity of a gaseous mixture. The relations (14.46) and (14.47) suggest an expression such as

$$\lambda = AT^{0.69} + BT + C. \tag{14.49}$$

The coefficient A is given by a relation analogous to (14.32) where μ_i is replaced by λ_i. For O_2 and N_2, only the first term of (14.46) and (14.47) is involved in the coefficient A. The coefficients B and C are given by [36]

$$B = \frac{1.9n(N_2)}{\sum_{i=1}^{5} \phi_{N_2 i} n_i} + \frac{2.55n(O_2)}{\sum_{i=1}^{5} \phi_{O_2 i} n_i} \tag{14.50}$$

and

$$C = \frac{51.4n(N_2)}{\sum_{i=1}^{5} \phi_{N_2 i} n_i} - \frac{92.7}{\sum_{i=1}^{5} \phi_{O_2 i} n_i} \tag{14.51}$$

where $\phi_{N_2 i}$ and $\phi_{O_2 i}$ are given in *Table 14.1.*

TABLE 14.1

COEFFICIENTS OF EQS. (14.50) AND (14.51)

	O ($i = 1$)	O_2 ($i = 2$)	N_2 ($i = 3$)	He ($i = 4$)	H ($i = 5$)
$\phi_{N_2 i}$:	0.771	0.975	1	0.301	0.195
$\phi_{O_2 i}$:	0.718	1	1.02	0.293	0.192

The thermal conductivity obtained from (14.49) is shown in *Fig. 14.4* for two atmospheric models. As for the viscosity, it is also possible to use an expression like (14.39). In this case, relation (14.48) should be adopted for O_2 and N_2. This procedure is rather good since it leads to an accuracy of the same order as for the approximation of $\lambda(O_2, N_2)$ shown in Figs. 14.2 and 14.3. Finally, it should be noted that the increase of the atmospheric

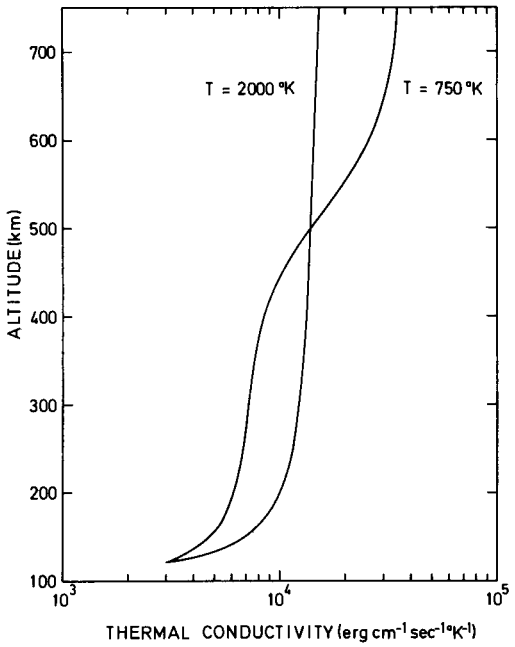


Fig. 14.4 Thermal conductivity of the atmosphere for two models with 750°K and 2000°K thermopause temperature.

thermal conductivity above 500 km (see Fig. 14.4) in the 750°K model is due to the presence of helium and atomic hydrogen. A similar effect appears also for higher temperatures, but at greater altitudes.

14.4 Energy Sources and Sinks

14.4.1 Atmospheric Heating

It has been shown in Chapter 5 that the slow decrease of the total density above 100 km is related to the diffusive separation of the atmospheric constituents and to the increase of temperature in the thermosphere. The gradients necessary to raise the temperature from above 200°K at 100 km to values ranging approximately from 600° to 2000°K at 500 km require the absorption of a certain amount of energy which is transformed into heat.

Since heat conduction is the principal transport process for thermal energy above 100 km, it follows from (14.22), (14.45), and (14.48) that

the vertical temperature gradient is given by

$$dT/dz = 13.2T^{-0.69}E \quad {}^{\circ}\mathrm{K\ km^{-1}} \tag{14.52}$$

in a pure atomic oxygen atmosphere and by

$$dT/dz = 17.8T^{-0.69}E \quad {}^{\circ}\mathrm{K\ km^{-1}} \tag{14.53}$$

in a molecular oxygen–nitrogen atmosphere. In (14.52) and (14.53) E is the absolute value of the downward heat flow expressed in erg $\mathrm{cm^{-2}\ sec^{-1}}$. Values of dT/dz for temperatures between 300° and 1000°K are given by expressions (5.25) and (5.26). It is clear from *Fig. 14.5* that a heat flow of the order of 1 erg $\mathrm{cm^{-2}\ sec^{-1}}$ can lead to temperature gradients between 35° and 10°K $\mathrm{km^{-1}}$ depending on the temperature of the altitude through which the heat is conducted. In a steady state, Eq. (14.23) shows that the divergence of the heat flow is simply the balance between the various heat sources and heat loss processes.

An important heat source during the day is solar ultraviolet radiation [13, 15, 16]. It has already been shown [16] how the temperature gradient in a sunlit atmosphere is related to the fraction of the absorbed solar ultraviolet energy. The heat production by ultraviolet absorption at wavelength λ is

$$P(\lambda, z) = \sum_i \varepsilon_i(\lambda, z)K_i(\lambda)n_i(z)E_{uv}(\lambda)e^{-\tau(\lambda,z)} \tag{14.54}$$

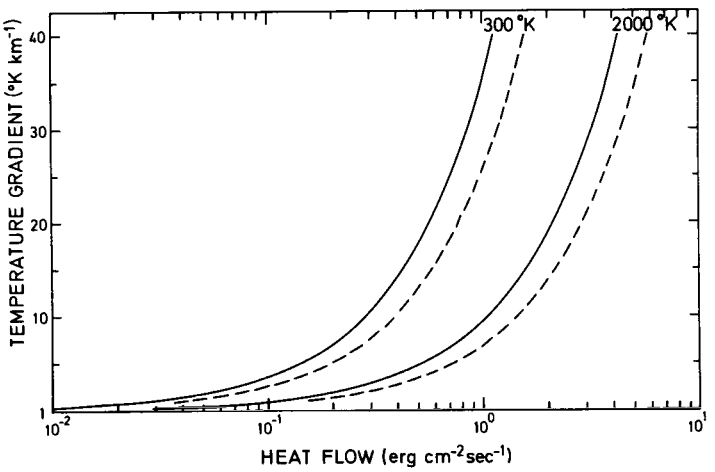


Fig. 14.5 Heat conduction flow as a function of the temperature gradient for two temperatures, namely 300°K and 2000°K. Solid curve, O_2, N_2 atmosphere; dashed curve, O atmosphere.

where $K_i(\lambda)$ is the absorption cross section of the constituent with concentration n_i. The summation is taken over the atmospheric constituents which can absorb the ultraviolet energy flux $E_{uv}(\lambda)$ available at the top of the atmosphere. The heat efficiency ε_i represents the fraction of the ultraviolet energy which is converted into heat. The optical depth $\tau(\lambda, z)$ is defined by

$$\tau(\lambda, z) = \sum_i \int_z^\infty n_i K_i(\lambda) F \, dz. \tag{14.55}$$

The optical depth factor F is equal to the secant of the zenith distance χ when $\chi < 75°$. For larger zenith angles, the earth's curvature has to be taken into account and F is given by the Chapman function for which several approximations are available [40, 41].

The total heat production over a certain wavelength interval is obtained by integrating (14.54) over λ. The relevant absorption cross sections have been discussed in Chapter 6 and data on the solar ultraviolet radiation are given in Chapter 7. The whole solar spectrum should be involved in the heat production, but Eq. (14.54) indicates that the maximum heat production occurs in the height range where the optical depth is practically unity. Therefore, the extent of the spectral region leading to a heat production is related to the optical absorption by the atmospheric region. For practical purposes, the solar spectrum can be divided into two parts: the Schumann–Runge continuum below 1750 Å and the wavelength region below Lyman β (1026 Å) down to 80 Å. Longer and shorter wavelengths need not be considered since they are not absorbed above 100 km altitude.

The absorption cross sections are relatively well known, with perhaps an exception for molecular nitrogen below 1000 Å. However, the major uncertainty in the heat production (14.54) results from the heat efficiencies ε_i which are poorly known compared to the other quantities. From the data described in Chapter 7, it is seen that the available energy flux in the Schumann–Runge continuum is of the order of 15 erg cm^{-2} sec^{-1}. Between 1026 and 80 Å the total ultraviolet flux can vary from 1.7 to 4.5 erg cm^{-2} sec^{-1} depending on the solar activity. In this interval the variation is, however, not the same for all wavelengths and a correlation with the solar decimetric flux can only lead to a rough approximation [42]. It is seen from Fig. 14.5 that a simultaneous knowledge of the solar flux and of the efficiencies is of fundamental importance for the values of the temperature gradients. Values for the efficiency between 0.1 and 1 have been used in the literature and it is very difficult to adopt an average value for the ε_i.

In the Schumann–Runge continuum, molecular oxygen is dissociated into $O(^3P) + O(^1D)$. The metastable ^1D state can undergo collisional deactivation to a ^3P state, releasing an energy of 1.967 eV in this process. Therefore, it has been assumed [43] that all the excess photon energy above the dissociation energy of O_2 into two normal atoms $O(^3P)$ is converted into heat. In such a way, the efficiency increases linearly with wavelength from 0.28 at 1750 Å to 0.59 at 1026 Å. In a more detailed analysis [44, 45], collisional deactivation of $O(^1D)$ and of $O_2(b\,^1\Sigma_g^+)$ as well as radiative emission of the excited states are taken into account. An average efficiency [45] of 0.3 is suggested between 1750 and 1350 Å. The altitude range for which heating occurs in the Schumann–Runge continuum depends on the absorption in this wavelength region. *Figure 14.6* shows the optical depth between 1750 and 1300 Å for three altitudes, namely 100, 120, and 150 km. It is clear that practically no heating occurs above 150 km, where the optical depth is less than 10^{-2}. The major absorption takes place below 120 km. *Figure 14.7*, corresponding to an average efficiency $\varepsilon = 0.3$, indicates that the maximum heat production in the Schumann–Runge continuum occurs around 100 km for an overhead sun.

Below the first ionization potential of O_2 at 1026 Å, the evaluation of the heat efficiency is even more complex since O, O_2, and N_2 simultaneously absorb strongly the solar radiation. The photoelectrons which are then produced can lead to secondary ionization and excitation. The ions, mole-

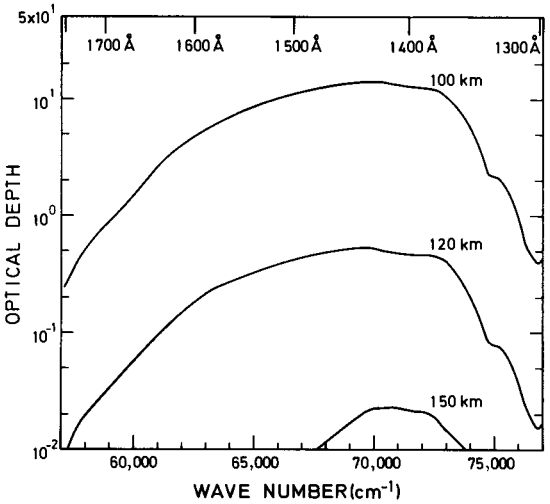


Fig. 14.6 Optical depth in the Schumann–Runge continuum for an overhead sun ($\chi = 0°$).

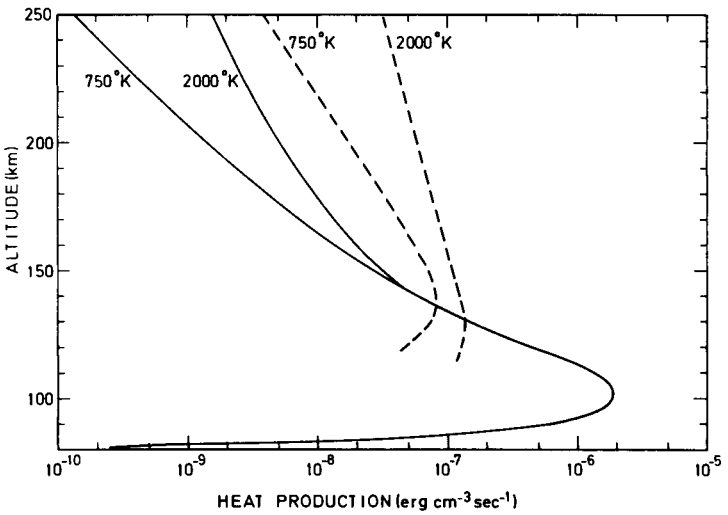


Fig. 14.7 Heat production as a function of altitude for 750° and 2000°K thermopause temperature. The heat efficiency is 0.3. Solid curve, Schumann–Runge continuum; dashed curve, $\lambda \leq 1026$ Å.

cules, and atoms react with each other and it is very difficult to estimate what fraction of the absorbed energy is converted into heat. Finally, one should keep in mind that for the whole spectrum the heat is not necessarily released at the height where the ultraviolet absorption occurs since mass transport cannot be neglected *a priori*. It is also possible that the heat efficiency depends on the solar cycle because the relative abundances of the different ions, atoms, and molecules are involved in the determination of the various ε_i.

The heat production below 1026 Å is shown in Fig. 14.7 for two atmospheric models corresponding respectively to thermopause temperatures of 750° and 2000°K. A constant efficiency $\varepsilon = 0.3$ has been used over the whole wavelength interval between 1026 and 80 Å. The 750°K curve corresponds to the minimum solar ultraviolet flux whereas the 2000°K one corresponds to the maximum values given in Chapter 7. Above 140 km, the ultraviolet heat production for $\lambda < 1026$ Å is higher than the production in the Schumann–Runge continuum. The heat energy available below 1026 Å is large enough to raise the thermopause temperature up to values between 600° and 2000°K. When the heating in the Schumann–Runge continuum is introduced, it is necessary to add a downward heat transport by turbulence [43] below 120 km since kinetic heat conduction alone would lead to extremely large temperature gradients around 100 km.

Other heat sources can play a role in the thermal structure of the upper atmosphere. The most important is probably the Joule heating [46, 47] arising from electric currents in the ionosphere. During geomagnetically disturbed periods, the global input of heat by Joule dissipation can be larger than that due to ultraviolet absorption. During the night [47] the Joule heating rate can exceed that in the day by a factor of two. Under such conditions, the whole thermosphere is perturbed and equatorward wind systems occur in the upper atmosphere. Even for geomagnetically quiet conditions, auroral Joule heating plays an important part in the dynamic and thermal structure of the thermosphere [48]. It is not excluded that auroral Joule heating alone is more important than the ultraviolet heating.

Joule heating in the regions outside the plasmasphere arises from localized auroral electric fields and the more widespread magnetospheric electric field responsible for plasma convection [48]. The magnitude of the convection field (10–100 mV m^{-1}) and its large geographic application (all regions poleward of 60° invariant latitude) are sufficient to imply a strong coupling between ion motions and the thermosphere, both in terms of direct heating and in the establishment of global wind patterns [49].

To illustrate the importance of the polar convection electric field, theoretical computations have been made of the rate of neutral gas heating when a 40 mV m^{-1} transverse electric field is applied to the summer polar cap in the form of a time quasi step-function ($E_\perp = 0$ for $t < 0$;

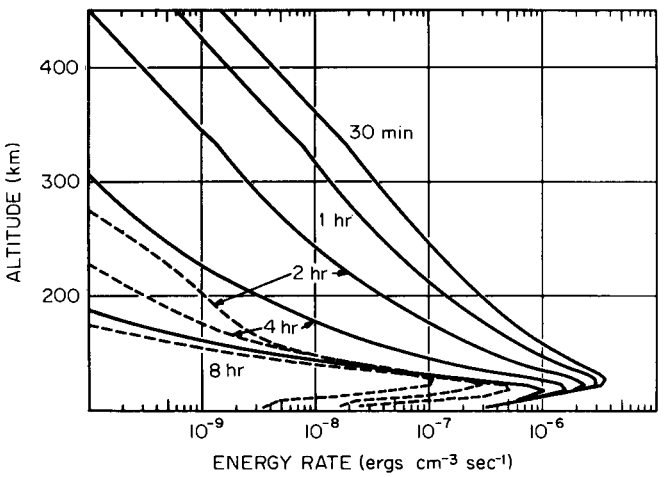


Fig. 14.8 Heat input to the polar thermosphere for a quasistep electric field of 40 mV m^{-1} at selected times after onset. The solid curves indicate the Joule heating rate while the dotted curves give the heating rate due to viscous dissipation.

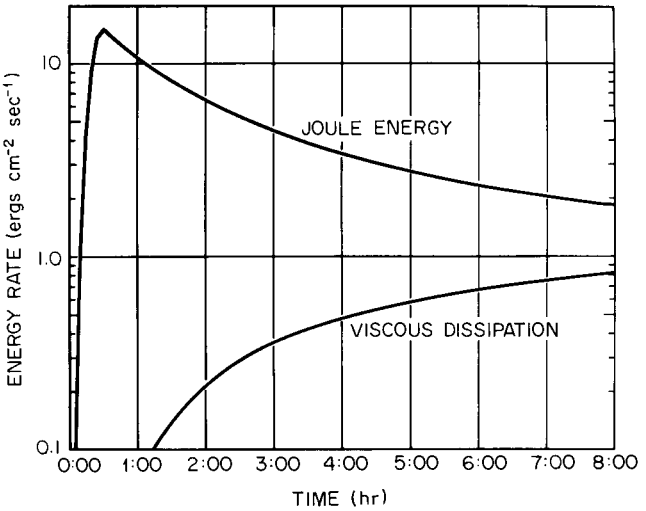


Fig. 14.9 The height integrated heating rates corresponding to Fig. 14.8 for a quasi-step function electric field.

$E_\perp = 40$ mV m^{-1} for $t > 1$ hr). The results, shown in *Figs. 14.8* and *14.9*, indicate that the combination of Joule and viscous dissipation is of the same order of magnitude as solar EUV heating (see Fig. 14.13). Equally important, however, is the horizontal momentum transferred to the thermosphere since the neutral wind velocities associated with the heating of Fig. 14.8 can reach 500 m sec^{-1} within 1 hr at 150 km altitude. Such results indicate the importance of the polar regions to the global energy and momentum budget of the thermosphere; i.e., the behavior of the thermosphere cannot be isolated from the terrestrial plasma environment.

It would be very interesting to include Joule heating in theoretical atmospheric models but more information is required for the external electric fields which drive the ions through the neutral gas. Since the heating occurs through ion-drag the relative speed between the ions and the neutral particles is a fundamental parameter in any evaluation of the Joule heating which is also accompanied by viscous heat dissipation through the thermosphere.

Tidal dissipation [25, 50] can also contribute to the heat input entering in the thermosphere from below. However, the excitation mechanisms of tides in the thermosphere have not yet been fully explored and it is extremely difficult to evaluate the effect of viscosity, thermal conduction, and hydromagnetic forces [51].

14.4.2 Atmospheric Cooling

If all the previous heat sources are really so effective as shown in the literature, heat sinks have to be introduced in the heat balance equation. The day and night airglow of the atmosphere in the infrared represents a possible heat loss. However, most of the infrared emissions of the earth's atmosphere arise below 100 km from minor constituents such as H_2O, OH, CO_2, and O_3. Since molecular nitrogen and oxygen do not possess a permanent dipole moment, they cannot emit in the infrared. Atomic oxygen can, however, radiate in the infrared at 63 and 147 μm. The ground state of neutral atomic oxygen is a triplet for which the $^3P_0$ and $^3P_1$ levels lie only 226.5 and 158.5 cm^{-1} above the ground level $^3P_2$. The excitation potentials, i.e., 0.028 and 0.020 eV are of the same order of magnitude as the kinetic energy of the atmospheric constituents. Since the collision frequency is high enough in the thermosphere, the following excitation mechanism has been suggested [13]:

$$X + O(^3P_J) \rightarrow X + O(^3P_{J'}) \tag{14.56}$$

where X is any atmospheric constituent. The quantum number J is equal to 2 or 1 and J' is equal to 1 or 0. If process (14.56) is fast enough, it is reasonable to assume that the oxygen atoms are distributed on the levels 0, 1, 2 according to a Boltzmann distribution. With the transition probabilities $A_{0-1} = 1.70 \times 10^{-5}$ sec^{-1} and $A_{12} = 8.95 \times 10^{-5}$ sec^{-1}, the emission rate at 63 μm and at 147 μm can be written

$$L_{63\mu m} = \frac{1.69 \times 10^{-18} n(O) e^{-228/T}}{1 + 0.6e^{-228/T} + 0.2e^{-326/T}} \quad \text{erg cm}^{-3} \text{ sec}^{-1} \tag{14.57}$$

and

$$L_{147\mu m} = \frac{4.59 \times 10^{-20} n(O) e^{-326/T}}{1 + 0.6e^{-228/T} + 0.2e^{-326/T}} \quad \text{erg cm}^{-3} \text{ sec}^{-1} \tag{14.58}$$

where $n(O)$ is the atomic oxygen concentration. These relations show that in a first approximation, the 147 μm emission is negligible compared to the 63 μm emission, which has been detected [52, 53] in the earth's atmosphere. The theoretical energy rate (erg sec^{-1}) emitted at 63 and 147 μm is given in *Table 14.2* as a function of the temperature. For temperatures between 300 and 2000°K, the infrared flux at 63 μm is given approximately by

$$F_{63\mu m}(z) \simeq 7 \times 10^{-19} \int_z^\infty n(O)\, dz \quad \text{erg cm}^{-2} \text{ sec}^{-1}. \tag{14.59}$$

TABLE 14.2

ENERGY[a] EMITTED AT 63 AND 147 μm

T (°K):	200	300	400	500	600	700	800	900	1000	1500	2000
$R_{63\mu m} \times 10^{19}$:	4.36	5.83	6.65	7.17	7.53	7.78	7.97	8.13	8.25	8.61	8.79
$R_{147\mu m} \times 10^{20}$:	0.73	1.15	1.42	1.61	1.75	1.85	1.93	1.99	2.04	2.20	2.29

[a] Values are in erg sec^{-1}.

The total contents of atomic oxygen above 120 and 150 km are respectively of the order of 1.8×10^{18} and 5.3×10^{17} cm^{-2} for a thermopause temperature of 750°K. These values lead to an infrared cooling rate of 1.3 erg cm^{-2} sec^{-1} at 120 km and 3.7×10^{-1} erg cm^{-2} sec^{-1} at 150 km, i.e., values of the same order of magnitude as the ultraviolet heating below 1026 Å.

The expressions (14.56) and (14.57) are, however, valid only for an optically thin atmosphere. For the 63 μm radiation, unit optical depth is reached around 100 km. It is therefore necessary to investigate the effect of the absorption of the 63 μm radiation and the effect of induced emission. This implies the solution of a radiative transfer equation [54–56]. At the top of the earth's atmosphere it can be assumed that the solar radiation at 63 μm has no effect, whereas at the lower boundary a blackbody emission corresponding more or less to the tropopause temperature can be introduced. The radiative transfer solution can be presented in a form such that [56]

$$L(z) = L(63\ \mu\text{m})[1 - X] \tag{14.60}$$

where X depends on the optical depth at 63 μm and $L(63\ \mu\text{m})$ is the optically thin expression (14.57). With a lower boundary emission corresponding to a blackbody at 190°K, the volume emission rate (14.60) is given in *Fig. 14.10* for an atmospheric model characterized by a 1000°K thermopause temperature. Below 100 km a small heating results from the lower boundary emission. Between 150 and 100 km, the cooling is always overestimated by expression (14.57). The departure from an optically thin layer is indicated in *Fig. 14.11*, where the reduction factor $1 - X$ is shown for two models corresponding to thermopause temperatures of 750° and 2000°K. A comparison between Figs. 14.10 and 14.7 indicates that the atomic oxygen infrared loss cannot be neglected in the thermal structure, despite the reduction resulting from reabsorption of the 63 μm radiation. The mean net flux is directed upwards [56] above 100 km and the infrared emission is lost into

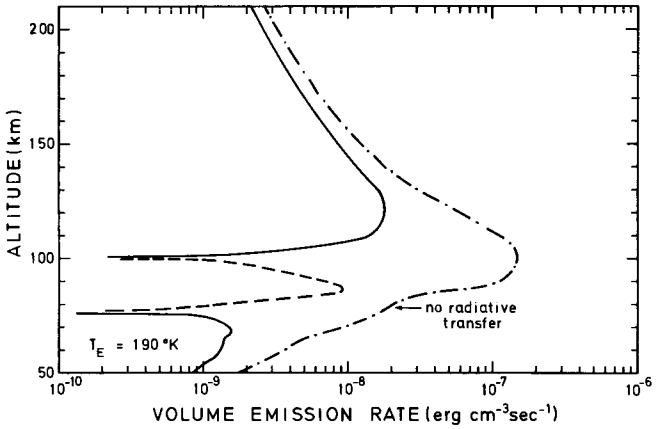


Fig. 14.10 Infrared volume emission rate at 63 μm in a 1000°K atmospheric model with an overhead sun. The radiative transfer curves are shown dashed for heating and solid for cooling.

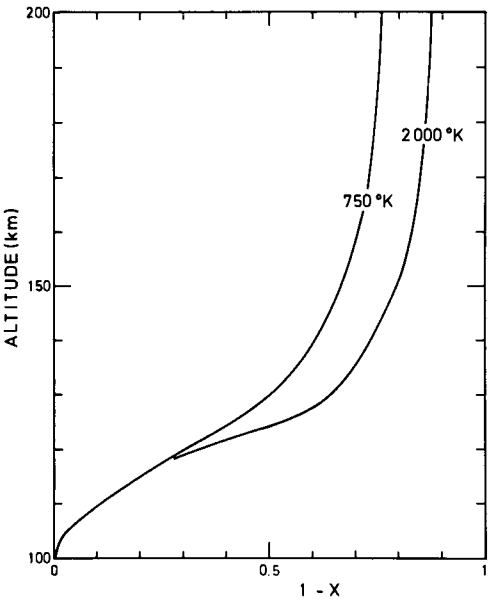


Fig. 14.11 Reduction factor resulting from radiative transfer. Values are for the atomic oxygen 63 μm emission.

the interplanetary space. At 300 km the mean upward infrared flux is between 0.1 and 0.2 erg cm^{-2} sec^{-1} for thermopause temperatures between 750° and 2000°K.

Since it appears that heat sources other than the ultraviolet heating should be introduced into the energy balance equation, it seems that the 63 μm infrared loss is not sufficient to avoid the buildup of very large temperature gradients and very high thermopause temperatures. Therefore, other loss mechanisms have to be discovered. The downward heat transport by turbulence [43] below 120 km offers an attractive possibility. It also cannot be excluded that a significant amount of the available energy is expended in the vibrational or rotational excitation of different neutral and ionic species or both [57]. Such a process is actually related to the heating efficiencies ε_i. Experimental determinations [58] indicate that in the 3–8 μm region a radiation flux between 1 and 10 erg cm^{-2} sec^{-1} sr^{-1} occurs above 90 km even under geomagnetically quiet conditions. Various excitation mechanisms [59] including electron impact and the effect of an electric field have been discussed in relation with this infrared emission.

It seems that the problem of the various heat sources and sinks is far from being completely solved. The importance of the different effects should emerge from a complete solution of the heat balance equation. At present there are, unfortunately, no available theoretical models which take all these effects into account.

14.5 Working Models

It is impossible at present to build atmospheric models which are able to represent in detail all the correct experimental facts. Two fundamental reasons can be advocated: First, the existent numerical techniques are not yet developed enough to perform the integration of the three-dimensional conservation equation. Second, all the physical processes responsible for the structure of the upper atmosphere are not yet completely understood. It is, however, necessary to have models which can be used as a guide for aeronomical investigations.

Using the assumption of diffusive equilibrium above a certain height, it is very easy to compute the concentration, pressure, and density when a vertical temperature distribution is adopted and when the partial concentrations are known at the lower boundary. An empirical expression for the temperature distribution is, for example [60],

$$T(z) = T_\infty + (T_0 - T_\infty) \exp(sz) \tag{14.61}$$

where T_0 and T_∞ are respectively the temperatures at the lower boundary and at the thermopause. The parameter s determines the shape of the curve. In recent models [61], the temperature profiles are given by polynomials and by an inverse tangent function. The success of this type of model results from its ability to help in the interpretation of satellite drag data. The choice of a specific model is made according to the thermopause temperature, which can be given by an empirical function [61, 62] of the solar decimetric flux at 10.7 cm or at 8 cm. For geomagnetically quiet conditions ($K_p = 0$) the nighttime minimum of the global temperature is given on a specific day by [61]

$$T_N = 379 + 3.24\bar{S}_{10.7} + 1.3(S_{10.7} - \bar{S}_{10.7}) \tag{14.62}$$

where $S_{10.7}$ is the daily solar radioelectric flux at 10.7 cm expressed in units of 10^{-22} W m^{-2} Hz^{-1}. The $S_{10.7}$ value should be the value for the previous day since temperature variations occur with a time lag [63] of the order of 1 day with respect to the solar flux. $\bar{S}_{10.7}$ is a smoothed solar flux over a period of 27 days.

The daytime maximum temperature is given by

$$T_D = 1.3T_N. \tag{14.63}$$

More complex formulas [61] are available to evaluate the temperature at a specific geographic location as a function of local time. When geomagnetic activity cannot be neglected, an increase of the temperature can be computed [64] as a function of the planetary geomagnetic index K_p.

Before describing the physical parameters given in the working models it is, however, interesting to discuss a time-dependent case. In the widely used one-dimensional time-dependent models [19, 20, 65] a hypothetical "second heat source" has been introduced for two reasons. First, without this "second heat source" the maximum temperature occurs around 17 hr local time and the amplitude of the diurnal variation is of the order of 2.5. With an arbitrarily adopted second heat source the diurnal temperature fluctuation amplitude was reduced to 1.5. The additional heat source was taken to have a maximum at 0900 LT with a total flux of 1 erg cm^{-2} sec^{-1} and a value of the order of 0.25 erg cm^{-2} sec^{-1} during the night.

Numerical integration of Eq. (14.23) by an implicit technique [66] leads to an amplitude of the order of 2 for the diurnal variation of the temperature when ultraviolet heating and infrared cooling are introduced. Since all the production and loss mechanisms are not exactly known, an arbitrary

production or loss can be introduced by

$$P_c = C \exp\left[-\frac{1}{2}\left(\frac{z - z_0}{s}\right)^2\right] \tag{14.64}$$

where z_0 is the altitude of the maximum value for P_c. The constant C is related to the height integrated flux E_c by

$$E_c = (2\pi)^{1/2} C s. \tag{14.65}$$

Adopting $s = 50$ km, one obtains $C = 8 \times 10^{-10}$ erg cm^{-3} sec^{-1} for an integrated flux $E_c = 0.1$ erg cm^{-2} sec^{-1}. When the peak of this production ($C > 0$) or loss ($C < 0$) is located at $z_0 = 350$ km, integration of (14.23) leads to the temperature variation shown in *Fig. 14.12*. The computation has been made for a geographic latitude of 30°N and a solar declination of 0°. These parameters enter in the ultraviolet heat production (14.54) through the optical depth factor F, which is a function of local time. The height integrated production or loss (14.65) is also shown on Fig. 14.12 as a function of local time. The total loss during the day is approximately

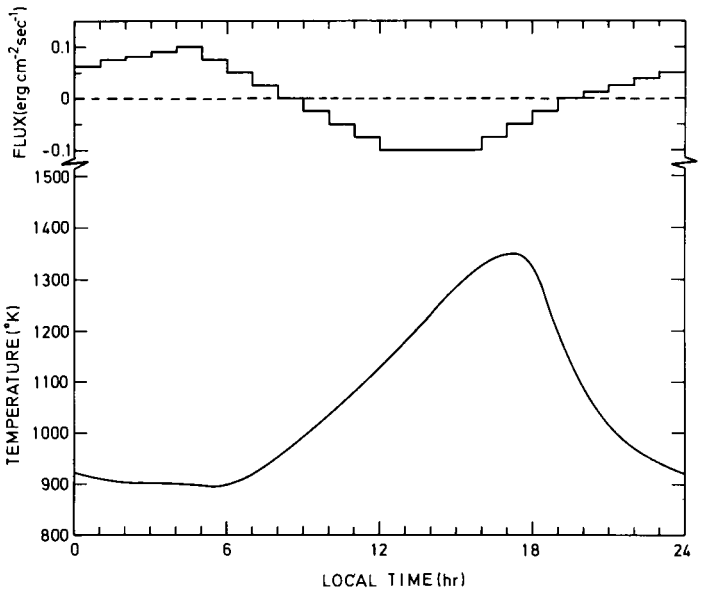


Fig. 14.12 Time dependent thermopause temperature showing the effect of an additional heat source or loss. The upper part of the graph shows the height integrated flux which is maximum at 350 km. Values are for a solar declination of 0° and a latitude of 30°.

equal to the total heat input and the absolute value of E_c never exceeds 0.1 erg cm^{-2} sec^{-1} during 1 hr. The diurnal amplitude of the temperature is equal to 1.5 with the additional production or loss P_c whereas it reaches 2 with the ultraviolet production and the infrared loss. A comparison between P_c and the ultraviolet production at 1200 LT is given in *Fig. 14.13*. The dashed curve corresponds to an integrated flux of 0.1 erg cm^{-2} sec^{-1} and the maximum ultraviolet heating flux is 1.7 erg cm^{-2} sec^{-1} at 1200 LT. It is clear that even a small additional source or sink can strongly influence the amplitude of the diurnal variation. Therefore, further studies are necessary to investigate all physical processes which could lead to additional production and/or loss terms in the heat conduction equation.

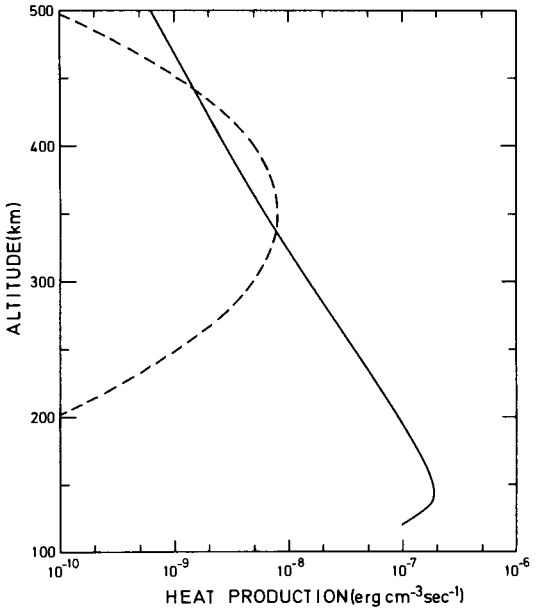


Fig. 14.13 Comparison between the UV heating at 1200 LT and the additional source.

The atmospheric models given in Appendix B, Tables B1–B11, are obtained in a slightly different way. They are numerical solutions of the heat conduction equation (14.23) where the heat input is the solar ultraviolet radiation below 1026 Å and the heat loss is the 63 μm radiation computed for the optically thin atmosphere. In this way the infrared loss is slightly overestimated between 120 and 150 km. The largest temperature gradients are probably still too high since turbulent conduction has been neglected.

No local time or latitude is given for the model since a one-dimensional solution of (14.23) cannot lead to a final description of the upper atmosphere. Table B7–B11 in Appendix B give the vertical temperature distributions for thermopause temperatures ranging from 600° to 2000°K with 50°K steps. The other atmospheric parameters are not given for these models since they can be easily computed from the temperature distributions. In these models the downward heat conduction flow ranges from 0.35 to 1.2 erg cm^{-2} sec^{-1} according to the thermopause temperature. The working models do not refer to a specific geographic location or to a specific local time. The boundary conditions have been taken constant at 120 km and correspond to the data given in Table 4.3d. The concentrations O, O_2, and N_2 are computed in diffusive equilibrium. The distributions of helium and hydrogen are described in the next chapter. The total density ϱ and the total concentration n are used to compute the mean molecular mass $m = \varrho/n$ which leads then to the atmospheric scale height

$$H = kT/mg \tag{14.66}$$

where $k = 1.38 \times 10^{-16}$ erg $°K^{-1}$ and g is the acceleration of gravity. Since the atmospheric scale height varies strongly with altitude, the gradient

$$\beta = dH/dz \tag{14.67}$$

has also been computed. When the temperature becomes constant with height above the thermopause, an analytical expression is available for β under diffusive equilibrium conditions. The gradient β goes successively through two maxima [67, 68] at the altitudes where $\varrho(\mathrm{He}) = \varrho(\mathrm{O})$ and $\varrho(\mathrm{H}) = \varrho(\mathrm{He})$.

Using the relations $p = nkT$ and $\varrho = nm$, the pressure and density variations may be written

$$\frac{dp}{p} = \frac{dn}{n} + \frac{dT}{T} = -\frac{dz}{H} \tag{14.68}$$

and

$$\frac{d\varrho}{\varrho} = \frac{dn}{n} + \frac{dm}{m} = -\frac{dz}{H_\varrho}. \tag{14.69}$$

From (14.68) and (14.69), the relation between the pressure scale height H and the density scale height H_ϱ becomes

$$H_\varrho = \frac{H}{1 + \beta - [2H/(R + z)]} \tag{14.70}$$

where R is the earth's radius. The density scale height is never greater than H and in the heterosphere H/H_ϱ varies and can reach values [68] of the order of 1.5. The density scale height H_ϱ and its gradient $\beta_\varrho = dH_\varrho/dz$ is extensively used in satellite drag data analysis [69]. It is important to note that β_ϱ is not less than β in the thermosphere. Above the thermopause β_ϱ can even become greater than the pressure scale height gradient. This can be seen by taking the derivative of (14.70) is which β is not constant.

The parameters which were briefly described are given in the tables of Appendix B for working models characterized by the following thermopause temperatures: 750°, 1000°, 1250°, 1500°, 1750°, and 2000°K.

REFERENCES

1. S. Chapman and T. G. Cowling, *The Mathematical Theory of Non-Uniform Gases*, 3rd ed. Cambridge Univ. Press, London and New York, 1970.
2. J. O. Hirschfelder, C. F. Curtiss, and R. B. Bird, *Molecular Theory of Gases and Liquids*. Wiley, New York, 1954.
3. L. D. Landau and E. M. Lifshitz, *Fluid Mechanics*. Pergamon, Oxford, 1959.
4. M. N. Izakov, *Space Sci. Rev.* **12**, 261 (1971).
5. M. P. Friedman, *Res. Space Sci., Smith. Inst. Astrophys. Obs., Spec. Rep.* **250** (1967).
6. L. G. Jacchia, in *CIRA* 1965, pp. 293–313. North-Holland Publ., Amsterdam, 1965.
7. W. Priester, M. Roemer, and H. Volland, *Space Sci. Rev.* **6**, 707 (1967).
8. H. Carru, M. Petit, and P. Waldteufel, *Planet. Space Sci.* **15**, 944 (1967).
9. J. S. Nisbet, *J. Atmos. Sci.* **24**, 586 (1967).
10. J. P. Mc Clure, *J. Geophys. Res.* **74**, 279 (1969).
11. P. Bauer, P. Waldteufel, and D. Alcayde, *J. Geophys. Res.* **75**, 4825 (1970).
12. L. Spitzer, Jr., in *The Atmospheres of the Earth and Planets* (G. P. Kuiper, ed.), pp. 213–249. Univ. of Chicago Press, Chicago, Illinois, 1949.
13. D. R. Bates, *Proc. Phys. Soc.* **64B**, 805 (1951).
14. A. N. Lowan, *J. Geophys. Res.* **60**, 421 (1955).
15. F. S. Johnson, *J. Geophys. Res.* **61**, 71 (1956).
16. M. Nicolet, *Planet. Space Sci.* **5**, 1 (1961).
17. D. C. Hunt and T. E. Van Zandt, *J. Geophys. Res.* **66**, 1673 (1961).
18. C. H. Cummack, *J. Atmos. Terr. Phys.* **24**, 691 (1962).
19. I. Harris and W. Priester, *J. Atmos. Sci.* **19**, 286 (1962).
20. I. Harris and W. Priester, *J. Geophys. Res.* **67**, 4585 (1962).
21. C. P. Lagos and J. R. Mahoney, *J. Atmos. Sci.* **24**, 88 (1967).
22. R. E. Dickinson, C. P. Lagos, and R. E. Newell, *J. Geophys. Res.* **73**, 4299, 6867 (1968).
23. H. Volland, *Planet. Space Sci.* **17**, 1581 (1969).
24. H.Volland, *Planet. Space Sci.* **17**, 1709 (1969).
25. H. Volland and H. G. Mayr, *Ann. Géophys.* **26**, 907 (1970).
26. H. Kohl and J. W. King, *J. Atmos. Terr. Phys.* **29**, 1045 (1967).
27. G. J. Bailey, R. J. Moffett, and H. Rishbeth, *J. Atmos. Terr. Phys.* **31**, 253 (1969).
28. G. E. Thomas and B. K. Ching, *J. Geophys. Res.* **74**, 1796 (1969).

29. R. E. Dickinson and J. E. Geisler, *Mon. Weather Rev.* **96**, 606 (1969).
30. F. G. Keyes, in *American Institute of Physics Handbook.* (J. Kestin, ed.), Sect. 2, p. 205. McGraw Hill, New York, 1957.
31. C. R. Wilke, *J. Chem. Phys.* **18**, 517 (1950).
32. T. G. Cowling, P. Gray, and P. G. Wright, *Proc. Roy. Soc.* **276A**, 69 (1963).
33. S. Mathur and S. C. Saxena, *Brit. J. Appl. Phys.* **16**, 389 (1965).
34. G. E. Childs and H. J. M. Hanley, NBS Tech. Note 350 (1966).
35. R. E. Walker, *J. Chem. Phys.* **34**, 2196 (1961).
36. L. A. Mata, *Aeronomica Acta* A59, Inst. Aéronomie Spatiale, Bruxelles (1969).
37. A. Dalgarno and F. J. Smith, *Planet. Space Sci.* **9**, 1 (1962).
38. S. I. Sandler, *Phys. Fluids* **11**, 2549 (1968).
39. S. C. Saxena, G. P. Gupta, and V. K. Saxena, in *Thermal Conductivity* (C. J. Ho and R. E. Taylor, eds.), pp. 125–139. Plenum Press, New York, 1969.
40. W. Swider, Jr., *Planet. Space Sci.* **12**, 761 (1964).
41. J. A. Fitzmaurice, *Appl. Opt.* **3**, 640 (1964).
42. L. A. Hall and H. E. Hinteregger, *J. Geophys. Res.* **75**, 6959 (1970).
43. F. S. Johnson and B. Gottlieb, *Planet. Space Sci.* **18**, 1707 (1970).
44. M. N. Izakov, *Geomagn. Aeron.* **10**, 279 (1970).
45. M. N. Izakov and S. K. Morozov, *Geomagn. Aeron.* **10**, 495 (1970).
46. K. D. Cole, *Aust. J. Phys.* **15**, 223 (1962).
47. K. D. Cole, *Planet. Space Sci.* **19**, 59 (1971); **20**, 2205 (1972).
48. P. M. Banks, *Space Res.* **12**, 1051 (1972).
49. J. A. Fedder and P. M. Banks, *J. Geophys. Res.* **77**, 2328 (1972).
50. R. S. Lindzen and D. Blake, *J. Geophys. Res.* **75**, 6868 (1970).
51. S. Kato, *Space Sci. Rev.* **12**, 421 (1971).
52. J. R. Houck and M. Harwit, *Science* **164**, 1271 (1969).
53. P. D. Feldman and D. P. Mc Nutt, *J. Geophys. Res.* **74**, 4791 (1969).
54. R. W. Stewart, *J. Atmos. Sci.* **25**, 744 (1968).
55. R. A. Craig and J. C. Gille, *J. Atmos. Sci.* **26**, 205, 790 (1969).
56. G. Kockarts and W. Peetermans, *Planet. Space Sci.* **18**, 271 (1970).
57. E. Bauer, R. Kummler, and M. H. Bortner, *Appl. Opt.* **10**, 1861 (1971).
58. M. N. Markov, *Cosmic Res.* **8**, 829 (1970).
59. B. F. Gordiets, M. N. Markov, and L. A. Shelepin, *Cosmic Res.* **8**, 398 (1970).
60. D. R. Bates, *Proc. Roy. Soc.* **253A**, 451 (1959).
61. L. G. Jacchia, *Res. Space Sci., Smith. Inst. Astrophys. Obs., Spec. Rep.* **332** (1971).
62. M. Nicolet, *J. Geophys. Res.* **68**, 6121 (1963).
63. M. Roemer, *Space Res.* **7**, 1091 (1967).
64. M. Roemer, *Space Res.* **11**, 965 (1971).
65. I. Harris and W. Priester, *J. Atmos. Sci.* **22**, 3 (1965).
66. R. D. Richtmyer and K. W. Morton, *Difference Methods for Initial-Value Problems*, 2nd ed. Wiley (Interscience), New York, 1967.
67. G. Kockarts, *Acad. Roy. Belg., Bull. Cl. Sci.* **49**, 1281 (1963).
68. G. Kockarts, *Ann. Géophys.* **22**, 161 (1966).
69. D. G. King-Hele, *Theory of Satellite Orbits in an Atmosphere.* Butterworth, London, 1964.

CHAPTER 15

Effects of Diffusion in the Heterosphere

15.1 Introduction

As mentioned previously, the relatively slow decrease of atmospheric density above 100 km altitude is reflected in the increase of the scale height $H = kT/mg$. When the hydrostatic equation is valid (see Chapter 3) such an increase can be produced through increases in neutral gas temperature or through a decrease in the mean molecular mass arising from diffusive separation of atmospheric constituents or through both effects.

The importance of molecular diffusion in determining the structure of the upper atmosphere was predicted from theory [1] and later confirmed by the first rocket observation [2] of the distribution of molecular oxygen to altitudes of 180 km. In addition, mass spectrometer measurements [3, 4] of argon and helium have shown that diffusive separation begins to be important near 110 km. Finally, the discovery of a Lyman α nightglow [5] indicated that atomic hydrogen must become an important atmospheric constituent at great altitudes. From these results it can be correctly concluded that diffusion is an important process in the atmosphere, both for major and minor constituents.

In this chapter the general diffusion equation is discussed with application to the minor constituents of the lower thermosphere. It is shown that minor constituents having atomic masses less than the mean atmospheric mass are subject to a diffusion condition which limits the maximum upward flow rate. This maximal condition can be used to estimate the effects of transport on the light gases.

When atmospheric constituents of low mass reach a certain height (called the critical level) where collisions become infrequent, a fraction of the particles, by virtue of their thermal kinetic energy, can escape from the earth's gravitational field. The net escape flux depends upon the temperature of the atmosphere and the supply of atoms available from below. Since there exists an ultimate limit to the atmospheric diffusive flow, the vertical distributions of the light gases are subject not only to the ballistic conditions for escape, but also to the diffusive properties of the neutral atmosphere.

The application of these ideas is given here for hydrogen, deuterium and helium distributions in the atmosphere. It is shown that the transport of these light constituents is such that even with concentration mixing ratios of 2×10^{-6} and 5×10^{-6} at 100 km for hydrogen and helium, respectively, these gases become the major constituents of the upper heterosphere and exosphere.

15.2 Diffusion Equation

For a binary mixture the general diffusion equation giving the relative diffusion velocity $\mathbf{v} = \mathbf{v}_1 - \mathbf{v}_2$ of gas 1 with respect to gas 2, can be written as [6]

$$\mathbf{v} = -D_{12}\left[\frac{n^2}{n_1 n_2}\nabla\left(\frac{n_1}{n}\right) + \frac{m_2 - m_1}{m}\nabla(\ln p) + \alpha_T \nabla(\ln T) - \frac{m_1 m_2}{mkT}(\mathbf{F}_1 - \mathbf{F}_2)\right] \tag{15.1}$$

where n_1, n_2 are respectively the concentration of particles 1 and 2, $n = n_1 + n_2$ is the total concentration of the binary mixture, T is the absolute neutral gas temperature, $p = p_1 + p_2$ is the total pressure, k is the Boltzmann constant, m_1, m_2 are the masses of particles 1 and 2, $m = (n_1 m_1 + n_2 m_2)/(n_1 + n_2)$ is the mean molecular mass, $\mathbf{F}_1$, $\mathbf{F}_2$ are the accelerations of particles 1 and 2 due to external forces, D_{12} is the molecular diffusion coefficient of gas 1 in gas 2, and α_T is the thermal diffusion factor.

In place of the thermal diffusion factor in (15.1) it is also possible to use the thermal diffusion ratio k_T or the thermal diffusion coefficient D_T defined by

$$k_T = (n_1 n_2/n^2)\alpha_T \tag{15.2}$$

and

$$D_T = k_T D_{12}. \tag{15.3}$$

While D_T and D_{12} retain physical dimensions, α_T and k_T are dimensionless quantities.

When neutral gases diffuse in a gravitational field, the term $\mathbf{F}_1 - \mathbf{F}_2$ is equal to zero. This term is, however, very important when ions and electrons diffuse in the presence of an electric or a magnetic field or both.

The vertical component of Eq. (15.1), when applied to neutral gases, can be written as

$$w_1 - w_2 = -D_{12}\left[\frac{n^2}{n_1 n_2}\frac{\partial(n_1/n)}{\partial z} + \frac{m_2 - m_1}{m}\frac{1}{p}\frac{\partial p}{\partial z} + \frac{\alpha_T}{T}\frac{\partial T}{\partial z}\right]. \tag{15.4}$$

This equation shows that diffusion is caused by concentration gradients, by pressure gradients, and by temperature gradients. If it is assumed that there is no net flow through an elementary surface at height z, i.e., if

$$n_1 w_1 + n_2 w_2 = 0, \tag{15.5}$$

then Eq. (15.4) can be transformed into

$$w_1 = -D_{12}\left[\frac{1}{n_1}\frac{\partial n_1}{\partial z} - \frac{1}{n}\frac{\partial n}{\partial z} + \frac{(m_2 - m_1)}{mn}\frac{n_2}{p}\frac{\partial p}{\partial z} + \alpha_T \frac{n_2}{n}\frac{1}{T}\frac{\partial T}{\partial z}\right]. \tag{15.6}$$

With the hydrostatic equation and the perfect gas law, Eq. (15.6) can be written for time-independent conditions as

$$w_1 = -D_{12}\left[\frac{1}{n_1}\frac{dn_1}{dz} + \frac{1}{H_1} + \left(1 + \alpha_T \frac{n_2}{n}\right)\frac{1}{T}\frac{dT}{dz}\right] \tag{15.7}$$

where $H_1 = kT/m_1 g$.

When component 1 is a minor constituent, (15.7) becomes

$$w_1 = -D_{12}\left[\frac{1}{n_1}\frac{dn_1}{dz} + \frac{1}{H_1} + (1 + \alpha_T)\frac{1}{T}\frac{dT}{dz}\right]. \tag{15.8}$$

For a multicomponent gas, the diffusion velocity w_i for the ith minor constituent can be written [6, 7] as

$$w_i = -D_i\left[\frac{1}{n_i}\frac{dn_i}{dz} + \frac{1}{H_i} + \frac{1}{T}\frac{dT}{dz}\right] \tag{15.9}$$

with an average diffusion coefficient D_i given by

$$1/D_i = \sum_{j \neq i} (n_j / n D_{ij}) \tag{15.10}$$

where $n = \sum n_j$ is the total concentration. In the past, thermal diffusion has been introduced [7] into Eq. (15.9) through analogy with (15.8) and in this way (15.9) becomes formally identical to (15.8) if $D_{12} = D_i$. It should be noted that the expression for the diffusion velocity of a major component is more complicated since the diffusion coefficient D_i or D_{12} and the thermal diffusion factor α_T depend strongly on the concentration of the major constituent.

Equation (15.8) does not represent all the possibilities giving rise to a vertical transport. Molecular diffusion tends to separate the atmospheric constituents according to their mass. Turbulence tends to mix the atmospheric constituents and in this way prevents any separation by molecular diffusion. Whereas turbulence mixing prevails in the homosphere, diffusive separation occurs in the heterosphere. There is, however, a region around 100 km where both processes are of the same order of magnitude. For this reason, Eq. (15.8) has to be modified. The vertical eddy diffusion velocity w_E for the constituent n_1 can be defined [8] by

$$w_E = \frac{-K[d(n_1/n)/dz]}{(n_1/n)} \tag{15.11}$$

where K is the eddy diffusion coefficient. Using the general relation

$$\frac{dp}{p} = \frac{dn}{n} + \frac{dT}{T} = -\frac{dz}{H} \tag{15.12}$$

where H is the atmospheric scale height, Eq. (15.11) becomes

$$w_E = -K\left[\frac{1}{n_1}\frac{dn_1}{dz} + \frac{1}{H} + \frac{1}{T}\frac{dT}{dz}\right]. \tag{15.13}$$

It is clear from (15.13) that a mixing distribution for n_1 leads to a zero eddy diffusion velocity. Using (15.8) and (15.13) the total transport velocity $w = w_1 + w_E$ can now be written in the form

$$\begin{aligned} w = &-D_{12}\left[\frac{1}{n_1}\frac{dn_1}{dz} + \frac{1}{H_1} + (1 + \alpha_T)\frac{1}{T}\frac{dT}{dz}\right] \\ &- K\left[\frac{1}{n_1}\frac{dn_1}{dz} + \frac{1}{H} + \frac{1}{T}\frac{dT}{dz}\right]. \end{aligned} \tag{15.14}$$

Diffusive equilibrium ($w_1 = 0$) leads to

$$n_1(z)/n_1(z_0) = (T_0/T)^{1+\alpha_T} \exp\left(-\int_{z_0}^{z} dz/H_1\right) \tag{15.15}$$

where $n_1(z_0)$ is the concentration at a height z_0 characterized by a temperature T_0.

Perfect mixing ($w_E = 0$) leads to

$$n_1(z)/n_1(z_0) = (T_0/T) \exp\left(-\int_{z_0}^{z} dz/H\right) \tag{15.16}$$

which is identical to (3.3). Usually, (15.16) is used in the homosphere and (15.15) is used above a certain altitude which is sometimes called the *turbopause*, i.e., the level above which turbulence is no longer effective [9]. Actually, there should be a smooth transition from perfect mixing to diffusive equilibrium. But the use of (15.16) in the homosphere and (15.15) above a level where diffusive equilibrium prevails, introduces a discontinuity in the concentration. This discontinuity is most important when the mass m_1 is very different from the mean molecular mass. The general equation (15.14) shows, however, that an equilibrium distribution ($w = 0$) can exist between mixing and diffusive equilibrium. With $\Lambda \equiv K/D_{12}$ and $w = 0$, integration of (15.14) gives the equilibrium distribution:

$$\frac{n_{eq}(z)}{n_1(z_0)} = \left(\frac{T_0}{T}\right) \exp -\left[\int_{z_0}^{z} \left(\frac{1}{H_1} + \frac{\Lambda}{H}\right)(1+\Lambda)^{-1}\, dz + \int_{z_0}^{z} \alpha_T (1+\Lambda)^{-1} \frac{dT}{T}\right]. \tag{15.17}$$

If $\Lambda = 0$, i.e., there is no turbulence, (15.17) reduces to the diffusive equilibrium solution (15.15). If $\Lambda = \infty$, i.e., no molecular diffusion, (15.17) leads to the perfect mixing distribution (15.16).

When a constituent 1 is subject to transport ($w \neq 0$), the total flux F is given by

$$F = n_1 w_1 + n_1 w_E. \tag{15.18}$$

Using (15.14) and the ratio $\Lambda = K/D_{12}$, the differential equation for the concentration n_1 is then

$$\frac{dn_1}{dz} + \left[\frac{1}{1+\Lambda}\left(\frac{1}{H_1} + \frac{\Lambda}{H}\right) + \left(1 + \frac{\alpha_T}{1+\Lambda}\right)\frac{1}{T}\frac{dT}{dz}\right] n_1 = -\frac{F}{D_{12}(1+\Lambda)}. \tag{15.19}$$

This flow is usually subject to certain continuity conditions which can involve chemical reactions or which are related to the escape of light constituents [10, 11].

When time-dependent problems are considered, the concentration n_1 must satisfy the general continuity equation

$$(\partial n_1/\partial t) + (\partial/\partial z)(n_1 w) = P - L \tag{15.20}$$

where P and L respectively are the eventual production and loss for the constituent n_1. Equation (15.20) can only be solved analytically for certain special cases [12, 13]. As an example, *Fig. 15.1* shows the time evolution for helium and argon between 100 and 120 km when $P = L = 0$ and for negligible eddy diffusion. The atmospheric parameters were taken from Table 4.3 characterized by atmospheric scale height gradients $\beta = 0.2$. The initial distributions at time $t = 0$ are assumed to be mixing distributions. The equilibrium diffusive distributions are computed with arbitrary turbopause levels at 105, 110, and 115 km. It is seen that Ar tends more rapidly toward diffusive equilibrium than He, since the difference between mixing and diffusive equilibrium is less important for argon than for helium.

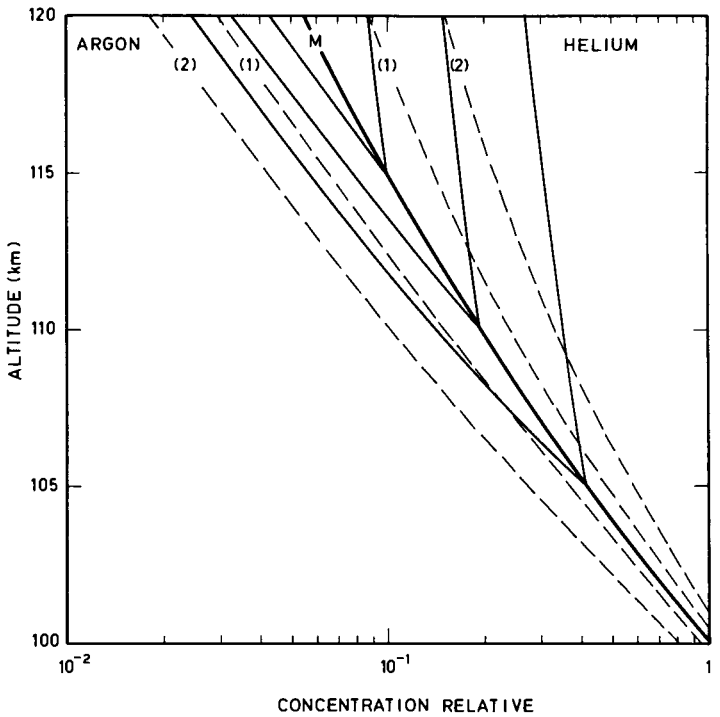


Fig. 15.1 Time evolution of helium and argon towards diffusive equilibrium. Mixing: (——); Diffusion: (——) equilibrium, (– –) after 10 days (1), (– –) after 30 days (2).

The tendency toward diffusive equilibrium can be estimated from the expression [13]

$$\tau_D = A(H^2/D_{12}) \tag{15.21}$$

where A is a numerical constant, H is the atmospheric scale height, and D_{12} is the molecular diffusion coefficient for the considered component. Usually the diffusion time τ_D is applied with $A = 1$. In this case, however, it gives only an order of magnitude accuracy. With the results of Fig. 15.1 it is possible to determine the constant A in a more precise manner. After 10 days, the He concentration at 120 km is the same as if diffusive equilibrium starts at 115 km; the time needed to decrease the diffusive equilibrium level by 5 km is then $\tau_D(\text{He}) = 9.6H^2/D_{12}$. For argon, one finds $\tau_D(\text{Ar}) = 1.6H^2/D_{12}$. In those cases, the diffusion times have a very precise meaning.

15.3 Diffusion Coefficients

In the previous sections it has been shown that three coefficients are used in the diffusion equation, namely the molecular diffusion coefficient D_{12}, the thermal diffusion factor α_T, and the eddy diffusion coefficient K. Numerical values for these quantities must be available for applications of the diffusion equation. Although D_{12} and α_T can be estimated from gas kinetic theory, the eddy diffusion coefficient is a much more speculative parameter. It is actually related to the hydrodynamical regime of the atmosphere and it represents, to a certain extent, the degree of turbulence. Measurements of the turbulence [14, 15] and theoretical estimates of the thermal balance [16, 17] indicate that the eddy diffusion coefficient becomes equal to the molecular diffusion coefficient in the 100–120 km region. Maximum values between 10^6 and 10^7 cm^2 sec^{-1} are possible and K is decreasing downwards to the mesopause. Although analysis has been made of the atmospheric stability [18] above the tropopause, it is not clear at the present time which values for the eddy diffusion coefficient should be used in the transport processes of the minor constituents in the homosphere. Direct or indirect measurements of the eddy diffusion coefficient are, however, of fundamental importance in any analysis of minor constituents in the stratosphere, mesosphere, and lower thermosphere (see Chapters 12 and 13).

The situation is clearer for the molecular diffusion coefficients. According to the classical gas kinetic theory [6, 19], the first approximation of the molecular diffusion coefficient D_{12} is given by

$$D_{12} = 3kT(m_1 + m_2)/16n\Omega_{12}m_1m_2 \tag{15.22}$$

where n is the total concentration $n_1 + n_2$ and Ω_{12} is a collision integral which can be written [19] as

$$\Omega_{12} = \frac{1}{2\pi^{1/2}} \left[\frac{m_1 m_2}{2kT(m_1 + m_2)}\right]^{5/2} P_{12}. \tag{15.23}$$

P_{12}, an integral depending on the relative speed g of the particles 1 and 2, is given by

$$P_{12} = \int_0^\infty q_D(g) g^5 \exp -[m_1 m_2 g^2/2(m_1 + m_2)kT]\, dg \tag{15.24}$$

where $q_D(g)$ is the momentum transfer cross section given by Eq. (9.31). For rigid elastic spheres, $q_D(g)$ does not depend on the velocity and is equal to πr_{12}^2. The radius r_{12} of the interaction sphere is the arithmetic mean value of the effective diameters r_1 and r_2. Since the atmospheric constituents are not perfect elastic spheres, a mean momentum transfer cross section $\bar{Q}_D$ can be written

$$\bar{Q}_D = f\pi r_{12}^2 \tag{15.25}$$

where f is a correction factor to the rigid sphere model. With a mean cross section $\bar{Q}_D$, Eq. (15.24) leads to

$$P_{12} = \bar{Q}_D [2kT(m_1 + m_2)/m_1 m_2]^3. \tag{15.26}$$

The diffusion coefficient (15.22) can now be written

$$D_{12} = \frac{3\pi}{32\bar{Q}_D n} \left(1 + \frac{m_1}{m_2}\right)^{1/2} \left(\frac{8kT}{\pi m_1}\right)^{1/2} \tag{15.27}$$

where $[1 + (m_1/m_2)]^{1/2}(8kT/\pi m_1)^{1/2}$ represents the relative speed of gas 1 with respect to gas 2.

With an effective interaction radius $f^{1/2} r_{12} = 3 \times 10^{-8}$ cm, the diffusion coefficient is given in centimeters squared per second by

$$D_{12} = 1.96 \times 10^6 \left(\frac{1}{m_1} + \frac{1}{m_2}\right)^{1/2} \frac{T^{1/2}}{n} \tag{15.28}$$

when m_1 and m_2 are expressed in grams or

$$D_{12} = 1.52 \times 10^{18} \left(\frac{1}{M_1} + \frac{1}{M_2}\right)^{1/2} \frac{T^{1/2}}{n} \tag{15.29}$$

when M_1 and M_2 are in amu. These expressions can be used for numerical

TABLE 15.1

DIFFUSION COEFFICIENTS[a] $D_{12} = AT^s/n$

System → ↓	Air		N_2		O_2		O	
	A	s	A	s	A	s	A	s
H_2	2.67×10^{17}	0.750	2.80×10^{17}	0.740	3.06×10^{17}	0.732	?	?
He	2.78×10^{17}	0.729	2.94×10^{17}	0.718	3.21×10^{17}	0.710	3.44×10^{17}	0.749
CH_4	7.56×10^{16}	0.747	7.34×10^{16}	0.750	7.51×10^{16}	0.759	?	?
CO	8.22×10^{16}	0.730	9.28×10^{16}	0.710	8.30×10^{16}	0.724	?	?
Ar	6.73×10^{16}	0.749	6.64×10^{16}	0.752	7.17×10^{16}	0.736	5.51×10^{16}	0.841
CO_2	6.42×10^{16}	0.735	6.58×10^{16}	0.752	5.77×10^{16}	0.749	?	?
O	?	?	9.69×10^{16}	0.774	9.69×10^{16}	0.774	—	—

[a] Values are for a temperature range of ~250° to 2000°K and are in $cm^2\ sec^{-1}$.

estimates of the diffusion processes in the atmosphere. In particular, when a minor constituent diffuses through the atmosphere, M_2 will be identified with the mean atmospheric molecular mass and n is then the total atmospheric concentration.

For a specific pair of gases (15.28) shows that the diffusion coefficient D_{12} is proportional to $T^{1/2}$ and inversely proportional to the concentration n. Equations (15.22)–(15.24) show however that D_{12} is proportional to some power of T, which depends on the adopted momentum transfer cross section; i.e., on the interaction potential. It can be shown [6, 19] that

$$D_{12} \propto T^s/n \tag{15.30}$$

where $\frac{1}{2} \leq s \leq 1$. The value $s = 1$ corresponds to Maxwellian molecules for which the repelling force varies inversely as the fifth power of the distance. The value $s = \frac{1}{2}$ corresponds to elastic spheres. From a detailed analysis of numerous experimental data [20], it is possible to represent the binary diffusion coefficients by expressions similar to (15.30). The coefficient of proportionality A entering in (15.30) and the exponent s are given in *Table 15.1* for several pairs of atmospheric gases [20]. The values of A and s given in Table 15.1 lead to diffusion coefficients which agree to at least within $\pm 10\%$ with the experimental data available. For certain gas mixtures more accurate expressions than (15.30) are available [20]. Since there exist practically no experimental data for mixture with atomic hydrogen, it is necessary to use the theoretical self-diffusion coefficients for H in order to compute the binary diffusion coefficients [21, 22]. When the results are presented in a form similar to Eq. (15.30), the coefficients A and s valid between 200° and 2000°K are given [23] in *Table 15.2*.

The final kinetic parameter involved in the diffusion equation is the thermal diffusion factor α_T which is associated with the temperature gra-

TABLE 15.2

BINARY DIFFUSION COEFFICIENTS FOR ATOMIC HYDROGEN[a]

System:	A ($\times 10^{17}$)	s
H–He	8.84	0.706
H–O	5.70	0.708
H–N_2	4.87	0.698
H–O_2	4.75	0.711

[a] Values are in $cm^2\ sec^{-1}$. $D_{12} = AT^s/n$.

dient. Theoretical expressions show [6] that α_T is strongly dependent on the interaction potential of the particles. On the other hand, the thermal diffusion factor varies with the ratio n_1/n_2 of the concentrations of particles 1 and 2. This means that in Eq. (15.7) α_T depends simultaneously on n_1 and n_2. The variation of α_T is illustrated in *Fig. 15.2* for Ar and for He diffusing through molecular nitrogen. The computation has been made for rigid spheres. Experimental values [24, 25] of α_T are usually 50% lower than in Fig. 15.2 when $n_1/(n_1 + n_2) = 0.5$. This difference reflects the effect of the interaction potential. However, for minor constituents the effect of the interaction potential is less important [26] and α_T can be taken as a constant for He, D, and H since the relative abundance of those constituents is always less than 5×10^{-4} in the region where important temperature gradients exist. Using the rigid sphere formulas [6] for minor con-

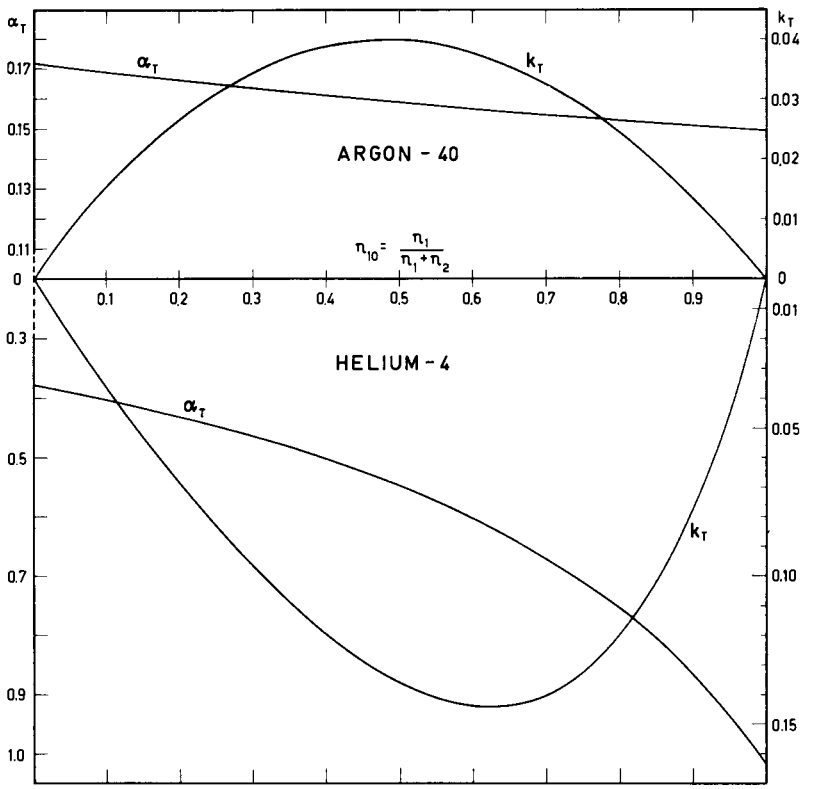


Fig. 15.2 Variation of the thermal diffusion factor α_T and of the thermal diffusion ratio k_T for argon-40 and helium-4 as a function of $n_1/(n_1 + n_2)$, when n_2 is molecular nitrogen.

stituents, one find that

$$\alpha_T(H) \simeq \alpha_T(D) \simeq \alpha_T(He^3) \simeq \alpha_T(He^4) \simeq -0.38 \tag{15.31}$$

and

$$\alpha_T(Ar) \simeq 0.17. \tag{15.32}$$

These values are obtained when the second component is N_2. The sign of the thermal diffusion factor is obtained from the following rule:

1. when $m_1 \neq m_2$, $\alpha_T > 0$ if $m_1 > m_2$,
2. when $m_1 \simeq m_2$, $\alpha_T > 0$ if $r_1 > r_2$.

This means that the heaviest (or the biggest) particles diffuse towards the coldest region. As an example, thermal diffusion increases the helium concentration [26] by approximately a factor of 2. For atomic hydrogen, the effect of α_T is less important since the large diffusion flow (see Section 15.8) leads to practically a mixing distribution in the region with large temperature gradients. For the major components (O, O_2, N_2), α_T is usually neglected.

15.4 Maximum Transport Velocities

In Section 15.2 a general expression for the concentration has been established when the vertical transport velocity is zero. Equation (15.19) shows, however, that any departure from an equilibrium solution is directly related to the importance of the transport flow F compared to $D_{12} + K$. It is therefore useful to estimate the magnitude of the flow which can be transported by molecular or by eddy diffusion without solving the differential equation for the actual concentration profile. The concept of maximum transport flow was introduced several years ago [27, 28] in relation with minor constituent distributions.

It is always possible to express the concentration gradient of a minor constituent n_1 as a function of the total concentration gradient in the following form:

$$\frac{1}{n_1}\frac{dn_1}{dz} = X(z)\frac{1}{n}\frac{dn}{dz} \tag{15.33}$$

where $X(z)$ is the vertical distribution factor which is height dependent. With (15.12), Eq. (15.33) can be transformed to

$$\frac{1}{n_1}\frac{dn_1}{dz} = -X(z)\left[\frac{1}{H} + \frac{1}{T}\frac{dT}{dz}\right]. \tag{15.34}$$

The total transport velocity (15.14) can now be written

$$w = \frac{D_{12}}{H}\left[X - \frac{H}{H_1} - \frac{H}{T}\frac{dT}{dz}(1 + \alpha_T - X)\right] + \frac{K}{H}[X - 1]. \quad (15.35)$$

The contributions due to molecular diffusion and to eddy diffusion are respectively represented by the terms proportional to D_{12} and to K.

When the minor constituent is characterized by a mixing distribution over a certain height range, the vertical distribution factor is such that $X = 1$. In this case (15.35) becomes simply

$$w = \frac{D_{12}}{H}\left[1 - \frac{H}{H_1} - \frac{\alpha_T H}{T}\frac{dT}{dz}\right] \quad (15.36)$$

or when α_T is negligible

$$w = \frac{D_{12}}{H}\left(1 - \frac{m_1}{m}\right) \quad (15.37)$$

where m is the atmospheric mean molecular mass. These equations give the *maximum* molecular diffusion velocity for a constituent which follows the distribution of the major constituents. When the mass m_1 of the minor constituent is less than the mean molecular mass, Eq. (15.37) shows that w is positive; i.e., an upwards velocity. When $m_1 > m$, w is negative and it corresponds to a downward velocity. With the atmospheric model of Table 4.4 and with the diffusion coefficient (15.29), the maximum diffusion velocities for ^{40}Ar, ^{4}He, ^{2}H, and ^{1}H are given in *Table 15.3*. The negative values for argon indicate that this constituent is subject to a maximum downward flow velocity. Around 100 km, the limiting molecular diffusion velocities

TABLE 15.3

MAXIMUM MOLECULAR DIFFUSION TRANSPORT VELOCITIES[a]

z (km)	^{40}Ar	^{4}He	^{2}H	^{1}H
90	-5.65×10^{-2}	3.01×10^{-1}	4.44×10^{-1}	6.40×10^{-1}
95	-1.43×10^{-1}	7.63×10^{-1}	1.13×10^{0}	1.62×10^{0}
100	-3.38×10^{-1}	1.78×10^{0}	2.62×10^{0}	3.78×10^{0}
105	-7.83×10^{-1}	3.94×10^{0}	5.82×10^{0}	8.34×10^{0}
110	-1.60×10^{0}	7.35×10^{0}	1.09×10^{1}	1.56×10^{1}
115	-3.09×10^{0}	1.32×10^{1}	1.96×10^{1}	2.82×10^{1}
120	-5.72×10^{0}	2.30×10^{1}	3.40×10^{1}	4.91×10^{1}

[a] Values are in cm sec^{-1}.

for ^{4}He, ^{3}He, ^{2}H, and ^{1}H are always of the order of a few centimeters per second. Once the concentration is known, the maximum transport velocity immediately gives the maximum flow which can be transported by diffusion. For example, applications of Eqs. (15.36) and (15.37) were made for nitric oxide in Chapter 12.

It is important to note that the maximum diffusion velocity is a characteristic parameter of the ambient medium and that it can be estimated without any knowledge of the concentration of the minor constituent. The magnitude of w depends, however, strongly on the molecular diffusion coefficient and any error in the momentum transfer cross section is reflected in the maximum diffusion velocity.

The concept of maximum diffusion velocity can also be used to deduce some requirements for the eddy diffusion coefficient in the chemosphere (see Section 13.6). If it is assumed that the minor constituent is distributed according to a concentration scale height $\mathscr{H}_1$ Eq. (15.33) leads to

$$X = \frac{H}{\mathscr{H}_1}\left[\frac{1}{1 + (H/T)(dT/dz)}\right]. \tag{15.38}$$

The term $(H/T)\,dT/dz$ is usually small compared to one and Eq. (15.35) is written

$$w = \frac{D_{12}}{H}\left[\left(\frac{H}{\mathscr{H}_1} - \frac{m_1}{m}\right) + A\left(\frac{H}{\mathscr{H}_1} - 1\right)\right]. \tag{15.39}$$

When the term $(H/T)\,dT/dz$ is included, it is necessary to define an effective mass [29, 30] m_1* to obtain an expression similar to (15.39). When a transport flow and a ratio $H/\mathscr{H}_1$ are adopted, Eq. (15.39) can be used to compute the corresponding value for $A = K/D_{12}$. In such a way, an eddy diffusion coefficient can be estimated to fulfill imposed transport conditions.

15.5 Effusion Velocities

The molecular diffusion velocity increases exponentially with altitude, since it is proportional to the diffusion coefficient D_{12}. Above a certain height, the diffusion equation can no longer be applied since collisions become less frequent. This altitude, termed the critical level, is the beginning of the exosphere which is discussed in the next chapter. At the critical level a substantial fraction of the particles with velocities greater than the escape velocity ($\sim$11 km sec^{-1}) can leave the heterosphere. When a Maxwellian velocity distribution function is integrated from the escape velocity to infinity over the upward hemisphere, one obtains an average velocity called

the effusion velocity. At a geocentric distance r, the effusion velocity v_e for a constituent characterized by a scale height H is given by [31, 32]

$$v_e = (g/2\pi)^{1/2} r H_1^{-1/2} (1 + H_1/r) e^{-r/H_1} \tag{15.40}$$

where g is the gravity acceleration at the distance r. The effusion velocity depends essentially on H_1, i.e., on the mass and on the temperature. Numerical values of v_e are given in *Table 15.4* for an altitude of 500 km. The effusion velocity increases slightly with the height, but it is shown in Section 16.4 that the escape flux is not very sensitive to the choice of the critical level height.

TABLE 15.4

EFFUSION VELOCITIES[a] AT 500 KM

Temperature (°K)	^{1}H	^{2}H	^{3}He	^{4}He
600	9.53×10^{0}	1.31×10^{-4}	1.48×10^{-9}	1.52×10^{-14}
700	4.74×10^{1}	3.36×10^{-3}	1.97×10^{-7}	1.06×10^{-11}
800	1.57×10^{2}	3.79×10^{-2}	7.66×10^{-6}	1.44×10^{-9}
900	3.98×10^{2}	2.48×10^{-1}	1.31×10^{-4}	6.49×10^{-8}
1000	8.30×10^{2}	1.11×10^{0}	1.27×10^{-3}	1.36×10^{-6}
1250	3.11×10^{3}	1.63×10^{1}	7.45×10^{-2}	3.21×10^{-4}
1500	7.45×10^{3}	9.65×10^{1}	1.11×10^{0}	1.21×10^{-2}
1750	1.38×10^{4}	3.41×10^{2}	7.57×10^{0}	1.60×10^{-1}
2000	2.20×10^{4}	8.75×10^{2}	3.18×10^{1}	1.10×10^{0}

[a] Values are in cm sec^{-1}.

Without loss or production in the upper atmosphere, the flow introduced in Eq. (15.19) must follow the continuity equation

$$F_1 r_1^2 = F_2 r_2^2 \tag{15.41}$$

between two levels at geocentric distances r_1 and r_2. Above a certain altitude, molecular diffusion is no longer effective and the flow must be supported through other processes such as thermal escape or polar wind escape (see Chapter 21). When thermal escape is considered, the time necessary to reduce the concentration by 50% at 500 km is given approximately by [11, 31]

$$\tau = 0.693 H_1(500 \text{ km})/v_e. \tag{15.42}$$

Figures 15.3 to *15.6* show the thermal escape time for ^{1}H, ^{2}H, ^{3}He, and

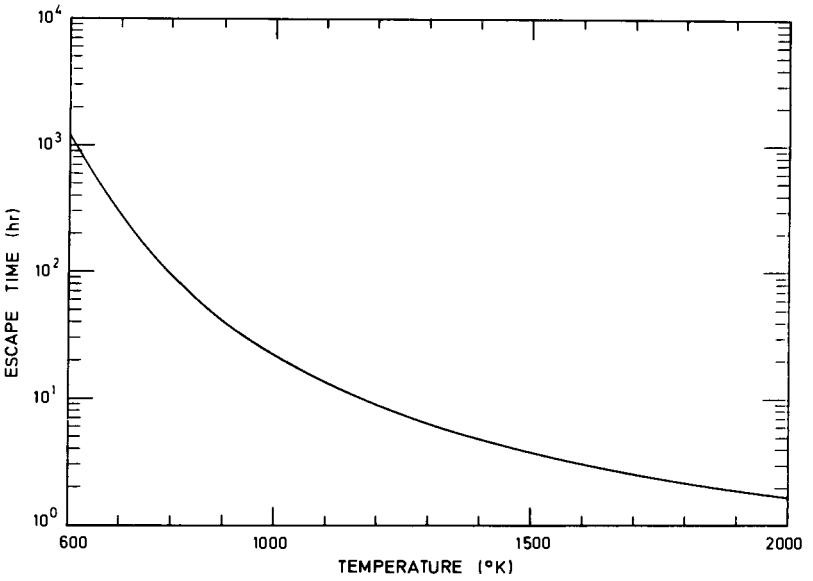


Fig. 15.3 Escape time for ^1H as a function of temperature.

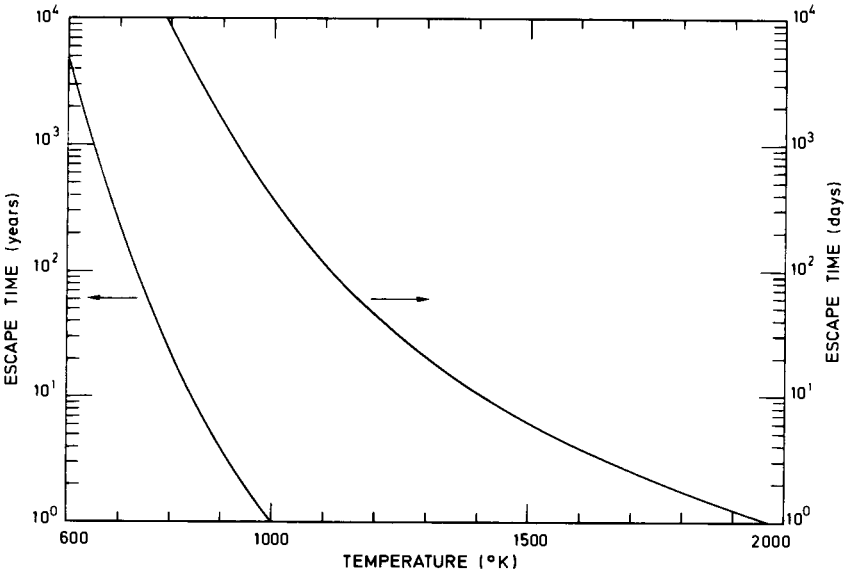


Fig. 15.4 Escape time for ^2H as a function of temperature.

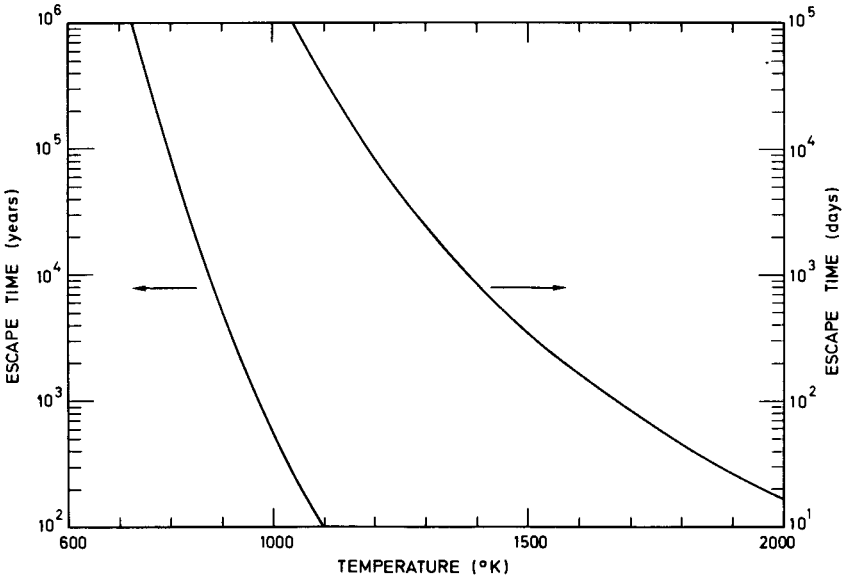


Fig. 15.5 Escape time for ^{3}He as a function of temperature.

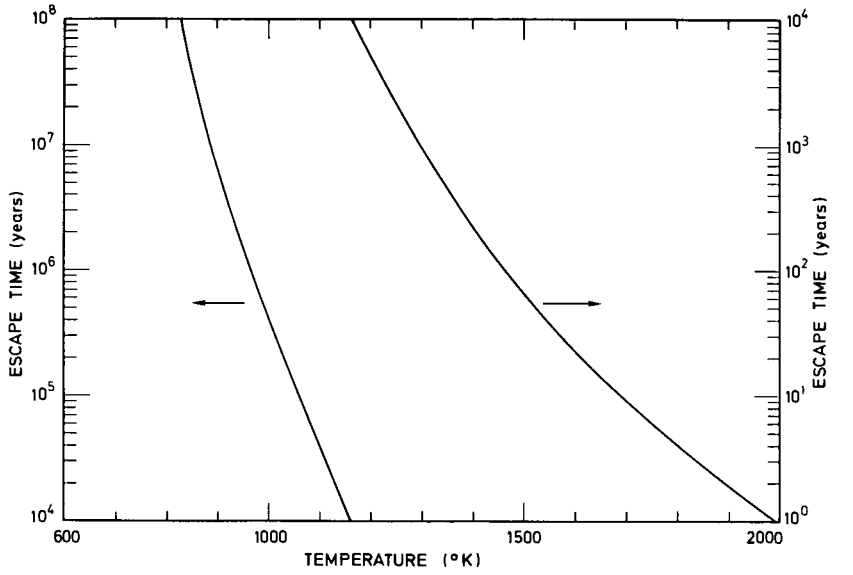


Fig. 15.6 Escape time for ^{4}He as a function of temperature.

^{4}He as a function of the thermopause temperature. It is clear that thermal escape has an appreciable effect in a very short time on the quantity of thermospheric atomic hydrogen. For helium-4, however, a temperature of 2000°K leads to a lifetime of the order of one year and upward diffusion transport should take less than one year to replenish the isothermal layer.

The effusion velocity (15.40), corresponding to a Maxwellian velocity distribution function, leads to the concept of a maximum thermal escape flow. This classical approach was introduced by Jeans [33]. Since particles from the high velocity tail of the distribution are escaping, the velocity distribution function cannot be exactly Maxwellian. In the past several years controversy has developed concerning the accuracy of the Jeans' escape flux [34–41]. Monte Carlo calculations have been used and conflicting results obtained. Recent analyses [42, 43] seem to indicate that in the earth's atmosphere the Jeans' escape formula can overestimate the actual escape flux by not more than 20 to 25%. Although such a departure is important for very accurate calculations, it cannot significantly modify the conclusions based on an expression similar to (15.40).

15.6 Helium Distribution

Around 1920 considerable discussion existed about the nature of the major constituent at high altitudes. With the assumption that diffusive equilibrium prevailed above 20 km, Chapman and Milne [44] concluded that helium was the major constituent above 100 km. Using a high abundance ($\sim 10^{-4}$) for H_2 at ground level, Jeans [33] concluded that hydrogen should be the predominant constituent above 75 km. At that time it was not realized that turbulence is effective up to 100 km and it was puzzling that no optical emissions of helium and hydrogen could be detected in the auroral features.

The first experimental evidence for the presence of helium in the upper atmosphere came from optical observations [45] of the orthohelium $2\,^3S$–$2\,^3P$ transition at 10,830 Å. But it was only in 1961 that helium was shown to be an important constituent in the upper atmosphere [46]. Later analysis of drag data [47, 48] of several satellites led to the conclusion that an increase of helium in the upper atmosphere occurs at high latitudes for winter conditions. This helium bulge has also been detected by mass spectrometric observations [49] and recent measurements [50] indicate a larger amplitude than was first indicated. The satellite drag data show an increase of a factor of 3 to 4 in atmospheric density between the summer pole and the winter

pole, whereas the mass spectrometric observations show an increase of approximately a factor of 10. Rocket observations [51] made at White Sands (32°N) give helium concentration between 6×10^{6} and 5×10^{8} cm^{-3} at 120 km whereas an observation [52] at Fort Churchill (58°N) indicates a concentration of 1.2×10^{8} cm^{-3} at 120 km. Drag data, satellite, and rocket mass spectrometric observations, and optical ground based observations [53] have clearly shown that a latitudinal variations occurs in the helium distribution.

It is now necessary to discuss the theory of the preceding sections in light of these experimental facts. It has been shown that an increase of 5 km for the beginning of the molecular diffusion equilibrium leads to a decrease by a factor of 2 in the helium concentration at high altitudes [11]. Such a variation of the turbopause level has been used several times to explain increases or decreases of the helium concentration. The transport flow of helium cannot affect the vertical distribution, since the actual flow relating to Eq. (15.19) is negligible compared to the maximum flow which can be transported upwards from the 100 km level. With a helium mixing ratio of 5.24×10^{-6} in the homosphere, the maximum diffusion velocity for ^{4}He (see Table 15.3) gives a maximum flow at 100 km

$$F(\mathrm{He}) \simeq 10^{8} \quad \mathrm{cm}^{-2}\,\mathrm{sec}^{-1}. \tag{15.43}$$

Recent measurements of the ^{4}He profile in the deep sea [54] indicate a flux of the order of 7.7×10^{5} cm^{2} sec^{-1}. Even with a value [31] of 1.7×10^{6} cm^{-2} sec^{-1}, it is clear that the true upward flow of helium originating from the radioactive decay of uranium and thorium in the crust and in the mantle of the earth is negligible compared to the maximum flow (15.43). Therefore, Eq. (15.19) can be used without the second term and the helium distribution is given by Eq. (15.17). Since the eddy diffusion coefficient is poorly known, *Fig. 15.7* gives helium distributions computed with several constant values for K. Generally, it can be seen that the introduction of an eddy diffusion coefficient produces steeper concentration gradients in the helium distribution. The available rocket observations [51, 52] fall practically between the two extreme curves of Fig. 15.7 and it is clear that large helium concentration gradients can be produced by introducing the effect of eddy diffusion.

The true atmospheric eddy diffusion coefficient is, however, not constant with altitude. *Figure 15.8* shows two possible distributions of K which are similar to the worldwide average values deduced from an analysis of the downward heat transfer by turbulence [55]. The corresponding helium

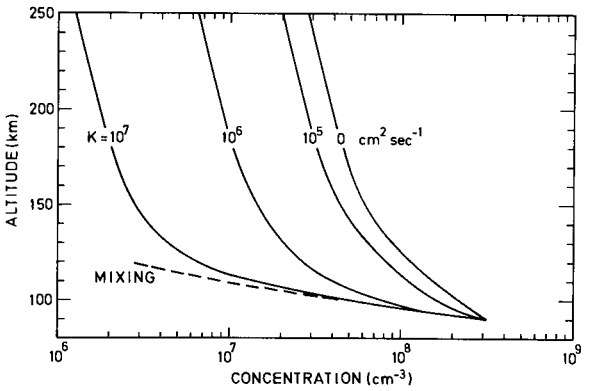


Fig. 15.7 Helium distribution for several eddy diffusion coefficients. The mixing distribution is shown for comparison. Values are for a 750°K thermopause temperature.

distributions are shown on *Fig. 15.9*. Actually, it is the peak value of the eddy diffusion coefficient which determines the helium concentration gradient in the 100–120 km range. In Fig. 15.9, the dotted curves corresponding to constant K values are shown for comparison. *Figure 15.10* shows the variation of the helium concentration at 120 km as a function of the eddy diffusion coefficient. When $K = 0$, the helium concentration at 120 km is 1.2×10^8 cm^{-3}. From Fig. 15.10, it is clear that a variation of a factor 10 is obtained when K varies by a factor of 50. Therefore, the helium bulge amplitude of a factor of 4 deduced by drag data can easily by explained by changes in the eddy diffusion coefficient.

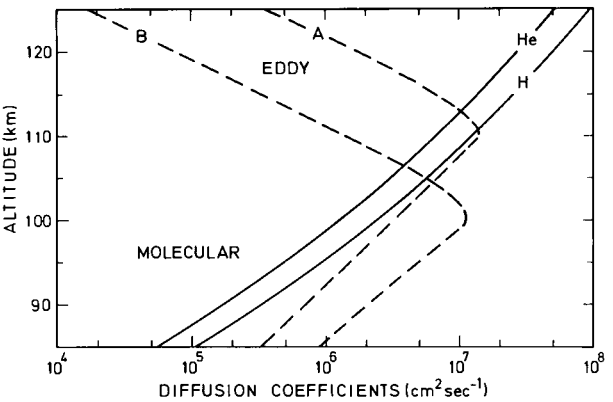


Fig. 15.8 Possible distributions for the eddy diffusion coefficients (curves A and B). The molecular diffusion coefficients for He and H are also shown.

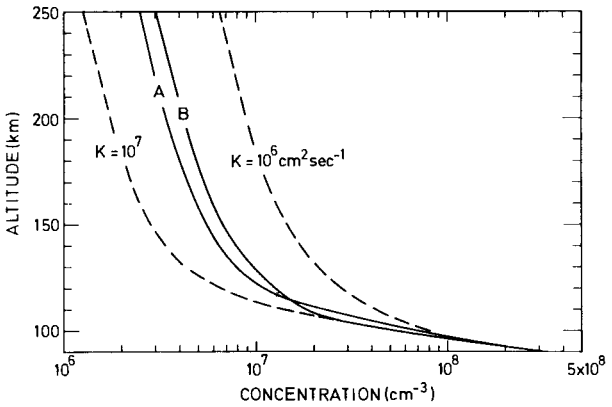


Fig. 15.9 Helium distribution with the eddy diffusion coefficients of Fig. 15.8 (curves A and B). The dashed curves correspond to constant K values. Values are for $T = 750°K$ at the thermopause.

Another explanation for the existence of the bulge is based on a meridional transport [55] combined with lateral flows [56, 57] in the exosphere. Such a wind system toward the winter polar region can also provide an increase of the helium concentration, but the effect of eddy diffusion cannot be neglected in a detailed explanation.

Satellite mass spectrometric observations [50] from OGO-6 indicate a variation of a factor of 10 between summer and winter helium densities. *Figure 15.11* gives an example of the observed variation as a function of geographic latitude. This variation is explained by eddy diffusion, if K changes with latitude as indicated on Fig. 15.11. The unsolved question is to know if such variations of K are really possible with latitude. Although wind and temperature data indicate [18] that the winter polar mesosphere is more turbulent than the summer polar mesosphere, there are not enough

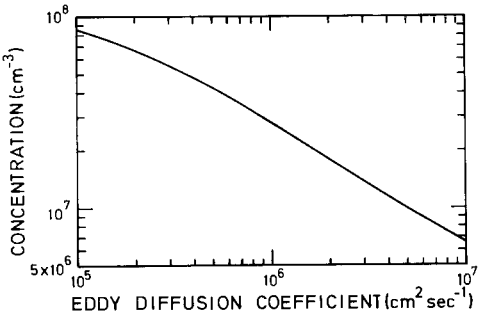


Fig. 15.10 Variation of the helium concentration at 120 km as a function of the eddy diffusion coefficient. $n(\mathrm{He})/n(\mathrm{M}) = 5.24 \times 10^{-6}$ at 90 km.

data available between 90 and 120 km to investigate a latitudinal variation in this height range. The fact that the winter high latitude thermosphere is not much cooler than the summer high latitude thermosphere seems to indicate that less heat is transported by turbulence toward the mesosphere. In the summer high latitude thermosphere, the solar ultraviolet heating and Joule heating are effective over long periods. Therefore, the same amount of heat should be transported downward by conduction in the thermosphere and by turbulence in the lower thermosphere. This implies larger eddy diffusion coefficients in the summer polar region.

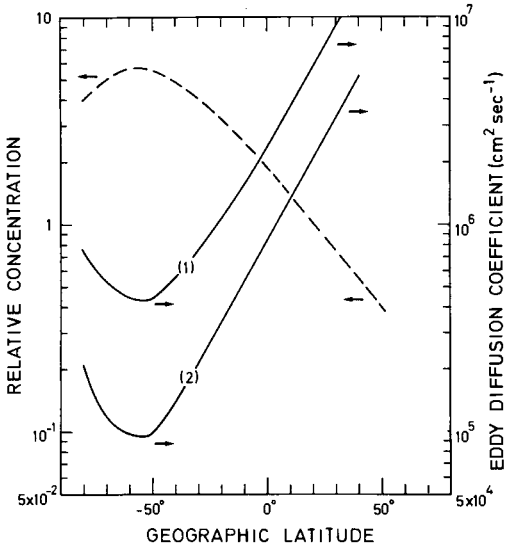


Fig. 15.11 Observed latitudinal variation of helium at 400 km and corresponding values of the eddy diffusion coefficient. The dashed curve is from Reber *et al.* [50]. (1) $n(\mathrm{He}) = 10^6\ \mathrm{cm}^{-3}$ at $\lambda = 20°\mathrm{N}$; (2) $n(\mathrm{He}) = 2 \times 10^6\ \mathrm{cm}^{-3}$ at $\lambda = 20°\mathrm{N}$.

From the previous discussion it is seen that the vertical transport flow has practically no effect on the helium distribution, since it is too small compared to the maximum diffusion flow. The helium concentration is, however, strongly dependent on the adopted eddy diffusion coefficient in the lower thermosphere. Therefore, the helium concentrations given in Appendix B actually correspond to an eddy diffusion coefficient of the order of $10^6\ \mathrm{cm}^2\ \mathrm{sec}^{-1}$. It should also be mentioned that the ^{3}He distribution has the same characteristics, although the ^{3}He thermal escape is more effective.

15.7 Deuterium Distribution

In the earth's atmosphere deuterium never becomes a major constituent. Its vertical distribution is, however, interesting since it involves all of the properties of the general diffusion equation. The production mechanism of deuterium is probably similar to the production of atomic hydrogen, i.e., above the mesopause the main production should result through photodissociation of deuterated water vapor. Therefore, reactions similar to those described in Chapter 13 have to occur, although isotropic effects could modify the effectiveness of certain processes.

The deuterium content of standard mean ocean water [58, 59] can be adopted as a working value for the atmospheric content. This leads to a concentration ratio of $n(\mathrm{D})/n(\mathrm{H}) = 1.6 \times 10^{-4}$. With an atomic hydrogen concentration of $3 \times 10^{7}\ \mathrm{cm}^{-3}$ at 100 km, the corresponding deuterium concentration is then $4.8 \times 10^{3}\ \mathrm{cm}^{-3}$.

Only a few experimental observations of deuterium have been made in the upper atmosphere. In 1965 deuterium ions [60, 61] were detected in the topside ionosphere. The ratio $n(\mathrm{D}^+)/n(\mathrm{H}^+)$ was estimated [61] to be of the order of 1.1×10^{-3} below 1000 km and it decreases by a factor of 10 above 2000 km. Optical observations [62, 63] of the solar Lyman α line seem to indicate an observation effect of terrestrial deuterium in the blue wing of the line at 1215.346 Å. The observed ratio $n(\mathrm{D}^+)/n(\mathrm{H}^+)$ and the optical absorption indicate that the ratio $n(\mathrm{D})/n(\mathrm{H})$ has to increase in the upper atmosphere. It has been shown [11] that the ratio $n(\mathrm{D})/n(\mathrm{H})$ can increase by a factor of 20 between 100 and 500 km when molecular diffusion is acting in the thermosphere. The effect of eddy diffusion has also been analyzed [64].

With a concentration $n(\mathrm{D}) = 4.8 \times 10^{3}\ \mathrm{cm}^{-3}$, the maximum diffusion velocity for $^2\mathrm{H} \equiv \mathrm{D}$ in Table 15.3 gives a maximum flow at 100 km

$$F(\mathrm{D}) = 1.3 \times 10^{4} \quad \mathrm{cm}^{-2}\,\mathrm{sec}^{-1}. \tag{15.44}$$

Since the real flow of deuterium is not known, the complete differential equation (15.19) should be used. Integration of this equation [65] leads to

$$n_1(z) = n_{\mathrm{eq}}\left[1 - \int_{z_1}^{z} \frac{F}{D_{12}(1 + \Lambda)n_{\mathrm{eq}}}\, dz\right] \tag{15.45}$$

where the zero flow distribution n_{eq} is given by (15.17). A similar equation [66, 67] has been applied in different studies in the atmosphere of Venus. When thermal escape is the mechanism for removing particles from the upper atmosphere, the flow F can be normalized to the effusion velocity

(15.40) since Eq. (15.19) is linear. Numerical results [64] of (15.45) are used in *Fig. 15.12*, which gives the deuterium concentration at different altitudes as a function of the thermopause temperature. It is seen that the deuterium concentration peaks at various heights for temperatures between 600° and 1500°K. Above 1500°K, n(D) always decreases with increasing temperature, i.e., shows a behavior similar to atomic hydrogen [10, 11]. This

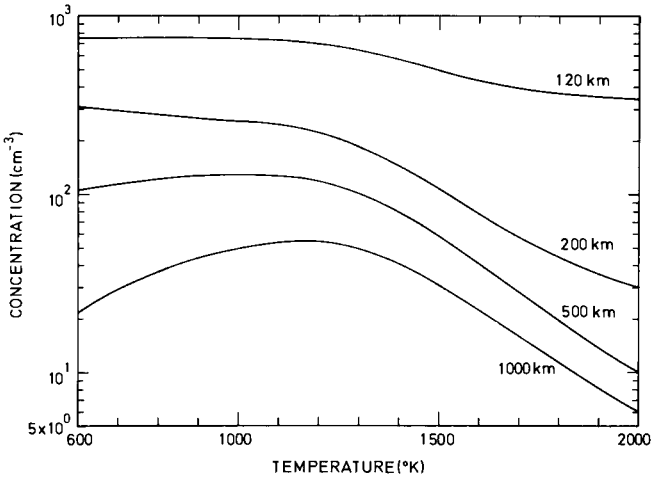


Fig. 15.12 Deuterium concentration at different altitudes as a function of the thermopause temperature. The eddy diffusion coefficient is $K = 10^7$ cm^2 sec^{-1}.

means that the thermal escape flux is only effective for temperatures above 1500 °K. For lower temperatures the deuterium distribution has a tendency to become similar to the helium distribution, since at 500 km there is practically no change in the concentration when the temperature varies. Combining the deuterium concentrations with the effusion velocities of Table 15.4, it is clear that the thermal escape flux cannot be constant over a wide range of temperatures, as is the case for atomic hydrogen. *Table 15.5* gives the thermal escape flux for three different values of the eddy diffusion coefficient. These fluxes have to be compared with the maximum diffusion flow of 1.3×10^4 cm^{-2} sec^{-1}. It is clear that a charge transfer process with atomic oxygen ions has to be considered in order to obtain an equivalent ionic escape flux through the polar wind which is described in Chapter 21.

It can be deduced from Table 15.5 that the effect of eddy diffusion is most important for low temperatures. *Figure 15.13* shows the variation of n(D) at 120 km as a function of the eddy diffusion coefficient. The most

TABLE 15.5

DEUTERIUM THERMAL ESCAPE FLUX[a]

T (°K)	$K = 10^7$ (cm^2 sec^{-1})	$K = 10^6$ (cm^2 sec^{-1})	$K = 0$ (cm^2 sec^{-1})
600	1.39×10^{-2}	4.61×10^{-2}	6.74×10^{-2}
700	3.85×10^{-1}	1.27×10^{0}	1.86×10^{0}
800	4.57×10^{0}	1.51×10^{1}	2.20×10^{1}
900	3.14×10^{1}	1.02×10^{2}	1.49×10^{2}
1000	1.43×10^{2}	4.56×10^{2}	6.56×10^{2}
1250	1.81×10^{3}	4.50×10^{3}	5.78×10^{3}
1500	5.59×10^{3}	9.25×10^{3}	1.05×10^{4}
1750	7.97×10^{3}	1.08×10^{4}	1.17×10^{4}
2000	8.92×10^{3}	1.13×10^{4}	1.21×10^{4}

[a] Values are in cm^{-2} sec^{-1}.

important variations appear for thermopause temperatures less than 1500°K. It should be noted that for helium (see Fig. 15.10) the variation of the concentration is independent of the thermopause temperature, since the thermal escape flow and the real diffusion flow are always negligible compared to the maximum diffusion flow. For deuterium, however, the thermal escape flow is of the same order of magnitude as the maximum diffusion flow for temperatures higher than 1500°K. The eddy diffusion coefficient becomes the leading factor only for temperatures below 1500°K.

The combined effect of eddy diffusion and of thermal escape influence therefore the vertical distribution of the ratio $n(\mathrm{D})/n(\mathrm{H})$ shown in *Fig. 15.14.*

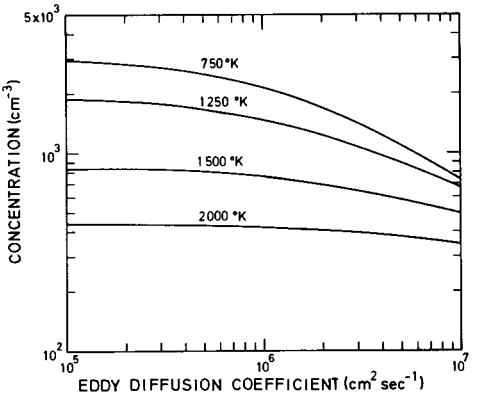


Fig. 15.13 Variation of the deuterium concentration at 120 km as a function of the eddy diffusion coefficient for several thermopause temperatures.

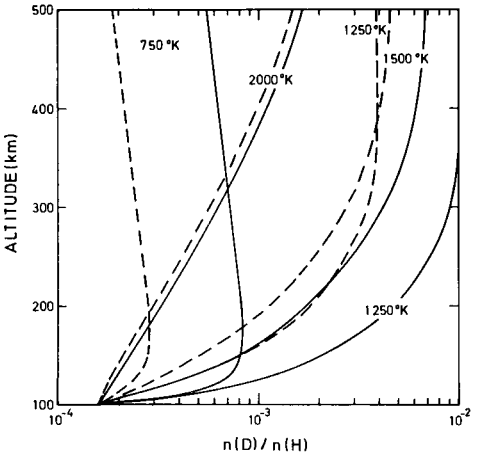


Fig. 15.14 Height dependence of the ratio $n(D)/n(H)$ for several thermopause temperatures. The eddy diffusion coefficients are $K = 0$ (solid curve) and 10^7 cm^2 sec^{-1} (dashed curve).

This ratio has been computed with the hydrogen distributions discussed in the next section. A maximum of $n(D)/n(H)$ occurs at an altitude depending on the thermopause temperature. Below 1500°K, the enhancement of $n(D)/n(H)$ depends on the adopted eddy diffusion coefficient. The maximum enhancement occurs however around 400 km for $T = 1250$°K and it corresponds to almost 60 times the natural abundance of 1.6×10^{-4} when $K = 0$ above 100 km. Such an enhancement is about a factor of 3 less than the experimental value [63] deduced at 160 km. The experimental ion ratio [61], $n(D^+)/n(H^+)$ is of the same order of magnitude as the results of Fig. 15.14. Above a certain height $n(D)/n(H)$ begins to decrease and reaches values less than the abundance at 100 km. Actually, diffusion can increase the ratio $n(D)/n(H)$ only over a limited height range.

Owing to its small relative abundance, deuterium is very difficult to observe in the earth's upper atmosphere. Since the deuterium concentration reaches the maximum value around 1250°K, and since the maximum enhancement of the ratio $n(D)/n(H)$ occurs above 200 km at the same temperature, it can be concluded that medium solar activity conditions offer the best possibilities for mass spectrometric and optical observations of deuterium in the upper atmosphere.

15.8 Atomic Hydrogen Distribution

The first far-ultraviolet study [5] of the night sky made in 1955 resulted in the discovery of the night Lyman α glow at 1216 Å. This measurement was used to compute a hydrogen distribution [10] in the thermosphere

with a concentration of 8.4×10^6 cm^{-3} at 100 km. A systematic analysis was then made [11, 68], using this value of n(H) at 100 km, in order to show the variation of atomic hydrogen in the thermosphere. It was found that the effect of the transport flow in Eq. (15.19) plays the essential role. It was shown that hydrogen for all practical purposes follows a mixing distribution between 100 and 120 km and that the concentration in the thermosphere is higher when the thermopause temperature decreases.

Since 1960 numerous Lyman α observations have been made by rockets and satellites. An analysis of the observations [69] indicates that the concentration at 100 km should be of the order of 3×10^7 cm^{-3}. Balmer α observations show [70] that atomic hydrogen is increasing from solar maximum to solar minimum. The OGO-4 observations [71] also require a concentration of 3×10^7 cm^{-3} at 100 km. However, other observations [72] seem to indicate values between 1.25×10^7 and 2×10^7 cm^{-3}. Actually, the Lyman α observations show a variation, or an uncertainty, of about a factor of 2 for the hydrogen concentration at 100 km. It is also true, however, that the Lyman α geocoronal observations require the solution of a radiative transfer equation [73] in an optically thick atmosphere which is not spherically symmetrical.

Above the mesopause, photodissociation of water vapor is the principal production mechanism [74] for atomic hydrogen. This process can also lead to a production of molecular hydrogen (see Chapter 13). Since there is an uncertainty in the reaction rate coefficients and in the eddy diffusion coefficient, it has been concluded [74] that mixing conditions lead to the best approximation for atomic hydrogen in the lower thermosphere below 100 km. Therefore, values between 10^7 and 3×10^7 cm^{-3} deduced from Lyman α observations may reflect in a certain way the complexity of the thermospheric processes.

With a concentration of 3×10^7 cm^{-3} and with the maximum diffusion velocity of Table 15.3, the maximum diffusion flow at 100 km is

$$F(\mathrm{H}) = 1.1 \times 10^8 \quad \mathrm{cm}^{-2}\,\mathrm{sec}^{-1}. \tag{15.46}$$

Since the real flow is of the same order of magnitude, it is necessary to compute the vertical distribution with Eq. (15.45). *Figure 15.15* gives the vertical distribution for two extreme values of the eddy diffusion coefficient. It is seen that the exact value of K is not important for high temperatures. *Figure 15.16* indicates how the hydrogen concentration varies at 120 km as a function of the eddy diffusion coefficient. Above 1000°K, the concentration is not affected by changes in the eddy diffusion transport

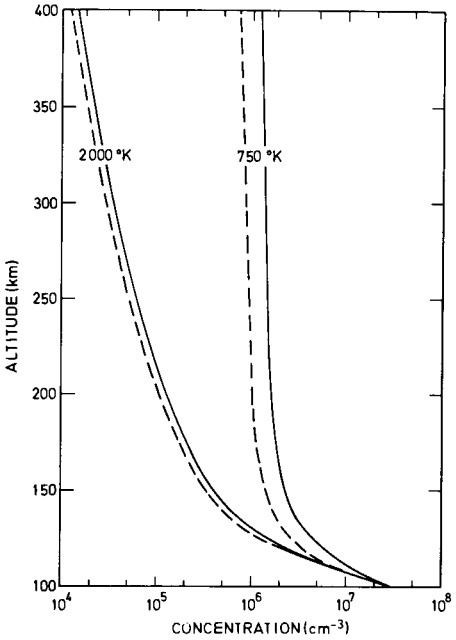


Fig. 15.15 Hydrogen vertical distribution for two thermopause temperatures. The eddy diffusion coefficients are $K = 0$ (solid curve) and 10^7 cm^2 sec^{-1} (dashed curve).

flow which leads practically to a mixing distribution between 100 and 120 km altitude. When the thermopause temperature is below 1000°K, the thermal escape becomes less efficient, as is shown in *Table 15.6*. This implies that for low temperatures the value of the eddy diffusion coefficient or the

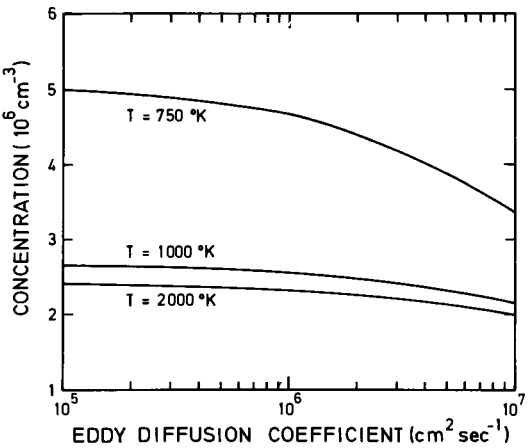


Fig. 15.16 Variation of the hydrogen concentration at 120 km as a function of the eddy diffusion coefficient for three thermopause temperatures.

TABLE 15.6

ATOMIC HYDROGEN THERMAL ESCAPE FLUX[a]

T (°K)	$K = 10^7$ (cm^2 sec^{-1})	$K = 10^6$ (cm^2 sec^{-1})	$K = 0$ (cm^2 sec^{-1})
600	1.40×10^7	3.40×10^7	4.20×10^7
700	3.24×10^7	7.39×10^7	8.28×10^7
800	6.72×10^7	9.27×10^7	9.95×10^7
900	7.90×10^7	9.95×10^7	1.05×10^8
1000	8.40×10^7	1.02×10^8	1.08×10^8
1250	8.89×10^7	1.06×10^8	1.11×10^8
1500	9.52×10^7	1.13×10^8	1.18×10^8

[a] Values are in cm^{-2} sec^{-1}.

height of the thermopause level influences the concentration and the escape flux at high altitudes.

The preceding computations are valid for steady state conditions. If the hydrogen gas responded instantaneously to the diurnal thermopause temperature variations, a day–night asymmetry as high as 20 might be expected in the hydrogen concentration during low solar activity conditions. This problem has recently been critically reviewed [75]. When a hydrogen buildup occurs during the night, a lateral flow should exist in the exosphere since there is a nonuniform concentration and temperature distribution over the globe. Calculations of such a flow have been made extensively [56, 76–79] and show that the maximum day-to-night variation can be of the order of 3 to 4. Recently, the atomic hydrogen concentration was derived from $n(H^+)$ measurements [80] using the equilibrium charge transfer between H^+ and O. This analysis shows a diurnal variation of about a factor of 2 for the period June 1966–January 1967, with a phase delay of about 3 hr between the temperature and the hydrogen concentration. A long term variation is superimposed on the day-to-night variation. This indicates that a significant increase of the atomic hydrogen concentration occurs during solar minimum conditions.

Up to this point the discussion of hydrogen, deuterium, and helium densities has been based on escape flows induced through pressure gradients established by thermal escape. In the regions outside the plasmasphere, however, there is a continual loss of ionization through the polar wind (see Chapter 21). Since this plasma ultimately derives from the photo-

ionization of the neutral atmosphere, such a loss can be just as effective as ballistic escape in affecting the vertical distributions of the light gases.

Although complete analyses have not been made, it appears that for hydrogen the polar wind flux is greater than the thermal escape flux for thermosphere temperatures below 1200°K. Thus, for higher temperatures the results of this section apply, but the effects for lower temperatures may be seriously modified at high latitudes. For example, polar wind ion fluxes are typically found to be $2\text{–}4 \times 10^8$ cm^{-2} sec^{-1}, somewhat larger than the maximum hydrogen flux of 1.1×10^8 cm^{-2} sec^{-1}. Thus, polar wind flow will always act to deplete the neutral hydrogen densities of the thermosphere. No complete analysis of this problem has yet been made, however.

For deuterium, ion escape can be important because, unlike thermal escape, the escape flux is not exponentially dependent upon the mass of the ion. Thus, the ratio of escape flows for hydrogen and deuterium ions is essentially the concentration ratio. As a consequence, the escape of ions along convecting field lines strongly affects the deuterium density and increases the temperatures at which thermal escape becomes more important than the polar wind. In polar regions, i.e., poleward of 60°–65° invariant latitude, it should be expected that the deuterium concentration show a great variability corresponding to the changes in magnetospheric convection.

With respect to helium, computations show that the polar wind flux is $\sim 2 \times 10^6$ ions cm^{-2} sec^{-1}, a value far less than the limiting flux. Thus, although ion escape plays a part in the global helium budget, it does not affect the altitude variation (see Chapter 21).

In summary, it has been shown how the general diffusion equation can be applied to minor constituents such as helium, deuterium, and atomic hydrogen. Actually the diffusion transport is such that helium and hydrogen, with relative abundances of the order of 10^{-6} at 100 km, become progressively the major components above 500 km altitude. Therefore these two constituents will be responsible for the structure of the exosphere discussed in the next chapter.

REFERENCES

1. M. Nicolet and P. Mange, *J. Geophys. Res.* **59**, 16 (1954).
2. E. T. Byram, T. A. Chubb, and H. Friedman, in *The Threshold of Space*, (M. Zelikoff, ed.), p. 211. Pergamon, Oxford, 1957.
3. E. B. Meadows and J. W. Townsend, *Ann. Géophys.* **14**, 80 (1958).
4. A. A. Pokhunkov, *Planet. Space Sci.* **9**, 269 (1962).
5. J. E. Kupperian, E. T. Byram, T. A. Chubb, and H. Friedman, *Ann. Géophys.* **14**, 329 (1958).

6. S. Chapman and T. G. Cowling, *The Mathematical Theory of Non-Uniform Gases*, 3rd ed. Cambridge Univ. Press, London and New York, 1970.
7. F. D. Colegrove, F. S. Johnson, and W. B. Hanson, *J. Geophys. Res.* **71**, 2227 (1968).
8. H. Lettau, in *Compendium of Meteorology* (T. F. Malone, ed.), p. 320. Amer. Meteorolog. Soc., Boston, Massachusetts, 1951.
9. J. E. Blamont and J. Barat, *Ann. Géophys.* **23**, 173 (1967).
10. D. R. Bates and T. N. L. Patterson, *Planet. Space Sci.* **5**, 257 (1961).
11. G. Kockarts and M. Nicolet, *Ann. Géophys.* **18**, 269 (1962).
12. P. S. Epstein, *Gerland's Beitr. Geophys.* **35**, 153 (1932).
13. P. Mange, *J. Geophys. Res.* **62**, 279 (1957).
14. J.-E. Blamont and J. Barat, *Ann. Géophys.* **24**, 375 (1968).
15. T. J. Keneshea and S. P. Zimmerman, *J. Atmos. Sci.* **27**, 831 (1970).
16. F. S. Johnson and B. Gottlieb, *Planet. Space Sci.* **18**, 1707 (1970).
17. P. B. Hays and J. J. Olivero, *Planet. Space Sci.* **18**, 1729 (1970).
18. S. P. Zimmerman, A. C. Faire, and E. A. Murphy, *Space Res.* **12**, 615 (1972).
19. J. O. Hirschfelder, C. F. Curtiss, and R. B. Bird, *Molecular Theory of Gases and Liquids*. Wiley, New York, 1954.
20. E. A. Mason and T. R. Marrero, *Advan. At. Mol. Phys.* **6**, 155 (1970).
21. S. Weissman and E. A. Mason, *J. Chem. Phys.* **36**, 791 (1962).
22. J. T. Vanderslice, S. Weissman, and E. A. Mason, *Phys. Fluids* **5**, 153 (1961).
23. L. Mata, Aeronomica Acta A 59, IAS, Brussels (1969).
24. K. E. Grew and T. L. Ibbs, *Thermal Diffusion in Gases*. Cambridge Univ. Press, London and New York, 1952
25. E. A. Mason, R. J. Munn, and F. J. Smith, *Advan. At. Mol. Phys.* **2**, 33 (1966).
26. G. Kockarts, *Acad. Roy. Belg., Bull. Cl. Sci.* **49**, 1135 (1963).
27. P. Mange, *Ann. Géophys.* **11**, 153 (1955).
28. P. Mange, *Ann. Géophys.* **17**, 277 (1961).
29. G. Kockarts, *Ann. Géophys.* **22**, 161 (1966).
30. M. Nicolet, *Geophys. J. Roy. Astronom. Soc.* **15**, 157 (1968).
31. M. Nicolet, *Ann. Géophys.* **13**, 1 (1957).
32. D. R. Bates and M. R. C. McDowell, *J. Atmos. Terr. Phys.* **16**, 393 (1959).
33. J. H. Jeans, *The Dynamical Theory of Gases*. Dover, New York, 1954.
34. S. K. Lew and S. V. Venkateswaran, *J. Atmos. Sci.* **22**, 623 (1965).
35. M. Liwshitz, *J. Atmos. Sci.* **23**, 816 (1966).
36. S. K. Lew and S. V. Venkateswaran, *J. Atmos. Sci.* **23**, 817 (1966).
37. M. Liwshitz and S. F. Singer, *Planet. Space Sci.* **14**, 541 (1966).
38. J. W. Chamberlain and F. J. Campbell, *Astrophys. J.* **149**, 687 (1967).
39. J. W. Chamberlain, *Astrophys. J.* **155**, 711 (1969).
40. R. T. Brinkmann, *Planet. Space Sci.* **18**, 449 (1970).
41. H. Fahr, in *Physics of the Upper Atmosphere* (F. Verniani, ed.), p. 348. Editrice Compositori, Bologna, 1971.
42. J. W. Chamberlain and G. R. Smith, *Planet. Space Sci.* **19**, 675 (1971).
43. R. T. Brinkmann, *Planet. Space Sci.* **19**, 791 (1971).
44. S. Chapman and E. A. Milne, *Quart. J. Roy. Meteorol. Soc.* **46**, 357 (1920).
45. A. V. Mironov, V. S. Prokudina, and N. N. Shefov, *Spectral Electropho. Radar Res. Aurora Airglow* **1**, 20 (1959).
46. M. Nicolet, *J. Geophys. Res.* **66**, 2263 (1961).
47. G. M. Keating, J. A. Mullins, and E. J. Prior, *Space Res.* **10**, 439 (1970).

48. G. E. Cook, *Planet. Space Sci.* **15**, 627 (1967).
49. C. A. Reber and M. Nicolet, *Planet. Space Sci.* **13**, 617 (1965).
50. C. A. Reber, D. N. Harpold, R. Horowitz, and A. E. Hedin, *J. Geophys. Res.* **76**, 1845 (1971).
51. W. T. Kasprzak, *J. Geophys. Res.* **74**, 894 (1969).
52. D. Muller and G. Hartmann, *J. Geophys. Res.* **74**, 1287 (1969).
53. A. B. Christensen, T. N. L. Patterson, and B. A. Tinsley, *J. Geophys. Res.* **76**, 1764 (1971).
54. H. Craig and W. B. Clarke, *Earth Planet. Sci. Lett.* **9**, 45 (1970).
55. F. S. Johnson and B. Gottlieb, *Planet. Space Sci.* **18**, 1707 (1970).
56. R. R. Hodges, Jr., *Planet. Space Sci.* **20**, 103 (1972).
57. J. R. McAfee, *Planet. Space Sci.* **15**, 599 (1967).
58. E. Roth, *J. Chim. Phys., Paris* **60**, 339 (1963).
59. R. Hageman, G. Nief, and E. Roth, *Tellus* **22**, 712 (1970).
60. J. H. Hoffman, *Science* **155**, 322 (1967).
61. J. H. Hoffman, C. Y. Johnson, J. C. Holmes, and J. M. Young, *J. Geophys. Res.* **74**, 6281 (1969).
62. E. C. Bruner, Jr. and T. E. Wilson, *J. Geophys. Res.* **74**, 6491 (1969).
63. R. A. Jones, E. C. Bruner, Jr., and W. E. Rense, *J. Geophys. Res.* **75**, 1849 (1970).
64. G. Kockarts, *Space Res.* **12**, 1047 (1972).
65. G. Kockarts, in *Physics of the Upper Atmosphere* (F. Verniani, ed.), p. 330. Editrice Compositori, Bologna, 1971.
66. T. M. Donahue, *J. Geophys. Res.* **74**, 1128 (1969).
67. M. B. McElroy and D. M. Hunten, *J. Geophys. Res.* **74**, 1720 (1969).
68. G. Kockarts and M. Nicolet, *Ann. Géophys.* **19**, 370 (1963).
69. T. M. Donahue, *Ann. Géophys.* **22**, 175 (1966).
70. B. A. Tinsley, in *Atmospheric Emissions* (B. M. McCormac and A. Omholt, eds.), p. 539. Van Nostrand-Reinhold, Princeton, New Jersey, 1969.
71. R. R. Meier and P. Mange, *Planet. Space Sci.* **18**, 803 (1970).
72. R. R. Meier and D. K. Prinz, *J. Geophys. Res.* **75**, 6969 (1970).
73. G. E. Thomas, *J. Geophys. Res.* **68**, 2639 (1963).
74. M. Nicolet, in *Mesospheric Models and Related Experiments* (G. Fiocco, ed.), p. 1. Reidel Publ., Dordrecht, The Netherlands, 1971.
75. T. N. L. Patterson, *Rev. Geophys.* **8**, 461 (1970).
76. W. B. Hanson and T. N. L. Patterson, *Planet. Space Sci.* **11**, 1035 (1963).
77. T. M. Donahue and J. R. McAfee, *Planet. Space Sci.* **12**, 1045 (1964).
78. T. N. L. Patterson, *Planet. Space Sci.* **14**, 425 (1966).
79. R. R. Hodges, Jr. and F. S. Johnson, *J. Geophys. Res.* **73**, 7307 (1968).
80. H. C. Brinton and H. G. Mayr, *J. Geophys. Res.* **76**, 6198 (1971).

CHAPTER 16

The Neutral Exosphere

16.1 Introduction

The first far-ultraviolet study of the night sky [1] in 1955 showed the presence of a substantial Lyman α emission, which indicated the existence of a large cloud of atomic hydrogen surrounding the earth. That such an envelope of light gas should be present in these regions can be predicted from the equations used in the last chapter to describe the altitude distribution of the constituents of the heterosphere. However, physical behavior of light gases such as H and He is greatly different from that for the heavier gases such as O, O_2, and N_2 as a result of gravitational escape.

In the heterosphere the major and minor constituents are subject to molecular diffusion in the earth's gravitational field. There the collision frequency between particles is large enough to ensure to high accuracy the existence of a Maxwellian velocity distribution. However, the mean free path for collisions varies inversely as the gas concentration, so that there is an exponential increase in free path with altitude. At sufficiently high altitudes collisions become infrequent and the velocity distribution function is no longer Maxwellian. This altitude corresponds to a *critical level* which defines the beginning of the exosphere. Particles entering the exosphere with sufficient energy are able to escape from the earth's gravitational field. This outwards flux alters the density distribution of the escaping gas so that the simple equation of hydrostatic equilibrium no longer applies. For the temperatures found in the earth's upper atmosphere escape is limited to hydrogen and helium.

In this chapter the general principles of exosphere behavior are discussed. These results are then applied to the distributions of light gases in the earth's atmosphere.

During the nineteenth century, it was shown [2, 3] that particles with sufficiently high velocities would escape from a planetary gravitational field if the ambient medium was such that collisions were infrequent. At the beginning of the present century, the first analysis of escape using Maxwellian velocity distributions [4, 5] was made and the effect of the earth's rotation was introduced [5]. It is now known that in addition to these effects the vertical distribution of an exosphere constituent is related to the interactions between the neutral and ionized gases, to the presence of a magnetic field, and to the winds prevailing in the upper atmosphere.

With a *Maxwellian velocity distribution*, the concentrations, n, of an exospheric constituent above the critical level located at a geocentric distance r_c is expressed by

$$n(y) = n(1) \exp[-E(1 - y)] \tag{16.1}$$

where

$$E = r_c/H(r_c) \tag{16.2}$$

and

$$y = r_c/r. \tag{16.3}$$

Equation (16.1) is the usual hydrostatic distribution characterized by the scale height $H(r_c) = kT(r_c)/mg(r_c)$. At the critical level $y = 1$ and at infinite distance $y = 0$. Such a result can be criticized [6], however, since the collision frequency in the exosphere is not high enough to provide a Maxwellian distribution and Eq. (16.1) cannot represent the correct vertical distribution. To do the problem correctly, a correction factor, based on the different types of trajectories of exospheric particles, must be deduced from an exospheric theory. In such an analysis it is of fundamental importance to consider the possible existence and importance of different types of trajectories, since the neutral gas is simultaneously subject to solar ultraviolet radiation and interaction with charged particles.

In a gravitational field the different types of trajectories above the critical level can be divided into two categories corresponding to

I. The particles which cross the critical level, and

II. The particles which never reach the critical level.

Four types of particles belong to the *first category* (see *Fig. 16.1*):

1. the ballistic particles leaving the critical level with a velocity less than the escape velocity,
2. the ballistic particles coming back to the critical level with a velocity less than the escape velocity,
3. the hyperbolic or parabolic particles escaping from the gravitational field, and
4. the hyperbolic or parabolic particles coming from interplanetary space.

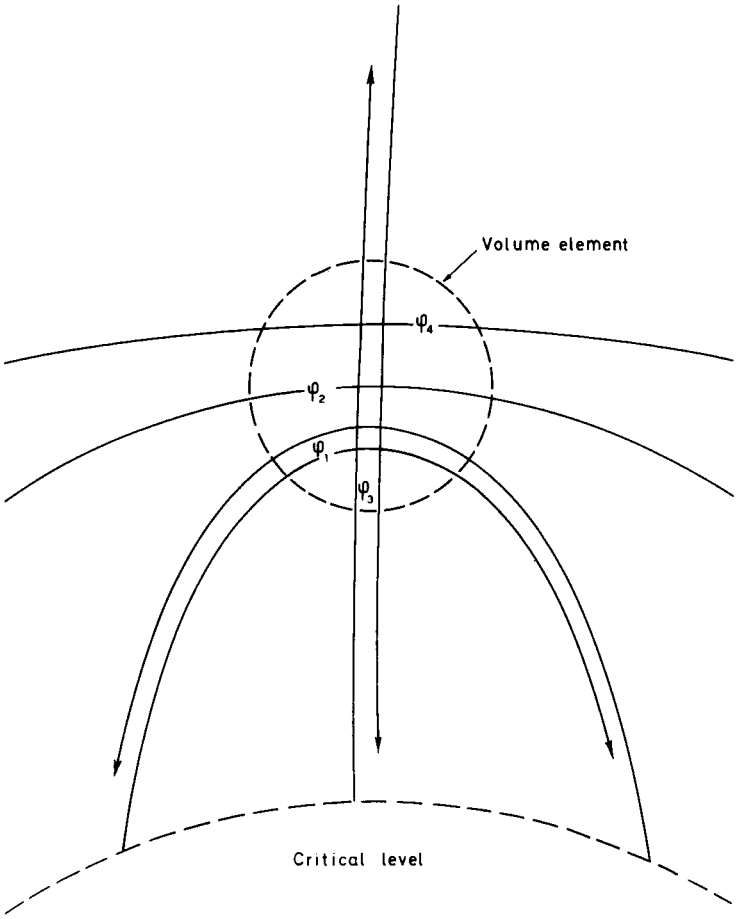


Fig. 16.1 Types of particles which can exist in an elementary volume above the critical level: ϕ_1 ballistic, ϕ_2 satellite, ϕ_3 hyperbolic, ϕ_4 external hyperbolic.

In a steady state the first two types of particles are of equal abundance and represent a fraction ϕ_1 of the hydrostatic concentration. In the same way, the hyperbolic particles crossing the critical level represent a fraction ϕ_3 of the total hydrostatic concentration.

The *second category* is composed of two types of particles:

1. the satellite particles whose perigees are above the critical level; they represent a fraction ϕ_2 of the total hydrostatic concentration, and
2. the external hyperbolic particles which come from interplanetary space; they represent a fraction ϕ_4 of the total hydrostatic concentration.

When all types of particles are present in the exosphere, the following relation is valid at all heights:

$$\phi_1 + \phi_2 + \phi_3 + \phi_4 = 1. \tag{16.4}$$

Two methods can be used to compute the fractions, ϕ_i. The first has been introduced by Öpik and Singer [6–8] and is based on Liouville's theorem. Öpik and Singer [7, 8] obtained integral expressions for the fractions ϕ_1 and $\frac{1}{2}\phi_3$ since they omitted particles coming from the interplanetary space with velocities greater than the escape velocity. Analytical expressions have been deduced [9–11] for these types of particles.

The second method, introduced by Johnson and Fish [12], is based on solutions for the Boltzmann equation. Since it is not possible to create satellite and external hyperbolic particles at the critical level, it is necessary to use the Boltzmann equation to compute the fractions ϕ_2 and ϕ_4. In addition, the same equation can be used to obtain the fractions ϕ_1 and ϕ_3. Although the methods based on Liouville's theorem and Boltzmann's equation are different, they lead to the same result for the fractions ϕ_1 and ϕ_3 which cross the critical level.

16.2 Method Based on Liouville's Theorem

According to Liouville's theorem, the distribution function, $f(r, v)$, of the velocities v at a geocentric distance r is related to the distribution function $f(r_c, v_c)$ at the critical level by

$$f(r, v) = f(r_c, v_c). \tag{16.5}$$

The quantities (r, v) are related to the critical level values (r_c, v_c) by energy

and momentum conservation. When a particle leaves the critical level r_c with a velocity v_c making an angle θ_c with the vertical, it is possible to compute the value of v and the angle θ at a geocentric distance r using the relations

$$v = [v_c^2 - 2g_c r_c(1 - y)]^{1/2} \tag{16.6}$$

and

$$v \sin \theta = v_c y \sin \theta_c \tag{16.7}$$

where g_c is the gravitational acceleration at the critical level and $y = r_c/r$. For a spherical symmetry, the concentration $n(r)$ at a geocentric distance r is then given by

$$n(r) = 4\pi \int\int f(r, v)v^2 \sin \theta \, dv \, d\theta \tag{16.8}$$

or, using (16.5), by

$$n(r) = 4\pi \int\int f(r_c, v_c)v^2 \sin \theta \, dv \, d\theta. \tag{16.9}$$

With the conservation laws (16.6) and (16.7), it is now possible to transform (16.9) into an integration over the velocity v_c and the angle θ_c at the critical level. This leads to

$$n(r) = 4\pi y^2 \int\int \frac{f(r_c, v_c)v_c^3 \cos \theta_c \sin \theta_c \, d\theta_c \, dv_c}{[v_c^2(1 - y^2 \sin^2 \theta_c) - 2g_c r_c(1 - y)]^{1/2}}. \tag{16.10}$$

The integration limits over the angle θ_c are given by

$$0 \leq \theta_c \leq \pi/2. \tag{16.11}$$

The integration limits over the velocity v_c can be obtained by expressing the fact that at the critical level r_c the particle has a velocity such that it can reach the altitude r, i.e., $v^2 \cos^2 \theta \geq 0$. Using Eqs. (16.6) and (16.7), this condition can be written

$$v_c \geq au \tag{16.12}$$

where

$$u^2 = (1 - y)/(1 - y^2 \sin^2 \theta_c) \tag{16.13}$$

and

$$a^2 = 2g_c r_c. \tag{16.14}$$

The quantity a can be recognized as the escape velocity at the critical level r_c.

In order to compute the concentration distribution from (16.10), it is necessary to determine the velocity distribution function $f(r_c, v_c)$ at the critical level. This is actually a very complex problem which has not been completely solved. Atomic hydrogen, for example, is subject to large diffusion fluxes in the thermosphere and finally escapes from the atmosphere. The velocity distribution function is therefore affected simultaneously by the vertical transport and by the depletion of particles with velocities greater than 11 km sec^{-1}. Several authors have studied this problem using mainly Monte Carlo techniques. Their results are somewhat different since the physical models did not have the same characteristics. It seems, however, that the escape flux computed from a Maxwellian velocity distribution function can be decreased by approximately 25% for atomic hydrogen [13, 14].

Two cases for the exospheric concentration distribution will be considered here. First, it will be assumed that at the critical level the velocity distribution function is Maxwellian, i.e., hyperbolic particles are coming from the interplanetary space. Second, a truncated Maxwellian distribution will be used in order to eliminate the particles coming from infinity and crossing the critical level.

16.2.1 Complete Maxwellian Velocity Distribution

At the critical level, the velocity distribution function can be written as

$$f(r_c, v_c) = n(1)(m/2\pi kT)^{3/2} \exp(-mv_c^2/2kT) \tag{16.15}$$

where $n(1)$ is the critical level concentration, m is the particle mass, k is Boltzmann's constant, and T is the temperature. The distribution function given by (16.15) corresponds to a steady state in which the ballistic particles reaching the critical level are in equal number. Since this distribution is isotropic, the two last types of particles of the first category (see Section 16.1) are present in the same amount. Therefore, introducing Eq. (16.15) into (16.10) one obtains the concentration

$$n_1 + n_3 = 4\pi n(1) y^2 \int_0^{\pi/2} \sin\theta_c \cos\theta_c \, J(\theta_c) \, d\theta_c \tag{16.16}$$

with

$$J(\theta_c) = \left(\frac{m}{2\pi kT}\right)^{3/2} \int_{au}^{\infty} \frac{v_c^3 \exp(-mv_c^2/2kT) \, dv_c}{[v_c^2(1 - y^2 \sin^2\theta_c) - 2g_c r_c(1 - y)]^{1/2}}. \tag{16.17}$$

Using Eqs. (16.2), (16.13), (16.14) and with the transformation $w = v_c/a$,

it can be shown that

$$ma^2/2kT = E, \tag{16.18}$$

$$mv_c^2/2kT = Ew^2, \tag{16.19}$$

and

$$v_c^2(1 - y^2 \sin^2 \theta_c) - 2g_c r_c(1 - y) = a^2(1 - y^2 \sin^2 \theta_c)(w^2 - u^2). \tag{16.20}$$

Therefore,

$$J(\theta_c) = \frac{(E/\pi)^{3/2}}{(1 - y^2 \sin^2 \theta_c)^{1/2}} \int_u^\infty \frac{w^3 \exp(-Ew^2)\, dw}{(w^2 - u^2)^{1/2}} \tag{16.21}$$

or

$$J(\theta_c) = \frac{(1 + 2Eu^2) \exp(-Eu^2)}{4\pi(1 - y^2 \sin^2 \theta_c)^{1/2}}. \tag{16.22}$$

Introducing (16.22) into (16.16) one finally obtains after integration

$$n_1(y) + n_3(y) = n(1) \exp[-E(1 - y)]\{1 - (1 - y^2)^{1/2} \exp[-Ey^2/(1 + y)]\}. \tag{16.23}$$

This expression [15] gives the concentration of the ballistic (n_1) and hyperbolic (n_3) particles crossing the critical level where a complete Maxwellian velocity distribution has been adopted. At infinity ($y = 0$), Eq. (16.23) leads to a zero concentration; this is not the case for a pure hydrostatic distribution.

16.2.2 Truncated Maxwellian Velocity Distribution

The introduction of hyperbolic particles coming from interplanetary space and crossing the critical level in a way such that the velocity distribution function becomes Maxwellian is rather arbitrary. Therefore, several authors [6, 8, 11, 12] have eliminated these particles by a truncation of the velocity distribution function. Actually the distribution function (16.15) has to be modified for the particles with velocities greater than the escape velocity given by Eq. (16.14). Since the distribution (16.15) implies equal concentrations for incoming and outgoing particles with velocities greater than $(2g_c r_c)^{1/2}$, the incoming hyperbolic particles can be eliminated by defining the velocity distribution function $f(r_c, v_c)$ in the following way:

$$f(r_c, v_c) = \alpha n(1)(m/2\pi kT)^{3/2} \exp(-mv_c^2/2kT) \tag{16.24}$$

with

$$\alpha = 1 \qquad \text{for} \quad v_c < a \tag{16.25}$$

and

$$\alpha = \tfrac{1}{2} \qquad \text{for} \quad v_c \geq a. \tag{16.26}$$

This distribution function will then lead to the concentration $n_1(y)+0.5n_3(y)$; i.e., the three first types of particles of the first category described in Section 16.1. With the previous notations, Eq. (16.10) leads to

$$J(\theta_c) = \frac{(1/8\pi)\exp(-Eu^2)\{(1 + 2Eu^2)[1 + \phi(x)] - x\phi'(x)\}}{(1 - y^2 \sin^2 \theta_c)^{1/2}} \tag{16.27}$$

with

$$x = E(1 - u^2), \tag{16.28}$$

$$\phi(x) = (2/\pi^{1/2}) \int_0^x \exp(-t^2)\, dt, \tag{16.29}$$

$$\phi'(x) = (2/\pi^{1/2}) \exp(-x^2). \tag{16.30}$$

Introducing this expression for $J(\theta_c)$ in an equation similar to (16.16) gives

$$n_1(y) + 0.5n_3(y) = 0.5n(1)(1 - y)^{1/2} \int_{(1-y)^{1/2}}^{(1+y)^{1/2}} \frac{\exp(-Eu^2)\{(1 + 2Eu^2)[1 + \phi(x)] - x\phi'(x)\}\, du}{u^2}. \tag{16.31}$$

Integration of (16.31) finally leads to

$$n_1(y) + 0.5n_3(y) = 0.5n(1)\exp[-E(1 - y)] \times \left\{1 + \psi(Ey) - (1 - y)^{1/2} \exp\left(-\frac{Ey^2}{1 + y}\right)\left[1 + \psi\left(\frac{Ey}{1 + y}\right)\right]\right\} \tag{16.32}$$

where the function $\psi(z)$ is defined by

$$\psi(z) = \phi(z^{1/2}) - 2(z/\pi)^{1/2} \exp(-z). \tag{16.33}$$

Expression (16.32) gives the concentration of all the ballistic particles and of the escaping hyperbolic particles. Öpik and Singer [8] obtained values for the correction factor to the hydrostatic equation by numerical integration of Eq. (16.10). Other authors [9–11] deduced analytical expressions equivalent to (16.32).

With a complete Maxwellian velocity distribution function at the critical level, Eq. (16.23) shows that $n_1 + n_3 = n(1)$, i.e., the concentration at the critical level. With the truncated Maxwellian distribution function, Eq. (16.32) indicates, however, that at the critical level ($y = 1$), the concentra-

tion is given by

$$n_1 + 0.5n_3 = 0.5n(1)[1 + \psi(E)]. \tag{16.34}$$

This expression shows that the difference $n(1) - (n_1 + 0.5n_3)$ increases when E decreases. For a fixed critical level a decrease of $E = r_c/H_c$ corresponds either to an increase of the temperature or to a decrease of the atomic mass. This means that the discontinuity introduced at the critical level by a truncated distribution is the most important for atomic hydrogen.

16.3 Method Based on Boltzmann's Equation

With the Boltzmann equation it is possible to compute the concentrations n_1, n_2, n_3, n_4, of the four types of particles defined in Section 16.1. When a particle reaches a point P in the exosphere, it will be considered as belonging to one of the four types if it has at that point a velocity characterizing one of the four types of particles. Therefore, the concentration $n_i(r)$ is given by

$$n_i(r) = 4\pi \iint f(r, v)v^2 \sin\theta \, d\theta \, dv \tag{16.35}$$

when the integration is extended over the velocity domain of the particles of the type i. Integral expressions have been deduced [12, 16] for the four types of particles. It is, however, possible to obtain analytical expressions for each type of particle.

At a certain point P the energy and momentum conservation equations can be written

$$v^2 - a^2y = v_P^2 - a^2y_P \tag{16.36a}$$

and

$$rv \sin\theta = r_P v_P \sin\theta_P. \tag{16.36b}$$

When v^2 is negative, zero, or positive at infinity, the trajectory is elliptic, parabolic, or hyperbolic. Equation (16.36a) leads to the following conditions:

$$v_P^2 < a^2y_P \quad \text{for elliptic trajectories} \tag{16.37}$$

$$v_P^2 \geq a^2y_P \quad \text{for parabolic or hyperbolic trajectories.} \tag{16.38}$$

Another criterion must be established in order to know whether or not a particle crosses the critical level. This can be done by determining the angle $\theta = \omega$ for which a particle, with a velocity v_P at the point P, has a trajectory tangent to the critical level r_c. When θ is smaller than ω, the particle crosses the critical level. At the tangent point $y = 1$ and $\theta = \pi/2$

and Eqs. (16.36a) and (16.36b) become

$$v^2 - a^2 = v_P^2 - a^2 y_P \tag{16.39}$$

$$r_c v = r_P v_P \sin \omega. \tag{16.40}$$

Therefore

$$v_P^2 \sin^2 \omega = y_P^2 [v_P^2 + a^2(1 - y_P)]. \tag{16.41}$$

If the velocity v_P is decomposed into its radial (v_r) and transversal (v_t) components, Eq. (16.41) leads to

$$(1 - y_P^2) v_t^2 - y_P^2 v_r^2 = a^2 y_P^2 (1 - y_P). \tag{16.42}$$

In the plane (v_r, v_t) this equation always defines a hyperbola since at any point P in the exosphere, $0 < y_P < 1$. The inside central region of the hyperbola corresponds to the trajectories crossing the critical level. According to Eqs. (16.37) and (16.38) the limit between elliptic and hyperbolic particles is given by

$$v_r^2 + v_t^2 = a^2 y_P. \tag{16.43}$$

The curves (16.42) and (16.43) fix the limits of the domains D_1, D_2, D_3, and D_4 for the particles with concentration n_1, n_2, n_3, and n_4. At any point P in the exosphere, these domains are similar to the example given in *Fig. 16.2.* The domain D_1 for the ballistic particles is inside the circle and the hyperbola; the satellite particle domain is inside the circle and outside the hyperbola; the domain D_3 for the hyperbolic particles is outside the circle and inside the hyperbola; and the external hyperbolic particles domain D_4 is outside the circle and the hyperbola.

Since the domains of existence are now defined for the different types of particles, the vertical distribution for the type i can now be obtained by introducing a Maxwellian distribution in Eq. (16.35) and by integrating over the domain D_i.

The results are

$$n_2(y) = n(1)(1 - y^2)^{1/2} \psi[Ey/(1 + y)] \exp[-Ey^2/(1 + y)], \tag{16.44}$$

$$n_1(y) + n_2(y) = n(1) \psi(Ey) \exp[-E(1 - y)], \tag{16.45}$$

$$n_4(y) = n(1)(1 - y^2)^{1/2} \{1 - \psi[Ey/(1 + y)]\} \exp[-Ey^2/(1 + y)], \tag{16.46}$$

$$n_3(y) + n_4(y) = n(1)[1 - \psi(Ey)] \exp[-E(1 - y)] \tag{16.47}$$

where $\psi(x)$ is defined by Eq. (16.33).

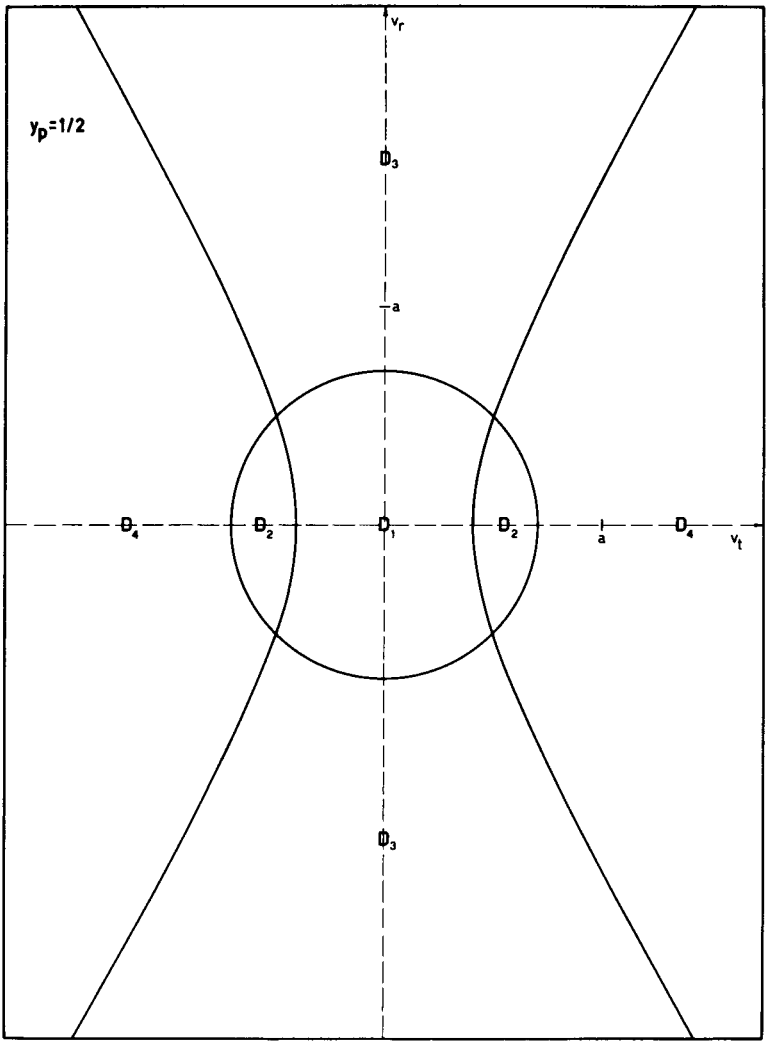


Fig. 16.2 Domains of existence for the different particles: D_1 ballistic, D_2 satellite, D_3 hyperbolic, and D_4 external hyperbolic particles.

It is easy to work with these formulas since the second term of Eq. (16.33) is half of the second derivative of the error function with $x^{1/2}$ as argument.

For $n_1 + n_3$ and $n_1 + 0.5n_3$, Eqs. (16.44)–(16.47) lead to expressions which are identical to those obtained with Liouville's theorem. This is a consequence of the fact that a Maxwellian velocity distribution is also a solution of the Boltzmann equation when the collision term is neglected.

When the four types of particles are present in the exosphere, Eqs. (16.45) and (16.47) clearly show that the vertical distribution of an exosphere constituent is given by the hydrostatic equation

$$\sum_{i=1}^{4} n_i = n(1) \exp[-E(1 - y)]. \tag{16.48}$$

Therefore, any departure from a hydrostatic distribution can be interpreted by the absence of one or several types of particles. This problem will be discussed in more detail in Section 16.6. For practical computations, it is often useful to represent the different types of particles by their fraction $\phi_i = n_i / \sum_{i=1}^{4} n_i$ of the hydrostatic distribution. These fractions are given by the following expressions:

for ballistic particles:

$$\phi_1 = \psi(Ey) - (1 - y^2)^{1/2} \psi[Ey/(1 + y)] \exp[-Ey^2/(1 + y)] \tag{16.49}$$

for satellite particles:

$$\phi_2 = (1 - y^2)^{1/2} \psi[Ey/(1 + y)] \exp[-Ey^2/(1 + y)] \tag{16.50}$$

for hyperbolic particles:

$$\phi_3 = 1 - \psi(Ey) - (1 - y^2)^{1/2} \exp[-Ey^2/(1 + y)]\{1 - \psi[Ey/(1 + y)]\} \tag{16.51}$$

for external hyperbolic particles:

$$\phi_4 = (1 - y^2)^{1/2} \exp[-Ey^2/(1 + y)]\{1 - \psi[Ey/(1 + y)]\}. \tag{16.52}$$

16.4 Critical Level

With a given velocity distribution function, it is possible to compute an escape flux at any height in the atmosphere. The effective value for the escape flux depends, however, on the number of collisions of the particles having velocities greater than the escape velocity. Therefore, Jeans [17] and Spitzer [18] defined the critical level as the height at which particles with great velocities have a probability $1/e$ to escape from the gravitational field without suffering any further collision. This probability is directly related to the mean free path of the particles. For a Maxwellian velocity distribution, the mean free path generally depends on the speed of the particles. When a particle 1 has a speed v_1, its mean free path L_1 is given by [19]

$$L_1(v_1) = v_1/(\nu_{11} + \nu_{12} + \nu_{13} + \cdots) \tag{16.53}$$

where ν_{1j} is the collision frequency of particle 1 with the particles of j other elements present in the ambient medium. The velocity dependent collision frequencies ν_{1j} are given by

$$\nu_{1j} = n_j Q_{1j}(2kT/\pi m_j)^{1/2}[\exp(-x_j^2) + (\pi^{1/2}/2)(2x_j + 1/x_j)\phi(x_j)] \quad (16.54)$$

where n_j is the concentration of the component with mass m_j and Q_{1j} is the collision cross section between particle 1 and j. The argument x_j of the error function $\phi(x_j)$ is given by $x_j = v_1(m_j/2kT)^{1/2}$. With Eq. (16.54), the mean free path can then be written

$$L_1(v_1) = \pi^{1/2}\left\{\sum_j n_j Q_{1j} F(x_j)/x_j^2\right\}^{-1} \quad (16.55)$$

where the function $F(x_j)$ is defined by

$$F(x_j) = x_j \exp(-x_j^2) + (\pi^{1/2}/2)(2x_j^2 + 1)\phi(x_j). \quad (16.56)$$

For particles with velocities greater than the escape velocity ($\sim$11 km sec^{-1}) a good approximation for Eq. (16.56) is given by

$$F(x_j)/x_j^2 \simeq \pi^{1/2}. \quad (16.57)$$

The mean free path for high velocity particles can therefore be written

$$L_1 = \left(\sum_j n_j Q_{1j}\right)^{-1}. \quad (16.58)$$

With the atmospheric models described in Chapter 14 it is possible to compute the mean free path as a function of height. *Figure 16.3* gives the vertical distribution for the atomic hydrogen mean free path computed for several thermopause temperatures with a mean collision cross section of 2.8×10^{-15} cm^{-2}. The mean free path increases rapidly with height, since the total concentration decreases exponentially. At a specific height the mean free path increases when the thermopause temperature decreases. At 500 km altitude, the atomic hydrogen mean free path is of the order of 15 km for a thermopause temperature of 2000°K, whereas, it reaches a value of 750 km for a temperature of 750°K. The altitudes at which the mean free path is equal to the atmospheric scale height are also shown on Fig. 16.3. This condition is often adopted as a definition for the critical level [18]. It should be noted, however, that expression (16.58) has been deduced for the case when the concentrations do not change along a mean

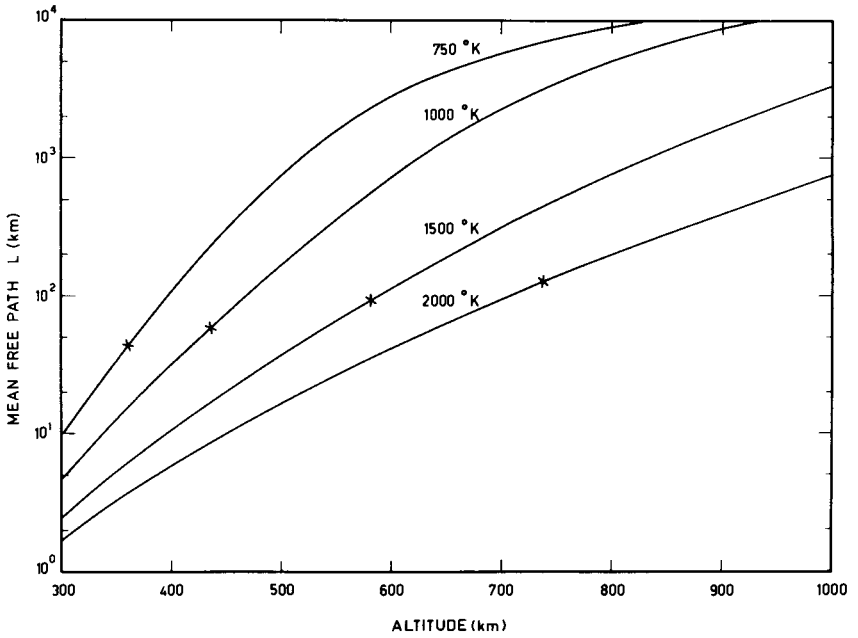


Fig. 16.3 Vertical distribution of the atomic hydrogen mean free path for several thermopause temperatures. The crosses indicate the altitude where the mean free path is equal to the atmospheric scale height ($H = L$).

free path. The results shown on Fig. 16.3 are therefore only valid along a line of equal density.

For the escaping particles, it is nevertheless necessary to consider the *vertical* mean free path. The probability P for an infinite mean free path above the critical level r_c is given by

$$P = \exp\left(-\int_{r_c}^{\infty} dr/L_1\right). \tag{16.59}$$

When the concentration is constant along the trajectory, Eq. (16.59) shows that the probability for an infinite mean free path is zero. When the concentration decreases with distance, the probability P can be different from zero and the total content of the different species must be known. Since the velocity distribution function is not Maxwellian in the exosphere, a correction factor has to be applied to the approximation $\int_{r_c}^{\infty} n_j\, dz = n_{jc}H_{jc}$. With a correction factor G_j defined by

$$G_j = \int_{r_c}^{\infty} n_j\, dr/n_{jc}H_{jc} \tag{16.60}$$

Eq. (16.59) can be written

$$P = \exp\left(-\sum_j Q_{1j} n_{jc} H_{jc} G_j\right). \tag{16.61}$$

The correction factor G_j becomes important for atomic hydrogen (see Section 16.8). In the height range where Eq. (16.61) has to be used, atomic hydrogen is however still a minor constituent and G_j can be taken equal to one. For an atmosphere with a single element, Spitzer [18] fixed the critical level at a height where

$$n_{1c} H_{1c} = Q_{11}^{-1}. \tag{16.62}$$

This level actually corresponds to an altitude where the particles s have a

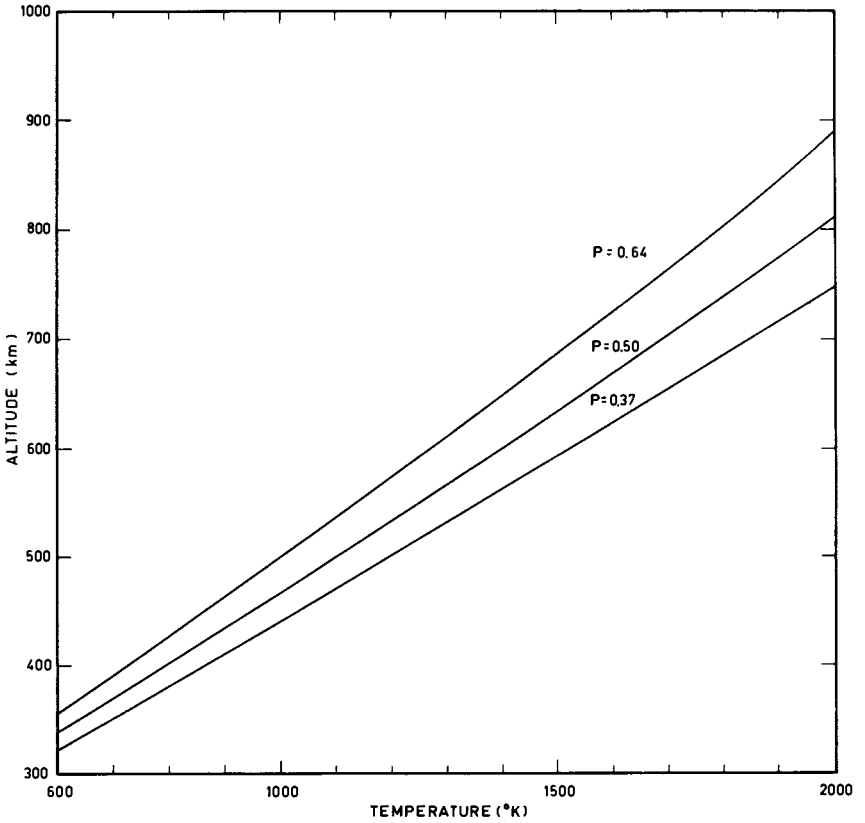


Fig. 16.4 Altitude of the critical level as a function of the thermopause temperature for the escape probabilities $P = 0.37$, 0.50, and 0.64.

probability e^{-1} for an infinite mean free path. This level is also the altitude where the horizontal mean free path is equal to the atmospheric scale height. Equation (16.61) shows that the altitude of the critical level depends on an arbitrary value of the probability P. This reflects the physical fact that the critical level is not a sharp transition between the heterosphere and the exosphere.

With an escape probability $P = (0.50 \pm 0.14)$, *Fig. 16.4* shows the altitude of the critical level as a function of the thermopause temperature. For a fixed value of P, the altitude of the critical level always increases the thermopause temperature. From Fig. 16.4 it can also be seen that the altitude of the critical level is approximately a linear function of the thermopause temperature. Round figures for the critical level height are given in *Table 16.1*.

TABLE 16.1

ALTITUDE OF THE CRITICAL LEVEL

Temperature (°K):	2000	1750	1500	1250	1000	750
Altitude (km):	800	700	650	550	450	400

With an escape probability of (0.50 ± 0.14) the critical level at 2000°K is determined within ± 50 km and at 750°K the uncertainty is of the order of ± 25 km. It is therefore necessary to know the effect of such an uncertainty on the escape flux, which is usually evaluated at the critical level.

The number of atoms escaping per unit time through a unit surface can be written [20]

$$F_c = n_c(g_c/2\pi)^{1/2}(r_c/H_c^{1/2})[1 + (H_c/r_c)]e^{-r_c/H_c} \tag{16.63}$$

where n_c and H_c are respectively the concentration and the scale height (kT/mg_c) of the escaping element at the critical level located at a geocentric distance r_c. With the notations of Section 16.1, expression (16.63) can be transformed into

$$F_c = n_c(g_c r_c/2\pi)^{1/2}[(E + 1)/E^{1/2}]e^{-E}. \tag{16.64}$$

If two arbitrary critical levels r_1 and r_2 are chosen for the same thermopause temperature, the ratio between the escape fluxes F_1 and F_2 is given by

$$\frac{F_1}{F_2} = \frac{r_2}{r_1}\left[\frac{E_1 + 1}{E_1 + (r_2/r_1)}\right]. \tag{16.65}$$

With the values given in Table 16.1, a variation of ± 50 km leads only to a change of the order of 1% for the escape flux. Therefore, the flux can be computed without an exact knowledge of the altitude of the critical level.

To complete the discussion, it is now necessary to analyze the behavior of the different types of particles at the critical level. According to Eqs. (16.50) and (16.52), there are no satellite and no external hyperbolic particles at the critical level ($\phi_2 = \phi_4 = 0$). The fractions of ϕ_1 and ϕ_3 of the particles crossing the critical level are given by

$$\phi_1 = \psi(E) \tag{16.66}$$

and

$$\phi_3 = 1 - \psi(E) \tag{16.67}$$

where the function $\psi(E)$ is defined by Eq. (16.33). *Figure 16.5* shows the effect of a variation of the critical level on the relative abundance ϕ_1 of the ballistic particles for atomic hydrogen. For low temperatures a variation of ± 250 km in the critical level altitude has no effect in the abundance of ballistic particles. At 2000°K, the number of ballistic particles changes only by 1%.

The critical level altitudes given in Table 16.1 are therefore sufficiently accurate for the computations of vertical exospheric distributions. Variations of ± 50 km in the critical level heights have no effect on the escape flux or on the abundance of ballistic particles.

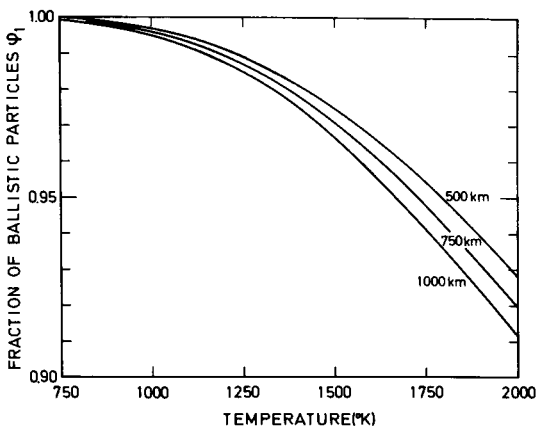


Fig. 16.5 Relative abundance ϕ_1 of the ballistic particles for atomic hydrogen as a function of the thermopause temperature for three arbitrary critical levels at 500, 750, and 1000 km altitude.

16.5 Terrestrial Exosphere up to 50,000 km Altitude

The earth's neutral exosphere is mainly composed of helium and atomic hydrogen since the concentration of light elements decreases less rapidly than the atomic oxygen concentration. It is necessary, however, to determine if atomic oxygen follows a hydrostatic distribution. This problem is only of importance below roughly 3500 km where the atomic oxygen con-

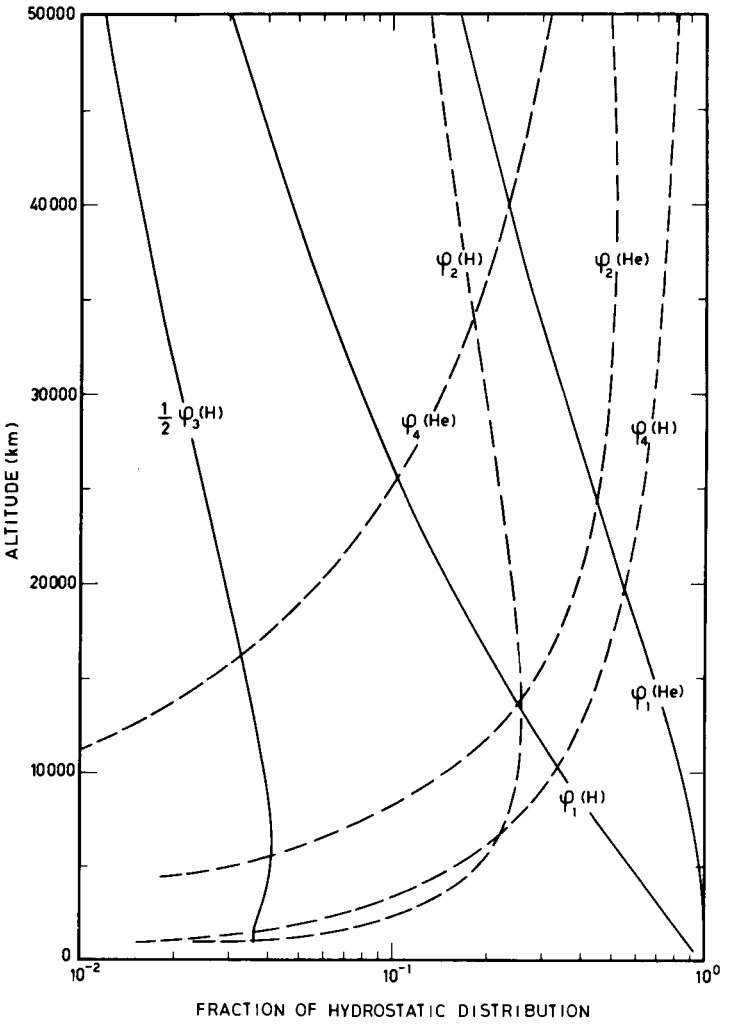


Fig. 16.6 Vertical distributions of the different types of particles for a thermopause temperature of 2000°K. E(H) = 3.36; E(He) = 13.3.

centration is greater than 1 particle cm^{-3}. At 3000 km, the fraction $\phi_1 + \phi_3$ of atomic oxygen particles always represents more than 99% of the hydrostatic distribution. Therefore, the atomic oxygen concentration is given by the hydrostatic approximation (16.1) with an accuracy better than 1%.

For helium and hydrogen the departure from a hydrostatic distribution is related to the presence or absence of the particles $\frac{1}{2}\phi_3$ and ϕ_4 and to the possible existence of the satellite particles ϕ_2. Before discussing this problem

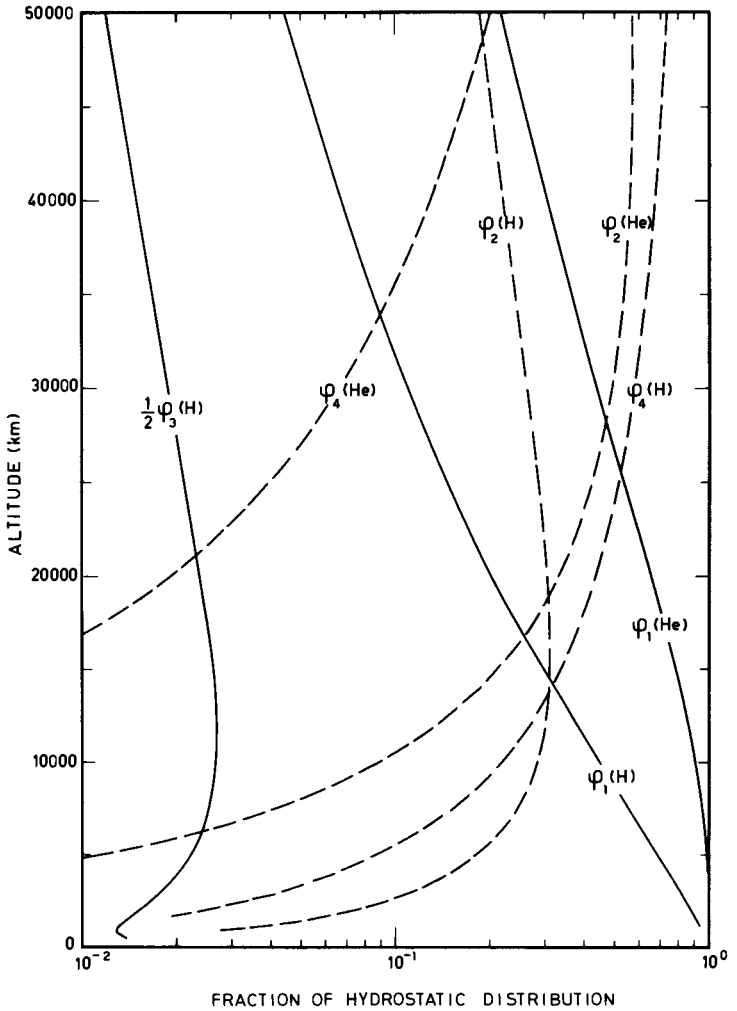


Fig. 16.7 Vertical distributions of the different types of particles for a thermopause temperature of 1500°K. E(H) = 4.57; E(He) = 18.1.

(see Section 16.6) it is interesting to present typical distributions for the four types of particles described in Section 16.1. *Figures 16.6–16.8* show the vertical distributions of the four types of particles obtained with the critical level of Table 16.1. It is seen that the fraction of escaping particles $\frac{1}{2}\phi_3$ decreases with temperature. The ballistic particles ϕ_1 however increase when the thermopause temperature decreases and the fraction ϕ_1 is more important for helium than for atomic hydrogen. Comparing the satellite particles ϕ_2

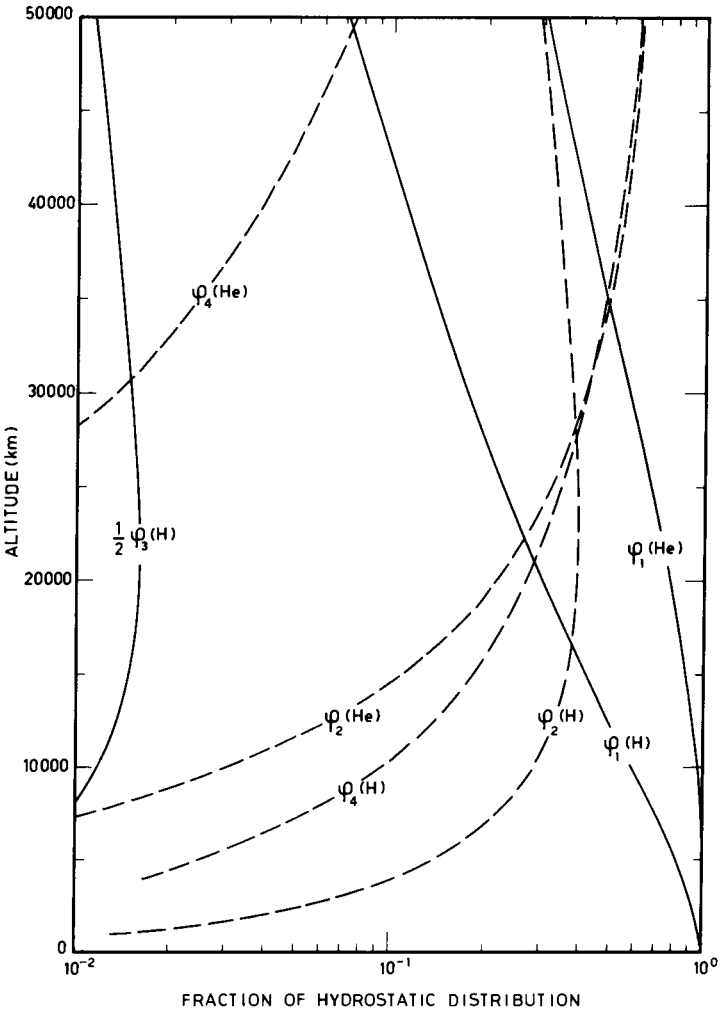


Fig. 16.8 Vertical distributions of the different types of particles for a thermopause temperature of 1000°K. E(H) = 7.06; E(He) = 28.0.

with the external hyperbolic particles, one sees that for helium ϕ_2 is always greater than ϕ_4 below 50,000 km whereas the opposite situation occurs for hydrogen at sufficiently high altitudes. Using Eqs. (16.50) and (16.52), the ratio ϕ_2/ϕ_4 is

$$\frac{\phi_2}{\phi_4} = \psi\left(\frac{Ey}{1+y}\right)\left[1 - \psi\left(\frac{Ey}{1+y}\right)\right]^{-1}. \tag{16.68}$$

Figure 16.9 shows the ratio ϕ_2/ϕ_4 as a function of $Z = [Ey/(1 + y)]^{1/2}$ which is the argument entering in the error function of Eq. (16.33). When Z is greater than 1.09 the satellite particles are always more abundant than the external hyperbolic particles. For the height range considered in Figs. 16.6–16.8, the parameter Z is always greater than 1.3 for helium. For atomic hydrogen, the values of Z are greater or less than 1.09 according to the thermopause temperature. This is the reason why the curves $\phi_2(H)$ and ϕ_4(H) cross each other at a height depending on the thermopause temperature.

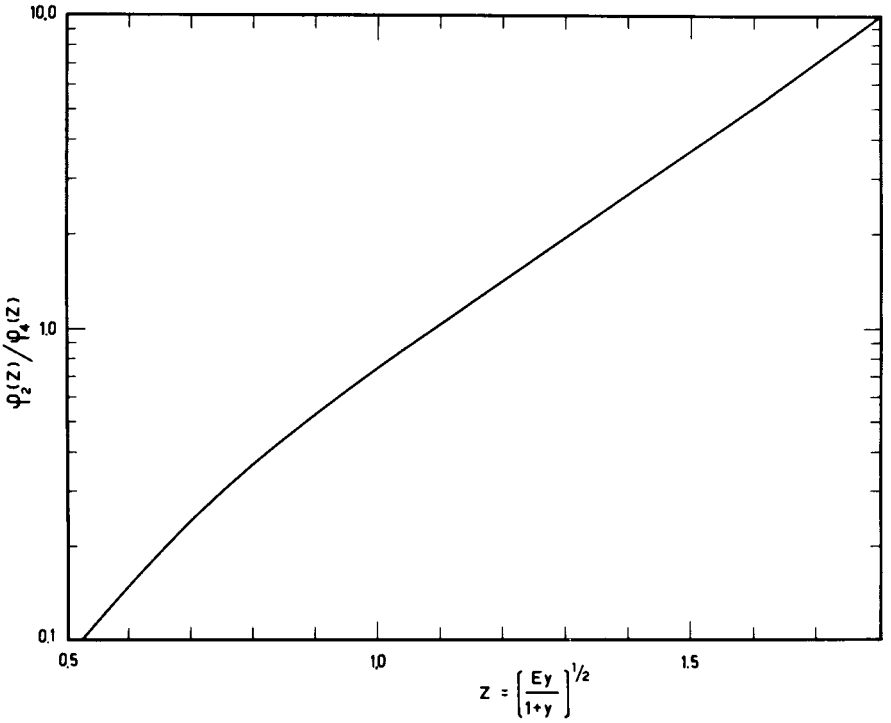


Fig. 16.9 Ratio between satellite and external hyperbolic particles as a function of $[Ey/(1 + y)]^{1/2}$.

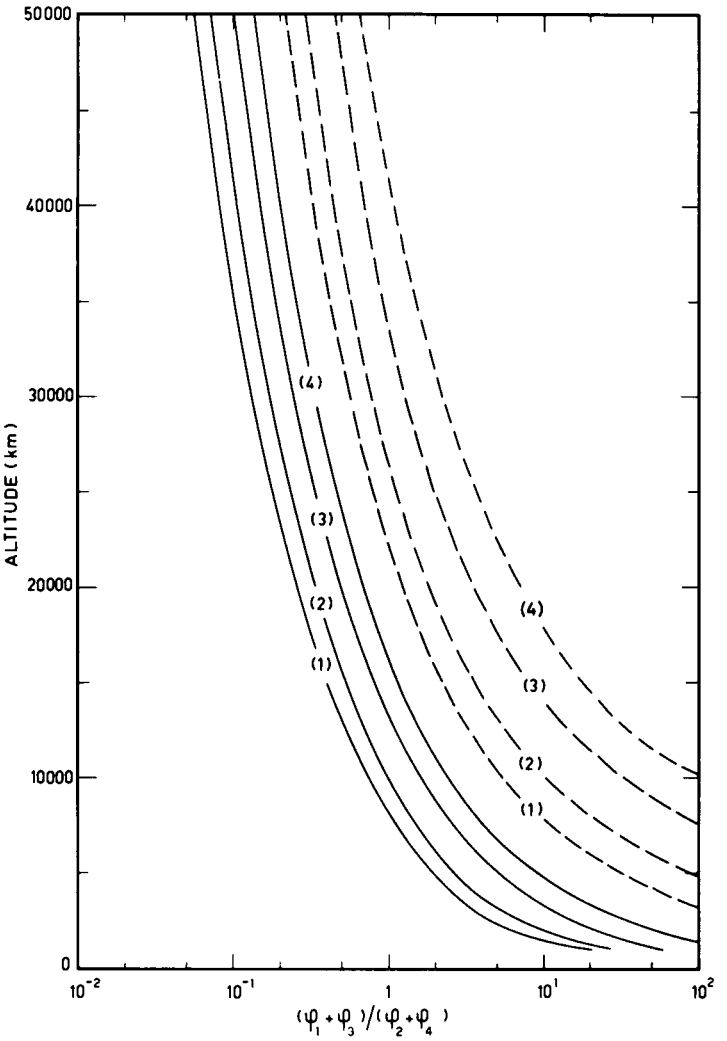


Fig. 16.10 Vertical distribution of the ratio between the particles crossing the critical level $\phi_1 + \phi_3$ and the particles $\phi_2 + \phi_4$ which never reach it. Solid curve, hydrogen; dashed curve, helium. Temperatures: (1) 2000°K, (2) 1500°K, (3) 1000°K, and (4) 750°K.

Using Eqs. (16.49)–(16.52), it is possible to compare the particles $\phi_1 + \phi_3$ which cross the critical level with those never reaching it. This ratio is given by

$$(\phi_1 + \phi_3)/(\phi_2 + \phi_4) = (1 - y^2)^{-1/2} \exp[Ey^2/(1 + y)] - 1. \quad (16.69)$$

Figure 16.10 shows that the particles crossing the critical level are more

TABLE 16.2

CONCENTRATIONS[a] OF THE DIFFERENT TYPES OF PARTICLES

Altitude (km)	n_1		n_3		n_2		n_4	
	H	He	H	He	H	He	H	He
$T = 2000°K$								
1000	3.61 (3)[b]	8.56 (5)	2.97 (2)	7.04 (0)	2.87 (1)	7.64 (1)	6.57 (1)	1.44 (0)
10,000	2.37 (2)	5.80 (2)	5.28 (1)	1.35 (0)	1.54 (2)	8.98 (1)	2.21 (2)	4.57 (0)
20,000	5.89 (1)	4.11 (1)	2.24 (1)	6.00 (−1)	9.01 (1)	2.80 (1)	2.16 (2)	4.25 (0)
30,000	2.41 (1)	9.74 (0)	1.26 (1)	3.51 (−1)	5.88 (1)	1.35 (1)	2.08 (2)	3.94 (0)
40,000	1.24 (1)	3.70 (0)	8.20 (0)	2.34 (−1)	4.19 (1)	8.04 (0)	2.01 (2)	3.70 (0)
50,000	7.38 (0)	1.80 (0)	5.78 (0)	1.69 (−1)	3.17 (1)	5.42 (0)	1.96 (2)	3.51 (0)
$T = 1500°K$								
1000	1.03 (4)	5.78 (5)	2.80 (2)	1.18 (−1)	9.54 (1)	1.17 (1)	8.61 (1)	1.93 (−2)
10,000	4.45 (2)	3.92 (1)	5.32 (1)	1.36 (−2)	2.58 (2)	3.36 (0)	2.18 (2)	4.65 (−2)
20,000	9.79 (1)	1.46 (0)	2.29 (1)	6.13 (−3)	1.41 (2)	7.18 (−1)	2.10 (2)	4.29 (−2)
30,000	3.79 (1)	2.61 (−1)	1.30 (1)	3.61 (−3)	8.92 (1)	2.88 (−1)	2.00 (2)	3.94 (−2)

40,000	1.90 (1)	8.49 (−2)	8.50 (0)	2.42 (−3)	6.24 (1)	1.55 (−1)	1.92 (2)	3.68 (−2)
50,000	1.10 (1)	3.75 (−2)	6.03 (0)	1.75 (−3)	4.66 (1)	9.81 (−2)	1.86 (2)	3.47 (−2)
$T = 1000°K$								
1000	7.87 (4)	2.40 (5)	2.57 (2)	2.18 (−5)	4.61 (2)	1.34 (−1)	1.04 (2)	2.18 (−6)
10,000	1.32 (3)	1.49 (−1)	5.24 (1)	1.20 (−6)	5.85 (2)	4.13 (−3)	2.10 (2)	4.12 (−6)
20,000	2.22 (2)	1.44 (−3)	2.30 (1)	5.41 (−7)	2.78 (2)	3.86 (−4)	1.98 (2)	3.75 (−6)
30,000	7.65 (1)	1.44 (−4)	1.32 (1)	3.21 (−7)	1.64 (2)	1.03 (−4)	1.86 (2)	3.42 (−6)
40,000	3.59 (1)	3.37 (−5)	8.72 (0)	2.16 (−7)	1.10 (2)	4.39 (−5)	1.77 (2)	3.16 (−6)
50,000	2.00 (1)	1.20 (−5)	6.23 (0)	1.58 (−7)	8.05 (1)	2.39 (−5)	1.70 (2)	2.97 (−6)
$T = 750°K$								
1000	4.64 (5)	9.11 (4)	1.90 (2)	2.78 (−10)	1.10 (3)	9.21 (−4)	8.07 (1)	2.78 (−10)
10,000	2.74 (3)	4.98 (−4)	3.96 (1)	1.04 (−10)	8.92 (2)	4.43 (−6)	1.54 (2)	3.16 (−10)
20,000	3.47 (2)	1.20 (−6)	1.76 (1)	4.20 (−11)	3.66 (2)	1.80 (−7)	1.44 (2)	2.85 (−10)
30,000	1.06 (2)	6.54 (−8)	1.02 (1)	2.49 (−11)	2.01 (2)	3.12 (−8)	1.34 (2)	2.59 (−10)
40,000	4.62 (1)	1.09 (−8)	6.77 (0)	1.69 (−11)	1.30 (2)	1.03 (−8)	1.27 (2)	2.39 (−10)
50,000	2.46 (1)	3.14 (−9)	4.86 (0)	1.23 (−11)	9.24 (1)	4.73 (−9)	1.21 (2)	2.23 (−10)

[a] Values are in cm^{-3}.
[b] $3.61(3) = 3.6 \times 10^{8}$.

important in the case of helium. On the other hand, the altitude at which $\phi_2 + \phi_4$ becomes more important than $\phi_1 + \phi_3$ is lower in the case of atomic hydrogen.

The fractions ϕ_j can be used to compute the absolute concentrations for each type of particle. *Table 16.2* gives the results for helium and hydrogen. The helium boundary concentration was taken to be 2×10^7 cm^{-3} at 120 km and the adopted hydrogen concentration is 3×10^7 cm^{-3} at 100 km

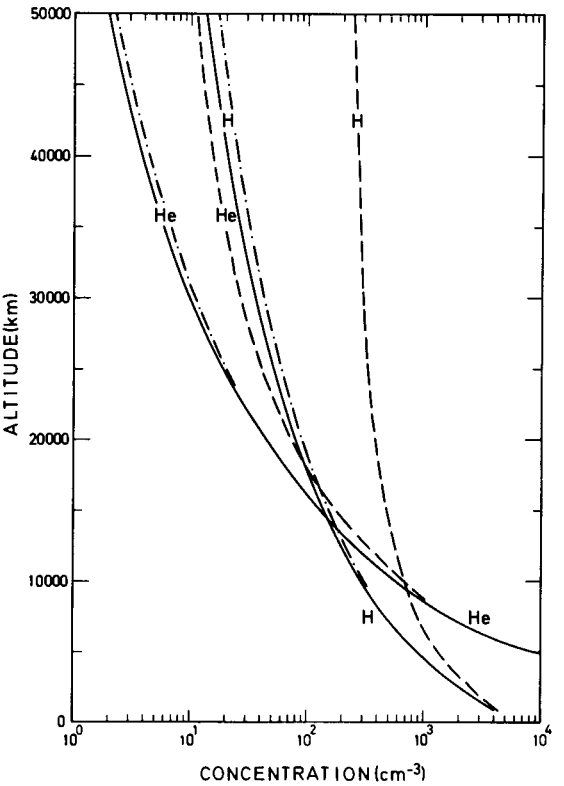


Fig. 16.11 Helium and hydrogen distributions for a temperature $T = 2000$°K. Comparison between the hydrostatic distribution (dashed curve), the minimum distribution $n_1 + \frac{1}{2}n_3$ (solid curve), and $n_1 + n_3$ (dotted dashed curve).

(see Chapter 15). Since important latitudinal variations of the helium concentration occur in the thermosphere (see Chapter 15), Table 16.2 is intended only to be a guide.

Even without discussing the possible existence of satellite and external hyperbolic particles, Table 16.2 shows that the hydrostatic distribution is

a good approximation for helium when the temperature is less than 1500°K. In the height range where helium plays a role in the total concentration, most of the helium particles are ballistic. *Figures 16.11–16.14* give the maximum hydrostatic distribution and the minimum distribution $n_1 + \frac{1}{2}n_3$ for the particles originating in the heterosphere. At 40,000 km, the ratio between the hydrostatic distribution and the distribution $n_1 + \frac{1}{2}n_3$ is 16 for H and 4 for He when $T = 2000$°K. This ratio decreases with temperature

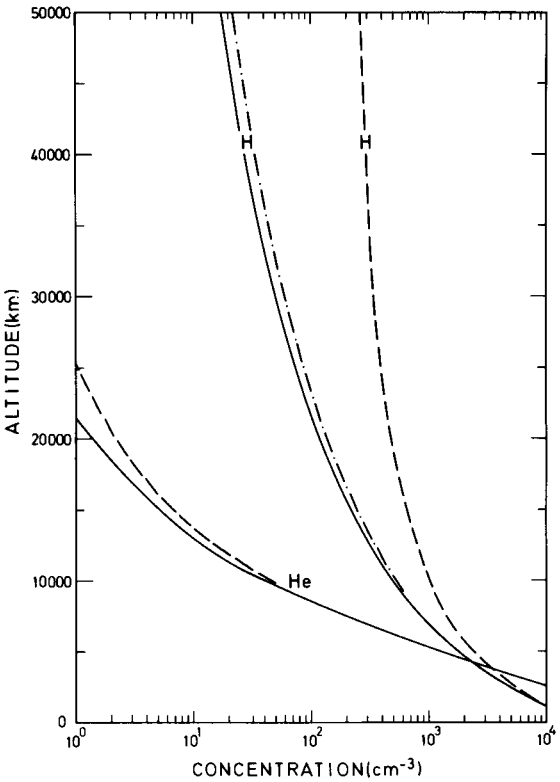


Fig. 16.12 Helium and hydrogen distributions for a temperature $T = 1500$°K. Comparison between the hydrostatic distribution and the minimum distribution $n_1 + \frac{1}{2}n_3$. See Fig. 16.11 for explanation of the curves.

and it reaches a value of 6 for H when $T = 750$°K. It is clear therefore that the satellite and external hyperbolic particles have to be analyzed for all thermopause temperatures in the case of atomic hydrogen. For helium, these particles can only play a role at very high temperatures of the order of 2000°K (see Fig. 16.11).

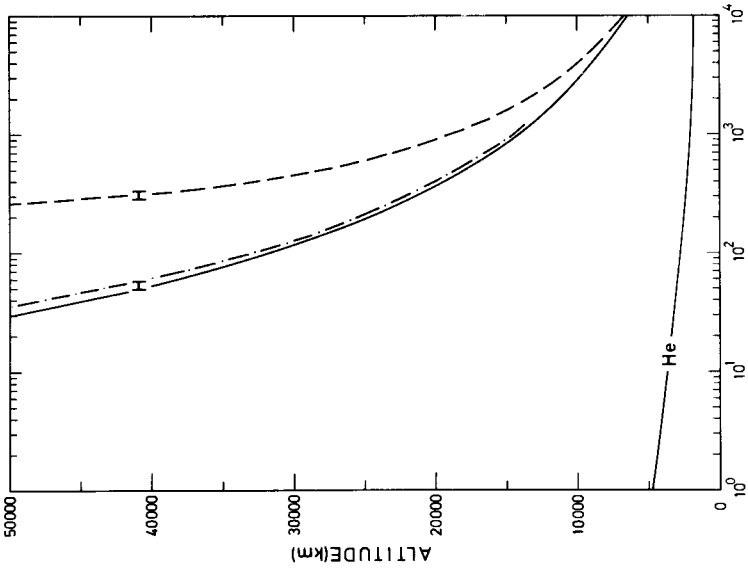


Fig. 16.14 Helium and hydrogen distributions for a temperature $T = 750°$K. Comparison between the hydrostatic distribution and the minimum distribution $n_1 + \frac{1}{2}n_3$. See Fig. 16.11 for explanation of the curves.

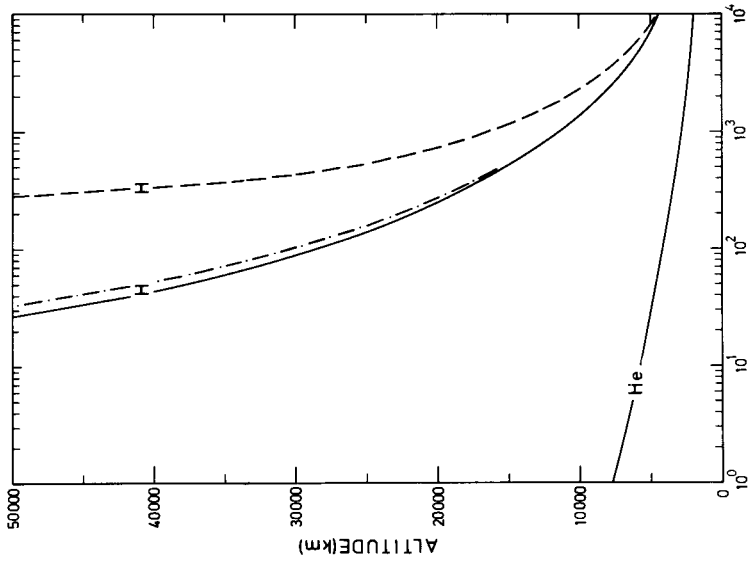


Fig. 16.13 Helium and hydrogen distributions for a temperature $T = 1000°$K. Comparison between the hydrostatic distribution and the minimum distribution $n_1 + \frac{1}{2}n_3$. See Fig. 16.11 for explanation of the curves.

16.6 Satellite and External Hyperbolic Particles

The importance of satellite particles has been discussed by Chamberlain [11] in terms of a *satellite particle critical level* above which the collisional creation of the satellite particles can be neglected. This level is fixed at a height where the production of satellite particles is balanced by several loss processes. It is, however, possible to study the behavior of satellite particles in a slightly different way.

A satellite particle X_s can be lost by photoionization

$$X_s + h\nu \rightarrow X^+ + e, \qquad \text{coefficient I} \quad (\text{sec}^{-1}), \tag{16.70}$$

by charge exchange

$$X_s + X^+ \rightarrow X_s^+ + X, \qquad \text{coefficient } \gamma n(X_s) \quad (\text{sec}^{-1}), \tag{16.71}$$

or by kinetic collisions with other particles.

The production of satellite particles is proportional to the concentration $n_1 + n_3 + n_4$ and to the kinetic collision frequency ν_k. Since certain angular and energetic conditions must be met to put a particle into orbit, it is necessary to introduce an efficiency factor ε. With Eqs. (16.70) and (16.71) the time dependent evolution for the satellite particles n_s is given by

$$dn_s/dt = \nu_k\varepsilon(n_1 + n_3 + n_4) - \nu_k(1 - \varepsilon)n_s - In_s - \gamma n_s n^+ \tag{16.72}$$

where n^+ is the positive ion concentration introduced in (16.71). The efficiency factor ε actually represents the probability of putting a particle into orbit by a collision with the other particles n_1, n_3, and n_4. The *maximum* efficiency is obtained for a complete Maxwellian distribution and from Fig. 16.2 it is seen that

$$\varepsilon = \int_{D_2} f(r, v)\, dV \Big(\sum_{i=1}^{4} \int_{D_i} f(r, v)\, dV \Big)^{-1} = n_2 \Big/ \sum_{i=1}^{4} n_i = \phi_2 \tag{16.73}$$

where dV is the volume element in the velocity space. From Eq. (16.73) it is clear that the efficiency factor is considerably reduced at great heights if the external hyperbolic particles are absent. Therefore Eq. (16.72) represents the most favorable case for putting particles into orbit when ε is given by (16.73), i.e., the maximum efficiency is equal to the relative abundance ϕ_2 of the satellite particles under steady state conditions. Equation (16.72) can now be written

$$dn_s/dt = \mu n_2 - Jn_s \tag{16.74}$$

with

$$\mu = \nu_k(1 - \varepsilon) = \nu_k(\phi_1 + \phi_3 + \phi_4) \tag{16.75}$$

and

$$J = I + \gamma n^+ + \mu \tag{16.76}$$

With $n_s(t = 0) = 0$, integration of Eq. (16.74) leads to

$$n_s(t) = (\mu n_2/J)[1 - e^{-Jt}]. \tag{16.77}$$

When the loss processes through ionization and charge exchange are neglected, the time necessary to reach 50% of the equilibrium value for the satellite particles is given by

$$\tau_{1/2} = 0.69/\mu. \tag{16.78}$$

The loss times through photoionization or through charge exchange are

$$\tau_{ion} = 1/I \tag{16.79}$$

and

$$\tau_{ex} = 1/\gamma n^+. \tag{16.80}$$

The question of whether or not satellite particles play a role is now answered by comparing the production time $\tau_{1/2}$ with the loss times τ_{ion} and τ_{ex}.

The charge exchange rate coefficient [21] for hydrogen is $\gamma(H) = 4.0 \times 10^{-9}$ cm^3 sec^{-1} at 2000°K and 2.6×10^{-9} cm^3 sec^{-1} at 1000°K. For helium, a value of 10^{-9} cm^3 sec^{-1} is sufficiently accurate for the present analysis. The ionization times for low solar activity can be estimated to be of the order of 8.2×10^6 sec for H and 1.3×10^7 sec for He. The vertical distribution of τ_{ex} requires the knowledge of the ion profiles up to 50,000 km.

TABLE 16.3

BOUNDARY VALUES[a] AT 500 KM FOR H^+, He^+, AND O^+

T (°K)	n^+(O)	n^+(He)	n^+(H)	Σn^+
2000	9.8×10^5	1.4×10^4	1.2×10^1	1.0×10^6
1000	1.8×10^5	1.6×10^4	3.0×10^2	2.0×10^5

[a] Values are for cm^{-3}.

Since there are large uncertainties at high altitude, the vertical profiles for H^+ and He^+ will be approximated by the usual ion diffusion equation [22]. The adopted boundary values are shown in *Table 16.3*. These should be considered only as indicative values necessary to illustrate the physical processes. *Figures 16.15* and *16.16* give the vertical distribution of the charge exchange time τ_{ex} and of the time $\tau_{1/2}$ necessary to reach 50% of a steady state satellite particle distribution. Figure 16.15 shows that, in the case of helium, charge exchange destroys satellite particles above 10,000 km and photoionization becomes important above 20,000 km. The loss processes are, however, not

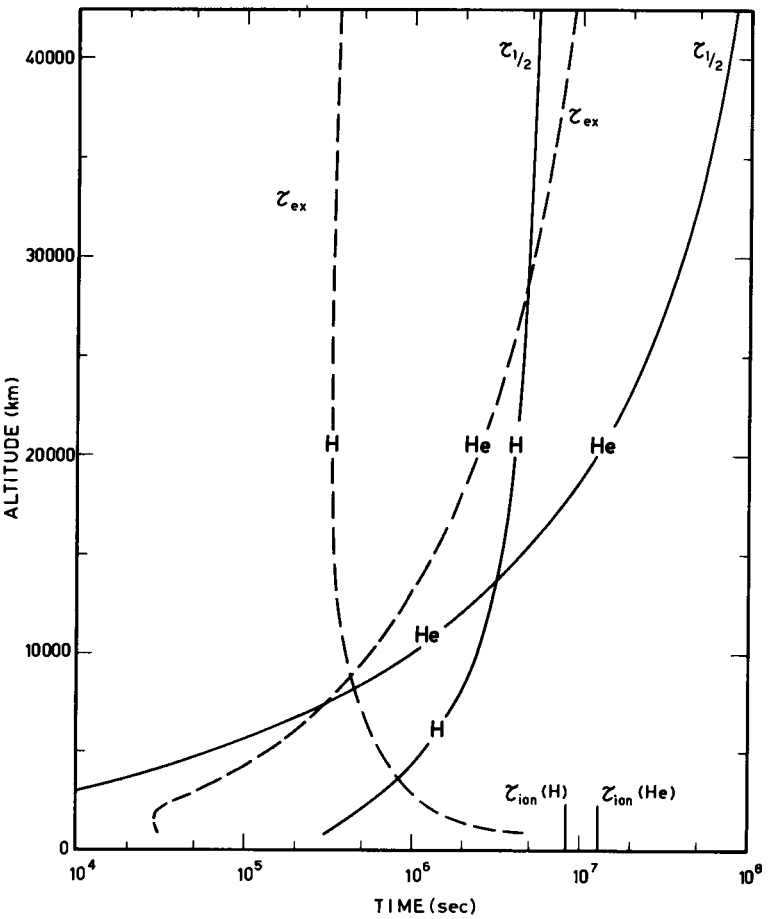


Fig. 16.15 Time $\tau_{1/2}$ necessary to reach 50% of the equilibrium value for the H and He satellite particles compared to the ionization time τ_{ion} and to the charge exchange time τ_{ex} for a thermopause temperature of 2000°K.

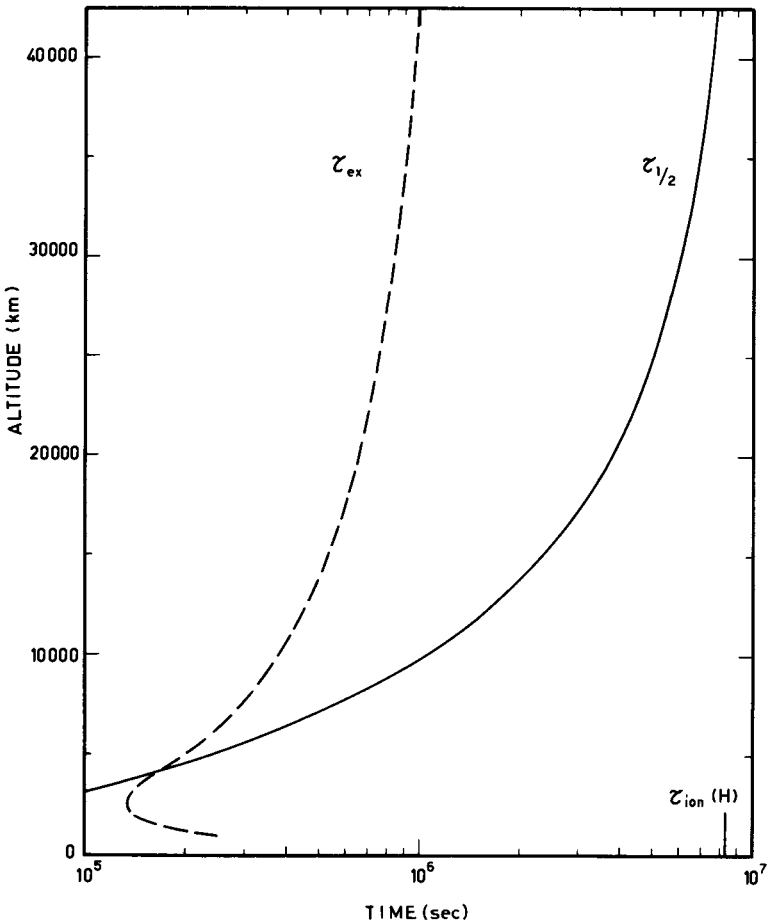


Fig. 16.16 Time $\tau_{1/2}$ necessary to reach 50% of the equilibrium value for the hydrogen satellite particles compared to the ionization time τ_{ion} and to the charge exchange time τ_{ex} for a thermopause temperature of 1000°K.

effective below 5000 km. Nevertheless, at those heights the helium satellite particles are negligible compared to the ballistic particles (see Fig. 16.6). It can, therefore, be concluded that photoionization and charge exchange are always effective for preventing the formation of an appreciable amount of helium satellite particles in the earth's exosphere. A similar conclusion is obtained for atomic hydrogen. Finally, it should be mentioned that, in any case, the production of satellite particles has been overestimated at great heights since external hyperbolic particles n_4 were assumed to be present.

The interplanetary hydrogen distribution has been computed [23] from

Lyman α observations and a concentration of $5\times10^{-2}\,\mathrm{cm}^{-3}$ was deduced for particles with a speed of several hundred kilometers per second in the vicinity of the earth's orbit. Such a value is negligible compared to the external hyperbolic particle concentrations shown in Table 16.2. Therefore the external hyperbolic particles n_4 should not be taken into account in a normal exospheric distribution. Actually, they are not necessary to explain the Lyman α observations in the earth's geocorona [24–26]. Even when atomic hydrogen flows enter into the solar system [27, 28], it is practically impossible for them to match a Maxwellian velocity distribution. Nevertheless, they can contribute to the Lyman α background which is observed beyond the geocorona.

Finally, it should be mentioned that the difference between the distributions $n_1 + n_3$ or $n_1 + \frac{1}{2}n_3$ is not significant below 50,000 km. Therefore, it can be concluded that the neutral earth's exosphere depends essentially on the ballistic particles and on the hyperbolic particles crossing the critical level.

16.7 Temperature in the Exosphere

The critical level is located in the isothermal region of the heterosphere where solar radiation cannot be sufficiently absorbed to create significant temperature gradients. Above the thermopause the physical parameters are usually computed in an isothermal atmosphere. The constant temperature is actually defined by the mean translational kinetic energy $\frac{1}{2}m\overline{v^2} = \frac{3}{2}kT$. The mean square velocity $\overline{v^2}$ is given by

$$\overline{v^2} = \int v^2 f(r, v)\, dV \Big/ \int f(r, v)\, dV \tag{16.81}$$

where $f(r, v)$ is the velocity distribution function and dV is the elementary volume in velocity space. The integration extends over all angles and velocities. Since the satellite and external hyperbolic particles can be neglected in the exosphere, the velocity distribution function is no longer Maxwellian. Using the notations of Section 16.2, it is however possible to deduce an expression for the mean square velocity $\overline{v^2_{ex}}$ in the exosphere,

$$\overline{v^2_{ex}} = \frac{\int v^4 f(r, v) \sin\theta\, d\theta\, dv}{\int v^2 f(r,v) \sin\theta\, d\theta\, dv} \tag{16.82}$$

or

$$\overline{v^2_{ex}} = \frac{4\pi n(1) y^2 \int_0^{\pi/2} \sin\theta_c \cos\theta_c K(\theta_c)\, d\theta_c}{n_1(y) + n_3(y)} \tag{16.83}$$

where

$$K(\theta_c) = \left(\frac{m}{2\pi kT}\right)^{3/2} \int_{au}^{\infty} \frac{v_c^3[v_c^2 - a^2(1-y)] \exp(-mv_c^2/2kT)\, dv_c}{[v_c^2(1 - y^2 \sin^2\theta_c) - a^2(1-y)]^{1/2}}. \quad (16.84)$$

The integrations in (16.83) and (16.84) lead to

$$\bar{v}_{ex}^2 = \frac{3kT}{m}\left\{1 - \frac{2}{3}\left(\frac{Ey^2}{1+y}\right)\left[\frac{1-(\phi_1+\phi_3)}{\phi_1+\phi_3}\right]\right\} \quad (16.85)$$

where T is the Maxwellian temperature at the thermopause.

Expression (16.85) can now be used to define an equivalent kinetic temperature T_{ex} for each exospheric constituent:

$$T_{ex} = T\left\{1 - \frac{2}{3}\left(\frac{Ey^2}{1+y}\right)\left[\frac{1-(\phi_1+\phi_3)}{\phi_1+\phi_3}\right]\right\}. \quad (16.86)$$

At the critical level $\phi_1 + \phi_3 = 1$ and $T_{ex} = T$, i.e., the usual Maxwellian

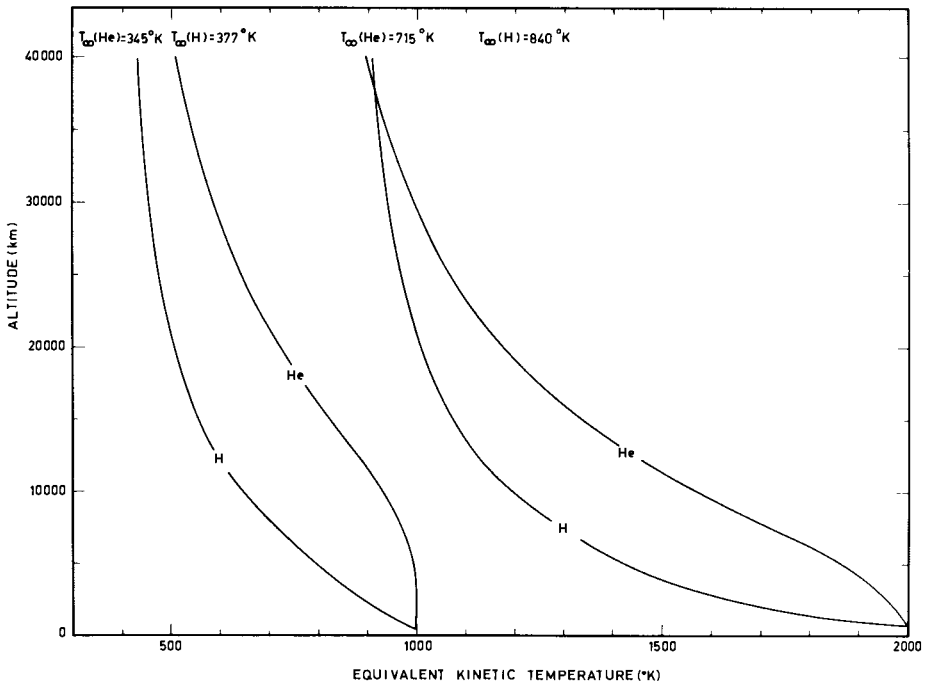


Fig. 16.17 Equivalent temperatures of helium and hydrogen in the exosphere when the thermopause temperature is 1000°K or 2000°K.

kinetic temperature. Above the critical level, the absence of certain particles in the velocity distribution function leads to a decrease of T_{ex}. *Figure 16.17* shows the vertical distribution of T_{ex} for thermopause temperatures of 2000°K. The decrease of T_{ex} is more pronounced for atomic hydrogen since in this case the departure from a Maxwellian velocity distribution function is more important. The asymptotic value of T_{ex} at infinity is given by

$$T_{ex}(\infty) = \tfrac{1}{3}T[(2E + 3)/(2E + 1)]. \tag{16.87}$$

Actually the equivalent kinetic temperature has no physical meaning at infinity since the concentration $n_1 + n_3$ becomes zero. The decrease of T_{ex} reflects the decrease of the velocity dispersion with altitude. The temperature T_{ex} defined in this section represents the mean kinetic energy in all directions. It is also possible to define a kinetic temperature in specific directions by changing the integration limits of Eq. (16.82).

16.8 Total Content

Optical observations of an exospheric constituent always require the knowledge of the total content $\int_r^\infty n\,dr$ above a certain geocentric distance r. Usually the expression nH is a good approximation in the thermosphere. However, when ballistic particles ϕ_1 and hyperbolic particles ϕ_3 are the most important, such an approximation is no longer valid. The correction factor G_j [see Eq. (16.60)] should be used. With a complete Maxwellian distribution at the critical level, one obtains

$$G(E) = \int_0^1 Ey^{-2}(\phi_1 + \phi_3)\exp[-E(1 - y)]\,dy. \tag{16.88}$$

Numerical integration of (16.88) leads to the results given in *Table 16.4*. It is seen that $G(E)$ is most important for atomic hydrogen since it changes between 1.5 and 1.3 when T ranges from 2000° to 750°K. For helium, $G(E)$ changes from 1.2 at 2000°K to 1.1 at 750°K. Since E is always greater than 50 for atomic oxygen, the correction factor is always less than 1.05. When a truncated Maxwellian distribution is adopted at the critical level, the correction factor is slightly decreased [9] for $E < 10$.

The total content for atomic hydrogen is shown in *Fig. 16.18* as a function of thermopause temperature. Two values have been adopted for the

TABLE 16.4

CORRECTION FACTOR $G(E)$

E	0.0	0.1	0.2	0.3	0.4	0.5	0.6	0.7	0.8	0.9
2. 1.	163	197	229	258	285	310	333	354	372	390
3.	405	418	431	442	451	459	466	472	478	482
4.	485	488	489	490	491	491	490	489	488	486
5.	484	481	478	475	472	468	464	460	456	452
6.	448	444	439	434	430	425	421	416	411	407
7.	402	397	392	388	383	379	374	370	365	361
8.	356	352	348	343	339	335	331	327	323	319
9.	315	311	308	304	300	297	293	290	286	283
10.	280	276	273	270	267	264	261	258	255	252
11.	249	247	244	241	239	236	234	231	229	226
12.	224	222	220	217	215	213	211	209	207	205
13.	203	201	199	197	195	193	192	190	188	186
14.	185	183	181	180	178	177	175	174	172	171
15.	169	168	167	165	164	163	161	160	159	158
16.	156	155	154	153	152	150	149	148	147	146
17.	145	144	143	142	141	140	139	138	137	136
18.	135	134	133	132	132	131	130	129	128	127
19.	126	126	125	124	123	123	122	121	120	120
20.	119	112	106	101	096	092	088	084	080	077
30.	074	072	069	067	065	063	061	059	057	056
40.	054	053	051	050	049	048	046	045	044	044
50.	043	042	041	040	039	038	038	037	036	036

eddy diffusion coefficient (see Chapter 15). For low temperature the total content changes in a substantial way. Even if atomic hydrogen distributions cannot respond instantaneously to diurnal temperature variations, an increase of the total content will however occur on a longer time scale during decreasing solar cycle activity.

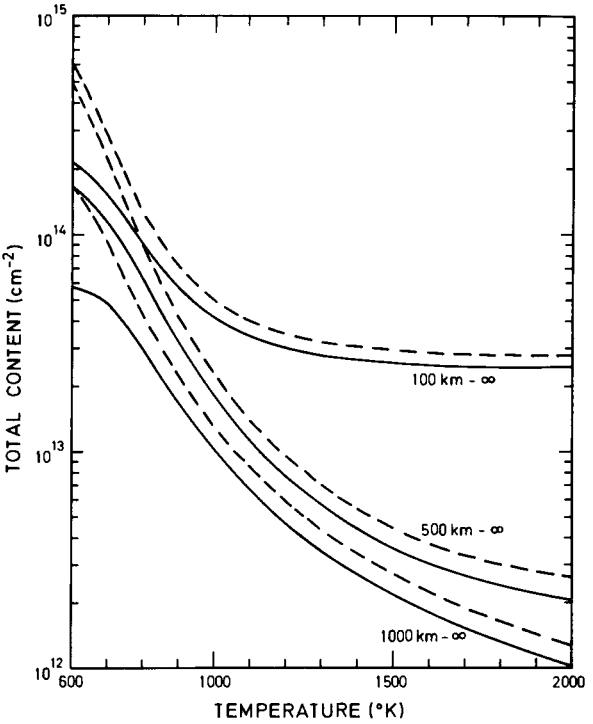


Fig. 16.18 Atomic hydrogen total content as a function of the thermopause temperature. Solid curve, $K = 10^7$ cm^2 sec^{-1}; dashed curve, $K = 0$.

REFERENCES

1. E. T. Byram, T. A. Chubb, H. Friedman, and J. Kupperian, in *The Threshold of Space* (M. Zelikoff, ed.), pp. 203–210. Pergamon, Oxford, 1957.
2. J. J. Waterston, *Phil. Trans. Roy. Soc. London* **183A**, 1 (1892).
3. G. J. Stoney, *Astrophys. J.* **7**, 25 (1898).
4. S. R. Cook, *Astrophys. J.* **11**, 36 (1900).
5. G. H. Bryan, *Phil. Trans. Roy. Soc. London* **196A**, 1 (1901).
6. E. J. Öpik and S. F. Singer, *Phys. Fluids* **2**, 653 (1959).
7. E. J. Öpik and S. F. Singer, *Phys. Fluids* **3**, 486 (1960).
8. E. J. Öpik and S. F. Singer, *Phys. Fluids* **4**, 221 (1961).
9. J. Herring and L. Kyle, *J. Geophys. Res.* **66**, 1980 (1961).
10. R. E. Aamodt and K. M. Case, *Phys. Fluids* **5**, 1019 (1962).
11. J. W. Chamberlain, *Planet. Space Sci.* **11**, 901 (1963).
12. J. S. Johnson and R. A. Fish, *Astrophys. J.* **131**, 502 (1960).
13. J. W. Chamberlain and G. R. Smith, *Planet. Space Sci.* **19**, 675 (1971).
14. R. T. Brinkmann, *Planet. Space Sci.* **19**, 791 (1971).
15. C. S. Shen, *J. Atmos. Sci.* **20**, 69 (1963).

16. F. S. Johnson, *Astrophys. J.* **133**, 701 (1961).
17. J. H. Jeans, *The Dynamical Theory of Gases*, 4th ed. Dover, New York, 1954.
18. L. Spitzer, Jr., in *The Atmospheres of the Earth and Planets* (G. P. Kuiper, ed.), pp. 213–249. Univ. of Chicago Press, Chicago, Illinois, 1949.
19. S. Chapman and T. G. Cowling, *The Mathematical Theory of Non-Uniform Gases*, 3rd ed. Cambridge Univ. Press, London and New York, 1970.
20. M. Nicolet, *Ann. Géophys.* **13**, 1 (1957).
21. A. Dalgarno, *Ann. Géophys.* **17**, 16 (1961).
22. G. Kockarts and M. Nicolet, *Ann. Géophys.* **19**, 370 (1963).
23. T. N. L. Patterson, F. S. Johnson, and W. B. Hanson, *Planet. Space Sci.* **11**, 767 (1963).
24. T. M. Donahue, *Ann. Géophys.* **22**, 175 (1966).
25. R. R. Meier and P. Mange, *Planet. Space Sci.* **18**, 803 (1970).
26. J.-L. Bertaux and J.-É. Blamont, *Space Res.* **10**, 591 (1970).
27. P. W. Blum and H. J. Fahr, *Astron. Astrophys.* **4**, 280 (1970).
28. J.-L. Bertaux and J.-É. Blamont, *Astron. Astrophys.* **11**, 200 (1971).

CHAPTER 17

Formation of the Ionosphere

17.1 Introduction

The preceding chapters have been devoted to the characteristics of the neutral atmosphere with only occasional reference to ionization processes or the dynamics of the ionosphere. In the historical sense such a progression reverses the actual way knowledge of the upper atmosphere has advanced. The first measurements of physical processes above 50 km were accomplished inadvertently through the use of radio waves for telecommunications [1]. Following the development of pulse echo transmitters and receivers [2], great progress was made in the exploration of the ionosphere with the discovery of the D, E, and F regions. Since the radio techniques relied upon the interaction between radio waves and free electrons, many early studies of the basic ionospheric processes tended to place undue emphasis on the behavior of the electrons. In fact, such emphasis was actually inevitable since it was not until 1946 that the first direct observations of the *in situ* neutral atmosphere and solar ultraviolet radiations were made possible through high altitude rocket flights. (For a more detailed bibliography of early accomplishments, see references given in Ratcliffe [3].)

During the past two decades a more complete understanding of the formation of the ionosphere has developed simultaneously with our knowledge of the composition and dynamics of the atmosphere and solar radiations. As rocket and satellite data have become available the older electron based ionosphere theories have given way to a more balanced perspective which recognizes the ionosphere as a multiconstituent plasma whose be-

havior is closely linked with that of the neutral atmosphere, the solar ionizing radiations, and the electrodynamic influences of the magnetosphere.

The main body of the ionosphere arises from ionization created by the atmospheric absorption of solar ultraviolet radiation of wavelengths less than 1026 Å. Such radiation ionizes O, O_2, and N_2. These initial ions are not necessarily the principal ionospheric ions, however, due to the secondary reactions which occur between these ions and the neutral gases. A typical profile of ion composition [4] in the ionosphere is given in *Fig. 17.1*. It is interesting to note that in the E and F regions NO^+ is an important ion, even through NO itself is a minor atmospheric constitutent.

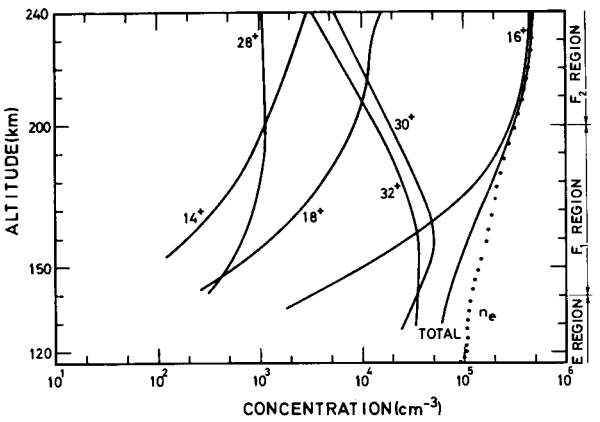


Fig. 17.1 Ion composition of the E and F_1 regions measured at White Sands, New Mexico on February 15, 1963 at 0934 MST for a solar zenith angle of 60° [30].

There are four major interrelated areas of scientific research relating to the ionospheric plasma. The first, and most explored area, is the ionic composition of the different regions including normal quiet diurnal variations, peculiarities arising from local phenomena, and the broader changes associated with seasonal and solar cycle effects. The dynamic motions of the ionospheric plasma is a second area of research with involves the diffusion of ions in response to gravity, pressure gradients, motions of the neutral atmosphere, and the presence of electric fields. Of more recent interest and perhaps the best understood field of study is concerned with the thermal structure of the ionosphere. This includes the different sources of heat, the possibility of different temperatures for the different plasma species, and the ultimate heat sinks. The fourth and most recent area of research concerns the question of the degree of interaction between magnetospheric processes and the behavior of the ionosphere. It is known,

for example, that the ionosphere provides most of the thermal plasma of the magnetosphere through a daily ebb and flow of ions along magnetic field lines. Perhaps more importantly, electric fields having their source in the magnetosphere can create widespread motions of the ionospheric plasma and, through collisions, winds in the neutral gases of the thermosphere.

In the following chapters the basic aspects of these physical processes are discussed in the way they affect the formation of the ionosphere and its subsequent behavior in the terrestrial environment. Although large collections of morphological data are available describing ionospheric behavior during the past half century, detailed discussions of such information are not attempted here. Details of the observed ionospheric behavior can be found in several of the general references listed at the end of Chapter 1 or in Ratcliffe [3].

This chapter introduces the problems of photoabsorption and photoionization in the upper atmosphere. The major portion of ionization in the upper atmosphere results from the absorption of solar ultraviolet radiation. As shown in Table 6.4, radiation of wavelengths less than 1026 Å is able to ionize the major atmospheric constituents and these are of principal interest for the formation of the ionosphere. However, radiation of longer wavelengths can be of importance in the ionization of minor constituents. The ionization of nitric oxide by solar Lyman α at 1216 Å, for example, provides an important contribution to the ionospheric D region.

Ionization by energetic particle impact can also be important. During normal conditions cosmic rays penetrate deeply into the atmosphere, creating ionization in the regions below 70 km altitude during both day and night. At lower energies, auroral particles create intense narrow rings of ionization in the polar regions. In the daytime auroral zones the particles are of relatively low energy ($\bar{\varepsilon} < 1$ keV) associated with the magnetosheath and cannot penetrate much below 200 km. In the nighttime auroral zones the average particle energy is greater than 1 keV and penetration to 100 km is a common occurrence. However, it is generally true that impact ionization is neither as consistent nor as dominating as that arising from the absorption of radiation.

17.2 Absorption of Radiation

Consider the problem of radiation entering an atmosphere and being gradually diminished in intensity by atomic and molecular absorption. If the radiation flux in the wavelength interval λ, $\lambda + d\lambda$ is represented as

$\phi(\lambda)$, the change in flux $d\phi$ due to absorption by a neutral gas in traveling a distance ds is

$$d\phi = -n\sigma_a\phi\, ds \tag{17.1}$$

where n is the altitude-dependent neutral gas concentration, σ_a is the wavelength-dependent absorption cross section, and ds is an increment of path length in the optical ray direction (see *Fig. 17.2*). This relation is valid only if there are no local sources of radiation and if resonance scattering of the radiation does not occur. These conditions are generally met in the terrestrial daytime atmosphere for the solar ultraviolet ionizing radiations.

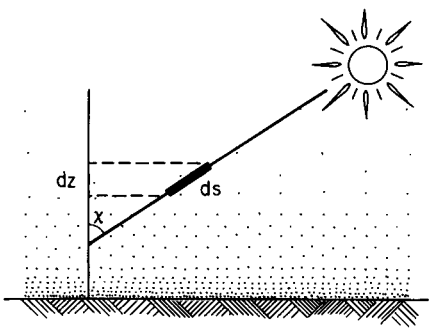


Fig. 17.2 The relationship between the increment of lengths, ds and dz, in a plane stratified atmosphere.

The altitude dependence of the incident photon flux follows from Eq. (17.1) as

$$\phi(\lambda) = \phi_\infty(\lambda) \exp\left(-\int_z^\infty n\sigma_a\, ds\right) \tag{17.2}$$

where $\phi_\infty(\lambda)$ is the radiation flux outside the atmosphere and the integration is taken from the observation altitude z along the optical ray path.

The argument of the exponential in Eq. (17.2) is called the optical depth and represented by the symbol τ:

$$\tau = \int_z^\infty n\sigma_a\, ds. \tag{17.3}$$

Radiation entering the earth's atmosphere is normally absorbed by several neutral gases, each with its own absorption cross section. The generalization of Eq. (17.3) to a multiconstituent atmosphere is straightforward and leads to the expression

$$\tau = \sum_i \sigma_a{}^i \int_z^\infty n_i\, ds \tag{17.4}$$

so that each constituent contributes to the attenuation in proportion to its cross section and column density.

Using Eqs. (17.2) and (17.4) the attenuation of $\phi(\lambda)$ due to atmospheric absorption can be written as

$$\phi(\lambda) = \phi_\infty(\lambda)e^{-\tau} \tag{17.5}$$

where the height dependence is implicitly contained in the optical depth. This equation can be used to estimate the atmospheric regions where absorption of a particular wavelength radiation will occur. Since most atmospheric gases vary exponentially with altitude, a similar behavior follows for τ. Thus, the condition $\tau = 1$ (unit optical depth) defines an altitude below which the incident radiation flux rapidly goes to zero. If $N_T = \int_z^\infty n\, ds$, the altitude where unit optical depth occurs can be found by searching for the altitude where the relation

$$N_T = 1/\sigma_a \tag{17.6}$$

is satisfied.

Accurate evaluation of the optical depth requires that the geometrical ray path be specified with respect to the vertical distribution of the absorbing gases. Consider first a simple model where the neutral gases are distributed according to the barometric law

$$dp/p = -dz/H \tag{17.7}$$

where H is the absorbing species scale height. A single integration of (17.7) gives

$$p = p_0 \exp\left[-\int_{z_0}^{z} dz'/H\right] \tag{17.8}$$

or, with the perfect gas relation $p = nkT$,

$$n = n_0(T_0/T) \exp\left[-\int_{z_0}^{z} dz'/H\right]. \tag{17.9}$$

Several possibilities exist for the altitude variation of the scale height and temperature. First, if one assumes T and H are constant, the density is

$$n = n_0 \exp[-(z - z_0)/H_0] \tag{17.10}$$

where the subscripts indicate evaluation at the altitude z_0. Second, it is possible to take g to be constant and permit the scale height to vary as

$$H = H_0 + \beta(z - z_0); \tag{17.11}$$

i.e., a linear variation with altitude with a scale height gradient β. In this case the density can be expressed as

$$n = n_0(H/H_0)^{-(1+\beta)/\beta} \tag{17.12}$$

if β is a constant.

To progress further in the derivation of the optical depth, it is necessary to find an expression relating the optical path distance ds to the altitude increment dz. As a first approximation, suppose that the atmosphere is plane stratified with the sun at an angle χ with respect to the zenith (see Fig. 17.2). From simple geometry the relation between ds and dz is given by $ds = -\sec \chi \, dz$. Using Eq. (17.3) the optical depth for the density distributions defined by Eqs. (17.10) and (17.12) can be obtained as

$$\tau = nH\sigma_a \sec \chi \tag{17.13}$$

for a single constituent atmosphere where the quantities are evaluated at the altitude for which the optical depth is needed. Following Eq. (17.4), the optical depth for an atmosphere of several gases, each obeying its own diffusive distribution, is

$$\tau = \sec \chi \sum_i n_i H_i \sigma_a{}^i. \tag{17.14}$$

Referring to Eqs. (17.10) and (17.12) it can be seen that τ increases exponentially with altitude. Since τ itself is the argument of an exponential, it follows that the absorption of radiation occurs extremely rapidly after the point $\tau = 1$ has been reached.

Both (17.13) and (17.14) show that the optical depth at each altitude increases as the solar zenith angle increases; i.e., as the sun moves towards the horizon the atmospheric column content becomes progressively larger. At large zenith angles, however, the sec χ factor appearing in Eqs. (17.13) and (17.14) is incorrect since the curvature of the earth makes the atmospheric column content a complicated function of solar zenith angle (see *Fig. 17.3*).

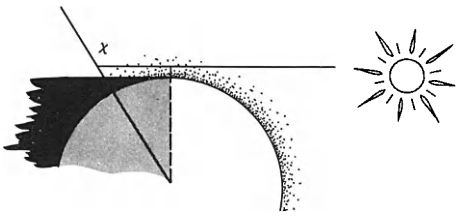


Fig. 17.3 The relationship between the optical ray path and atmospheric density for large zenith angles in a spherically stratified atmosphere.

A number of studies [4–10] have been made to correct the optical depth expression for large solar zenith angles ($\chi \gtrsim 70°$). The formulas derived are themselves approximations to the actual behavior and for accurate computations numerical integration of Eq. (17.2) is necessary. For some purposes, however, approximate expressions are useful. These methods express the optical depth at an altitude z in the form

$$\tau(X, \chi) = nH\sigma_a F(X, \chi) \tag{17.15}$$

where $X = (R_E + z)/H$ with R_E being the earth's radius, H is the local scale height, n the local gas concentration, and $F(X, \chi)$ some given function. Tabulations of $F(X, \chi)$ are available for different conditions. For a constant scale height atmosphere $F(X, \chi)$ is commonly written as $\mathrm{Ch}(X, \chi)$ and referred to as the Chapman function [4, 11].

When more general atmospheric conditions apply, approximate analytic forms for $F(X, \chi)$ can be used. Several of the more common forms are given below [7, 8, 10]:

$$F(X, \chi) = -X\cos\chi + [1 + X(1 + \sin\chi)]^{1/2}\{[X(1 - \sin\chi)]^{1/2} + (\pi^{1/2}/2)(1 - \mathrm{erf}[X(1 - \sin\chi)]^{1/2})\exp[X(1 - \sin\chi)]\} \tag{17.16}$$

$$F(X, \chi) = (\pi X/2)^{1/2}\exp[(X/2)\cos^2\chi]\{1 - \mathrm{erf}[(X/2)^{1/2}\cos\chi]\} \tag{17.17}$$

$$F(X, \chi) = \exp[\chi^2/2/(1 - 0.115\chi^2 - \alpha\chi^4)]$$
$$\alpha = \frac{0.284 - 2.47/\ln(\pi X/2)}{6.09}. \tag{17.18}$$

Analysis of the accuracy of these expressions has shown [10] that (17.16) differs by less than 0.5% from the result for $\mathrm{Ch}(X, \chi)$. However, (17.17) and (17.18) are accurate to better than 2% and represent a considerable decrease in computation.

For $\chi > \pi/2$ these expressions must be used in the form

$$\tau = n(a)H(a)\sigma_a F(Y, \chi \geq \pi/2) \tag{17.19}$$

where

$$F(Y, \chi \geq \pi/2) = 2F(Y, \pi/2) - F(X, \pi - \chi) \cdot \exp Y(1 - csc\,\chi) \tag{17.20}$$

with Y being the parameter X evaluated at the minimum height, a, of the grazing solar ray (see Fig. 17.3). As an approximation, (17.20) can be replaced by

$$F(Y, \chi \geq \pi/2) = (\pi Y/2)^{1/2}\{1 + \mathrm{erf}[-\cot\chi(Y/2)^{1/2}]\}. \tag{17.21}$$

17.3 Production of Ionization

Values of the atmospheric density and solar ultraviolet radiation absorption cross sections have been given in previous chapters. Using the unit optical depth condition the formation of the different ionospheric regions can be related to portions of the solar ultraviolet spectrum in the following way:

A. The D *region* is formed by radiation whose absorption cross section is smaller than 10^{-19} cm^2. This includes solar x rays having wavelengths less than 10 Å and ultraviolet radiation of wavelengths greater than 1750 Å. In addition, Lyman α (1216 Å) can penetrate deeply into the atmosphere because the O_2 absorption reaches a very small value ($\sim 10^{-20}$ cm^2) at this wavelength. Thus, x rays ionize O_2 and N_2, while Lyman α ionizes NO and other low ionization potential gases.

B. The E *region* is formed by radiation whose absorption cross section is less than 5×10^{-18} cm^2. Solar radiation in the range 100–31 Å and $\lambda > 800$ Å are of principal importance. The solar Lyman β line at 1025 Å and the C(III) line at 977 Å are of special importance since they both ionize O_2. The Lyman continuum at $\lambda < 910$ Å also contributes through ionization of O.

C. The F *region* derives from radiation whose absorption cross section is greater than 10^{-17} cm^2. This includes the range $100 < \lambda < 800$ Å and results in the photoionization of N_2, O_2, and O.

The vertical distribution of ionization in the upper atmosphere depends on both the rate of ion production and the different ion loss processes. Using Eq. (17.5), the ionization resulting from a flux $\phi(\lambda)$ of radiation is

$$q_j = n_j \sigma_I^j \phi_\infty(\lambda) e^{-\tau} \tag{17.22}$$

where n_j is the concentration of the jth ionizable gas and σ_I^j is the wavelength-dependent ionization cross section. Following the method introduced in Chapter 7, the product of the ionization cross section and solar flux can be combined to give the photoionization rate coefficient, $I_j(\lambda) = \sigma_I^j \phi_\infty(\lambda)$. Thus, (17.22) becomes

$$q_j = n_j I_j(\lambda) e^{-\tau} \tag{17.23}$$

with the total jth species ionization rate, Q_j, given by a summation over the different wavelength bands:

$$Q_j = \sum_\lambda q_j = n_j \sum_\lambda I_j(\lambda) e^{-\tau(\lambda)}. \tag{17.24}$$

Depending upon the assumption affecting the altitude distribution of the neutral gases, Eq. (17.23) can be manipulated to find the altitude of the peak ionization rate and the shape of the ionization production layer [4, 11, 12].

Since numerical analysis has largely replaced analytical approximation for computations, the basic ideas of ionization production are best illustrated in terms of absorption and ionization in a single constituent, constant scale height atmosphere. For such a model the neutral gas can be represented by

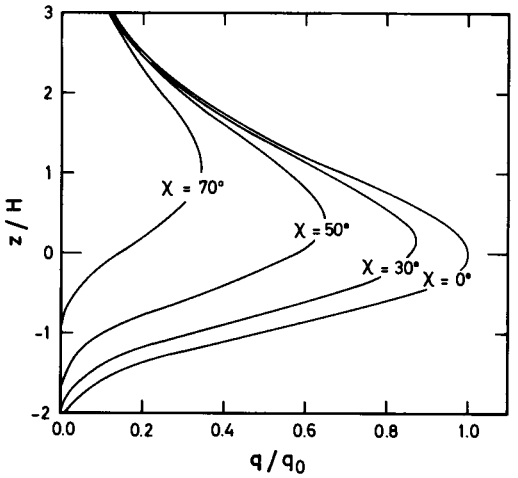


Fig. 17.4 Normalized values of ion production for a Chapman layer in an idealized isothermal, plane-stratified atmosphere for different solar zenith angles.

(17.10) and, as shown by *Fig. 17.4*, a production layer is formed. The maximum ion production rate, q_m of this layer can be obtained as

$$q_m = \sigma_I \phi_\infty e^{-1} \cos \chi / \sigma_a H \tag{17.25}$$

which occurs at an altitude where the implicit relation

$$n = (\sigma_a H \sec \chi)^{-1} \tag{17.26}$$

is satisfied; i.e., at unit optical depth.

The altitude dependence of the ion production rate follows from (17.22), (17.25), and (17.26) in the form

$$q = q_m \exp[1 - z/H - e^{-z/H} \sec \chi] \tag{17.27}$$

where the altitude z is measured relative to unit optical depth for $\chi = 0$; i.e., where

$$n = (\sigma_a H)^{-1} \tag{17.28}$$

is satisfied.

Equation (17.27) is the classical Chapman formula which predicts the form for ionization production due to the absorption of solar radiation in an isothermal atmosphere. At high altitudes absorption of the radiation is small; i.e., $\exp(-z/H)$ can be neglected and the ion production rate increases proportionately to the neutral gas density. Eventually, however, absorption reduces the intensity of the radiation so that a maximum rate is reached at unit optical depth, followed by a very rapid decrease at lower altitudes.

The normalized form for (17.27) is shown in Fig. 17.4 for different solar zenith angles. As χ increases the magnitude of the peak decreases according to (17.25) while the peak altitude moves upward as predicted by (17.26).

Using Chapman's expression for ion production, it is possible to anticipate the results of the next chapter and assume that electrons and ions are lost in a dissociative recombination process of the typical form

$$AB^+ + e \rightarrow A + B \tag{17.29}$$

with a recombination coefficient α. The equation for ionization equilibrium follows from (17.27) and (17.29) as

$$\alpha n_e^2 = q \tag{17.30}$$

or

$$n_e = (q/\alpha)^{1/2} \tag{17.31}$$

giving

$$n_e = (q_m/\alpha)^{1/2} \exp \tfrac{1}{2} [1 - z/H - e^{-z/H} \sec \chi] \tag{17.32}$$

as the vertical distribution of ionization in a simple Chapman layer.

Using (17.25) for the peak production rate it follows that the peak electron density depends on solar zenith angle as

$$n_{e|max} = (\sigma_I \Phi_\infty e^{-1} \cos \chi / \sigma_a H \alpha)^{1/2} \tag{17.33}$$

which has formed the basis for many experimental analyses.

Although the Chapman formulas provide a very convenient analytical form to describe the formation of the ionosphere, they are subject to substantial correction. In the first place there are a large number of wave-

length bands which contribute to the overall ionization of the D, E, and F regions. These radiations are absorbed by three gases (O, O_2, N_2) having different cross sections and vertical distributions. This problem is especially important for the ionization of atomic oxygen since in the wavelength range 910–796 Å N_2 is not itself ionized but acts as an absorber preventing the penetration of radiation. Next, the distribution of gases in the atmosphere is not the simple isothermal expression of (17.10) but more complicated owing to the presence of important thermal gradients arising from the absorption of solar radiation. Using (17.12) it is possible to derive expressions equivalent to (17.33) for an atmosphere where there is a constant scale height gradient [13]. However, such an analytical form is useful only to the extent that it gives physical insight for the problem of photoabsorption. For example, the extension of Eq. (17.33) to conditions appropriate to a constant scale height gradient atmosphere shows that the peak density of a Chapman layer becomes

$$n_e\big|_{\max} \propto (\cos \chi)^{(1+\beta)/2}, \tag{17.34}$$

showing that the existence of a scale height gradient can appreciably affect the dependence of the peak density upon solar zenith angle.

Nevertheless, for the actual atmospheric conditions it is usually necessary to use numerical methods to integrate the density of atmospheric species along the optical path through regions which have substantially different conditions than those found lying directly above the observation point.

17.4 Calculations of Atmospheric Photoionization

The absorption of solar radiation is the initial process in the chain of complicated actions ultimately resulting in the ionosphere. The emphasis of the preceding chapters has been directed towards the presentation of the basic physical quantities which affect the aeronomical processes of the upper atmosphere. At this point, however, it is possible to combine basic atomic cross-section data, the most recently available information concerning the solar ultraviolet radiations, and a set of working models of the atmospheric composition to give an indication of the expected ionizations which can take place. In such a synthesis of information it cannot be claimed that an accurate representation of the actual ionosphere productions has been made. Nevertheless, the results are consistent within the approximations adopted and serve as guides to further studies.

Any discussion of ionospheric ionization processes divides naturally at about the mesopause. Above this altitude the E and F regions are produced by long wavelength x rays and the extreme ultraviolet, while below the mesopause the D region ions arise from short wavelength x rays, cosmic rays, and Lyman α. This division of processes is emphasized in the separate treatments given in the following two sections.

17.4.1 Production of Ionization in the E *and* F *Regions*

The basic photoabsorption and photoionization data needed to compute the altitude distribution of initial ions have been given in Chapters 6 and 7. The atmospheric models are those described in Appendix B. To show the actual penetration of the adopted bands of radiation, *Fig. 17.5* shows the transmission of the solar flux for two model thermospheres: The 1000°K model to represent low solar activity and the 1500°K model for maximum solar activity. It can be inferred that the absorption by N_2 is especially effective in the range 796–275 Å and acts to prevent ionization deep in the atmosphere by these radiations. Because of the greater column densities, absorption in the 1500°K model takes place at a substantially higher altitude than for the 1000°K model. Although the changes associated with varying

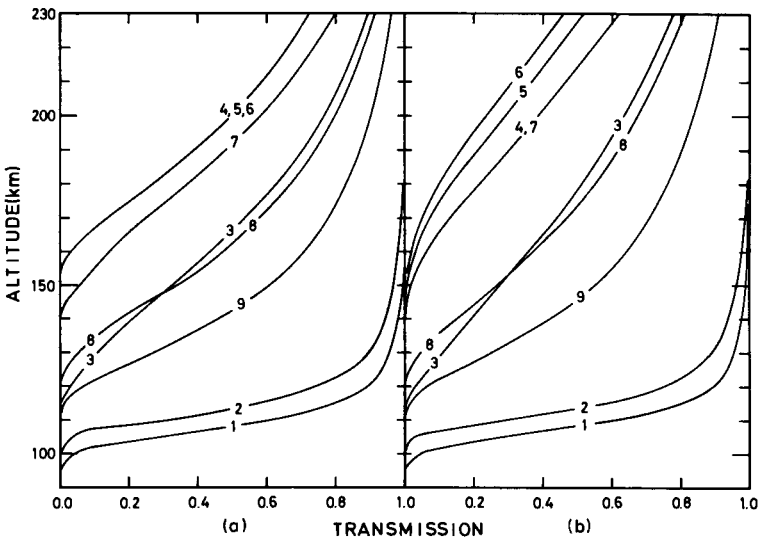


Fig. 17.5 Penetration of solar radiation 1026–80 Å at a 60° zenith angle into two model thermospheres. (a) $T = 1000°K$; (b) $T = 1500°K$; (1) 1026 Å, (2) 977 Å, (3) 910–796 Å, (4) 796–732 Å, (5) 732–665 Å, (6) 665–375 Å, (7) 375–275 Å, (8) 275–150 Å, and (9) 150–80 Å.

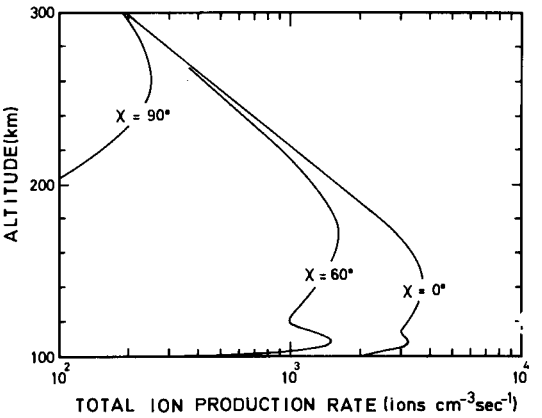


Fig. 17.6 Total ion production rate for various solar zenith angles in a 1000°K model thermosphere using photoionization rates for low solar activity.

the solar zenith angle from 0° to 60° are not dramatic, they represent real effects. At twilight such a behavior is more pronounced.

To show the dependence of the total ion production rates on solar zenith angle and thermopause temperature, the ionization rate coefficients given in Table 7.19 have been applied to the $T = 1000°K$ and $T = 1500°K$ model thermospheres. The results, shown in *Figs. 17.6* and *17.7*, include three solar zenith angles ($\chi = 0°, 60°, 90°$) and take account of all ground state and excited ions of a given species. As expected, it is found that the ionization maxima moves upward in the warmer atmospheric model with some slight

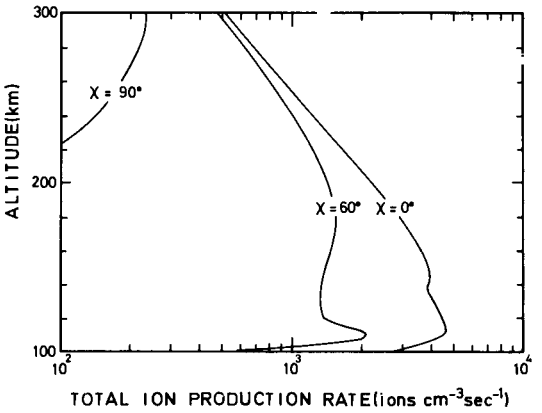


Fig. 17.7 Total ion production rate for various solar zenith angles in a 1500°K model thermosphere for high solar activity.

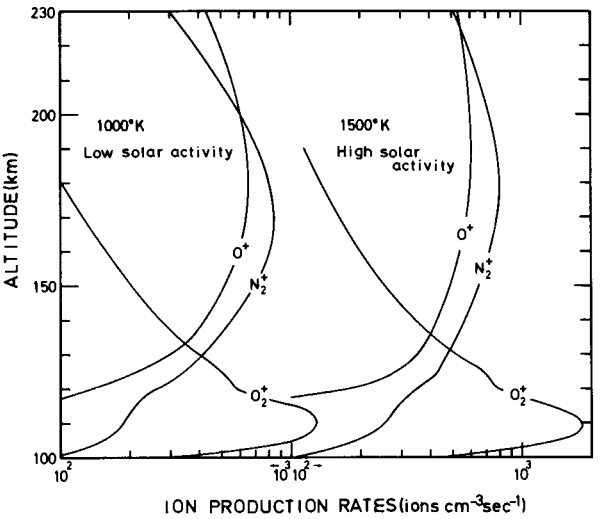


Fig. 17.8 Individual ion production rates for a 60° solar zenith angle in 1000° and 1500°K model thermospheres for low solar activity and high solar activity, respectively.

change in initial abundances due to the N_2 absorption effect. The production rates for individual ions at $\chi = 60°$ are shown in *Fig. 17.8*.

As indicated in the discussion of Chapter 6, substantial numbers of the initial photoions are created in excited states. For metastable states this

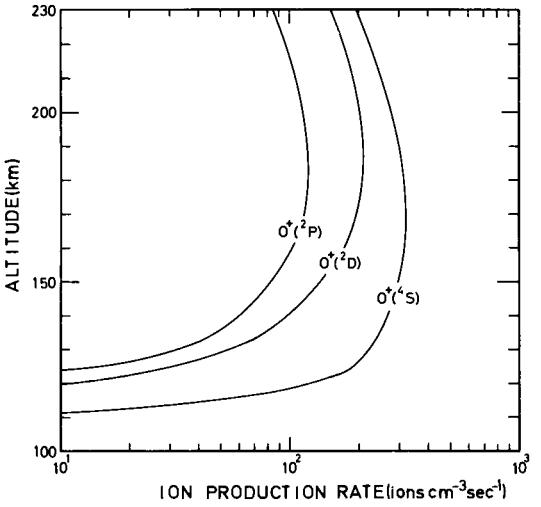


Fig. 17.9 Production rates of O^+ in a 1000°K model thermosphere at 60° solar zenith angle for low solar activity.

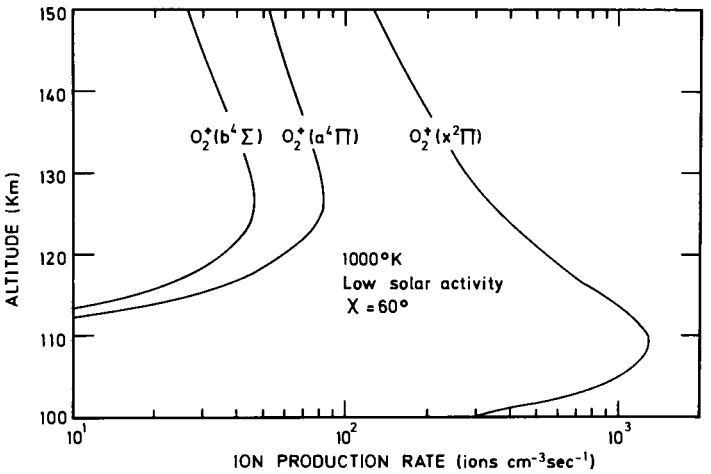


Fig. 17.10 Production rates of O_2^+ in a 1000°K model thermosphere at 60° solar zenith angle for low solar activity.

introduces the possibility of additional reactions which cannot be accomplished with ground state ions. Production rates of the major excited species are shown in *Figs. 17.9–17.11* for the 1000°K thermospheric model for a zenith angle of 60°. The production of $O^+(^2D)$ is of special importance since it leads to a direct charge exchange reaction with N_2, producing N_2^+ rather than the NO^+ which follows $O^+(^4S)$ reactions.

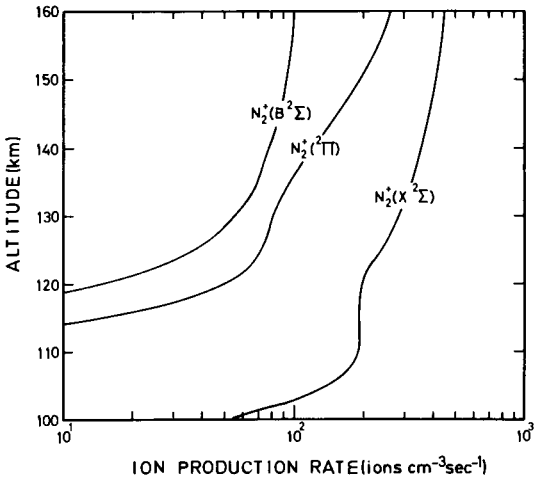


Fig. 17.11 Production rates of N_2^+ in a 1000°K model thermosphere at 60° solar zenith angle for low solar activity.

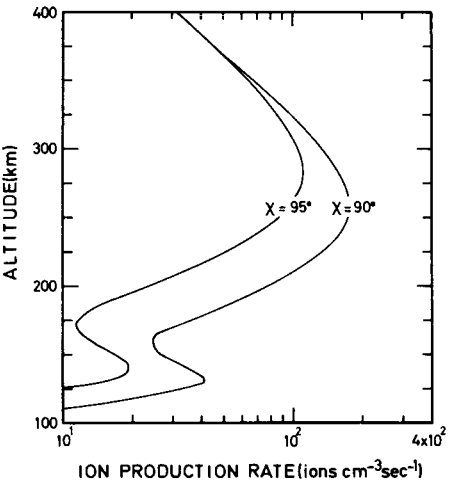


Fig. 17.12 Total ion production rates for a 1000°K model thermosphere at two solar zenith angles for low solar activity.

To illustrate twilight effects, *Fig. 17.12* shows the total ion production rates for zenith angles of 90° and 95°. These computations are based on a laterally uniform 1000°K model thermosphere. It is seen that the ionization rate becomes rapidly less at lower altitudes with an upward change of the E-region ionization production.

17.4.2 Production of Ionization in the D *Region*

Penetration of radiation into the mesosphere is governed by the absorption cross sections of the major constituents and, in at least one case, by a minor constituent. For the range $100 < \lambda < 910$ Å, N_2 and O absorb strongly and solar radiations of these wavelengths are absent in the mesosphere. This is not the case, however, for radiations of both shorter and longer wavelength. At the x-ray side of the spectrum, absorption cross sections become progressively smaller so that solar x rays are an important source of ionization in the upper mesosphere.

The situation for $\lambda > 910$ Å is somewhat more complex. Here O_2 presents an absorption cross section which is very irregular, permitting penetration of radiation in some windows having cross sections as small as 4×10^{-21} cm^2 while absorbing radiations only a few angstroms away with cross sections of 10^{-18} cm^2. Thus, by chance Lyman α is not greatly absorbed and is available to ionize low ionization potential molecules such as NO down to 75 km.

It is generally thought that the ionization of NO by Lyman α is the principal source of ions in the upper mesosphere [14]. However, because the x-ray spectrum changes greatly during periods of solar disturbance

there are times when the x-ray production of O_2^+ and N_2^+ is able to be of the same magnitude as the Lyman α photoionization of NO. Deeper in the atmosphere, i.e., from 70 km down to 30 km, galactic cosmic rays produce a steady ionization through particle impact. Since these energetic particles are ions, they are deflected by the geomagnetic field and a magnetic latitude dependence is introduced into the ion densities of these lower regions. Following large solar flares in the proper solar sector, large fluxes of MeV protons penetrate the mesosphere, producing intense ionization for several days following the onset [15].

Because the D region is subject to these various ionization sources, it is useful to discuss separately the effects of long wavelength x rays, Lyman α, short wavelength x rays, galactic cosmic rays, and solar protons.

$31 < \lambda < 80$ and Lyman β

X radiation in the range $31 < \lambda < 80$ Å and Lyman β (1026 Å) have sufficiently large absorption cross sections such that unit optical depth is reached above 100 km. Consequently, the ionization rate decreases very rapidly on the bottom side of the E region [16].

Because a large fraction of the ionization produced by these long wavelength x rays depends upon secondary electron impact, calculations of the ionization yield in air mixtures are necessary. This problem involves evaluation of all possible channels of electron energy loss including ionization and excitation. Because the various cross sections are not known with sufficient accuracy only estimates can be made of the fractions of different ions. From a recent study [15], if q is the total ion production rate, the individual ion production rates are expected to be in the ratios:

$$q(O_2^+)/q = 0.17,\ q(N^+)/q = 0.14,\ q(N_2^+)/q = 0.62,\ \text{and}\ q(O^+)/q = 0.07.$$

Lyman β is able to penetrate deeply into the atmosphere since O_2 is the only effective absorber. Unit optical depth for this radiation is reached near 115 to 120 km. Thus, ionization from this source decreases rapidly in intensity below 100 km and is very sensitive to minor changes in O_2 column content. The altitude profiles for the Lyman β O_2^+ production are included in Fig. 17.6 for several solar zenith angles.

Lyman α

Through a chance of nature Lyman-α radiation falls in an absorption window of O_2 and reaches unit optical depth near 75 km. Although the ionization thresholds of the major atmospheric constituents lie at shorter wavelengths than Lyman α, ionization of NO occurs and is a major source

of ions in the upper D region [14, 17]. Ionization rate coefficients for NO have already been given in Table 7.16 for three solar zenith angles but the absolute production rate for NO^+ remains in doubt because the NO concentration is not satisfactorily known. (The discussion of these uncertainties is given in Chapter 12.) The ion production rate shown in Fig. 17.14 has been obtained assuming that $n(NO) = 1 \times 10^7\ cm^{-3}$. Thus, the NO^+ production rate profiles illustrated cannot be regarded as definite.

Nonflare Solar X Rays (1–10 Å)

The altitude of unit optical depth for x rays in the wavelength range 1–10 Å varies from 58 to 100 km (compare the absorption cross sections of Tables 6.1 and 6.2 with the atmospheric column contents of Table 3.2). As shown by the ionization rate coefficients of Table 7.6, the relative importance of these radiations is closely linked with the degree of solar activity, a range of 10^3 existing between the completely quiet and disturbed conditions. These variations obviously affect the mesospheric ionization rate and introduce a degree of variability connected with solar rotation. Plots of the ionization production rate for the rates of Chapter 7 are given in *Fig. 17.13.* The actual initial ion ratios can be obtained from the factors quoted in the last section.

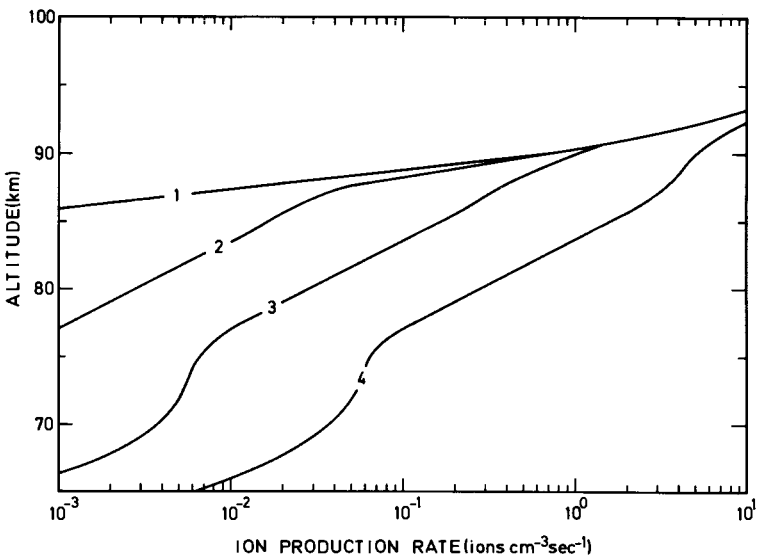


Fig. 17.13 Ion production arising from 1 to 10 Å x rays with a solar zenith angle of 60° for several solar conditions given in Chapters 6 and 7. Solar activity: (1) completely quiet, (2) quiet, (3) lightly disturbed, and (4) disturbed.

Galactic Cosmic Rays

Cosmic rays of galactic origin penetrate deeply into the atmosphere creating ionization in proportion to the atmospheric density. Scattering of cosmic rays occurs in the interplanetary medium, but the principal effect on the global distribution arises from their interaction with the geomagnetic field [17]. This effect is reflected in the exclusion of particles lacking a minimum magnetic rigidity. Experiments have shown a solar cycle effect on cosmic ray fluxes near the earth, presumably related to the structure of the solar wind. Measurements of global ionization rates [18, 19] during 1954 showed a factor of 10 increase between 0° and 60° magnetic latitude, with little change from 60° to the poles. At solar maximum (1958) the latitudinal increase was reduced to a factor of 5 while the 1954 flux was about twice the 1958 flux.

The variation of the incident cosmic ray flux with latitude is important, but an insufficient number of studies have been made to deduce its dependence upon geomagnetic coordinates. *Table 17.1* gives the dependence of the overall ionization rate upon geometric latitude for solar minimum and

TABLE 17.1

GALACTIC COSMIC RAY IONIZATION COEFFICIENTS[a]

Geometric latitude (deg)	Ionization coefficient (10^{-18} sec^{-1})	
	Solar maximum	Solar minimum
0	2	3
10	2	3
20	2	4
30	3	6
40	5	9
50	8	14
60	9	19
70	9	21
80	9	22
90	9	23

[a] From Swider [16].

solar maximum conditions [16]. As a form adequate for approximation, the expression [17]

$$p = 10^{-17} n(\text{air}) \quad \text{ions cm}^{-3}\,\text{sec}^{-1} \tag{17.35}$$

has been used for conditions at 50° geomagnetic latitude. Depending upon the concentration of NO, cosmic ray produced ionization becomes the largest source of ions between 60 and 70 km (see *Figure 17.14*).

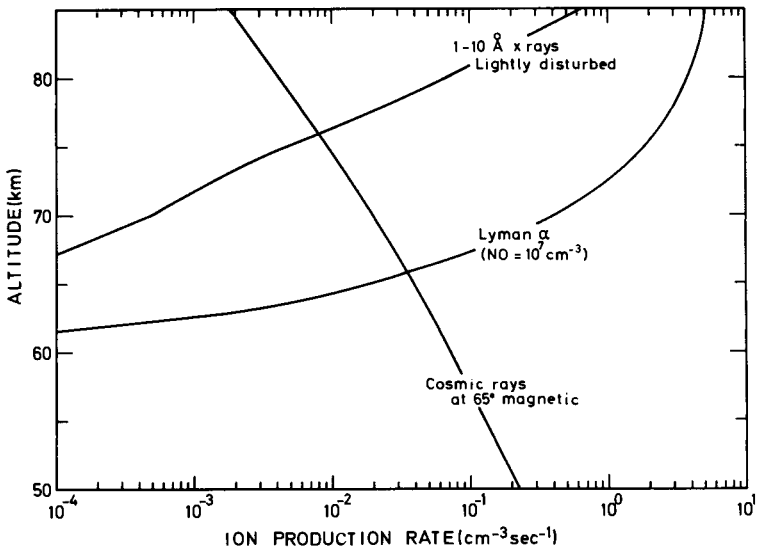


Fig. 17.14 D-region ion production profiles.

Solar Flare X Rays

During solar flares the short wavelength x-ray spectrum is greatly enhanced and extra ionization is produced in the D region as low as 60 km altitude. Both the magnitude and shape of the spectrum vary from flare to flare, but typical ionization coefficients associated with this activity have been given in Table 7.6 showing factors of 10^5 increase over completely quiet conditions. The profiles of ion production associated with such disturbances are shown in Fig. 17.13.

Photoionization of $O_2(^1\Delta_g)$

Appreciable quantities of $O_2(^1\Delta_g)$ have been observed in the mesosphere. The ionization threshold of this molecule lies at 1118 Å and a possibility exists for its photoionization deep in the atmosphere due to the presence

of an O_2 absorption minimum in the vicinity of 1108 Å [20, 21]. The first calculations [16, 20] of this process were based on an absorbing O_2 atmosphere and showed that unit optical depth for the ionization of $O_2(^1\Delta_g)$ occurred between 80 and 90 km. The peak production rate for this process was thought to be an order of magnitude greater than that for long wavelength x rays (10–100 Å) or Lyman α. In a more recent study [22] the importance of this ionization source was questioned on the basis that the solar radiation is absorbed not only by O_2, but also by CO_2. It was shown that the effect of CO_2 is to greatly reduce the $O_2(^1\Delta_g)$ ionization rate to values somewhat smaller than those found for the more conventional ionization processes. Nevertheless, it is still thought that this source of O_2^+ may be needed to explain the altitude variation of electron densities in the upper mesosphere [23] (see Chapter 18).

17.4.3 Nightsky Radiations

The ionization processes discussed in the last two sections arise from direct solar illumination. As the solar zenith angle increases beyond 90° such radiations are rapidly absorbed by the atmosphere and become ineffective in producing ionization. Nevertheless, the analysis of experimental data suggests that additional ultraviolet radiations are needed to explain the maintenance of a low density E region throughout the night [24–26].

The importance of the resonance scattering of solar Lyman α in the hydrogen corona of the earth was deduced directly following the first rocket measurements [27]. The theory of this process is well understood and computations of the nightsky intensities have been made [28], showing that Lyman α photon fluxes of the order 10^9 photons cm^{-2} sec^{-1} are available to ionize NO in the D and E regions.

In addition to Lyman α, the existence of other resonantly scattered radiations capable of ionizing the atmosphere was suggested in 1960 [29]. Subsequently, Lyman β and He(II) (304 Å) have been found to be important features of the night airglow [30–32]. The Lyman β radiation is of the order $5\text{–}10 \times 10^6$ photons cm^{-2} sec^{-1} while the He(II) (304 Å) intensity appears to be slightly less. Both sources are capable of producing E-region ionization, although in different altitude regions, the peak 304 Å contribution occurring near 140 km [32] as opposed to 115 km for Lyman β.

Computations of the expected variation of the nightsky ionization rates are complex owing to the necessity for including radiative transport through the hydrogen and helium geocorona. Nevertheless, it is clear that these radiations are responsible for the principal portion of the nighttime E and upper D regions.

17.5 Other Sources of Ionization

The processes described in the last three sections are the principal known sources of ionization in the mesosphere and thermosphere. However, no mention was made of the photoionization of H and He, auroral ionization, or solar proton events. The first two topics are discussed further in Chapter 21, while the impact ionization associated with electron, proton, and α particle bombardment requires a more detailed discussion than can be given here. Reviews of the basic processes for these ionizations are available in the literature [15, 33–35].

REFERENCES

1. E. V. Appleton and M. A. F. Barnett, *Proc. Roy. Soc.* **A109**, 621 (1925).
2. G. Breit and M. A. Tuve, *Phys. Rev.* **28**, 554 (1926).
3. J. A. Ratcliffe, (ed.) *Physics of the Upper Atmosphere.* Academic Press, New York, 1960.
4. S. Chapman, *Proc. Phys. Soc. (London)* **43**, 483 (1931).
5. E. O. Hulburt, *Phys. Rev.* **55**, 639 (1939).
6. M. V. Wilkes, *Proc. Phys. Soc. (London)* **B67**, 304 (1954).
7. A. E. S. Green, C. S. Lindenmeyer, and M. Griggs, *J. Geophys. Res.* **69**, 493 (1964).
8. J. A. Fitzmaurice, *Appl. Opt.* **3**, 640 (1964).
9. W. Swider, *Planet. Space Sci.* **12**, 761 (1964).
10. W. Swider and M. E. Gardner, *Appl. Opt.* **8**, 725 (1969).
11. S. Chapman, *Proc. Phys. Soc. (London)* **43**, 26 (1931).
12. S. Chapman, *Proc. Phys. Soc. (London)* **51**, 93 (1939).
13. M. Nicolet, *J. Atmos. Terr. Phys.* **1**, 141 (1951).
14. M. Nicolet, *Mem. Inst. Meteorol. Belg.* **19**, 83 (1945).
15. D. K. Bailey, *Planet. Space Sci.* **12**, 495 (1964).
16. W. Swider, *Rev. Geophys.* **7**, 573 (1969).
17. M. Nicolet and A. Aikin, *J. Geophys. Res.* **65**, 1469 (1960).
18. H. V. Neher and J. R. Anderson, *J. Geophys. Res.* **67**, 1309 (1962).
19. H. V. Neher, *J. Geophys. Res.* **72**, 1527 (1967).
20. D. M. Hunten and M. B. McElroy, *J. Geophys. Res.* **73**, 2421 (1968).
21. K. Watanabe, *Advan. Geophys.* **5**, 153 (1958).
22. R. E. Huffman, D. E. Paulsen, J. C. Larrabee, and R. B. Cairns, *J. Geophys. Res.* **76**, 1028 (1971).
23. T. Donahue, *Radio Sci* **7**, 73 (1972).
24. W. Swider, *Space Res.* **5**, 212 (1965).
25. T. Ogawa and T. Tohmatsu, *Rep. Ionos. Space Res. Japan* **20**, 395 (1966).
26. T. Tohmatsu, *Space Res.* **10**, 608 (1970).
27. E. T. Byram, T. A. Chubb, and H. Friedman, in *The Threshold of Space* (M. Zelikoff, ed.), p. 203. Pergamon, Oxford, 1957.
28. R. R. Meier and P. Mange, *Planet. Space Sci.* **18**, 803 (1970).
29. H. Friedman, in *Physics of the Upper Atmosphere* (J. A. Ratcliffe, ed.), p. 202, Academic Press, New York, 1960.

30. J. M. Young, G. R. Carruthers, J. C. Holmes, C. Y. Johnson, and N. P. Patterson, *Science* **160**, 990 (1968).
31. C. Y. Johnson, J. M. Young, and J. C. Holmes, *Science* **171**, 379 (1971).
32. J. M. Young, C. S. Weller, C. Y. Johnson, and J. C. Holmes, *J. Geophys. Res.* **76**, 3710 (1971).
33. M. H. Rees, *Planet. Space Sci.* **11**, 1209 (1963).
34. J. C. G. Walker and M. H. Rees, *Planet. Space Sci.* **16**, 459 (1968).
35. G. W. Adams and A. J. Masley, *J. Atmos. Terr. Phys.* **21**, 289 (1965).

CHAPTER 18

Ionospheric Processes

18.1 Introduction

Many years of intensive research have been devoted to the complex problems associated with the formation and subsequent dynamical behavior of ionospheric ions and electrons [1]. Prior to the era of rocket and satellite experiments it was necessary to deduce the nature of ionospheric processes from measured values of electron density obtained through ground based radio experiments. Deductions obtained in this way were always incomplete, however, since the identity of the ions associated with the electrons could only be surmised on the basis of a sketchy knowledge of the composition of the neutral atmosphere.

With the possibility of *in situ* measurements of both ion and neutral gas composition the earlier models of the ionosphere have been extensively modified and improved. The principal processes associated with the E, F, and topside regions are thought to be reasonably well understood [2, 3] although various difficulties associated with reaction rates and the effects of excited gas species remain to be resolved. In the D region, however, such a comprehensive view has not been possible and models have had to be revised to include complex cluster ions whose mechanisms of production and loss are not yet known in detail [4–6].

A typical daytime profile of measured ion composition above 100 km at midlatitudes has been shown in Fig. 17.1. It illustrates an essential problem of ionospheric chemistry; i.e., how to explain the virtual absence of N_2^+, the principal photoion between 130 and 220 km, and the dominance

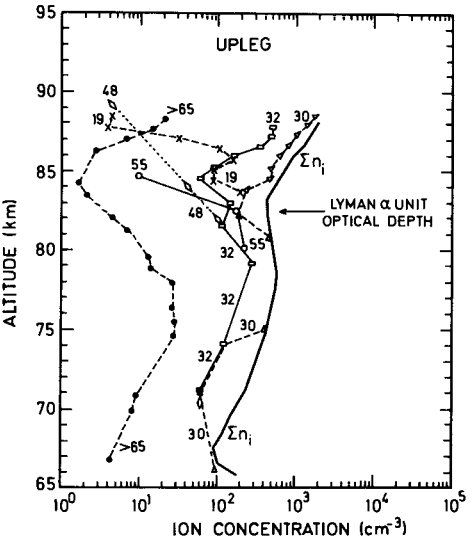


Fig. 18.1 Daytime D-region positive ion composition obtained [7] at Thumba, India on March 19, 1970 at a solar zenith angle of 53.2 degrees. The solid curve, $\sum n_j$ represents the total ions. *Key*: crosses, H_3O^+; triangles, NO^+; rectangles, O_2^+; diamonds, NO^+H_2O; open circles, $H_3O^+(H_2O)_2$; closed circles, total >65.

of NO^+, an ion whose parent neutral is present in the upper atmosphere only as a trace constituent.

To illustrate the positive ions of the D region, the results of an equatorial rocket measurement [7] are shown in *Fig. 18.1*. Concentrations of negative ions in the same altitude range but obtained at high latitudes [8, 9], are shown in *Fig. 18.2*. With regard to the positive ions, it is observed that the atomic and molecular ions found above 100 km are largely absent. In their place heavy water vapor ion clusters are present in large numbers.

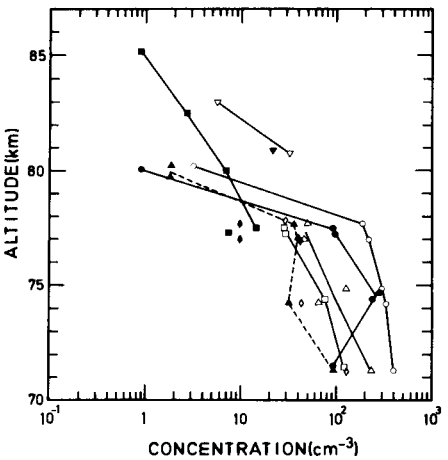


Fig. 18.2 Nighttime negative ion composition obtained by rocket measurements (F22 upleg and downleg) at high altitude [8], Andoya, Norway, on March 23, 1970 at 2358 LT. *Key*: open circle, 60 (CO_3^-); closed circle, 35 (Cl^-); open triangle △, 61 (HCO_3^-); closed triangle ▲, 62 (NO_3^-); open square, 37 (Cl^-); closed square, 32 (O_2^-); open diamond, 93 ($NO_2^- \cdot HNO_2$); closed diamond, 76 (CO_4^-); open triangle ▽, 111 ± 1; closed triangle ▼, 125 ± 1.

As will be discussed in Section 18.3, not only is the chemistry of this region exceedingly complex but also it is not clear if all the fundamental ionization processes are yet known [5].

In the preceding chapter definitions of the ionospheric regions were given in terms of the absorption of certain spectral bands of solar radiation. Using present knowledge of the ionosphere obtained through both direct measurements and laboratory reaction data, it is possible to give definitions of the ionospheric regions which are based on the characteristic ion processes rather than on the older boundaries related to the variations of electron density measured by radio wave reflections.

Anticipating the results of this chapter, the D region can be considered as the lowest portion of the ionosphere where water vapor cluster ions, both positive and negative, tend to dominate the ion composition and chemistry. Such a definition gives a nebulous lower boundary near 50 km and a rather abrupt upper edge near 85 km where there is a rapid transition to the molecular ions NO^+ and O_2^+ as major constituents as well as O^+ and metallic ions as minor constituents. Owing to diurnal and seasonal variations in minor constituent concentrations in the neutral atmosphere it is clear that such an upper boundary cannot remain fixed in time or altitude.

Above 85 km the cluster ions give way to the molecular ions of the E region, O_2^+ and NO^+. As a consequence of atmospheric absorption of radiation for $\lambda < 910$ Å, the principal initial ion of the E region is O_2^+ resulting from Lyman β and the C(III) line at 977 Å. A peak in the electron density distribution is frequently observed with a gradual change in the ratio NO^+/O_2^+ such that NO^+ becomes dominant near 140 km. As shown in Fig. 17.1 this transition corresponds to a conventional upper boundary for the E layer. Such a definition is somewhat arbitrary, however, since the ion reaction chains are essentially the same at lower and higher altitudes; it is only the relative abundance of the initial photoions and the changing atmospheric composition which alters the steady state ion ratios.

A more reasonable boundary to the E region, but one which conflicts with the layers deduced from radio measurements, can be based on the transition from the molecular ions NO^+ and O_2^+ to the atomic ion, O^+. This transition can occur as low as 170 km in the daytime or as high as 220 km at night. As illustrated in Fig. 17.1, the dominance of O^+ is rapidly established as a consequence of the change in the neutral atmosphere from molecular to atomic particles.

Although the F_1-region definitions are rather vague, the transition to O^+ ions is an important feature. Above 200 km the vertical distribution of ions and electrons is increasingly governed by the mechanical forces of gravity

and pressure gradients with the result that at high altitudes (250–350 km) the O^+ concentration reaches a maximum value, then decreases with height. The ionospheric regime where diffusive motions occur is the F_2 region. Although the ion reaction chains of the F_2 region are identical with those of the F_1 and E regions, the process of ion diffusion acts as the major distinguishing feature with O^+, the principal photoion, as the dominant thermal ion.

In this chapter analysis are given of the ion reaction chains thought to be important in the middle (E and F_1 regions) and lower (D region) ionosphere; i.e., those regions where ion transport can generally be neglected and the individual ion concentrations are determined from the equation of continuity:

$$\partial n_i/\partial t = p_i - l_i \tag{18.1}$$

where n_i is the ith ion concentration, p_i and l_i are the production and loss rates, and charge neutrality is assumed in the form $n_e = \sum n_i$. After an initial discussion of simple ionospheric behavior, the progression of topics is upwards from the poorly understood D region into the E and F_1 regions where the basic processes appear to be well known.

18.2 Simple Models of the Ionosphere

The reaction chains leading from initial photoions to steady state ion densities are sufficiently complex to require numerical analysis [10, 11]. Insight with regard to the most important processes can be obtained, however, through consideration of simple models involving electrons, a positive ion species, and, in the D region, negative ions. While the results given by analysis of such models cannot be completely accurate, they do provide convenient analytical expressions which can be compared with the actual behavior.

18.2.1 The D *Region*

Consider a simple model of the D region where a single positive molecular ion, n^+, is created through photoionization at a rate In with I the altitude dependent photoionization coefficient ($I \sim 10^{-7}$ sec^{-1}) and n the neutral gas concentration. Once created, the positive ions remain until dissociative recombination (coefficient $\alpha_D \sim 10^{-6}$ cm^3 sec^{-1}) with electrons or mutual neutralization with negative ions (coefficient $\alpha_i \sim 10^{-6}$ cm^3 sec^{-1}) occurs. Negative ions are formed in this model through three-body collisional

attachment (see Chapter 10 and the formation of O_2^-) at a rate an^2n_e. Negative ions can be destroyed through photodetachment (coefficient $d \sim 0.4\ \text{sec}^{-1}$ for O_2^-) or associative detachment through ionic reactions (coefficient $f \sim 10^{-10}\ \text{cm}^3\ \text{sec}^{-1}$) with minor constituents (density n_m).

The time dependent equations describing the time variation of such a system are

$$dn^+/dt = In - \alpha_D n_e n^+ - \alpha_i n^+ n^- \tag{18.2}$$

$$dn^-/dt = an^2 n_e - n^-(d + fn_m + \alpha_i n^+) \tag{18.3}$$

$$dn_e/dt = In - \alpha_D n_e n^+ - an^2 n_e + n^-(d + fn_m). \tag{18.4}$$

If the ratio $\lambda = n^-/n^+$ is introduced, the various densities can be expressed as

$$n^+ = n_e + n^- = n_e(1 + \lambda). \tag{18.5}$$

Using Eqs. (18.5) and (18.2)–(18.4), the time variation of electron density can be written as

$$\frac{dn_e}{dt} = \frac{nI}{1 + \lambda} - (\alpha_D + \lambda\alpha_i)n_e^2 - \frac{n_e}{1 + \lambda}\frac{d\lambda}{dt} \tag{18.6}$$

or, in alternative form,

$$\frac{dn_e}{dt} = \frac{an^2 n_e}{\lambda} - n_e[d + fn_m + (1 + \lambda)\alpha_i n_e) - \frac{n_e}{\lambda}\frac{d\lambda}{dt}. \tag{18.7}$$

These equations can also be used to determine the time variation of λ:

$$\frac{1}{\lambda(\lambda + 1)}\frac{d\lambda}{dt} = \left[\frac{an^2}{\lambda} - (d + fn_m)\right] - \left[\frac{nI}{(1 + \lambda)n_e} + (\alpha_i - \alpha_D)n_e\right]. \tag{18.8}$$

Steady state values of λ can be considered for three different conditions related to the effects of solar radiation:

a. In a sunlit atmosphere

$$\lambda = \frac{an^2 - [\lambda/(\lambda + 1)][nI/n_e)}{d + fn_m + (\alpha_i - \alpha_D)n_e}. \tag{18.9}$$

b. For twilight conditions where $I = 0$ due to the absorption of ultraviolet ionizing radiation

$$\lambda = \frac{an^2}{d + fn_m + (\alpha_i - \alpha_D)n_e}. \tag{18.10}$$

c. For nighttime conditions where $I = 0$ and $d = 0$

$$\lambda = \frac{an^2}{fn_m + (\alpha_i - \alpha_D)n_e}. \tag{18.11}$$

The typical behavior of the negative ion ratio can be discussed in terms of a modified form of Eq. (18.9):

$$\lambda = \frac{an^2}{d + fn_m}\left[1 + \frac{In}{(1+\lambda)n_e(d+fn_m)} + \frac{(\alpha_i - \alpha_D)n_e}{d + fn_m}\right]^{-1}. \tag{18.12}$$

Substitution of the order of magnitude values for the rate coefficients already given shows that the second and third terms in the denominator of (18.12) are much smaller than 1. Thus, the steady state approximation, λ_s, can be written as

$$\lambda_s \simeq an^2/(d + fn_m) \tag{18.13}$$

showing that λ will decrease with altitude owing to the simultaneous decrease in attachment rate and increase in the associative detachment rate (n_m is principally atomic oxygen which increases with altitude in the lower D region).

Using the reaction rates given in Chapter 9, (18.13) can be evaluated for O_2^- as

$$\lambda = \frac{1.6\times 10^{-30} n^2(O_2)}{0.3 + 2.5\times 10^{-10}[n(O) + n(O_2\,{}^1\Delta_g)]} \tag{18.14}$$

where atomic oxygen and $O_2(^1\Delta_g)$ are taken as the effective detachment gases. As discussed in the next section, λ is normally thought to be less than 1 below 70 to 75 km in the daytime. At night (18.14) predicts an increase in λ since photodetachment would no longer be an effective removal process.

The time variation of λ starting from some initial value λ_0 at $t = 0$ follows from (18.8). Neglecting the unimportant second term on the right, one obtains

$$\lambda(t) = \frac{\lambda_s - [(\lambda_s - \lambda_0)/(\lambda_0 + 1)]e^{-t/\tau}}{1 + [(\lambda_s - \lambda_0)/(\lambda_0 + 1)]e^{-t/\tau}} \tag{18.15}$$

where λ_s is the steady state value given by (18.13) and the decay time τ is

$$\tau = [an^2 + d + fn_m]^{-1}. \tag{18.16}$$

Using numerical coefficients for O_2^-, $\tau \leq 2$ sec for typical D-region con-

ditions. Thus, equilibrium of negative ions is the usual state in the sunlit D region, even allowing for the greatly altered negative ion chemistry that actually prevails.

Returning to the problem of D-region electron densities, Eq. (18.7) can be written ignoring $d\lambda/dt$; i.e.,

$$\frac{dn_e}{dt} = \frac{nI}{1+\lambda} - (\alpha_D + \lambda\alpha_i)n_e^2 \tag{18.17}$$

so that the steady-state electron density is

$$n_{es} = \left[\frac{nI}{(1+\lambda)(\alpha_D + \lambda\alpha_i)}\right]^{1/2} \tag{18.18}$$

while the time dependent variation starting from some initial value n_{eo} is

$$r(t) = \frac{1 + [(r_0 - 1)/(r_0 + 1)]e^{-t/\tau}}{1 - [(r_0 - 1)/(r_0 + 1)]e^{-t/\tau}} \tag{18.19}$$

where $r = n_e/n_{es}$, $r_0 = n_{eo}/n_{es}$, and the time constant τ is given by

$$\tau = [2(\alpha_D + \lambda\alpha_i)n_{es}]^{-1}. \tag{18.20}$$

18.2.2 The E *Region*

The ionic processes of the E region are linked to the presence of O_2^+ and the lack of negative ions. In the absence of convective motions the plasma equation of continuity is

$$dn_e/dt = In - \alpha_D n_e^2 \tag{18.21}$$

where I is to photoionization coefficient, α_D is the dissociative recombination coefficient for the molecular ion n^+, and $n_e = n^+$.

The steady state electron density corresponding to (18.21) is

$$n_{es} = [In/\alpha_D]^{1/2} \tag{18.22}$$

and the time-dependent variation starting from some initial electron density n_{eo} is

$$r(t) = \frac{1 + [(r_0 - 1)/(r_0 + 1)]e^{-t/\tau}}{1 - [(r_0 - 1)/(r_0 + 1)]e^{-t/\tau}} \tag{18.23}$$

where $r = n_e/n_{es}$, $r_0 = n_{eo}/n_{es}$, and the time constant τ is

$$\tau = [2\alpha_D n_{es}]^{-1}. \tag{18.24}$$

Since $\alpha_D \simeq 10^{-7}$ cm^3 sec^{-1} in the E region, while a typical value of n_e is 5×10^5 cm^{-3}, $\tau \simeq 10$ sec; i.e., the electron density closely follows variations in the production rate.

The form of (18.21) can be used to deduce the decay of ionization from some initial value n_{eo} when ionic production suddenly vanishes. The result is

$$n_e(t) = n_{eo}/(1 + \alpha_D n_{eo} t). \tag{18.25}$$

Owing to the presence of low level nightsky radiations, however, the approximation given by (18.25) cannot be entirely accurate. Equation (18.23) correctly represents the variation of electron density for an instantaneous decrease in ion production.

18.2.3 The F_1 Region

Above about 170 km atomic oxygen ions become important to the overall ionization balance. Owing to the slowness of radiative recombination for atomic ions, ionization created through photoionization of atomic oxygen is lost through ion–atom interchange followed by molecular dissociative recombination.

To show the basic features, consider the following processes:

$$(I): \quad O + h\nu \rightarrow O^+ + e \tag{18.26}$$

$$(\gamma): \quad O^+ + N_2 \rightarrow NO^+ + N \tag{18.27}$$

$$(\alpha_D): \quad NO^+ + e \rightarrow N^* + O^*. \tag{18.28}$$

The time-dependent behavior of this system is described by the equations

$$\frac{dn(O^+)}{dt} = In(O) - \gamma n(N_2) n(O^+) \tag{18.29}$$

$$\frac{dn(NO^+)}{dt} = \gamma n(N_2) n(O^+) - \alpha_D n(NO^+) n_e. \tag{18.30}$$

Since NO itself is a minor atmospheric constituent, it can safely be omitted from (18.30) for the purposes of this illustrative behavior.

The steady state O^+ concentration follows from (18.29) as

$$n_s(O^+) = In(O)/\gamma n(N_2) \tag{18.31}$$

showing the exponential increase in $n(O^+)$ with altitude arising from the balance between ion production and loss. Taking the typical values

$I(O^+\ ^4S) = 1.6\times10^{-7}\ \text{sec}^{-1}$, $\gamma = 6\times10^{-13}\ \text{cm}^3\ \text{sec}^{-1}$, this expression becomes

$$n_s(O^+) \simeq 2.7\times10^5 n(O)/n(N_2) \quad \text{cm}^{-3} \tag{18.32}$$

in the absence of ion diffusion.

The time variation of $n(O^+)$ follows directly from (18.29) as

$$n(O^+) = n_s(O^+) + [n_0(O^+) - n_s(O^+)]e^{-t/\tau} \tag{18.33}$$

where

$$\tau = [\gamma n(N_2)]^{-1}.$$

Using the value given above for γ, $\tau \simeq 1.7\times10^{12}/n(N_2)$ sec so that the time constant characteristic of changes at 200 km is $\tau \leq 1000$ sec.

With regard to NO^+ in the F_1 region, its steady state concentration follows from (18.29) and (18.30) as

$$n_s(NO^+) = \tfrac{1}{2}n_s(O^+)(\{1 + [4In(O)/\alpha_D n(O^+)]\}^{1/2} - 1) \tag{18.34}$$

so that if α_D is sufficiently large the NO^+ concentration becomes much smaller than that of O^+; i.e., the rate of ion interchange reactions acts as a limit determining the total electron density. Thus, following sunset in the F_1 region of the ionosphere, it can be expected that NO^+ will decrease rapidly in concentration, leaving O^+ as the dominant ion which produces NO^+ at a rather slow rate.

18.3 Ionization in the D Region

The distribution of electrons in the D region has received extensive theoretical and experimental study [4, 5]. This interest arises both from the peculiar behavior of this region and from its more practical effect upon radio waves which suffer considerable attenuation in their passage to and from the reflecting ionospheric layers located at higher altitudes.

Examples of the electron density profile as obtained through rocket measurements [12] at Wallops Island, Virginia are shown in *Fig. 18.3* for different seasons at a solar zenith angle of 60°. Rather low electron densities exist at low altitudes, but there is a rapid rise until near 80 km a sudden jump occurs taking the electron density from $\sim2\times10^2$ to $\sim2\times10^3\ \text{cm}^{-3}$ in an altitude interval of only a few kilometers. Referring to the discussion of the last section, such a jump implies either a rapid increase in ion production or a decrease in the effective recombination rate (which is actually the case) [4]. Unfortunately, electron densities alone are not adequate to

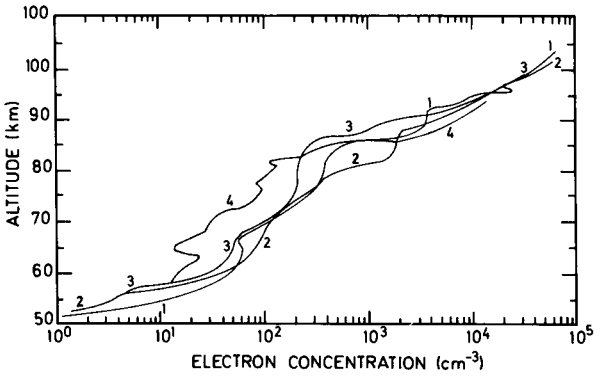


Fig. 18.3 Daytime D-region electron density profiles obtained [12] at Wallops Island, Virginia for different seasons of the year at a constant zenith angle of 60°. Curve 1, April 1964, Nike Apache No. 14.143; Curve 2, June 1965, No. 14.246; Curve 3, September 1965, No. 14.244; Curve 4, December 1965, No. 14.247.

infer the essential processes leading to variations in recombination or the presence of negative ions.

Although preliminary analyses of D-region ion chemistry were made more than a decade ago [13], a true appreciation of the actual physical situation was possible only after the first direct measurements of positive ion composition [14] in 1965 and negative ion composition [8, 15] in 1971. While the theoretical work [13] had predicted the presence of O_2^+, NO^+, and O_2^- in varying quantities, the unexpected results were that H_3O^+, $H_5O_2^+$, and other water vapor cluster ions actually dominated below 85 km. In a similar fashion, instead of O_2^- alone, the negative ions of CO_3^-, HCO_3^-, NO_3^-, and CO_4^- were observed [8, 15]. Results of such a negative ion composition taken from a recent rocket experiment have already been shown in Fig. 18.2.

From the analysis of the last chapter it follows that ionization in the D region is produced through x rays, Lyman α, and cosmic rays. (During disturbed periods energetic particles and bremstrahlung may also contribute). The initial positive ions are N_2^+, O_2^+, NO^+, and to a much lesser extent, O^+. Starting from these initial ions and their corresponding electrons, the essential problem of D-region ion chemistry is to trace the respective positive and negative ion reaction chains which yield the observed composition [16–19]. Owing to the presence of water vapor these reaction chains are difficult to analyze. The principal significance of these complex ions lies in their net reduction of the effective brecombination coefficient below values appropriate to simple diatomic molecular ions [4].

18.3.1 Positive Ions

The first measurements of the positive ion composition of the D region [14] are shown in *Fig. 18.4*. Analysis of these and similar results has shown the existence of two key positive ion reaction chains leading from O_2^+ and NO^+ to hydrated hydronium ions [5].

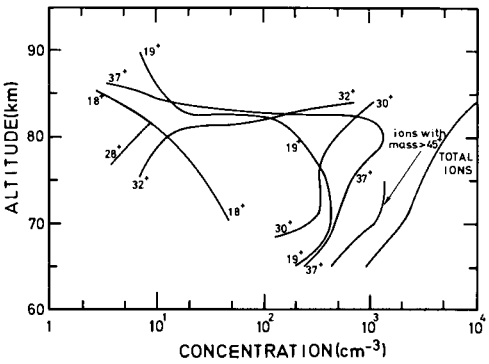


Fig. 18.4 The first direct measurements of the positive ion composition of the D region [14].

The O_2^+ reaction scheme leading to water vapor cluster ions, shown in the upper portion of *Fig. 18.5* is

$$(\varkappa_1): \quad O_2^+ + O_2 + M \rightarrow O_4^+ + M \tag{10.222}$$

$$(\varkappa_3): \quad O_4^+ + H_2O \rightarrow O_2^+ \cdot H_2O + O_2 \tag{10.224}$$

$$(\varkappa_6): \quad O_2^+ \cdot H_2O + H_2O \rightarrow H_3O^+ \cdot OH + O_2 \tag{10.231}$$

$$(\varkappa_7): \quad \rightarrow H_3O^+ + OH + O_2 \tag{10.232}$$

$$(\varkappa_{20}): \quad H_3O^+ \cdot OH + H_2O \rightarrow H_3O^+ \cdot H_2O + OH \tag{10.261}$$

$$(\varkappa_{21}): \quad H_3O^+ \cdot H_2O + H_2O + M \rightarrow H_3O^+ \cdot (H_2O)_2 + M. \tag{10.262}$$

The dimer ion O_4^+ plays a large role in this sequence, providing the switching mechanism whereby H_2O is able to replace O_2 in (10.231). As shown by Eq. (10.223), atomic oxygen is important in determining the number of O_4^+ ions available to participate in the clustering reactions:

$$(\varkappa_2): \quad O_4^+ + O \rightarrow O_2^+ + O_3. \tag{10.223}$$

The equilibrium ratio of O_4^+ is given by

$$n(O_4^+) = \frac{\varkappa_1 n(O_2) n(M)}{\varkappa_3 n(H_2O) + \varkappa_2 n(O)} \tag{18.35}$$

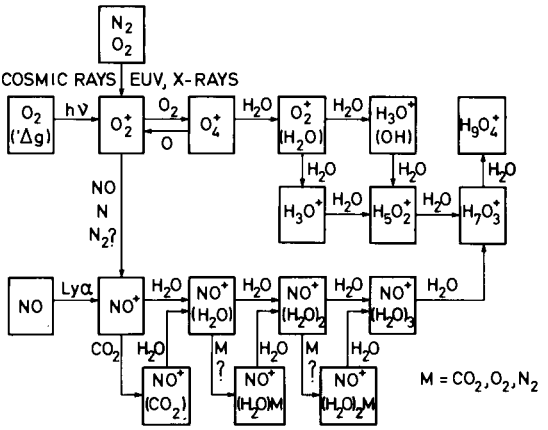


Fig. 18.5 D-region positive ion reactions [5].

showing that diurnal variations in atomic oxygen can be important in determining the concentration of O_4^+. At 75 km, for example, $n(O) \simeq 5 \times 10^9$ cm^{-3} while $n(H_2O) \simeq 2 \times 10^9$ cm^{-3}. Hence, using the appropriate reaction rates $\varkappa_2 n(O) > 4\varkappa_3 n(H_2O)$ so that atomic oxygen greatly affects the overall formation of cluster ions originating in the O_2^+ sequence. Examination of the atomic oxygen profiles of Chapter 12 indicates that it is the presence of atomic oxygen which leads to the rapid decrease of cluster ions found between 80 and 85 km [7, 9].

The second clustering sequence, which originates with NO^+ produced principally through the photoionization of NO by Lyman α, presents far more difficulty [3]. Direct reactions between NO^+ and water vapor are possible, but slow (see the bottom section of Fig. 18.5):

$$(\varkappa_{15}): \quad NO^+ + H_2O + N_2 \rightarrow NO^+ \cdot H_2O + N_2 \tag{10.249}$$

followed by

$$NO^+ \cdot (H_2O)_n + H_2O + M \rightarrow NO^+ \cdot (H_2O)_{n+1} + M \tag{18.36}$$

with the ultimate conversion

$$(\varkappa_{18}): \quad NO^+ \cdot (H_2O)_3 + H_2O \rightarrow H_3O^+ \cdot (H_2O)_2 + HNO_2. \tag{10.253}$$

Analysis of this reaction scheme has shown it to be too slow to explain the observed absence of NO^+ and intermediate NO^+ hydrates. A further difficulty arises from the relative production profiles of NO^+ and O_2^+.

Below 75 km there is little direct production of N_2^+ or O_2^+: Lyman α ionization of NO dominates. Nevertheless, experiments show that $H_5O_2^+$ dominates to 65 km with NO^+ present as a minor ion. Hence, there exists some rapid conversion of NO^+ into water cluster ions which must avoid the limitations set by (10.249) and (10.253).

A possible reaction sequence which shortens the time for NO^+ conversion involves CO_2 [5]:

$$(\varkappa_{12}): \quad NO^+ + CO_2 + N_2 \rightarrow NO^+ \cdot CO_2 + N_2 \tag{10.242}$$

which can be followed by the switching reaction

$$(\varkappa_{14}): \quad NO^+ \cdot CO_2 + H_2O \rightarrow NO^+ \cdot H_2O + CO_2 \tag{10.247}$$

which is effective because CO_2 is more abundant than water vapor.

Once formed, cluster ions appear to be stable in the presence of sunlight [5, 20]. Experiments have shown, however, that considerable fractionation may occur in high speed rocket measurements [7].

Further progress in the study of the positive ions of the D region cannot be made without further information on reaction processes and the presence of minor mesospheric constituents. Topical reviews, such as given in Ref. [5], must remain a principal source of summary knowledge until the basic reactions can be determined with accuracy.

18.3.2 Negative Ions

The negative ion structure of the D region is not well known, but the first measurements [8, 15] give a complexity equivalent to that found for the positive ions. An outline of the negative ion sequence of reactions as they are presently understood is shown in *Fig. 18.6*.

The negative ion reaction sequence is initiated by the attachment reaction

$$(\phi_1): \quad e + O_2 + O_2 \rightarrow O_2^- + O_2. \tag{10.270}$$

The two-body reaction involving electrons and O_3, given by (10.274), is very slow and cannot compete with (10.270).

Once created, there are five important processes for O_2^-:

a. photodetachment at a rate 0.3 sec^{-1},
b. associative detachment with atomic oxygen at a rate $\lambda_1 n(O)$, or with $O_2(^1\Delta_g)$ at a rate $\lambda_3 n(O_2\ ^1\Delta_g)$,
c. charge transfer with O_3 at a rate $\delta_1 n(O_3)$,
d. three-body association to form O_4^- at a rate $\delta_3 n^2(O_2)$, and
e. the direct formation of a water cluster ion at a rate $\delta_6 n(H_2O) n(O_2)$.

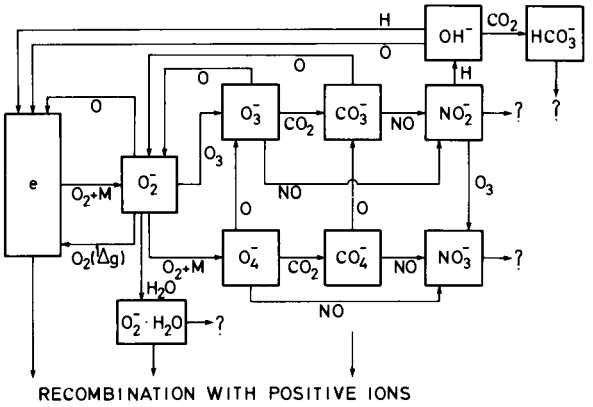


Fig. 18.6 D-region negative ion reactions [5].

These, together with the subsequent reactions shown in Fig. 18.6, act to determine the total negative ion density. Atomic oxygen plays a particularly important role in the upper D region since it is able to successively convert CO_3^- to O_2^-, O_3^- to O_2^-, and O_2^- to O_2. A similar role is found for ozone at lower altitudes. In fact, atomic oxygen and ozone are more effective than sunlight as detaching agents in most of the D region. It is through these reactions that the negative ion to electron ratio is kept at less than one above 75 km in the daytime.

Owing to the complexity of the ion reaction chains, numerical solutions are needed to determine the various ion densities [9, 18]. A typical computation of the daytime fractional negative ion composition taken from a recent study is shown in *Fig. 18.7*. The extent to which negative ion hydration is important is not well known and substantial work remains to be done [21].

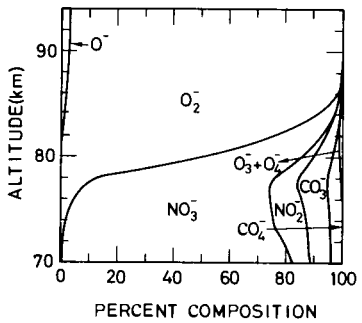


Fig. 18.7 Computed negative ion composition as a function of altitude [3].

18.4 Ionization in the E Region

The ionization processes leading to the formation of the E region can be summarized as:

1. the ionization of O_2 by x rays in the range $100 < \lambda < 31$ Å, by Lyman β at 1025.7 Å, and by ultraviolet radiation in the Lyman continuum, $\lambda < 910$ Å,
2. the ionization of N_2 by x rays in the range $100 < \lambda < 31$ Å, and
3. the ionization of O by Lyman continuum radiation and by x rays in the range $100 < \lambda < 31$ Å.

It is thought that photoionization of NO, N, and metallic constituents contribute negligibly to the overall ionization balance, even though ions of these neutrals may reach large densities through secondary ionization exchange processes. As shown by the results of the last chapter, O_2^+ and N_2^+ are the dominant initial ions of the E region. Owing to the effects of the various reaction chains discussed here, O_2^+ and NO^+ dominate the ion composition, even though appreciable quantities of O^+ and N_2^+ are produced initially [10]. A typical profile of ion composition for a midlatitude daytime E region is shown in Fig. 17.1.

Owing to the relatively low molecular oxygen density of the E region, three-body electron attachment to form O_2^- and the continuing sequence of negative ions is slow. In addition, electron detachment through collisions of negative ions with atomic oxygen is very rapid.

The reactions governing the concentration of O^+ in the E region are shown in *Fig. 18.8*. Because there are two initial states of O^+, it is necessary to distinguish between $O^+(^4S)$, leading to the formation of NO^+, and $O^+(^2D)$,

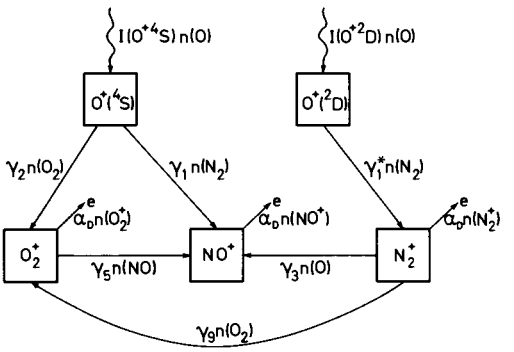


Fig. 18.8 Reactions of E-region ions.

leading to N_2^+ and, subsequently, O_2^+ and NO^+. Taking account of these processes, it is found that for the steady state

$$n(O^+ {}^4S) = \frac{I({}^4S)n(O) + \gamma_{15}n(N^+)n(O)}{\gamma_1 n(N_2) + (\gamma_4 + \gamma_{4a})n(NO) + \gamma_2 n(O_2) + \gamma_{21}n(CO_2)} \quad (18.37)$$

and

$$n(O^+ {}^2D) = \frac{I({}^2D)n(O)}{\gamma_1^* n(N_2)}. \quad (18.38)$$

Considerable simplification for (18.37) follows when it is noted that the product $(\gamma_4 + \gamma_{4a})n(NO)$ must be very small owing to the low reaction rate coupled with modest NO densities. Furthermore, N^+ is a minor ion. With regard to (18.38), examination of the ion production curves presented in Fig. 17.9 shows that $I({}^2D)$ is very small below 150 km so that $O^+({}^2D)$ must be completely negligible. Consequently, the O^+ density in the E region can be expressed as

$$n(O^+) = \frac{I({}^4S)n(O)}{\gamma_1 n(N_2) + \gamma_2 n(O_2) + \gamma_{21}n(CO_2)}. \quad (18.39)$$

Numerical evaluation of (18.39) shows that $n(O^+) < 10^3$ for virtually all conditions below 140 km. Typical values will be shown later in Fig. 18.9.

N_2^+ is a minor ion in the E region as a result of blanketing absorption of its ionizing radiations by the atmosphere above 140 km. Furthermore, the reactions of N_2^+ with O_2 and O to form O_2^+ and NO^+, respectively, are very rapid. At 120 km the lifetime of N_2^+ with respect to the formation of O_2^+ is 0.5 sec, while the transformation to NO^+ requires only 0.07 sec. In comparison, dissociative recombination is a relatively slow process: At this altitude it requires about 80 sec for a density of 10^5 electrons cm^{-3}.

The principal ionization product of the E region is O_2^+. The important reaction processes for this ion and NO^+ are shown in Fig. 18.8. In a steady state the daytime ion densities may be approximated as

$$n(O_2^+) = \frac{I(O_2)n(O_2)}{\gamma_5 n(NO) + \alpha_D(O_2^+)n_e} \quad (18.40)$$

$$n(NO^+) = \frac{\gamma_5 n(NO)n(O_2^+) + I(N_2)n(N_2)}{\alpha_D(NO^+)n_e} \quad (18.41)$$

since almost all N_2^+ formed in the E region forms NO^+.

Typical mid-day results [22–24] show that $n(O_2^+) > n(NO^+)$. In this situation the NO^+ density can be written as

$$n(NO^+) = \frac{\gamma_5 n(NO)}{\alpha_D(NO^+)} + \frac{I(N_2)n(N_2)}{\alpha_D(NO^+)n(O_2^+)} \quad (18.42)$$

while the O_2^+ density is given by

$$n(O_2^+) = \frac{[\gamma_5^2 n^2(NO) + 4\alpha_D(O_2^+)I(O_2)n(O_2)]^{1/2} - \gamma_5 n(NO)}{2\alpha_D(O_2^+)}. \quad (18.43)$$

Computations of the E-region ion composition based on the complete reaction scheme shown in Fig. 18.8 are given in *Fig. 18.9* for a 1000°K model thermosphere at 60° solar zenith angle. The reaction rates, atmospheric densities, and temperatures have been taken from values given in previous chapters. The principal peak in O_2^+ density at 115 km is caused by the absorption of C(III) and Lyman β radiation. This peak is superimposed on additional ionization resulting from x rays. Since the absorption cross section of C(III) (977 Å) is about 2.5 times greater than that of Lyman β, the individual ionization peaks of these radiations differ by about 8 km.

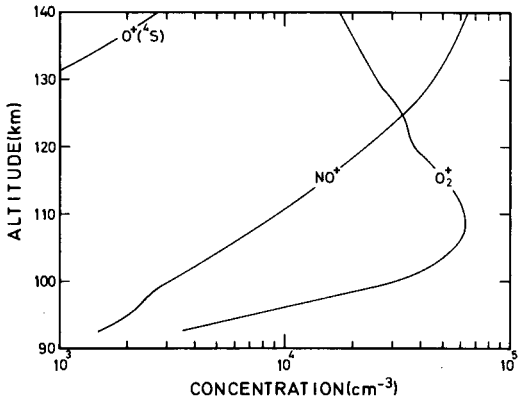


Fig. 18.9 E-region ion densities for a 1000°K thermosphere with $\chi = 60°$. Thermal equilibrium between electrons and neutrals is assumed. The NO density is taken as curve I of Figs. 12.14 and 12.15. $NO|_{120} = 1 \times 10^7$ cm^{-3}.

The shape of the electron density below the principal peak is related [23] to the spectral distribution of x rays. For example, the region near the mesopause should be dependent upon the flux of photons in the range 31–40 Å.

As illustrated by Fig. 18.9, the daytime E layer is dominated by O_2^+. The equation for the electron density follows from Eq. (18.21) as

$$dn_e/dt = I(O_2^+)n(O_2) - \alpha_D(O_2^+)n_e^2 \quad (18.44)$$

with a time constant given by (18.24). In the steady state, E-region electron densities are given by

$$n_e = [I(O_2)n(O_2)/\alpha_D(O_2^+)]^{1/2} \tag{18.45}$$

if charge exchange losses to NO can be neglected. As discussed later, this may frequently be a poor assumption.

Variations in E-region composition can be expected when there are changes in solar zenith angle, especially near twilight when the production of different ion species is greatly dependent upon the effective column density. E-region profiles for $\chi = 0°$, 60°, and 90° are shown in *Fig. 18.10.*

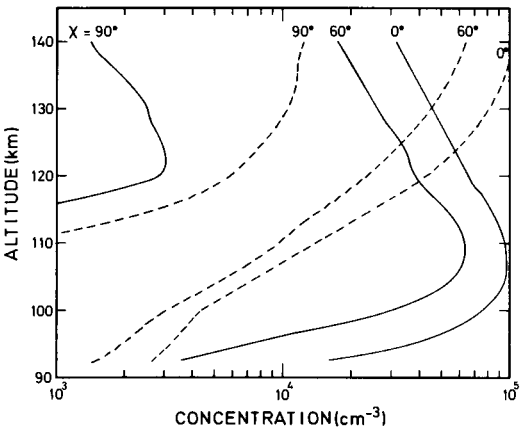


Fig. 18.10 E-region ion densities for $\chi = 0°$, 60°, and 90° for conditions described in Fig. 18.8. $T = 1000°K$. Solid curves, O_2^+; dashed curves, NO^+.

Even more important than midday solar zenith angle changes, however, is the effect of NO. If the NO density is of the order of 3×10^7 cm^{-3} or greater, charge exchange to form NO^+ becomes more important for O_2^+ loss than dissociative recombination [3]. Furthermore, since NO^+ is lost only through dissociative recombination, its concentration rises rapidly with increasing O_2^+ to NO^+ charge transfer. Examples of this behavior are shown in *Fig. 18.11* where the NO concentration has been given the values 5×10^7 and 5×10^8 cm^{-3}. In general, larger NO densities can frequently be responsible for a change from O_2^+ to NO^+ dominance [25–27].

Ion densities of the nighttime E region have been obtained through rocket measurements [22]. The data shown in *Fig. 18.12* were obtained near midnight at midlatitudes [22]. Following sunset it might be expected

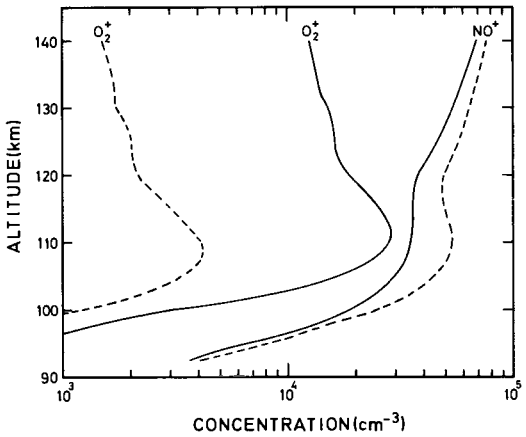


Fig. 18.11 E-region ion densities for the model of Fig. 18.8 using two altitude independent values of the NO concentration. $T = 1000°K$; $\chi = 60°$; solid curve, NO $= 5 \times 10^7$ cm^{-3}; dashed curve, NO $= 5 \times 10^8$ cm^{-3}.

that virtually no ionization would be present in the E region owing to the relatively short time constant for plasma decay [28]. The measurements showed, however, that even in the absence of direct solar illumination there is appreciable ionization in the form of NO^+.

It is thought that the source of the nighttime E region lies in the nightsky radiations of Lyman α, Lyman β, and He II (304 Å) [10, 29, 30]. Photometric observations [31, 32] have shown the presence of Lyman β with an intensity of $5–10 \times 10^6$ photons cm^{-2} sec^{-1} which, if interpreted in terms

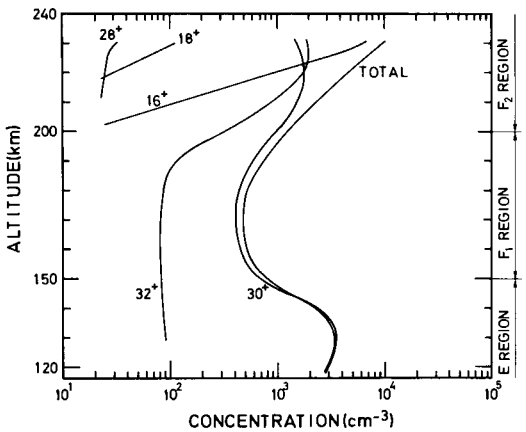


Fig. 18.12 Nighttime E-region ion composition obtained at 0106 MST at White Sands, New Mexico on August 1, 1963 [22].

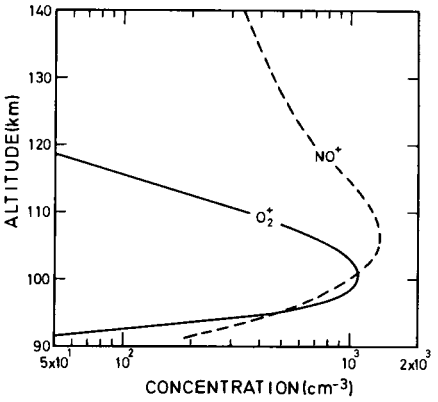


Fig. 18.13 Effects of nightsky radiation on the formation of the E region. A Lyman β source of 5×10^6 photons $cm^{-2}\,sec^{-1}$ is assumed in a 1000°K model thermosphere.

of an incident flux, leads to an ionization rate of $\sim5\times10^{-12}\,sec^{-1}$. This rate, although small compared with the direct O_2 photoionization rate, is adequate to support the observed ion densities (see *Fig. 18.13*).

In further explanation of Fig. 18.12, although Lyman β ionizes O_2, charge exchange with NO must be effective and lead to the NO^+ which, because of its low loss rate via dissociative recombination, becomes the dominant ion. In this case the O_2^+ density is given by

$$n(O_2^+) = p(O_2^+)/\gamma_5 n(NO) \tag{18.46}$$

while the NO^+ density becomes

$$n(NO^+) = p(O_2^+)/\alpha_D(NO^+)n_e \tag{18.47}$$

so that the relative composition can be expressed as

$$n(O_2^+)/n(NO^+) = \alpha_D n_e/\gamma_5 n(NO). \tag{18.48}$$

Using the data of Fig. 18.12 and the appropriate values for γ_5 and $\alpha_D(NO^+)$, it follows that $n(NO) \simeq 4\times10^7\,cm^{-3}$ to explain the results on the basis of this simple model.

The importance of NO in altering the E-region composition has been found in auroral E-region measurements [33–35]. The dominant ion in the narrow ionization ledges produced by auroral particles [36] (see *Fig. 18.14*) is NO^+, to the great exclusion of O_2^+. In one measurement [35], at 110 km the NO^+ density was measured at $10^6\,cm^{-3}$, while the O_2^+ was less than $10^3\,cm^{-3}$. In this case the NO concentration was measured as $2\times10^{11}\,cm^{-3}$. The explanation for such a large NO density remains to be found.

Rocket measurements of ion composition in the upper D and lower E regions have shown the presence of alkali and alkali–earth metal ions in

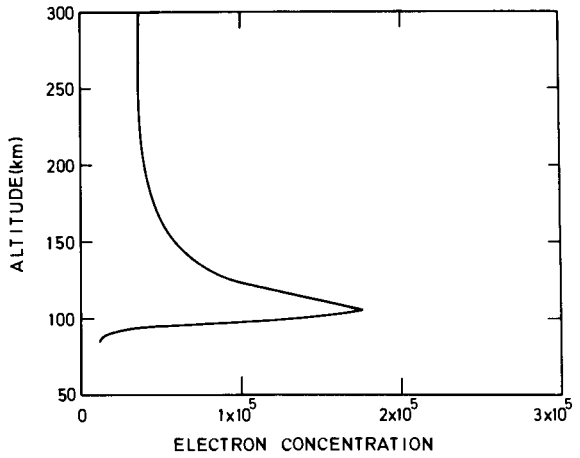


Fig. 18.14 Electron density profile of a weak aurora obtained by incoherent scatter radar observations February 14, 1972 0057–0106 AST at Chatanika, Alaska. Sample width was 7 km. The slope of the electron density above the peak is twice that of the neutral atmosphere. (Courtesy J. R. Doupnik and M. Baron.)

significant numbers [7, 9, 14, 24, 37, 38] (see Figs. 18.1 and 18.3). Sodium, magnesium, and calcium have been tentatively identified. The source of the neutral gases is thought to be associated with ablated meteoritic debris [39]. Once present in neutral form, the low ionization potential of these atoms assures their ultimate ionization through charge exchange with any of the major ionospheric species (except NO^+). Such ionization is lost very slowly since only radiative recombination (rate $\sim 10^{-12}$ cm^3 sec^{-1}) with electrons, ion–ion mutual neutralization (rate $\sim 10^{-6}$–10^{-7} cm^3 sec^{-1}), or dissociative recombination of metallic oxide ions [40, 41] are operative.

One practical importance for such ions appears to be their relationship to the formation of dense E-region layers (sporadic E) associated with large changes in neutral wind direction (a general review is given by Whitehead [42]). Theory predicts, and some experiments show, that ionization is mechanically compressed in such a region. If atomic ions of low ionization potential are present, the ambient electron density rises, effectively increasing the dissociative recombination coefficient and eliminating molecular ions.

18.5 Ionization in the F_1 Region

The E region is effectively shielded from solar radiation in the range $100 < \lambda < 910$ Å by absorption occurring at higher altitudes; N_2^+ and O^+ photoions are produced in meager quantity. As one progresses upwards

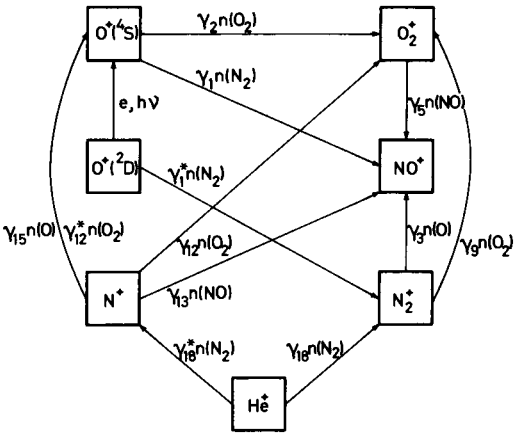


Fig. 18.15 Ion reactions of the F_1 region.

from 120 km, however, such a shielding is rapidly lost and N_2^+ and O^+ become the principal initial positive ions. The O_2^+ photoions, in contrast, diminish in importance as a result of the decrease in molecular oxygen density. The molecular nitrogen density is decreasing almost as rapidly, but the increase in photoionization rate is able to counter this effect, at least up to 170 km. This behavior is illustrated in Fig. 17.8.

In the F_1 region one finds a profusion of atomic and molecular ion reactions with a consequently complex problem of ion chemistry [2, 3, 11]. The extent of the interrelationships is illustrated in *Fig. 18.15*. Of key importance is the presence of NO^+ as an end product for most of the ion reactions involving nitrogen. Owing to this fact, NO^+ becomes the dominant total ion and molecular ion above 140 km. It is reduced again to secondary importance only above about 170 km where O^+, with its much slower loss rate, reaches a greater density.

Consider first the behavior of N_2^+ which, as shown by the data of Fig. 17.1, is a minor ion having a peak density of the order 10^3 ions cm^{-3}. The important processes leading to ionization equilibrium are included in the expression

$$n(N_2^+) = \frac{I(N_2)n(N_2) + \gamma_1^* n(N_2)n(O^+\,{}^2D)}{\gamma_3 n(O) + \gamma_9 n(O_2) + \alpha_D(N_2^+)n_e}. \tag{18.49}$$

Referring to the production rate data of Figs. 17.8 and 17.9, the direct photoionization of N_2 is the most important source of this ion below about 220 km, while at higher altitudes reactions involving $O^+(^2D)$ are most effective.

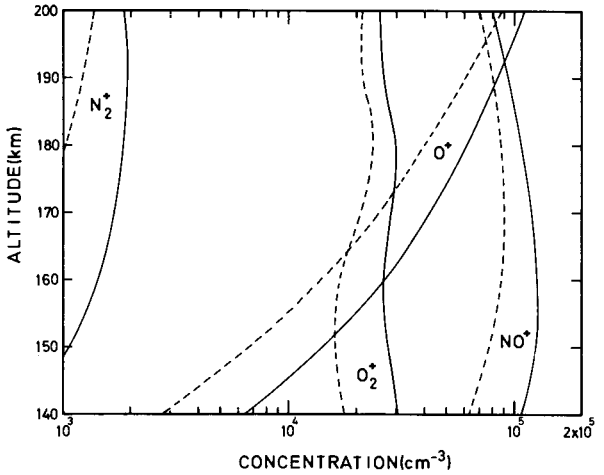


Fig. 18.16 F_1-region ion densities for a 1000°K thermosphere at low solar activity with $\chi = 60°$ (dashed curve) and 0° (solid curve). An electron temperature profile varying linearly from 324°K at 120 km to 1600°K at 200 km has been adopted. The NO density is taken as Curve IV of Figs. 12.14 and 12.15.

Computations of the N_2^+ density in the F_1 region are shown in *Fig. 18.16*. Using the adopted rate coefficients it is found that the principal loss process is that involving atomic oxygen; i.e., (18.49) can be written for practical purposes as

$$n(N_2^+) = \frac{I(N_2)n(N_2)}{\gamma_3 n(O)} + \frac{I(O^+\,{}^2D)}{\gamma_3} \tag{18.50}$$

or, for zero optical depth,

$$n(N_2^+) = 8.6\times 10^2 + 3.5\times 10^3 n(N_2)/n(O) \quad \text{cm}^{-3} \tag{18.51}$$

when diffusion is absent and dissociative recombination is negligible.

With regard to N^+, possible sources include direct photoionization, dissociative charge transfer from He^+ reacting with N_2, and charge transfer from N_2^+. Taking account of the most important processes shown in Fig. 18.15, the equilibrium density can be written as

$$n(N^+) = \frac{I(N)n(N) + \gamma_{18}^* n(He^+)n(N_2) + \gamma_{10} n(N)n(N_2^+)}{(\gamma_{12} + \gamma_{12}^*)n(O_2) + \gamma_{13} n(NO) + \gamma_{15} n(O)} \tag{18.52}$$

with the term $(\gamma_{12} + \gamma_{12}^*)n(O_2)$ being of principal importance for the loss of N^+. Owing to the lack of rapid loss processes and the relatively slow decrease in production with altitude, N^+ has a greater density than N_2^+ above 250 km and is frequently observed in the topside ionosphere.

The behavior of O_2^+ in the F_1 region where O^+ is the dominant ion is determined in the steady state by the relation

$$n(O_2^+) = \frac{I(O_2)n(O_2) + \gamma_2 n(O_2)n(O^+\,{}^4S) + \gamma_9 n(O_2)n(N_2^+)}{\gamma_5 n(NO) + \alpha_D(O_2^+)n_e} \quad (18.53)$$

or, eliminating the N_2^+ reaction which does not contribute greatly,

$$n(O_2^+) = \frac{I(O_2)n(O_2) + \gamma_2 n(O_2)n(O^+\,{}^4S)}{\gamma_5 n(NO) + \alpha_D(O_2^+)n_e}. \quad (18.54)$$

Numerical values for the O_2^+ density are shown in Fig. 18.16. Throughout much of the F_1 region the O_2^+ density is about a factor of 4 less that that of NO^+. Below 170 km the attenuation of solar radiation decreases the N_2^+ production rate, causing a decrease in the relative abundance of NO^+.

NO^+ in the F_1 region results mainly from the photoions $O^+(^4S)$ and N_2^+. The equilibrium density follows from Fig. 18.15 as

$$n(NO^+) = \frac{\gamma_1 n(N_2)n(O^+\,{}^4S) + \gamma_3 n(O)n(N_2^+) + \gamma_5 n(NO)n(O_2^+)}{\alpha_D(NO^+)n_e}. \quad (18.55)$$

The importance of the NO^+ arising from O_2^+ to NO charge exchange is difficult to determine. If $n(NO) \geq 10^8$ cm^{-3} it is dominant but for smaller values the other processes become important. As in the E region, the NO^+/O_2^+ ratio depends strongly upon the density of NO.

Above about 200 km O^+ becomes the dominant ion. Its equilibrium density can be expressed as

$$n(O^+) = \frac{I(O^+\,{}^4S)n(O)}{\gamma_1 n(N_2) + \gamma_2 n(O_2)} \quad (18.56)$$

where the presence of $O^+(^2D)$ is neglected.

Steady state ion densities in a 1000°K model thermosphere with $\chi = 60°$ are given in Fig. 18.16. Such results depend upon a number of assumptions concerning the composition of the neutral atmosphere, the electron temperature, and the importance of certain neutral species.

To illustrate the variations expected for different solar zenith angles, *Fig. 18.17* gives the ion composition for $\chi = 90°$. Comparing Figs. 18.16 and 18.17, it is seen that in the lower F_1 region NO^+ is greatly affected with the NO^+/O_2^+ ratio declining as χ increases.

The dependence of the ion composition upon NO density is shown in *Fig. 18.18*. A range of altitude independent values from 5×10^6 to 5×10^8 cm^{-3} are chosen to indicate the possible influence of this neutral species.

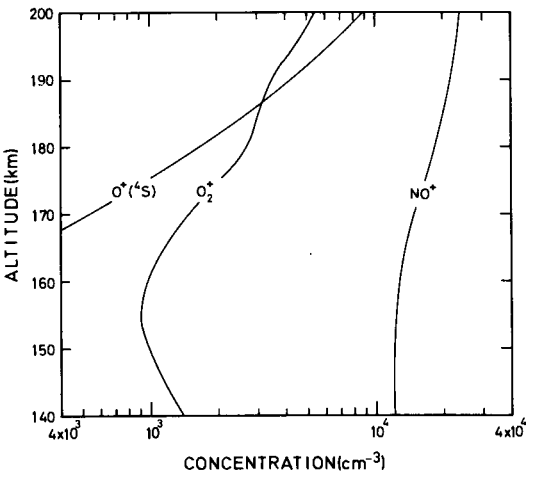


Fig. 18.17 F_1-region ion densities for $\chi = 90°$ using the atmospheric parameters described in Fig. 18.16. $T = 1000°K$.

The ion most strongly affected is O_2^+. In fact, it is clear that the NO^+/O_2^+ ratio provides a strong measuring tool for the determination of the NO density.

The behavior of the F_1 region following local sunset is interesting since it illustrates the importance of the ion reaction chains. Experimental data

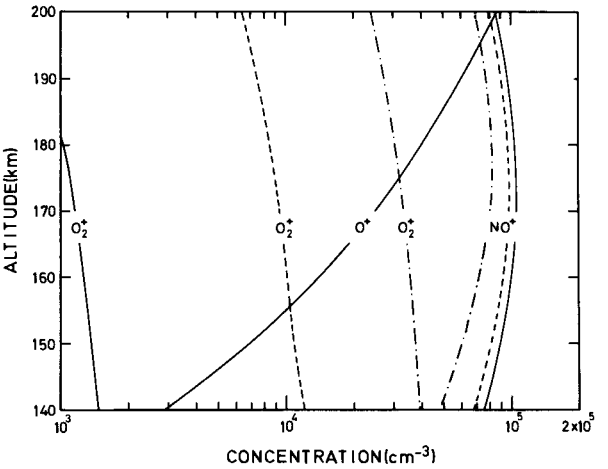


Fig. 18.18 F_1-region ion composition for the model of Fig. 18.16 using three altitude independent NO concentrations. $T = 1000°K$; $\chi = 60°$. Solid curve, NO $= 5 \times 10^8$ cm^{-3}; dashed curve, NO $= 10^7$ cm^{-3}; dotted dashed curve, NO $= 5 \times 10^6$ cm^{-3}.

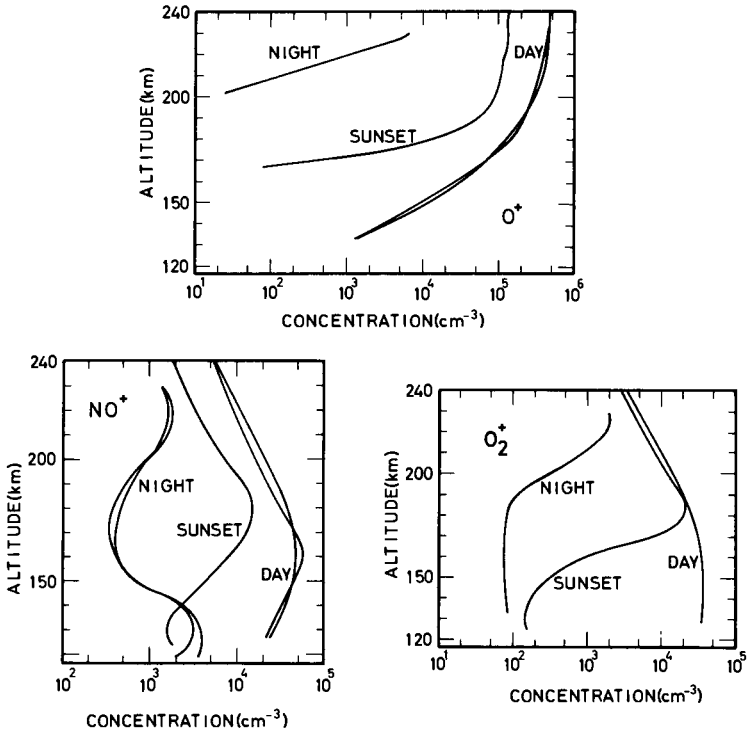


Fig. 18.19 Altitude profiles of ion composition for daytime, sunset, and nighttime conditions [22, 38]. Data obtained at White Sands, New Mexico at $\chi = 60°$ (February 15, 1963), $\chi = 103°$ (January 26, 1966), and at 0106 MST (August 1, 1963).

showing the decay of this region are shown in *Fig. 18.19*. Considering first the O^+ density, it is seen that there is a steady reduction from the daytime densities. Taking account of the two important O^+ loss processes, the following expression describes $n(O^+\,{}^4S)$ from its initial value $n_0(O^+)$:

$$n(O^+) = n_0(O^+) \exp\{-[\gamma_1 n(N_2) + \gamma_2 n(O_2)]t\}. \tag{18.57}$$

Evaluation of the indicated rates and densities shows that above 180 km the decay time is of the order of hours. Because the N_2 and O_2 densities increase exponentially with decreasing altitude, the time constant becomes shorter and, at a given time after sunset, the O^+ concentration is exponentially less, as shown in Fig. 18.19.

The nighttime behaviors of NO^+ and O_2^+ are linked through O_2^+ reactions with NO. Above 200 km, O^+ reactions with N_2 and O_2 produce about equal amounts of NO^+ and O_2^+. Dissociative recombination results in nearly

identical densities. At lower altitudes the effect of NO becomes more pronounced since there is a decrease in the total electron density and the effectiveness of dissociative recombination. Thus, the O_2^+ density tends to drop relative to NO^+.

Throughout the night diffusion acts to bring F_2-region O^+ downwards into the upper F_1 region [43]. This provides a continuing source of ionization which is consumed through the dissociative recombination of NO^+ and O_2^+. The maintenance of the nighttime upper F_1 region arises principally from such a source and the slow rate of ion–molecule reaction. In addition, near 160 to 180 km some nighttime maintenance arises from nightsky helium radiations which ionize N_2, O, and O_2 [31, 32, 44–47].

REFERENCES

1. See articles contained in J. A. Ratcliffe (ed.), *Physics of the Upper Atmosphere.* Academic Press, New York, 1960.
2. T. M. Donahue, *Science* **159**, 489 (1968).
3. T. M. Donahue, *Radio Sci.* **7**, 73 (1972).
4. G. C. Reid, *J. Geophys. Res.* **75**, 2551 (1970).
5. E. E. Ferguson, *Rev. Geophys.* **9**, 997 (1971).
6. L. Thomas, *J. Atmos. Terr. Phys.* **33**, 157 (1970).
7. R. A. Goldberg and A. C. Aikin, *J. Geophys. Res.* **76**, 8352 (1971).
8. F. Arnold, J. Kissel, D. Krankowsky, H. Wieder, and J. Zähringer, *J. Atmos. Terr. Phys.* **33**, 1169 (1971).
9. D. Krankowsky, F. Arnold, and H. Wieder, in *Magnetosphere-Ionosphere Interactions* (K. Folkestadt, ed.), p. 19. Univ. of Oslo Press, Oslo, 1971.
10. T. J. Keneshea, R. S. Narcisi, and W. Swider, *J. Geophys. Res.* **75**, 845 (1970).
11. M. Nicolet and W. Swider, *Planet. Space Sci.* **11**, 1459 (1963).
12. E. A. Mechtley and L. G. Smith, *J. Atmos. Terr. Phys.* **30**, 1555 (1968).
13. M. Nicolet and A. C. Aikin, *J. Geophys. Res.* **65**, 1469 (1960).
14. R. S. Narcisi and A. D. Bailey, *J. Geophys. Res.* **70**, 3687 (1965).
15. R. S. Narcisi, A. D. Bailey, L. Della Luca, C. Sherman, and D. M. Thomas, *J. Atmos. Terr. Phys.* **33**, 1147 (1971).
16. F. C. Fehsenfeld and E. E. Ferguson, *J. Geophys. Res.* **74**, 2217 (1969).
17. E. E. Ferguson and F. C. Fehsenfeld, *J. Geophys. Res.* **74**, 5743 (1969).
18. H. Kamiyama, *J. Geomag. Geoelect.* **22**, 403 (1970).
19. R. S. Narcisi and W. Roth, *Advan. Electron Phys.* **29**, 79 (1970).
20. A. Johannessen, D. Krankowsky, F. Arnold, W. Riedler, M. Friedrich, K. Folkestad, G. Skovli, E. V. Trans, and J. Tröim, *Nature* (London) **235**, 215 (1972).
21. E. E. Ferguson, *Ann. Geophys.* **26**, 589 (1970).
22. J. C. Holmes, C. V. Johnson, and J. M. Young, *Space Res.* **5**, 756 (1965).
23. R. E. Bourdeau, A. C. Aikin, and J. L. Donley, *J. Geophys. Res.* **71**, 727 (1966).
24. C. R. Smith, H. C. Brinton, M. W. Pharo, and H. A. Taylor, *J. Geophys. Res.* **72**, 2357 (1967).
25. R. E. Bourdeau, *Space Sci. Rev.* **1**, 683 (1963).

26. M. W. Pharo, L. R. Scott, H. G. Mayr, L. H. Brace, and H. A. Taylor, *Planet. Space Sci.* **19**, 15 (1971).
27. J. H. Hoffman, C. Y. Johnson, J. C. Holmes, and J. M. Young, *J. Geophys. Res.* **74**, 6281 (1969).
28. W. Swider, *J. Geophys. Res.* **70**, 4859 (1965).
29. T. M. Donahue, *Planet. Space Sci.* **14**, 33 (1966).
30. T. Ogawa and T. Tohmatsu, *Rep. Ionosphere Res. Japan* **20**, 395 (1966).
31. J. M. Young, G. R. Carruthers, J. C. Holmes, C. Y. Johnson, and N. P. Patterson, *Science* **160**, 990 (1968).
32. J. M. Young, C. S. Weller, C. Y. Johnson and J. C. Holmes, *J. Geophys. Res.* **76**, 3710 (1971).
33. C. Y. Johnson, E. B. Meadows, and J. C. Holmes, *J. Geophys. Res.* **63**, 443 (1958).
34. T. M. Donahue, E. C. Zipf, and T. D. Parkinson, *Planet. Space Sci.* **18**, 171 (1970).
35. E. C. Zipf, W. L. Borst, and T. M. Donahue, *J. Geophys. Res.* **75**, 6371 (1970).
36. M. H. Rees, *Space Sci. Rev.* **10**, 413 (1969).
37. V. G. Istomin, *Space Res.* **3**, 209 (1963).
38. J. M. Young, C. Y. Johnson, and J. C. Holmes, *J. Geophys. Res.* **72**, 1473 (1967).
39. H. R. Lehmann and C. U. Wagner, *J. Atmos. Terr. Phys.* **28**, 617 (1966).
40. E. E. Ferguson and F. C. Fehsenfeld, *J. Geophys. Res.* **73**, 6215 (1962).
41. W. Swider, *Nature (London)* **217**, 438 (1968).
42. J. D. Whitehead, *Rev. Geophys.* **8**, 65 (1970).
43. H. Rishbeth, *Rev. Geophys.* **6**, 33 (1968).
44. J. C. Brandt, *Astrophys. J.* **134**, 975 (1961).
45. T. M. Donahue and J. B. Kumer, *J. Geophys. Res.* **76**, 145 (1971).
46. C. Y. Johnson, J. M. Young, and J. C. Holmes, *Science* **171**, 379 (1971).
47. T. Ogawa and T. Tohmatsu, *J. Geophys. Res.* **76**, 6136 (1971).

CHAPTER 19

Plasma Transport

19.1 Introduction

The motions of individual plasma species in the ionosphere are determined by pressure gradients, gravity, and external electric and magnetic fields. Within the E region plasma drifts across magnetic field lines result from the flow of polarization currents and establishment of local and global electric fields. In the F_2 region the diffusion of ions parallel to the geomagnetic field plays an important part in determining the ionic composition of the middle and upper ionosphere. Further, electric fields perpendicular to the magnetic field cause lateral and radial plasma motions reflecting the importance of magnetospheric processes and neutral winds in the E region.

In this chapter the equations of motion for electrons and ions are presented as they apply to the ionospheric environment; that is, a partially ionized, collision dominated plasma moving in a neutral atmosphere under the forces of gravity and electric and magnetic fields.

19.2 Equations of Plasma Transport

Consider a partially ionized plasma of electrons, ions, and neutral particles. The equations of motion for the electron and ion gases within the approximation where inertial effects can be ignored are [1, 2]

$$\frac{\partial \mathbf{C}_e}{\partial t} + \frac{1}{\varrho_e} \nabla p_e - \mathbf{g} - \frac{q_e}{m_e} \left(\mathbf{E} + \frac{1}{c} \mathbf{C}_e \times \mathbf{B} \right) = \frac{\mathbf{A}_e}{\varrho_e} \tag{19.1}$$

$$\frac{\partial \mathbf{C}_i}{\partial t} + \frac{1}{\varrho_i} \nabla p_i - \mathbf{g} - \frac{q_i}{m_i} \left(\mathbf{E} + \frac{1}{c} \mathbf{C}_i \times \mathbf{B} \right) = \frac{\mathbf{A}_i}{\varrho_i} \tag{19.2}$$

where the subscripts apply to electrons and ions, and

$\mathbf{C}$ is the bulk transport velocity,
$p = nkT$ is the isotropic gas pressure,
$\mathbf{g}$ is the acceleration of gravity,
$\mathbf{E}$ is the total electric field,
$\mathbf{B}$ is the magnetic field,
q is the particle charge, including sign,
n is the concentration,
k is Boltzmann's constant (1.38×10^{-16} erg $^{\circ}K^{-1}$),
T is the gas temperature,
$\varrho = mn$ is the mass density,
m is the particle mass,
c is the speed of light (3.0×10^{10} cm sec^{-1}), and
$\mathbf{A}_j = \sum \mathbf{A}_{jk}$ is the collision term describing the dynamical effects of friction between gases of differing transport velocity.

The form of the collision term follows directly from the Boltzmann equation as [3]

$$\mathbf{A}_j = \int m_j \mathbf{v}_j (\partial f_j / \partial t)_c \, d\mathbf{v}_j \tag{19.3}$$

where $(\partial f_j/\partial t)_c$ is the collision term, $\mathbf{v}_j$ is the jth particle velocity, and $\mathbf{A}_j$ represents the rate of change of the jth species momentum due to collisions. Expansion of the collision term for elastic collisions between j and k type particles leads to the expression

$$\mathbf{A}_{jk} = [m_j m_k/(m_j + m_k)] \iint (\mathbf{v}_k - \mathbf{v}_j)(\nu_{jk}/n_k) f_j f_k \, d\mathbf{v}_n \, d\mathbf{v}_k \tag{19.4}$$

where the subscript j applies to electrons or ions, the subscript k applies to other neutral or ionized gas species, and $\mathbf{v}$ is the velocity of particles, f the velocity distribution functions, $d\mathbf{v}$ the velocity space volume elements, and $\nu_{jk} = n_k \mid \mathbf{v}_j - \mathbf{v}_k \mid q_D$ is the velocity dependent momentum transfer collision frequency given by Eq. (9.32).

The general expression for $\mathbf{A}_j$ involves arbitrary bulk velocities, $\mathbf{C}_j$, and the possibility of non-Maxwellian velocity distribution functions for the different species. Further, if several different species are present, the total collision term in the jth species momentum equation is the sum of individual contributions; i.e., $\mathbf{A}_j = \sum_k \mathbf{A}_{jk}$.

The reduction of Eq. (19.4) to a particular result is possible only after the velocity dependence of the momentum transfer collision cross section

has been specified. However, the general form of the result can be written as [2]

$$\mathbf{A}_{jk} = [m_j m_k/(m_j + m_k)]n_j\bar{\nu}_{jk}(\mathbf{C}_k - \mathbf{C}_j)f(v/\alpha) \tag{19.5}$$

where $\bar{\nu}_{jk}$ is the momentum transfer collision frequency, $v = |\mathbf{C}_k - \mathbf{C}_j|$, and $\alpha^2 = 2k(T_j/m_j + T_k/m_k)$. The term $f(v/\alpha)$ in this expression is important only when the relative speed of gas transport approaches the speed of sound; i.e., $v/\alpha \gtrsim 1$. For low speed flow $f(v/\alpha) \to 1$. Thus, as will become evident from subsequent discussion, $f(v/\alpha)$ is a high speed correction term which accounts for changes in both relative speed and cross section.

An explicit expression for $\mathbf{A}_{jk}$ can be obtained if the jth and kth type particles are assumed to interact with a momentum transfer cross section which varies inversely with v. [See Equation (9.70) for ion–neutral collisions.] If f_j and f_k are displaced Maxwellian distributions with parameters T_j, T_k, $\mathbf{C}_j$, and $\mathbf{C}_k$, then [2]

$$\mathbf{A}_{jk} = [m_j m_k/(m_j + m_k)]n_j\bar{\nu}_{jk}(\mathbf{C}_k - \mathbf{C}_j) \tag{19.6}$$

where $\bar{\nu}_{jk}$ is the momentum transfer collision frequency [Eq. (9.33)] for the proper cross section [Eq. (9.71)]. This expression shows that the effective frictional interaction acting between two gases in relative motion is linearly dependent upon the difference in transport velocities with the term $f(v/\alpha) = 1$. Such a result is not general, but is a property of the assumed inverse velocity dependence of the collision cross section. For convenience, however, it is common to assume that Eq. (19.6) is valid even when arbitrary cross sections are used and high speed gas flow is present. The limitations of such an assumption are obvious and, depending upon the actual velocity dependence of $q_D(v)$ and the magnitude of v, can lead to appreciable error.

For illustration, the collision term appropriate for *hard sphere collisions* of cross section $\pi\sigma^2$ is [2]

$$\mathbf{A}_{jk} = [m_j m_k/(m_j + m_k)]n_j\bar{\nu}_{jk}(\mathbf{C}_k - \mathbf{C}_j)f(v/\alpha) \tag{19.7}$$

where

$$\bar{\nu}_{jk} = \frac{4}{3}\, n_k\left[\frac{8k}{\pi}\left(\frac{T_j}{m_j} + \frac{T_k}{m_k}\right)\right]^{1/2}\pi\sigma^2 \tag{19.8}$$

$$f\left(\frac{v}{\alpha}\right) = \left\{\frac{3\pi^{1/2}}{8}\left(\frac{v}{\alpha} + \frac{\alpha}{v} - \frac{\alpha^3}{4v^3}\right)\operatorname{erf}\left(\frac{v}{\alpha}\right) + \frac{3}{8}\left[1 + \frac{\alpha^2}{2v^2}\exp\left(\frac{-v^2}{\alpha^2}\right)\right]\right\} \tag{19.9}$$

$$\alpha = \left[2k\left(\frac{T_j}{m_j} + \frac{T_k}{m_k}\right)\right]^{1/2}. \tag{19.10}$$

When $v/\alpha \ll 1$, $f(v/\alpha) \to 1$, but for increasing values of v/α, $f(v/\alpha)$ becomes larger than 1 with an eventual proportionality to v/α at speeds large relative to the thermal speed of the gas mixture.

For *Coulomb interactions* between particles of masses m_j and m_k and charge $Z_j e$, $Z_k e$, the collision term can be written as [2]

$$A_{jk} = [m_j m_k/(m_j + m_k)]\bar{\nu}_{jk}(\mathbf{C}_k - \mathbf{C}_j)f(v/\alpha) \tag{19.11}$$

where $\bar{\nu}_{jk}$ is the momentum transfer collision frequency for Coulomb collisions [see Eq. (9.106)] and the high speed correction factor $f(v/\alpha)$ is

$$f(v/\alpha) = \tfrac{4}{3}\pi^{1/2}[(\alpha/v)^3 \operatorname{erf}(v/\alpha) - (2/\pi^{1/2})(\alpha/v)^2 \exp(-v^2/\alpha^2)] \tag{19.12}$$

with α defined previously by (9.10).

Although further explicit results [4] are available for particular forms of the collision cross section, in subsequent discussion of this chapter, Eq. (19.4) is adopted as representing the essential features of collisional momentum transfer. Such a choice may not represent the true momentum transfer rate for the ionospheric gases.

Before returning to the individual species momentum equations one further step is helpful in reducing the apparent complexity of the collision term. For simplicity a diffusion collision frequency

$$\nu_{jk} = [m_k/(m_j + m_k)]\bar{\nu}_{jk} \tag{19.13}$$

can be adopted so that Eqs. (19.1) and (19.2) can be written as

$$\frac{\partial \mathbf{C}_e}{\partial t} + \frac{1}{\varrho_e}\nabla p_e - \mathbf{g} - \frac{q_e}{m_e}\left(\mathbf{E} + \frac{1}{c}\mathbf{C}_e \times \mathbf{B}\right) = -\sum_k \nu_{ek}(\mathbf{C}_e - \mathbf{C}_k) \tag{19.14}$$

$$\frac{\partial \mathbf{C}_i}{\partial t} + \frac{1}{\varrho_i}\nabla p_i - \mathbf{g} - \frac{q_i}{m_i}\left(\mathbf{E} + \frac{1}{c}\mathbf{C}_i \times \mathbf{B}\right) = -\sum_k \nu_{ik}(\mathbf{C}_i - \mathbf{C}_k). \tag{19.15}$$

When one considers a multiconstituent plasma, both collisional and electric field coupling is present between the various ions and the electrons. In this situation the complete solution for individual ion and electron velocities cannot be made without a simultaneous solution to Maxwell's equation:

$$\nabla \cdot \mathbf{E} = 4\pi e(n_e - \sum n_i). \tag{19.16}$$

However, for most applications the polarization electric field given by (19.16) is sufficiently strong to insure that $n_e \simeq \sum n_i$ to a very high degree of accuracy. Thus, Eqs. (19.1) and (19.2) can be closed through the explicit

assumption

$$n_e = \sum n_i \tag{19.17}$$

which is used here. Such an approximation is not valid in the formation of electric double layers such as may occur above auroras.

19.3 Ambipolar Diffusion

An important application of Eqs. (19.1) and (19.2) is to ambipolar diffusion where, owing to a proper choice of boundary conditions, no net electrical current is permitted to flow in the plasma [5]. The particular conditions for which ambipolar motion can exist follow for a single ion species from (19.14) and (19.15) with $\mathbf{C}_e = \mathbf{C}_i \triangleq \mathbf{C}$ and $n_e = n_i$. Adding the two equations gives

$$\begin{aligned}(\varrho_e + \varrho_i)\frac{\partial \mathbf{C}}{\partial t} + \nabla(p_e + p_i) + (\varrho_e + \varrho_i)\mathbf{g} \\ = -\varrho_e \sum_k \nu_{ek}(\mathbf{C} - \mathbf{C}_k) - \varrho_i \sum_k \nu_{ik}(\mathbf{C} - \mathbf{C}_k)\end{aligned} \tag{19.18}$$

showing that for the assumed ambipolar conditions the plasma equation of motion is independent of the applied electric and magnetic fields. The boundary conditions necessary for obtaining this result are of some practical interest, however. In the ionosphere, for example, suppose that the gradient in plasma pressure and the force of gravity act only in the vertical direction. Taking the cross product of the unit vector $\hat{z}$ in the z direction twice with (19.14) with $\partial \mathbf{C}/\partial t = 0$, one obtains, after some manipulation [5],

$$\mathbf{E} = E_z\hat{z} - (1/c)C_z(\hat{z} \times \mathbf{B}). \tag{19.19}$$

Thus, the total electric field acting in the plasma is composed of two terms. The first, in the z direction, arises from gravitational separation of the electrons and ions and acts to keep the electron and ion gas together such that $n_e \simeq n_i$. The second term of (19.19) is a balancing electric field which is necessary to counteract the magnetic defecting force which tends to separate electrons and ions. In general, this component of $\mathbf{E}$ can be established only if the flow of currents is prevented through appropriate boundary conditions, i.e., the plasma must be polarized in some manner by the magnetic field. An example of this type of a situation is found at the geomagnetic equator where there is a vertical ambipolar flow of plasma in response to an east-west electric field arising from the interaction of neutral winds with ions in the E region [6].

19.4 Ionospheric Motions: Diffusion and Convection

The problem of plasma diffusing in a stationary neutral gas permeated by an external magnetic field can be approached using Eqs. (19.14) and (19.15). For this model we assume $q_e = -e$; $q_i = +e$; and $n_e = \sum n_i$, that the electron and ion pressures depend only upon the vertical coordinate z, and that steady-state conditions exist. Taking $\mathbf{B} = B_x\hat{x} + B_z\hat{z}$ and $\mathbf{C} = u\hat{x} + v\hat{y} + w\hat{z}$, the electron and ion momentum equations can be decomposed into rectangular components (see *Fig. 19.1*) as follows:

$$x: \quad v_i\Omega_z{}^i = \sum \nu_{ik}(u_i - u_k) - (eE_x/m_i) \tag{19.20}$$

$$v_e\Omega_z{}^e = -\sum \nu_{ek}(u_e - u_k) - (eE_x/m_e) \tag{19.21}$$

$$y: \quad u_i\Omega_z{}^i = w_i\Omega_x{}^i - \sum \nu_{ik}(v_i - v_k) + (eE_y/m_i) \tag{19.22}$$

$$u_e\Omega_z{}^e = w_e\Omega_x{}^e + \sum \nu_{ek}(v_e - v_k) + (eE_y/m_e) \tag{19.23}$$

$$z: \quad \frac{1}{\varrho_i}\frac{\partial p_i}{\partial z} + g - \frac{eE_z}{m_i} + v_i\Omega_x{}^i = -\sum \nu_{ik}(w_i - w_k) \tag{19.24}$$

$$\frac{1}{\varrho_e}\frac{\partial p_e}{\partial z} + g + \frac{eE_z}{m_e} - v_e\Omega_x{}^e = -\sum \nu_{ek}(w_e - w_k) \tag{19.25}$$

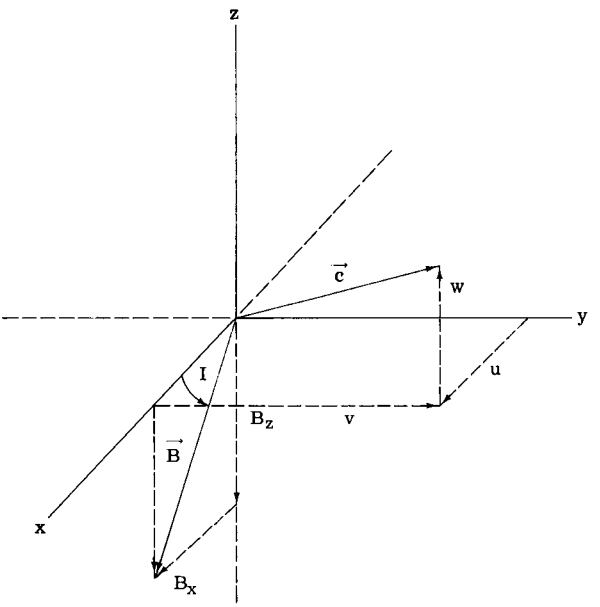


Fig. 19.1 Coordinate system used in the derivation of the plasma transport equations.

where $\Omega_k^j = eB_k/cm_j$ is the jth species gyrofrequency, and the collision terms include effects due both to plasma and neutral gas motions.

Using Eqs. (19.20) and (19.21) the x and y components of plasma motion can be written, neglecting electron–ion collisions, as

$$v_i(\Omega_z^{i^2} + \nu_i^2) = w_i\Omega_x{}^i\nu_i + \nu_i(eE_y/m_i) - \Omega_z{}^i(eE_x/m_i) + \nu_i{}^2v_n - \Omega_z{}^i\nu_iu_n \tag{19.26}$$

$$v_e(\Omega_z^{e^2} + \nu_e^2) = -w_e\Omega_x{}^e\nu_e - \Omega_z{}^e(eE_x/m_e) - \nu_e(eE_y/m_e) + \nu_e{}^2v_n + \Omega_z{}^e\nu_eu_n \tag{19.27}$$

$$u_i(\Omega_z^{i^2} + \nu_i^2) = \Omega_z{}^i\Omega_x{}^iw_i + \nu_i(eE_x/m_1) + \Omega_z{}^i(eE_y/m_i) + \nu_i{}^2u_n + \Omega_z{}^i\nu_iv_n \tag{19.28}$$

$$u_e(\Omega_z^{e^2} + \nu_e^2) = \Omega_z{}^e\Omega_x{}^ew_e - \nu_e(eE_x/m_e) + \Omega_z{}^e(eE_y/m_e) + \nu_e{}^2u_n - \Omega_z{}^e\nu_ev_n \tag{19.29}$$

where the subscript n refers to the neutral gas and $\nu_j = \sum \nu_{jk}$.

At very low altitudes ($z < 70$ km) the ion and electron collision frequencies are much larger than their respective gyrofrequencies ($\nu_e{}^2 \gg \Omega_z^{e^2}$; $\nu_i{}^2 \gg \Omega_z^{i^2}$) and magnetic field coupling of the plasma motion vanishes (see *Table 19.1*). Each component of the motion is determined independently in terms of the applied forces; i.e., Eqs. (19.26) and (19.27) become (with

TABLE 19.1

ELECTRON AND ION COLLISION PARAMETERS[a]

z (km)	$(\nu_e/\Omega_z{}^e)^2$	$(\nu_i/\Omega_z{}^i)^2$			
	$B_z = 0.5$	$B_z = 0.3$	$B_z = 0.4$	$B_z = 0.5$	$B_z = 0.6$
100	3.0×10^{-5}	1.4×10^{3}	8.0×10^{2}	5.4×10^{2}	3.6×10^{2}
110	2.5×10^{-6}	5.6×10^{1}	3.2×10^{1}	2.0×10^{1}	1.4×10^{1}
120	3.2×10^{-7}	3.8×10^{0}	2.1×10^{0}	1.4×10^{0}	9.5×10^{-1}
130	6.8×10^{-8}	3.8×10^{-1}	2.1×10^{-1}	1.4×10^{-1}	9.5×10^{-2}
140	2.2×10^{-8}	7.8×10^{-2}	4.3×10^{-2}	2.8×10^{-2}	1.9×10^{-2}
150	9.2×10^{-9}	2.3×10^{-2}	1.3×10^{-2}	8.4×10^{-5}	5.9×10^{-3}

[a] $O_2{}^+$ ions are assumed in a 1000°K model thermosphere. Values of B_z are in gauss.

$\Omega_x^{i,e}/\Omega_z^{i,e} \ll 1$)

$$v_i = (1/\nu_i)(eE_y/m_i) + v_n \tag{19.30}$$

$$v_e = -(1/\nu_e)(eE_y/m_e) + v_n \tag{19.31}$$

and

$$u_i = (1/\nu_i)(eE_x/m_i) + u_n \tag{19.32}$$

$$u_e = -(1/\nu_e)(eE_x/m_e) + u_n. \tag{19.33}$$

Using Eqs. (19.30)–(19.33) and the definition of an electric current

$$\mathbf{j} = e(\sum n_i \mathbf{C}_i - n_e \mathbf{C}_e) \tag{19.34}$$

the conductivity, σ, of the plasma is given by

$$\mathbf{j} = \sigma \mathbf{E} \tag{19.35}$$

where

$$\sigma = n_e e^2 \left(\sum \frac{n_i}{m_i \nu_i} + \frac{1}{m_e \nu_e} \right). \tag{19.36}$$

Thus, at sufficiently low altitudes the conductivity is isotropic and current flow follows the direction of the electric field. In addition, (19.36) indicates that almost all the current is carried by electrons since $m_i \nu_i \gg m_e \nu_e$.

For altitudes between 70 and 130 km a peculiar effect occurs from the fact that the electron gyrofrequency ($\sim 4.8 \times 10^6$ sec^{-1} at midgeomagnetic latitudes) is larger than the ion gyrofrequency by the factor m_i/m_e. Hence, the electrons are magnetically dominated while the ions are essentially free to move across the magnetic field line in response to pressure gradients, electric fields, or motions in the neutral atmosphere. The application of this circumstance has been made in the dynamo theory which explains small diurnal variations in the geomagnetic field as resulting from ionospheric electric currents associated with tidal motions of the neutral atmosphere [6]. Using the conditions $\nu_e^2 \ll \Omega_z^{e^2}$ and $\nu_i^2 \gg \Omega_z^{i^2}$ in Eqs. (19.26)–(19.29), the ion and electron velocities become

$$v_i = (1/\nu_i)(eE_y/m_i) + v_n \tag{19.37}$$

$$v_e = -eE_x/\Omega_z^e m_e \tag{19.38}$$

and

$$u_i = (1/\nu_i)(eE_x/m_i) + u_n \tag{19.39}$$

$$u_e = eE_y/\Omega_z^e m_e \tag{19.40}$$

and the conductivity becomes anisotropic. Using (19.34) and (19.35) the components of current are

$$j_x = n_e e\left[eE_y \sum \frac{n_i/n_e}{m_i \nu_i} + v_n + \frac{eE_x}{\Omega_z^e m_e}\right] \tag{19.41}$$

$$j_y = n_e e\left[eE_x \sum \frac{n_i/n_e}{m_i \nu_i} + u_n - \frac{eE_y}{\Omega_z^e m_e}\right]. \tag{19.42}$$

Thus, electric fields applied to the E region will result in current flow. Similarly, motions of the neutral atmosphere will establish currents and electric fields consistent with appropriate boundary conditions [6]. The interrelationship among the neutral winds, the flow of currents, and the establishment of polarization electric fields is well demonstrated by the dynamo theory of diurnal geomagnetic variations observed at the surface of the earth. In essence, global wind patterns are created in the E region by solar radiation heating the neutral atmosphere. Through collisions ion currents are established [Eqs. (19.41) and (19.42)] such that polarization electric fields are created with consequent influence upon electrons [Eqs. (19.38) and (19.40)] and ions. In the steady state, self-consistent solutions for the electric field and currents are found through the requirement that

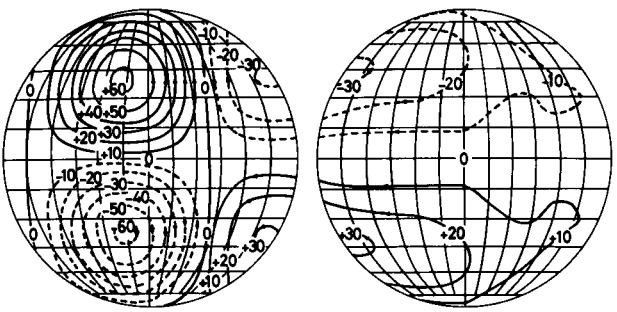


Fig. 19.2 Global current pattern associated with atmospheric winds for northern summer day (left) and night (right) [7].

$\nabla \cdot \mathbf{j} = 0$. *Figure 19.2* illustrates a computed global current pattern associated with diurnal atmospheric motions [7]. The theoretical models are complex and usually deal with height averaged densities and velocities. Furthermore, spatial gradients of conductivity (electric density) can be particularly important in determining the global potential distribution.

Referring to Table 19.1, at sufficiently high altitudes, $\nu_i^2 \ll \Omega_z^{i^2}$ and $\nu_e^2 \ll \Omega_z^{e^2}$ and it is found that

$$v_i = -eE_x/\Omega_z{}^i m_i \tag{19.43}$$

$$v_e = -eE_x/\Omega_z{}^e m_e \tag{19.44}$$

and

$$u_i = eE_y/m_i\Omega_z{}^i \tag{19.45}$$

$$u_e = eE_y/m_e\Omega_z{}^e \tag{19.46}$$

showing that in the absence of collisions, electric fields applied perpendicular to the magnetic field cannot cause currents to flow. Instead, there is an **E×B** drift of both electrons and ions. This result follows directly from (19.1) and (19.2) as

$$\mathbf{C}_e = \mathbf{C}_i = -c(\mathbf{E}\times\mathbf{B}/B^2). \tag{19.47}$$

Thus, electric fields established within the E region will affect the drift motion of plasma at high altitudes, producing not only the general rotation

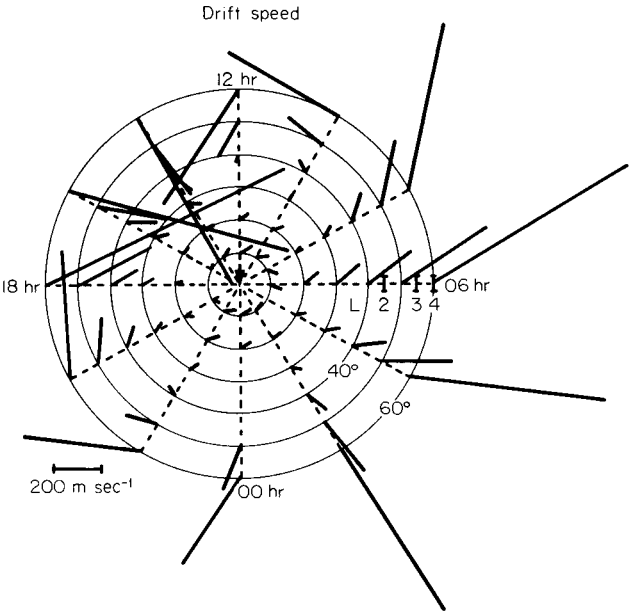


Fig. 19.3 Plasma velocities in the magnetic equatorial plane associated with atmospheric winds. Effects of atmospheric rotation are not included; i.e., the plasma rotation velocity must be added to obtain the total plasma velocity [8].

of the plasma with the neutral atmosphere (and hence, the earth) but also variations associated with the neutral winds, which are gas motions referred to the frame of atmospheric rotation. The plasma velocities associated with these winds are generally small; a typical result [8] is shown in *Fig. 19.3.*

The vertical components of plasma motion can be obtained for electrons and ions using Eqs. (19.14) and (19.15):

$$\frac{1}{\varrho_e}\frac{dp_e}{dz} + g + \frac{eE_z}{m_e} + \frac{\Omega_x^e \nu_e}{\Omega_z^{e2} + \nu_e^2}\left[\frac{eE_y}{m_e} + \frac{\Omega_z^e eE_x}{m_e \nu_e} - \nu_e v_n - \Omega_z^e u_n\right]$$
$$= -\nu_e w_e\left[1 + \frac{\Omega_x^{e2}}{\nu_e^2 + \Omega_z^{e2}}\right] + \nu_e w_n \tag{19.48}$$

$$\frac{1}{\varrho_i}\frac{dp_i}{dz} + g - \frac{eE_z}{m_i} + \frac{\Omega_x^i \nu_i}{\Omega_z^{i2} + \nu_i^2}\left[\frac{eE_y}{m_i} - \frac{\Omega_z^e eE_x}{m_i \nu_i} + \nu_i v_n - \Omega_z^i u_n\right]$$
$$= -\nu_i w_i\left[1 + \frac{\Omega_x^{i2}}{\nu_i^2 + \Omega_z^{i2}}\right] + \nu_i w_n. \tag{19.49}$$

Without making the ambipolar hypothesis, E_z can be eliminated from (19.48) and (19.49) to give

$$\frac{1}{n_e}\frac{dp_e}{dz} + \frac{1}{n_i}\frac{dp_i}{dz} + (m_e + m_i)g + eE_y\left[\frac{\Omega_x^i \nu_i}{\Omega_z^{i2} + \nu_i^2} + \frac{\Omega_x^e \nu_e}{\Omega_z^{e2} + \nu_e^2}\right]$$
$$+ eE_x\left[\frac{\Omega_x^e \Omega_z^e}{\Omega_z^{e2} + \nu_e^2} - \frac{\Omega_x^i \Omega_z^i}{\Omega_z^{i2} + \nu_i^2}\right] + v_n\left[\frac{m_i \Omega_x^i \nu_i^2}{\Omega_z^{i2} + \nu_i^2} - \frac{m_e \Omega_x^e \nu_e^2}{\Omega_z^{e2} + \nu_e^2}\right]$$
$$- u_n\left[\frac{m_e \Omega_x^e \Omega_z^e \nu_e}{\Omega_z^{e2} + \nu_e^2} + \frac{m_i \Omega_x^i \Omega_z^i \nu_i}{\Omega_z^{i2} + \nu_i^2}\right]$$
$$= -\nu_i m_i w_i\left[1 + \frac{\Omega_x^{i2}}{\nu_i^2 + \Omega_z^{i2}}\right] - \nu_e m_e w_e\left[1 + \frac{\Omega_x^{e2}}{\nu_e^2 + \Omega_z^{e2}}\right]$$
$$+ w_n(m_e \nu_e + m_i \nu_i). \tag{19.50}$$

The z component of the electric field can be obtained as [9]

$$eE_z = -\frac{m_e \nu_e(\nu_e^2 + \Omega_e^2)}{\nu_e^2 + \Omega_z^{e2}} w_e - \frac{1}{n_e}\frac{dp_e}{dz} - m_e g - \frac{\Omega_x^e \Omega_z^e}{\nu_e^2 + \Omega_z^{e2}} eE_x$$
$$- \frac{\Omega_x^e \nu_e}{\nu_e^2 + \Omega_z^{e2}} eE_y - \frac{\nu_e}{\nu_e^2 + \Omega_z^{e2}}$$
$$\{-\Omega_z^e \Omega_x^e u_n - \nu_e \Omega_x^e v_n - (\nu_e^2 + \Omega_z^{e2}) w_n\} \tag{19.51}$$

where $\Omega_j^2 = \Omega_x^{j2} + \Omega_z^{j2}$. The first term on the right-hand side arises princi-

pally from field aligned currents while succeeding terms represent diffusion, perpendicular electric field effects, and convection by the neutral atmosphere.

Further reduction of Eq. (19.50) can be made by noting that $m_i \nu_i w_i$ is normally much larger than $m_e \nu_e w_e$. Thus, the equation of motion for the ith ion gas can be taken as

$$w_i = -\frac{(\nu_i^2 + \Omega_z^{i^2})}{m_i \nu_i (\nu_i^2 + \Omega_i^2)} \left\{ \frac{1}{n_i} \frac{dp_i}{dz} + \frac{1}{n_e} \frac{dp_e}{dz} + m_i g \right\} + \phi_i \quad (19.52)$$

where the first term represents the effect of particle diffusion and the second term, ϕ_i, arises from external forces which produce convection:

$$\begin{aligned} \phi_i = -\frac{\nu_i^2 + \Omega_z^{i^2}}{\nu_i(\nu_i^2 + \Omega_i^2)} \Bigg[& -\left(\frac{\nu_i \Omega_x^{\,i} \Omega_z^{\,i}}{\nu_i^2 + \Omega_z^{i^2}} + \frac{\nu_e \Omega_x^{\,e} \Omega_z^{\,e}}{\nu_e^2 + \Omega_z^{e^2}} \right) u_n \\ & + \left(\frac{\nu_i^2 \Omega_x^{\,i}}{\nu_i^2 + \Omega_z^{i^2}} - \frac{\nu_e^2 \Omega_x^{\,e}}{\nu_e^2 + \Omega_z^{e^2}} \right) v_n - (\nu_e + \nu_i) w_n \\ & - \left(\frac{\Omega_x^{\,i} \Omega_z^{\,i}}{\nu_i^2 + \Omega_z^{i^2}} - \frac{\Omega_x^{\,e} \Omega_z^{\,e}}{\nu_e^2 + \Omega_z^{e^2}} \right) \frac{eE_x}{m_i} + \left(\frac{\Omega_x^{\,i} \nu_i}{\nu_i^2 + \Omega_z^{i^2}} + \frac{\Omega_x^{\,e} \nu_e}{\nu_e^2 + \Omega_z^{e^2}} \right) \frac{eE_y}{m_i} \Bigg]. \end{aligned} \quad (19.53)$$

Equations (19.52) and (19.53) are applicable to general ionospheric conditions for arbitrary magnetic latitudes and altitudes. Solutions for ionospheric ion densities and transport velocities are possible using the condition

$$n_e = \sum n_i \quad (19.54)$$

and the time-dependent equation of continuity

$$\partial n_i / \partial t + \nabla \cdot n \mathbf{C}_i = p_i - l_i. \quad (19.55)$$

Within the D, E, and F_1 regions principal interest relates to Eqs. (19.27)–(19.29) with vertical plasma motions being generally neglected except in special cases such as the equatorial ionosphere or sporadic-E ionization produced through neutral wind shears. The essential problem in the E-region behavior relates to the total electric field, having been formed in connection with Hall and Pederson currents.

The plasma transport conditions applicable for F-region heights excluding the equatorial regions can be obtained from (19.52) and (19.53) by taking $(\nu_i/\Omega_i)^2 \ll 1$, $(\nu_e/\Omega_e)^2 \ll 1$, and neglecting terms of order m_e/m_i:

$$\begin{aligned} w_i = & -\left(\frac{\Omega_z^{i^2}}{\Omega_i^2} \right) \frac{1}{m_i \nu_i} \left(\frac{1}{n_i} \frac{dp_i}{dz} + \frac{1}{n_e} \frac{dp_e}{dz} + m_i g \right) \\ & + \frac{\Omega_x^{\,i} \Omega_z^{\,i}}{\Omega_i^2} u_n - \frac{\nu_i \Omega_x^{\,i}}{\Omega_i^2} v_n + \frac{\Omega_z^{i^2}}{\Omega_i^2} w_n - \frac{\Omega_x^{\,i}}{\Omega_i^2} \frac{eE_y}{m_i}. \end{aligned} \quad (19.56)$$

Noting that $\mathbf{B} = B_0 \cos I\,\hat{x} - B_0 \sin I\,\hat{k}$, where I is the dip angle taken to be positive in the northern hemisphere, (19.56) can be reexpressed as

$$w_i = -\frac{\sin^2 I}{m_i \nu_i}\left(\frac{1}{n_i}\frac{dp_i}{dz} + \frac{1}{n_e}\frac{dp_e}{dz} + m_i g\right) - (\sin I \cos I)u_n - \left(\frac{\nu_i}{\Omega_i}\cos I\right)v_n + (\sin^2 I)w_n - \left(c\,\frac{\cos I}{B_0}\right)E_y. \tag{19.57}$$

Using the definition

$$D_{in} = (kT_i/m_i)/\sum \nu_{ik} \tag{19.58}$$

for the ion-neutral diffusion coefficient, (19.57) can be reexpressed in the standard form

$$w_i = -D_{in}\sin^2 I\left[\frac{1}{n_i}\frac{dn_i}{dz} + \frac{T_e/T_i}{n_e}\frac{dn_e}{dz} + \frac{m_i g}{kT_i} + \frac{1}{T_i}\frac{d}{dz}(T_e + T_i)\right] - c\cos I\frac{E_y}{B_0} - \frac{\nu_i}{\Omega_i}\cos I\, v_n - \sin I\cos I\, u_n + \sin^2 I\, w_n. \tag{19.59}$$

For the motion of a plasma having one ion species, $n_e = n_i$ and (19.59) becomes

$$w_i = -D_a \sin^2 I\left[\frac{1}{n_e}\frac{dn_e}{dz} + \frac{m_i g}{k(T_e + T_i)} + \frac{1}{T_e + T_i}\frac{d(T_e + T_i)}{dz}\right] - c\cos I\frac{E_y}{B_0} - \frac{\nu_i}{\Omega_i}\cos I\, v_n + \sin^2 I\, w_n - \sin I\cos I\, u_n \tag{19.60}$$

where the ambipolar diffusion coefficient is $D_a = (1 + T_e/T_i)D_{in}$. Comparison of this result with the equations of Chapters 14 and 15 for uncharged gases shows an enhancement of plasma diffusion due to the charge separation electric field established by the large diffusivity of the electron gas.

19.5 Diffusion in the Ionosphere: Multiple Ion Species

The results of the preceding section apply to a plasma composed of electrons and several ion species placed in an external magnetic field. In the upper ionosphere one generally must deal with the possibility of several ion species with differing flow velocities. As a result, not only do ion–ion friction effects become important, but there is also an electric field coupling term which acts to maintain the overall local electrical neutrality of the plasma.

Rather than attempting a complete derivation as was done in the last section, the basic problems can be described by assuming plasma flow is present only parallel to the magnetic field lines.

For low speed electron flows an adequate approximation to the electron momentum equation is

$$(1/n_e)\, dp_e/ds = -eE_{\parallel} \tag{19.61}$$

while the ith ion species momentum equation can be obtained from (19.15) as

$$\frac{1}{n_i m_i}\frac{dp_i}{ds} + g_{\parallel} - \frac{eE_{\parallel}}{m_i} = -\nu_{in} w_i - \sum_j \nu_{ij}(w_i - w_j) \tag{19.62}$$

where ν_{ij} is the ion–ion collision frequency relating to the friction arising from the differing ion flow velocities [6], w is the parallel velocity, and the effects of external electric fields perpendicular to the magnetic field are omitted.

Using (19.61) to eliminate $eE_{\parallel}$ from (19.62) one obtains the ith ion species equation of motion:

$$\frac{1}{n_i m_i}\frac{dp_i}{ds} + \frac{1}{n_e m_i}\frac{dp_e}{dz} + g = -\nu_{in} w_i - \sum \nu_{ij}(w_i - w_j). \tag{19.63}$$

In the previous section a similar equation was derived with the assumption $n_e = n_i$; $w_i = w_j$ such that an explicit expression for w_i could be derived. Equation (19.63) shows that such a simple form is not available when multiple ion flows are present because of both the friction terms and the electric field coupling involved in the term $(1/n_e m_e)dp_e/dz$ with $n_e = \sum n_i$. In general no further reduction of (19.63) is possible and to obtain the individual flow velocities numerical techniques must be applied.

The special example of a minor constituent diffusing through a dominant ion species follows from (19.63) as

$$w_i = -\frac{kT_i/m}{\sum \nu_{ij} + \nu_{in}}\left[\frac{1}{n_i}\frac{dn_i}{ds} + \frac{T_e/T_i}{n_e}\frac{dn_e}{ds} + \frac{m_i g}{kT_i} + \frac{1}{T_i}\frac{d}{dz}(T_e + T_i)\right] - \frac{\sum \nu_{ij} w_j}{\sum \nu_{ij} + \nu_{in}}. \tag{19.64}$$

Since $n_i \ll n_e$, the term involving dp_e/ds determines $E_{\parallel}$ and the transport speed of the minor ion can be greatly affected; for example, as with the downward flow of He^+ within the plasmasphere resulting from rapid loss through reactions with N_2.

19.6 Ion Diffusion Coefficients

Calculations of the ion diffusion coefficient can be made through evaluation of Eq. (19.3) once the interaction between ions and scattering particles is known. For ionospheric conditions this implies that ion-neutral resonance charge exchange, ion-neutral polarization, and ion–ion Coulomb interactions must be considered. In the first two cases account must be taken of differing ion and neutral gas temperatures, while for ions it is known that in the ionosphere the ion gases have approximately the same temperature [10, 11].

19.6.1 Resonance Charge Exchange [12, 13]

$$D_{\text{in}} = \frac{3(\pi/2)^{1/2}}{8n_{\text{n}}\bar{Q}_{\text{E}}} \left(\frac{kT_{\text{i}}}{m_{\text{i}}}\right)^{1/2} \frac{1}{(1 + T_{\text{n}}/T_{\text{i}})^{1/2}} \tag{19.65}$$

where T_{i} and T_{n} are the ion and neutral gas temperatures, m_{i} is the ion (or neutral particle) mass, n_{n} is the neutral gas density, and $\bar{Q}_{\text{E}}$ is the charge exchange cross section. The charge exchange cross section of principal importance for low speed flows has been given in Chapter 9. *Table 19.2*

TABLE 19.2

DIFFUSION COEFFICIENTS DUE TO CHARGE EXCHANGE
$\log_{10}(T_{\text{e}} + T_{\text{i}}) = 3.4771$

Species	D_{in} (cm^2 sec^{-1})	
O^+–O	$\frac{3.1 \times 10^{17}}{n(\text{O})}$	$\frac{T_{\text{i}}^{1/2}}{(1 + T_{\text{n}}/T_{\text{i}})^{1/2}}$
H^+–H	$\frac{8.0 \times 10^{17}}{n(\text{H})}$	$\frac{T_{\text{i}}^{1/2}}{(1 + T_{\text{n}}/T_{\text{i}})^{1/2}}$
He^+–He	$\frac{6.8 \times 10^{17}}{n(\text{He})}$	$\frac{T_{\text{i}}^{1/2}}{(1 + T_{\text{n}}/T_{\text{i}})^{1/2}}$
N_2^+–N_2	$\frac{1.3 \times 10^{17}}{n(\text{N}_2)}$	$\frac{T_{\text{i}}^{1/2}}{(1 + T_{\text{n}}/T_{\text{i}})^{1/2}}$
O_2^+–O_2	$\frac{2.4 \times 10^{17}}{n(\text{O}_2)}$	$\frac{T_{\text{i}}^{1/2}}{(1 + T_{\text{n}}/T_{\text{i}})^{1/2}}$

presents values of the resonance charge exchange diffusion coefficients for different ionospheric ion species using the data of Table 9.12 with the assumption that $T_i + T_n = 3000°K$ in the logarithm terms.

19.6.2 Elastic Collisions with Neutrals

$$D_{in} = kT_i/\mu_{in}\bar{\nu}_{in} \tag{19.66}$$

where μ_{in} is the ion-neutral reduced mass and $\bar{\nu}_{in}$ is the ion-neutral momentum transfer collision frequency of Eq. (9.33). In practical form (19.66) becomes

$$D_{in} = (8.31 \times 10^7 T_i)/\mu_A \bar{\nu}_{in} \quad \text{cm}^2\,\text{sec}^{-1} \tag{19.67}$$

with μ_A the reduced mass in atomic units. Values of the ion-neutral elastic diffusion coefficient are given in *Table 19.3* for different ions and neutral gases based on the 1000°K collision frequencies of Table 9.11.

TABLE 19.3

DIFFUSION COEFFICIENT FOR ELASTIC ION-NEUTRAL COLLISIONS

Species	D_{in} (cm^2 sec^{-1})
O^+–N_2	$8.5 \times 10^{15} T_i/n(N_2)$
O^+–O_2	$7.2 \times 10^{15} T_i/n(O_2)$
O^+–He	$5.6 \times 10^{16} T_i/n(He)$
N_2^+–O_2	$9.7 \times 10^{15} T_i/n(O_2)$
N_2^+–O	$1.1 \times 10^{16} T_i/n(O)$
O_2^+–N_2	$9.4 \times 10^{15} T_i/n(N_2)$
O_2^+–O	$1.7 \times 10^{16} T_i/n(O)$
NO^+–air	$4.5 \times 10^{15} T_i/n(\text{air})$

19.6.3 Ion–Ion Coulomb Interaction

$$D_{12} = (3\gamma/32n_2)(2kT_i/\mu\pi)^{1/2}(2kT_i/e^2)^2(1/\ln \Lambda) \tag{19.68}$$

where T_i is the ion temperature, μ is the ion–ion reduced mass, n_2 is the density of the ion gas through which type 1 ions are diffusing, $\ln \Lambda$ is related to the Debye shielding distance, and γ is a correction factor determined from kinetic theory [14]. In practical terms, (19.68) becomes

$$D_{12} = (6.5 \times 10^7 \gamma T_i^{5/2})/n_2 \mu_A^{1/2} \quad \text{cm}^2\,\text{sec}^{-1} \tag{19.69}$$

where μ_A is the ion–ion reduced mass in atomic mass units and $\ln \Lambda = 15$. For the ionospheric regions above 250 km the diffusion of minor ions is generally determined by Coulomb collisions with the dominant ion species rather than through collisions with the neutral gas particles.

Values of γ appropriate for H^+, He^+, and N^+ moving through O^+ are $\gamma = 1.36$, 2.51, and 1.75, respectively [14].

19.6.4 Electron–Ion Coulomb Interaction

$$D_{ei} = 3(2/\pi)^{1/2}(kT_e)^{5/2}/(8n_e e^4 m_e^{1/2} \ln \Lambda) \tag{19.70}$$

or

$$D_{ei} = (2.8 \times 10^{11} T_e^{5/2})/n_e \quad \text{cm}^2 \text{ sec}^{-1}. \tag{19.71}$$

REFERENCES

1. J. P. Dougherty, *J. Atmos. Terr. Phys.* **20**, 167 (1961).
2. J. M. Burgers, *Flow Equations for Composite Gases.* Academic Press, New York, 1969.
3. E. H. Holt and R. E. Haskell, *Foundations of Plasma Dynamics.* MacMillan, New York, 1965.
4. J. M. Smith, An Exact Calculation of Momentum and Energy Exchange Collision Integrals over Displaced Maxwellian Distribution Functions. General Electric Co., Missile and Space Div., R64SD54, August (1964) [Available as ASTIA Document AD607333].
5. V. C. A. Ferraro, *J. Atmos. Terr. Phys.* **29**, 913 (1964).
6. J. A. Fejer, Motions of Ionization, in *Physics of the Earth's Upper Atmosphere* (C. O. Hines, I. Paghis, T. R. Hartz and J. A. Fejer, eds.). Prentice-Hall, Englewood Cliffs, New Jersey, 1965.
7. S. Chapman and J. Bartels, *Geomagnetism*, Vols. 1 and 2. Oxford Univ. Press, London and New York, 1949.
8. S. Matsushita, *Radio Sci.* **6**, 279 (1971).
9. W. I. Axford, D. M. Cunnold, L. J. Gleeson, *Planet. Space Sci.* **14**, 909 (1966).
10. P. M. Banks, *Planet. Space Sci.* **15**, 77 (1967).
11. J. C. G. Walker and A. Dalgarno, *Planet. Space Sci.* **15**, 200 (1967).
12. P. M. Banks and T. E. Holzer, *Planet. Space Sci.* **16**, 1019 (1968).
13. A. Dalgarno, M. R. C. McDowell, and A. Williams, *Proc. Roy. Soc.* (*London*) **A250**, 411 (1958).
14. R. W. Schunk and J. C. G. Walker, *Planet. Space Sci.* **18**, 1319 (1970).

CHAPTER 20

Ionospheric Transport Processes

20.1 Introduction

The profiles of ion concentration in the ionosphere are determined by a competition between chemical and transport processes. At low altitudes in the D and E regions the neutral gases are sufficiently dense to greatly retard plasma motions associated with gravity and pressure gradients. Thus, since the time scale for plasma transport is much greater than that for ionic production and loss, the ion composition and concentration is determined by local effects. Above 150 to 200 km the time scale for transport becomes comparable with that for ionic reactions so that ion densities are no longer determined by local effects but by the much more complicated couplings involving diffusion of ions from regions of production to those of loss [1–10].

For general conditions the altitude distribution of each ion species is implicit in the equation of continuity:

$$\partial n_i/\partial t + \nabla \cdot n_i \mathbf{C}_i = q_i - l_i \tag{20.1}$$

where n_i is the ith ion species concentration, $\mathbf{C}_i$ is the mean ion transport velocity, and q_i and l_i are the respective rates of ion production and loss.

Solutions for the ion concentration cannot be obtained without a knowledge of $\mathbf{C}_i$. In the last chapter the ion momentum equation was given in terms of various forces acting in a partially ionized plasma. The general case of time-dependent diffusion is difficult to discuss, however, since numerical solutions are needed. Thus, in the following sections various simplified models of plasma transport are discussed to illustrate the basic principles which govern the behavior of ions and electrons in the ionosphere.

20.2 Transport with a Single Ion Species

Consider a simple model of plasma transport where pressure gradients and gravity act only in the vertical direction and $n_e = n_i$. The continuity equation giving the vertical distribution of ionization is

$$(\partial n_i/\partial t) + (\partial n_i w_i/\partial z) = q_i - l_i \tag{20.2}$$

where changes in the volume of the magnetic field tube are omitted (see Chapter 21).

With the restriction of the present model to the case of a plasma with a single ionic constituent, the vertical transport velocity, valid for low speed motions, is given by Eq. (19.60) as

$$w_i = -D_a \sin^2 I \left(\frac{1}{n_i}\frac{\partial n_i}{\partial z} + \frac{1}{T_p}\frac{\partial T_p}{\partial z} + \frac{1}{H_p}\right) - \frac{cE_y}{B_0}\cos I - \frac{\nu_n \nu_{in}}{\Omega_i}\cos I - u_n \sin I \cos I + w_n \sin^2 I \tag{19.60}$$

where $D_a = (1 + T_e/T_i)D_{in}$ is the ambipolar diffusion coefficient, $T_p = T_e + T_i$, and $H_p = kT_p/m_i g$ is the plasma scale height.

The altitude variation of w_i depends upon the diffusion coefficient, the external electric field, and winds in the neutral atmosphere. Since D_a is inversity proportional to the neutral gas density, while the pressure gradients and gravity are limited to some range of values, it follows that the effects of diffusive transport become progressively smaller as one goes to lower altitudes. In the absence of transport, Eq. (20.1) reduces to

$$\partial n_i/\partial t = q_i - l_i \tag{20.3}$$

with the steady state solution $q_i = l_i$ as was assumed in the preceding chapters dealing with D, E, and lower F region ionic and neutral chemistry.

Even if diffusive motions are suppressed, changes can occur in the vertical ion density profile as a result of winds and electric fields. Thus, if $D_a \to 0$, the ion vertical velocity is

$$w_D = -\frac{cE_y}{B_0}\cos I - \frac{\nu_n \nu_i}{\Omega_i}\cos I - u_n \sin I \cos I + w_n \sin^2 I \tag{20.4}$$

which can be important to ion density profiles in the lower F and upper E regions. Equation (20.4) has, of course, a restricted validity dependent upon the conditions $\nu_i \ll \Omega_z{}^i$ and $D_a \to 0$.

At high altitudes ($z \geq 250$ km) the ambipolar diffusion coefficient becomes sufficiently large to permit substantial ion gas diffusive motions in response to density and temperature gradients. Time-dependent plasma diffusion involves a wide spectrum of possible variations which must be treated using numerical methods. On the other hand, it is possible to obtain analytical solutions for steady state distributions in high altitude regions. These results are of fundamental importance to our understanding of the ionospheric environment and plasma transport processes.

To obtain the equation describing the ion concentration profile at all altitudes for steady state conditions with a simple model of plasma transport the ion equation of continuity (20.2) and the momentum equation (20.42) can be combined to give [3, 4, 9, 10]

$$\frac{d^2 n_e}{dz^2} + \left[\frac{1}{H_p} + \frac{1}{D_a}\frac{dD_a}{dz} - \frac{w_D}{D_a \sin^2 I}\right]\frac{dn_e}{dz} + \left[\frac{1}{D_a H_p}\frac{dD_a}{dz} - \frac{1}{D_a \sin^2 I}\frac{dw_D}{dz}\right] n_e = \frac{l_i - q_i}{D_a \sin^2 I}. \quad (20.5)$$

Here both diffusion and drift have been included and constant values of T_e, T_i, and g are assumed.

The form of Eq. (20.5) is linear and of second order with two linearly independent solutions. At low altitudes, where $D_a \to 0$, these solutions are degenerate, but at high altitudes, such as in the F_2 region and above, the degeneracy is removed by the influence of diffusion.

Analytic solutions to Eq. (20.5) are difficult to obtain [3, 4, 10] and the linearly independent solutions must usually be found through numerical methods as discussed later and shown in *Fig. 20.1*. In the case at high altitudes where w_D, q_i and l_i are negligible, however, the two solutions can be readily obtained.

Consider the limiting form of Eq. (20.5) valid for high altitudes above the F_2 region neglecting drift terms:

$$\frac{d^2 n_e}{dz^2} + \left(\frac{1}{H_p} + \frac{1}{D_a}\frac{dD_a}{dz}\right)\frac{dn_e}{dz} + \left(\frac{1}{D_a H_p}\frac{dD_a}{dz}\right) n_e = 0. \quad (20.6)$$

The solution to (20.6) can be written as

$$n_e(z) = A n_1(z) + B n_2(z) \quad (20.7)$$

where $n_1(z)$ and $n_2(z)$ are the linearly independent solutions and A and B are constants chosen to match the ionospheric boundary conditions, to be discussed later.

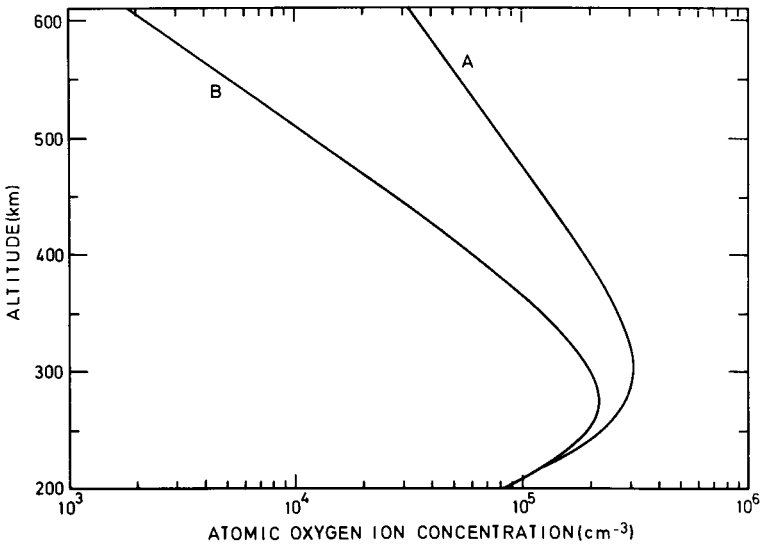


Fig. 20.1 Plot of the F_2-region O^+ density showing diffusive equilibrium (curve A) and full upwards flow (curve B) for a daytime 1000°K model thermosphere with a vertical magnetic field.

The first of the two independent solutions to (20.6) can be found from the assumption $w_i = 0$, corresponding to diffusive equilibrium of the plasma at high altitudes under the influence of gravity:

$$n_1(z) = n_{1a}(T_{pa}/T_p) \exp\left(-\int_a^z (m_i g/kT_p)dz'\right). \tag{20.8}$$

Here a is a reference altitude from which the distance z is measured. Actually, this equation is more general than the solution to (20.6) since it applies to conditions where T_p and g vary with altitude. If, however, T_p and g are constants, (20.8) reduces to the static distribution

$$n_1(z) = n_{1a} \exp[-(z - a)/H_p]. \tag{20.9}$$

This result shows that the plasma scale height for diffusive equilibrium is at least twice as large as the scale height of a neutral gas having the same atomic mass. Therefore, the plasma density decreases less rapidly with altitude than the parent neutral gas. This feature of the plasma density distribution arises from the gravitational separation of ions and electrons with the consequent establishment of a vertical electric field which tends to neutralize the downward force of gravity for the ions and enhance the

net downward force acting on electrons. The magnitude of the electric field acting in diffusive equilibrium for a single ion species can be obtained from the electron momentum equation

$$(1/n_e)(dp_e/dz) = -eE_z \tag{20.10}$$

so that, from (20.9)

$$eE_z = m_i g/(1 + T_i/T_e), \tag{20.11}$$

positive in the upward direction. It is the long range effect of this charge separation electric field which serves to couple the electrons and ions in a manner not possible in a mixture of neutral gases.

The form of the second solution to the ion density equation (20.6) depends upon the altitude dependence of D_a. Suppose the ambipolar diffusion coefficient varies with altitude as $D_a = D_a{}^a \exp[(z - a)/H]$, where H is the scale height corresponding to the neutral gas through which the ion gas diffuse and $D_a{}^a$ is the value of D_a at the reference altitude a where $z = a$. For this model the second solution is

$$n_2(z) = n_{2a} \exp[-(z - a)/H] \tag{20.12}$$

where n_{2a} is the density at the altitude a. When the scale height of the neutral gas is less than that of the plasma, this solution corresponds to an upward flow of plasma supported through a plasma pressure gradient which is larger than that needed for diffusive equilibrium. Since there is no production of ionization in this model, the ion flux is constant.

The diffusion velocity corresponding to (20.12) can be obtained as

$$w_i = -D_a{}^a e^{(z-a)/H} \sin^2 I \left[\frac{1}{H_p} - \frac{1}{H}\right]. \tag{20.13}$$

For an ion gas diffusing through its parent neutral gas, such as O^+ through O, the scale height factors of (20.13) reduce to give

$$w_i = -\frac{D_a{}^a e^{(z-a)/H}}{H} \sin^2 I \left[\frac{T_n}{T_e + T_i} - 1\right], \tag{20.14}$$

showing that for the ionosphere, where $T_e \geq T_i \geq T_n$, the diffusive flow is upwards and continually increasing in velocity. Further, as mentioned above, since $q_i = l_i = 0$, the total ion flux is conserved, i.e., $n_1 w_1 = n_{1a} w_{1a}$ at any point.

The ion flow derives in part from the steep gradient in electron density which, by Eq. (20.10), is equivalent to a vertical component of the electric field. This electric field can be found to be

$$eE_z = m_i g(T_e/T_i); \tag{20.15}$$

a value sufficient to overcome the force of gravity on each ion since $T_e/T_i \geq 1$ in the upper ionospheric regions where this analysis applies.

The limiting flux, $F = n_i w_i$, of ions leaving the ionosphere in the steady flow solution to the diffusion equation follows from (20.13) and (20.14) as

$$F = \frac{D_a{}^a n_{ea}}{H}\left[1 - \frac{T_n}{T_e + T_i}\right]\sin^2 I. \tag{20.16}$$

Since the ion flux F is constant, the decrease of electron density given by (20.12) implies that the ion velocity, w_i must increase exponentially with altitude. Eventually, above a certain height the ion inertia term $w_i\,\partial w_i/\partial z$, which was neglected in the present ion momentum equation, becomes more important than ion neutral friction in limiting the rate at which the ion velocity can increase with altitude. A complete description of this effect is given in Chapter 21.

To determine the actual altitude variation of electron density two boundary conditions are needed [6, 7, 11]. Since the present model lacks production or loss of ionization it is difficult to apply the purely exponential solutions to a physical situation. Nevertheless, suppose that the value $n_e = n_{ea}$ is given at $z = a$, and the upward ion flux at this point is ϕ. Using Eqs. (20.7) and (20.16) the electron density profile is

$$n_e(z) = [1 - (\phi/F)]n_{ea}e^{-(z-a)/H_p} + (\phi/F)n_{ea}e^{-(z-a)/H}. \tag{20.17}$$

If the boundary value ion flux ϕ is zero, then diffusive equilibrium exists and $n_e(z) = n_{ea}\exp[-(z - a)/H_p]$. As ϕ/F is increased, larger amounts of $n_2(z)$ are linearly mixed with $n_1(z)$, producing a sharp change in slope of the electron density profile. Eventually, a point is reached where $\phi = F$ and $n_e(z) = n_{ea}\exp[-(z - a)/H]$. From (20.17) attempts to increase ϕ to values greater than F will result in negative electron densities. Hence, F represents the critical or limiting flux of ionization which can be transported through diffusion (but not by vertical drifts).

The model used to derive Eq. (20.17) neglected ion production or loss. Nevertheless, solutions to Eq. (20.5) which take these terms into account have a behavior very similar to (20.17). This is illustrated in Fig. 20.1 for the two solutions for the case of O^+ in the F_2 region where production and

loss of ions is important. At low altitudes the two solutions are degenerate, but at high altitudes they become distinct. The actual electron density profile for any real situation involves linear combinations to match specified ion flux conditions (outward or inward flow) at the upper boundary.

When time-dependent ion profiles are computed it is found that the concept of the limiting ion flux is important and that an outflow is needed to fill magnetic flux tubes with plasma. Thus, the maximum rate at which a density profile can change is governed not only by ion production and loss, but also by the magnitude of the ion diffusion coefficient and the neutral gas scale height. It should be noted, however, that while there is a restriction to the rate of outward O^+ flow from the ionosphere, there is no limit to the rate of plasma inflow [$\phi < 0$; see Eq. (20.17)] and rapid changes consistent with plasma pressure gradients are possible.

It is clear that the motion of ionization must involve elements of the steady flow solutions; that is, for rapid changes in boundary pressures and temperatures the ion density distribution cannot remain in diffusive equilibrium, but must reflect the characteristics of ion flow. The specific altitude dependence of the ion density in a predawn F_2 region, for example, can be that of diffusive equilibrium. After sunrise, with photoelectron heating and an increase in the lower boundary plasma pressure, there will be an upward flow of plasma into the magnetosphere with there being some decrease in the effective plasma scale height of the F_2 region corresponding to a transition toward limiting flow.

20.3 The F_2 Region

20.3.1 Basic Processes

The discussion of the last section concerned the form of the solutions to the electron density equation. The relation of these two independent solutions to the structure of the ionosphere was not explicit, however, and in the present section an introduction to the current theory of the F_2 region will be made.

The ionospheric F_2 region extends upward from about 225 km, past the electron density peak which is formed through competition between ion transport and chemical process, and into the topside ionosphere at 300 to 500 km altitude [10–13]. The principal ion of the F_2 region is $O^+(^4S)$, and the predominant neutral gas is O, although N_2 and O_2 play an important part in the O^+ loss process. Through solar ultraviolet radiation ($\lambda < 910$ Å) the atomic oxygen atoms of the F_2 region are ionized and free to participate

in plasma transport or chemical reactions. Generally speaking, the $O^+(^4S)$ is lost through slow ion–molecule reactions with N_2 or O_2 to form NO^+, N_2^+, or O_2^+. These molecular ions, in turn, recombine with electrons through the rapid process of dissociative recombination as discussed in Chapters 10 and 18.

The altitude profile of ion density in the F_2 region is determined both by ionic reactions and ion transport. In the absence of diffusion or convection processes the ion density in a steady state distribution would be expected to continually rise with altitude owing to the rapid decrease in the effective ion recombination coefficient. At sufficiently high altitudes, however, the time constant for chemical processes becomes comparable with that for ion transport and a peak in the ion density is reached, followed by a density distribution which decreases with altitude.

In the steady state, atomic oxygen ions produced in the upper F_2 region diffuse downward through the peak of the F_2 region to lower altitudes where ion loss processes are important. Typical downward velocities at the F_2 peak are in the range 10–20 m sec^{-1} [4, 11, 13]. A series of electron density profiles typical of the midlatitude F_2 region are shown in *Fig. 20.2*.

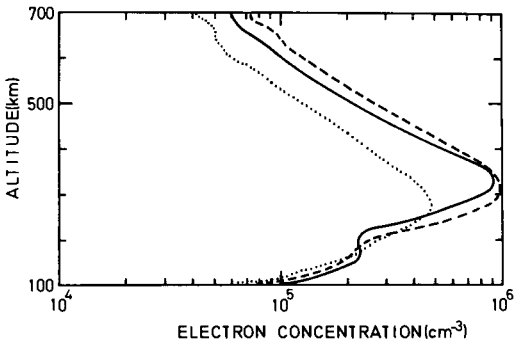


Fig. 20.2 Ionospheric electron density profiles at Arecibo, Puerto Rico measured on July 22, 1965 using the incoherent scatter technique. Key to the time (AST): dotted curve, 0800; solid curve, 1100; dashed curve, 1600. (Courtesy of Dr. J. R. Doupnik.)

The formation of the F_2 region is established by short wavelength solar ultraviolet radiation ($\lambda < 910$ Å) which ionizes atomic oxygen at the rate

$$q(O^+) = I(O)n(O) \tag{20.18}$$

where $I(O) = (3.2 \pm 1.3) \times 10^{-7}$ sec^{-1} (see Chapter 7) is the net photoionization rate coefficient leading to all important ion internal energy states;

that is, $O^+(^4S)$, $O^+(^2D)$, and $O^+(^2P)$. Although it is common to ignore the final ion states, recent work [14–18] has shown that photoionizations leading to the $O^+(^2D)$ state are important as a result of the rapid reaction

$$(\gamma_1^*): \quad O^+(^2D) + N_2(X^1\Sigma_g, v' = 0) \rightarrow O(^3P) + N_2^+(A\ ^2\Pi_u; v' = 1) \tag{10.108}$$

which has an estimated [17] reaction rate $\gamma_1^* \simeq 10^{-9}\ \text{cm}^3\ \text{sec}^{-1}$. Reaction (10.108) is far more rapid than those involving ground state $O^+(^4S)$:

$$(\gamma_1): \quad O^+(^4S) + N_2 \rightarrow NO^+ + N \tag{10.104}$$

$$(\gamma_2): \quad O^+(^4S) + O_2 \rightarrow O_2^+ + O \tag{10.105}$$

where $\gamma_1 = (1.1 \pm 0.3) \times 10^{-12}\ \text{cm}^3\ \text{sec}^{-1}$ and $\gamma_2 = (2 \pm 0.2) \times 10^{-11}\ \text{cm}^3\ \text{sec}^{-1}$. As a result of the difference between γ_1^* and γ_1, $O^+(^2D)$ is largely absent from the F_2 region and, in terms of the ion density structure, only $O^+(^4S)$ reactions and transport are important.

When solar ultraviolet radiation or energetic electrons ionize atomic oxygen, there is a large probability that the resulting ion will be in an excited state [14, 15]. Of particular importance for ionospheric problems are the long lifetimes ($\tau = 2.1 \times 10^4$ and 5.6×10^3 sec) for $O^+(^2D_{5/2})$ and $O^+(^2D_{3/2})$ that permit these excited ions to participate in reactions with the molecular gases of the neutral atmosphere.

The production of $O^+(^4S)$, $O^+(^2D)$, and $O^+(^2P)$ occurs in the atmosphere as a result of the removal of an outer shell electron through photoionization with ionization thresholds of 911, 732, and 663 Å, respectively. The ionization processes involving the removal of an inner shell electron, which lead to $O^+(^4P)$ and $O^+(^2P)$ states (thresholds of 434 and 310 Å), can be neglected because of their relatively small cross sections.

Both the $O^+(^2D)$ and $O^+(^2P)$ states can be destroyed through quenching collisions with electrons, through superelastic collisions or chemical reactions with neutral particles, or through radiative transitions eventually leading to the ground state $O^+(^4S)$. From the data of Fig. 6.14 it can be seen that direct excitation to $O^+(^2P)$ is important, even though the ^2P state has a relatively short lifetime, since it provides an additional source of $O^+(^2D)$ through photon emission (the auroral lines $\lambda = 7319$, 7320, 7330, and 7331 Å arise from $^2P_{3/2,1/2} \rightarrow {}^2D_{5/2,3/2}$ transitions). With lifetimes of 6.2 and 5.7 sec, $O^+(^2P_{1/2})$ and $O^+(^2P_{3/2})$ can either decay to $O^+(^2D_{5/2,3/2})$ or $O^+(^4S_{3/2})$, respectively, or become directly involved in an atmospheric collision. In the upper F region and above, the mean times for collision are somewhat greater than 6 sec and radiative cascading must occur. At lower

altitudes, collisions and reactions will be of importance. Here, it is convenient to make the assumption that the ^2P states are free to radiate to ^2D and ^4S states. This assumption can lead to an underestimate of the number of excited ions participating in ionospheric ion–molecule reactions but, since the radiative transition ratio

$$(^2P \rightarrow {}^4S)/(^2P \rightarrow {}^2D) = 0.27$$

is small (assuming a population of ^2P states according to statistical weights), no large effect should occur unless the $O^+(^2P)$ reaction with N_2 is significantly slower than that for $O^+(^2D)$.

Electron quenching of the ^2P and ^2D states can occur and acts as a heat source for the ionospheric electron gas. Using available data, the rate for electron quenching between the different energy levels of O^+ is [19]

$$\bar{\nu}_{n,n'} = [8.6 \times 10^{-6} \Omega(n, n') n_e]/\omega_n T_e^{1/2} \quad \text{sec}^{-1} \tag{20.19}$$

where $\Omega(n, n')$ is the normalized cross section for transition between the states n and n' (given in Fig. 6.14), and ω_n is the statistical weight of the originating level. Since the electron deexcitation rates are roughly the same for $^2P \rightarrow {}^2D$, $^2P \rightarrow {}^4S$, and $^2D \rightarrow {}^4S$ transitions, the effect of $^2P \rightarrow {}^2D$ quenching can be neglected at this point, but is considered again as a general process that will tend to deactivate the ^2D levels.

Cross sections for ultraviolet photoionization have been calculated and can be used to obtain the relative rates of $O^+(^4S)$, $O^+(^2P)$, and $O^+(^2D)$ ionization [20–22].

With the assumption that the ^2P states created by photoionization are populated in proportion to their statistical weights, the proportion of $O^+(^2P)$ radiative transitions that terminate in the ^2D states is 79%. Thus, the total ionization rate leading to the production of $O^+(^2D)$ is

$$I(^2D) = \left[\frac{\sigma(^2D)}{\sigma_t} + 0.79\,\frac{\sigma(^2P)}{\sigma_t}\right] \sum_{\Delta\lambda} \Delta I_\infty(\lambda) e^{-\tau(\lambda)} \Delta\lambda \tag{20.20}$$

where σ_t is the total O^+ photoionization cross section,

$$\Delta I_\infty(\lambda) = n(O)\sigma_t \, \Delta\Phi_\infty(\lambda)$$

is the total O^+ ionization rate outside the atmosphere per unit wavelength, $\Delta\Phi_\infty(\lambda)$ is the solar flux per unit wavelength, and $\tau(\lambda)$ is the optical depth.

Calculations based on (20.20) have been made for the total production rates of $O^+(^4S)$ and $O^+(^2D)$ for the different atmospheric models used here.

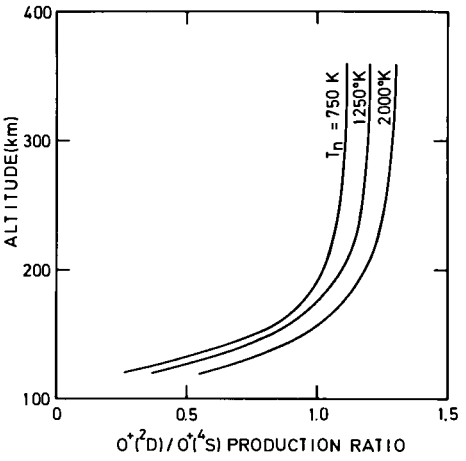


Fig. 20.3. Ratio of $O^+(^2D)$ to $O^+(^4S)$ photoproduction for three levels of solar activity for an overhead sun.

Figure 20.3 plots the ratio $I(^2D)/I(^4S)$ as a function of altitude for several of these models. Generally, solar photoionization leads to approximately 50% of all initial photoions being in the ^2D state.

The conditions for which electron deactivation of $O^+(^2D)$ is of importance can be established through comparison of (10.104) and (20.19). Thus, when $n_e > 1.1 \times 10^{-2} n(N_2)$, deactivation of $O^+(^2D)$ will be more important than ion–molecule charge exchange. Since limiting values of $n(N_2)$ at 350 km range between 7×10^7 and $3 \times 10^8\,cm^{-3}$ for $800° < T_n < 1400°K$, it follows that deactivating electron collisions are important only for particular situations of very high electron density. Further, since T_e is generally greater than 1000°K, the deexcitation rate will usually be smaller than 3×10^{-8} $cm^3\,sec^{-1}$.

The most important consequences of the present treatment can be seen through solutions for the ion continuity equations considering only processes (10.104), (10.100), and (10.101) with the assumptions that dissociative recombination is very rapid and that electron deactivation collisions are negligible. For steady state conditions

$$\frac{n(^2D)}{n(^4S)} = \frac{\gamma_1^* n(N_2) + \gamma_2 n(O_2)}{\gamma_1 n(N_2) + \gamma_2 n(O_2)} \frac{I(^2D)}{I(^4S)} \tag{20.21}$$

so that in the F_2 region $n(^2D)/n(^4S) \simeq 4.5 \times 10^{-3}$.

In practical terms (20.21) indicates that computations of the O^+ density profile should be made taking into account only those processes involving $O^+(^4S)$, both in photoionization and ion loss. The effective photoionization rates for O^+ characteristic of differing levels of solar activity are given in *Table 20.1.*

TABLE 20.1

$O^+(^4S)$ PHOTOIONIZATION RATES

Solar conditions	Rate (sec^{-1})
Minimum activity (750°, 1000°K models)	1.1×10^{-7}
Low activity (1250°K model)	1.6×10^{-7}
Medium activity (1500°K model)	2.2×10^{-7}
High activity (1750°, 2000°K models)	3.3×10^{-7}

20.3.2 Theoretical Results

The application of these results to theoretical models of the F_2 region can be made using the electron density equation derived previously in (20.5), along with the O^+–O, O^+–N_2, and O^+–O_2 diffusion coefficients discussed in Chapter 19. The rates of $O^+(^4S)$ production appropriate for an overhead sun for several typical model neutral atmospheres can be obtained from the Tables of Chapter 7 and Appendix B.

The results, shown in *Figs. 20.4–20.7*, have been obtained for several values of the electron temperature with no vertical drift effects. The ion

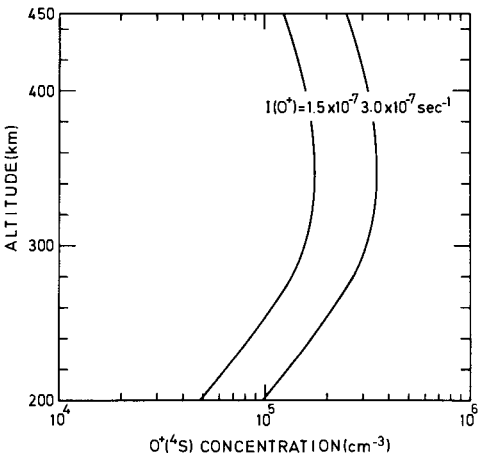


Fig. 20.4 F_2-region ion density profile for diffusive equilibrium in a 1500°K model thermosphere, overhead sun, and vertical magnetic field ignoring the effects of vertical ion drifts due to winds. A constant electron temperature of 2000°K has been used ($\sin^2 I = 1$; $w_D = 0$; $T_i = T_n$).

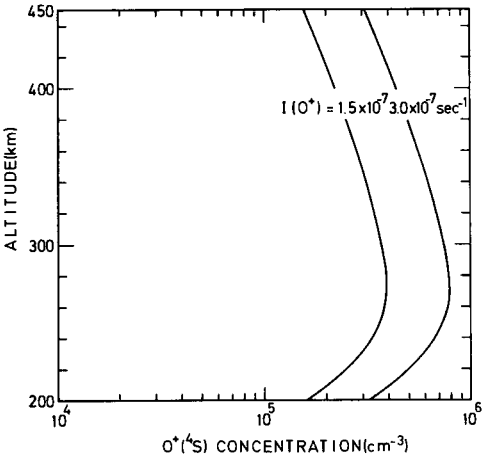


Fig. 20.5 F_2-region ion density profile for a 1000°K model thermosphere and conditions identical to Fig. 20.4.

temperatures have been calculated in a self-consistent fashion using the energy transfer rates of Chapter 22. The boundary conditions appropriate to these examples correspond to chemical equilibrium at low altitudes [$w(O^+) = 0$] followed by zero diffusion velocity at high altitudes. Thus, in addition to the expected peak in ion density, it is found that at high altitudes the plasma density varies as predicted by Eq. (20.9); i.e., $n_e = n_{ea} \exp[-z/H_p]$ with $H_p = kT_p/m(O^+)g$.

Increases in the plasma temperature generally tend to decrease the magnitude of the F_2 peak by increasing the value of the diffusion coefficient [23]. The height of the peak, in contrast, tends to be raised somewhat for higher

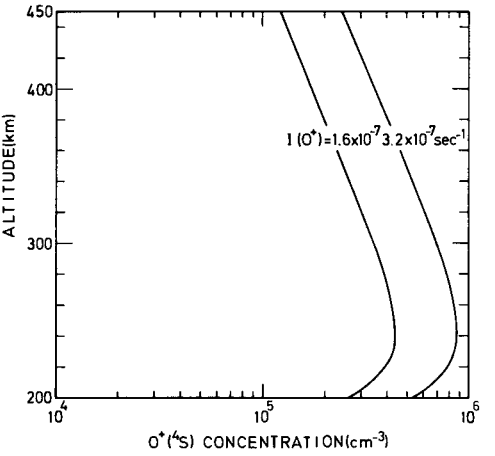


Fig. 20.6 F_2-region ion density profile for a 750°K model thermosphere and conditions identical to Fig. 20.4.

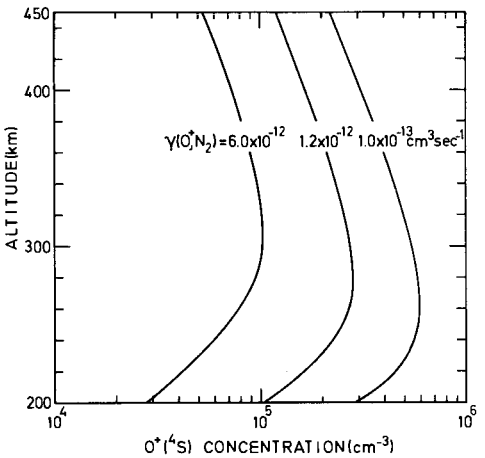


Fig. 20.7 F_2-region ion density profiles for a 1000°K model thermosphere with different values of the O^+-N_2 loss rate. An overhead sun, vertical magnetic field, and a constant electron temperature of 2000°K have been assumed.

temperatures. A slight change in scale height above the F_2 peak is caused by the transition of the ion temperature from the neutral gas temperature at 300 km towards the electron temperature near 800 km.

Changes in the neutral atmosphere strongly affect both the magnitude and height of the F_2 peak. For increasing thermospheric temperatures there exists an implied increase in solar flux and ion production rates [23–25]. Because increases in temperature lead to higher neutral gas pressures in the F_2 region, the F_2 peak tends to move upward. This tendency towards an increased height of the F_2 peak is enhanced by the vibrational excitation of N_2. As shown in Fig. 10.10, the higher neutral gas temperatures lead to increased vibrational temperatures and more rapid ion loss; i.e., an effectively greater N_2 density. Thus, when the exospheric temperature increases the peak density decreases and the location of the peak shifts upward [25]. To show this in more detail, Fig. 20.7 has been prepared using an order of magnitude variation in the O^+–N_2 loss rate for a 1000°K model neutral atmosphere.

An additional factor relates to uncertainty in the O^+–O diffusion coefficient. *Figure 20.8* gives the F_2-region profiles resulting from changes in D_a for a 1000°K model atmosphere and a constant electron temperature of 2000°K. The variations seen also relate to changes in the magnetic dip angle since the term $\sin^2 I$ acts to reduce the vertical component of ion diffusion.

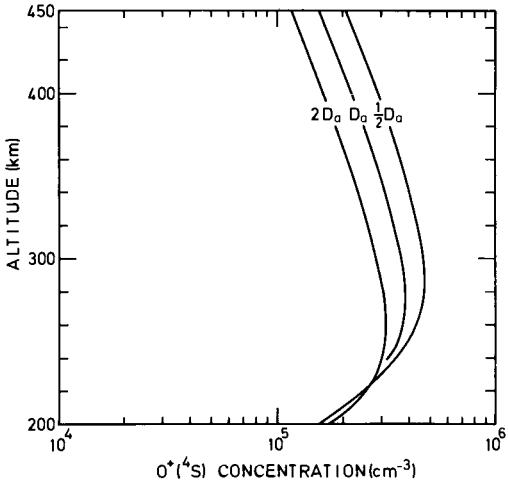


Fig. 20.8 Effects of changing the O^+-O diffusion coefficient in a 1000°K model thermosphere using the conditions listed for Fig. 20.4.

Up to this point the examples of F_2-region behavior have been based upon diffusive equilibrium at high altitudes. In contrast, an example of a steady outward flow of O^+ has been shown in Fig. 20.1 for a 1000°K model thermosphere. In that figure curve A represents the solution pertaining to a hydrostatic plasma distribution with no net ion flux at high altitudes. Curve B, on the other hand, represents the density distribution appropriate to a continual outwards flow of ionospheric ionization at the maximum possible rate in the absence of upward drift.

The choice of a proper linear combination of the two solutions clearly relates to the physical boundary conditions to be imposed. In polar regions, where the magnetic field lines are open to interplanetary plasma pressures, continual escape can occur [26, 27]. In this circumstance a natural boundary condition for the O^+ flow must depend upon the rate at which H^+ can be produced and removed; i.e., a two-ion model must be introduced as is done in Chapter 22. In this situation, time-independent flows of ions appear to be appropriate.

Outside the regions of open field lines upward flows must involve dynamic effects. Inside the plasmasphere it has been found that there is a continual exchange of ionization between the ionosphere and inner magnetosphere [28–31]. As a result of this and many other influences there occur diurnal variations in O^+ pressure in the F_2 regions. During early morning hours the F_2 region must replenish the high altitude magnetic field tubes with new ionization to replace that lost during the night as a result of recombina-

tion in the F_2 region. This upward flow of plasma involves a flux $\phi \sim 2\text{–}4 \times 10^8$ ions cm^{-2} sec^{-1}. However, since the limiting upward flux for O^+ moving through O is about 2×10^9 ions cm^{-2} sec^{-1}, the upward flow can be supported with only a small flattening in the O^+ density profile.

In the evening a general influx of O^+ (created through H^+ to O^+ charge exchange) is forced into the upper F_2 region. Since inward flow is not subject to a limiting condition, the density profile remains nearly that for hydrostatic equilibrium. *Figure 20.9* gives the theoretical F_2-region density profile which results from an ionization influx during the daytime when photoionization is present (overhead sun). In contrast, *Fig. 20.10* shows similar profiles when there is no local ionization process; i.e., a situation similar to the nighttime maintenance of the F_2 region through ionization flow from the plasmasphere.

The effects of neutral winds and a perpendicular electric field have not been included in the last examples. Returning to Eq. (19.60) these external drifts can be written as

$$w_D = -\frac{cE_y \cos I}{B_0} + v_n \frac{\nu_i}{\Omega_i} \cos I - u_n \sin I \cos I + w_n \sin^2 I. \quad (20.22)$$

Figure 20.11 has been calculated for different values of w_D and a constant electron temperature of 2000°K with $\sin^2 I = 0.75$. These velocities

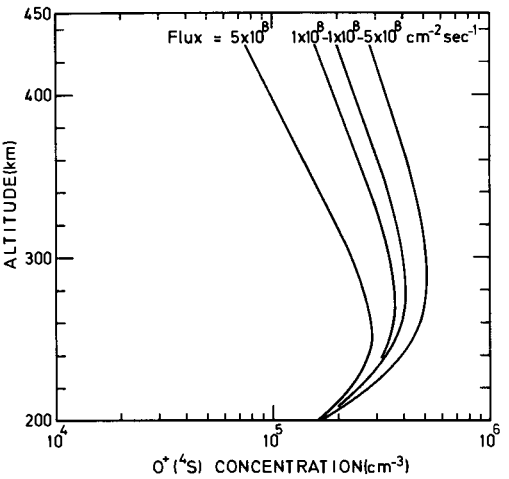


Fig. 20.9 Changes in the F_2 region when ionization flows from the topside ionosphere. A 1000°K thermosphere has been used with various values of the ion flux for a vertical magnetic field when full daytime photoionization is present. (See conditions listed for Fig. 20.4.)

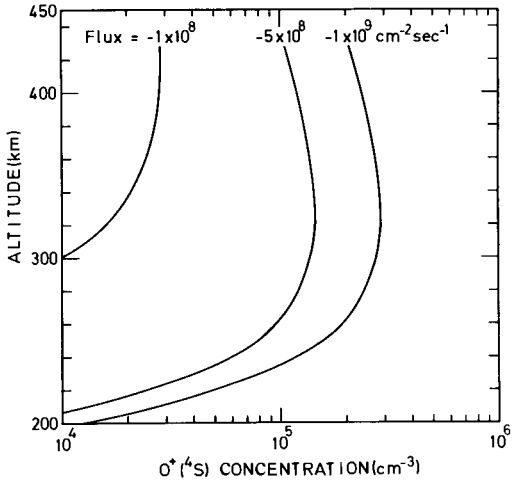


Fig. 20.10 Maintenance of the F_2-region ionization through ionization inflow for a 1000°K thermosphere. (See conditions listed for Fig. 20.4 and $I(O^+) = 0$.)

can be converted to values of E_y, v_n, u_n, or w_n using (20.22). An upward drift tends to raise the peak of the F_2 layer to a somewhat higher altitude than normal, while a downward motion has the opposite effect [23]. Since the present coordinate system is aligned in the northern hemisphere with the x axis pointing toward the north magnetic pole, neutral winds blowing

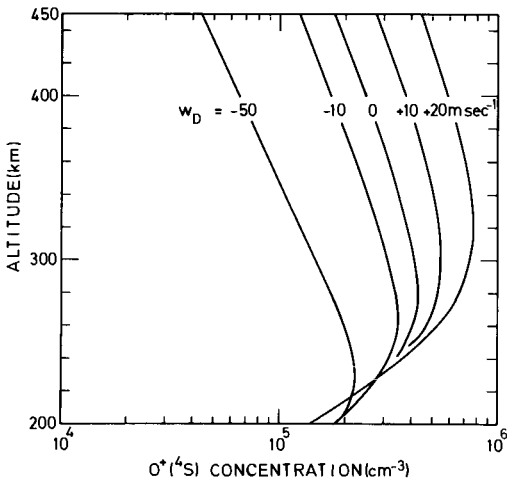


Fig. 20.11 Effects of ion drift upon the F_2 region for a sunlit 1000°K thermosphere. ($\sin^2 I = 0.75$; $T_e = 2000$°K; $T_i = T_n$.)

from north to south tend to move ionization up magnetic field lines, enhancing the F_2 layer and the height of the peak [24, 28, 32–40]. Since winds in the neutral atmosphere are established through solar ultraviolet heating [34], Joule dissipation [41, 42], and ion convection [43] at high latitudes (discussed in the next section) the global response of the F_2 region is very complex. In addition, the winds themselves are modified by the ionosphere so that a large degree of coupling is present making analysis difficult. Initial attempts to solve these problems have been based on models which ignore the dynamic effects present at high latitudes.

The effectiveness of external electric fields in altering F_2-region profiles has been studied extensively [28, 38, 44, 45]. Such fields can have their origin either in the magnetosphere or in the dynamo region of the ionosphere [46]. Although fields as large as 10^{-1} V m^{-1} have been observed during magnetic storms in polar regions [47–49], the large magnetic dip angle there results primarily in a lateral drift of ionization. Within the quiet time plasmasphere electric fields are typically less than 10^{-3} V m^{-1} and the plasma transport effects are thought to be rather small except during geomagnetic disturbances [46] and except for the narrow belt about the geomagnetic equator (equatorial electrojet).

20.3.3 Global Dynamics

Using the theoretical ideas discussed in the last sections it is possible to isolate the different processes affecting the distribution of ionization in the F_2 region. However, the analysis of global electron density data has shown that the F_2-region ionosphere is extremely variable in its maximum density and peak altitude [50]. An example of this is shown in *Fig. 20.12* giving the predicted F_2-layer critical frequencies for the Western Zone, in December 1954. Large gradients in ionization are clearly evident corresponding to sunrise and sunset. In addition, other less explicable features are present such as the increase in density at night in the southern hemisphere ($-60°$ latitude) [50].

Of particular interest is the latitudinal variation of the regions of greatest electron density. An idealized sketch of this behavior, given previously by King [50], is shown in *Fig. 20.13*. Depending upon its relation to the geomagnetic equator, a given station will observe a complicated variation in the F_2-layer peak density with there being one or more relative maxima occurring during the course of a day, as shown in *Fig. 20.14*, also adopted from King [50].

Attempts to reproduce the diurnal variation of the F_2 layer [32–40] have

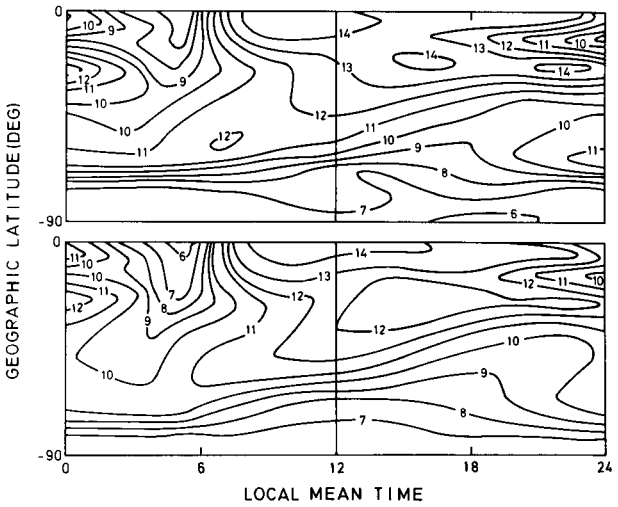


Fig. 20.12 Predicted values of the F_2-region critical frequency (MHz) for the southern hemisphere for December 1958 (upper) and January 1959 (lower) [20].

shown that the observed complicated patterns can be explained only through plasma drifts having vertical velocities in the range of ± 50 m sec^{-1}. The principal source for these drifts appears to be winds in the upper F region [32], although during periods of magnetic disturbance transverse electric fields could be responsible for substantial drift velocities [44, 45].

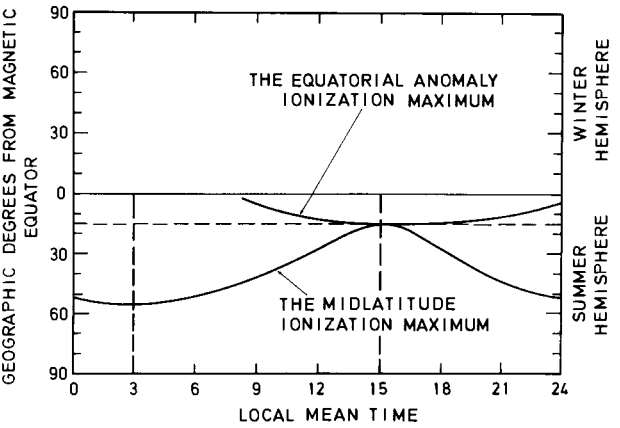


Fig. 20.13 Schematic form of the geographic variations in the location of maximum values in the peak F_2-region density as a function of local time. The equatorial maximum is associated with the electrojet formation, while the midlatitude ionization maximum arises from the combination of neutral winds and electric fields [50].

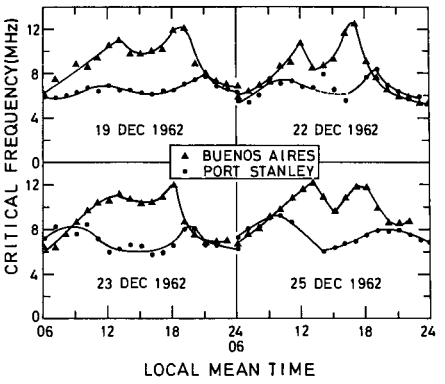


Fig. 20.14 Diurnal variations of F_2-region critical frequency at Buenos Aires (23°S geomagnetic) and Port Stanley (40°S geomagnetic) during the summer. The double peak is consistent with the sketch of Fig. 20.14 [50].

Following the discussion of Chapter 14, neutral winds are produced in the F region in response to pressure gradients associated with solar EUV heating as well as the momentum transferred by ion drag over the polar caps. The winds are affected by Coriolis forces, viscosity, inertia, and momentum transfer to the ambient ionosphere. Calculations based on global models of these effects [32–40] give wind patterns (relative to the rotating earth) which are directed away from the regions of greatest pressure (about 1400 LT in the vicinity of the equator) toward the regions of least pressure (about 0200–0300 LT). The results of one computation are shown in *Fig. 20.15*, taken from Kohl and King [33]. Referring to Eq. (20.4), it follows that the poleward component of the neutral wind will tend to drive

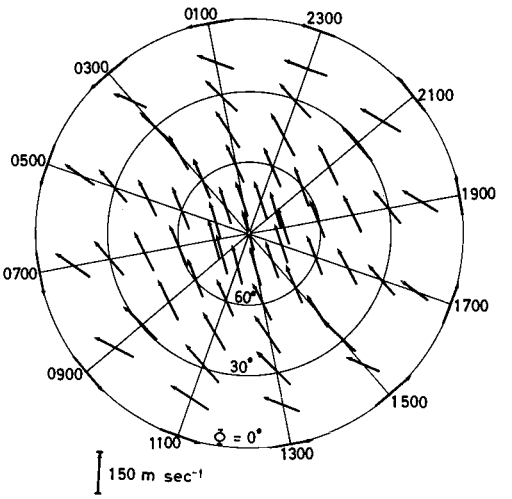


Fig. 20.15 Computed global thermospheric winds at 300 km [33].

the F_2 layer downward with consequent diminution of the peak density while equatorward flow will give an upward motion, thereby enhancing the peak density.

Even though the effects of neutral winds can explain the gross features of daily F_2-region changes, accurate computations are extremely difficult since the neutral winds and F_2-region plasma form a strongly coupled system having a response time on the order of several days. Although the mid-latitude ionosphere is relatively stationary with respect to the earth's surface, at high latitudes large transverse electric fields can drive plasma through the neutral atmosphere so that a substantial amount of momentum can be transferred to the neutral gas [41, 43]. Since the electric fields in the polar caps undergo continual fluctuation, the global neutral winds may never reach a steady state but always remain in dynamic motion. This, in turn, would affect the diurnal variation of the F-region electron density over large areas of the earth.

Studies have been made of the electric fields which would be necessary to explain diurnal variations of F_2-region electron density [44, 45]. Although electric fields can be derived to reproduce these variations in adequate detail, the magnitude of the fields ($5\ \text{mV m}^{-1}$) appears to be excessively large compared with experiment [47–49] and the predictions of the dynamo theory so that the role of electric fields in governance of the F_2 region is still an open question.

Other regular and anomalous features of the F region can be identified such as the equatorial fountain, the seasonal anomaly, maintenance of the nighttime ionosphere, and so forth. Complete descriptions of these phenomena can be found elsewhere (for example, King [50]).

REFERENCES

1. H. Rishbeth and D. W. Barron, *J. Atmos. Terr. Phys.* **18**, 234 (1960).
2. J. P. Dougherty, *J. Atmos. Terr. Phys.* **20**, 167 (1961).
3. J. E. C. Gliddon and P. C. Kendall, *J. Atmos. Terr. Phys.* **24**, 1073 (1962).
4. S. A. Bowhill, *J. Atmos. Terr. Phys.* **24**, 503 (1962).
5. W. B. Hanson and T. N. L. Patterson, *Planet. Space Sci.* **12**, 979 (1964).
6. J. E. C. Gliddon and P. C. Kendall, *J. Atmos. Terr. Phys.* **26**, 721 (1964).
7. H. Rishbeth, *J. Atmos. Terr. Phys.* **26**, 657 (1964).
8. J. E. C. Gliddon, *Planet. Space Sci.* **13**, 959 (1965).
9. T. Shimazaki, *J. Atmos. Terr. Phys.* **27**, 593 (1965).
10. T. Yonezawa, *Space. Sci. Rev.* **5**, 3 (1966).
11. H. Rishbeth, *J. Atmos. Terr. Phys.* **29**, 225 (1967).
12. H. Rishbeth, *Rev. Geophys.* **6**, 33 (1968).

13. G. Vasseur, *J. Atmos. Terr. Phys.* **34**, 397 (1969).
14. A. Dalgarno and M. B. McElroy, *Planet. Space Sci.* **13**, 947 (1965).
15. A. Dalgarno and M. B. McElroy, *Planet. Space Sci.* **14**, 1321 (1966).
16. A. Omholt, *J. Atmos. Terr. Phys.* **10**, 320 (1957).
17. B. R. Turner, J. A. Rutherford, and D. M. J. Compton, *J. Chem. Phys.* **48**, 1602 (1968).
18. L. Wallace and M. B. McElroy, *Planet. Space Sci.* **14**, 677 (1966).
19. M. J. Seaton and D. E. Osterbrock, *Astrophys. J.* **125**, 66 (1957).
20. A. Dalgarno, R. J. W. Henry, and A. L. Stewart, *Planet. Space Sci.* **12**, 235 (1964).
21. R. J. W. Henry, *Planet. Space Sci.* **15**, 1747 (1967).
22. E. J. McGuire, *Phys. Rev.* **175**, 20 (1968).
23. T. Yonezawa, *Ann. Géophys.* **26**, 581 (1970).
24. P. Stubbe, *J. Atmos. Terr. Phys.* **32**, 865 (1970).
25. H. Rishbeth and D. W. Barron, *J. Atmos. Terr. Phys.* **18**, 234 (1960).
26. P. M. Banks and T. E. Holzer, *J. Geophys. Res.* **74**, 6317 (1969).
27. P. M. Banks, Dynamical behavior of the polar topside ionosphere, in *Magnetosphere-Ionosphere Interactions* (K. Folkestadt, ed.) p. 87. Univ. of Oslo Press, Oslo, 1972.
28. W. B. Hanson and T. N. L. Patterson, *Planet. Space Sci.* **12**, 979 (1964).
29. J. E. Geisler and S. A. Bowhill, *J. Atmos. Terr. Phys.* **27**, 1119 (1965).
30. P. M. Banks, A. F. Nagy, and W. I. Axford, *Planet. Space Sci.* **19**, 1053 (1971).
31. C. Park, *J. Geophys. Res.* **75**, 4249 (1970).
32. J. W. King and H. Kohl, *Nature (London)* **206**, 699 (1965).
33. H. Kohl and J. W. King, *J. Atmos. Terr. Phys.* **29**, 1045 (1967).
34. J. E. Geisler, *J. Atmos. Terr. Phys.* **29**, 1469 (1967).
35. H. Rishbeth, *J. Atmos. Terr. Phys.* **29**, 225 (1967).
36. H. Rishbeth, *J. Atmos. Terr. Phys.* **30**, 63 (1968).
37. G. J. Bailey, R. J. Moffett, and H. Rishbeth, *J. Atmos. Terr. Phys.* **31**, 253 (1969).
38. P. Stubbe, *J. Atmos. Terr. Phys.* **30**, 243 (1968).
39. H. Kohl, J. W. King, and D. Eccles, *J. Atmos. Terr. Phys.* **30**, 1733 (1968).
40. D. Eccles, J. W. King, P. Rothwell, *J. Atmos. Terr. Phys.* **33**, 371 (1971).
41. K. D. Cole, *Planet. Space Sci.* **19**, 59 (1971); **20**, 2205 (1972).
42. P. M. Banks, *Space Res.* **12**, 1051 (1972).
43. J. A. Fedder and P. M. Banks, *J. Geophys. Res.* **77**, 2328 (1972).
44. E. N. Bramley, *J. Atmos. Terr. Phys.* **31**, 1223 (1969).
45. P. Stubbe and S. Chandra, *J. Atmos. Terr. Phys.* **32**, 1909 (1970).
46. S. Matsushita, *Radio Sci.* **6**, 279 (1971).
47. D. P. Cauffman and D. A. Gurnett, *J. Geophys. Res.* **76**, 6014 (1971).
48. N. C. Maynard, Electric fields in the ionosphere and magnetosphere, in *Magnetosphere-Ionosphere Interactions* (K. Folkestadt, ed.) p. 155. Univ. of Oslo Press, Oslo, 1972.
49. L. A. Frank and D. A. Gurnett, *J. Geophys. Res.* **76**, 6829 (1971).
50. J. W. King, in *Annals of the IQSY*, Volume 5, *Solar-Terrestrial Physics: Terrestrial Aspects*, p. 131. MIT Press, Cambridge, Massachusetts, 1969.

CHAPTER 21

Physical Processes in the Topside Ionosphere

21.1 Introduction

At progressively greater distances from the earth the equations governing the distribution of ions under the effect of gravity predict that the mean ionic mass should continually decrease, with the particles of smallest mass being predominant in the furthest regions. Thus, when early measurements [1] of radio whistlers indicated the presence of an envelope of substantial electron densities surrounding the earth to distances of many earth radii, it was clear that hydrogen ions should be involved. Although the hydrogen ions were at first thought to have a solar origin, it was later shown through theoretical analysis [2, 3] that these ions are a direct result of ion–neutral reactions taking place within the F_2 region.

The presence of helium ions in the topside ionosphere was suggested [4, 5] in 1961 as a consequence of the discovery that neutral helium is an important constituent of the upper atmosphere. Experimental observations of helium ions were soon reported from rocket and satellite data [6–10] and it was generally thought that the ionosphere above the peak of the F_2 layer was a ternary mixture of successively O^+, He^+, and H^+ ions residing largely in diffusive equilibrium [11]. While early measurements indicated He^+ was plentiful in the topside ionosphere, more recent experiments [12–26] have shown that He^+ is generally a minor concentration ion except during active portions of the solar cycle when atomic hydrogen densities are very low.

Because the neutral atmosphere is very thin in the topside ionosphere,

ion–neutral particle collisions are relatively unimportant in the ion momentum equations and, in the absence of perpendicular electric fields, plasma can flow only along magnetic field lines. Even in the absence of ion–neutral collisions, however, the topside ions remain strongly coupled through the action of a charge separation electric field and ion–ion collisions. These forces are of fundamental importance to the behavior of the topside ionosphere and the establishment of ion flux boundary conditions for the F_2 layer.

21.2 Hydrogen Ions

The key reaction of importance to the production hydrogen ions in the F_2 region and above is accidentally resonant charge exchange [2, 27]:

$$O^+(^4S) + H(^2S) \rightleftharpoons O(^3P_J) + H^+ + \Delta\varepsilon. \tag{9.81}$$

Since the energy defects of (9.81) are small relative to thermospheric energies ($kT \sim 0.05$ to 0.1 eV) the charge exchange proceeds rapidly in both directions.

For given reactant concentrations the continuity equation governing the H^+ number density is

$$(\partial n_i/\partial t) + \nabla \cdot (n_i \mathbf{C}_i) = p_i - l_i \tag{21.1}$$

where

$$p_i = I(\mathrm{H})n(\mathrm{H}) + \bar{Q}_E n(\mathrm{H})n(O^+)(8kT_n/\pi m(\mathrm{H}))^{1/2} \tag{21.2}$$

$$l_i = \tfrac{8}{9}\bar{Q}_E n(\mathrm{O})n(H^+)(8kT_i/\pi m(\mathrm{H}))^{1/2}. \tag{21.3}$$

Here $I(\mathrm{H})n(\mathrm{H})$ represents the direct photoionization of atomic hydrogen, $\bar{Q}_E = (1.5 \pm 0.5) \times 10^{-15}$ cm^2 is the charge exchange cross section for (O^+, H) collisions, T_n and T_i are the neutral and ion gas temperatures, and $m(\mathrm{H})$ is the mass of the hydrogen atom. The direct recombination of H^+ and electrons is ignored because of its very slow rate compared with charge exchange and diffusion.

The H^+ density for chemical equilibrium ($\mathbf{C}_i = 0$; $\partial n_i/\partial t = 0$) follows from (21.2) and (21.3) as

$$\frac{n(H^+)}{n(O^+)} = \frac{9}{8}\frac{n(\mathrm{H})}{n(\mathrm{O})}\left(\frac{T_n}{T_i}\right)^{1/2}\left[1 + \frac{I(\mathrm{H})}{\bar{Q}_E n(O^+)(8kT_n/\pi m(\mathrm{H}))^{1/2}}\right]. \tag{21.4}$$

Using rates for photoionization and charge exchange given in Chapters 7

and 9, it is found that photoionization is important only when the oxygen ion density is less than about 10^2–10^3 cm^{-3}; i.e., values far less than are normally observed in the ionospheric F_2 region. As a consequence, for most conditions (21.4) can be reduced to

$$\frac{n(H^+)}{n(O^+)} = \frac{9}{8}\frac{n(H)}{n(O)}\left(\frac{T_n}{T_i}\right)^{1/2} \tag{21.5}$$

so that the hydrogen to oxygen ion density ratio increases rapidly with altitude owing to the different scale heights of atomic hydrogen and oxygen.

To show this explicitly consider hydrostatic distributions for the two neutral gases with normalization to the reference altitude r_a. It follows from (21.5) that the chemical equilibrium density ratio is

$$\frac{n(H^+)}{n(O^+)} = \frac{9}{8}\left(\frac{T_n}{T_i}\right)^{1/2}\frac{n_a(H)}{n_a(O)}\exp\left[\frac{15}{16}\frac{r_a}{h(O)}\left(1-\frac{r_a}{r}\right)\right] \tag{21.6}$$

where $h(O) = kT_n/m(O)g_a$ is the atomic oxygen scale height with g_a the acceleration of gravity at the radius r_a. From this result it is clear that even without ion diffusion effects, hydrogen ions would eventually become the dominant ion species at a sufficiently large distance from the earth.

As a guide to expected ionospheric conditions, H^+/O^+ concentration ratios characteristic of different altitudes and thermospheric temperatures are listed in *Table 21.1* for $T_n = T_i$.

TABLE 21.1

HYDROGEN TO OXYGEN ION DENSITY RATIOS: CHEMICAL EQUILIBRIUM

Altitude (km)	Thermospheric temperatures					
	750°K	1000°K	1250°K	1500°K	1750°K	2000°K
200	4.6 (−4)[a]	6.9 (−5)	3.3 (−5)	2.8 (−5)	2.8 (−5)	2.9 (−5)
250	1.4 (−3)	1.4 (−4)	4.5 (−5)	3.1 (−5)	2.8 (−5)	2.8 (−5)
300	4.2 (−3)	3.0 (−4)	7.0 (−5)	3.8 (−5)	3.0 (−5)	2.8 (−5)
350	1.2 (−3)	6.7 (−4)	1.2 (−4)	5.1 (−5)	3.4 (−5)	2.9 (−5)
400	3.5 (−2)	1.4 (−3)	2.1 (−4)	7.3 (−5)	4.1 (−5)	3.2 (−5)
450	8.8 (−2)	3.1 (−3)	3.7 (−4)	1.1 (−4)	5.3 (−5)	3.7 (−5)
500	2.7 (−1)	6.8 (−3)	6.8 (−4)	1.7 (−4)	7.2 (−5)	4.4 (−5)

[a] 4.6 (−4) = 4.6×10^{-4}.

The steady state solution for the chemical equilibrium hydrogen ion density does not depend upon the charge exchange rate. At one time theoretical estimates [28, 29] indicated a small cross section ($\sim 10^{-17}$ cm^2) for $\bar{Q}_E$, thereby enhancing the importance of alternate processes of hydrogen ion production, such as photoionization or accretion from the solar wind. Recent laboratory evidence, however, gives a much larger cross section at thermal energies ($Q_E \sim 1.5 \times 10^{-15}$ cm^{-2}), thereby assuring that charge exchange is the dominant source of protons in the upper ionosphere.

From Eq. (21.3) the time constant for changes in $n(H^+)$ when other parameters are fixed is

$$\tau(H^+) = [\tfrac{8}{9} n(O) \bar{Q}_E (8kT_i/\pi m(H))^{1/2}]^{-1}. \tag{21.7}$$

Values of $\tau(H^+)$ given in *Table 21.2* indicate that chemical equilibrium is reached fairly rapidly above the F_2 region. Eventually, however, ionic

TABLE 21.2

TIME CONSTANTS[a] FOR O^+–H CHARGE EXCHANGE

Altitude (km)	Atmospheric model thermospheric temperatures					
	750°K	1000°K	1250°K	1500°K	1750°K	2000°K
200	2.3 (−1)[b]	2.3 (−1)	1.9 (−1)	1.6 (−1)	1.1 (−1)	8.2 (−2)
250	8.0 (−1)	6.2 (−1)	4.4 (−1)	3.5 (−1)	2.4 (−1)	1.6 (−1)
300	2.6 (0)	1.5 (0)	9.4 (−1)	6.6 (−1)	4.3 (−1)	2.8 (−1)
350	8.1 (0)	3.6 (0)	1.9 (0)	1.2 (0)	7.3 (−1)	4.5 (−1)
400	2.5 (1)	8.3 (0)	3.7 (0)	2.2 (0)	1.2 (0)	7.1 (−1)
450	7.6 (1)	1.9 (1)	7.3 (0)	3.8 (0)	1.9 (0)	1.1 (0)
500	2.2 (2)	4.3 (1)	1.4 (1)	6.5 (0)	3.1 (0)	1.7 (0)

[a] Values are in sec.
[b] 2.3 (−1) = 2.3 × 10^{-1}.

diffusion becomes important and controls the distribution of ionization. As shown later, however, a coincidence of nature intervenes at this point so that for regions where $n(O^+) \gg n(H^+)$, the chemical and diffusive equilibrium solutions for the hydrogen ion density are nearly the same [30, 31]. As a consequence, the transition from chemical to diffusive equilibrium does not greatly affect H^+ distributions and significant departures from the

theoretical density ratio given by (21.5) for times longer than $\tau(H^+)$ must be attributed to deviations from diffusive equilibrium arising from ion transport.

21.3 Helium Ions

Helium ions are produced in the upper ionosphere through photoionization by solar radiation with $\lambda < 504$ Å:

$$He(^1S) + h\nu\ (\lambda < 504\ \text{Å}) \rightarrow He^+(^2S) + e. \tag{21.8}$$

The laboratory measurements summarized in Chapter 10 indicate that the principal loss processes involve charge transfer [(10.148) and (10.150)] and dissociative charge transfer [(10.147) and (10.149)] with O_2 and N_2.

The continuity equation for He^+ follows as

$$\partial n_i/\partial t + \nabla \cdot (n_i \mathbf{C}_i) = I(\text{He})n(\text{He}) - n(\text{He}^+)[(\gamma_{17} + \gamma_{17}^*)n(O_2) + (\gamma_{18} + \gamma_{18}^*)n(N_2)] \tag{21.9}$$

where $I(\text{He})$ is the helium photoionization rate.

For chemical equilibrium with no bulk transport, the helium ion density is

$$n(\text{He}^+) = \frac{I(\text{He})n(\text{He})}{(\gamma_{17}^* + \gamma_{17})n(O_2) + (\gamma_{18}^* + \gamma_{18})n(N_2)} \tag{21.10}$$

indicating that He^+, like H^+, increases in density with altitude for chemical equilibrium. At sufficiently high altitudes the chemical processes are too slow to compete with diffusion, however, and ion diffusion processes eventually determine the density distribution. As indicated in Chapter 10, the rate coefficients γ_{17}^*, γ_{17}, γ_{18}^*, and γ_{18} are large, being at least 10^{-9} cm^3 sec^{-1}. Since $n(N_2) \gg n(O_2)$ above 300 km, the principal channel of He^+ loss is through molecular nitrogen.

The rapidity at which He^+ loss takes place in the upper ionosphere represented a difficult problem several years ago. Taking account of the helium photoionization rate and the indicated He^+ loss processes, it was found that computed He^+ densities were substantially greater than the observed values. It was then suggested [30] that this dilemma resulted from the application of laboratory reaction rates to ionospheric conditions. Laboratory measurements, however, indicate that little change occurs in He^+ reaction rates due to internal excitation of the molecular species. Thus, the trend toward

lower measured He^+ densities could indicate the presence of experimental errors in the earlier observations. Recent data obtained by satellite mass spectrometers give good agreement with the theoretical He^+ densities [21].

The time constant associated with (21.9) for a constant production of He^+ and no ion transport follows directly as

$$\tau(He^+) = \frac{1}{(\gamma_{17}^* + \gamma_{17})n(O_2) + (\gamma_{18}^* + \gamma_{18})n(N_2)} \tag{21.11}$$

or, numerically with $\gamma \simeq 10^{-9}$ cm^3 sec^{-1},

$$\tau(He^+) \simeq \frac{10^9}{n(O_2) + n(N_2)} \text{ sec.} \tag{21.12}$$

Since $n(O) \gg n(O_2) + n(N_2)$ above 300 km, $\tau(He^+)$ is substantially greater than $\tau(H^+)$ so that at a given altitude diffusion effects are more important for He^+ than H^+. Furthermore, the He^+ density profile does not increase as rapidly with altitude for diffusive equilibrium (as a minor constituent in O^+) as it does for chemical equilibrium. [There is a factor of six difference in effective scale heights: Compare (21.10) and (21.25).]

21.4 Ion Density Distributions

The discussion of the last two sections has been directed to the chemical processes affecting the production and loss of H^+ and He^+. Above 500 to 700 km, however, ionic reactions become unimportant relative to ion diffusion and convection and the ion distributions are controlled by mechanical forces such as electric and magnetic fields, gravity, centrifugal force, and ion partial pressure gradients. Nevertheless, because the ionosphere at lower altitudes is a source (and sink) for the topside plasma the behavior of the F_2-region ionosphere and the topside ionosphere are strongly coupled.

Electric fields of magnetospheric origin are of particular importance to the distribution of thermal plasma in the topside ionosphere. These fields result in plasma convective motions perpendicular to the geomagnetic field and, in certain circumstances, can lead to the permanent loss of ionospheric plasma from the topside ionosphere [32–35].

Referring to *Fig. 21.1* we can visualize three basic diffusive states for plasma in the topside ionosphere. The first state, diffusive equilibrium, corresponds to no net transport of ionization along the tubes of magnetic force. Although such a state is reached only at rare intervals, it provides a

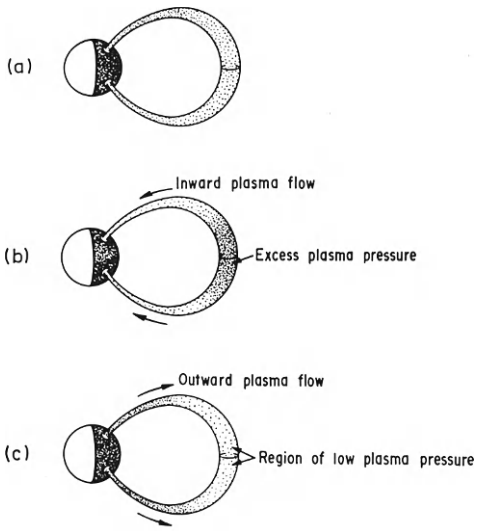


Fig. 21.1 Illustrating the three basic states of motion for the topside ionosphere: diffusive equilibrium, plasma inflow, and plasma outflow. (a) Diffusive equilibrium: static distribution of plasma with small inward flow at low altitudes to accommodate ion losses in the F_2 region. (b) Inward diffusive flow: plasma moves inward and is lost in the F_2 region. Speed of flow may become supersonic if excess plasma pressure is sufficiently large. (c) Outward diffusive flow: plasma moves outward to equalize plasma pressure. Speed of flow may become supersonic if pressure deficit is large.

useful theoretical basis for understanding the consequences of inward or outward flow, the remaining two states [35, 36].

Inward diffusive flow results when there is an excess of plasma pressure at high altitudes somewhere along a magnetic field tube. Both H^+ and He^+ can be driven inwards to regions where ion-neutral reactions convert these ions into other ions such as O^+ and N_2^+. As a result, there is a net downward transport of the light ions from the topside which tends to enhance the ion density of the F_2 region. The inward flow can be either subsonic or supersonic, depending upon the specific pressure conditions. If the flow is supersonic inwards a shock front with its associated heating and an ion density jump must eventually occur at some altitude. Otherwise, if the flow is subsonic the gravitational potential energy of the flow is gradually released through both compressional ion heating and collisions with particles of the neutral atmosphere. As shown later, the density profiles characteristic of subsonic inward diffusive flow are virtually the same as those for diffusive equilibrium, even though the net inward transport of ions may be large.

Outward diffusive flow of light ions results from a deficit of plasma

pressure at some point along a magnetic field tube. In this situation plasma pressure gradients and small gravitationally induced electric fields parallel to the magnetic field lines drive the light ions outward. Such a flow is always subsonic below 800 to 1000 km, but can, in proper circumstances, become supersonic at higher altitudes. In the absence of magnetospheric electric fields other than that due to corotation, the upward flowing plasma must eventually fill the field tube along which it moves towards diffusive equilibrium. Such a behavior is typical of the recovery of the topside ionosphere following magnetic storms [35].

At high latitudes it is known that a large scale magnetospheric field exists which periodically drives thermal plasma out of the magnetosphere [37]. In this situation the plasma pressure remains low along the magnetic field lines and a continual upward flow of plasma (the polar wind) results.

The dynamical properties of the topside ionosphere are complex owing to the large time constants associated with ion flow parameters and the frequent occurrence of plasma disturbances. As a result, only the topside ionosphere at low latitudes ever has an opportunity to reach the state of diffusion equilibrium. At mid and high latitudes there appears to be continual disequilibrium with prolonged periods of plasma outflow or inflow taking place.

21.5 Basic Equations

The ion density profiles in the topside ionosphere can be determined from the equations of continuity and momentum for each ion species, neglecting for the moment the problem of the ionospheric temperatures. For the jth type ion gas, the one-dimensional momentum equation parallel to the lines of geomagnetic force is

$$\frac{\partial w_j}{\partial t} + w_j \frac{\partial w_j}{\partial s} + \frac{1}{n_j{}^+ m_j} \frac{\partial p_j}{\partial s} + g_{\parallel} - \frac{Z_j e E_{\parallel}}{m_j} = -\sum_k \nu_{jk}(w_j - w_k) \quad (21.13)$$

where $p_j = n_j k T_j$, $Z_j e$ is the ion atomic charge, $g_{\parallel}$ is the acceleration of gravity parallel to the magnetic field (positive inwards), w_j is the ion bulk transport velocity parallel to the magnetic field direction, w_k is the parallel component of velocity of the other ion and neutral species, ν_{jk} is the ion collision frequency between the jth and kth species (see Chapter 19), and s is a coordinate along **B**. The collision term includes the effects of ion–ion and ion–neutral collisions in retarding (or enhancing) the jth ion gas bulk speed. Equation (21.13) ignores the effect of ion production in the frame of the neutral gas. The effect of centrifugal force has not been included.

The equation of continuity for the jth species is

$$\frac{\partial n_j^+}{\partial t} + \frac{1}{A}\frac{\partial (n_j^+ w_j A)}{\partial s} = q_j - l_j \tag{21.14}$$

where l is the ion loss rate. The quantity A is the area of the magnetic field flux tube at the point s. It arises in the transition from the gradient operator of Eq. (21.1) to the magnetic field coordinate system used in (21.14).

To a high degree of approximation the electron momentum equation can be expressed as

$$\frac{1}{n_e}\frac{\partial p_e}{\partial s} + eE_{\parallel} = 0; \tag{21.15}$$

that is, in the topside ionosphere gravitation, inertial, and frictional effects for the electron gas are unimportant in comparison with the parallel electric field induced through charge separation. Substitution of (21.15) into (21.13) gives the equations of motion for a multiconstituent plasma:

$$\frac{\partial w_j}{\partial t} + w_j\frac{\partial w_j}{\partial s} + \frac{1}{n_j^+ m_j}\frac{\partial p_j}{\partial s} + g_{\parallel} + \frac{Z_j e}{n_e m_j}\frac{\partial p_e}{\partial s} = -\sum_k \nu_{jk}(w_j - w_k) \tag{21.16}$$

subject to the constraint of local charge neutrality

$$n_e = \sum_j Z_j n_j^+. \tag{21.17}$$

Owing to the nonlinear nature of (21.16) and the complications brought about through frictional coupling and the differing rates of ion production and loss, it is difficult to solve Eqs. (21.14) and (21.16) in an analytic fashion to obtain the various flow velocities and densities for arbitrary conditions. Consequently, in the following three sections approximations to the actual flow conditions are derived and discussed. These include diffusive equilibrium, low speed flow, and high speed flow.

21.6 Diffusive Equilibrium for a Multicomponent Plasma

The mathematical difficulties associated with solutions for the ion density distributions can be overcome for the particular case of diffusive equilibrium between ion species. By assuming that all $w_j = 0$, explicit results can be obtained for the ion densities giving the equilibrium density distributions of a multicomponent ionosphere [38, 39].

With $w_j = 0$ and ignoring centrifugal force, Eq. (21.13) can be written for each ion for steady state conditions as

$$\frac{1}{n_j^+}\frac{\partial p_j}{\partial s} + m_j g_{\parallel} - Z_j e E_{\parallel} = 0, \tag{21.18}$$

while for electrons

$$\frac{1}{n_e}\frac{\partial p_e}{\partial s} + e E_{\parallel} = 0. \tag{21.19}$$

When a multiconstituent plasma is placed in a gravitational field, a parallel electric field is established which arranges the ions in layers with the lightest ions in the regions of weakest gravity. Using (21.16)–(21.19), this parallel electric field can be derived for diffusive equilibrium as

$$e E_{\parallel} = \frac{g_{\parallel} \sum (Z_j n_j^+ m_j / n_e) + k T_i [\partial / \partial s (\ln T_i / T_e)]}{(T_i / T_e) + \sum (Z_j^2 n_j^+ / n_e)}. \tag{21.20}$$

For the topside ionospheric regions where atomic oxygen ions are the dominant ion species [$n^+(O) \gg 16 n^+(H)$; $n^+(O) \gg 4 n^+(He)$], the vertical electric field due to charge separation is

$$e E_{\parallel} \simeq \frac{m(O^+) g_{\parallel} + k T_i [\partial / \partial s (\ln T_i / T_e)]}{1 + T_i / T_e}, \tag{21.21}$$

showing that for diffusive equilibrium the electrical force tends to dilute the effect of gravity [see Eq. (21.18)] upon the ion gases. A similar expression can be derived for H^+ which involves $m(H^+)$ rather than $m(O^+)$ when H^+ is the dominant constituent.

Using (21.20), $e E_{\parallel}$ can be eliminated from the individual ion momentum equations to give the coupled equations for the electron and ion density variation as

$$\frac{1}{n_e}\frac{\partial n_e}{\partial s} = -\frac{g_{\parallel} \sum Z_j (Z_j + 1) n_j^+ \mu_j / n_e + k T_i [\partial \ln (T_i / T_e) / \partial s]}{k T_i + k T_e \sum (Z_j^2 n_j^+ / n_e)} - \frac{\partial \ln T_e}{\partial s} \tag{21.22}$$

$$\frac{1}{n_j^+}\frac{\partial n_j^+}{\partial s} = -\frac{m_j g_{\parallel}}{k T_i} + Z_j \left[\frac{T_e}{T_i}\right] \left[\frac{g_{\parallel} \sum Z_j (Z_j + 1) n_j^+ \mu_j / n_e + k T_i [\partial / \partial s (\ln T_i / T_e)]}{k T_i + k T_e \sum (Z_j^2 n_j^+ / n_e)}\right] - \frac{\partial \ln T_i}{\partial s} \tag{21.23}$$

where the effective mass of the jth ion of charge state Z_j is defined as

$$\mu_j = m_j/(Z_j + 1). \tag{21.24}$$

Examination of the ion momentum equation (21.23) shows that the first term arises from the parallel component of gravitational force while the second term represents the effect of the electric field arising from charge separation.

If the jth type ion is a minor species in a plasma dominated by singly charged k-type ions, then the altitude dependence of the minor constituent n_j^+, for diffusive equilibrium and $\partial T_i/\partial s = \partial T_e/\partial s = 0$, follows from (21.23) as

$$\frac{1}{n_j^+}\frac{\partial n_j^+}{\partial s} \simeq -\frac{m_j g_\parallel}{kT_i}\left[1 - \frac{Z_j m_k/m_j}{1 + (T_i/T_e)}\right], \tag{21.25}$$

showing that the density of n_j^+ can increase or decrease with altitude depending upon the sign of the bracketed quantity. In fact, for particular temperature and mass ratios, there is a balance between gravity and the charge separation electric field so that the density of the minor ion can be independent of altitude [40].

Returning to the general problem of the ion distributions, a further reduction of Eqs. (21.22) and (21.23) is possible when the mean effective ionic mass is introduced:

$$\mu^+ = \sum Z_j(Z_j + 1)n_j^+\mu_j / \sum Z_j(Z_j + 1)n_j^+. \tag{21.26}$$

Since, however, the principal ions of the terrestrial ionosphere are singly ionized μ^+ reduces to

$$2\mu^+ = n_j^+ m_j/n_e = m^+ \tag{21.27}$$

where m^+ is the mean ionic mass.

Using this definition for the mean ionic mass, the expressions for the electron and ion density can be rewritten as

$$\frac{1}{n_e}\frac{\partial n_e}{\partial s} = -\frac{m^+ g_\parallel}{k(T_e + T_i)} - \frac{\partial \ln(T_e + T_i)}{\partial s} \tag{21.28}$$

and

$$\frac{1}{n_j^+}\frac{\partial n_j^+}{\partial s} = -\frac{m_j g_\parallel}{kT_i} + \frac{m^+ g_\parallel}{k(T_e + T_i)}\left[\frac{T_e}{T_i}\right] - \frac{\partial \ln(T_e + T_i)}{\partial s} \tag{21.29}$$

showing more clearly the coupling between electrons and ions in terms of the mean ion mass. When $m^+ = m_i$, these equations reduce to the previous results for a plasma with a single ionic constituent.

If Eqs. (21.28) and (21.29) are integrated along the magnetic field between the limits $s' = a$ and s, the coupled equations for the electron and ion densities become

$$n_e = n_{ea} \frac{(T_e + T_i)_a}{(T_e + T_i)} \exp\left[- \int_a^s \frac{g_{\parallel} m^+(s')\, ds'}{k(T_e + T_i)} \right] \tag{21.30}$$

$$n_j^+ = n_{ja}^+ \frac{(T_e + T_i)_a}{(T_e + T_i)} \exp\left[- \int_a^s \frac{g_{\parallel} m_j\, ds'}{kT_i} + \int_a^s \frac{T_e}{T_i} \frac{m^+(s') g_{\parallel}\, ds'}{k(T_e + T_i)} \right] \tag{21.31}$$

where the altitude dependence of the mean ionic mass is noted explicitly.

The altitude variation of ion density deduced from (21.31) shows that the ordinary balance between gravity and kinetic pressure (the first integral) is offset by an electric field induced through electron–ion charge separation (the second integral). For arbitrary electron and ion temperature variations Eqs. (21.27), (21.30), and (21.31) must be solved numerically to obtain the electron and ion density distributions.

Analytic expressions for the ion and electron densities can be obtained if it is assumed that the plasma temperatures are independent of altitude. Noting that $\mathbf{g} = -\nabla\varphi$ where the magnitude of the gravitational acceleration g is $g_a r_a^2/r^2$ with g_a the acceleration of gravity at r_a, one obtains

$$\left[\frac{n_e}{n_{ea}} \right]^{(T_e + T_i)/T_i} = \frac{\sum n_{ja}^+ \exp\{-(r_a/h_j)[1 - (r_a/r)]\}}{n_{ea}} \tag{21.32}$$

$$n_j^+ = n_{ja}^+ \exp\left[- \frac{r_a}{h_j} \left(1 - \frac{r_a}{r} \right) \right] \left[\frac{n_{ea}}{n_e} \right]^{T_e/T_i} \tag{21.33}$$

where $h_j = kT_i/m_j g_a$. In this approximation a knowledge of the ion density values at the height r_a is adequate to determine the plasma density and composition at all other heights. From the form of (21.32) it is clear that in diffusive equilibrium a multicomponent plasma will arrange itself so that layers of ions are formed in inverse order of their atomic masses.

Numerous satellite and rocket measurements [20–22, 41–43] have shown that the important ions above the maximum of the F_2 layer are singly ionized H^+, O^+, and He^+ with trace concentrations of N^+, N^{2+}, D^+, O_2^+, N_2^+, O^{2+}, He^{2+}, Fe^+, and perhaps others (see *Fig. 21.2*). To illustrate the theoretical altitude dependence of H^+ and He^+ for diffusive equilibrium, profiles of ion composition have been obtained from Eqs. (21.30) and

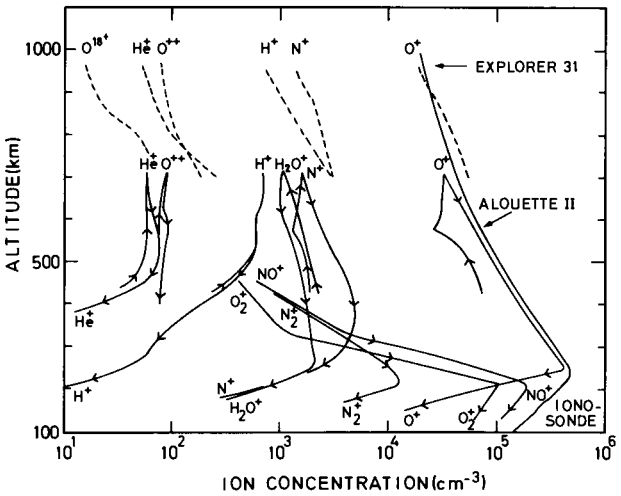


Fig. 21.2 Ion concentrations in the topside ionosphere measured by a rocket borne ion mass spectrometer launched August 15, 1966 from Wallops Island, Virginia. Also shown are Explorer 31 ion composition data and the Alouette II electron density profile [21].

(21.31) by assuming chemical equilibrium within the F_2 region using the ionic reactions discussed in Chapters 9 and 10. Because the ion density profiles are sensitive to the values of the electron and ion temperatures, a thermal model based on magnetospheric heat conduction has been adopted. Using the results of Chapter 22 the electron temperature profile corresponds to that of a constant heat flux with $T_e = 2500°K$ at 500 km. The ion temperature has been calculated from Eq. (23.2) taking into account electron heating and neutral gas cooling.

The results of these computations are shown in *Figs. 21.3–21.6* for four different models of the thermosphere. For the atmospheres having thermopause temperatures less than 1500°K, H^+ dominates above the O^+ regions of the F_2 layer. The He^+ profiles given in these figures are not accurate models of the He^+ behavior for these conditions. This is a consequence of the adoption of an ionic equilibrium He^+ density at an arbitrary boundary (500 km) with zero diffusion velocity. In fact, for steady state conditions He^+ created by photoionization at high altitudes diffuses downward to the F_2-region heights where ionic equilibrium is eventually reached.

Changes in the plasma temperature also affect the diffusive equilibrium distribution of ions. *Figure 21.7* shows the results for two values of the magnetospheric heat flux spanning the range of normal ionospheric interest.

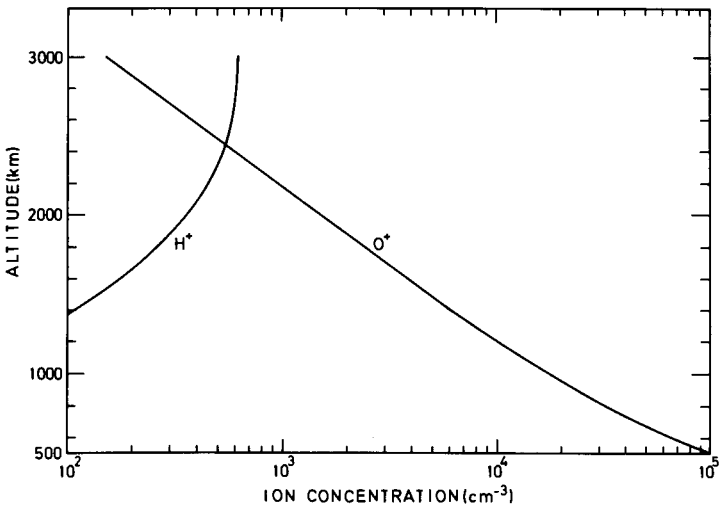


Fig. 21.3 Ion concentrations for diffusive equilibrium in a 2000°K model thermosphere with a magnetospheric electron gas heat flux Φ_e of 5×10^9 eV cm^{-2} sec^{-1}. The electron temperature is taken as 2500°K at 500 km altitude.

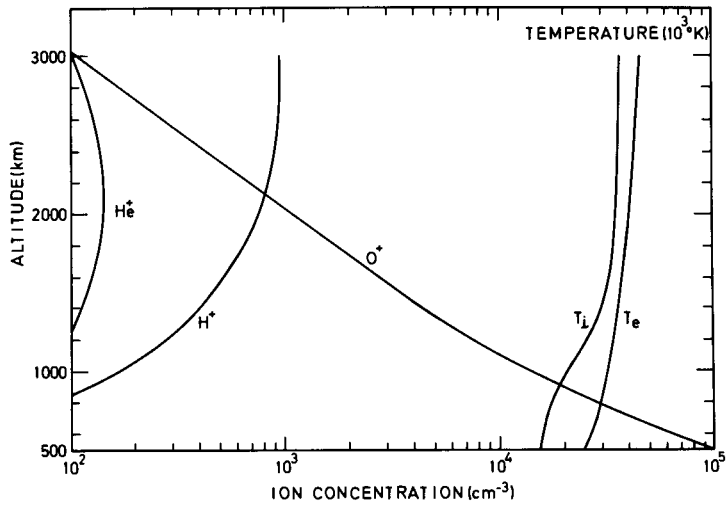


Fig. 21.4 Ion concentrations for diffusive equilibrium in a 1500°K model thermosphere with a magnetospheric electron gas heat flux Φ_e of 5×10^9 eV cm^{-2} sec^{-1}. The electron temperature is taken as 2500°K at 500 km altitude.

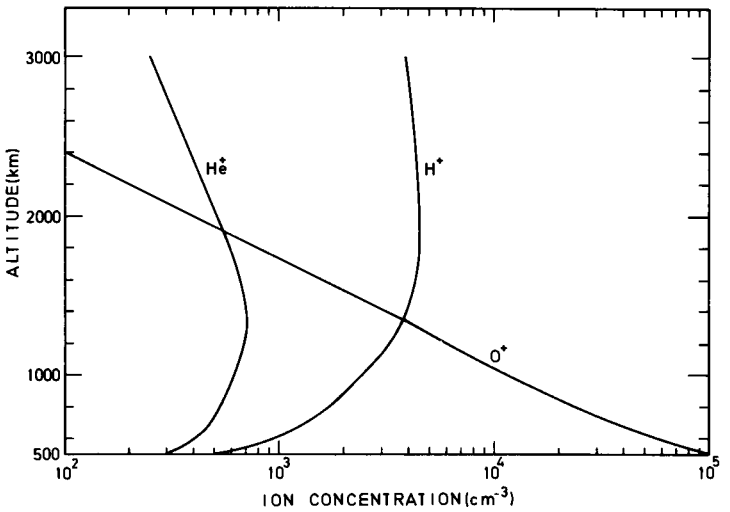


Fig. 21.5 Ion concentrations for diffusive equilibrium in a 1000°K model thermosphere with a magnetospheric electron gas heat flux Φ_e of 5×10^9 eV cm^{-2} sec^{-1}. The electron temperature is taken as 2500°K at 500 km altitude.

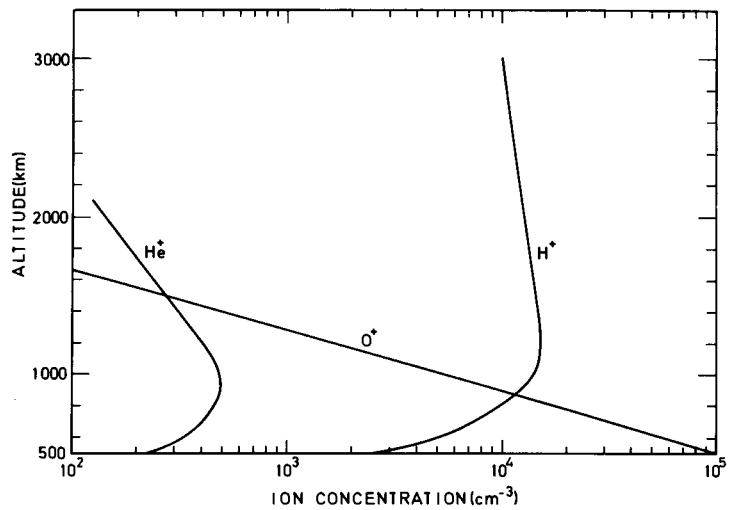


Fig. 21.6 Ion concentrations for diffusive equilibrium in a 750°K model thermosphere with a magnetospheric electron gas heat flux Φ_e of 5×10^9 eV cm^{-2} sec^{-1}. The electron temperature is taken as 2500°K at 500 km altitude.

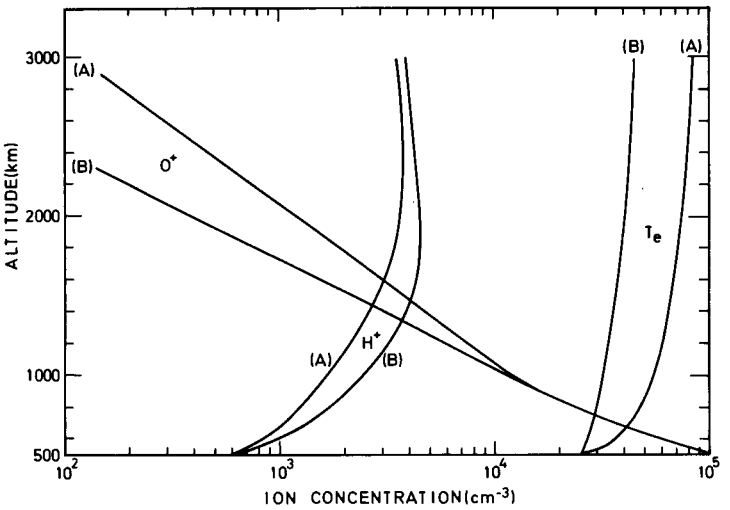


Fig. 21.7 Ion concentrations for diffusive equilibrium in a 1000°K model thermosphere for magnetospheric heat fluxes of (B) 5×10^9 and (A) 5×10^{10} eV cm^{-2} sec^{-1}.

Generally, as the heat flux and $T_e + T_i$ increase for a fixed neutral atmospheric temperature, the transition altitude from O^+ to a light ion moves to a higher altitude. However, the high altitude H^+ density remains virtually the same.

21.7 Low Speed Plasma Flow

The state of diffusive equilibrium between different ion species provides a convenient, but inaccurate, approximation to the description of the real topside ionosphere. It is known from experiments that a strong coupling exists between the ionosphere and inner magnetosphere such that dynamical processes involving continual ion transport must be important.

The problem of ion flow in the topside ionosphere differs from that of the F_2 region in that several ion species are involved with the eventual transition from O^+ to H^+. Consequently, the electric field coupling term involving the gradient of electron pressure introduces an awkward nonlinearity into the ion equations of motion [44–47].

The low speed approximation to the jth species ion momentum equation follows from (21.16) by ignoring the inertial term:

$$\frac{\partial w_j}{\partial t} + \frac{1}{n_j m_j} \frac{\partial p_j}{\partial s} + g_{\parallel} + \frac{Z_j e}{n_e m_j} \frac{\partial p_e}{\partial s} = -\sum \nu_{jk}(w_j - w_k) \quad (21.34)$$

with $n_e = \sum n_j^+$. This approximate form for the ion equation of motion is valid as long as $w_j \ll (kT_i/m_j)^{1/2}$; i.e., for the subsonic flow regime.

Analytic solutions for the complete transition from O^+ to H^+ with arbitrary low speed flow boundary conditions have not been obtained. The essential features of low speed ion flow in the regions below 1000 km can be derived, however, by noting that in these regions H^+ and He^+ are generally minor constituents which do not contribute greatly to the overall ion density nor, consequently, to the electron pressure gradient term of (21.34). In this situation the nonlinear coupling between ions is broken and analytic results for the minor ion density and velocity can be derived for steady state conditions [46].

Consider the model where a minor concentration ion species, indicated by the subscript j, diffuses through a stationary background ion gas of density n_i with $n_j \ll n_i$ and $n_i \simeq n_e$ where n_e is the electron density. The steady state equations of motion for electrons and the ions are

$$\frac{1}{n_e}\frac{dp_e}{ds} + eE_{\parallel} = 0 \tag{21.35}$$

$$\frac{1}{m_i n_i}\frac{dp_i}{ds} + g_{\parallel} - \frac{eE_{\parallel}}{m_i} = \nu_{ij} w_j \tag{21.36}$$

$$\frac{1}{m_j n_j}\frac{dp_j}{ds} + g_{\parallel} - \frac{eE_{\parallel}}{m_j} = -\nu_{ji} w_j \tag{21.37}$$

where p is the pressure, $E_{\parallel}$ is the parallel electric field, n is the concentration, $w_i = 0$, $g_{\parallel}$ represents the parallel component of the acceleration of gravity, and ν_{ji} is defined such that $n_i m_i \nu_{ij} n_i = n_j m_j \nu_{ji} n_j$. It is also assumed that the temperatures of the two ion species are identical.

Using (21.35) to eliminate $eE_{\parallel}$ from (21.37), one obtains the equation of motion for the minor concentration ion as

$$w_j = -D_{ji}\left[\frac{1}{n_j}\frac{dn_j}{ds} + \frac{m_j g_{\parallel}}{kT_i} + \frac{T_e/T_i}{n_e}\frac{dn_e}{ds} + \frac{1}{T_i}\frac{d(T_e + T_i)}{ds}\right] \tag{21.38}$$

where $D_{ji} = (kT_i/m_j)/\nu_{ji}$.

To progress further the variation of electron density with altitude must be specified. In most real cases this relates to the distribution of O^+ at high altitudes. If it is assumed that the O^+ is not greatly affected by the momentum transferred from the minor constituent (see later discussion, however), nor by chemical effects, it is possible to adopt

$$\frac{1}{m_i n_e}\frac{d(p_i + p_e)}{ds} = -g_{\parallel} \tag{21.39}$$

and

$$\frac{1}{n_e}\frac{dn_e}{ds} \simeq -\frac{m_i g_{\parallel}}{k(T_e + T_i)} - \frac{1}{T_e + T_i}\frac{d(T_e + T_i)}{ds}. \tag{21.40}$$

Defining the plasma scale height H_p through the relation

$$H_p = \frac{k(T_e + T_i)}{m_i g_{\parallel}}, \tag{21.41}$$

Eq. (21.38) can be reduced to

$$w_j = -D_{ji}\left[\frac{1}{n_j}\frac{dn_j}{ds} + \frac{1}{H_j} - \frac{T_e/T_i}{H_p} + \frac{1}{T_e + T_i}\frac{d(T_e + T_i)}{ds}\right]. \tag{21.42}$$

To determine the steady state altitude profile of the minor ion concentration, Eq. (21.42) must be incorporated into the jth species equation of continuity

$$\frac{1}{A}\frac{d(n_j w_j A)}{ds} = q_j - \beta n_j \tag{21.43}$$

where q_j is the ion production rate and β is the loss coefficient. The result is a linear, second-order differential equation of the form

$$\frac{d^2 n_j}{ds} + B(s)\frac{dn_j}{ds} + C(s)n_j = D(s) \tag{21.44}$$

similar to that obtained for the density of O^+ in the F_2 region (see Chapter 20).

Although numerical methods are required to solve (21.44) for suitable boundary conditions when production, loss, thermal gradients, and the altitude dependence of gravity are included [44–46, 48], analytic forms can be obtained when these effects can be neglected. In this case, which corresponds to minor ion diffusion at altitudes above 1000 to 1500 km, the two linearly independent solutions for n_j are obtained as

$$n_j = n_{ja} \exp\left\{\left[\frac{T_e/T_i}{H_p} - \frac{1}{H_j}\right](s - a)\right\} \tag{21.45}$$

and

$$n_j = n_{ja} \exp[-(s - a)/H_p] \tag{21.46}$$

where a represents the lower reference point.

The first solution (21.45) corresponds to a nondiffusing minor constituent which, if $1/H_j > (T_e/T_i)/H_p$, increases in density with altitude

until the condition $n_j \ll n_i$ is violated. For this solution, the upward electric field established by the dominant ion (O^+) acts to reduce the net gravitational force acting on the minor constituent ions.

The second solution given by (21.46) gives a minor ion density which decreases with altitude with the dominant ion (O^+) scale height. When this solution is substituted into the jth ion velocity equation (21.42) the velocity w_j is found to be

$$w_j = D_{ji}\left(\frac{1 + T_e/T_i}{H_p} - \frac{1}{H_j}\right) \tag{21.47}$$

so that if $H_j^{-1} < (1 + T_e/T_i)/H_p$, as is true for H^+ and He^+ in O^+, the minor constituent ion moves upward with a speed which varies with altitude as $\exp[(s - a)/H_p]$ as a consequence of the ith ion density implicit in D_{ji}.

The net jth species ion flux associated with this solution is found from (21.45) to be

$$F = n_j w_j = n_j^a D_{ji}^a\left(\frac{1 + T_e/T_i}{H_p} - \frac{1}{H_j}\right) \tag{21.48}$$

where D_{ji}^a is the ion diffusion coefficient at the altitude a. This height independent flux represents the maximum rate at which ions can flow through the frictional medium provided by the dominant species ion gas. The existence of a limit to the outward flow of minor constituent ions is entirely analogous to the flow of hydrogen atoms through the thermosphere (Chapter 14) or O^+ ion through the atomic oxygen atoms of the F_2 region (Chapter 20).

The general solution to (21.44) which describes the minor ion altitude density distribution when ion production, loss, and other quantities are included is of the form

$$n_j(s) = Af(s) + Bg(s). \tag{21.49}$$

The first term, $f(s)$, represents the distribution appropriate to diffusive equilibrium while the second corresponds to the flowing solution described in the preceding paragraphs.

For the particular problem of H^+ moving through O^+, an analytic expression [46] has been obtained for the limiting flux for thermal equilibrium neglecting the altitude variation of gravity. The result is

$$F = 3.1 \times 10^{-3}[n_0\,(O^+)^{5/8}/n_0(O)^{3/8}]n_0(H)T^{3/2} \quad \text{cm}^{-2}\,\text{sec}^{-1} \tag{21.50}$$

where the neutral gas and O^+ densities are evaluated at the altitude $z = z_0$. Note that the combination of densities in (21.50) is almost independent of

altitude. Typical limiting fluxes for the different model thermospheres are listed in *Table 21.3*. Since (21.50) is restricted to thermal equilibrium it underestimates the limiting flux; numerical computations based on more realistic conditions give somewhat larger fluxes.

TABLE 21.3

H^+ LIMITING FLUXES[a]

T_n (°K)	n(O) (cm^{-3})	n(H) (cm^{-3})	$n(O^+)$ (cm^{-3})	Flux ($cm^{-2}\ sec^{-1}$)
750	4.3×10^5	7.7×10^6	5×10^4	3.2×10^8
			1×10^5	4.9×10^8
			2×10^5	7.5×10^8
			5×10^5	1.4×10^9
			1×10^6	2.0×10^9
1000	4.4×10^6	1.2×10^5	5×10^4	3.2×10^8
			1×10^5	5.0×10^8
			2×10^5	7.5×10^8
			5×10^5	1.4×10^9
			1×10^6	2.1×10^9
1250	1.7×10^7	3.3×10^4	5×10^4	7.4×10^6
			1×10^5	1.1×10^7
			2×10^5	1.7×10^7
			5×10^5	3.1×10^7
			1×10^6	4.7×10^7
1500	3.6×10^7	1.4×10^4	5×10^4	3.2×10^6
			1×10^5	5.0×10^6
			2×10^5	7.5×10^6
			5×10^5	1.4×10^7
			1×10^6	2.1×10^7

[a] Densities evaluated at 600 km.

For atmospheric models having thermospheric temperatures less than 1000°K the limiting flux of H^+ is $2\text{–}4 \times 10^8\ cm^{-2}\ sec^{-1}$. A similar analysis for He^+ gives a limiting flux $2\text{–}3 \times 10^6\ cm^{-2}\ sec^{-1}$; the difference between the H^+ and He^+ fluxes is related to the different modes of ionization production and loss. Since He^+ undergoes a rapid ionic reaction with N_2,

its density at high altitudes is small in comparison with H^+ giving, by (21.48), a relatively low limiting flux.

The limiting flux for H^+ is directly proportional to the atomic hydrogen density. Thus, the maximum outward H^+ flux must change during the solar cycle so that the refilling of the plasmasphere following magnetic storms or in the dawn period following normal nighttime losses may change by a factor of 10 or more. This behavior is reenforced by the tendency for $n(O)$ to increase as $n(H)$ decreases [see Eq. (21.50)].

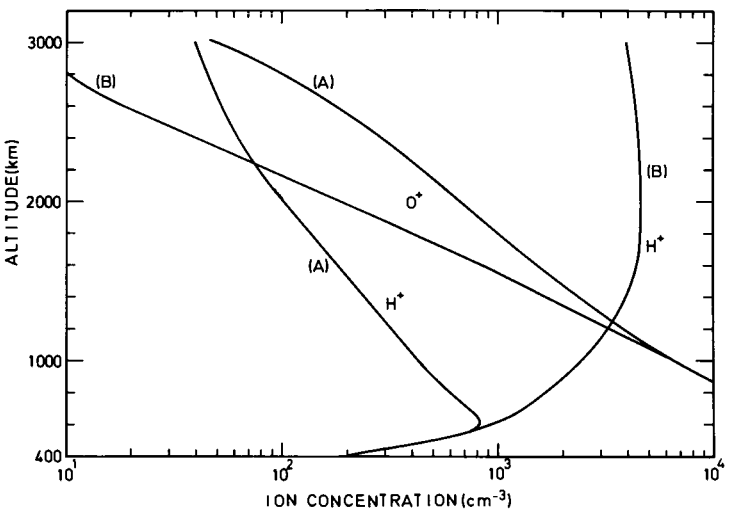


Fig. 21.8 H^+ ion profiles corresponding to different conditions for the given O^+ distribution and plasma temperature. A 1000°K model neutral atmosphere was used along with $T_e = T_i = 2500$°K at 400 km altitude. Curve A indicates the profile for maximum H^+ efflux, while Curve B indicates the densities valid for diffusive equilibrium. $\Phi_e = 5 \times 10^9$ eV cm^{-2} sec^{-1}; H^+ escape flux, 7.4×10^7 cm^{-2} sec^{-1}.

The discussion of the foregoing paragraphs relates to approximate forms for the minor ion densities. Numerical computations based on the coupled equations can be used to examine the general results when H^+ and He^+ are no longer minor ions. A typical result for H^+ in the ionosphere is shown in *Fig. 21.8*. Here it is assumed that H^+ is created through charge exchange in a 1000°K model neutral atmosphere. The oxygen ion density profile is typical for the midlatitude ionosphere for moderate solar activity with a value of 2×10^5 cm^{-3} at 400 km. Curve A of Fig. 21.8 corresponds to the density profile of H^+ characteristic for a maximum efflux of H^+ from the atmosphere consistent with O^+–H^+ friction. Curve B represents the solution

valid for diffusive equilibrium at high altitudes. The maximum outward flux possible in this particular model is $F(H^+) = 7.4 \times 10^7$ cm^{-2} sec^{-1}.

Although the present method gives an indication of the maximum outward ion fluxes which are consistent with a particular set of conditions, it does not predict the actual flux valid for a particular model where the density distribution is neither in a flux limited condition nor in diffusive equilibrium. The actual flux for this situation can be found only through a numerical solution to the transport equations [44, 45, 49] (see *Fig. 21.9*). Nevertheless, a knowledge of the maximum flux is useful, both with regard to the polar regions where the polar wind normally removes ionization at the maximum possible rate and at midgeomagnetic latitudes [48] when just after sunrise there is a large upward surge of H^+ into the magnetosphere. In this latter case the upward flow of H^+ changes the H^+ density from a distribution characteristic of diffusive equilibrium, shown as curve B of Fig. 21.8, to approximately a state of flowing equilibrium, shown as curve A.

Although similar considerations apply to the midlatitude behavior of He^+ in early morning hours, an additional factor should be taken into account. While O^+ provides a stationary frictional background for He^+, outward flowing H^+ transfers momentum to He^+ by means of H^+–He^+

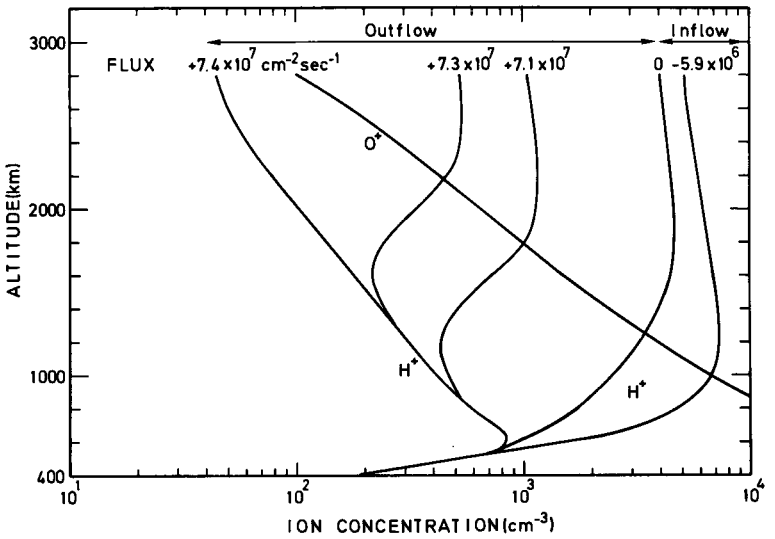


Fig. 21.9 H^+ density profiles for a 1000°K model thermosphere and different escape fluxes. The O^+ profile applies to the largest outflow ($O^+|_{400km} = 2 \times 10^5$ cm^{-3}). $\Phi_e = 5 \times 10^9$ eV cm^{-2} sec^{-1}; $T_e|_{400km} = 2500$°K.

Coulomb collisions. To evaluate this effect, the He^+ momentum equation can be written as

$$\frac{1}{m_j n_j}\frac{dp_j}{ds} + g_{\parallel} + \frac{1}{n_e m_j}\frac{dp_e}{ds} = -\nu(He^+, O^+)w_j - \nu(He^+, H^+)(w_j - w_k) \tag{21.51}$$

where the subscripts j and k apply to He^+ and H^+, respectively. Collecting terms, (21.51) becomes

$$w_j = \frac{1}{\nu(He^+, O^+) + \nu(He^+, H^+)}\left(\frac{1}{m_j n_j}\frac{dp_j}{ds} + g_{\parallel} + \frac{1}{n_e m_j}\frac{dp_e}{ds}\right) + \frac{\nu(He^+, H^+)w_k}{\nu(He^+, O^+) + \nu(He^+, H^+)} \tag{21.52}$$

or, through reduction of the ion–ion collision frequencies (see Chapters 9 and 19),

$$w(He^+) = \frac{1}{\nu}\left\{\frac{1}{m_j n_j}\frac{dp_j}{ds} + g_{\parallel} + \frac{1}{n_e m_j}\frac{dp_e}{ds}\right\} + \frac{w(H^+)}{1 + 4(n^+(O)/n^+(H))} \tag{21.53}$$

where $\nu = \nu(He^+, O^+) + \nu(He^+, H^+)$. The last term of this equation represents the effect of (H^+, He^+) collisions adding momentum to the He^+ flow.

Since $n^+(O)/n^+(H) > 1$ in the regions of concern, the additional term of (21.53) can be reduced to give

$$w(He^+) = \frac{1}{\nu}\left\{\frac{1}{m_j n_j}\frac{dp_j}{ds} + g_{\parallel} + \frac{1}{n_e m_j}\frac{dp_e}{ds}\right\} + \frac{\phi(H^+)}{4n^+(O)} \tag{21.54}$$

where $\phi(H^+) = w(H^+)n(H^+)$ is the H^+ flux.

With $\phi(H^+) \simeq 2 \times 10^8\ cm^{-2}\ sec^{-1}$ and $n^+(O) \sim 10^4$–$10^5\ cm^{-3}$ the He^+ ions can be given a velocity of 5 to 50 m sec^{-1} as a result of H^+–He^+ collisions. This additional velocity component acts to alter the He^+ density distribution and to enhance the net flux of He^+ leaving the ionosphere at the expense of the H^+ flux or to deplete He^+ in the nighttime ionosphere.

In a similar manner, the H^+ flow affects the altitude distribution of O^+, acting as an additional force acting in opposition to gravity. To evaluate the importance of this effect, the H^+ frictional drag can be expressed

$$f_d = \frac{m(H^+)}{m(O^+) + m(H^+)}\bar{\nu}(O^+, H^+)w(H^+) \tag{21.55}$$

or, using Eq. (9.115),

$$f_d = 7.2\times 10^{-2}\phi(H^+)T_i^{-3/2} \quad \text{cm sec}^{-2}. \tag{21.56}$$

Substitution of typical parameters into (21.56) indicates that H^+ frictional drag is usually only 10% of the acceleration due to gravity.

At very great altitudes H^+ becomes the dominant ion of the topside ionosphere and ion-neutral and H^+–O^+ collisions are completely negligible in determining the ion density profile along the magnetic field line. In this circumstance the equation of motion becomes

$$\frac{\partial w}{\partial t} + \frac{1}{n_e}\frac{\partial(p_e + p_i)}{\partial s} + g_{\parallel} = 0, \tag{21.57}$$

i.e., for low speed flow where $w\,\partial w/\partial s$ can be neglected the ion density profile is approximately that for diffusive equilibrium, even if the plasma is in motion. Thus, an inward flow of H^+ at high altitudes would give a density profile exactly that expected for diffusive equilibrium. Below 1000 to 2000 km, however, (H^+, O^+) collisions and the (O^+–e) charge separation electric field tend to slightly increase the H^+ density. The flow, however, would remain inward and the excess H^+ is converted to O^+ through charge exchange. The overall H^+ density profile for this situation is very similar to that for diffusive equilibrium even though substantial H^+ fluxes may be involved. Values of the H^+ density profiles for both inward and outward flow are given in Fig. 21.9 for 1000°K model atmosphere.

Finally, the approximation of low speed flow is difficult to maintain when the outward flux of ions approaches the limiting flux. In the limiting flux approximation the ion flow velocity increases exponentially with altitude with a scale height equal to that of O^+. Thus, even if the initial speed is low, over a distance of 1000 km the light ion speed may approach the sonic velocity so that the omission of the ion inertial term becomes important in limiting the acceleration of the ions.

Since the H^+ escape flux is of the order $10^8\,\text{cm}^{-2}\,\text{sec}^{-1}$, H^+ densities lower than $10^3\,\text{cm}^{-3}$ in a flow situation indicate the possibility of a transition to supersonic speeds.

21.8 High Speed Plasma Flow

The previous discussion was arbitrarily restricted to situations where ion inertia effects were negligible. At low geomagnetic latitudes changes in ionospheric plasma densities and temperatures are accompanied by rela-

tively slow gas motions. In these cases the use of the low speed plasma diffusion equations appears to be justified [50].

In contrast, outside the plasmapause where magnetic field lines periodically open to the tail of the magnetosphere, it is predicted theoretically and observed experimentally that supersonic ion flows can take place. In addition, following magnetic storms plasma depletion of the topside ionosphere is so severe that the initial stages of refilling could involve supersonic flow. These processes can be properly described only when the effects of inertia are included in the ion momentum equations.

Consider the possible motions of a plasma moving in a neutral atmosphere where production and loss of ionization occurs [51]. A strong magnetic field is assumed present such that all plasma transport occurs parallel to the lines of force and only one spatial coordinate s along the field lines is of importance.

The momentum equations for the ion gases have been given previously by Eq. (21.13) as

$$\frac{\partial w_i}{\partial t} + w_i \frac{\partial w_i}{\partial s} + \frac{1}{n_i m_i} \frac{\partial p_i}{\partial s} - \frac{eE_\parallel}{m_i} + g_\parallel = -\sum_j \nu_{ij}(w_i - w_j). \quad (21.58)$$

To proceed further a stipulation must be made with regard to the net current flow in the system under consideration; that is, one can deal with an ambipolar condition specified by $n_e w_e = \sum n_i w_i$ or the case where there is a net electric current, $j_\parallel = -en_e w_e + \sum en_i w_i$. In many cases of geophysical and astrophysical interest the ambipolar motion is most important. For the remaining discussion here it is assumed that an ambipolar motion is present.

The parallel component of electric field can be eliminated from (21.58) using the electron pressure gradient of Eq. (21.15) to give

$$m_i \frac{\partial w_i}{\partial t} + m_i w_i \frac{\partial w_i}{\partial s} + \frac{1}{n_e} \frac{\partial p_e}{\partial s} + \frac{1}{n_i} \frac{\partial p_i}{\partial s} + m_i g_\parallel = -m_i \sum_n \nu_{ij}(w_i - w_j). \quad (21.59)$$

To reduce (21.59) further the perfect gas relation $p = nkT$ can be introduced for each of the species with the result

$$m_i \frac{\partial w_i}{\partial t} + m_i w_i \frac{\partial w_i}{\partial s} + \frac{1}{n_e} \frac{\partial p_e}{\partial s} + \frac{kT_i}{n_i} \frac{\partial n_i}{\partial s} + k \frac{\partial T_i}{\partial s} + m_i g_\parallel = -m_i \sum_j \nu_{ij}(w_i - w_j). \quad (21.60)$$

Using the equations of continuity for the ith ion species (21.14), it is possible to eliminate the ion pressure gradient term of (21.60) for steady state conditions to give

$$\frac{1}{w_i}\frac{dw_i}{ds}\left[w_i^2 - \frac{kT_i}{m_i}\right] = -g_{\parallel} + \frac{kT_i}{m_i}\frac{d\ln A}{ds} - \sum_j \nu_{ij}(w_i - w_j) - \frac{kT_i}{m_i}\frac{d\ln T_i}{ds} - \frac{kT_i}{m_i}\frac{d\ln Q_i}{ds} - \frac{1}{n_e m_i}\frac{dp_e}{ds} \tag{21.61}$$

where

$$Q_i = \int_a^s (q_i - l_i)A(s')\,ds' \tag{21.62}$$

is the net ion flux flowing through the magnetic field tube arising from the effects of particle production and loss.

With the definition of the isothermal sound speed, $C_i^2 = kT_i/m_i$, (21.61) can be put in the form [51, 52]

$$\frac{1}{w_i}\frac{dw_i}{ds}\left[\frac{w_i^2}{C_i^2} - 1\right] = -\frac{g_{\parallel}}{C_i^2} + \frac{1}{A}\frac{dA}{ds} - \frac{1}{T_i}\frac{dT_i}{ds} - \frac{1}{C_i^2}\sum_j \nu_{ij}(w_i - w_j) - \frac{1}{Q_i}\frac{dQ_i}{ds} - \frac{1}{C_i^2 n_e m_i}\frac{dp_e}{ds} \tag{21.63}$$

showing that a singularity appears in the ith ion momentum equation when $w_i = \pm C_i$; that is, at the point of transition to supersonic flow.

To emphasize the high speed nature of (21.63) a local ion Mach number, M_i, can be defined as

$$M_i = w_i/C_i \tag{21.64}$$

and introduced into (21.63). For steady state conditions the result is

$$\frac{1}{M_i}\frac{dM_i}{ds}(M_i^2 - 1) = -\frac{g_{\parallel}}{C_i^2} + \frac{1}{A}\frac{dA}{ds} - \frac{1}{C_i^2}\sum_j \nu_{ij}(M_i C_i - w_j) - \frac{1}{Q_i}\frac{dQ_i}{ds} - \frac{1}{2T_i}\frac{dT_i}{ds}[M_i^2 + 1] - \frac{1}{T_i}\frac{dT_e}{ds} - \frac{T_e/T_i}{n_e}\frac{dn_e}{ds}. \tag{21.65}$$

It is important to note that M_i is the Mach number for the ith ion species along and does not necessarily represent the Mach number for the overall plasma flow.

The general theory described above applies to a plasma composed of electrons and several ion species. The details of such flows are usually complicated. However, the case of a single ion species where the charge separation electric field arises from only one source does permit further progress. For this situation it is possible to take $n_e = n_i$. Using (21.65) one obtains the single ion species ambipolar equation:

$$\frac{1}{M}\frac{dM}{ds}[M^2 - 1] = -\frac{g_{\parallel}}{C^2} + \frac{1}{A}\frac{dA}{ds} - \frac{C_i^2}{C^2}\frac{1}{T_i}\frac{dT_i}{ds} - \frac{C_e^2}{C^2}\frac{1}{T_e}\frac{dT_e}{ds} - \frac{1}{Q}\frac{dQ}{ds} - \sum_n \frac{\nu_{in}}{C^2}(w_i - w_n) - \frac{1}{T_e + T_i}\frac{d(T_e + T_i)}{ds} \tag{21.66}$$

where $C^2 = k(T_e + T_i)/m_i$, $C_e^2 = kT_e/m_i$, $C_i^2 = kT_i/m_i$, and the plasma Mach number is defined as $M = w/C$.

A plot of the different solutions for (21.66) is shown schematically in *Fig. 21.10*.

For $M > 0$, corresponding to plasma flow away from the earth, it is possible to identify both subsonic ($M < 1$) and supersonic regions ($M > 1$). Particular importance must be attached to the critical solutions A and B which pass through the singular point $M = 1$ of Eq. (21.66). Only along one of these two solutions is it possible to pass from the region $M < 1$ to $M > 1$, or vice versa.

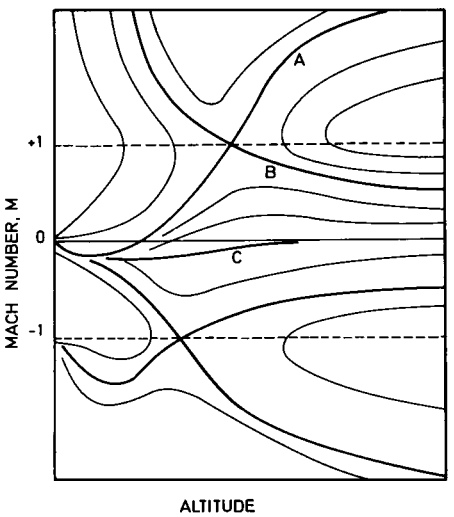


Fig. 21.10 Ion Mach number diagram showing transition to supersonic flow for outward and inward solutions.

For curve A the critical point or point of transition to supersonic flow (subsonic flow for curve B) occurs at an altitude where $M = 1$ and the right-hand side of (21.66) is simultaneously zero. For altitudes below the critical point $M_A\ (s \to 0) \to 0$, $M_B\ (s \to 0) \to \infty$, while for the regions above the critical point $M_A\ (s \to \infty) \to \infty$, $M_B\ (s \to \infty) \to 0$.

For $M < 1$ a group of subsonic solutions exist which reach some maximum value beyond the critical point, decreasing thereafter to low Mach numbers.

For $M > 1$ a group of supersonic solutions exist which start at initially large values, reach minimum values near the critical point, and thereafter increase in magnitude with increasing distance.

The behavior of M at large distances from the earth depends strongly upon the plasma thermal gradients. At high latitudes $g_{\parallel} \propto 1/r^2$ while $(1/A)\,\partial A/\partial r = n/r$ where $n = 2$ for a radical expansion and $n = 3$ for plasma motion in a dipole field. Hence, far out of the earth's atmosphere (21.66) becomes

$$\frac{1}{M}\frac{dM}{ds}[M^2 - 1] = \frac{n}{s} \tag{21.67}$$

for constant temperatures. This result may be integrated for the limiting circumstances of high and low Mach number flow to give

$$s \to \infty \begin{cases} M \gg 1: & M^2 = M_0^2 + 2n \ln(s/s_0) \quad (21.68) \\ M \ll 1: & M = M_0(s_0/s)^n \quad (21.69) \end{cases}$$

where M_0 is the Mach number at the point s_0. Using the equation of continuity and the perfect gas relation, $p = nkT$, these results imply that for $M \gg 1$ the plasma pressure at large s tends toward zero, while for subsonic flows ($M \ll 1$) the pressure eventually becomes constant.

The above discussion has been directed toward the solutions $M > 0$, corresponding to plasma escape from the earth. It is clear from Fig. 21.10, however, that adequate solutions exist which describe inward, or accretive, plasma motion.

To choose a correct solution for a specific physical problem requires a statement of the applicable boundary conditions. Generally, the earth's atmosphere at low altitudes is sufficiently dense to greatly retard plasma motion. Hence, solutions with $M \to 0$ as $s \to 0$ are generally sought. For outward plasma flow this choice restricts the correct solution to either the set of subsonic values or to the one critical solution leading to supersonic flow. To determine the actual solution it is necessary either to impose a point velocity boundary value or, more generally, to establish the plasma

pressure at the boundary surrounding the model under consideration. For example, in current models of the solar wind [53] this outer boundary condition is assumed to be imposed by the pressure of interstellar space. For the polar wind the plasma pressure of the high latitude magnetotail must be considered.

Essentially, each of the curves of Fig. 21.10 has a limiting pressure value as $s \rightarrow \infty$. For all curves lying above $M = 1$ the pressure at large distances from the earth is zero, while all curves lying below $M = 1$ have progressively greater pressures for lower values of M. In this regard, the asymptotic pressure of curve B, the descending critical solution, is of key importance. If the imposed boundary plasma pressure lies within $0 \leq p(\infty) < p_B(\infty)$ then the only correct solution to the ion Mach number equation is the ascending critical solution which starts at low values near the earth, passes through the critical point, and continues onward until a shock front is reached. At this point M drops to a subsonic value such that the proper pressure boundary is reached as $s \rightarrow \infty$. This behavior is sketched in *Fig. 21.11*. The physical location of the shock must be determined by application of the Rankin–Hugoniot relations.

If the plasma boundary pressure is chosen to be greater than that of the descending critical solution, curve B of Fig. 21.10, then only subsonic flow will be present in the model and the proper solution can be determined directly through numerical techniques. At some sufficiently large boundary pressure a hydrostatic distribution of plasma will result with a slight inward velocity at low altitudes to take account of ionic loss processes. Curve C of Fig. 21.10 illustrates this particular solution.

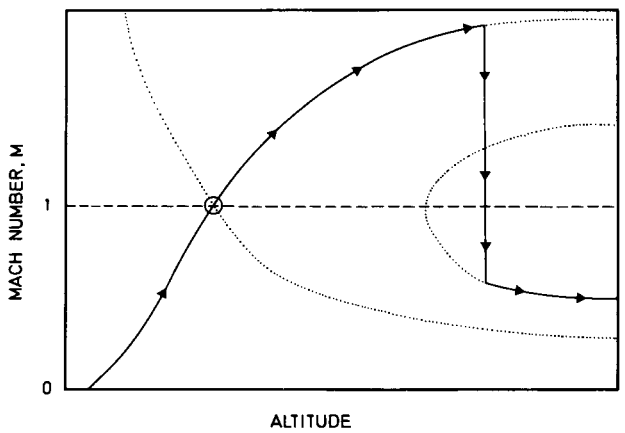


Fig. 21.11 Ion Mach number diagram with shock front formation.

If the boundary plasma pressure is enhanced still further, inward accretive plasma flow will result as indicated by the various solutions of Fig. 21.10 for $M < 0$.

Although the discussion in this section has emphasized the general aspects of single ion flow, the basic principles remain the same for multi-ion flow typical of the transition from the F_2 region to the topside ionosphere. The results of computations for such multi-ion models are discussed in the next section.

21.9 The Polar Wind

21.9.1 Introduction

Satellite measurements of topside electron density and ion composition in polar regions have shown many effects which are absent at lower geomagnetic latitudes [54–70]. Among the varieties of anomalous behavior can be included:

1. O^+ remains as the principal ionospheric ion to great altitudes ($\sim$4000 km).
2. The polar nighttime electron densities are very small with values less than 30 cm^{-3} being observed at 3000 km.
3. Above 2000 km a change in ion composition from H^+ to O^+ occurs near a magnetic latitude of 60° as one progresses polewards.
4. Large-scale upward fluxes of H^+ have been observed outside the plasmapause.

On a global scale, regions of enhanced plasma density are restricted to the plasmasphere, a torus-like volume lying about the geomagnetic equator whose outer surface ($L \simeq 4$–6) is roughly coincident with the lines of force of the geomagnetic field [71–73], as shown in *Fig. 21.12.* Outside the relatively sharp plasmapause boundary, much lower electron densities are found although local features, such as the auroral zone precipitation enhancements, do exist. Direct measurements of ion composition at large distances from the earth show clearly the plasmapause boundary [16, 18, 73]. *Figure 21.13*, taken from OGO-5 satellite results, shows the typical decrease in H^+ at 60° to 65° invariant latitude for different magnetic activities [73].

Measurements at lower altitudes have also been obtained and show directly the peculiar characteristics of the transplasmapause region. Typical results for O^+, H^+, N^+, and He^+ are shown in *Fig. 21.14.* In this figure, the plasmapause transition appears as a sharp decrease in the H^+ and He^+

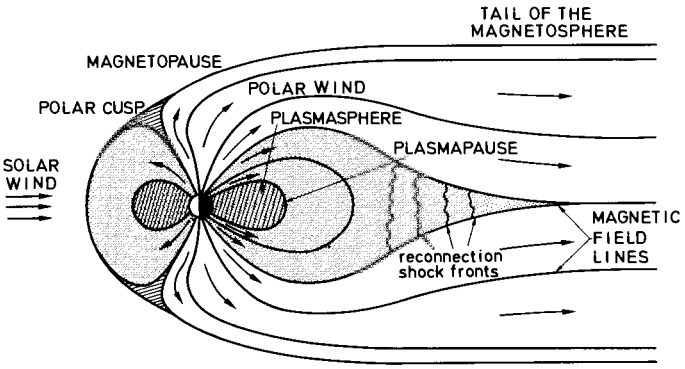


Fig. 21.12 The different regions of the magnetosphere. In the plasmasphere field lines are closed and, to a large extent, corotate with the earth. At very high latitudes the field lines are open to the tail of the magnetosphere. Between the plasmapause and open regions field lines are closed, but convect around the earth.

densities at invariant latitude of $\sim 60^\circ$ with considerable structure existing in the transplasmapause region. O^+, on the other hand, does not exhibit such a variation and becomes the dominant ionic constituent in the polar regions.

Further direct evidence illustrating the depletion of light ions in the transplasmapause region has been obtained through the Explorer 31 sat-

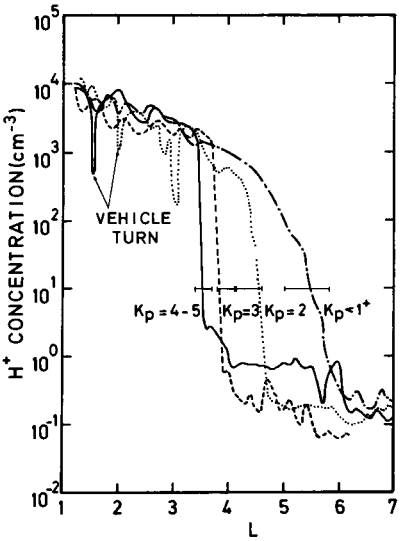


Fig. 21.13 Plasma density measurements obtained in the vicinity of the plasmapause by the OGO-5 mass spectrometer [73]. Solid curve, March 25, 1968, $K_p = 4$–5; dashed curve, April 22, 1968, $K_p = 3$; dotted curve, April 4, 1968, $K_p = 2$; and dotted dashed curve, April 12, 1968, $K_p < 1^+$.

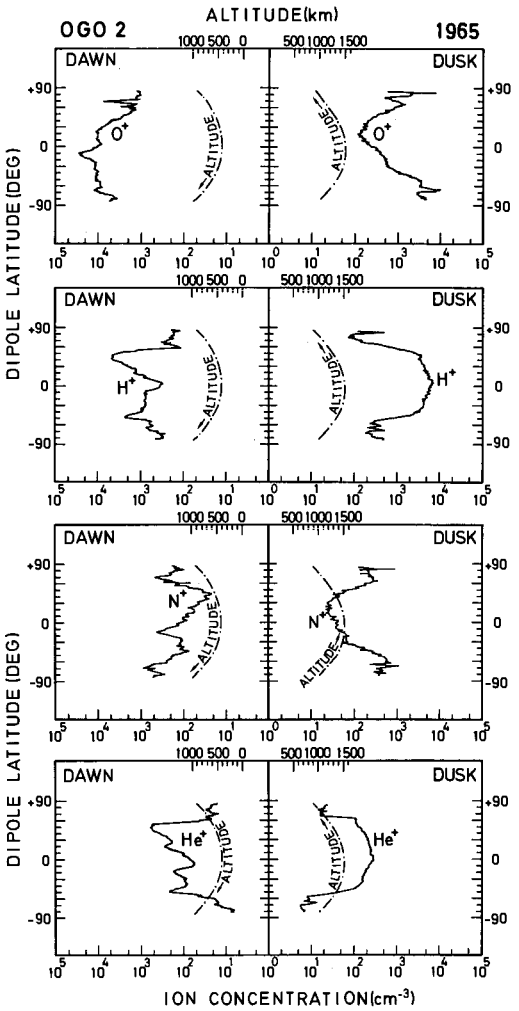


Fig. 21.14 Concentrations of O^+, H^+, N^+, and He^+ as a function of magnetic dipole latitude on October 15, 1965 as obtained from OGO-2 measurements [61] .The plasmapause boundary is most evident in the H^+ and He^+ curves at a latitude of 60°.

ellite. *Figure 21.15* shows winter results [68] for December 16, 1965. Within the plasmasphere at an altitude of 2100 km H^+ and He^+ are the two most important positive ions. Between 60° and 70° invariant latitude, however, the situation changes radically with the previously absent O^+ becoming the dominant ion in a region where deep troughs and spikes of ionization appear to predominate with average densities less than 100 cm^{-3}.

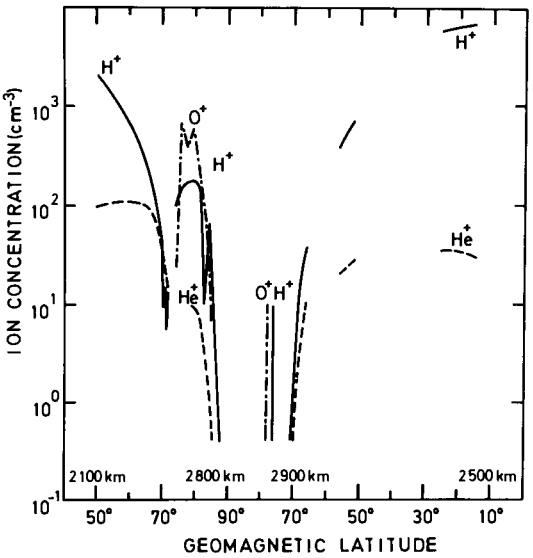


Fig. 21.15 Ion composition measurements of the winter north pole from the Explorer 31 satellite on December 16, 1965 at 19:10–19:40 GMT showing the transition from the plasmasphere to polar cap conditions [68].

Earlier results from Alouette I demonstrated the same behavior in terms of the mean ionic mass [67, 74].

Direct measurements of light ion flow were made by Explorer 31. The results for summer and winter conditions are shown in *Figs. 21.16* and *21.17* [70]. The full arrows indicate portions of satellite passes where H^+ speeds greater than several kilometers per second were observed. The dotted arrows indicate passes where no H^+ flow could be detected.

Although the foregoing discussion has emphasized the anomalous high altitude characteristics of the topside polar region, other data are available which show the existence of strong effects in the F_2 region. The identification of midlatitude and high latitude troughs (or decreases in the maximum F_2-region electron density) was first made from Alouette I ionograms [75]. Further analysis has shown that the occurrence of multiple troughs is related to the existence of several depletion regions [59, 62] in the polar cap, as indicated by *Fig. 21.18*. Depending upon the particular track of a satellite, one or more F_2-region troughs can be observed.

The first qualitative ideas relating to the structure of the high latitude ionosphere and the absence of light ions were based upon the concept of an open magnetosphere [33, 76–78]. In an open topology (that is, in an open magnetosphere) the usual magnetic field confinement of plasma pre-

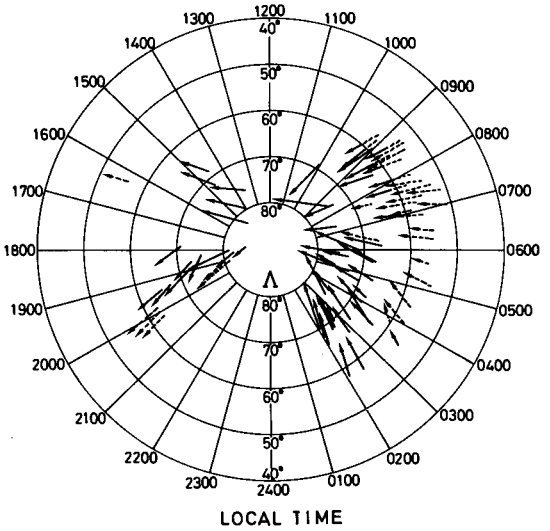


Fig. 21.16 Observations of polar wind flow in the summer polar cap by the Explorer 31 satellite in the summer of 1966 from 2000 to 3000 km. All available data is shown with direction and duration of satellite pass indicated by arrow. Solid lines indicate the presence of ion flow (H^+–O^+ phase shift), while the dotted line indicates its absence (No phase shift); Λ = invariant latitude. (Courtesy of Dr. J. H. Hoffman. See also Banks [70].)

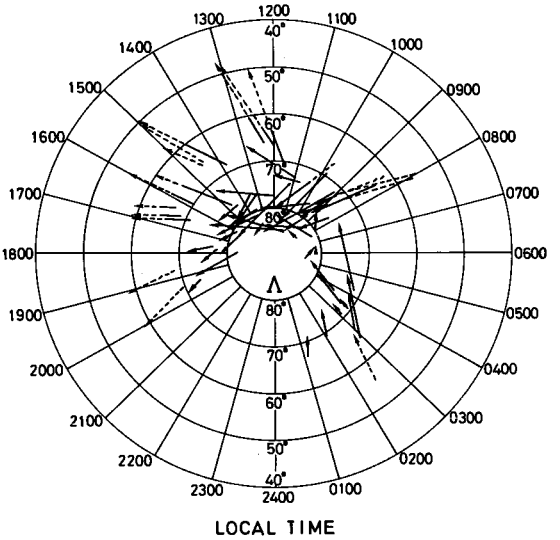


Fig. 21.17 Observations of polar wind flow in the winter polar region obtained from the Explorer 31 satellite during the winter of 1966 from 2000 to 3000 km. See Fig. 21.16 for key. (Courtesy of Dr. J. H. Hoffman. See also Banks [70].)

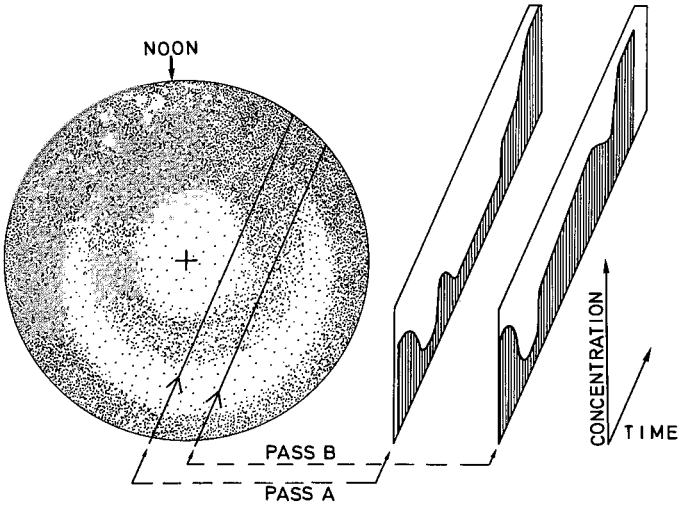


Fig. 21.18 Model distribution of F_2-region electron density above the winter pole where darker shading represents larger electron concentrations. Both a polar cap depletion and the main low latitude trough are present. On the right are sketched two possible density-time records which can be obtained from different satellite trajectories [59].

sent at low latitudes (where field lines form closed loops) cannot be effective at high latitudes and plasma, if sufficiently energetic to escape the earth's gravitational field, can escape into the magnetospheric tail. This plasma flow, when sufficiently large, reduces the ambient electron density below those values found for diffusive equilibrium.

At low geomagnetic latitudes, where lines of magnetic force form closed loops which corotate with the earth, a state of near-diffusive equilibrium can generally prevail with no significant loss of plasma from a given field tube. In contrast, at high geomagnetic latitudes where the field lines connect to the interplanetary environment via the tail of the magnetosphere, a steady outward flow of H^+ can occur with consequent low H^+ densities within the topside ionosphere [52, 79]. Moreover, since O^+ in polar regions remains as the dominant ion to higher altitudes than at lower geomagnetic latitudes, it follows from the relatively small scale height of O^+ that the overall electron densities along open field lines should be very low.

A fundamental restriction in early work was that H^+ escape could only be expected along open magnetic field lines. Radio whistler studies [71, 72, 80] and satellite density measurements [16, 18, 73] on the other hand indicate that the plasmapause occurs at relatively low magnetic latitudes where from trapped particle measurements the field lines are known to be

closed. Hence, it initially appeared that the formation of the plasmapause could not be related directly to the flow of ionization out of the open polar cap field lines. It was soon pointed out [33], however, that magnetic field tube convection, coupled with plasma escape from the open field lines leading into the tail of the magnetosphere, could lead in a natural manner to the establishment of a plasmapause in the region of closed field lines. According to the theory of magnetospheric convection open field lines are thought to continually sweep over the polar caps into the tail of the magnetosphere where they eventually reconnect in the vicinity of the neutral sheet and migrate in the sunwards direction at relatively low geomagnetic latitudes [37]. Near the front of the magnetosphere disconnection of the field lines again occurs and the convection process repeats. The ionospheric projection of plasma motions during the convection cycle is shown in *Fig. 21.19.*

During that portion of the convection cycle following disconnection, the geomagnetic field lines are open to the tail of the magnetosphere and plasma escape occurs with consequent depletion of H^+ and He^+. Following reconnection the field tubes, with their low ion densities, continue to circulate to lower geomagnetic latitudes before moving sunwards in their convective paths. Thus, it was proposed that because ionospheric replenishment of ionization is a relatively slow process, the regions of field tube

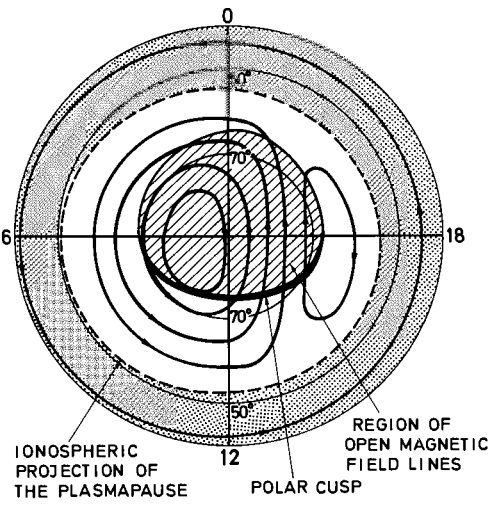


Fig. 21.19 The streamlines of flux tube motion projected into the north polar ionosphere. The plasmapause is shown by dashed lines, while the region of open field tubes is cross-hatched. The single dark line represents roughly the location of the polar cusp [70].

convection would be characterized by low electron densities, with the plasmapause boundary representing the outer shell of field tubes not participating in the magnetospheric convective motions.

Initial calculations of the light ion depletion effect [77, 78] were based upon simple models of evaporative escape similar to the problem of neutral hydrogen escape. In fact, such an approach ignores the electric field coupling existing between electrons and positive ions which substantially alters the classical escape problem. In recent work [34, 52, 79, 81] calculations based upon the hydrodynamic plasma equations have been used to show that a dynamic plasma expansion process is operative in the polar regions such that H^+ and He^+ are rapidly accelerated to supersonic speeds along the open magnetic field lines. The resulting outward flow, called the polar wind, has been found to result in a great depletion of ionization in the polar regions.

In the last section the theory of high speed, multiconstituent plasma flow has been developed. In the following paragraphs models appropriate to the polar topside ionosphere are presented.

21.9.2 Model for the Polar Wind Theory

The essential features of polar plasma flow involve a number of different processes for the conversion of random thermal energy and electric potential energy into directed energy of bulk motion. Briefly, O^+ is created by photoionization (summer conditions) or soft particle precipitation (winter conditions) or both such that, through competition between diffusion and ion loss processes, a typical F_2 layer is formed between 200 and 350 km altitude. The altitude distribution of O^+ above the F_2 peak is not quite that of diffusive equilibrium, but must be a mixture of the static and flowing distributions needed to take account of the effects of a small O^+ escape flux, a much larger flux needed to support the escape flux of H^+ by means of O^+–H charge exchange, and H^+–O^+ frictional acceleration.

Below about 600 km the steady state H^+ densities are determined by charge exchange but, as shown in Section 21.7, upward H^+ transport eventually results in lower H^+ densities than those appropriate to chemical or diffusive equilibrium. Although the initial H^+ velocity in the vicinity of 600 km is small, the rapid decrease with altitude of O^+, with a consequent decrease in H^+–O^+ friction, permits the O^+–e electric field and the H^+ pressure gradient to eject the H^+ out of the polar ionosphere with increasingly greater velocity. Although the usual low speed plasma transport equations (Section 21.7) are adequate to describe the H^+ motions below about 1000 km, above this altitude ion inertia becomes important in de-

termining the H^+ velocity and the high speed transport equations are necessary.

At an altitude of 2000 to 4000 km, a precise value depending upon a number of factors, the H^+ flow velocity becomes supersonic and further acceleration continues with the H^+ pressure gradients being of progressively less importance as compared with the O^+–e and H^+–e charge separation electric fields and the H^+ inertia. Net H^+ escape fluxes of the order of 5×10^7 to 5×10^8 cm^{-2} sec^{-1} appear to be typical for polar summer conditions.

With regard to He^+ an ejection process similar to that of H^+ takes place following photoionization of He; that is, the O^+–e electric field and the He^+ pressure gradient drive the outward flow against the frictional retardation of He^+–O^+ collisions. The critical point (transition point to supersonic flow) for He^+ is slightly higher than that for H^+ and escape fluxes of the order of $2\text{–}4\times10^6$ cm^{-2} sec^{-1} are typical for a wide range of conditions.

21.9.3 Theoretical Results

Typical results for H^+ transport velocities are shown in *Fig. 21.20* for several values (altitude independent) of the electron and ion temperatures for the 1000°K neutral atmosphere. At low altitudes, where charge exchange occurs rapidly, the H^+ flow is inward with H^+ being converted to O^+ which, in turn, is eventually lost through ion–molecule reactions and rapid dissociative recombination. The H^+ density distribution for chemical equilibrium and transport as a minor ion are identical for thermal equilibrium among electrons, ions, and neutral particles; no downward flow results. With $T_e \geq T_i > T_n$, however, a balance between diffusion and charge exchange can be met only with a downward flux of H^+.

Above about 600 to 800 km charge exchange and friction weaken to such an extent that upward H^+ flow can begin. Under the action of the H^+ pressure gradient and the O^+–e electric field (H^+ is a minor constituent to well past its critical point), H^+ is rapidly accelerated, and the critical point, or transition to supersonic flow, occurs in the range 1500–4000 km, depending upon the particular model involved. The location of the critical point is determined by the condition that $w(H^+) = C(H^+)$ at the point where gravity, friction, electric fields, ion temperature gradients, and particle production are in balance. In the polar wind acceleration produced by the H^+ pressure gradient and the O^+–e charge separation electric field, modified by the effect of gravity upon H^+, is essentially balanced by H^+–O^+ friction at the critical point; the term $d \ln A/dr$ of Eq. (21.63) being relatively unimportant.

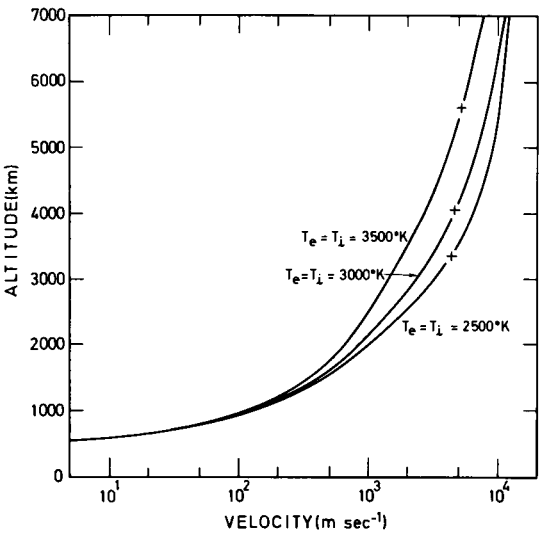


Fig. 21.20 Daytime polar region H^+ velocity profiles for $T_n = 1000°K$ and several values of T_e and T_i. Decreases in T_e and T_i lead to a faster flow owing to the complementary effects of the electric field and H^+–O^+ friction. Below 600 km the H^+ flow is downward as a result of charge exchange. Crosses mark the H^+ critical point. Escape flux (cm^{-2} sec^{-1}) normalized to 1000 km: 2500°K—$F(H^+) = 4.3 \times 10^8$, $F(He^+) = 1.6 \times 10^6$; 3000°K—$F(H^+) = 5.8 \times 10^8$, $F(He^+) = 1.8 \times 10^6$; 3500°K—$F(H^+) = 7.5 \times 10^8$, $F(He^+) = 1.7 \times 10^6$.

Changes in T_e and T_i affect the H^+ flow in several ways. First, the H^+–O^+ collision frequency at low velocities is proportional to $T_i^{-3/2}$ so that decreases in T_i tend to enhance H^+–O^+ friction. In opposition, the O^+ density depends upon $(T_e + T_i)$ through the O^+ density profile such that decreases in temperature decrease H^+–O^+ friction. The general result of these counteracting tendencies is to increase the altitude of the critical point for increases in plasma temperature, although the reverse behavior can result for particular conditions.

The effect of differing neutral gas models upon the H^+ velocity is shown in *Fig. 21.21* for fixed ion and electron temperatures of 3000°K. The lower neutral gas densities of the cooler models (the increasing density of H does not strongly affect the H^+ velocity) result in progressively smaller values of $n(O^+)$, thereby reducing H^+–O^+ friction and permitting higher H^+ velocities. The crosses of Fig. 21.19 indicate the H^+ critical points and show the direct relationship between the thermospheric temperature and the altitude of the transition to supersonic (with respect to H^+) flow.

The relative ion composition of the topside ionosphere is strongly affected

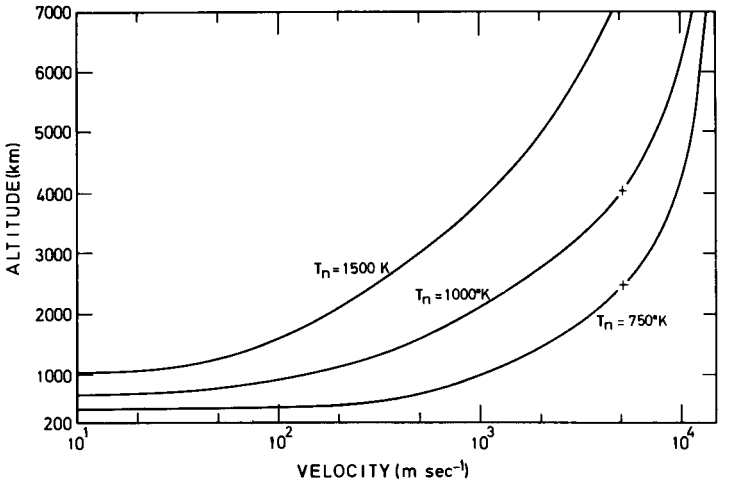


Fig. 21.21 Daytime polar region H^+ velocity profiles for $T_e = T_i = 3000°K$ and three models of the neutral atmosphere. The flows are faster for lower values of the thermospheric temperature owing to decreased frictional resistance. Crosses mark the H^+ critical point. Escape flux (cm^{-2} sec^{-1}) normalized to 1000°K: $F(H^+, 750°K) = 6.6 \times 10^8$, $F(He^+, 750°K) = 1.5 \times 10^6$; $F(H^+, 1000°K) = 5.8 \times 10^8$, $F(He^+, 1000°K) = 1.8 \times 10^6$; $F(H^+, 1500°K) = 3.8 \times 10^8$, $F(He^+, 1500°K) = 3.7 \times 10^6$.

by the escape of H^+ and He^+. Results for two model neutral atmospheres are shown in *Figs. 21.22* and *21.23*.

Several features of these figures are of interest. First, the altitude distribution of H^+ corresponds to a condition of maximum flow consistent with H^+–O^+ friction. Below 600 to 800 km the H^+ density is determined largely by charge exchange and has a positive gradient somewhat past the point where the O^+–e portion of the total electric field, acting in opposition to the H^+ pressure gradient and gravity, is able to begin to accelerate the H^+ upward. Above 600 to 800 km $dn(H^+)/dr < 0$ and the H^+ pressure gradient acts to further accelerate the flow; it is retarded mainly by H^+–O^+ friction. For $T_e/T_i = 1$ the electric field due to O^+–e charge separation and the H^+ pressure gradient contribute equally to the flow velocity.

In the regions above the H^+ critical point $n(H^+)$ increases relative to $n(O^+)$ such that H^+ becomes the dominant ion at altitudes of 3000 to 7000 km, depending upon the particular model involved. At these altitudes the gradual decline in importance of O^+ does not remove the accelerating forces acting upon H^+; the H^+–e electric field acts to continue to increase the speed of the flow into the regions where the spreading of field lines becomes slight.

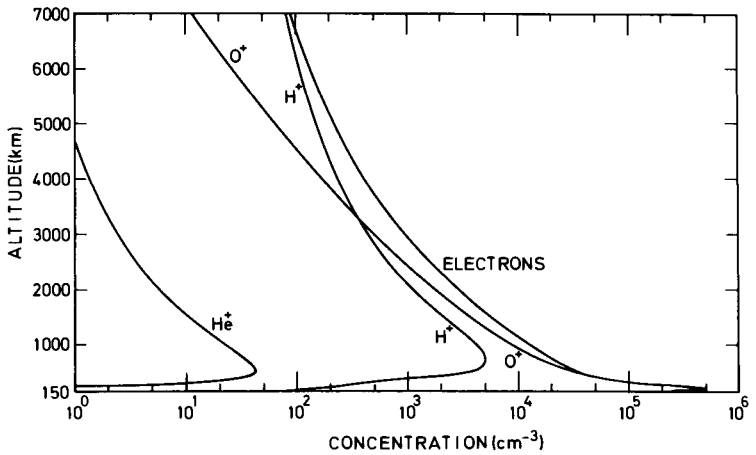


Fig. 21.22 Daytime polar region ion density profiles for $T_e = T_i = 3000°K$ and a 750°K model neutral atmosphere. The large concentration of H in this model, in conjunction with the relative absence of O, leads to a rapid loss of H^+. To support the H^+ flow a large upwards flux of O^+ is present. As a consequence of this flow, O^+ is not in diffusive equilibrium below 3000 km. Escape flux (normalized to 1000 km): $F(H^+) = 6.6 \times 10^8\ cm^{-2}\ sec^{-1}$; $F(He^+) = 1.5 \times 10^6\ cm^{-2}\ sec^{-1}$.

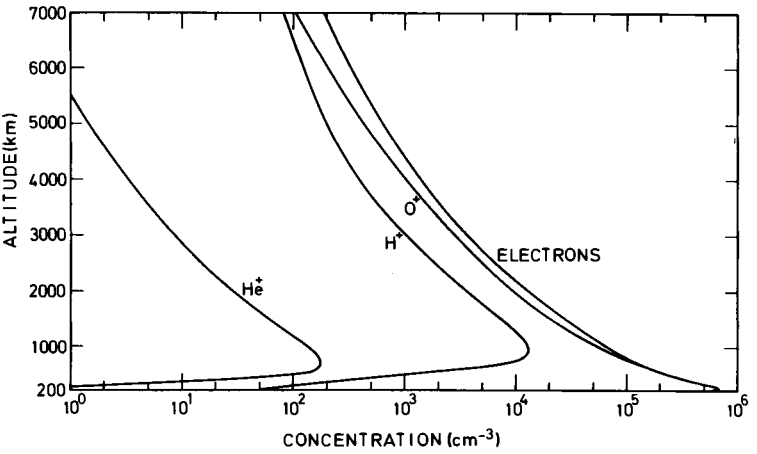


Fig. 21.23 Daytime polar region ion density profiles for $T_e = T_i = 3000°K$ and a 1000°K model neutral atmosphere. Due to the low H concentration of this model, the net H^+ escape flux is small compared with that of Fig. 21.20. As a consequence, the requirement for the upward O^+ flux is reduced and the O^+ density profile is closer to diffusive equilibrium with substantially greater densities. Owing to these factors the O^+–H^+ transition level changes from 3400 km (Fig. 21.20) to 7500 km. Escape flux (normalized to 1000 km): $F(H^+) = 5.8 \times 10^8\ cm^{-2}\ sec^{-1}$; $F(He^+) = 1.8 \times 10^6\ cm^{-2}\ sec^{-1}$.

As a result of the rapid efflux of H^+ from the ionospheric regions above 800 km, O^+ is left as the dominant ion and, due to its relatively small scale height, the electron density rapidly falls to much lower values than would be found at the same altitude for diffusive equilibrium; H^+ remains as a minor constituent to very high altitudes. With respect to O^+, the effect of ion flow is most apparent slightly above the F_2 peak where O^+–O friction is effective in limiting the maximum possible efflux rate to $\sim 10^9$ cm^{-2} sec^{-1}. In some cases the O^+ flux required for H^+ escape approaches the limiting O^+ flux, and, for the 750°K model, $n(O^+)$ falls off with the atomic oxygen density (a maximum flux condition) for some distance above the F_2 peak. Owing to the upward flux and H^+–O^+ friction above 600 to 800 km, O^+ is not in diffusive equilibrium.

The He^+ density profile is determined through a combination of chemical and transport effects. As a minor ion He^+ is accelerated upward through its own partial pressure gradient and the O^+–e electric field. For low He^+ speeds, this outward acceleration is matched by He^+–O^+ friction, gravity, He^+–H^+ friction, and other forces. At high speeds friction becomes less important than inertia. Because of the rapidity of He^+–N_2 reactions, the

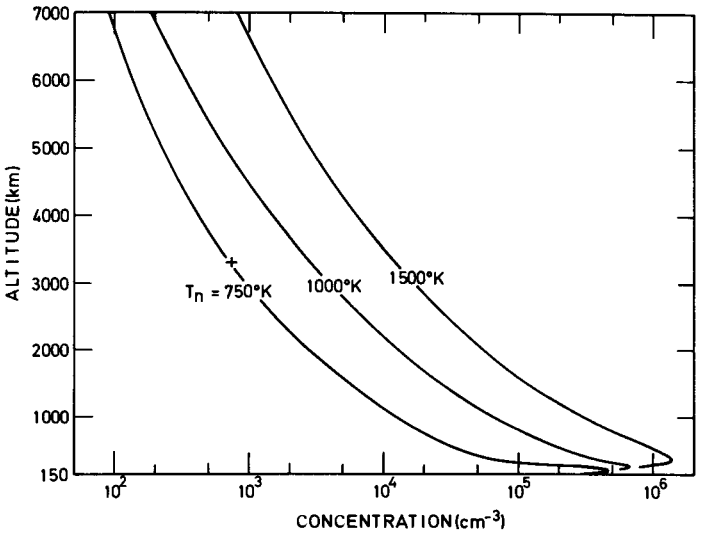


Fig. 21.24 Daytime polar region electron density profiles for $T_e = T_i = 3000$°K and three model neutral atmospheres. Crosses mark the level of transition from O^+ to H^+ dominance. The H^+ escape flux is larger for a low density, rapidly flowing model than for a high density, slowly flowing model. Escape flux (cm^{-2} sec^{-1}) normalized to 1000 km: $F(H^+, 750°K) = 6.6 \times 10^8$, $F(He^+, 750°K) = 1.5 \times 10^6$; $F(H^+, 1000°K) = 5.8 \times 10^8$, $F(He^+, 1000°K) = 1.8 \times 10^6$; $F(H^+, 1500°K) = 3.8 \times 10^8$, $F(He^+, 1500°K) = 3.7 \times 10^6$.

He^+ density is at least 100 times smaller than $n(O^+)$ throughout the regions below 5000 km.

Electron density profiles typical of steady state, daytime conditions in the polar models are shown in *Fig. 21.24* for three model neutral atmospheres. In each case O^+ is the dominant ion up to at least 4000 km even though the relative amount of neutral atomic hydrogen changes greatly between 750° and 1500°K. In fact, the cooler models involve substantially larger escape fluxes of H^+ placing more stringent requirements upon the upward transport of O^+. Progressing from $T_n = 1500°K$, the smaller O^+ scale heights above the F_2 peak indicate the extent to which the escaping H^+ flux is limited by the rate at which O^+ can diffuse upward. The changes in slope of these curves do not arise from composition changes or thermal gradients but are due only to transport effects. As a consequence, interpretation of high latitude electron density profiles in terms of diffusive equilibrium conditions can be expected to give no more than qualitative results.

Variations in plasma temperature also affect the high altitude electron density, as shown in *Fig. 21.25*. While the peak density remains approximately fixed, both the escape fluxes and densities increase with plasma temperature.

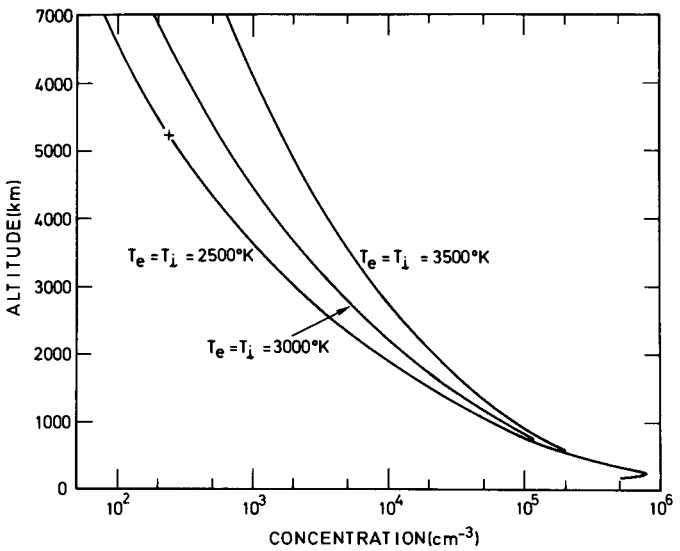


Fig. 21.25 Daytime polar region electron density profiles for $T_n = 1000°K$ and several values of T_e and T_i. Crosses mark the O^+–H^+ transition point. Escape flux ($cm^{-2}\,sec^{-1}$) normalized to 1000 km: 2500°K—$F(H^+) = 4.3 \times 10^8$, $F(He^+) = 1.6 \times 10^6$; 3000°K—$F(H^+) = 5.8 \times 10^8$, $F(He^+) = 1.8 \times 10^6$; 3500°K—$F(H^+) = 7.5 \times 10^8$, $F(He^+) = 1.7 \times 10^6$.

21.9.4 The Polar Wind for Collisionless Conditions

At sufficiently great altitudes the mean free path for H^+–O^+ collisions exceeds the O^+ scale height. As a result, the flow ceases to be collision dominated and an individual particle treatment must be adopted to determine the increasingly greater pressure anisotropies. With respect to the polar wind, H^+ and He^+ are accelerated by their own pressure gradients and the overall charge separation electric field. For subsonic flows pressure gradients play an important part in determining the ion flow velocity, while for supersonic flows the pressure gradient can be neglected. To determine the validity of the assumption that both the ion and electron pressures are isotropic about their individual flow velocities, several approximations can be introduced. The first, mentioned above, involves the ratio between the local mean free path and the scattering medium scale height $\lambda(H^+, O^+)/H(O^+)$. If $\lambda(H^+, O^+)/H(O^+) \ll 1$ the flow is considered to be collision dominated and the concepts of an isotropic pressure and the usual thermal conductivity should apply.

A second measure of collision dominance can be defined, however, in terms of the collision frequency, the bulk flow velocity u, and the local scattering scale height: vH/u. If vH/u is $\gg 1$ collision dominance is assumed to exist. While the λ/H criterion is based upon individual particle behavior, the vH/u standard takes into account the actual flow velocity and collision frequency.

As an example of the approach to collisionless conditions in the polar wind, consider the problem of H^+ moving through O^+. Suppose the O^+ density gradient is defined through the relation

$$\left| \frac{1}{n(O^+)} \frac{dn(O^+)}{dr} \right| = \frac{1}{\alpha} \left[\frac{m(O^+)g_{\parallel}}{k(T_e + T_i)} \right] \tag{21.70}$$

where α is a parameter normally less than one.

At the H^+ critical point $u^2(H^+) = kT_i/m(H^+)$ and an explicit relation can be obtained for $\lambda(H^+, O^+)/H(O^+)$:

$$\frac{\lambda(H^+, O^+)}{H(O^+)} = 1.18\alpha \left[\frac{T_e}{T_i} + \alpha \frac{H(O^+)}{h} \right]^{-1} \tag{21.71}$$

where

$$h^{-1} = \frac{3}{r} - \frac{m(H^+)g_{\parallel}}{kT_i}. \tag{21.72}$$

Since $\alpha H(O^+)/h \ll 1$ and $T_e \geq T_i$ in normal circumstances it is clear that $\lambda(H^+, O^+)/H(O^+) \leq 1$ at and below the critical point. As a result the

isotropic pressure assumption can be adopted with a fair degree of confidence in the ionospheric regions below the critical point for both summer and winter conditions.

Above the critical point H^+–O^+ collisions become increasingly infrequent and an anisotropic pressure should develop with narrowing of H^+ pitch angles into the direction of motion. Calculations of the polar wind flow characteristic in this high altitude region can be used as boundary conditions for various models of ion exospheres [82, 83]. As such, the details of the escape flux, the separate ion densities, and the individual species flow velocities are determined by ionospheric parameters below the critical point [84].

REFERENCES

1. L. R. O. Storey, *Phil. Trans. Roy. Soc. (London)* **A246**, 113 (1953).
2. J. W. Dungey, *The Physics of the Ionosphere*, p. 406. Phys. Soc., London, 1955.
3. F. S. Johnson, *J. Geophys. Res.* **65**, 577 (1960).
4. M. Nicolet, *J. Geophys. Res.* **66**, 2263 (1961).
5. D. R. Bates and T. N. L. Patterson, *Planet. Space Sci.* **5**, 257 (1961).
6. W. B. Hanson, *J. Geophys. Res.* **67**, 183 (1963).
7. R. W. Bourdeau, E. C. Whipple, J. L. Donley, and S. J. Bauer, *J. Geophys. Res.* **67**, 467 (1962).
8. D. N. Anderson, W. H. Bennett, and L. C. Hale, *J. Geophys. Res.* **70**, 1031 (1965).
9. H. A. Taylor, L. H. Brace, H. C. Brinton, and C. R. Smith, *J. Geophys. Res.* **68**, 5339 (1963).
10. P. J. Bowen, R. L. F. Boyd, W. J. Raitt, and A. P. Willmore, *Proc. Roy. Soc.* **A281**, 504 (1964).
11. S. J. Bauer, B. V. Krishnamurthy, *Planet. Space Sci.* **16**, 653 (1968).
12. J. H. Hoffman, *Science* **155**, 322 (1967).
13. J. H. Hoffman, *J. Geophys. Res.* **72**, 1883 (1967).
14. H. A. Taylor, H. G. Mayr, and H. C. Brinton, *Space Res.* **10**, 663 (1970).
15. S. S. Prasad, *J. Geophys. Res.* **73**, 6795 (1968).
16. H. C. Brinton, R. A. Pickett, and H. A. Taylor, *Planet. Space Sci.* **16**, 899 (1968).
17. D. R. Moorcroft, *J. Geophys. Res.* **74**, 315 (1969).
18. H. A. Taylor, H. C. Brinton, and C. R. Smith, *J. Geophys. Res.* **70**, 5769 (1965).
19. S. S. Prasad, *J. Geophys. Res.* **75**, 1911 (1970).
20. H. G. Mayr, L. H. Brace, and G. S. Dunham, *J. Geophys. Res.* **72**, 4391 (1967).
21. J. H. Hoffman, C. Y. Johnson, J. C. Holmes, and J. M. Young, *J. Geophys. Res.* **74**, 6281 (1969).
22. J. H. Hoffman, *Science* **155**, 322 (1967).
23. C. Y. Johnson, *J. Geophys. Res.* **71**, 330 (1966).
24. H. C. Carlson and W. E. Gordon, *J. Geophys. Res.* **71**, 5573 (1966).
25. D. T. Farley, *Ann. Géophys.* **22**, 448 (1966).
26. V. G. Istomin, *Ann. Géophys.* **22**, 255 (1966).
27. W. B. Hanson and I. B. Ortenburger, *J. Geophys. Res.* **66**, 1425 (1961).
28. D. R. Bates and N. Lynn, *Phil. Trans. Roy. Soc.* **253A**, 141 (1959).

29. D. Rapp, *J. Geophys. Res.* **68**, 1773 (1963).
30. S. J. Bauer, *Ann. Géophys.* **22**, 247 (1966).
31. S. J. Bauer, *Proc. IEEE* **57**, 1114 (1969).
32. W. I. Axford and C. O. Hines, *Can. J. Phys.* **39**, 1433 (1961).
33. A. Nishida, *J. Geophys. Res.* **71**, 5669 (1966).
34. P. M. Banks and T. E. Holzer, *J. Geophys. Res.* **74**, 6317 (1969).
35. P. M. Banks, A. F. Nagy, and W. I. Axford, *Planet. Space Sci.* **19**, 1053 (1971).
36. C. G. Park, *J. Geophys. Res.* **75**, 4249 (1970).
37. W. I. Axford, *Rev. Geophys.* **7**, 421 (1969).
38. G. Kockarts and M. Nicolet, *Ann. Géophys.* **19**, 370 (1963).
39. J. Angerami and J. O. Thomas, *J. Geophys. Res.* **69**, 4537 (1964).
40. P. M. Banks and J. W. McGowan, *J. Geophys. Res.* **73**, 5008 (1969).
41. H. C. Brinton, R. A. Pickett, and H. A. Taylor, *J. Geophys. Res.* **16**, 899 (1968).
42. E. J. R. Maier, *J. Geophys. Res.* **74**, 815 (1969).
43. H. C. Brinton, M. W. Pharo, H. G. Mayr, and H. A. Taylor, *J. Geophys. Res.* **74**, 2941 (1969).
44. W. B. Hanson and T. N. L. Patterson, *Planet. Space Sci.* **12**, 979 (1964).
45. H. G. Mayr, L. H. Brace, and G. S. Dunham, *J. Geophys. Res.* **72**, 4391 (1967).
46. J. E. Geisler, *J. Geophys. Res.* **72**, 81 (1967).
47. H. G. Mayr, J. M. Grebowsky, and H. A. Taylor, *Planet. Space Sci.* **18**, 1123 (1970).
48. H. C. Brinton, J. M. Grebowsky, and H. G. Mayr, *J. Geophys. Res.* **76**, 3738 (1971).
49. T. M. Watt, *J. Geophys. Res.* **76**, 3095 (1971).
50. A. F. Nagy, P. Bauer, and E. G. Fontheim, *J. Geophys. Res.* **73**, 6259 (1968).
51. P. M. Banks and T. E. Holzer, *J. Geophys. Res.* **74**, 6304 (1969).
52. P. M. Banks and T. E. Holzer, *J. Geophys. Res.* **73**, 6846 (1968).
53. E. N. Parker, *Interplanetary Dynamical Processes.* Wiley, New York, 1963.
54. P. J. Bowen, R. L. F. Boyd, W. J. Raitt, and A. P. Willmore, *Proc. Roy. Soc.* **A281**, 504 (1964).
55. G. P. Serbu and E. J. R. Maier, *Space Res.* **7**, 527 (1966).
56. E. L. Hagg, *Can. J. Phys.* **45**, 27 (1967).
57. J. L. Donley, NASA Rep. X-615-67-335, Goddard Space Flight Center, Greenbelt, Maryland (1967).
58. J. H. Hoffman, *Trans. Amer. Geophys. Un.* **49**, 253 (1968).
59. J. O. Thomas and M. K. Andrews, *J. Geophys. Res.* **73**, 7407 (1968).
60. P. Timleck and G. L. Nelms, *Proc. IEEE* **57**, 1164 (1969).
61. H. A. Taylor, H. C. Brinton, M. W. Pharo, and N. K. Rahman, *J. Geophys. Res.* **73**, 5521 (1968).
62. T. Sato and L. Colin, *J. Geophys. Res.* **74**, 2193 (1969).
63. T. Sato and L. Colin, *J. Geophys. Res.* **74**, 2208 (1969).
64. H. A. Taylor, H. C. Brinton, D. L. Carpenter, F. M. Bonner, and R. L. Heyborne, *J. Geophys. Res.* **74**, 3517 (1969).
65. D. L. Carpenter, C. G. Park, H. A. Taylor, and H. C. Brinton, *J. Geophys. Res.* **74**, 1837 (1969).
66. G. W. Sharp, *J. Geophys. Res.* **71**, 1345 (1966).
67. R. E. Barrington, *Proc. IEEE* **57**, 1036 (1969).
68. J. H. Hoffman, *Proc. IEEE* **57**, 1063 (1969).
69. G. L. Nelms and J. H. Chapman, in *The Polar Ionosphere and Magnetospheric Processes* (G. Scovli, ed.). p. 233 Gordon and Breach, New York (1970).

70. P. M. Banks, in *Physics of the Polar Magnetospheric*, p. 75. Univ. of Oslo Press, Oslo, 1971.
71. D. L. Carpenter, *J. Geophys. Res.* **68**, 1675 (1963).
72. D. L. Carpenter, *J. Geophys. Res.* **71**, 693 (1966).
73. C. R. Chappell, K. K. Harris, and G. W. Sharp, *J. Geophys. Res.* **75**, 50 (1970).
74. S. D. Shawhan, and D. A. Gurnett, *J. Geophys. Res.* **71**, 47 (1966).
75. B. D. Muldrew, *J. Geophys. Res.* **70**, 2635 (1965).
76. J. W. Dungey, *Phys. Rev. Lett.* **6**, 47 (1961).
77. S. J. Bauer, *Electron density profiles*, in *Ionosphere and Exosphere* (J. Frihagn, ed.) p. 1. North-Holland Publ., Amsterdam, 1966.
78. A. J. Dessler and F. C. Michel, *J. Geophys. Res.* **71**, 1421 (1966).
79. W. I. Axford, *J. Geophys. Res.* **73**, 6855 (1968).
80. J. J. Angerami and D. L. Carpenter, *J. Geophys. Res.* **71**, 711 (1966).
81. K. Marubashi, *Rep. Ionos. Space Res.* **24**, 322 Japan (1970).
82. T. E. Holzer, J. A. Fedder, and P. M. Banks, *J. Geophys. Res.* **76**, 2453 (1971).
83. J. Lemaire and M. Scherer, *Planet. Space Sci.* **18**, 103 (1970).
84. J. Lemaire, *J. Atmos. Terr. Phys.* **34**, 1647 (1972).

CHAPTER 22

Thermal Processes of the Ionosphere

22.1 Introduction

Only in the past decade have extensive studies been made of the thermal structure of the ionosphere. Although calculations of ion density profiles in the ionosphere require a knowledge of both the electron and ion gas temperatures to evaluate plasma transport effects, prior to 1960 it was common to assume that the various modes of energy exchange between the neutral and ionized gases were sufficiently rapid to assure thermal equilibrium [1].

The importance of electrons created in the photoionization of the neutral atmosphere as a source of electron gas heating was first pointed out in 1946 [2]. When a solar photon ionizes a neutral atom or molecule a certain excess energy, corresponding to the difference between the initial photon energy and the energy of the final ion state, is given to the free photoelectron. As the photoelectron travels through the atmospheric gases it loses this excess kinetic energy ($\sim$15 eV per photoelectron) through excitation of the neutral atmospheric gases. At energies near 1.5 eV the number of excitation processes available to the photoelectron becomes small and elastic collisions with other electrons and ions become important. In these final stages of photoelectron thermalization a substantial amount of energy is given to the ambient electron gas which increases the electron temperature above that of the neutral gases.

Langmuir probe measurements [3] at Fort Churchill in November 1958 gave the first indication of elevated ionosphere electron temperatures

($T_e \sim 2000°K$ at 150 km). In 1961 a theory of ionospheric heating by photoelectrons was presented [4] which predicted electron temperatures up to 1500°K, or about 500°K hotter than the neutral atmosphere. Confirmation of thermal disequilibrium between electron and neutral gases was obtained in 1962 and 1963 from rocket experiments with plasma probes [5, 6]. At about the same time incoherent scatter radar measurements also showed the absence of thermal equilibrium between electrons and ions [7, 8]. A typical result taken from later rocket measurements [9] is shown in *Fig. 22.1*. While there is still some doubt of the validity of the rocket results below 150 km, it is clear that the major prediction of the photoelectron heating theory is correct; the electron temperature is substantially elevated above the neutral gas temperature over a wide altitude range.

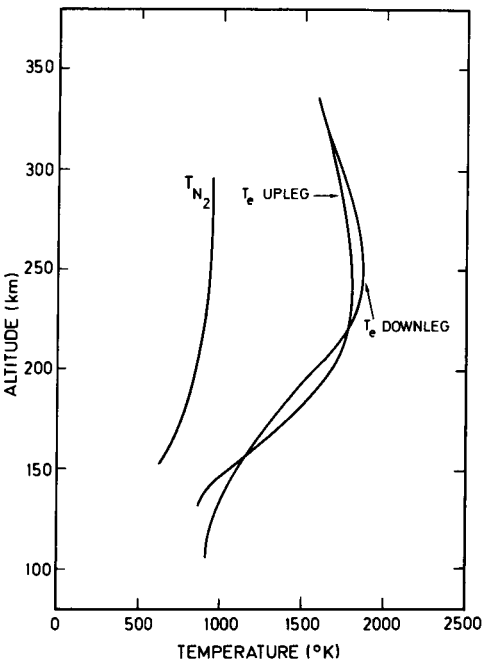


Fig. 22.1 Molecular nitrogen and electron temperatures from the NASA 6.07 rocket probe [9] of April 18, 1963 at 16:04 EST at Wallops Island, Virginia ($X = 60°$).

Later developments in the theory of ionospheric temperatures have sketched more accurately the roles of various processes. An important contribution was the deduction [10] that electron heat conduction is important in maintaining $T_e > T_n$ even at very high altitudes where the local energy production is small. It was also recognized that substantial numbers of photoelectrons could escape the upper atmosphere and travel along the

lines of magnetic force into the magnetosphere. These energetic electrons heat the electron gas at great altitudes and, in the absence of high altitude energy loss processes, this thermal energy is removed by conduction along the lines of magnetic force back into the ionosphere [11].

Although photoelectrons are able to heat the ambient electron gas, they do not transfer a significant amount of energy to the ion gases. The thermal electrons, on the other hand, provide an important heat source for the ions and thermal equilibrium between ions and neutral particles is found only in the regions below 300 km where the ion gases are rapidly cooled by the neutral atmosphere [10]. At low altitudes it is observed that $T_i \simeq T_n$. Above 300 km the energy given to the ions by the electron gas can be dissipated only if $T_i > T_n$. Thus, a transitional behavior for T_i is expected [12], with T_i approaching T_e near 600 to 800 km, depending upon the specific ionic composition involved.

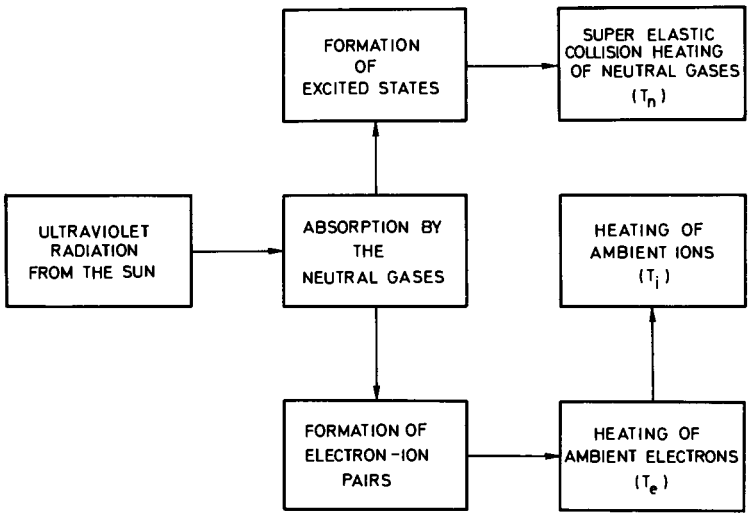


Fig. 22.2 Energy sources for the electrons, ions, and neutral particles within the ionosphere.

The overall flow of thermal energy in the upper atmosphere and ionosphere described in the preceding paragraphs has been summarized in *Fig. 22.2*. At low and middle magnetic latitudes most of the heating for both the neutral and ionized gas originates from solar ultraviolet radiation. Absorption of these short wavelength photons leads to enhanced neutral gas and plasma temperatures [13]. At high latitudes electric fields having

their source in the magnetosphere are responsible for considerable Joule dissipation which may be more important in these regions than solar ultraviolet radiation [14, 15].

In the following sections attention will be given to each of the important aspects of the thermal balance of the ionosphere.

22.2 Energy Balance Equations

Consider a plasma composed of electrons, several ion species, and neutral gases, each of which is described by a displaced Maxwellian velocity distribution function in terms of the density n_r, temperature T_r, and bulk flow velocity $\mathbf{C}_r$. For this model the energy balance equation for each species can be derived from Boltzmann's equation as [16]

$$\tfrac{3}{2}n_r k\,\partial T_r/\partial t + \tfrac{3}{2}n_r k\mathbf{C}_r \cdot \nabla T_r + n_r k T_r \nabla \cdot \mathbf{C}_r + \nabla \cdot \boldsymbol{\phi}_r = M_r - \mathbf{A}_r \cdot \mathbf{C}_r \tag{22.1}$$

where n_r is the gas number density, T_r the gas temperature relative to a surface moving with velocity $\mathbf{C}_r$, $\mathbf{C}_r$ the rth species transport velocity, $\boldsymbol{\phi}_r$ the rth species heat flux vector,

$$M_r = \tfrac{1}{2}\int m_r \mathbf{v}_r \cdot \mathbf{v}_r (\partial f_r/\partial t)_c \, d\mathbf{v}_r$$

is the kinetic energy moment of the collision term of Boltzmann's equation, and

$$\mathbf{A}_r = \int m_r \mathbf{v}_r (\partial f_r/\partial t)_c \, d\mathbf{v}_r$$

is the momentum moment of the collision term of Boltzmann's equation.

Equation (22.1) is often rewritten in another form to eliminate the friction term $\mathbf{A}_r \cdot \mathbf{C}_r$ from the right-hand side. Using the momentum equation

$$n_r m_r D\mathbf{C}_r/Dt + \nabla p_r + n_r m_r \mathbf{F}_{\text{ext}} = \mathbf{A}_r \tag{22.2}$$

where $\mathbf{F}_{\text{ext}}$ represents the external mechanical forces acting on the rth species [usually gravity and electric and magnetic fields: see Equation (19.1)], Eq. (22.1) can be reduced to the form [17]

$$n_r(DE_r/Dt) - (\partial p_r/\partial t) = M_r + n_r \mathbf{F}_r \cdot \mathbf{C}_r - \nabla \cdot \boldsymbol{\phi}_r \tag{22.3}$$

where

$$E_r = \tfrac{5}{2}kT_r + \tfrac{1}{2}mC_r^2 \tag{22.4}$$

and

$$DE_r/Dt = (\partial E_r/\partial t) + \mathbf{C}_r \cdot \nabla E_r \tag{22.5}$$

is the time derivative following the rth species motion.

The advantage of (22.3) lies in the more simplified separation of density and temperature effects and the explicit inclusion of external forces. However, (22.1) and (22.3) are entirely equivalent and lead to the same description of temperature variations in dynamical systems.

The term M_r in both forms of the energy balance equation represents the effects of energy exchange between gas components. This includes energy transfer due to differing gas temperatures as well as part of the collisional transfer of energy resulting from gases having different mean flow velocities. Although specific expressions for M_r depend upon the choice of cross section, the general form of the energy exchange term is, including s species,

$$M_r = \sum_s M_{rs} \tag{22.6}$$

where for elastic collisions,

$$\begin{aligned} M_{rs} = {} & [2m_r m_s/(m_r + m_s)^2]n_r\bar{\nu}_{rs}[\tfrac{3}{2}k(T_s - T_r)f(v/\alpha) \\ & + \tfrac{1}{2}(m_s\mathbf{C}_s + m_r\mathbf{C}_r) \cdot (\mathbf{C}_s - \mathbf{C}_r)g(v/\alpha)] \end{aligned} \tag{22.7}$$

with $\bar{\nu}_{rs}$ the momentum transfer collision frequency of Eq. (9.33). Also,

$$v = |\,\mathbf{C}_s - \mathbf{C}_r\,| \tag{22.8}$$

$$\alpha^2 = 2k[(T_r/m_r) + (T_s/m_s)] \tag{22.9}$$

and $f(v/\alpha)$ and $g(v/\alpha)$ are functions determined by the velocity dependence of the interaction cross section.

For the particular case of particles which have an inverse velocity dependent cross section (see the discussion of ion-neutral collisions in Section 9.6) Eq. (22.7) can be written as

$$M_{rs} = [2m_r m_s/(m_r + m_s)^2]n_r\bar{\nu}_{rs}[\tfrac{3}{2}k(T_s - T_r) + \tfrac{1}{2}(m_s\mathbf{C}_s + m_r\mathbf{C}_r) \cdot (\mathbf{C}_s - \mathbf{C}_r)] \tag{22.10}$$

eliminating the high speed correction terms altogether. Using the results of Chapter 19 for $\mathbf{A}_r$ for the same inverse velocity-dependent cross section,

the rth species energy balance equation becomes

$$\tfrac{3}{2}n_r k(\partial T_r/\partial t) + \tfrac{3}{2}n_r k\mathbf{C}_r \cdot \nabla T_r + n_r k T_r \nabla \cdot \mathbf{C}_r + \nabla \cdot \boldsymbol{\phi}_r = \sum_s [2m_r m_s/(m_r + m_s)^2] n_r \bar{\nu}_{rs} [\tfrac{3}{2}k(T_s - T_r) + \tfrac{1}{2}m_s(\mathbf{C}_s - \mathbf{C}_r)^2]. \quad (22.11)$$

This result shows explicitly the effects of thermal energy transfer and the possibilities of converting the kinetic energy of relative motion into heat. Such a process is important, for example, in the polar E region where electric fields can move ions with a substantial velocity relative to the neutral gas. For such a situation the rise in ion temperature is, as discussed later, approximately

$$T_i - T_n = m_n(\mathbf{C}_n - \mathbf{C}_i)^2/3k. \quad (22.12)$$

Returning to Eq. (22.11), analysis of the second term on the right side of the equation shows that it accounts for the dissipation of translational kinetic energy as thermal energy; i.e., it represents the rth species portion of Joule heating. From the form of this equation it can be found that a fraction $m_s/(m_r + m_s)$ of the total Joule heating is given to the rth species. Using (22.11) and including both the r and s gases, the total Joule heating in a two-component system is

$$\text{Joule heating rate} = \mu_{rs}\bar{\nu}_{rs} n_r (\mathbf{C}_s - \mathbf{C}_r)^2 \quad (22.13)$$

where μ_{rs} is the reduced mass.

It can also be noted that while the right side of Eq. (22.1) appears to be asymmetric in $\mathbf{C}_r$, the final result given by (22.11) depends only upon the relative speed $|\mathbf{C}_s - \mathbf{C}_r|$.

The alternate form for the energy balance equation is given by Eq. (22.3). Using the special relations developed immediately preceding, we have

$$n_r(DE_r/Dt) - (\partial p_r/\partial t) = n_r \mathbf{F}_r \cdot \mathbf{C}_r - \nabla \cdot \boldsymbol{\phi}_r + \sum_s \frac{2m_r m_s}{(m_r + m_s)^2} n_r \bar{\nu}_{rs} [\tfrac{3}{2}k(T_s - T_r) + \tfrac{1}{2}(m_s\mathbf{C}_s + m_s\mathbf{C}_r) \cdot (\mathbf{C}_s - \mathbf{C}_r)]. \quad (22.14)$$

Equations (22.11) and (22.14) have been developed for the particular cross section which depends inversely upon relative speed. Explicit results are also available for other cross sections; for example, hard sphere and

Coulomb collisions. Expressions for the energy transfer term for these interactions are given below using the form of Eq. (22.7) [16, 18]:

Hard Sphere Interaction:

$$f\left(\frac{v}{\alpha}\right) = \frac{\pi^{1/2}}{2}\left(\frac{v}{\alpha} + \frac{\alpha}{2v}\right)\operatorname{erf}\left(\frac{v}{\alpha}\right) + \frac{1}{2}\exp\left(-\frac{v^2}{\alpha}\right) \tag{22.15}$$

$$g\left(\frac{v}{\alpha}\right) = \frac{3\pi^{1/2}}{8}\left(\frac{v}{\alpha} + \frac{\alpha}{v} - \frac{\alpha^3}{4v^3}\right)\operatorname{erf}\left(\frac{v}{\alpha}\right) + \frac{3}{8}\left(1 + \frac{\alpha^2}{2v^2}\right)\exp\left(-\frac{v^2}{\alpha^2}\right) \tag{22.16}$$

$$\bar{\nu}_{rs} = \frac{4}{3}n_s\left[\frac{8k}{\pi}\left(\frac{T_r}{m_r} + \frac{T_s}{m_s}\right)\right]^{1/2}\pi\sigma^2 \tag{22.17}$$

Coulomb Interaction:

$$f(v/\alpha) = \exp(-v^2/\alpha^2) \tag{22.18}$$

$$g\left(\frac{v}{\alpha}\right) = \frac{3\pi^{1/2}}{4}\left(\frac{\alpha}{v}\right)^3\operatorname{erf}\left(\frac{v}{\alpha}\right) - \frac{3}{2}\left(\frac{\alpha}{v}\right)^2\exp\left(-\frac{v^2}{\alpha^2}\right) \tag{22.19}$$

$$\bar{\nu}_{rs} = \frac{16\pi^{1/2}}{3}\frac{n_s Z_r^2 Z_s^2 e^4 \ln \Lambda}{\mu\alpha^{3/2}}. \tag{22.20}$$

Up to this point, the effect of an external magnetic field has been introduced only through the term $\mathbf{F}_{\text{ext}}$ of (22.14). The principal consequence of such a field is found in the heat flow vector $\boldsymbol{\phi}_r$ which, as the ratio of the collision frequency to gyrofrequency becomes small, becomes increasingly anisotropic so that most heat flow is parallel to the magnetic field. Since electron or ion heat conduction is seldom important below 150 km it is sometimes useful to consider the energy balance equation in terms of a cylindrical coordinate system whose axis is parallel to the magnetic field. If changes of intensity of **B** are taken into account, the heat balance equation can be expressed as

$$\frac{3}{2}n_r k\frac{\partial T_r}{\partial t} + \frac{3}{2}n_r k w_r\frac{\partial T_r}{\partial s} + \frac{n_r k T_r}{A}\frac{\partial A w_r}{\partial s} - \frac{1}{A}\frac{\partial}{\partial s}\left(AK_r\frac{\partial T_r}{\partial s}\right)$$
$$= \sum \frac{2m_r m_s}{(m_r + m_s)^2}n_r\bar{\nu}_{rs}\left[\frac{3}{2}k(T_s - T_r) + \frac{1}{2}m_s(\mathbf{C}_s - \mathbf{C}_r)^2\right] \tag{22.21}$$

where s is a coordinate parallel to **B**, $A \propto |\,\mathbf{B}\,|^{-1}$, K_r is the rth species thermal conductivity, w_r is the velocity component parallel to **B**, and the collision term of Eq. (22.10) has been chosen.

22.3 The Electron Energy Balance

The principal heat source for the ionosphere above 150 km arises from the kinetic energy given to photoelectrons in the photoionization of the neutral gases of the upper atmosphere. The general outline of the problem can be made as follows [19]: First, knowing the ultraviolet flux spectrum of the sun, the composition of the neutral atmosphere, and the relevant ionization and absorption cross sections, it is necessary to calculate the initial photoelectron energy spectrum. Next, by taking into account photoelectron collisions with ions, electrons, and neutral particles, the steady-state electron energy distribution must be found as a function of altitude. From the energy distribution thus obtained both the electron number density and kinetic temperature can be derived.

In practice, the precise calculation of the complete electron energy distribution is too complicated to undertake and certain approximations have normally been made to separate the electron gas into two distinct components: First, a low energy ($\bar{\varepsilon} \sim 0.01$–$0.3$ eV) Maxwellian distribution having some characteristic temperature, T_e, and, second, a collection of much more energetic electrons arising from photoionization which lie far out in the tail of the ambient electron energy distribution. In this model the energetic electrons introduce heat into the ambient electrons by means of electron–electron collisions and superelastic electron–excited particle collisions. Although this arbitrary segregation of electrons according to characteristic energies leads to somewhat ambiguous results in the range 0.5–1.5 eV, on the whole it is well justified as a result of the small degree of interaction between thermal electrons and those of energy greater than a few electron volts.

The rate of energetic electron energy loss by means of elastic electron–electron collisions is [20, 21]

$$d\varepsilon/dt = -(2\sqrt{2}\,\pi n_e e^4 \ln G)/(m_e\varepsilon)^{1/2} \tag{22.22}$$

or

$$d\varepsilon/dt = -7.7\times 10^{-6}(n_e \ln G/\varepsilon^{1/2}) \quad \text{eV sec}^{-1} \tag{22.23}$$

where ε is the photoelectron energy in electron volts, n_e is the ambient electron density, and G is obtained from the conditions

$$G = \frac{m_e v_e^3}{\gamma e^2 \omega_p} \qquad kT_e \ll \varepsilon < \frac{m_e^4}{2\hbar^2}, \tag{22.24}$$

$$G = \frac{m_e v_e^2}{\hbar\omega_p} \qquad \varepsilon > \frac{m_e e^4}{2\hbar^2} \quad (\sim 14 \text{ eV}) \tag{22.25}$$

where $\omega_p^2 = (4\pi n_e e^2/m_e)$, ln γ is Euler's constant, and $\hbar$ is Planck's constant divided by 2π. Values of ln G are substantially greater than those for ln Λ (see Section 9.7); i.e., a range (21 ± 2) applies over the range $2 < \varepsilon < 30$ eV.

When a flux Φ of fast electrons of energy ε passes through a thermal electron gas, energy is given to the ambient electrons by means of Coulomb collisions at the rate

$$P_e = (2 \pm 0.5) \times 10^{-12}(n_e \Phi/\varepsilon) \quad \text{eV cm}^{-3}\,\text{sec}^{-1} \tag{22.26}$$

where ε is the fast electron energy in electron volts and $\varepsilon \gg \frac{3}{2} n_e k T_e$. For photoelectrons escaping the neutral atmosphere and traveling along magnetic field lines into the magnetosphere, (22.26) can be used to calculate the rate of local heat production. In fact, within the magnetosphere (22.26) may represent a lower limit to the local energy production since other plasma processes may act to enhance energetic particle thermalization.

The energy balance equations of the last section have emphasized the importance of elastic collisions. While such an approach is adequate to describe the interactions of ions and neutral particles, energy transfer processes involving electrons are more complex. Several factors contribute to this situation. First, because of the mass factors of (22.11) electron energy exchange via elastic collisions is slow, while the available excitation channels with neutral atoms and molecules are rapid. Thus, as described in Section 22.6, phenomenological energy loss rates involving inelastic collisions tend to be most important for thermal energy loss [22]. Second, as described above, the principal heat source for the thermal electron gas is energetic electrons whose energy spectrum varies with aeronomic conditions and cannot be given a simple analytic form.

As a consequence of these factors, the electron energy balance is best described in the form [23, 24]

$$\begin{aligned} \tfrac{3}{2} n_e k \frac{\partial T_e}{\partial t} + \tfrac{3}{2} n_e k \mathbf{C}_e \cdot \nabla T_e + n_e k T_e \nabla \cdot \mathbf{C}_e + \nabla \cdot \boldsymbol{\phi} \\ = P_e - L_e + \sum_s m_e n_e \bar{\nu}_{es} (\mathbf{C}_s - \mathbf{C}_e)^2 \end{aligned} \tag{22.27}$$

where P_e is the rate of thermal energy production due to photoelectrons or other mechanisms other than Joule dissipation or a combination of these, L_e the rate of energy loss due to inelastic and elastic collisions, and $\sum_s m_e n_e \bar{\nu}_{es} (\mathbf{C}_s - \mathbf{C}_e)^2$ is the rate of energy production due to elastic thermal electron collisions with neutral gases and ions: Joule dissipation.

In the following section a discussion is given of ionospheric photoelectrons and the processes affecting the rate of thermal energy production in the electron gas. Expressions for electron energy loss are then given in a subsequent section.

22.4 Photoelectrons

The initial source spectrum of photoelectrons generally reflects the gross features of the spectral distribution of solar photons, but considerable local distortion occurs as a result of the many different thresholds and ionization energies for the atmospheric gases [13, 25]. Since a given singly charged ion may have several internal energy states above the ground state, a given photoionization can yield a photoelectron having one of several possible energies, depending upon the energy of the original photon and the relative cross sections for different ionization states.

The photoelectron energy ε, arising from a photon of energy $h\nu$, is given by

$$\varepsilon = h\nu - I_p \tag{22.28}$$

where I_p is the ionization potential of the particular ion state. *Table 22.1* lists the ionization potentials for the atmospheric gases [26] but does not indicate the relative probabilities for photoelectrons of different energies when more than one ionization state is accessible; such information is difficult to obtain either from experiment or theory.

The importance of the various ionization states lies in the possibility that the photoelectron energy may, in the excitation of a higher than ground level energy state, be less than that calculated by assuming only a single ionization threshold. An upper limit can always be placed on the photoelectron heating rate, however, by assuming that only ground state ionizations occur and that all photoelectron energy is given to the ambient electrons.

In the absence of adequate cross section data, several semiquantitative methods have been used to evaluate the relative excitation probabilities for the different ion states. Although the first studies assumed probabilities in proportion to the statistical weights of the available channels [19], further modifications have been made by different authors on the basis of new information [25, 27, 28]. The results of a recent study [28] are listed in *Table 22.2* and have been used in the literature to obtain estimates of the photoelectron energy spectrum. A plot of the initial energy spectra of photoelectrons at different altitudes for an overhead sun is given in *Fig. 22.3*.

TABLE 22.1

IONIZATION THRESHOLDS FOR ATMOSPHERIC IONS

Neutral gas	Ion state	Threshold	
		(eV)	(Å)
$H(^2S)$	p	13.6	910
$He(^1S)$	$He^+(^1S)$	24.8	504
$O_2(^3\Sigma_g^-)$	$O_2^+(^2\Pi_g)$	12.1	1026
	$O_2^+(^4\Pi_u)$	16.1	770
	$O_2^+(^2\Pi_u)$	17.0	737
	$O_2^+(^4\Sigma_g^-)$	18.2	682
	$O_2^+(^2\Pi_u)$	28.5	435
	$O_2^+(^2\Pi_g)$	~40	310
$N_2(^1\Sigma_g^+)$	$N_2^+(^2\Sigma_g^+)$	15.6	796
	$N_2^+(^2\Pi_u)$	16.7	743
	$N_2^+(^2\Sigma_g^+)$	~35	354
$O(^3P)$	$O^+(^4S)$	13.6	910
	$O^+(^2D)$	16.9	732
	$O^+(^2P)$	18.6	665
	$O^+(^4P)$	28.5	435
	$O^+(^2P)$	40	310

TABLE 22.2

RELATIVE PROBABILITIES FOR PHOTOIONIZATION STATES

Ion state	Threshold (eV)	Statistical weights	Computations[a]
$O^+(^4S)$	13.6	1	1.0
$O^+(^2D)$	16.9	2.5	1.5
$O^+(^2P)$	18.6	1.5	1.0
$O^+(^4P)$	28.5	3.0	0.4
$O^+(^2P)$	40	1.5	0.3
$O_2^+(^2\Pi_g)$	12.1	1.0	1.0
$O_2^+(^4\Pi_u)$	16.1	2.0	0.67
$O_2^+(^2\Pi_u)$	17.0	1.0	0.33
$O_2^+(^4\Sigma_g^-)$	18.2	1.0	0.30
$N_2^+(^2\Sigma_g^+)$	15.6	1.0	1.0
$N_2^+(^2\Pi_u)$	16.7	2.0	2.0
$N_2^+(^2\Sigma_g^+)$	18.8	1.0	0.27

[a] Shea *et al.* [28].

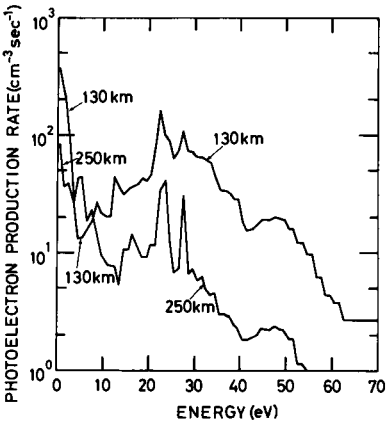


Fig. 22.3 Initial energy spectrum of photoelections at two altitudes for an overhead sun and 1250°K model thermosphere. The strong peaks between 20 and 30 eV arise from He(II)(304) [32].

The photoelectron energies and excitation probabilities corresponding to the photon ranges of Chapter 7 are shown in *Table 22.3.*

Using the photoionization rates developed in Chapter 7 for each of the solar spectral ranges given in Table 22.3, the average photoelectron energy at zero optical depth can be calculated. The results are:

$$O_2: \ \bar{\varepsilon}_p = 21 \ \text{eV} \qquad N_2: \ \bar{\varepsilon}_p = 19 \ \text{eV} \qquad O: \ \bar{\varepsilon}_p = 14 \ \text{eV}.$$

TABLE 22.3

PHOTOELECTRON ENERGIES AND EXCITATION PROBABILITIES

Spectral range	Mean energy (eV)	O_2	N_2	O
Lyman β (1025.7 Å)	12.1	0	0	0
C(III) (977 Å)	12.7	0.6 (1.0)	0	0
Lyman continuum	13.6	1.1 (1.0)	0	0
910–796 Å	14.6	2.5 (1.0)	0	1.0 (1.0)
796–665 Å	17.1	5.0 (0.6)	1.1 (1.0)	2.65 (0.45)
		1.0 (0.4)		4.15 (0.29)
				0.85 (0.26)
665–375 Å	26	14 (0.6)	9.8 (0.8)	12.2 (0.29)
		10 (0.4)	7.0 (0.2)	8.9 (0.45)
				7.2 (0.20)
375–275 Å	39	37 (0.6)	23.0 (0.8)	25.4 (0.30)
		33 (0.4)	20.2 (0.2)	22.1 (0.47)
				20.9 (0.23)
275–150 Å	64	52 (0.6)	48.0 (0.8)	50.4 (0.32)
		48 (0.4)	45 (0.2)	47.1 (0.42)
				45.4 (0.26)

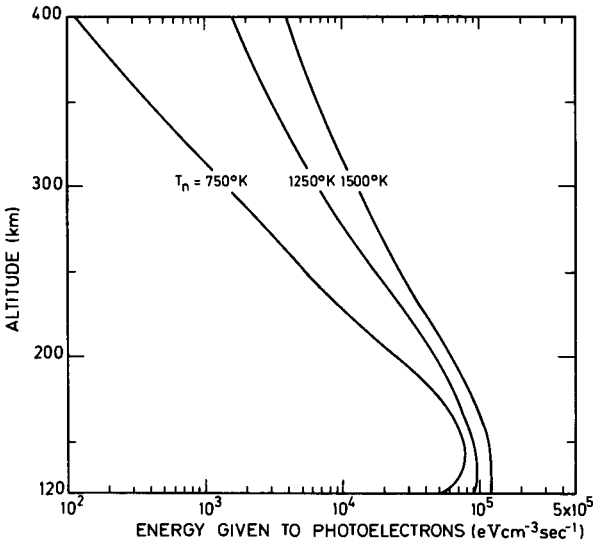


Fig. 22.4 Initial photoelectron energy production rates for three model neutral atmospheres. The photoionization channels leading to ion states above the ground state were included in these calculations.

TABLE 22.4

INITIAL PHOTOELECTRON KINETIC ENERGY[a]

Altitude (km)	750°K	1250°K	1500°K
120	5.6(4)[b]	9.2(4)	1.2(5)
150	7.5(4)	8.8(4)	1.2(5)
200	2.4(4)	4.6(4)	6.1(4)
250	5.4(3)	1.7(4)	2.6(4)
300	1.4(3)	6.6(3)	1.3(4)
350	4.0(2)	3.0(3)	6.8(3)
400	1.1(2)	1.6(3)	4.0(3)
450	3.3(1)	6.1(2)	2.4(3)
500	1.2(1)	3.0(2)	7.4(2)

[a] Values are in eV cm^{-3} sec^{-1}.
[b] 5.6(4) = 5.6 × 10^4.

Calculations have been made of the rate at which photoelectron energy is created at various altitudes in the atmosphere for several model neutral atmospheres. The results, shown in *Fig. 22.4* and tabulated in *Table 22.4*, indicate the general trend toward larger production rates with the hotter model atmospheres with both changes in relative composition and in the strength of the ionizing fluxes in the different spectral ranges being taken into account.

The preceding estimates of the initial kinetic energy given to photoelectrons serve only to indicate the maximum possible energy production rates for the ambient electron gas. In fact, as soon as the photoelectrons are created significant energy losses occur, with photoelectrons losing most of their excess kinetic energy in excitation of N_2 and O_2 with only a modest proportion of the original energy being eventually deposited in the thermal electron gas.

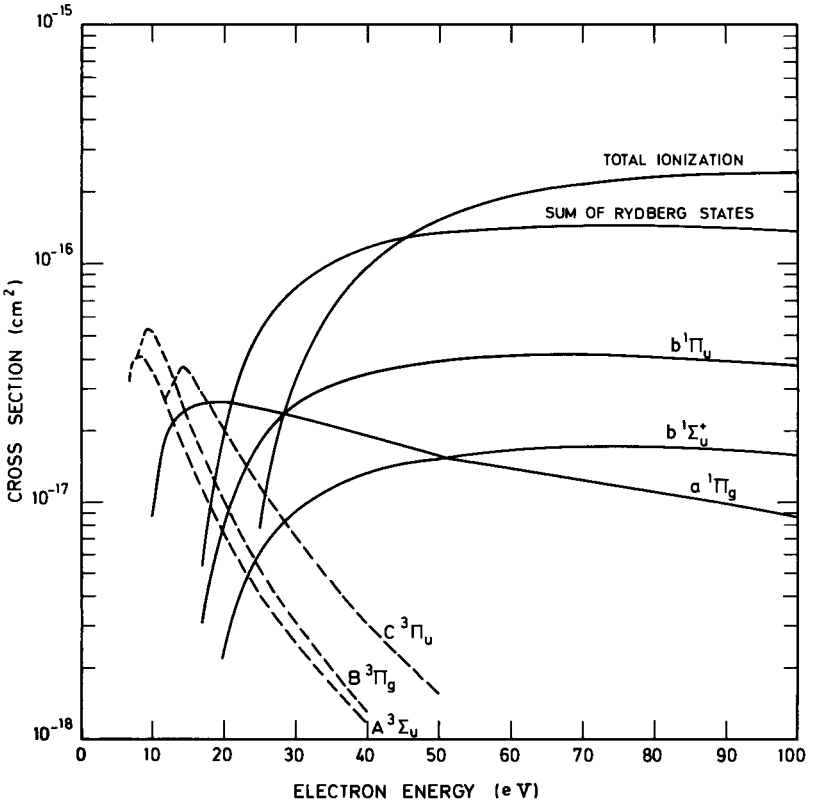


Fig. 22.5 Cross sections for electron energy loss in molecular nitrogen.

Detailed studies of the slowing down of fast photoelectrons have been reported in the literature and these take into account ionization and the excitation of electronic, vibrational, and rotational states of N_2, O_2, and O [19, 27, 29–33]. Cross sections associated with these different processes are shown in *Figs. 22.5–22.7* and described in Chapter 9. Essentially, above 4 to 6 eV fast electrons lose most of their excess energy through excitation of N_2, O_2, and O electronic states. For energies below 4 to 6 eV the chief

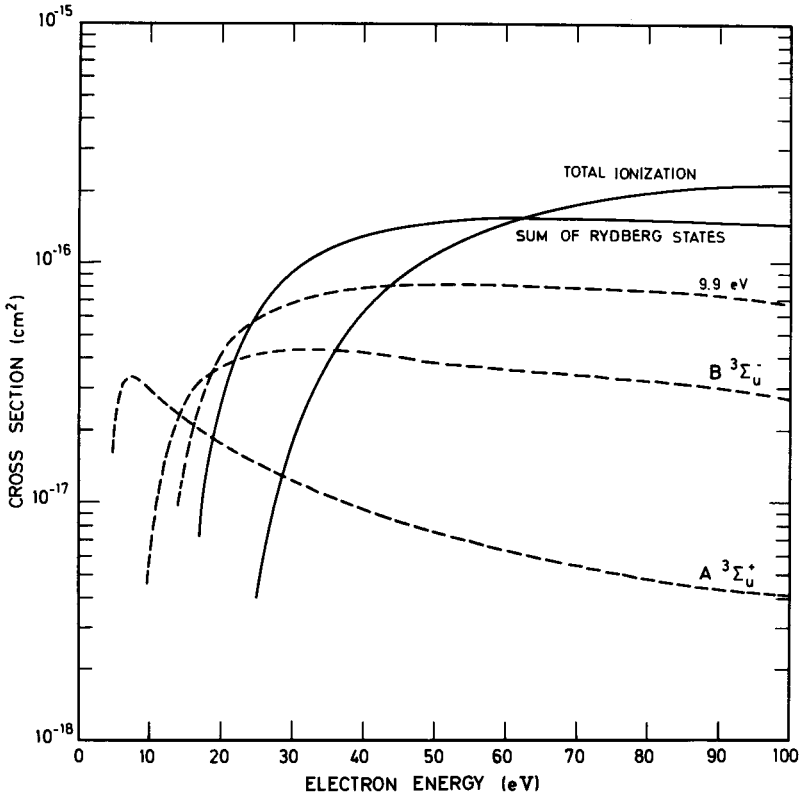


Fig. 22.6 Cross sections for electron energy loss in molecular oxygen.

energy loss occurs through vibrational excitation of N_2, although rotational excitation cannot be altogether excluded. Below 2 eV the cross section for vibrational excitation of N_2 decreases rapidly to small values and the final stage of photoelectron thermalization must continue through elastic collisions with electrons, ions, and neutrals, as well as a variety of rotational and vibrational processes in N_2 and O_2.

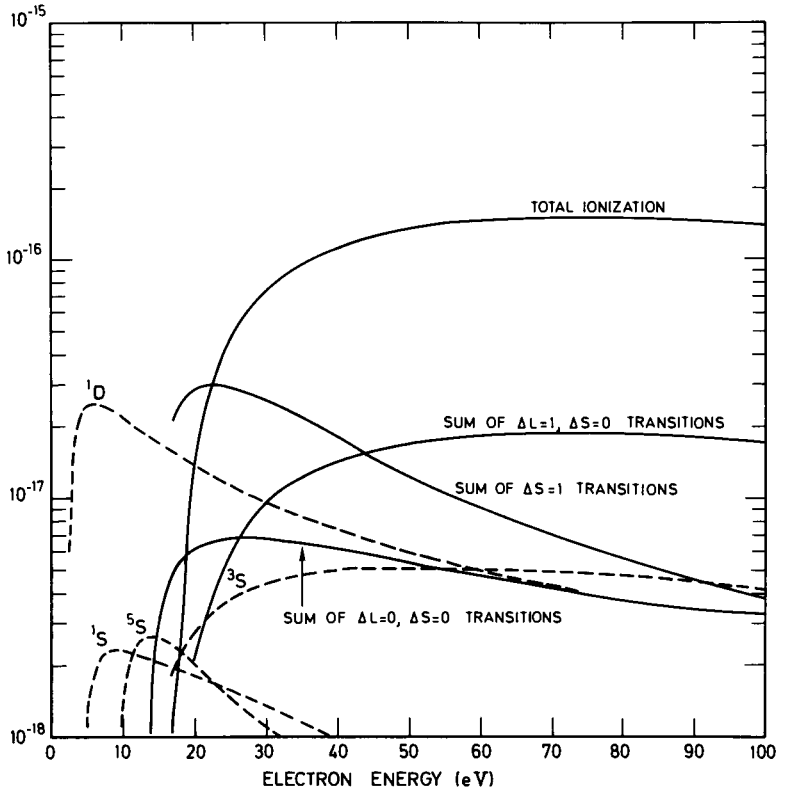


Fig. 22.7 Cross sections for electron energy loss in atomic oxygen.

Typical photoelectron energy spectra calculated for low altitudes using the different production and loss processes are shown in *Fig. 22.8.*

Photoelectrons with energies less than several electron volts tend to lose their energy by elastic collisions to ambient electrons rather than ions or neutral particles. On the other hand, if rapid inelastic processes such as rotational or vibrational excitation are involved, energy loss to neutrals can be more rapid.

This latter condition is generally true below about 150 km in the ionosphere where almost all of the initial photoelectron energy is expended in inelastic electron–molecule collisions. Above 150 km proportionately more energy is given to ambient electrons due primarily to photoelectrons which have cooled to about 1.5 eV; that is, below the energy of maximum vibrational excitation for N_2. At progressively higher altitudes the neutral gas densities become exponentially less dense and electron–electron collisions

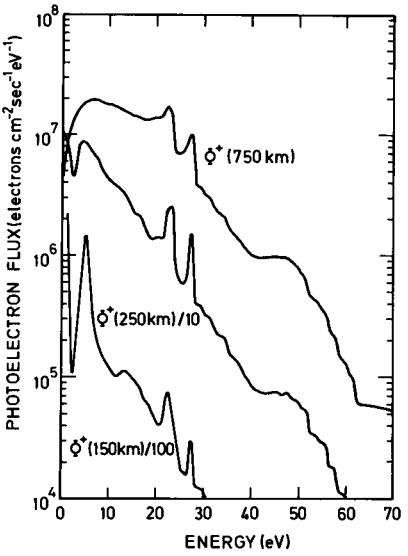


Fig. 22.8 Daytime photoelectron energy spectra at 150, 250, and 750 km for a 750°K model thermosphere and overhead sun ($\chi = 0°$) [32].

become proportionately more important, converting a greater fraction of the initial photoelectron kinetic energy into electron gas thermal energy.

Measurements of photoelectron energy spectra have been made with rocket and spacecraft experiments for a variety of atmospheric conditions and solar illumination angles [34–37]. A comparison of recent theoretical and experimental results is shown in *Fig. 22.9*. In general, the theoretical spectra give a more jagged appearance than that actually observed. At energies less than 10 eV experiments tend to show more electrons than calculated, possibly resulting in more thermal electron heating than expected.

22.4.1 Local Photoelectron Heating

Consider the ionizing effect of a single ultraviolet spectral line of flux Φ incident upon a neutral atmosphere of density n_n. If σ_i and σ_a are the cross sections for ionization and absorption ($\sigma_a \geq \sigma_i$), then the local ionization rate q is

$$q = n_n \sigma_i \Phi e^{-\tau} \tag{22.29}$$

where the optical depth τ is given by

$$\tau = \int_z^\infty n_n \sigma_a \, ds \tag{22.30}$$

with the integration being along the optical ray path. If $\varepsilon(z)$ is the energy per photoionization given locally to the electron gas, then the rate of heat

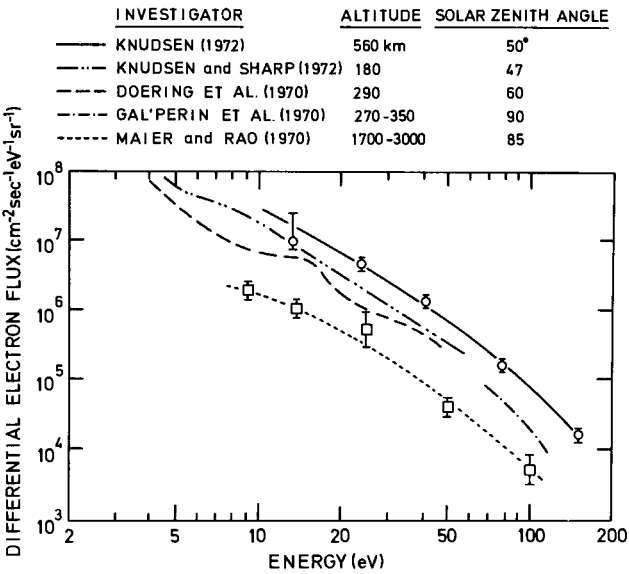


Fig. 22.9 Experimental values for the differential photoelectron flux at various altitudes and solar zenith angles [36].

input, $P(z)$, is

$$P(z) = \varepsilon(z) n_n \sigma_i \Phi e^{-\tau} \tag{22.31}$$

Equation (22.31) can be applied to the particularly simple case of an isothermal hydrostatic neutral atmosphere of temperature T_n;

$$n_n = n_n^a \exp(-z/H_n) \tag{22.32}$$

where $H_n = kT_n/m_n g$ is the scale height, g is the acceleration of gravity, and z is the distance above the point of density n_n^a. The rate of heat input to the electron gas is

$$P(z) = \varepsilon(z) n_n^a \Phi \sigma_i \exp[-(z/H_n) - n_n^a \sigma_a e^{-z/H_n}] \tag{22.33}$$

which is similar in form to a Chapman layer.

At low altitudes where optical depth effects are important $P(z)$ depends strongly upon the form of $\varepsilon(z)$, which is not known in great detail. In any case, due to the absorption of the solar radiation, $P(z) \to 0$ as $z \to -\infty$. At high altitudes, usually above 200 km, the absorption term in the brackets of (22.33) becomes small and

$$P(z) = \varepsilon(z) n_n \sigma_i \Phi \tag{22.34}$$

showing that $P(z)$ must decline with the neutral gas scale height since $\varepsilon(z)$

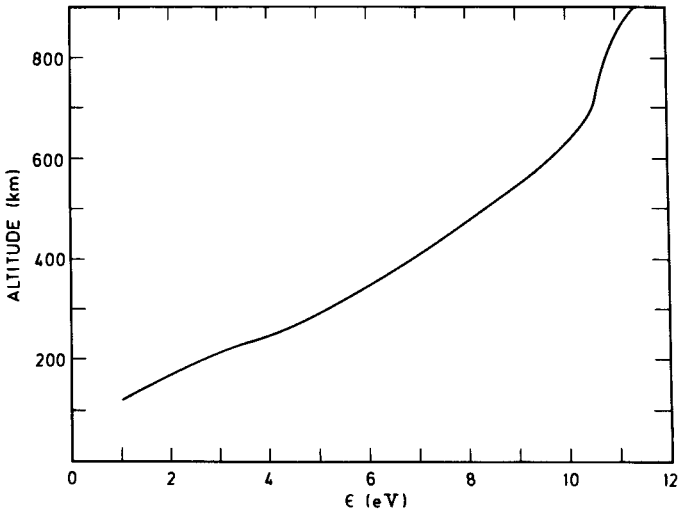


Fig. 22.10 Altitude profile of the mean electron gas heating energy per photoionization calculated for 1200 EST, July 1963, at Millstone Hill, Massachusetts [27].

is limited by the total amount of kinetic energy available in the photoelectron. To illustrate, a typical altitude profile for $\varepsilon(z)$ is shown in *Fig. 22.10*, along with a calculated profile for electron gas energy production in *Fig. 22.11*.

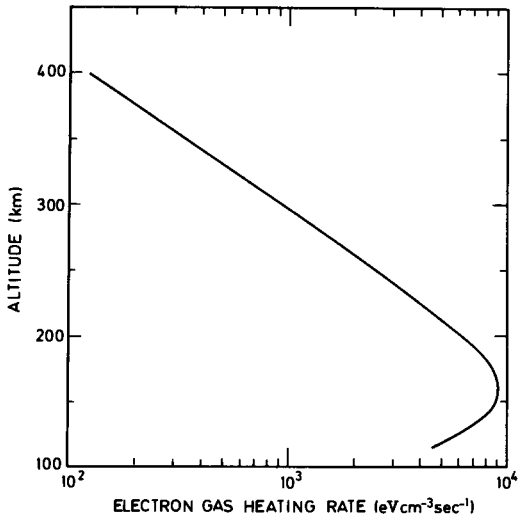


Fig. 22.11 Altitude profile of the total electron gas heating rate derived for 0800 EST, July 1963, at Millstone Hill, Massachusetts [27]. $T_n(\infty) = 766°K$; $\chi = 50.2°$.

22.4.2 Photoelectron Transport

The electron gas heating theory presented above is based on the assumption that photoelectrons lose their excess energy in the same spatial region where they are created; the migration of photoelectrons toward regions of lower neutral gas density is neglected. Transport and eventual atmospheric escape of photoelectrons can be expected to occur, however, in those regions of the atmosphere where the electron free path λ_e approaches or is larger than the scale height H_n of the neutral atmosphere [10]. If one adopts a total scattering cross section of 5×10^{-16} cm^2 for atomic oxygen, the dominant neutral gas in the regions where photoelectron escape occurs, one finds that the condition $\lambda_e = H_n$ obtains at the altitude where $n(O) \simeq 10^{11}/T_n$ cm^{-3}. Using the model atmospheres discussed previously, it is found that photoelectron escape develops near 300 to 350 km altitude. In this region and above photoelectrons can spiral along the geomagnetic field lines out of the neutral atmosphere into the magnetosphere. The escaping fast electrons represent a loss of energy from the atmosphere but, by depositing their energy in high altitude regions where the local heating rate is small, they increase the local electron heating rate above the value which would be found if the escaping flux were neglected [38–43].

Detailed theories of photoelectron transport have been developed in the literature [31, 32, 38, 44]. A reasonable estimate of the magnitude of the escaping photoelectron flux can be made on the basis of a simple absorption and scattering model [45]. Suppose that in traveling along the field lines, photoelectrons in a certain energy range ε, $\varepsilon + d\varepsilon$ interact with the neutral atmosphere through elastic scattering collisions of cross section σ_e and through inelastic collisions of cross section σ_a. The effect of an elastic collision is to alter the pitch angle of the incident electron. For isotropic scattering the probability of reversing the direction of a photoelectron per collision is $\frac{1}{2}$. For a simple model, consider only two angular sectors corresponding to photoelectrons traveling either up or down a field line. Backscattering by elastic collisions is assumed to be the fraction $p_e\sigma_e$ where $p_e \leq 1$ and $p_e = \frac{1}{2}$ for isotropic scattering, $p_e < \frac{1}{2}$ for preferential scattering in the original direction of motion, $p_e > \frac{1}{2}$ for preferential backscattering.

In addition to elastic scattering, inelastic processes occur which are assumed to remove the photoelectron from its original energy range; i.e., removal to a lower energy range is assumed to occur with a cross section σ_a. To describe the total steady state photoelectron flux, equations of continuity can be written for the upward (Φ^+) and downward (Φ^-) fluxes of

photoelectrons in the energy range ε, $\varepsilon + d\varepsilon$:

$$\frac{d\Phi^+}{ds} = \frac{-1}{\langle \cos\theta \rangle} \sum_k n_k [\sigma_a{}^k + p_e{}^k \sigma_e{}^k] \Phi^+ + \frac{1}{\langle \cos\theta \rangle} \sum_k n_k p_e{}^k \sigma_e{}^k \Phi^- + \frac{q}{2} + \frac{q^+}{\langle \cos\theta \rangle} \tag{22.35}$$

$$-\frac{d\Phi^-}{ds} = \frac{-1}{\langle \cos\theta \rangle} \sum_k n_k [\sigma_a{}^k + p_e{}^k \sigma_e{}^k] \Phi^- + \frac{1}{\langle \cos\theta \rangle} \sum_k n_k p_e{}^k \sigma_e{}^k \Phi^+ + \frac{q}{2} + \frac{q^-}{\langle \cos\theta \rangle} \tag{22.36}$$

where

$$\begin{aligned} \sigma_a{}^k &= \sum_j \sigma_{aj}^k \\ q^+(\varepsilon, s) &= \sum_k n_k(s) \sum_{\substack{j \\ E>\varepsilon}} \{p_{aj}^k(E)\sigma_{aj}^k(E \to \varepsilon)\Phi^-(E, s) \\ &\quad + [1 - p_{aj}^k(E)]\sigma_{aj}^k(E \to \varepsilon)\Phi^+(E, s)\} \\ q^-(\varepsilon, s) &= \sum_k n_k(s) \sum_{\substack{j \\ E>\varepsilon}} \{p_{aj}^k(E)\sigma_{aj}^k(E \to \varepsilon)\Phi^+(E, s) \\ &\quad + [1 - p_{aj}^k(E)]\sigma_{aj}^k(E \to \varepsilon)\Phi^-(E, s)\} \end{aligned} \tag{22.37}$$

and

s	is the distance along a magnetic field line (positive outward),
$\Phi^+(\varepsilon, s)$	is the photoelectron flux outward along s,
$\Phi^-(\varepsilon, s)$	is the photoelectron flux inward along s,
$n_k(s)$	is the kth species number density,
$p_e{}^k(\varepsilon)$	is the photoelectron backscatter probability for elastic collisions with the kth species,
$\sigma_e{}^k(\varepsilon)$	is the photoelectron total scattering cross section for elastic collisions with the kth species,
$q(\varepsilon, s)$	is the photoelectron production rate in the range ε to $\varepsilon + d\varepsilon$ due to direct ionization processes,
$q^\pm$	is the photoelectron production in the range ε to $\varepsilon + d\varepsilon$ due to cascading from higher energy photoelectrons undergoing inelastic collisions,
p_{aj}^k	is the photoelectron backscatter probability for collisions with the kth species resulting in the jth inelastic process,
σ_{aj}^k	is the inelastic cross section for the jth excitation of the kth particle species, and
$\langle \cos\theta \rangle$	is the mean pitch angle for Φ^+ and Φ^- photoelectrons.

Equations (22.35) and (22.36) provide a direct means for computing photoelectron energy spectra and fluxes in the ionosphere. These can then be used with Eq. (22.27) to compute the electron heating rate.

Numerical solutions to (22.35) and (22.36) are normally needed to include the many excitation cross sections and photoelectron production rates complicated by energy cascading [32, 46]. Analytic solutions for Φ^+ and Φ^- can be obtained, however, for a simple model of a single constituent, sunlit, isothermal atmosphere with photoelectrons produced at a single energy ε. Thus, from (22.35) and (22.36) the fluxes of electrons of energy ε can be derived as

$$\Phi^+ = \frac{I\langle\cos\theta\rangle}{2\sigma_a}\left\{1 - R\left[1 - \frac{2\sigma_a}{I\langle\cos\theta\rangle}\Phi^-(\infty)\right]e^{-H/\lambda}\right\} \tag{22.38}$$

$$\Phi^- = \frac{I\langle\cos\theta\rangle}{2\sigma_a}\left\{1 - R\left[1 - \frac{2\sigma_a}{I\langle\cos\theta\rangle}\Phi^-(\infty)\right]e^{-H/\lambda}\right\} \tag{22.39}$$

where

$$R = \frac{1 - [\sigma_a/(\sigma_a + 2p_e\sigma_e)]^{1/2}}{1 + [\sigma_a/(\sigma_a + 2p_e\sigma_e)]^{1/2}} \tag{22.40}$$

$$\lambda = \frac{\langle\cos\theta\rangle \sin I_d}{n_n[\sigma_a(\sigma_a + 2p_e\sigma_e)]^{1/2}} \tag{22.41}$$

and

I is the photoionization rate,
σ_a is the inelastic cross section,
H is the neutral gas scale height,
n_n is the neutral gas density,
I_d is the magnetic dip angle, and
$\Phi^-(\infty)$ is the downcoming photoelectron flux far from the atmosphere.

At low altitudes where $\lambda \ll H$, Eqs. (22.38) and (22.39) reduce to

$$\Phi^+ = \Phi^- = I\langle\cos\theta\rangle/2\sigma_a \tag{22.42}$$

showing no net transport of photoelectrons.

In the limit $z \to \infty$, the photoelectron escape flux, $\Phi^+(\infty)$, is found to be

$$\Phi^+(\infty) = [I\langle\cos\theta\rangle/2\sigma_a](1 - R) \tag{22.43}$$

so that elastic scattering actually reduces the photoelectron escape flux below values obtained in its absence.

If, in addition to photoelectrons produced in the local atmosphere, one introduces a downward electron flux $\Phi^-(\infty)$ such as might be present from a magnetically conjugate hemisphere the escape flux becomes

$$\Phi^+(\infty) = \frac{I\langle\cos\theta\rangle}{2\sigma_a}\left\{1 - R\left(1 - \frac{2\sigma_a}{I\langle\cos\theta\rangle}\Phi^-(\infty)\right)\right\} \tag{22.44}$$

showing that a fraction of the incident photoelectrons introduced as $\Phi^-(\infty)$ are scattered upward and escape from the local atmosphere.

The altitude where photoelectron escape is substantial follows from (22.38) and (22.39) as the region where the neutral atmospheric density satisfies the relation $\lambda \simeq H$ or

$$n_n \approx \frac{\langle\cos\theta\rangle \sin I_d}{H[\sigma_a(\sigma_a + 2p_e\sigma_e)]^{1/2}}. \tag{22.45}$$

A crude estimate of magnitude of the escaping photoelectron flux may be obtained by noting that the principal constituent of the neutral atmosphere near 300 km is atomic oxygen. Taking approximate values the escape flux, Φ^+(escape) is about $1\text{–}3 \times 10^9$ cm^{-2} sec^{-1}. Since photoelectrons arising from atomic oxygen have an average energy of about 15 eV, a total energy flux of about $1.5\text{–}4.5 \times 10^{10}$ eV cm^{-2} sec^{-1} is involved which, if the electrons are thermalized in the magnetosphere, represents a substantial source of high altitude heating.

Using typical values for the pertinent parameters, photoelectron escape altitudes have been tabulated in *Table 22.5* for the six model atmospheres described in Chapter 14.

Detailed theoretical calculations of the ionospheric photoelectron fluxes

TABLE 22.5

PHOTOELECTRON ESCAPE ALTITUDES

T_n (°K)	Escape altitude (km)
750	261
1000	303
1250	346
1500	381
1750	425
2000	466

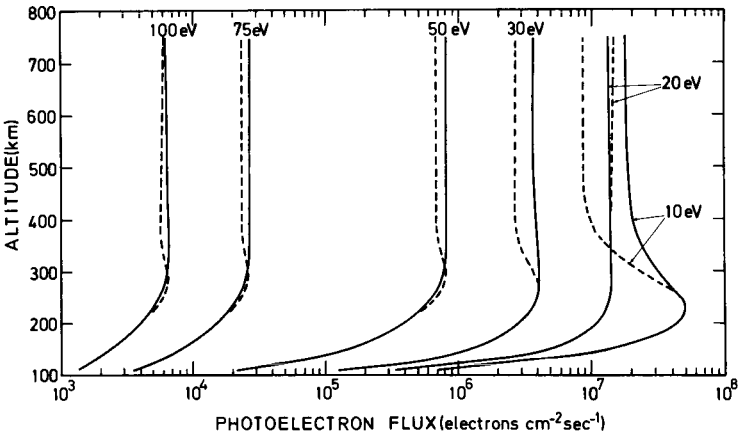


Fig. 22.12 Photoelectron fluxes for a sunlit 750°K thermosphere and overhead sun. Solid curves, Φ^+; dashed curves, Φ^-.

have been made including the effects of transport [31, 32]. Typical results are shown in *Figs. 22.12* and *22.13* for sunlit 750° and 1250°K thermospheres. Both the upward (+) and downward (−) fluxes are shown for several energies. The net escape flux can be found at Φ^+ evaluated at sufficiently high altitudes. The difference between Φ^+ and Φ^- is especially large at low energies, principally as a result of the strong photoelectron–thermal electron energy transfer rate which affects both conjugate and local photoelectrons.

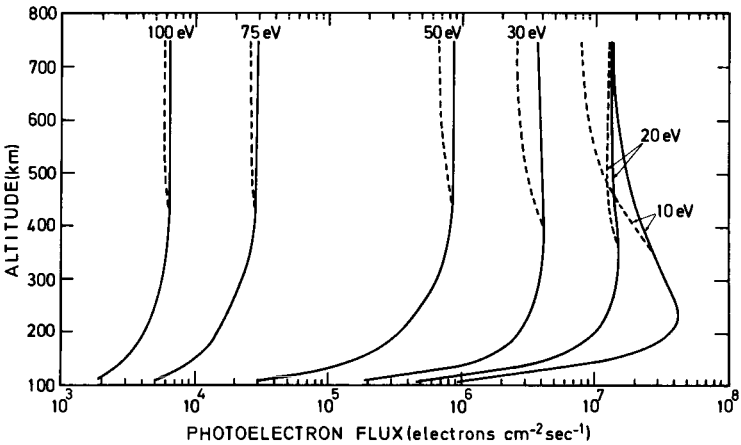


Fig. 22.13 Photoelectron fluxes for a sunlit 1250°K thermosphere and overhead sun. Solid curves, Φ^+; dashed curves, Φ^-.

Comparison of the two photoelectron models shown in Figs. 22.12 and 22.13 shows that the escape fluxes are relatively insensitive to changing atmospheric conditions. In addition, it is found that there is no strong dependence upon solar zenith angle for angles less than 70° to 80° [36].

22.5 Other Sources of Plasma Heating

22.5.1 Electrons

When an electric field is applied perpendicular to the geomagnetic field, charged particles drift through the neutral gases. Collisions between the different charged and neutral species act to limit the final transport velocities and some conversion of directed motion into random thermal energy occurs. Such a condition is thought to be important in the auroral and polar ionospheres and descriptions of the various processes have been presented in the literature [14, 15, 47, 48]. For an electric field **E**, the electron heating rate follows from Eqs. (22.27), (19.38), and (19.40) as

$$P_e = m_e n_e \bar{\nu}_{en}\{[(cE_y/B_z) - u_n]^2 + [(cE_x/B_z) - v_n]^2 + (w_e - w_n)^2\} \quad (22.46)$$

where a single neutral gas (subscript n) is assumed to be present. The rate of electron heating caused by this process is substantially smaller than that produced in the ion gases for the same values of E_x and E_y. If the electron energy loss proceeded by means of elastic collisions, the rise of electron temperature would be given by an equation similar to (22.12). Owing to the importance of inelastic processes, however, such a relation cannot be valid for electrons and the Joule heating created by electric fields and neutral winds is dissipated through inelastic processes.

When electric currents flow in plasma the electron and ion transport velocities differ and collisional Joule heating again occurs [24]. The rate of electron gas heating due to this effect follows from (22.28) and (9.112) as

$$P_e = m_e n_e \bar{\nu}_{ei}(\mathbf{C}_e - \mathbf{C}_i)^2 g(v/\alpha) \quad (22.47)$$

where

$$g\left(\frac{v}{\alpha}\right) = \frac{3\pi^{1/2}}{4}\left(\frac{\alpha}{v}\right)^3 \operatorname{erf}\left(\frac{v}{\alpha}\right) - \frac{3}{2}\left(\frac{\alpha}{v}\right)^2 \exp\left(-\frac{v^2}{\alpha^2}\right) \quad (22.48)$$

and

$$v = |\mathbf{C}_e - \mathbf{C}_i|, \quad (22.49)$$

$$\alpha^2 = 2kT_e/m_e. \quad (22.50)$$

Another source of electron heating, principally effective at altitudes below 150 km, has been postulated [49] to explain the apparent high electron temperatures in the ionospheric E region (100–140 km) measured by rockets carrying Langmuir probes. The most rapid energy conversion process taking place in the E region involves the absorption of solar radiation in the Schumann–Runge continuum of molecular oxygen and leads to metastable atomic oxygen atoms in the ^1D state. It has been hypothesized [49] that the excited oxygen atoms are quenched through collisions with molecular nitrogen with a substantial number of molecules being vibrationally excited. Through N_2*–N_2 collisions the vibration levels are thought to quickly attain a Boltzmann distribution with a characteristic temperature as high as 3300°K. Thermal electrons, in collisions with the excited N_2 molecules, will be heated (or cooled) through deexcitation (or excitation) of the different N_2 vibration states. Due to the long time required to deactivate the excited N_2 molecules, the vibration temperature will remain substantially greater than the neutral gas temperature throughout the night, thus providing a long-term nocturnal heat source for electrons. One difficulty with this particular model involves the rapidity with which N_2* can be deactivated through quenching. In fact, the quenching of N_2* by CO_2 could prove to be important in limiting the usefulness of excited N_2 as an electron heat source [50].

22.5.2 Ions

The electron gas acts, by means of elastic Coulomb collisions, as a heat source for the ion gases. The rate of thermal energy transfer between electrons and ions follows from (22.11) as

$$P_i = 7.7\times 10^{-6} n_e n_i [(T_e - T_i)/A_i T_e^{3/2}] \quad \text{eV cm}^{-3}\,\text{sec}^{-1} \qquad (22.51)$$

where A_i is the ion mass in atomic mass units. Equation (22.51) is based on the assumption that the electron and ion gases have separate Maxwellian velocity distributions. Theoretical models of various plasma processes have shown that the ionospheric constituents maintain independent Maxwellian forms over a wide range of conditions [51–53].

In addition to heating by the electron gas, other possible sources of ion thermal energy involving dissipation of wave energy, electric fields, chemical reactions, or inelastic collisions have been postulated. However, from observational evidence there is strong support for the choice of the electron gas as the primary source of ion heating at altitudes above 300 km.

Below 300 km, electric fields of magnetospheric and ionospheric origin, neutral winds, and electric currents can strongly affect the ion temperature through conversion of bulk transport into random thermal motions. The expressions for this type of ion heating follow from Eq. (22.11) as special cases of the relation

$$P_i = \mu_{in} n_i \bar{\nu}_{in} [m_n/(m_i + m_n)](\mathbf{C}_i - \mathbf{C}_n)^2 \tag{22.52}$$

where μ_{in} is the ion-neutral reduced mass.

To evaluate the importance of various effects, it is possible to adopt Eqs. (19.26)–(19.29) giving the steady state ion motions in a horizontally stratified medium. Although the general case is cumbersome, it is possible to deal with the approximations $\bar{\nu}_{in}^2 \gg \Omega_z^{i^2}$ and $\bar{\nu}_{in}^2 \ll \Omega_z^{i^2}$. These give, omitting explicit expressions for the vertical components of velocity,

$\bar{\nu}_{in}^2 \gg \Omega_z^{i^2}$:

$$P_i = (n_i/m_i \bar{\nu}_{in})(eE_\perp)^2 \tag{22.53}$$

$\bar{\nu}_{in}^2 \ll \Omega_z^{i^2}$:

$$P_i = \frac{\mu_{in}^2}{m_i} n_i \bar{\nu}_{in} \left[\left(\frac{cE_y}{B_z} - u_n \right)^2 + \left(\frac{cE_x}{B_z} + v_n \right)^2 \right] \tag{22.54}$$

where $\bar{\nu}_{in}$ is the ion-neutral momentum transfer collision frequency. Equation (22.53), valid below about 140 km, shows that heating results when a perpendicular electric field drives plasma through the neutral atmosphere. Because the ion-neutral collision frequency is much larger than the ion gyrofrequency neutral winds do not enter into the expression. In the absence of an electric field the ions are forced to move with the neutral atmosphere.

At higher altitudes, Eq. (22.54) shows that both electric fields and neutral gas motions heat the ion gas. Thus, even if the electric field vanishes (in the coordinate frame of the rotating earth) neutral gas motions relative to the rotating earth result in substantial ion heating.

Up to now, Eq. (22.11) as applied to ions in the neutral atmosphere has been arbitrarily separated into two parts, one of which corresponds to heat production, the second to energy loss to the neutral atmosphere. Actually, the same collisional processes act in both parts. Consequently, for steady-state conditions, it is possible to find the ion temperature from an equation similar to Eq. (22.11). This gives

$$T_i = T_n + m_n[(\mathbf{C}_i - \mathbf{C}_n)^2/3k]F(v/\alpha), \tag{22.55}$$

irrespective of the actual elastic ion-neutral collision frequency, with $F(v/\alpha)$

a normalized function of relative speed and temperature such that $F(v/\alpha)\rightarrow 1$ as $v/\alpha \rightarrow 0$. For the model of Eq. (22.11), $F(v/\alpha) = 1$, permitting (22.55) to be written as

$\bar{\nu}_{in}^2 \gg \Omega_z^{i^2}$:

$$T_i = T_n + (m_n e^2/3k\mu_{in}^2\bar{\nu}_{in}^2)(E_x^2 + E_y^2) \tag{22.56}$$

$\bar{\nu}_{in}^2 \ll \Omega_z^{i^2}$:

$$T_i = T_n + \frac{m_n}{3k}\left[\left(\frac{cE_y}{B_z} - u_n\right)^2 + \left(\frac{cE_x}{B_z} + v_n\right)^2\right]. \tag{22.57}$$

For a stationary neutral atmosphere, this last relation reduces at polar latitudes to

$$T_i = T_n + 1217(E_\perp/55)^2 \ ^\circ\text{K} \tag{22.58}$$

with $E_\perp$ measured in millivolts per meter. The time needed to establish such a temperature difference is of the order $1/\bar{\nu}_{in}$. Consequently, fluctuations of ion temperature provide a measure of the magnitude and time variations of both electric fields and neutral winds. In the low collision frequency regime, $T_i - T_n$ is independent of plasma or neutral densities. Only when $\bar{\nu}_{in}^2$ becomes of the order $\Omega_z^{i^2}$ or larger are density factors important.

With regard to ion gas heating due to dissipation of energy from current flow, Eqs. (22.11) and (9.112) give

$$P_i = (m_e^2/m_i)n_e\bar{\nu}_{ei}(\mathbf{C}_e - \mathbf{C}_i)^2 g(v/\alpha) \tag{22.59}$$

since $n_i\bar{\nu}_{ie} = n_e\bar{\nu}_{ei}$ for a single ion species. The different quantities in this expression are given following Eq. (22.47). Because of the extra mass factor m_e/m_i, heating by electron currents is much slower for ions than for electrons [see Eq. (22.47)].

22.6 Energy Losses of Electrons and Ions

The exact expression for the rate of energy transfer by means of elastic collisions between the constituent particles of two stationary gases having different temperatures and particle masses can be obtained [54] from the energy moment of the collision term of Boltzmann's equation [see Eq. (22.7)]

$$dU_1/dt = -[2m_1m_2/(m_1 + m_2)^2]n_1\bar{\nu}_{12}(\tfrac{3}{2}kT_1 - \tfrac{3}{2}kT_2) \tag{22.60}$$

where

$$\bar{\nu}_{12} = \tfrac{4}{3} n_2 (8k/\pi)^{1/2} [(T_1/m_1) + (T_2/m_2)]^{1/2} \bar{Q}_D \tag{22.61}$$

$$\bar{Q}_D = K^3 \int_0^\infty g^5 q_D(g) \exp(-Kg^2)\, dg \tag{22.62}$$

$$U_1 = \frac{1}{2} \int m_1 v_1^2 f_1\, d^3v \triangleq \tfrac{3}{2} n_1 k T_1 \tag{22.63}$$

$$K = [(2kT_1/m_1) + (2kT_2/m_2)]^{-1} \tag{22.64}$$

$$q_D(g) = 2\pi \int \sigma(g, \theta)[1 - \cos\theta] \sin\theta\, d\theta \tag{22.65}$$

and

$\bar{\nu}_{12}$ is the average momentum transfer collision frequency,
$\bar{Q}_D$ is the average momentum transfer cross section,
g is the relative velocity,
q_D is the velocity dependent momentum transfer cross section,
f is the distribution function, and
σ is the differential scattering cross section.

Through numerous experimental and theoretical studies it is known that a substantial portion of the energy exchange between the different gases of the ionosphere occurs not as a result of elastic collisions but through excitation of internal energy states of the colliding particles [13, 19, 27]. The excitation of an internal energy state (rotation, vibration, electronic) of an atom or molecule is an important mechanism for particle energy loss because it permits the direct transfer of kinetic energy to the colliding particles without the intervening mass factor which limits the rate of elastic collision energy transfer. As a consequence of the mass factor in (22.60) inelastic collisions tend to play a much more important part in determining the rate of electron gas cooling in a neutral atmosphere than that for ions. Unlike the case for elastic collisions, light particles can lose or gain energy relatively rapidly owing to inelastic collisions. In particular, electrons in a heavy neutral gas have an energy decrement of $2m_e/m_n$ per collision as a result of elastic processes. For inelastic collisions, the mass factor is absent and a rapid change in kinetic energy is possible.

Ions, in contrast, can have an energy decrement of up to one-half $[2m_1m_2/(m_1 + m_2)^2 \simeq \frac{1}{2}]$ for elastic collisions in a neutral gas composed of particles of nearly the same atomic mass. Hence, inelastic processes

cannot be expected to radically increase the rate of energy exchange unless the cross section for a given excitation is substantially larger than the elastic momentum transfer cross section.

Further evaluation of the equations of energy transfer for inelastic processes is useful only in particular cases where the specific cross section involved can be identified. Such, for example, is the case for electron excitation of molecular rotational states and ion-neutral resonance charge exchange.

22.6.1 Thermal Electron Cooling Processes

The rate at which a heated electron gas cools in the atmosphere as a result of elastic collision with neutral particles is [54]

$$dU_e/dt = -(3m_e/m_n)n_e k\bar{\nu}_e[T_e - T_n] \tag{22.66}$$

where $\bar{\nu}_e$ is the electron-neutral momentum transfer collision frequency defined by

$$\bar{\nu}_e = \tfrac{4}{3}n_n(8kT_e/\pi m_e)^{1/2}\bar{Q}_D, \tag{22.67}$$

$$\bar{Q}_D = (m_e/2kT_e)^3 \int_0^\infty vq_D \exp(-m_e v^2/2kT_e)\, dv, \tag{22.68}$$

and v is the electron velocity. Using the electron collision frequencies of Chapter 9, the energy transfer rates for elastic electron-neutral collisions in the atmospheric gases become

$$\left.\frac{dU_e}{dt}\right|_{N_2} = -1.2\times10^{-19}n_e n(N_2)[1 - 1.2\times10^{-4}T_e]T_e(T_e - T_n) \quad \text{eV cm}^{-3}\,\text{sec}^{-1} \tag{22.69}$$

$$\left.\frac{dU_e}{dt}\right|_{O_2} = -7.9\times10^{-19}n_e n(O_2)[1 + 3.6\times10^{-2}T_e^{1/2}]T_e^{1/2}(T_e - T_n) \quad \text{eV cm}^{-3}\,\text{sec}^{-1} \tag{22.70}$$

$$\left.\frac{dU_e}{dt}\right|_{O} = -7.2\times10^{-18}n_e n(O)T_e^{1/2}(T_e - T_n) \quad \text{eV cm}^{-3}\,\text{sec}^{-1} \tag{22.71}$$

$$\left.\frac{dU_e}{dt}\right|_{H} = -6.3\times10^{-16}n_e n(H)[1 - 1.35\times10^{-4}T_e]T_e^{1/2}(T_e - T_n) \quad \text{eV cm}^{-3}\,\text{sec}^{-1}. \tag{22.72}$$

From numerous experiments and theoretical analyses, it is known that electron energy transfer by means of elastic collisions with N_2 is never of great importance in the upper atmosphere. In fact, the rotational excitation

of N_2 and O_2 provides a rapid channel for energy loss which avoids the unfavorable mass factor appearing in (22.66). Although a precise theory is not available it is possible to adopt [55, 56]

$$\left.\frac{dU_e}{dt}\right|_{\substack{N_2 \\ \text{rotational}}} = -2\times 10^{-14} n_e n(N_2) \frac{(T_e - T_n)}{T_e^{1/2}} \quad \text{eV cm}^{-3}\,\text{sec}^{-1} \quad (22.73)$$

for N_2 with a possible uncertainty of a factor of 2.

For molecular oxygen the situation is not clear. Experimental studies [57, 58] show that O_2 is a more efficient electron coolant than N_2, in contradiction to predictions based on the long range quadrupole interaction. Recent theoretical studies have indicated the importance of short range interactions and a tentative energy loss rate of

$$\left.\frac{dU_e}{dt}\right|_{\substack{O_2 \\ \text{rotation}}} = -7\times 10^{-14} n_e n(O_2) \frac{(T_e - T_n)}{T_e^{1/2}} \quad \text{eV cm}^{-3}\,\text{sec}^{-1} \quad (22.74)$$

has been suggested [55] but this result is very uncertain. In any case, the effect of O_2 rotational excitation upon the overall electron energy balance is not great at altitudes above 150 km since O_2 rapidly becomes a minor constituent.

For electron temperatures above about 1500°K vibrational excitation of N_2 leads to more rapid electron cooling than rotational excitation. Calculations [55, 59] based upon theoretical values of the N_2 vibration cross section lead to the electron energy loss rates tabulated in *Table 22.6*, and

TABLE 22.6

ELECTRON ENERGY LOSS RATES[a] FOR N_2 VIBRATIONAL EXCITATION

T_e (°K)	$\frac{dU_e}{dt}\frac{1}{n_e n(N_2)}$	T_e (°K)	$\frac{dU_e}{dt}\frac{1}{n_e n(N_2)}$
200	3×10^{-19}	2500	1×10^{-11}
300	7×10^{-17}	3000	5×10^{-11}
500	7×10^{-15}	3500	1×10^{-10}
1000	2×10^{-13}	4000	3×10^{-10}
1500	8×10^{-13}	4500	2×10^{-9}
2000	2×10^{-12}	5000	7×10^{-9}

[a] Values are in eV cm^3 sec^{-1}.

approximated by the expression [60]

$$dU_e/dt = -1.3\times10^{-4}n_e n(N_2)\{1 - \exp[3200([1/T_e - 1/T_n])]\}A \quad \text{eV cm}^{-3}\,\text{sec}^{-1} \tag{22.75}$$

where

$$A = \begin{cases} 5.715\times10^{-8}e^{-3352.6/T_e}, & T_e < 1000^\circ\text{K} \\ 2.0\times10^{-7}e^{-4605.2/T_e}, & 1000^\circ < T_e < 2000^\circ\text{K} \\ 2.53\times10^{-6}T_e^{1/2}e^{-17620./T_e}, & T_e > 2000^\circ\text{K}. \end{cases}$$

For elevated electron temperatures N_2 vibrational excitation is certainly one of the principal means of electron energy loss in the ionosphere.

Vibration cross sections for electron cooling in O_2 are available from an analysis of transport phenomena [61] and theory [62]. However, since the O_2 vibration cross sections tend to be of the same order of magnitude, or smaller, than those for N_2, the inclusion of O_2 vibrational excitation is relatively unimportant in the electron gas energy budget, especially at altitudes above 200 km.

Electronic excitation of N_2 is not a significant energy loss process for ionospheric electrons due to the relatively large (6.2 eV) excitation potential of the first excited state $A\,^3\Sigma_u$ of N_2. In contrast, the first O_2 electronic state ($a\,^1\Delta_g$) lies only 0.96 eV above the ground state and, with a sufficiently large cross section, could be a significant sink for electron thermal energy. Laboratory measurements and theoretical analysis tend to indicate, however, that the direct excitation cross section leading to the $O_2(^1\Delta_g)$ state is very small ($\sim10^{-19}$ cm^2) [63].

In the middle ionosphere electron collisions with atomic oxygen are known to bring about impact induced fine structure transitions according to the process [64]

$$e + O(^3P_J) \rightarrow e + O(^3P_{J'}) \tag{22.76}$$

since the $^3P_0$ and $^3P_1$ levels are 0.028 and 0.020 eV above the ground state $^3P_2$ level. Cross sections for (22.76) have been used to calculate the energy loss rate expression as [60]

$$\begin{aligned} dU_e/dt = {} & -3.0\times10^{10}n_e n(O)T_e^{-1/2}[5 + 3e^{-\Delta_2/kT_n} + e^{-\Delta_3/kT_n}]^{-1} \\ & \times \{(6.28\times10^{-17} + 4.75\times10^{-21}T_e)\,\Delta_2 kT_e[e^{-\Delta_2/kT_e} - e^{-\Delta_2/kT_n}] \\ & + (1.16\times10^{-17} + 2.3\times10^{-21}T_e)\,\Delta_3 kT_e[e^{-\Delta_3/kT_e} - e^{-\Delta_3/kT_n}] \\ & + (2.2\times10^{-17} + 3.0\times10^{-21}T_e)\,\Delta_1 kT_e[e^{-\Delta_1/kT_e} - e^{-\Delta_1/kT_n}] \\ & \times e^{-\Delta_2/kT_n}\} \quad \text{eV cm}^{-3}\,\text{sec}^{-1} \end{aligned} \tag{22.77}$$

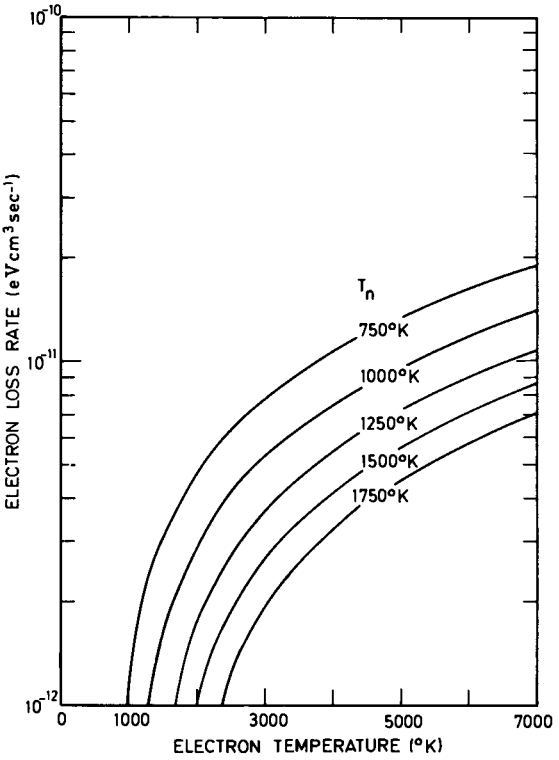


Fig. 22.14 Electron energy loss rate due to fine structure transitions of $O(^3P)$.

where $\Delta_1 = 0.00833$ eV, $\Delta_2 = 0.01965$ eV, $\Delta_3 = 0.02798$ eV, and $k = 8.63 \times 10^{-5}$ eV $^\circ K^{-1}$.

A plot of the energy loss rate as a function of electron and neutral gas temperature is given in *Fig. 22.14*. These results show that atomic oxygen is an important sink of electron thermal energy. Recent work [27] indicates that the inclusion of this process in models of the ionospheric thermal structure tends to give good agreement between predicted and observed electron temperature profiles.

The first excited state of atomic oxygen $O(^1D)$ lies 1.97 eV above the $O(^3P)$ ground state. For electron temperatures above several thousand degrees electron impact excitation of the ^1D state can be important [60]. The energy loss rate has been calculated as [65]

$$dU_e/dt = -1.1 \times 10^{-10} n_e n(O) T_e^{1/2} e^{-2.27\times10^4/T_e} \{(0.406 + 0.357 \times 10^{-4} T_e) - (0.333 + 0.183 \times 10^{-4} T_e)\, e^{-1.37\times10^4/T_e} - (0.456 + 0.174 \times 10^{-4} T_e) e^{-2.97\times10^4/T_e}\} \text{ eV cm}^{-3} \text{ sec}^{-1} \quad (22.78)$$

assuming a Maxwellian electron velocity distribution and thermal distribution of $O(^3P_J)$ states.

The excitation of $O(^1S)$ is not a major sink of electron energy for the temperatures normally observed within the ionosphere due to its threshold of 4.2 eV.

The elastic scattering of electrons by ions leads to a rapid electron–ion energy transfer rate as a consequence of the large Coulomb cross section. Using (22.66)

$$\left.\frac{dU_e}{dt}\right|_{\text{ions}} = -\frac{3m_e}{m_i} n_e k \bar{\nu}_{ei}(T_e - T_i) \tag{22.79}$$

where

$$\bar{\nu}_{ei} = \tfrac{4}{3}(2\pi)^{1/2} n_i \frac{(Z_i e^2)^2}{m_e^{1/2}} \frac{\ln \Lambda}{(kT_e)^{3/2}}. \tag{22.80}$$

Hence, the electron–ion energy transfer rate is

$$\left.\frac{dU_e}{dt}\right|_{\text{ions}} = -4(2\pi)^{1/2} n_e n_i \frac{m_e^{1/2}}{m_i} \frac{(Z_i e^2)^2 \ln \Lambda}{(kT_e)^{3/2}} k(T_e - T_i), \tag{22.81}$$

the subscript i applying to ion parameters. Numerically, this becomes

$$\left.\frac{dU_e}{dt}\right|_{\text{ions}} = -(7.7 \pm 0.8) \times 10^{-6} n_e n_i \frac{(T_e - T_i)}{A_i T_e^{3/2}} \quad \text{eV cm}^{-3} \text{ sec}^{-1} \tag{22.82}$$

where A_i is the ion atomic mass in atomic mass units. The indicated uncertainty reflects the problem of choosing an adequate cutoff for the Coulomb potential.

For a fixed ion temperature in Eq. (22.82) there is a maximum energy transfer rate when $T_e = 3T_i$; that is,

$$\left.\frac{dU_e}{dt}\right|_{\max} = -\frac{3.0 \times 10^{-6} n_e n_i}{A_i T_i^{1/2}} \quad \text{eV cm}^{-3} \text{ sec}^{-1}. \tag{22.83}$$

For local energy production in the electron gas greater than (22.83) the electron temperature must rise until thermal transport or energy losses to the local neutral atmosphere becomes important.

22.6.2 Thermal Ion Cooling Processes

At low temperature ($T < 300°K$) the most important ion-neutral interaction arises from an induced dipole attraction which was discussed in Chapter 9.

For temperatures greater than about 300°K other effects besides polarization become important. Unfortunately the specific nature of these effects depends intimately upon the identity of the colliding particles. Because there are almost no data available for either the cross sections or collision frequencies at high temperatures, the ion-neutral energy transfer rates for many ionospheric processes must remain somewhat uncertain. In these cases the rates can be estimated using the low temperature polarization interaction with a suitable truncation repulsive potential to simulate short range quantum effects.

In this approximation the ion neutral collision frequency for singly charged ions is given by Eq. (9.73) as

$$\bar{\nu}_{in} = 2.6\times 10^{-9} n_n(\alpha_0/\mu_A)^{1/2} \quad \text{sec}^{-1} \tag{9.73}$$

where μ_A is the ion-neutral reduced mass in atomic units and α_0 is the neutral gas polarizability in units of 10^{-24} cm^3. From (22.60) the ion-neutral elastic energy transfer rate is

$$\left.\frac{dU_i}{dt}\right|_{\text{neutrals}} = -2.6\times 10^{-4} \frac{A_i A_n n_i}{(A_i + A_n)^2} \bar{\nu}_{in}(T_i - T_n) \quad \text{eV cm}^{-3}\,\text{sec}^{-1} \tag{22.84}$$

where $A_{i,n}$ is the atomic mass of the indicated particle. The energy transfer rates of ions can be approximated as

$$dU_i/dt = -n_i n_n \beta_{in}(T_i - T_n). \tag{22.85}$$

Values of β_{in} are listed in *Table 22.7.*

TABLE 22.7

ION ENERGY LOSS RATES[a]

Species	β_{in}	Species	β_{in}
N_2^+, N_2	5.9	O^+, N_2	4.0
O_2^+, O_2	5.3	He^+, N_2	4.5
O^+, O	5.6	H^+, N_2	2.8
H^+, H	1.9	O_2^+, O	1.3
He^+, He	5.4	NO^+, O	1.4
N^+, N	6.5	N_2^+, O	1.5
O_2^+, N_2	2.6	He^+, O	4.1

[a] Values are in 10^{-14} eV cm^3 °K^{-1} sec^{-1}.

Care must be taken applying these rates to ion scattering in homonuclear gases such as O_2 and N_2. In these cases the probability of rotational excitation at thermal energies is large and a substantial part of the scattering may actually be inelastic. The true processes involved are complex, however, and the rates of Table 22.7 can be used as typical values subject to future correction.

In addition to the collisional energy transfer described by (22.84) there exists for ions a second method of energy loss by means of resonance charge exchange which, while fundamentally elastic in nature (no internal energy states are excited), requires an evaluation of the collision term in Boltzmann's equation to obtain the ion-neutral energy transfer rate. For Maxwellian distributions the ion-neutral energy exchange rate is [54]

$$dU_i/dt = -\tfrac{3}{2}n_i k\bar{\nu}_E(T_i - T_n) \tag{22.86}$$

where $\bar{\nu}_e$ is the charge exchange collision frequency. Using values given in Chapter 9, the rates of energy transfer for the ions of the upper atmosphere have the form

$$\left.\frac{dU_i}{dt}\right|_{\substack{\text{charge}\\ \text{exchange}}} = n_i n_n \gamma_{in}(T_i + T_n)^{1/2}(T_i - T_n). \tag{22.87}$$

Table 22.8 lists values of γ_{in} for resonance charge exchange.

TABLE 22.8

RESONANCE CHARGE EXCHANGE ENERGY LOSS COEFFICIENTS[a]

Species	γ_{in}	Species	γ_{in}
O^+, O	2.1	N_2^+, N_2	2.8
H^+, H	13.0	O_2^+, O_2	1.4
He^+, He	3.9	N^+, N	2.2

[a] Values are in 10^{-15} eV cm^3 °K$^{-3/2}$ sec^{-1}.

As a result of differing rates of energy production in the ionospheric ion gases there exists a tendency for there to be minor differences in the ion kinetic temperatures [66–69]. An important factor preventing substantial differences is the rapid ion–ion energy exchange rate based on the

Coulomb interaction. From (22.60) the ion–ion energy exchange rate is

$$\left.\frac{dU_i}{dt}\right|_{\text{ion–ion}} = -\frac{3m_1m_2}{(m_1+m_2)^2} n_1 k \bar{\nu}_{12}(T_1 - T_2) \tag{22.88}$$

where the subscripts apply to two ion gases and $\bar{\nu}_{12}$ is defined by Eq. (9.114). Numerically, (22.88) becomes

$$\left.\frac{dU_i}{dt}\right|_{\text{ion–ion}} = -\frac{3.3\times 10^{-4} n_1 n_2 (T_1 - T_2)}{A_1 A_2 [(T_1/A_1) + (T_2/A_2)]^{3/2}} \text{ eV cm}^{-3}\text{ sec}^{-1} \tag{22.89}$$

where the subscripts apply to the two ion species and A is the ion mass in atomic mass units.

22.7 Plasma Thermal Conductivity

Owing to the large difference between the electron gas and ion gas mean thermal speeds, most of the thermal energy flow in a plasma takes place through the electron gas in response to electron temperature gradients [70, 71]. As a result, the electron temperature profile in the ionosphere is more strongly affected by energy transport than is that for the ion gases. Nevertheless, the ion thermal conductivity cannot be ignored altogether since at high altitudes, where the rate of energy transfer between electrons and ion gases is slow, the transport of thermal energy through the ion gas can measurably alter the ion temperature profile [12, 72].

In both neutral gases and plasmas, particle collisions determine the magnitude of the thermal conductivity. In ionized gases, however, there is a further effect since electric fields established through charge separation between electrons and ions can substantially reduce the flow of electrons and thus act to determine an effective thermal conductivity which is substantially smaller than the conductivity appropriate for Coulomb collisions alone.

When the bulk transport velocity is much smaller than the mean thermal speed of the gas, the principal contribution to the jth species heat flow, $\Phi_{\parallel}^{j}$, arises from thermal conduction and is given by the relation

$$\Phi_{\parallel}^{j} = -K_j' \, \partial T_j/\partial s \tag{22.90}$$

where K_j' is the jth species thermal conductivity.

22.7.1 Electron Thermal Conductivity

From simple mean free path arguments the energy flux Φ_e arising from a gradient in the electron temperature is [73]

$$\Phi_e = -\tfrac{3}{4} n_e \bar{v} k \lambda (dT_e/dz) \tag{22.91}$$

where n_e is the electron density, $\bar{v}$ is the average electron thermal speed, k is Boltzmann's constant, λ is the electron mean free path, principally determined by electron–ion Coulomb collisions in a fully ionized plasma, and s is a coordinate along the magnetic field.

Using the basic transport relation

$$\lambda = 1/n\sigma \tag{22.92}$$

where n is the number density of the scattering particles and σ is the scattering cross section, the thermal conductivity becomes

$$K_e' = \tfrac{3}{4}(\bar{v} k n_e/\sigma n). \tag{22.93}$$

For a fully ionized gas, where the electrons are scattered by Coulomb collisions with ions, it is possible to take $n_e = n$ and (22.93) becomes

$$K_e' \simeq \tfrac{3}{4}(\bar{v} k/\sigma_c) \tag{22.94}$$

independent of the charged particle number density. A further reduction could be made by using the electron–ion momentum transfer cross section in place of σ_c in (22.94). This gives

$$K_e' \simeq \frac{3\sqrt{2}}{\pi^{3/2}} \frac{k(kT_e)^{5/2}}{m_e^{1/2} e^4 \ln \Lambda} \tag{22.95}$$

where the different symbols have been defined in Section 9.7. More exact derivations, which take into account the nonlinear effects of electron–electron collisions through direct evaluation of Boltzmann's equation give the result [16, 74]

$$K_e' = 20(2/\pi)^{3/2} k[(kT_e)^{5/2}\delta/m_e^{1/2} e^4 \ln \Lambda] \tag{22.96}$$

which, with $\delta = 0.225$ and $\ln \Lambda = 15$, becomes

$$K_e' = 1.8 \times 10^6 T_e^{5/2} \quad \text{eV cm}^{-1} \text{ sec}^{-1} \text{ °K}^{-1} \tag{22.97}$$

uncorrected for any thermoelectric effects which may exist in the plasma.

Before proceeding with the analysis needed to derive the effective thermal conductivity valid for a partially ionized plasma, it is necessary to discuss two aspects of the thermal conductivity which are important for the ionospheric plasma. The first revolves about the already mentioned effect of the geomagnetic field in constraining the motions of electrons into helical paths along the magnetic lines of force. For such conditions the thermal conductivity becomes anisotropic with different values parallel and perpendicular to the field lines [75]. While the component of conductivity parallel to the field lines is the same as derived here for the field-free case, the perpendicular component is reduced by the factor $\nu_e/(\nu_e^2 + \Omega_e^2)$ where Ω_e is the electron cyclotron frequency and ν_e is essentially a mean collision frequency. Since $\Omega_e \sim 10^7$ sec^{-1} and $\nu_e \sim 10^{-9} n_n$ sec^{-1} for the earth's magnetic field and atmosphere, it is found that there will be essentially no energy conducted through the electron gas perpendicular to the magnetic field for altitudes above about 80 km. Thus, only the component of the electron temperature gradient parallel to the field will be effective in transporting energy through the electron gas. The thermal conductivity derived here will be considered as the component parallel to the direction of the magnetic field lines and the effect of the perpendicular component will be ignored (see Eq. (22.91)).

The second effect, which plays an important part in reducing the thermal conductivity of a plasma, arises from the possibility of different thermoelectric effects inhibiting the flow of electrons [16, 24, 74]. When a weak electric field $E_\parallel$, temperature gradient dT_e/ds, and electron pressure gradient dp_e/ds, are present in a plasma and acting parallel to the imposed magnetic field, then the steady state electron current j_e and electron heat flow Φ_e can be expressed in phenomenological terms as

$$j_e = \sigma\left(E_\parallel + \frac{1}{en_e}\frac{dp_e}{ds}\right) + \phi\frac{dT_e}{ds}, \tag{22.98}$$

$$\Phi_e = -K_e'\frac{dT_e}{ds} - T_e\phi\left(E_\parallel + \frac{1}{en_e}\frac{dp_e}{ds}\right). \tag{22.99}$$

As a consequence of these relations the electron flux and heat flow are closely related in the sense that for a given applied temperature gradient, pressure gradient, or electric field there will be a net flow of electric current and heat.

In many physical situations geometrical or magnetic effects may be present which prohibit a flow of electron current. The magnetic field lines equatorward of the auroral zones, in particular, require that any currents generated

through temperature or density gradients or electric fields must pass along the field lines to the ionospheric E region where the transverse electrical conductivities become large enough to support lateral current flow towards the geomagnetic conjugate region. Because of the relatively poor electrical conductivity of the lower ionosphere and the long path length involved, very little current is able to flow in such a system; a secondary electric field must be established along the lines of magnetic force which, in effect, reduces the electron current flow to zero. The magnitude of this secondary field follows from (22.98) with $j_e = 0$:

$$E_{\parallel} = -\frac{1}{en_e}\frac{dp_e}{ds} - \frac{\phi}{\sigma}\frac{dT_e}{ds}. \tag{22.100}$$

With the substitution of the secondary electric field of (22.100) into (22.99), the net electron heat flux Φ_e through the electron gas becomes

$$\Phi_e = -\left(K_e' - \frac{T_e\phi^2}{\sigma}\right)\frac{\partial T_e}{\partial s} \tag{22.101}$$

and the effective coefficient of thermal conductivity is reduced to $K_e = \varepsilon K_e'$ where the reduction factor ε is given by

$$\varepsilon = [1 - (T_e\phi^2/K_e'\sigma)] \tag{22.102}$$

so that the thermal energy flux becomes

$$\Phi_e = -K_e(\partial T_e/\partial s). \tag{22.103}$$

The condition that no electric current flow along the lines of magnetic force, which has been met above through the requirement that $j_e = 0$, could also follow from an ambipolar hypothesis: $j_e = j_i$. However, owing to the large ion to electron mass ratio, the ambipolar requirement does not appreciably alter the results obtained for the case of no electron flow.

In a fully ionized gas the electron free path is determined by collisions with ions and, indirectly, through collisions with other electrons. For these circumstances the thermal conductivity has been evaluated [74] numerically to give

$$K_{ei}' = 1.8\times 10^6 T_e^{5/2} \quad \text{eV cm}^{-1}\,\text{sec}^{-1}\,{}^\circ\text{K}^{-1} \tag{22.104}$$

or, with the calculated value $\varepsilon = 0.419$,

$$K_{ei} = 7.7\times 10^5 T_e^{5/2} \quad \text{eV cm}^{-1}\,\text{sec}^{-1}\,{}^\circ\text{K}^{-1} \tag{22.105}$$

independent of the plasma number density.

For the limit of a weakly ionized plasma the distortion of the electron velocity distribution function arising from electron–electron collisions can be neglected and the thermal conductivity can be found from the Lorentzian approximation as [75]

$$K'_{\mathrm{en}} = \frac{4\pi}{3} n_{\mathrm{e}} k \int_0^\infty f_{\mathrm{e}}^M \frac{v^4}{\nu_{\mathrm{e}}} \left[\frac{v^2}{c^2} - \frac{5}{2}\right]^2 dv \tag{22.106}$$

where v is the electron speed, ν_{e} is the velocity dependent collision frequency between electrons and neutrals and f_{e}^M represents the Maxwellian velocity distribution function for the electron gas.

In order to reduce (22.106) to a practical form it is necessary to introduce a specific velocity dependence for the electron-neutral collision frequency. This, in general, is difficult since there are a number of effects which act to determine the magnitude of the scattering cross section at different energies. Only for certain simple interaction models is it possible to obtain analytical solutions. To take the velocity variations of the electron collision frequency into account it is adequate to introduce the average momentum transfer cross section $\bar{Q}_{\mathrm{D}}$ [see Eq. (9.38)] into Eq. (22.106) in place of the velocity-dependent momentum transfer cross q_{D}. In terms of $\bar{Q}_{\mathrm{D}}$ the electron thermal conductivity becomes

$$K'_{\mathrm{en}} = \tfrac{3}{4}(8kT_{\mathrm{e}}/\pi m_{\mathrm{e}})^{1/2}(n_{\mathrm{e}}/n)(k/\bar{Q}_{\mathrm{D}}) \tag{22.107}$$

where the various values of $\bar{Q}_{\mathrm{D}}$ for the atmospheric gases have been given in Chapter 9. The error involved in the process is very small for simple power law cross sections. Since the actual values of $q_{\mathrm{D}}(v)$ are only known to within 20% for O_2 and N_2, the approximation is adequate for ionospheric applications.

Numerical values for the reduction factor ε can be calculated for electron-neutral collision from (22.102) and the Lorentzian relations

$$\phi = \frac{4\pi}{3} \frac{n_{\mathrm{e}} e}{T_{\mathrm{e}}} \int_0^\infty \frac{v^4}{\nu_{\mathrm{en}}} \left(\frac{v^2}{c^2} - \frac{5}{2}\right) f_{\mathrm{e}}^M \, dv, \tag{22.108}$$

$$\sigma = \frac{4\pi}{3} \frac{n_{\mathrm{e}} e^2}{kT_{\mathrm{e}}} \int_0^\infty \frac{v^4}{\nu_{\mathrm{en}}} f_{\mathrm{e}}^M \, dv. \tag{22.109}$$

If we adopt the approximation

$$\nu_{\mathrm{en}} = n\bar{Q}_{\mathrm{D}} v \tag{22.110}$$

then $\varepsilon = \frac{8}{9}$ and the effective thermal conductivity K_{en} becomes

$$K_{en} = \tfrac{2}{3}(8kT_e/\pi m_e)^{1/2}(n_e/n_n)(k/\bar{Q}_D). \tag{22.111}$$

In a fully ionized gas the electron mean free path is determined by the effect of collisions with ions and, to a lesser extent, with other electrons. In a partially ionized plasma, however, it is necessary to take into account the presence of neutral particles since, for sufficiently large neutral particle concentrations, the free path will be determined by electron-neutral collisions alone.

For situations where only a rough estimate is required for the thermal conductivity of a partially ionized plasma a mean free path mixing rule can be adopted. In this case the electron free path can be expressed as

$$\lambda = 1 \Big/ \sum_j n_j Q_j \tag{22.112}$$

where n_j is a particle number density and Q_j is the appropriate scattering cross section for the jth species. Equation (22.112) may be further decomposed as

$$\lambda = \lambda_c/(1 + \lambda_c/\lambda_n) \tag{22.113}$$

where λ_c is the electron-charged particle free path and

$$\lambda_n = 1 \Big/ \sum_k n_n \bar{Q}_D \tag{22.114}$$

is the electron-neutral free path which includes the effects of k different neutral-gas species.

With Eqs. (22.113) and (22.114) it is now possible to write the total electron thermal conductivity as [23, 76]

$$K_e = \frac{K_{ei}}{1 + K_{ei}[\sum_k (1/K_{en})]} \tag{22.115}$$

where K_{ei} is the electron thermal conductivity of a fully ionized gas and K_{en} is the conductivity of electrons in a very dense neutral gas of the nth species where charged particle collisions are unimportant. This result is identical with the more common thermodynamic problem of the heat conductivity of combined slabs of insulating materials.

Equation (22.115) shows that at low neutral particle densities, where λ_n and K_n become large, $K_e \simeq K_{ei}$, while for large neutral particle densities λ_n and K_n become small, leading to $K_e \simeq 1/\sum_n (1/K_{en})$.

In terms of K_{ei} and K_{en} given by (22.105) and (22.111), the effective electron thermal conductivity for the mean free path mixing rule becomes

$$K_e = \frac{7.7\times 10^5 T_e^{5/2}}{1 + 3.22\times 10^4 (T_e^2/n_e)\sum_k n_n \bar{Q}_D} \quad \text{eV cm}^{-1}\,\text{sec}^{-1}\,^\circ\text{K}^{-1} \tag{22.116}$$

where the summation in the denominator is taken over all neutral gas species present. For low neutral particle densities this expression reduces to Eq. (22.105) for a fully ionized gas. At the opposite extreme, however, the correction factor is large and the thermal conductivity becomes

$$K_e = \frac{23.9 n_e T_e^{1/2}}{\sum_n n_n \bar{Q}_D} \quad \text{eV cm}^{-1}\,\text{sec}^{-1}\,^\circ\text{K}^{-1}. \tag{22.117}$$

This result indicates the relative insensitivity of the electron thermal conductivity to changes of temperature in a dense neutral atmosphere. The transition between the two limiting conditions is shown in *Fig. 22.15* where the thermal conductivity is plotted for several values of T_e as a function of the density reduced cross section $\sum_n (n_n/n_e)\bar{Q}_D$. Since K_{ei} is independent of the number densities, the departure of the curves from the horizontal indicates the effect of the neutral gases.

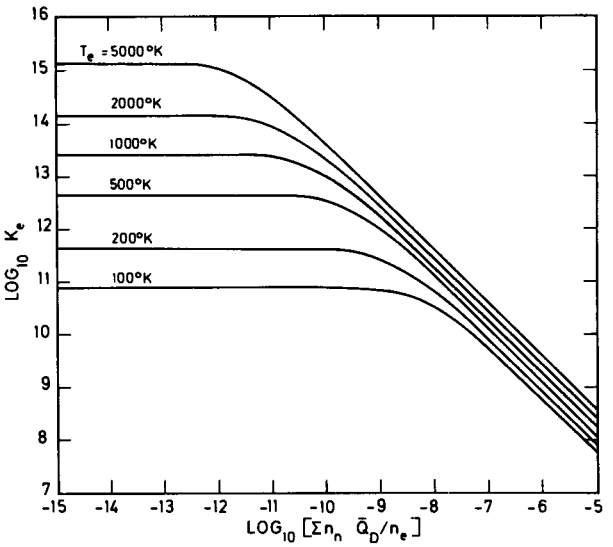


Fig. 22.15 Electron thermal conductivity for several values of electron temperature.

An alternative to the relatively inaccurate free path mixing rule has been developed [70] on the basis of the Lorentzian coefficients given by (22.107–22.109). If one adopts a modified electron–ion collision frequency for the total collision frequency ν_e in these equations it is possible to obtain an accuracy far better than the simple mixing rule and somewhat better than even the twelfth order Sonine-polynomial approximation. Formulas for K'_{en}, σ, and ϕ are obtained in this technique through the replacements [70]

$$\nu_e(K'_{en})_e = \nu_{en}(v) + 2.70\bar{\nu}_{ei}(2kT_e/m_e v^2) \tag{22.118}$$

$$\nu_e(\sigma) = \nu_{en}(v) + 1.27\bar{\nu}_{ei}(2kT_e/m_e v^2) \tag{22.119}$$

$$\nu_r(\phi) = \nu_{en}(v) + 1.80\bar{\nu}_{ei}(2kT_e/m_e v^2) \tag{22.120}$$

$$\bar{\nu}_{ei} = \tfrac{4}{3}[(2\pi)^{1/2} n_i e^4 \ln \Lambda / m_e^{1/2}(kT_e)^{3/2}] \tag{22.121}$$

respectively. The thermal conductivity resulting from this method is generally smaller than that obtained using the free path mixing rule.

There have been several laboratory measurements of the electron thermal conductivity [77–79]. In each of these experiments it was found that the electron thermal conductivity was independent of the neutral gas pressure. However, analysis of the experimental conditions has shown that in all cases the laboratory parameters of T_e, n_e, and n_n were not adequate to lead to any appreciable reduction in the conductivity.

The practical importance of the neutral gas reduction of the electron gas thermal conductivity in the ionosphere is felt principally below 200 km. During the daytime the electron density is generally high enough to ensure that the effect of the neutral atmosphere enters only at altitudes below 140 to 150 km. During the night, however, the electron density in the regions below 200 km falls to values of the order of 10^3 cm^{-3} and it is found that there is essentially no thermal conduction acting within the electron gas: The electron temperature is determined through local energy production and loss. On this basis there is a substantial thermal decoupling of the high altitude electron gas from the important electron energy losses of the E region of the ionosphere. If electron–neutral collisions did not reduce the electron thermal conductivity, large fluxes of electron thermal energy could be conducted rapidly to low altitudes with the net result that the electron temperature would be lower in the regions of energy production [76]. An example of this behavior is shown in *Fig. 22.16*.

22.7.2 Ion Thermal Conductivity

In response to gradients in ion temperature, a flux Φ_i of ion thermal energy flows along the lines of magnetic force. For a single ion gas the

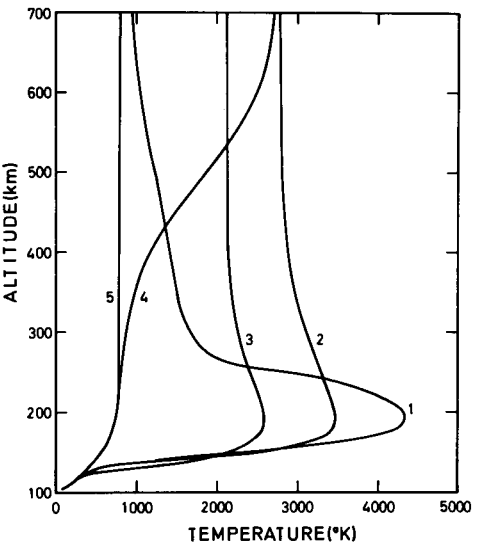


Fig. 22.16 Charged and neutral gas temperatures typical of quiet solar conditions. Curve 1 is the solution to the daytime electron energy balance equation which ignores heat conduction through the electron gas. When heat conduction is included the electron temperature profile is substantially changed, as shown by curves 2 and 3. Curve 2 results when an effective thermal conductivity including the effects of electron–neutral particle collisions is introduced. For curve 3 the thermal conductivity for a fully ionized gas was used. Curves 4 and 5 are the calculated ion and the assumed neutral atmosphere temperatures.

heat flux is given by Eq. (22.90) but when mixtures of ions are involved additional terms enter into the expression corresponding to thermal diffusion effects. However, evaluation of the heating influences of conduction and diffusion indicates that heat conduction is generally dominant. Only for circumstances of low ion temperatures and densities can diffusion heating or cooling due to ion transport be important.

The calculation of the ion thermal conductivity K_i for a single ion gas of atomic mass A_i follows from kinetic theory as

$$K_i = 4.6 \times 10^4 A_i^{-1/2} T_i^{5/2} \quad \text{eV cm}^{-1} \text{ sec}^{-1} \text{ °K}^{-1} \tag{22.122}$$

where the correction factor appropriate for the second approximation has been applied. The analysis of the thermal conductivity for the electron component of a fully ionized gas has shown that thermoelectric effects are important. Thus the stipulation that there is no net electron current flow in a plasma leads to the establishment of an electric field within the plasma

that opposes the electron current flow associated with the gradient in electron temperature and reduces the electron thermal conductivity by a factor of 2.3. When the simultaneous ion and electron heat and current flow equations are introduced, it is possible to require a condition of no net electric current through the ambipolar hypothesis. In this case the electric field established by electrons tends to increase the effective ion thermal conductivity. It is found, however, that this enhancement is generally small and can be neglected in the ionosphere, giving the result that $\varepsilon = 1$ for the ion heat flow component.

For the ion gases of the ionosphere, an extension of (22.122) must be made to include the effects of differing conductivities for each ion species. An exact expression is difficult to obtain and an approximate, density weighted, thermal conductivity can be used in the form

$$K_i = 1.2 \times 10^4 [n^+(O) + 2n^+(He) + 4n^+(H)] T_i^{5/2} n_e^{-1} \quad \text{eV cm}^{-1} \text{ sec}^{-1} \text{ °K}^{-1} \tag{22.123}$$

which leads to errors of less than several percent in binary mixtures. The effects of ion–neutral collisions, which tend to reduce the thermal conductivity below the value given by (22.123) can be neglected above 300 km.

An example of the effect of the ion thermal conductivity upon the profile of ion temperature is shown in Fig. 23.13 for quiet solar conditions. The principal effect is to maintain a permanent separation between ion and electron temperatures at high altitudes when the electron densities are sufficiently low.

22.8 Effects of Electron Heat Conduction

Owing to the dependence of the electron thermal conductivity upon temperature, electron heat flow due to conduction leads to particular temperature profiles along magnetic lines of force at high altitudes. Thus, from (22.21) for a fully ionized gas at rest

$$-\frac{K_0}{A}\frac{d}{ds}\left(AT_e^{5/2}\frac{\partial T_e}{\partial s}\right) = P_e(s) - L_e(s) \tag{22.124}$$

where both the production and loss of thermal energy may depend upon altitude and temperature, A is the area of a given field tube, and $K_0 = 7.7 \times 10^5$ eV cm^{-1} °K$^{-7/2}$ sec^{-1}.

A single integration of (22.124) can be performed immediately to give

$$A(s)T_e^{5/2}(dT_e/ds) = A(a)T_e^{a\,5/2}(dT_e/ds)_a + (1/K_0)\int_a^s [L(s') - P(s')]A(s')\,ds' \qquad (22.125)$$

where the subscript a refers to some reference level.

At very high altitudes ($z > 1000$ km) it is frequently assumed that there is no local energy production or loss; thermal energy is conducted downwards along the magnetic field line from heat sources located within the magnetosphere, perhaps in the vicinity of the geomagnetic equator. In this situation (22.125) can be integrated to give the conductive temperature profile as

$$T_e(s) = T_e^a\left\{1 + \frac{7}{2}\left[\frac{d}{ds}(\ln T_e)\right]_a \int_a^s \frac{A(a)}{A(s')}\,ds'\right\}^{2/7} \qquad (22.126)$$

showing that the electron temperature must continually rise as one goes away from the earth in order to maintain the same net rate of heat flow downwards along the magnetic field lines.

Over a sufficiently short distance the variation of $A(s')$ with s' can be neglected so that

$$T_e(s) = T_e^a\left\{1 + \frac{7}{2}\left[\frac{d}{ds}(\ln T_e)\right]_a (s - a)\right\}^{2/7} \qquad (22.127)$$

giving the temperature variation along the field line in terms of the values T_e^a and $(dT_e/ds)_a$.

For some purposes it is convenient to retain the value of the heat flux in an expression similar to (22.126). Thus,

$$T_e(s) = T_e^{a\,7/2} - \frac{7}{2}\frac{\Phi_{\parallel}^a}{K_0}\int_a^s \frac{A(a)}{A(s')}\,ds' \qquad (22.128)$$

where $\Phi_{\parallel}^a$ is the boundary value heat flux, and $A(s')$ is the area of the magnetic field flux tube normalized to A ($s = a$).

REFERENCES

1. N. C. Gerson, *Rep. Progr. Phys.* **14**, 316 (1951).
2. G. Drukarev, *J. Phys.* (*USSR*) **10**, 81 (1946).
3. R. L. Bogges, L. H. Brace, and N. W. Spencer, *J. Geophys. Res.* **64**, 1627 (1959).
4. W. B. Hanson and F. S. Johnson, *Mem. Soc. Roy. Sci., Liege Ser.* 5 **4**, 390 (1961).

5. N. W. Spencer, L. H. Brace, and G. R. Carignan, *J. Geophys. Res.* **67**, 157 (1962).
6. A. F. Nagy, L. H. Brace, G. R. Carignan, and M. Kanal, *J. Geophys. Res.* **68**, 6401 (1963).
7. J. V. Evans, *J. Geophys. Res.* **67**, 4914 (1962).
8. V. C. Pineo and D. P. Hynek, *J. Geophys. Res.* **67**, 5119 (1962).
9. N. W. Spencer, L. H. Brace, G. R. Carignan, D. R. Taeusch, and H. Niemann, *J. Geophys. Res.* **70**, 2665 (1965).
10. W. B. Hanson, *Space Res.* **3**, 282 (1963).
11. J. E. Geisler and S. A. Bowhill, *J. Atmos. Terr. Phys.* **27**, 457 (1965).
12. P. M. Banks, *J. Geophys. Res.* **72**, 3365 (1967).
13. P. M. Banks, *Proc. IEEE* **57**, 258 (1969).
14. K. D. Cole, *Planet. Space Sci.* **19**, 59 (1971); **20**, 2205 (1972).
15. J. A. Fedder and P. M. Banks, *J. Geophys. Res.* **77**, 2328 (1972).
16. J. M. Burgers, *Flow Equations for Composite Gases.* Academic Press, New York 1969.
17. L. J. Gleeson and W. I. Axford, *Planet Space Sci.* **15**, 123 (1967).
18. J. M. Smith, An Exact Calculation of Momentum and Energy Exchange Collision Integrals Over Displaced Maxwellian Distribution Functions. General Electric Co., Missile and Space Div., R64SD54, August (1964) (Available as ASTIA Document AD60733).
19. A. Dalgarno, M. B. McElroy, and R. J. Moffett, *Planet Space Sci.* **11**, 463 (1963).
20. R. W. Schunk and P. B. Hays, *Planet Space Sci.* **19**, 113 (1971).
21. Y. Itakawa and O. Aono, *Phys. Fluids* **9**, 1259 (1966).
22. K. Takayangi and Y. Itikawa, *Space Sci. Rev.* **11**, 380 (1970).
23. R. W. Schunk and J. C. G. Walker, *Planet Space Sci.* **18**, 1535 (1970).
24. M. H. Rees, R. A. Jones, and J. C. G. Walker, *Planet Space Sci.* **19**, 313 (1971).
25. T. Tohmatsu, T. Ogawa and H. Tsuruta, *Rep. Ionosphere Space Res. Japan* **19**, 482 (1965).
26. J. C. Brandt and M. B. McElroy, *The Atmospheres of Mars and Venus*, p. 251. Gordon and Breach, New York, 1963.
27. A. Dalgarno, M. B. McElroy, M. H. Rees, and J. C. G. Walker, *Planet. Space Sci.* **16**, 1371 (1968).
28. M. F. Shea, R. D. Sharp, and M. B. McElroy, *J. Geophys. Res.* **73**, 4199 (1968).
29. W. F. Hoegy, J. P. Fournier, and E. G. Fontheim, *J. Geophys. Res.* **70**, 5464 (1965).
30. E. G. Fontheim, A. E. Beutler, and A. F. Nagy, *Ann. Géophys.* **24**, 489 (1968).
31. J. S. Nisbet, *J. Atmos. Terr. Phys.* **30**, 1257 (1968).
32. A. F. Nagy and P. M. Banks, *J. Geophys. Res.* **75**, 6260 (1970).
33. A. Dalgarno, M. B. McElroy, and A. I. Stewart, *J. Atmos. Sci.* **26**, 753 (1969).
34. J. P. Doering, W. G. Fastie, and P. D. Feldman, *J. Géophys. Res.* **75**, 4787 (1970).
35. M. L. Duboin, G. Lejeune, M. Petit, and G. Weill, *J. Atmos. Terr. Phys.* **30**, 563 (1968).
36. W. C. Knudsen, *J. Geophys. Res.* **77**, 1233 (1972).
37. E. J. R. Maier and B. C. N. Rao, *J. Geophys. Res.* **75**, 7168 (1970).
38. J. E. Geisler and S. A. Bowhill, *J. Atmos. Terr. Phys.* **27**, 457 (1965).
39. R. C. Whitten, *J. Atmos. Terr. Phys.* **30**, 1523 (1968).
40. K. V. S. Nathan, *Planet. Space Sci.* **14**, 717 (1966).
41. J. R. Catchpole, *J. Atmos. Terr. Phys.* **29**, 949 (1967).
42. J. R. Catchpole, *J. Atmos. Terr. Phys.* **29**, 70 (1967).

43. J. V. Evans, *Planet. Space Sci.* **15**, 1557 (1967).
44. R. J. Cicerone and S. A. Bowhill, *Radio Sci.* **5**, 49 (1970).
45. P. M. Banks and A. F. Nagy, *J. Geophys. Res.* **75**, 1902 (1970).
46. A. F. Nagy and P. M. Banks, *Space Res.* **11**, 1123 (1971).
47. M. H. Rees and J. C. G. Walker, *Ann. Géophys.* **24**, 193 (1968).
48. J. C. G. Walker, in *The Radiating Atmosphere* (B. M. McCormac, ed.). Reidel Publ., Dordrecht, The Netherlands, 1971.
49. J. C. G. Walker, *Planet. Space Sci.* **16**, 321 (1968).
50. J. C. G. Walker, R. S. Stolarski, and A. F. Nagy, *Ann. Géophys.* **25**, 831 (1969).
51. L. R. Megill and J. H. Cahn, *J. Geophys. Res.* **69**, 5041 (1964).
52. P. M. Banks and G. J. Lewak, *Phys. Fluids* **11**, 804 (1968).
53. P. M. Banks, *Planet. Space Sci.* **16**, 759 (1968).
54. P. M. Banks, *Planet. Space Sci.* **14**, 1078 (1966).
55. A. Dalgarno, *Advan. At. Mol. Phys.* **4**, 381 (1968).
56. M. H. Mentzoni and R. V. Row, *Phys. Rev.* **130**, 2312 (1963).
57. M. H. Mentzoni and K. V. Narasinga Rao, *Phys. Rev. Lett.* **14**, 779 (1965).
58. M. H. Mentzoni, *J. Geophys. Res.* **73**, 4444 (1968).
59. A. Dalgarno and R. J. W. Henry, *Proc. Roy. Soc. London* **A288**, 521 (1965).
60. R. G. Roble, A Theoretical and Experimental Study of the Stable Mid-Latitude Red Arc. Ph.D. Thesis, Univ. of Michigan, March (1969).
61. R. D. Hake and A. V. Phelps, *Phys. Rev.* **158**, 70 (1967).
62. N. F. Lane and A. Dalgarno, *J. Geophys. Res.* **74**, 3011 (1969).
63. G. J. Schulz and J. T. Dowell, *Phys. Rev.* **128**, 174 (1962).
64. A. Dalgarno and T. C. Degges, *Planet. Space Sci.* **16**, 125 (1968).
65. M. H. Rees, J. C. G. Walker and A. Dalgarno, *Planet. Space Sci.* **15**, 1097 (1967).
66. P. M. Banks, *Planet. Space Sci.* **15**, 77 (1967).
67. A. Dalgarno and J. C. G. Walker, *Planet. Space Sci.* **15**, 200 (1967).
68. J. R. Herman and S. Chandra, *Planet. Space Sci.* **17**, 815 (1969).
69. P. Stubbe, *J. Atmos. Terr. Phys.* **32**, 865 (1970).
70. C. Kruger, M. Mitchner, U. Daybilge, *Proc. IEEE* **56**, 1458 (1968).
71. E. L. Walker and B. S. Tanenbaum, *Phys. Fluids* **11**, 1955 (1968).
72. P. M. Banks, *Earth Planet. Sci. Lett.* **1**, 270 (1966).
73. S. Chapman, *Smithsonian Contrib. Astrophys.* **2**, 1 (1956).
74. L. Spitzer and R. Harm, *Phys. Rev.* **89**, 977 (1953).
75. S. Chapman and T. G. Cowling, *Mathematical Theory of Nonuniform Gases*, 3rd ed. Cambridge Univ. Press, London and New York, 1970.
76. P. M. Banks, *Ann. Géophys.* **22**, 577 (1966).
77. L. Goldstein and T. Sekiguchi, *Phys. Rev.* **109**, 625 (1958).
78. T. Sekiguchi and R. C. Herndon, *Phys. Rev.* **112**, 1 (1958).
79. F. Rostas, K. Bhattacharya, and J. H. Cahn, *Phys. Rev.* **129**, 495 (1963).

CHAPTER 23

Electron and Ion Temperatures

23.1 Electron Temperatures

Using the basic steady state energy balance equations for electrons and ions with the various heating and cooling processes described in the preceding chapter, it is possible to compute theoretical profiles of temperature appropriate for different model neutral atmospheres and ranges of parameters. Typical results taken from recent work [1] are shown in *Fig. 23.1* to illustrate the theoretical variation in electron temperature through the course of an undisturbed day in July 1963 at Millstone Hill, Massachusetts.

Several features of these theoretical profiles are of interest since they relate to the general features of ionospheric temperatures. First, below 150 km thermal equilibrium between the electron and neutral gases is predicted as a result of the rapid electron-neutral energy loss rates which are present even for minor temperature differences. (Although it has been postulated [2] that $T_e > T_n$ within the E region due to electron deexcitation of N_2 vibration states, the heat source appropriate to this process has not been included in the calculations of Fig. 23.1.)

Next, as shown in the same figure, the electron temperature has a positive temperature gradient to very high altitudes, even though it is known that the altitude of maximum heat input to the electron gas occurs between 160 and 180 km. A temperature profile of this character is typical of an electron energy budget dominated by thermal conduction and can usually be found either during periods of low solar activity when the F_2-region electron densities are depressed and electron to ion energy losses are rel-

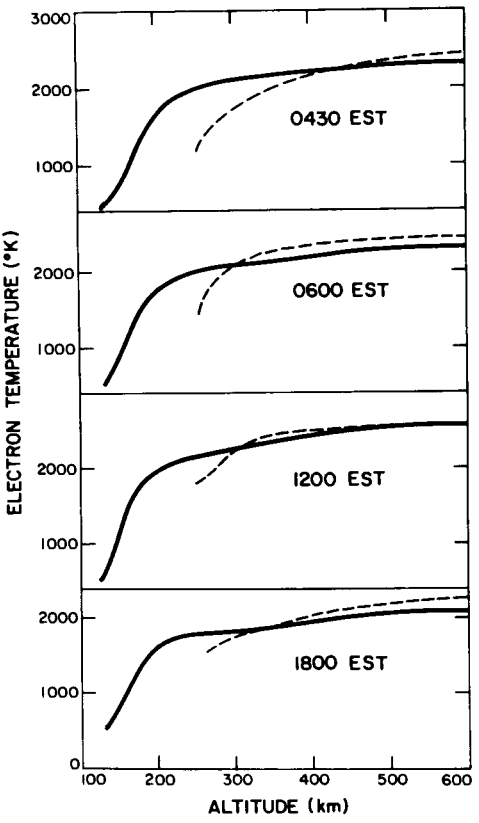


Fig. 23.1 Electron temperature profiles in July 1963 at various times throughout the day. The solid lines are the theoretical predictions while the dashed curves are the experimental incoherent scatter data at Millstone Hill [1].

atively unimportant, or at times when large downward heat fluxes emerge from the magnetosphere [3–6]. Under these circumstances much of the heat produced in the F_2 region and above is conducted downwards and eventually lost to the neutral atmosphere below 200 km.

For more intense solar activity the energy losses associated with F_2-region ions become important. While the production of electron thermal energy depends roughly upon the electron density, the energy losses vary as n_e^2. Thus, for the elevated electron densities characteristic of moderate and active solar conditions, T_e will tend to decrease with altitude in the F_2 region, bringing about a closer semblance of thermal equilibrium at high altitudes [7]. A temperature profile illustrating this effect is shown in *Fig. 23.2*. Thermal conduction is effective at all altitudes but, in contrast to the temperature profiles characteristic of low electron density shown in Fig. 23.1, the F_2-region energy losses in the present case are sufficiently large to cause a negative temperature gradient to appear. In a certain sense

these high density temperature profiles are very similar to older predictions which ignored thermal transport effects [8].

When the effect of magnetospheric heating is included, however, it is found that the F_2-region temperature minimum is no longer followed by a relatively cool, isothermal region, but rather there occurs a strong positive electron temperature gradient with high temperatures ($T_e \sim$ 3000–4000°K) being found at altitudes above 1000 km [3, 5, 9–12].

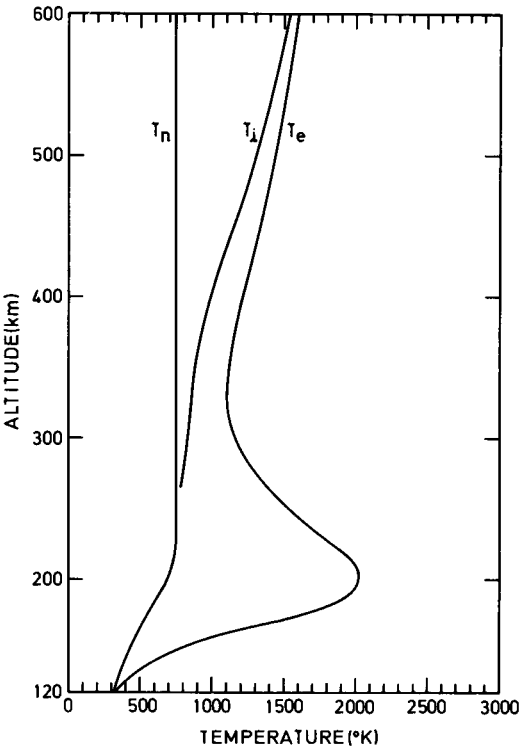


Fig. 23.2 Electron and ion temperature profile for a 750°K model neutral atmosphere, overhead sun, a vertical magnetic field, a 10% photoelectron heating efficiency, and a magnetospheric heat source of 10^9 eV cm^{-2} sec^{-1} at 600 km altitude.

One important consequence of large F_2-region energy losses is that the temperature profile at altitudes below the F_2 region becomes virtually independent of magnetospheric energy processes. Thermal energy conducted downwards from the inner magnetosphere (having its origin in low energy electrons, photoelectrons, etc.) will affect only the temperatures in the ionospheric regions near and above the F_2 peak. This thermal isolation will

be present only if the electron–ion heat losses are a large part of the F_2-region heat budget. In marginal cases, such as may occur in the normal ionosphere at minimum solar activity, the presence of a large, downward heat flux of the order of 5×10^9 to 5×10^{10} eV cm^{-2} sec^{-1} could convert a loss dominated profile (Fig. 23.2) into a conduction dominated profile (Fig. 23.1).

The theoretical prediction of ionospheric electron temperatures is subject to a number of uncertainties associated with a lack of precise knowledge of atomic and molecular excitation ionization processes. In particular, the rate at which photoelectron energy is introduced into the thermal electron gas cannot be accurately calculated as a result of the large number of possible photoion energy states, the inexactness of photoelectron cooling cross sections for O_2 and N_2, and the possibility of photoelectron transport [13]. Consequently, accepting the basic range of values for the rate at which the electron gas is heated, it is more important to know the general behavior of the ionospheric temperatures with respect to particular trends in the parameters of the neutral and ionized atmospheres rather than the specific values calculated for a single model.

To illustrate the effects associated with the uncertainty in the photoelectron heating rate, the electron temperatures of *Fig. 23.3* have been

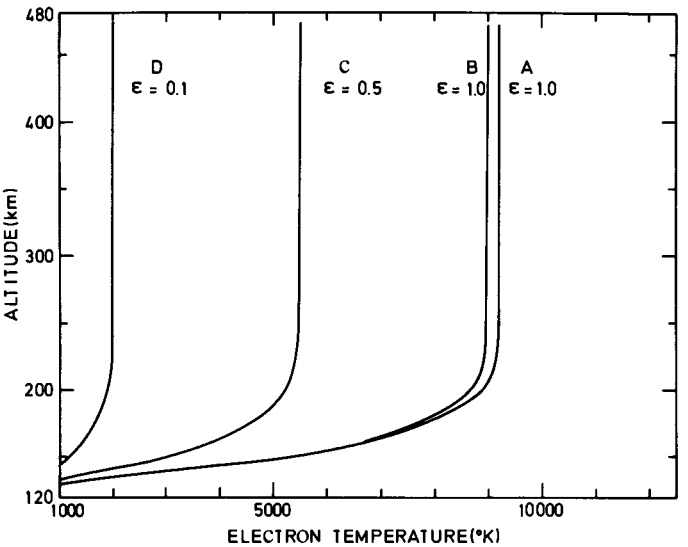


Fig. 23.3 Electron temperature profiles for a 1250°K model neutral atmosphere and differing efficiencies for photoelectron to electron energy conversion.

calculated for a 1250°K model neutral atmosphere with several different rates of electron gas energy production taken from Chapter 22. Curve A of Fig. 23.3 is the electron temperature profile which would result if all photoionizations resulted in ground state photoions with all photoelectron energy being given to thermal electrons; that is, the photoelectrons are given the maximum possible proportion of the available initial solar EUV photon energy which, in turn, is transferred exclusively to the electron gas. In contrast, Curve B represents the temperature profile arising from an energy production rate based upon the actual distribution of photoion internal energy states and the assumption that all photoelectron energy is given locally to the electron gas. Since only a small fraction of the photoelectron energy initially available actually is given to the electron gas, curves C and D indicate the temperature profiles resulting when 50% and 10% of the photoelectron energy production is given locally to the electron gas.

In the four cases listed above it has been assumed that $T_i = 1250°K$ and a self-consistent electron density profile has been calculated using the production, loss, and diffusion rates discussed in the preceding chapters. No downward heat flux from the magnetosphere has been included.

Changing solar conditions affect both the structure of the neutral atmosphere and the ionosphere. Profiles of electron temperature for neutral gas models characterized by thermospheric temperatures of $T_n = 750°$, 1250°, 1500°, and 2000°K are shown in *Figs. 23.4–23.6* for three different energy production rates; full, one-half, and one-tenth the total amount of energy initially given to photoelectrons, taking into account the different photoion energy states. For each of the neutral atmospheres the changes in solar flux have been taken into account and self-consistent model ionospheres have been calculated.

At low activity, as typified by $T_n = 750°K$, and depending upon the peak electron density, the F_2-region energy losses are not sufficiently large to bring about $dT_e/dz < 0$ at any altitude and a conduction dominated profile results. For higher thermospheric temperatures the peak F_2-region density increases significantly such that $dT_e/dz < 0$ for $z > 250$ km and $T_e \to T_n$ at high altitudes in the absence of downward heat conduction.

The importance of thermal energy transported downward from the magnetosphere into the upper ionosphere should not be underestimated in its effect upon the electron temperature profile. From incoherent scatter radar [9, 11, 12] data and direct rocket probes [10, 14] it is known that the magnitude of the heat flux entering the daytime midlatitude ionosphere ranges between 5×10^9 and 2×10^{10} eV cm^{-2} sec^{-1}. In the absence of high altitude energy production or loss the electron temperature gradient corresponding

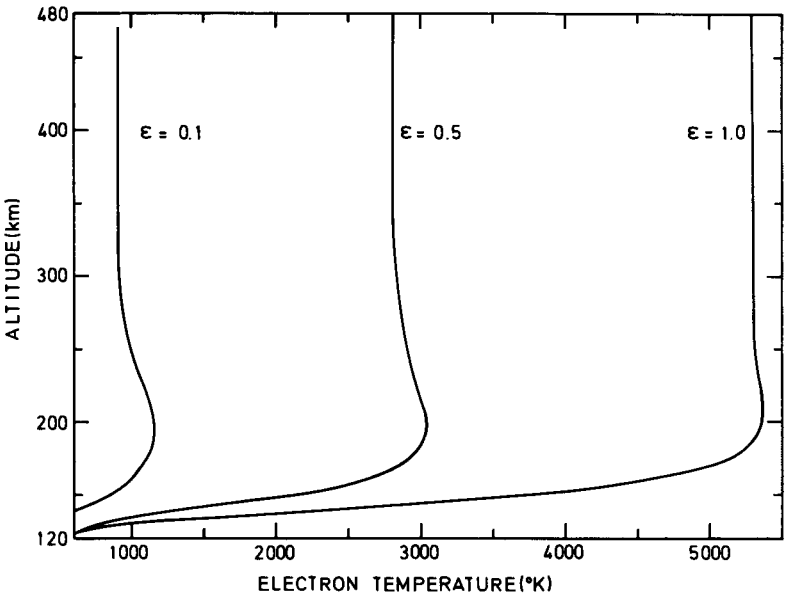


Fig. 23.4 Electron temperature profiles for a 750°K model neutral atmosphere and differing photoelectron energy conversion efficiencies.

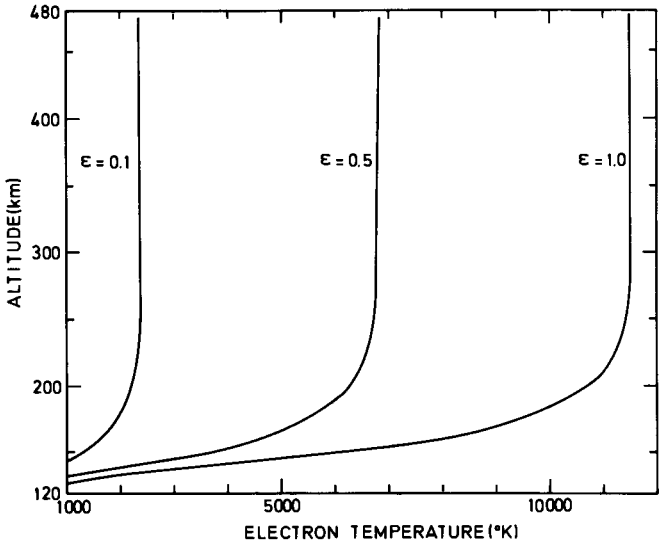


Fig. 23.5 Electron temperature profiles for a 1500°K model neutral atmosphere and differing photoelectron energy conversion efficiencies.

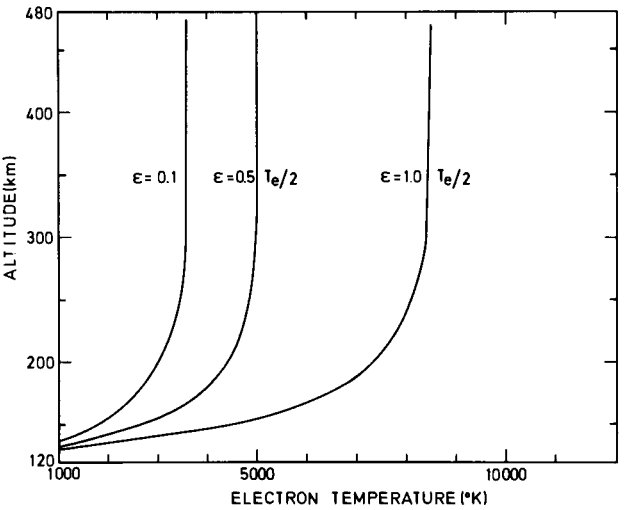


Fig. 23.6 Electron temperature profiles for a 2000°K model neutral atmosphere and differing photoelectron energy conversion efficiencies.

to a heat flux Φ_E is

$$dT_e/dz = -(1.3\times 10^{-1}\Phi_E)/T_e^{5/2} \quad {}^\circ\text{K km}^{-1} \tag{23.1}$$

which, for $T_e = 4000^\circ$K, indicates the presence of thermal gradients as large as 2.5°K km^{-1} in the regions between 500 and 1000 km. Altitude profiles of electron temperature showing the effect of downward thermal conduction are given in *Fig. 23.7* for downward energy fluxes between 1×10^9 and 5×10^{10} eV cm^{-2} sec^{-1} using a 1250°K model neutral atmosphere and a self-consistent ionosphere.

It has been postulated that the major source of heating for the inner magnetosphere arises from photoelectrons which escape the neutral atmosphere [3, 5, 9, 15]. As discussed in Chapter 22, the calculation of the magnitude and energy spectrum of this flux is very difficult and subject to a number of complications which make any predictions of the net upward energy flow rather uncertain [6, 16–19]. In a steady state the upward energy flow carried by photoelectrons is matched by an equal downward flow by thermal conduction. In addition, to preserve electrical neutrality the upward photoelectron flux must be matched by a downward flow of thermal electrons which, in itself, can result in a significant heat flux.

Direct measurements of ionospheric electron temperatures are now available for a substantial portion of the solar cycle [3, 4, 14, 20–43]. To date,

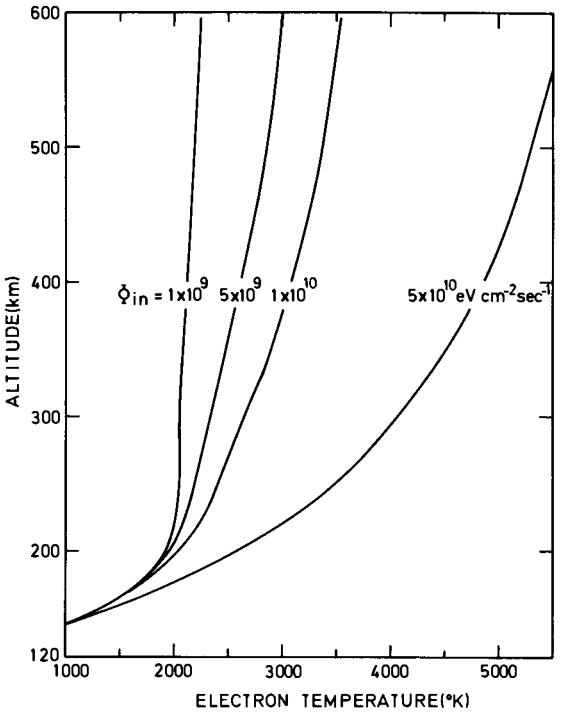


Fig. 23.7 Altitude profiles of electron temperature for a 1250°K model atmosphere, overhead sun, and various downward magnetospheric heat fluxes.

the results of rocket-borne Langmuir probes have provided the best opportunities to compare theoretical models of the electron energy budget with the real ionospheric environment. Since the rockets pass rapidly through the ionospheric plasma, the inherent difficulties of time dependent fluctuations can be avoided to a large extent.

A typical result from rocket probes has already been shown in Fig. 22.1. In this experiment not only was it possible to measure directly the electron temperature profile but, through computation of the N_2 scale height $[H(N_2) = kT_n/m(N_2)g]$, the neutral gas temperature could also be found. In the example shown a relatively large degree of thermal disequilibrium is clearly evident.

A typical series of electron temperatures, obtained at the Arecibo, Puerto Rico incoherent scatter facility [29] is shown in *Fig. 23.8*. These data illustrate the fluctuating nature of the electron temperatures in response to changes in both the ionospheric electron density and the character of the neutral atmosphere. As mentioned previously, in the upper F region a

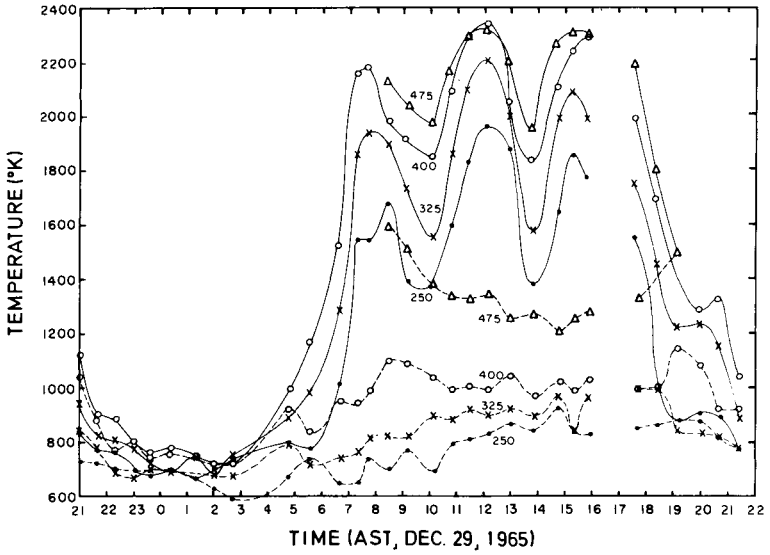


Fig. 23.8 Electron and ion temperature variations throughout December 29, 1965, as measured at the Arecibo, Puerto Rico incoherent scatter facility [29]. Solid curve, T_e; dashed curve, T_i.

balance exists between chemical processes and bulk transport such that the electron density, temperature, and diffusion velocity are coupled. Fluctuations in any of the external parameters of the plasma system, especially those relating to the structure of the neutral atmosphere and its winds, can lead to substantial changes in the observed densities and temperatures. Thus, large increases (or decreases) in F_2-region electron density depress (or enhance) the local electron temperature, and the electron density is the dominant member of the coupled system. From theoretical considerations, an increase in T_e can enhance the rate of ion diffusion and lower the electron density near the F_2 peak, thus decreasing the electron to ion energy transfer rate and supporting a further increase in T_e. It has been shown [44, 45], however, that a process of this type is rapidly self-limiting and cannot explain the large changes in electron temperature shown in Fig. 23.8. A better explanation lies in the effects of neutral winds which move F_2-layer ionization along geomagnetic field tubes by means of ion-neutral collisions. The introduction of a given wind may greatly enhance (or diminish) the peak F_2-layer electron density, thereby increasing (or decreasing) the electron to ion energy losses and lowering (or raising) T_e.

Theoretical studies are concerned with local, steady state models of the ionosphere [1, 7, 8, 46]. Incoherent scatter radar results, in contrast, are

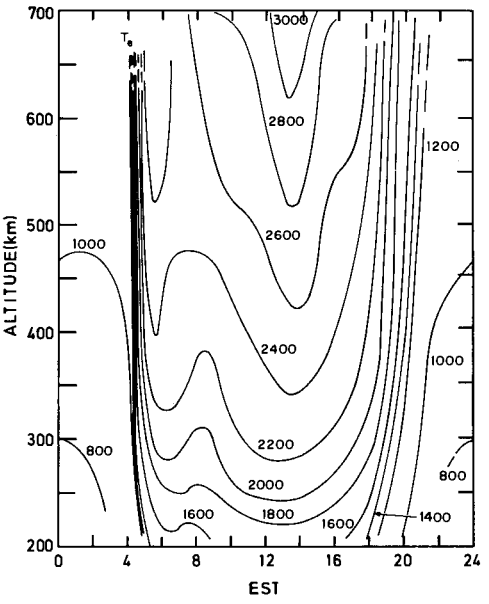


Fig. 23.9 Mean monthly behavior of the electron temperature during July 1964 measured at Millstone Hill, Massachusetts, using the incoherent scatter technique [3].

most effective when applied to time-dependent phenomena. *Figures 23.9* and *23.10*, for example, show the daily variations in electron temperature during the months of July (summer) and November (winter), 1964 as measured at Millstone Hill, Massachusetts. It is clear that significant dif-

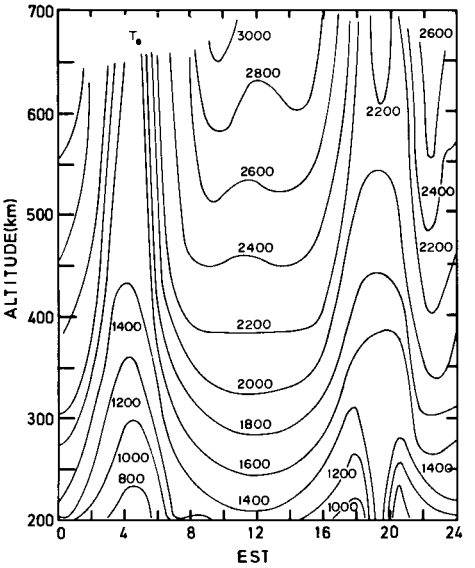


Fig. 23.10 Mean monthly behavior of the electron temperature during November 1964 measured at Millstone Hill, Massachusetts, using the incoherent scatter technique. The temperature rise near dawn is generally much less rapid in winter than in summer [3].

ferences exist between the two seasons of the year and that to explain these would require a detailed theory relating not only to the ionosphere, but to geographical and geomagnetic factors, the seasonal behavior of the upper atmospheric composition and temperature, and variations in horizontal neutral gas transport (winds).

In contrast to rocket and radar experiments, which are well suited to investigate ionospheric phenomena on a local scale, satellite measurements are principally useful to the extent that they yield information on the global distributions of temperature and density over extended time periods. *Figure 23.11* illustrates the diurnal variation in T_e as a function of geomagnetic latitude for the 1965 vernal equinox as measured by the Explorer XXII satellite at an altitude of 1000 $\pm$ 100 km. Such data, coupled with theoretical models of plasma diffusion and the electron heat balance, have been

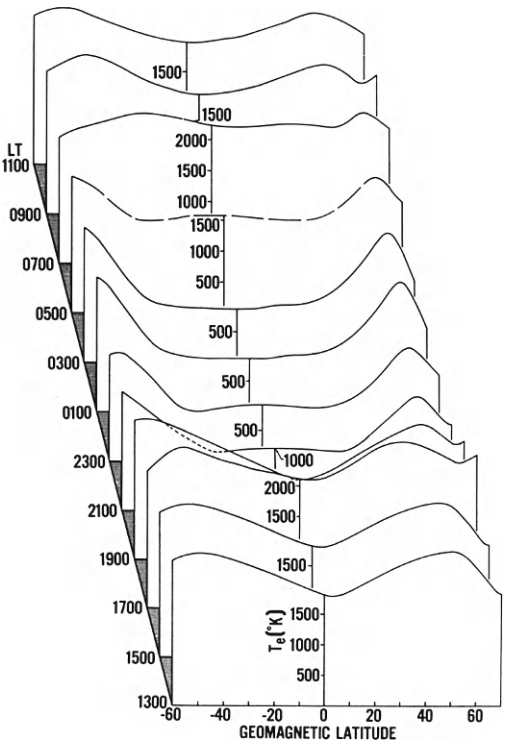


Fig. 23.11 Averaged latitudinal and local time behavior of the electron temperature at 1000 $\pm$ 100 km altitude as measured by Explorer XXII in 1965 near vernal equinox. The nighttime cooling of the electron gas proceeds rapidly at low geomagnetic latitudes owing to the low heat capacity of the low latitude photonosphere magnetic field tubes [33].

used to increase our knowledge of plasma behavior in the inner magnetosphere.

Within the constraints of the geomagnetic field, plasma in a given tube has been found to behave much like a compressible fluid [47–49], undergoing expansion as a result of daytime photoelectron heating and contraction as a result of nighttime heat loss to the lower ionospheric regions. At low geomagnetic latitudes, where the volume and heat capacity of the field tubes are small, the thermal energy introduced into the field tube by photoelectrons and thermal conduction can be rapidly lost to the F_2 region at night, leading to rapid decreases in electron temperature. For progressively higher latitudes, however, the heat capacity of field tubes increases rapidly and eventually a steady state behavior is reached with only moderate variations in density and temperature between day and night [50].

23.2 Ion Temperatures

Owing to the rapid loss of ion thermal energy to the neutral gases for small temperature separations, $T_i \simeq T_n$ to within a few percent in the E and F_1 regions if only heating by the ambient electron gas is considered. Equating the ion thermal energy input from electron–ion collision to that lost through collisions with neutral particles, an approximate expression for the ion temperature can be obtained for steady state conditions, ignoring thermal conduction, as [51]

$$T_i = \frac{T_n + (\alpha n_e/n_n)T_e^{-1/2}}{1 + (\alpha n_e/n_n)T_e^{-3/2}} \tag{23.2}$$

where from the energy exchange rates of Chapter 22, $\alpha \simeq 6 \times 10^6$ and n_n is the neutral gas number density. At high altitudes, where n_e/n_n is large, $T_i \to T_e$. This transitional temperature dependence is shown in *Fig. 23.12* for a 1000°K model neutral atmosphere and various constant values of the electron temperature.

The approximate result given by (23.2) is adequate for large (10–50 eV cm^{-3} sec^{-1}) high altitude electron–ion energy transfer rates. During periods of low solar activity, however, the local energy production and loss rates at altitudes above 500 km become small and thermal conduction through the ion gases begins to play a part in determining the actual ion temperature profile [51]. The principal effect appears as a modest separation between T_e and T_i at very high altitudes, as shown in *Fig. 23.13*.

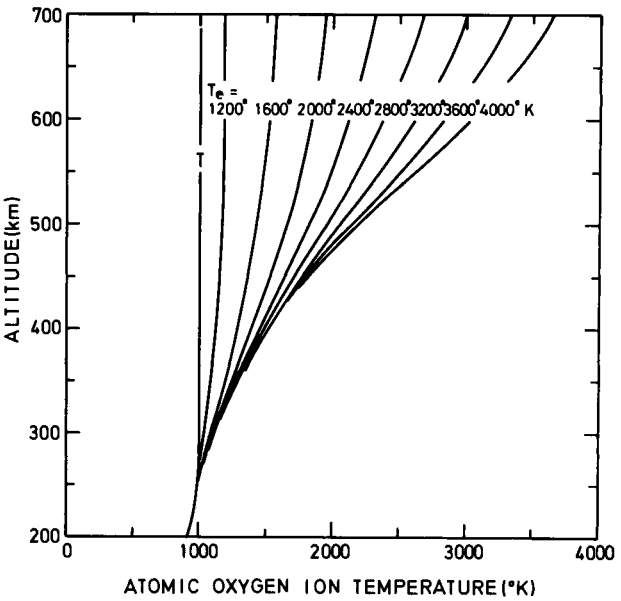


Fig. 23.12 Temperature of atomic oxygen ions for different constant electron temperatures and a neutral atmospheric temperature of 1000°K. Below 300 km electron gas heating is not sufficient to enhance the ion temperature. At high altitudes, however, the neutral gas is ineffective in cooling the ions and the ion temperature approaches the electron temperature [55].

The altitude profile of ion temperature depends strongly upon the composition and temperature of the neutral atmosphere as well as on ionospheric parameters. For neutral gas models having increasing temperature the concentrations of the major constituents increase at a given altitude and serve, through ion-neutral collisions, to bind the ion temperature more tightly to the neutral gas temperature. However, it is generally true that the electron density is larger during the periods of enhanced solar activity characteristic of the warmer neutral atmospheric models and, as a consequence, it is difficult to predict from a limited set of geophysical data the actual ion temperature profile at a given time.

The time-dependent behavior of the ion gas has been studied theoretically [51]. For altitudes below 500 to 600 km the effect of thermal conduction is small and the time constant for changes in the ion temperature is determined by ion-neutral charge exchange and elastic ion–electron collisions. *Table 23.1* lists typical time constants. It appears that for normal diurnal changes in ionospheric parameters T_i will have essentially its steady-state value.

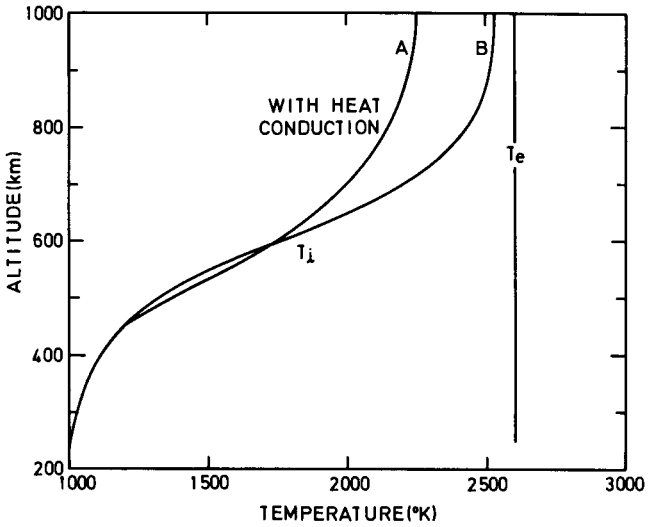


Fig. 23.13 Calculated ion temperature profiles. The effect of ion gas heat conduction is included in curve A but excluded in curve B. The thermal energy given to the ion gases above 600 km in A is transported downwards and is lost between 450 and 600 km, slightly raising the ion temperature above the value for B [51]. ($T_n = 1000°K$; $T_e = 2600°K$; $I = 90°$.)

Because of the relatively slow ion thermal speeds (1–4 km sec^{-1}) rocket and satellite probe measurements of ion temperature are relatively difficult to perform [14, 22, 41, 52, 53]. A recent result is shown in *Fig. 23.14* along with the observed values of T_e.

Measurements based upon the electromagnetic properties of the local plasma permit the determination of ion temperatures. Investigations using

TABLE 23.1

ION TEMPERATURE TIME CONSTANTS

Altitude (km)	τ (sec)
300	3.6
400	15
500	72
600	240
700	540

satellite borne experiments [54], for example, have deduced ion composition and temperatures from VLF plasma resonances and topside radio sounding data taken with the Alouette 1 satellite. The most extensive experimental studies of ion temperature have been made by incoherent scatter radars. These data, as do the rocket results, tend to confirm in detail the altitude transitional behavior of the ion temperature and, by implication, the choice of the electron gas as the ion gas heating agent. *Figure 23.15* shows a typical set of electron and ion temperature profiles obtained in 1964 at Millstone Hill, Massachusetts [3]. Also shown is the oxygen ion temperature calculated [51] using the ion heating, cooling, and transport processes discussed in the preceding sections.

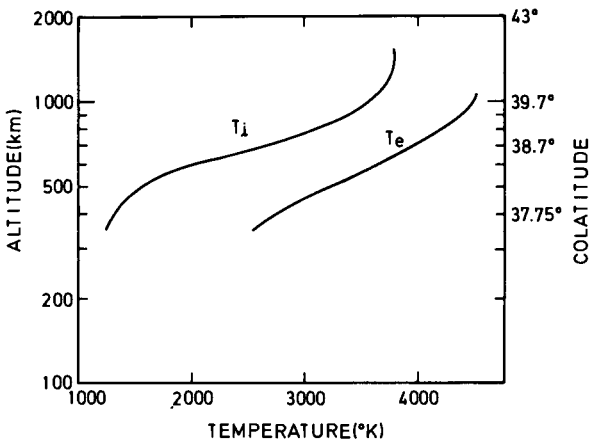


Fig. 23.14 Electron and ion temperature profiles measured above Wallops Island, Virginia, on June 21, 1967, using rocket and satellite sensors [10].

Another aspect of the thermal balance of the ion gases relates to the degree to which the different ion gases have the same temperature. Several studies [51–57] have been made which predict that H^+ and He^+ should be several hundred degrees Kelvin warmer than O^+ ions due to the differing rates of electron–ion energy transfer. Direct calculations of the H^+ velocity distribution [58] have shown some distortion from Maxwellian due to this heating, but the deviation is not large. Likewise, solutions for the O^+ velocity distribution function using Boltzmann's equation including the effects of charge exchange ($O^+ + O \rightleftharpoons O + O^+$), electron–ion collisions, and ion–ion collisions have shown [59] that there should be no important departure of O^+ ions from the Maxwellian velocity distribution, even for large rates of ion heating and cooling.

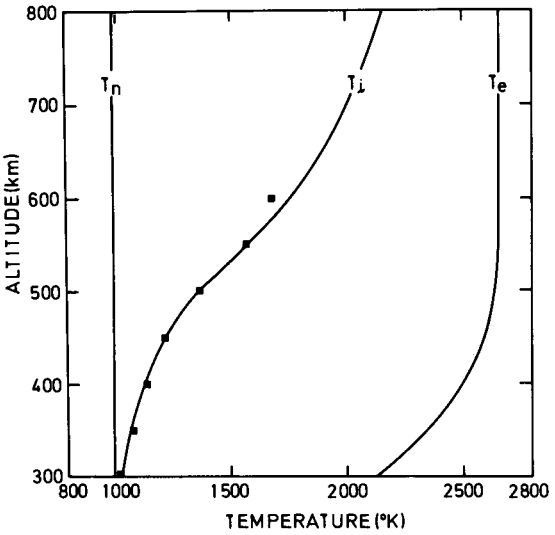


Fig. 23.15 Comparison of computed and experimental ion temperatures using a 1000°K model neutral atmosphere and the incoherent scatter data of J. V. Evans (shown by squares) for 1200 EST, September, 1963 [51]. $N_e = 3.4 \times 10^5\ cm^{-3}$ at 300 km.

23.3 Conjugate Region Heating

It has been observed [43, 60–65] that local enhancement in electron temperature occurs in the upper F region at a particular location during the dark early morning hours when local sunrise (and local photoelectron production) follows several hours after the sunrise in the geomagnetic conjugate region. A possible explanation for this phenomenon, illustrated in *Fig. 23.16*, is that energetic photoelectrons created in the small optical depth regions of the geomagnetically conjugate ionosphere are able to travel through the magnetosphere from the conjugate region to the local, predawn region along the lines of magnetic force. In passing downward into the dark hemisphere the photoelectrons suffer inelastic collisions with the neutral atmospheric particles and finally release some fraction of their energy to the ambient electron gas. A theoretical prediction [16] for the low latitude (Arecibo, Puerto Rico) energy spectrum of incident photoelectrons for various solar zenith angles is shown in *Fig. 23.17*.

As discussed previously, a substantial flux of photoelectrons is able to escape the normal daytime ionosphere and travel along the lines of geomagnetic force into the magnetosphere. The distance these electrons can travel before being thermalized by the ambient electron gas is contained

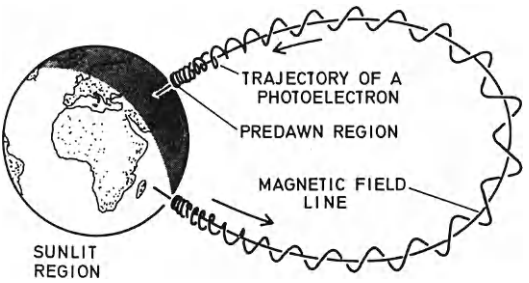


Fig. 23.16 Geomagnetic conjugate region heating by photoelectrons. Due to geographic and geomagnetic factors, magnetically conjugate ionospheres are not symmetrically illuminated by the sun. At certain times of the year photoelectrons can travel into dark predawn regions, bringing about enhancements in electron and ion temperatures and airglow emissions.

implicitly in the equation

$$\varepsilon^2 = \varepsilon_a{}^2 - \frac{3.9\times 10^{-12}}{\cos\theta}\int_a^s n_e(s')\,ds' \quad (\text{eV})^2 \tag{23.3}$$

where θ is the electron pitch angle, ε_a is the initial electron energy in electron volts, ε is the final electron energy at the point s, s' is a coordinate along the magnetic field lines, and n_e is the electron density.

In order for there to be any appreciable penetration of photoelectrons

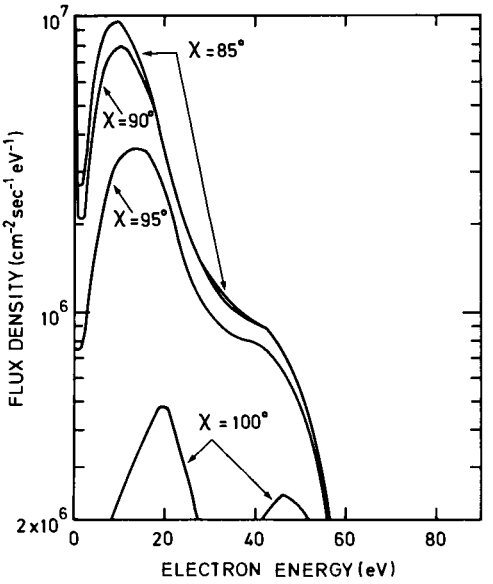


Fig. 23.17 Flux spectrum of photoelectrons entering the predawn ionosphere at 1000 km for different solar zenith angles, χ (referred to the daytime ionosphere) [16].

through the magnetosphere into a conjugate region, the electron column content must be less than that required by (23.3) to make $\varepsilon = 0$. During the early morning hours, when conjugate heating occurs, typical field tube ionization contents at Arecibo [18] tend to be of the order $0.5\text{–}1.0 \times 10^{13}$ electrons cm^{-2}, establishing a threshold of about 4.5 to 5.2 eV for an initial photoelectron to be able to travel the field line and produce any appreciable heating. This implies that only short wavelength solar photons ($\lambda \lesssim 665$ Å) are important for conjugate region energy production.

During the middle of the day, when magnetospheric electron densities are larger, the energy threshold is substantially increased and most of the photoelectron energy is dissipated within the magnetosphere and eventually lost to the ionospheric regions by means of thermal conduction.

The range equation (23.3) also indicates that a geomagnetic latitude effect should be present. At low latitudes essentially all photoelectrons can travel to their conjugate regions. For increasingly higher latitudes the length of the field lines becomes rapidly larger and only electrons of progressively higher energy are able to completely traverse the field lines.

The possibility of observing conjugate region effects depends upon both geographical and geomagnetic factors. Normally, significant predawn heating is seen only for relatively short periods during the course of a year [50].

23.4 Subauroral Red Arcs

An important feature of worldwide magnetic storms was discovered in 1957 [60] in connection with observations of O(I) (λ 6300–6364 Å) atmospheric emissions from stable red arcs occurring at subauroral latitudes. The SAR-arc, which is not normally visible, appears equatorwards of the normal auroral zone as a long, thin emission band within the F region and oriented parallel to lines of magnetic latitude. A peculiarity of SAR-arcs is the lack of emissions other than those originating at the $O(^1D)$ state, the lowest electronic energy level of the oxygen atom.

The SAR-arcs have been found to be stable and persist over time periods as long as 10 hr while undergoing slow (5–50 m sec^{-1}) equatorward drifts. *Figure 23.18* shows the relationship of the SAR-arcs to the auroral zones and the general near-earth environment. A discussion of the relevant observations is given in Nagy *et al.* [67].

A number of theories have been advanced to explain the SAR-arc phenomenon. The most plausible explanation involves heated ambient electrons exciting atomic oxygen in such a manner that while the $O(^1D)$ is

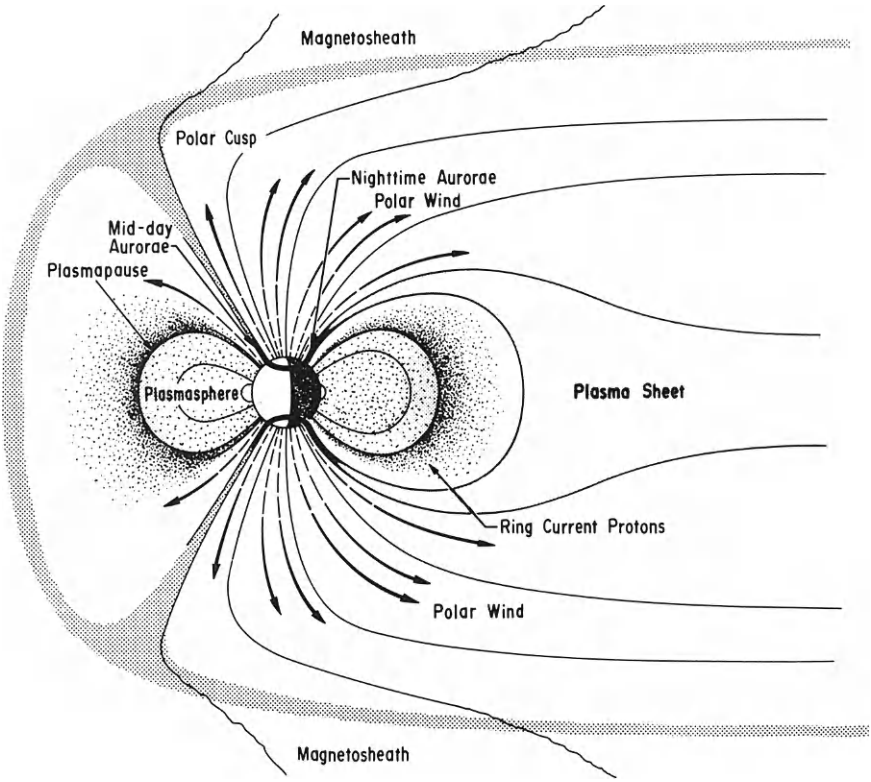


Fig. 23.18 The relationship between auroras, the polar cap glow, and SAR arcs in terms of the earth's plasma and magnetic field plasma. It has been postulated that ring current particles heat the magnetospheric plasma and, by thermal conduction, the ionosphere.

significantly populated, virtually no excitation of O(I)(^{1}S) leading to O(I) (λ 5577 Å), is involved [68, 69].

It has been suggested [70] that the decay of energetic ring current particles by means of a wave–particle interaction within the magnetosphere would provide a large heat source at high altitudes which could, by means of thermal conduction, be used to heat F-region electrons and produce the observed emissions. If heat conduction from above is the local heating mechanism for the F region, then a substantial electron temperature gradient must exist and electron temperatures greater than 5000°K must be expected at 1000 km [71]. Because the efficiency of the wave–particle interaction depends upon the electron density, it has been argued [70] that SAR arcs occur at the plasmapause where the ring current particles are continually

eroded away. In the recovery phase of a magnetic storm the plasmapause and ring current particles are found at relatively low magnetic latitudes. As the plasmasphere refills with ionospheric plasma, the ring current particles are removed with the most rapid conversion of energetic particle energy into wave energy being found at the plasmasphere boundary. Through interaction of the plasma waves with thermal electrons a body of hot electrons of average energy 1–2 eV is formed at the plasmapause. Subsequent thermal conduction can lead to elevated electron temperatures and 6300 Å emission.

23.5 Thermal Effects of Auroras

The precipitation of energetic (~5 keV) electrons into the atmosphere at high latitudes (65°–70° magnetic) is normally observed during large scale geomagnetic storms and polar magnetic substorms. Although the basic acceleration process of the electrons is not yet known, our understanding of the atmospheric processes governing the emission of infrared, optical, and ultraviolet radiations is well advanced [72] and can be summarized as follows: As the incident fast electrons penetrate the atmosphere, ionizing and exciting collisions with the neutral gas particles occur and large numbers of secondary electrons of relatively low (10–50 eV) energy are created. The secondary particles, in turn, create further excitation of the neutral gases while thermalizing. Eventually, most of the fast electrons are stopped near 100 km, the lower altitude limit of auroral displays. The excited atoms and molecules return to their ground states either through quenching collisions with other particles or through the emission of characteristic radiation. The peculiar forms and apparent motions of auroras are due to the spatial distributions of the fast electrons and to changes in the location of the incident particles.

Generally, electron temperatures in auroras are as high as 4000°K as a result of two energy sources. First, in analogy with the photoelectron heating problem, the secondary electrons of auroras are able to transfer some of their excess kinetic energy directly to the ambient electron gas [73]. In addition, electron deexcitation of atoms and molecules in excited states is an important source of thermal energy to an extent not normally seen in a quiet, sunlit atmosphere.

A second heat source relates to the heating of ambient electrons by the electric fields thought to exist in some types of intense auroral forms [74, 75]. Adopting electric fields perpendicular to the geomagnetic field with mag-

nitudes on the order of 10^{-2} V m^{-1}, it has been predicted that this heat source for both electrons and ions can lead to peak temperatures on the order of 3500°K at 300 km altitude in agreement with experiment.

23.6 The Polar Wind

Within the auroral oval the geomagnetic field lines lead into the tail of the magnetosphere and interplanetary space. The theory predicts that much of the ionization associated with the polar topside icnosphere is lost from the earth by means of a large scale outward hydrodynamic expansion very similar to the expansion of the solar corona which gives the solar wind. The escaping ionospheric ion flux, termed the polar wind, involves the conversion of random thermal energy and electric potential energy into the energy of bulk motion and has associated with it the requirement for a continual heat input to overcome the energy losses of ion-neutral friction and gravitational potential energy. In the absence of external energy sources the polar wind process would be expected to cool the ionospheric plasma to temperatures substantially below that of the neutral atmosphere. If, on the other hand, external heat sources are present, and the polar wind plays an unimportant part in the polar ionosphere electron heat budget, the electron temperature profiles would be expected to have certain characteristic shapes, depending upon whether F-region heat sources (soft precipitating electrons) or magnetospheric (thermal conduction) heat sources were involved.

At the present time very little is known about the temperature profiles of the polar regions. During winter periods photoionization cannot be an effective heat source, yet satellite measurements [76] indicate electron temperatures as high as 3000°K at 3000 km. Ion temperature measurements from low altitude (200 km) satellites [52, 53] have given values of T_i as large as 6000°K, but the separation of kinetic temperature from bulk motion is difficult. Many problems relating to the polar ionosphere remain to be solved and it can be expected that the solutions will relate not only to the upper atmosphere of the earth but also to external influences typical of the solar wind and the magnetospheric tail.

REFERENCES

1. A. Dalgarno, M. B. Mc Elroy, M. H. Rees, and J. C. G. Walker, *Planet. Space Sci.* **16**, 1371 (1968).
2. J. C. G. Walker, *Planet. Space Sci.* **16**, 321 (1968).
3. J. V. Evans, *Planet. Space Sci.* **15**, 1557 (1967).

4. J. V. Evans, *Planet. Space Sci.* **15**, 1387 (1967).
5. J. V. Evans and G. P. Mantas, *J. Atmos. Terr. Phys.* **30**, 563 (1968).
6. A. F. Nagy, E. G. Fontheim, R. S. Stolarski, and A. E. Beutler, *J. Geophys. Res.* **74**, 4667 (1969).
7. P. M. Banks, *Ann. Géophys.* **22**, 577 (1966).
8. A. Dalgarno, M. B. Mc Elroy, and R. J. Moffett, *Planet. Space Sci.* **11**, 463 (1963).
9. J. V. Evans, *Space Res.* **8**, 717 (1968).
10. S. Sanatani and W. B. Hanson, *J. Geophys. Res.* **75**, 769 (1970).
11. P. Bauer, G. Lejeune, and M. Petit, *Planet. Space Sci.* **18**, 1447 (1970).
12. J. V. Evans, *Planet. Space Sci.* **18**, 1225 (1970).
13. W. B. Hanson and R. Cohen, *J. Geophys. Res.* **73**, 831 (1968).
14. W. B. Hanson, S. Sanatani, L. H. Brace, and J. A. Findlay, *J. Geophys. Res.* **74**, 2229 (1969).
15. W. B. Hanson, *Space Res.* **3**, 282 (1963).
16. E. G. Fontheim, A. E. Beutler, and A. F. Nagy, *Ann. Géophys.* **24**, 489 (1968).
17. M.-L. Duboin, G. Lejeune, M. Petit, and G. Weill, *J. Atmos. Terr. Phys.* **30**, 299 (1968).
18. J. S. Nisbet, *J. Atmos. Terr. Phys.* **30**, 1257 (1968).
19. A. F. Nagy and P. M. Banks, *J. Geophys. Res.* **75**, 6260 (1970).
20. R. L. Boggess, L. H. Brace, and N. W. Spencer, *J. Geophys. Res.* **64**, 1627 (1959).
21. N. W. Spencer, L. H. Brace, and G. R. Carignan, *J. Geophys. Res.* **67**, 157 (1962).
22. A. F. Nagy, L. H. Brace, G. R. Carignan, and M. Kanal, *J. Geophys. Res.* **68**, 6401 (1963).
23. J. V. Evans, *J. Geophys. Res.* **67**, 4914 (1962).
24. N. W. Spencer, L. H. Brace, G. R. Carignan, D. R. Taeusch, and H. Niemann, *J. Geophys. Res.* **70**, 2665 (1965).
25. L. H. Brace, N. W. Spencer, and G. R. Carignan, *J. Geophys. Res.* **68**, 5397 (1963).
26. J. V. Evans, *J. Geophys. Res.* **72**, 3343 (1967).
27. J. V. Evans, *Planet. Space Sci.* **13**, 1031 (1965).
28. D. T. Farley, *Ann. Géophys.* **22**, 448 (1966).
29. J. R. Doupnik and J. S. Nisbet, *J. Atmos. Terr. Phys.* **30**, 931 (1968).
30. L. H. Brace, N. W. Spencer, and A. Dalgarno, *Planet. Space Sci.* **13**, 647 (1965).
31. P. J. Bowen, R. L. F. Boyd, C. L. Henderson, and A. P. Willmore, *Proc. Roy. Soc.* **281A**, 526 (1964).
32. L. H. Brace, H. G. Mayr, and B. M. Reddy, *J. Geophys. Res.* **73**, 1607 (1968).
33. L. H. Brace, B. M. Reddy, and H. G. Mayr, *J. Geophys. Res.* **72**, 265 (1967).
34. L. H. Brace, H. C. Carlson, and K. K. Mahajan, *J. Geophys. Res.* **74**, 1883 (1969).
35. S. Chandra, B. E. Troy, Jr., J. L. Donley, and R. E. Bourdeau, *J. Geophys. Res.* **75**, 3867 (1970).
36. D. T. Farley, J. P. Mc Clure, D. L. Sterling, and J. L. Green, *J. Geophys. Res.* **72**, 5837 (1967).
37. J. P. Mc Clure, *J. Geophys. Res.* **74**, 279 (1969).
38. S. S. Prasad, *J. Geophys. Res.* **73**, 6795 (1968).
39. S. S. Prasad, *J. Geophys. Res.* **75**, 1911 (1970).
40. P. B. Rao, *J. Geophys. Res.* **73**, 1661 (1968).
41. S. Sanatani and W. B. Hanson, *J. Geophys. Res.* **75**, 769 (1970).
42. R. H. Wand, *J. Geophys. Res.* **75**, 829 (1970).
43. H. Carru, M. Petit, and P. Waldtenfel, *J. Atmos. Terr. Phys.* **29**, 351 (1967).

44. J. R. Doupnik, Density and Temperature Fluctuations in the Daytime F-region of the Ionosphere. Ph. D. Dissertation, Pennsylvania State Univ., Univ. Park, Pennsylvania, August 10 (1967).
45. W. F. Utlaut and R. Cohen, *Science* **174**, 245 (1971).
46. A. V. da Rosa, *J. Geophys. Res.* **71**, 4107 (1966).
47. H. G. Mayr, L. H. Brace, and G. S. Dunham, *J. Geophys. Res.* **72**, 4391 (1967).
48. A. F. Nagy, P. Bauer, and E. G. Fontheim, *J. Geophys. Res.* **73**, 6259 (1968).
49. P. M. Banks, A. F. Nagy, and W. I. Axford, *Planet. Space Sci.* **19**, 1053 (1971).
50. J. V. Evans, *J. Geophys. Res.* **73**, 3489 (1968).
51. P. M. Banks, *J. Geophys. Res.* **72**, 3365 (1967).
52. W. C. Knudsen and G. W. Sharp, *J. Geophys. Res.* **70**, 143 (1965).
53. W. C. Knudsen and G. W. Sharp, *J. Geophys. Res.* **72**, 1061 (1967).
54. R. E. Barrington, J. S. Belrose, and G. L. Nelms, *J. Geophys. Res.* **70**, 1647 (1965).
55. P. M. Banks, *Planet. Space Sci.* **15**, 77 (1967).
56. A. Dalgarno and J. C. G. Walker, *Planet. Space Sci.* **15**, 200 (1967).
57. S. Chandra and J. R. Herman, *Planet. Space Sci.* **17**, 841 (1969).
58. P. M. Banks, *Planet. Space Sci.* **16**, 759 (1968).
59. P. M. Banks and G. J. Lewak, *Phys. Fluids* **11**, 804 (1968).
60. D. Barbier, *Ann. Géophys.* **14**, 334 (1958).
61. H. C. Carlson, Jr., *J. Geophys. Res.* **71**, 195 (1966).
62. H. C. Carlson, Jr., in *Aurora and Airglow* (B. M. McCormac, ed.), pp. 643–647. Van Nostrand–Reinhold, Princeton, New Jersey, 1967.
63. H. C. Carlson and G. M. Weill, *Ann. Géophys.* **23**, 569 (1967).
64. R. T. Bennett, *J. Geophys. Res.* **74**, 381 (1969).
65. C. S. Deehr, *Ann. Géophys.* **25**, 867 (1969).
66. C. S. Deehr, *Ann. Géophys.* **25**, 881 (1969).
67. A. F. Nagy, R. G. Roble, and P. B. Hays, *Space Sci. Rev.* **11**, 709 (1970).
68. K. D. Cole, *J. Geophys. Res.* **70**, 1689 (1965).
69. K. D. Cole, *Space Sci. Rev.* **5**, 699 (1966).
70. J. M. Cornwall, F. V. Coroniti, and R. M. Thorne, *J. Geophys. Res.* **76**, 4428 (1971).
71. R. G. Roble, R. B. Norton, J. A. Findlay, and E. Marovich, *J. Geophys. Res.* **76**, 7648 (1971).
72. R. S. Stolarski, *Planet. Space Sci.* **16**, 1265 (1968).
73. J. C. G. Walker and M. H. Rees, *Planet. Space Sci.* **16**, 459 (1968).
74. M. H. Rees and J. C. G. Walker, *Ann. Géophys.* **24**, 193 (1968).
75. M. H. Rees, R. A. Jones, and J. C. G. Walker, *Planet. Space Sci.* **19**, 313 (1971).
76. J. L. Donley, *Space Res.* **8**, 381 (1968).

APPENDIX B

Working Models of the Thermosphere

The following tables contain six model thermospheres for thermopause temperatures of 750°, 1000°, 1250°, 1500°, 1750°, and 2000°K. Data are provided for the altitude, temperature, concentrations of the five principal neutral species, the total atmospheric pressure, the pressure scale height, the total neutral gas concentration, the total neutral gas mass density, the mean molecular mass, the total pressure scale height gradient, the mass density scale height, and the mass density scale height gradient.

Atmospheric models corresponding to other thermopause temperatures can be constructed from the data of Tables B7 through B11 which give the altitude variation of temperature for thermopause temperatures ranging from 600° to 2000°K in 50°K increments.

TABLE B1a

750°K THERMOPAUSE

Temperature and Concentrations of Neutral Species

Z (KM)	T (K)	N(O) (CM-3)	N(O2) (CM-3)	N(N2) (CM-3)	N(HE) (CM-3)	N(H) (CM-3)
120	323.6	10.00E 10	4.00E 10	4.00E 11	2.00E 07	4.28E 06
130	418.6	4.73E 10	1.16E 10	1.31E 11	1.51E 07	2.88E 06
140	504.6	2.65E 10	4.38E 09	5.47E 10	1.22E 07	2.27E 06
150	573.5	1.67E 10	1.98E 09	2.68E 10	1.03E 07	1.94E 06
160	624.2	1.14E 10	9.98E 08	1.46E 10	9.11E 06	1.75E 06
170	660.2	8.13E 09	5.40E 08	8.46E 09	8.20E 06	1.62E 06
180	685.6	6.01E 09	3.06E 08	5.12E 09	7.50E 06	1.54E 06
190	703.5	4.53E 09	1.79E 08	3.19E 09	6.92E 06	1.47E 06
200	716.2	3.47E 09	1.06E 08	2.02E 09	6.43E 06	1.42E 06
210	725.2	2.68E 09	6.43E 07	1.30E 09	6.00E 06	1.38E 06
220	731.6	2.08E 09	3.93E 07	8.43E 08	5.62E 06	1.35E 06
230	736.3	1.63E 09	2.41E 07	5.50E 08	5.27E 06	1.32E 06
240	739.7	1.28E 09	1.49E 07	3.61E 08	4.95E 06	1.29E 06
250	742.2	1.01E 09	9.29E 06	2.38E 08	4.66E 06	1.27E 06
260	744.1	7.94E 08	5.79E 06	1.58E 08	4.38E 06	1.25E 06
270	745.4	6.27E 08	3.63E 06	1.05E 08	4.13E 06	1.23E 06
280	746.5	4.97E 08	2.27E 06	6.95E 07	3.89E 06	1.21E 06
290	747.3	3.94E 08	1.43E 06	4.63E 07	3.67E 06	1.19E 06
300	747.9	3.12E 08	9.02E 05	3.09E 07	3.46E 06	1.17E 06
310	748.3	2.48E 08	5.69E 05	2.07E 07	3.27E 06	1.15E 06
320	748.7	1.97E 08	3.60E 05	1.39E 07	3.09E 06	1.13E 06
330	749.0	1.57E 08	2.28E 05	9.29E 06	2.92E 06	1.12E 06
340	749.2	1.25E 08	1.45E 05	6.24E 06	2.75E 06	1.10E 06
350	749.4	9.97E 07	9.20E 04	4.20E 06	2.60E 06	1.09E 06
360	749.5	7.95E 07	5.85E 04	2.83E 06	2.46E 06	1.07E 06
370	749.6	6.35E 07	3.73E 04	1.91E 06	2.32E 06	1.05E 06
380	749.7	5.07E 07	2.38E 04	1.29E 06	2.20E 06	1.04E 06
390	749.7	4.05E 07	1.52E 04	8.70E 05	2.08E 06	1.02E 06
400	749.8	3.24E 07	9.75E 03	5.89E 05	1.96E 06	1.01E 06
450	749.9	1.07E 07	1.07E 03	8.51E 04	1.49E 06	9.42E 05
500	749.9	3.61E 06	1.21E 02	1.27E 04	1.13E 06	8.80E 05
550	750.0	1.24E 06	1.41E 01	1.93E 03	8.67E 05	8.22E 05
600	750.0	4.29E 05	1.71E 00	3.04E 02	6.65E 05	7.69E 05
650	750.0	1.51E 05	2.12E-01	4.90E 01	5.13E 05	7.20E 05
700	750.0	5.41E 04		8.10E 00	3.96E 05	6.75E 05
750	750.0	1.96E 04		1.37E 00	3.08E 05	6.33E 05
800	750.0	7.23E 03		2.39E-01	2.40E 05	5.95E 05
850	750.0	2.70E 03			1.87E 05	5.59E 05
900	750.0	1.02E 03			1.47E 05	5.26E 05
950	750.0	3.91E 02			1.16E 05	4.95E 05
1000	750.0	1.52E 02			9.12E 04	4.66E 05
1500	750.0				1.01E 04	2.68E 05
2000	750.0				1.46E 03	1.65E 05
2500	750.0				2.61E 02	1.07E 05
3000	750.0				5.63E 01	7.26E 04

TABLE B1b (*continued*)

750°K THERMOPAUSE

Temperature, Total Pressure, Pressure Scale Height, Total Concentration, and Total Density

Z (KM)	T (K)	P (TORR)	H (KM)	N (CM-3)	RHO (GM/CM3)
120	323.6	1.81E-05	10.9	5.40E 11	2.34E-11
130	418.6	8.22E-06	14.6	1.90E 11	7.95E-12
140	504.6	4.47E-06	18.2	8.56E 10	3.48E-12
150	573.5	2.70E-06	21.4	4.55E 10	1.79E-12
160	624.2	1.74E-06	24.0	2.70E 10	1.03E-12
170	660.2	1.17E-06	26.3	1.71E 10	6.38E-13
180	685.6	8.12E-07	28.2	1.14E 10	4.14E-13
190	703.5	5.76E-07	29.8	7.91E 09	2.78E-13
200	716.2	4.15E-07	31.3	5.60E 09	1.92E-13
210	725.2	3.04E-07	32.6	4.05E 09	1.35E-13
220	731.6	2.25E-07	33.9	2.97E 09	9.66E-14
230	736.3	1.68E-07	35.0	2.21E 09	7.02E-14
240	739.7	1.27E-07	36.1	1.66E 09	5.16E-14
250	742.2	9.68E-08	37.0	1.26E 09	3.83E-14
260	744.1	7.41E-08	37.9	9.63E 08	2.87E-14
270	745.4	5.72E-08	38.8	7.41E 08	2.17E-14
280	746.5	4.43E-08	39.6	5.73E 08	1.66E-14
290	747.3	3.45E-08	40.3	4.46E 08	1.27E-14
300	747.9	2.70E-08	41.0	3.49E 08	9.81E-15
310	748.3	2.12E-08	41.7	2.74E 08	7.60E-15
320	748.7	1.67E-08	42.3	2.16E 08	5.92E-15
330	749.0	1.32E-08	42.9	1.71E 08	4.63E-15
340	749.2	1.05E-08	43.5	1.35E 08	3.64E-15
350	749.4	8.35E-09	44.0	1.08E 08	2.87E-15
360	749.5	6.66E-09	44.6	8.59E 07	2.26E-15
370	749.6	5.34E-09	45.3	6.88E 07	1.79E-15
380	749.7	4.29E-09	45.9	5.52E 07	1.42E-15
390	749.7	3.46E-09	46.6	4.45E 07	1.13E-15
400	749.8	2.79E-09	47.4	3.60E 07	9.04E-16
450	749.9	1.03E-09	53.3	1.33E 07	3.01E-16
500	749.9	4.38E-10	65.6	5.64E 06	1.06E-16
550	750.0	2.27E-10	91.0	2.93E 06	4.00E-17
600	750.0	1.45E-10	137.6	1.86E 06	1.71E-17
650	750.0	1.07E-10	205.6	1.38E 06	8.63E-18
700	750.0	8.74E-11	281.5	1.13E 06	5.20E-18
750	750.0	7.46E-11	349.5	9.61E 05	3.63E-18
800	750.0	6.53E-11	405.1	8.42E 05	2.78E-18
850	750.0	5.81E-11	451.3	7.49E 05	2.25E-18
900	750.0	5.23E-11	492.1	6.74E 05	1.88E-18
950	750.0	4.74E-11	530.3	6.11E 05	1.61E-18
1000	750.0	4.33E-11	567.0	5.58E 05	1.39E-18
1500	750.0	2.16E-11	869.7	2.78E 05	5.16E-19
2000	750.0	1.29E-11	1062.5	1.66E 05	2.85E-19
2500	750.0	8.31E-12	1215.7	1.07E 05	1.80E-19
3000	750.0	5.64E-12	1363.5	7.26E 04	1.22E-19

TABLE B1c (*continued*)

750°K THERMOPAUSE

Mean Molecular Mass, Atmospheric Scale Height, Gradient of H, Density Scale Height HRO, and Gradient of HRO

Z (KM)	T (K)	M (AMU)	H (KM)	BETA	HRO (KM)	BETAR
120	323.6	26.1	10.9	0.377	8.0	0.300
130	418.7	25.3	14.6	0.372	10.7	0.276
140	504.7	24.5	18.3	0.344	13.6	0.305
150	573.6	23.8	21.4	0.292	16.7	0.298
160	624.2	23.1	24.1	0.242	19.5	0.267
170	660.3	22.4	26.3	0.204	22.0	0.232
180	685.7	21.8	28.2	0.176	24.2	0.201
190	703.6	21.2	29.9	0.155	26.1	0.176
200	716.2	20.6	31.3	0.140	27.7	0.158
210	725.2	20.1	32.7	0.128	29.2	0.144
220	731.7	19.6	33.9	0.118	30.6	0.133
230	736.4	19.1	35.0	0.110	31.9	0.124
240	739.8	18.7	36.1	0.102	33.1	0.117
250	742.3	18.3	37.1	0.095	34.2	0.110
260	744.1	18.0	38.0	0.088	35.3	0.104
270	745.5	17.7	38.8	0.082	36.3	0.098
280	746.5	17.4	39.6	0.076	37.2	0.091
290	747.3	17.2	40.4	0.071	38.1	0.085
300	747.9	16.9	41.1	0.067	38.9	0.078
310	748.4	16.7	41.7	0.063	39.7	0.072
320	748.8	16.5	42.3	0.061	40.4	0.067
330	749.0	16.4	42.9	0.059	41.0	0.061
340	749.2	16.2	43.5	0.058	41.6	0.056
350	749.4	16.0	44.1	0.059	42.2	0.052
360	749.5	15.9	44.7	0.061	42.7	0.049
370	749.7	15.7	45.3	0.064	43.1	0.046
380	749.7	15.5	46.0	0.069	43.6	0.043
390	749.8	15.3	46.7	0.075	44.0	0.041
400	749.8	15.1	47.5	0.083	44.4	0.040
450	750.0	13.7	53.3	0.164	46.5	0.045
500	750.0	11.3	65.6	0.349	49.3	0.073
550	750.0	8.2	91.0	0.698	54.5	0.141
600	750.0	5.5	137.5	1.167	64.6	0.281
650	750.0	3.8	205.4	1.497	84.2	0.519
700	750.0	2.8	281.1	1.471	117.5	0.811
750	750.0	2.3	348.9	1.230	163.7	1.003
800	750.0	2.0	404.4	1.001	214.2	0.983
850	750.0	1.8	450.5	0.859	259.9	0.836
900	750.0	1.7	491.4	0.784	298.0	0.698
950	750.0	1.6	529.6	0.746	330.7	0.619
1000	750.0	1.5	566.3	0.724	360.7	0.591
1500	750.0	1.1	869.3	0.474	694.0	0.697
2000	750.0	1.0	1062.3	0.327	989.9	0.477
2500	750.0	1.0	1215.6	0.296	1190.3	0.349
3000	750.0	1.0	1363.4	0.298	1354.1	0.312

TABLE B2a

1000°K THERMOPAUSE

Temperature and Concentrations of Neutral Species

Z (KM)	T (K)	N(O) (CM-3)	N(O2) (CM-3)	N(N2) (CM-3)	N(HE) (CM-3)	N(H) (CM-3)
120	323.6	10.00E 10	4.00E 10	4.00E 11	2.00E 07	2.61E 06
130	472.7	4.32E 10	1.09E 10	1.23E 11	1.41E 07	1.22E 06
140	596.4	2.44E 10	4.40E 09	5.37E 10	1.12E 07	7.53E 05
150	692.5	1.59E 10	2.17E 09	2.84E 10	9.53E 06	5.41E 05
160	765.2	1.13E 10	1.20E 09	1.67E 10	8.42E 06	4.25E 05
170	819.8	8.38E 09	7.12E 08	1.05E 10	7.63E 06	3.54E 05
180	861.0	6.45E 09	4.43E 08	6.88E 09	7.02E 06	3.07E 05
190	892.2	5.08E 09	2.85E 08	4.66E 09	6.52E 06	2.74E 05
200	915.9	4.07E 09	1.87E 08	3.22E 09	6.11E 06	2.50E 05
210	934.0	3.29E 09	1.25E 08	2.26E 09	5.75E 06	2.32E 05
220	948.0	2.69E 09	8.48E 07	1.60E 09	5.44E 06	2.18E 05
230	958.8	2.21E 09	5.80E 07	1.15E 09	5.16E 06	2.07E 05
240	967.2	1.83E 09	3.99E 07	8.26E 08	4.90E 06	1.98E 05
250	973.7	1.52E 09	2.77E 07	5.99E 08	4.67E 06	1.90E 05
260	978.9	1.26E 09	1.93E 07	4.36E 08	4.45E 06	1.84E 05
270	983.0	1.05E 09	1.35E 07	3.18E 08	4.24E 06	1.79E 05
280	986.2	8.79E 08	9.43E 06	2.33E 08	4.05E 06	1.74E 05
290	988.8	7.36E 08	6.63E 06	1.71E 08	3.87E 06	1.70E 05
300	990.8	6.17E 08	4.67E 06	1.26E 08	3.70E 06	1.67E 05
310	992.5	5.18E 08	3.30E 06	9.28E 07	3.54E 06	1.64E 05
320	993.9	4.36E 08	2.33E 06	6.85E 07	3.39E 06	1.61E 05
330	995.0	3.66E 08	1.65E 06	5.07E 07	3.24E 06	1.58E 05
340	995.9	3.09E 08	1.17E 06	3.76E 07	3.11E 06	1.56E 05
350	996.6	2.60E 08	8.33E 05	2.79E 07	2.98E 06	1.54E 05
360	997.2	2.19E 08	5.93E 05	2.07E 07	2.85E 06	1.51E 05
370	997.7	1.85E 08	4.23E 05	1.54E 07	2.73E 06	1.49E 05
380	998.1	1.56E 08	3.01E 05	1.14E 07	2.62E 06	1.47E 05
390	998.5	1.32E 08	2.15E 05	8.52E 06	2.51E 06	1.46E 05
400	998.7	1.12E 08	1.54E 05	6.36E 06	2.41E 06	1.44E 05
450	999.6	4.87E 07	2.93E 04	1.49E 06	1.95E 06	1.36E 05
500	999.9	2.15E 07	5.72E 03	3.56E 05	1.59E 06	1.29E 05
550	1000.1	9.61E 06	1.14E 03	8.70E 04	1.30E 06	1.22E 05
600	1000.1	4.35E 06	2.34E 02	2.17E 04	1.07E 06	1.16E 05
650	1000.2	1.99E 06	4.89E 01	5.53E 03	8.78E 05	1.11E 05
700	1000.2	9.21E 05	1.05E 01	1.43E 03	7.24E 05	1.05E 05
750	1000.2	4.31E 05	2.29E 00	3.79E 02	5.99E 05	1.00E 05
800	1000.2	2.04E 05	5.12E-01	1.02E 02	4.96E 05	9.57E 04
850	1000.2	9.72E 04	1.17E-01	2.80E 01	4.13E 05	9.14E 04
900	1000.2	4.69E 04		7.84E 00	3.44E 05	8.73E 04
950	1000.2	2.29E 04		2.23E 00	2.87E 05	8.34E 04
1000	1000.2	1.13E 04		6.44E-01	2.41E 05	7.98E 04
1500	1000.2	1.54E 01			4.62E 04	5.27E 04
2000	1000.2				1.08E 04	3.65E 04
2500	1000.2				2.98E 03	2.64E 04
3000	1000.2				9.44E 02	1.98E 04

TABLE B2b (*continued*)

1000°K THERMOPAUSE

Temperature, Total Pressure, Pressure Scale Height, Total Concentration, and Total Density

Z (KM)	T (K)	P (TORR)	H (KM)	N (CM-3)	RHO (GM/CM3)
120	323.6	1.81E-05	10.9	5.40E 11	2.34E-11
130	472.7	8.65E-06	16.4	1.77E 11	7.42E-12
140	596.4	5.10E-06	21.4	8.25E 10	3.38E-12
150	692.5	3.33E-06	25.5	4.64E 10	1.86E-12
160	765.2	2.31E-06	28.9	2.91E 10	1.14E-12
170	819.8	1.66E-06	31.8	1.96E 10	7.48E-13
180	861.0	1.23E-06	34.3	1.38E 10	5.15E-13
190	892.2	9.26E-07	36.4	10.00E 09	3.67E-13
200	915.9	7.09E-07	38.3	7.48E 09	2.68E-13
210	934.0	5.49E-07	40.0	5.68E 09	1.99E-13
220	948.0	4.30E-07	41.6	4.38E 09	1.50E-13
230	958.8	3.40E-07	43.0	3.42E 09	1.15E-13
240	967.2	2.70E-07	44.4	2.70E 09	8.91E-14
250	973.7	2.16E-07	45.6	2.15E 09	6.96E-14
260	978.9	1.74E-07	46.8	1.72E 09	5.48E-14
270	983.0	1.41E-07	48.0	1.39E 09	4.35E-14
280	986.2	1.15E-07	49.0	1.13E 09	3.47E-14
290	988.8	9.40E-08	50.0	9.18E 08	2.79E-14
300	990.8	7.71E-08	51.0	7.52E 08	2.25E-14
310	992.5	6.35E-08	51.9	6.18E 08	1.83E-14
320	993.9	5.25E-08	52.8	5.10E 08	1.49E-14
330	995.0	4.35E-08	53.6	4.22E 08	1.22E-14
340	995.9	3.61E-08	54.3	3.51E 08	10.00E-15
350	996.6	3.01E-08	55.1	2.92E 08	8.27E-15
360	997.2	2.51E-08	55.8	2.44E 08	6.84E-15
370	997.7	2.10E-08	56.4	2.04E 08	5.67E-15
380	998.1	1.76E-08	57.1	1.71E 08	4.72E-15
390	998.5	1.48E-08	57.7	1.43E 08	3.93E-15
400	998.7	1.25E-08	58.3	1.21E 08	3.29E-15
450	999.6	5.41E-09	61.2	5.23E 07	1.38E-15
500	999.9	2.44E-09	64.4	2.36E 07	5.99E-16
550	1000.1	1.15E-09	68.9	1.11E 07	2.68E-16
600	1000.1	5.75E-10	75.6	5.56E 06	1.24E-16
650	1000.2	3.09E-10	86.3	2.98E 06	5.91E-17
700	1000.2	1.81E-10	102.9	1.75E 06	2.95E-17
750	1000.2	1.17E-10	127.4	1.13E 06	1.56E-17
800	1000.2	8.24E-11	160.0	7.96E 05	8.87E-18
850	1000.2	6.22E-11	198.5	6.01E 05	5.48E-18
900	1000.2	4.95E-11	238.4	4.78E 05	3.68E-18
950	1000.2	4.07E-11	275.5	3.94E 05	2.66E-18
1000	1000.2	3.43E-11	307.7	3.32E 05	2.03E-18
1500	1000.2	1.02E-11	537.4	9.89E 04	3.96E-19
2000	1000.2	4.90E-12	865.9	4.73E 04	1.33E-19
2500	1000.2	3.04E-12	1254.6	2.94E 04	6.40E-20
3000	1000.2	2.14E-12	1605.2	2.07E 04	3.93E-20

TABLE B2c (*continued*)

1000°K THERMOPAUSE

Temperature, Mean Molecular Mass, Pressure Scale Height, Pressure Scale Height Gradient, Density Scale Height, and Density Scale Height Gradient

Z (KM)	T (K)	M (AMU)	H (KM)	BETA	HRO (KM)	BETAR
120	323.6	26.1	10.9	0.595	6.9	0.435
130	472.7	25.3	16.5	0.529	10.8	0.391
140	596.4	24.7	21.4	0.454	14.8	0.398
150	692.6	24.1	25.6	0.376	18.7	0.374
160	765.3	23.5	29.0	0.312	22.2	0.336
170	819.9	23.0	31.9	0.264	25.4	0.297
180	861.1	22.5	34.3	0.228	28.2	0.262
190	892.2	22.0	36.4	0.200	30.6	0.231
200	915.9	21.6	38.3	0.179	32.8	0.206
210	934.1	21.1	40.0	0.163	34.8	0.186
220	948.0	20.7	41.6	0.150	36.6	0.170
230	958.8	20.3	43.0	0.140	38.2	0.158
240	967.2	19.9	44.4	0.131	39.7	0.148
250	973.8	19.5	45.7	0.123	41.2	0.139
260	978.9	19.2	46.9	0.116	42.5	0.132
270	983.0	18.9	48.0	0.110	43.8	0.126
280	986.2	18.6	49.1	0.104	45.0	0.121
290	988.8	18.3	50.1	0.099	46.2	0.115
300	990.9	18.0	51.0	0.093	47.4	0.110
310	992.6	17.8	52.0	0.088	48.4	0.105
320	993.9	17.6	52.8	0.084	49.5	0.100
330	995.0	17.4	53.6	0.079	50.4	0.096
340	995.9	17.2	54.4	0.075	51.4	0.091
350	996.6	17.1	55.1	0.071	52.3	0.086
360	997.3	16.9	55.8	0.068	53.1	0.081
370	997.7	16.8	56.5	0.065	53.9	0.077
380	998.2	16.6	57.1	0.063	54.6	0.072
390	998.5	16.5	57.7	0.061	55.3	0.068
400	998.8	16.4	58.3	0.059	56.0	0.065
450	999.6	15.9	61.3	0.059	58.8	0.050
500	1000.0	15.3	64.5	0.073	61.2	0.044
550	1000.1	14.5	68.9	0.107	63.4	0.047
600	1000.2	13.4	75.6	0.168	66.0	0.059
650	1000.2	11.9	86.3	0.266	69.5	0.084
700	1000.2	10.2	102.9	0.406	74.7	0.129
750	1000.2	8.3	127.3	0.573	82.9	0.201
800	1000.2	6.7	159.9	0.721	95.4	0.305
850	1000.2	5.5	198.3	0.797	113.8	0.436
900	1000.2	4.6	238.0	0.778	139.0	0.569
950	1000.2	4.1	275.0	0.693	170.0	0.660
1000	1000.2	3.7	307.1	0.591	203.7	0.675
1500	1000.2	2.4	536.1	0.525	386.0	0.251
2000	1000.2	1.7	864.4	0.759	556.8	0.456
2500	1000.2	1.3	1253.4	0.759	849.1	0.703
3000	1000.2	1.1	1604.3	0.642	1235.2	0.807

TABLE B3a

1250°K THERMOPAUSE

Temperature and Concentrations of Neutral Species

Z (KM)	T (K)	N(O) (CM-3)	N(O2) (CM-3)	N(N2) (CM-3)	N(HE) (CM-3)	N(H) (CM-3)
120	323.6	10.00E 10	4.00E 10	4.00E 11	2.00E 07	2.41E 06
130	523.2	4.01E 10	1.04E 10	1.16E 11	1.33E 07	1.01E 06
140	677.5	2.29E 10	4.40E 09	5.28E 10	1.05E 07	5.90E 05
150	796.5	1.53E 10	2.29E 09	2.93E 10	8.96E 06	3.99E 05
160	888.4	1.11E 10	1.34E 09	1.81E 10	7.94E 06	2.94E 05
170	959.9	8.43E 09	8.43E 08	1.19E 10	7.21E 06	2.28E 05
180	1015.9	6.65E 09	5.55E 08	8.21E 09	6.65E 06	1.85E 05
190	1060.2	5.37E 09	3.77E 08	5.83E 09	6.20E 06	1.54E 05
200	1095.5	4.41E 09	2.63E 08	4.23E 09	5.83E 06	1.31E 05
210	1123.6	3.66E 09	1.86E 08	3.12E 09	5.52E 06	1.14E 05
220	1146.3	3.07E 09	1.34E 08	2.33E 09	5.24E 06	1.01E 05
230	1164.6	2.60E 09	9.71E 07	1.76E 09	5.00E 06	9.05E 04
240	1179.4	2.21E 09	7.11E 07	1.33E 09	4.78E 06	8.22E 04
250	1191.5	1.89E 09	5.24E 07	1.02E 09	4.57E 06	7.54E 04
260	1201.3	1.62E 09	3.88E 07	7.84E 08	4.39E 06	6.99E 04
270	1209.4	1.39E 09	2.89E 07	6.05E 08	4.21E 06	6.53E 04
280	1216.1	1.20E 09	2.16E 07	4.69E 08	4.05E 06	6.14E 04
290	1221.6	1.04E 09	1.62E 07	3.64E 08	3.90E 06	5.82E 04
300	1226.2	8.96E 08	1.22E 07	2.83E 08	3.76E 06	5.54E 04
310	1230.0	7.77E 08	9.17E 06	2.21E 08	3.62E 06	5.30E 04
320	1233.1	6.74E 08	6.93E 06	1.73E 08	3.49E 06	5.10E 04
330	1235.8	5.86E 08	5.24E 06	1.36E 08	3.37E 06	4.92E 04
340	1238.0	5.09E 08	3.97E 06	1.06E 08	3.25E 06	4.77E 04
350	1239.9	4.44E 08	3.02E 06	8.35E 07	3.14E 06	4.63E 04
360	1241.5	3.87E 08	2.29E 06	6.57E 07	3.03E 06	4.51E 04
370	1242.9	3.37E 08	1.75E 06	5.17E 07	2.93E 06	4.40E 04
380	1244.0	2.94E 08	1.33E 06	4.08E 07	2.83E 06	4.30E 04
390	1245.0	2.57E 08	1.02E 06	3.22E 07	2.73E 06	4.22E 04
400	1245.9	2.24E 08	7.76E 05	2.54E 07	2.64E 06	4.14E 04
450	1248.6	1.15E 08	2.05E 05	7.94E 06	2.23E 06	3.82E 04
500	1249.9	5.99E 07	5.54E 04	2.53E 06	1.90E 06	3.60E 04
550	1250.6	3.14E 07	1.53E 04	8.18E 05	1.61E 06	3.42E 04
600	1250.9	1.67E 07	4.29E 03	2.70E 05	1.38E 06	3.27E 04
650	1251.1	8.92E 06	1.23E 03	9.03E 04	1.18E 06	3.13E 04
700	1251.2	4.82E 06	3.59E 02	3.07E 04	1.01E 06	3.00E 04
750	1251.2	2.62E 06	1.06E 02	1.06E 04	8.66E 05	2.89E 04
800	1251.2	1.44E 06	3.21E 01	3.72E 03	7.46E 05	2.78E 04
850	1251.3	7.98E 05	9.85E 00	1.32E 03	6.43E 05	2.68E 04
900	1251.3	4.46E 05	3.07E 00	4.77E 02	5.56E 05	2.58E 04
950	1251.3	2.51E 05	9.74E-01	1.75E 02	4.82E 05	2.49E 04
1000	1251.3	1.42E 05	3.14E-01	6.47E 01	4.18E 05	2.40E 04
1500	1251.3	7.32E 02			1.12E 05	1.72E 04
2000	1251.3	7.07E 00			3.50E 04	1.29E 04
2500	1251.3	1.15E-01			1.25E 04	9.93E 03
3000	1251.3				4.99E 03	7.87E 03

TABLE B3b (*continued*)

1250°K THERMOPAUSE

Temperature, Total Pressure, Pressure Scale Height, Total Concentration, and Total Density

Z (KM)	T (K)	P (TORR)	H (KM)	N (CM-3)	RHO (GM/CM3)
120	323.6	1.81E-05	10.9	5.40E 11	2.34E-11
130	523.2	9.01E-06	18.2	1.66E 11	7.01E-12
140	677.5	5.62E-06	24.2	8.01E 10	3.30E-12
150	796.5	3.86E-06	29.1	4.69E 10	1.89E-12
160	888.4	2.80E-06	33.2	3.05E 10	1.21E-12
170	959.9	2.11E-06	36.6	2.12E 10	8.23E-13
180	1015.9	1.62E-06	39.6	1.54E 10	5.88E-13
190	1060.2	1.27E-06	42.2	1.16E 10	4.34E-13
200	1095.5	1.01E-06	44.5	8.90E 09	3.28E-13
210	1123.6	8.11E-07	46.6	6.97E 09	2.52E-13
220	1146.3	6.57E-07	48.5	5.54E 09	1.97E-13
230	1164.6	5.37E-07	50.3	4.46E 09	1.56E-13
240	1179.4	4.42E-07	51.9	3.62E 09	1.24E-13
250	1191.5	3.65E-07	53.4	2.96E 09	10.00E-14
260	1201.3	3.04E-07	54.9	2.44E 09	8.15E-14
270	1209.4	2.54E-07	56.3	2.03E 09	6.66E-14
280	1216.1	2.13E-07	57.6	1.69E 09	5.48E-14
290	1221.6	1.79E-07	58.8	1.42E 09	4.53E-14
300	1226.2	1.52E-07	60.0	1.20E 09	3.76E-14
310	1230.0	1.29E-07	61.2	1.01E 09	3.14E-14
320	1233.1	1.09E-07	62.3	8.58E 08	2.63E-14
330	1235.8	9.34E-08	63.3	7.30E 08	2.22E-14
340	1238.0	7.98E-08	64.4	6.23E 08	1.87E-14
350	1239.9	6.84E-08	65.3	5.33E 08	1.58E-14
360	1241.5	5.88E-08	66.3	4.58E 08	1.35E-14
370	1242.9	5.06E-08	67.1	3.94E 08	1.15E-14
380	1244.0	4.37E-08	68.0	3.39E 08	9.80E-15
390	1245.0	3.77E-08	68.8	2.93E 08	8.39E-15
400	1245.9	3.27E-08	69.6	2.53E 08	7.20E-15
450	1248.6	1.62E-08	73.2	1.26E 08	3.46E-15
500	1249.9	8.33E-09	76.4	6.44E 07	1.72E-15
550	1250.6	4.39E-09	79.6	3.39E 07	8.84E-16
600	1250.9	2.38E-09	83.2	1.83E 07	4.65E-16
650	1251.1	1.32E-09	87.7	1.02E 07	2.49E-16
700	1251.2	7.62E-10	93.8	5.89E 06	1.36E-16
750	1251.2	4.57E-10	102.2	3.53E 06	7.60E-17
800	1251.2	2.87E-10	113.9	2.22E 06	4.35E-17
850	1251.3	1.90E-10	130.0	1.47E 06	2.56E-17
900	1251.3	1.33E-10	151.2	1.03E 06	1.56E-17
950	1251.3	9.81E-11	177.7	7.58E 05	9.92E-18
1000	1251.3	7.57E-11	208.7	5.84E 05	6.60E-18
1500	1251.3	1.68E-11	441.1	1.30E 05	7.91E-19
2000	1251.3	6.20E-12	572.8	4.79E 04	2.54E-19
2500	1251.3	2.91E-12	769.0	2.24E 04	9.97E-20
3000	1251.3	1.67E-12	1059.5	1.29E 04	4.63E-20

TABLE B3c (*continued*)

1250°K THERMOPAUSE

Temperature, Mean Molecular Mass, Pressure Scale Height, Pressure Scale Height Gradient, Density Scale Height, and Density Scale Height Gradient

Z (KM)	T (K)	M (AMU)	H (KM)	BETA	HRO (KM)	BETAR
120	323.6	26.1	10.9	0.826	6.0	0.556
130	523.3	25.4	18.2	0.659	11.0	0.482
140	677.6	24.8	24.2	0.542	15.8	0.464
150	796.5	24.3	29.1	0.448	20.3	0.430
160	888.4	23.8	33.2	0.375	24.4	0.389
170	959.9	23.4	36.7	0.320	28.0	0.350
180	1016.0	23.0	39.7	0.277	31.4	0.313
190	1060.3	22.6	42.3	0.244	34.3	0.281
200	1095.5	22.2	44.6	0.219	37.0	0.253
210	1123.7	21.8	46.7	0.199	39.4	0.230
220	1146.3	21.4	48.6	0.182	41.6	0.210
230	1164.6	21.1	50.3	0.169	43.6	0.194
240	1179.4	20.7	52.0	0.158	45.5	0.180
250	1191.5	20.4	53.5	0.149	47.2	0.169
260	1201.4	20.1	54.9	0.141	48.9	0.159
270	1209.5	19.8	56.3	0.134	50.4	0.151
280	1216.1	19.5	57.6	0.128	51.9	0.145
290	1221.7	19.2	58.9	0.123	53.3	0.139
300	1226.2	19.0	60.1	0.117	54.7	0.134
310	1230.0	18.7	61.2	0.112	56.0	0.129
320	1233.2	18.5	62.3	0.108	57.2	0.124
330	1235.9	18.3	63.4	0.103	58.5	0.120
340	1238.1	18.1	64.4	0.099	59.6	0.116
350	1240.0	17.9	65.4	0.095	60.8	0.112
360	1241.6	17.7	66.3	0.091	61.9	0.108
370	1242.9	17.6	67.2	0.087	62.9	0.104
380	1244.1	17.4	68.1	0.084	64.0	0.100
390	1245.1	17.3	68.9	0.081	65.0	0.097
400	1245.9	17.1	69.7	0.078	65.9	0.093
450	1248.6	16.6	73.3	0.067	70.1	0.075
500	1250.0	16.1	76.5	0.063	73.5	0.062
550	1250.6	15.7	79.7	0.066	76.3	0.053
600	1251.0	15.3	83.3	0.079	78.9	0.050
650	1251.1	14.7	87.8	0.103	81.4	0.052
700	1251.2	13.9	93.8	0.141	84.2	0.059
750	1251.3	13.0	102.2	0.197	87.5	0.074
800	1251.3	11.8	113.9	0.274	91.7	0.098
850	1251.3	10.5	129.9	0.370	97.4	0.133
900	1251.3	9.1	151.1	0.477	105.3	0.184
950	1251.3	7.9	177.6	0.578	116.1	0.252
1000	1251.3	6.8	208.5	0.651	130.7	0.337
1500	1251.3	3.7	439.9	0.252	385.9	0.315
2000	1251.3	3.2	571.2	0.311	486.5	0.174
2500	1251.3	2.7	767.0	0.482	586.3	0.234
3000	1251.3	2.2	1057.2	0.678	728.0	0.338

TABLE B4a

1500°K THERMOPAUSE

Temperature and Concentrations of Neutral Species

Z (KM)	T (K)	N(O) (CM-3)	N(O2) (CM-3)	N(N2) (CM-3)	N(HE) (CM-3)	N(H) (CM-3)
120	323.6	10.00E 10	4.00E 10	4.00E 11	2.00E 07	2.37E 06
130	527.9	3.98E 10	1.03E 10	1.15E 11	1.33E 07	9.73E 05
140	702.1	2.23E 10	4.30E 09	5.16E 10	1.03E 07	5.53E 05
150	844.9	1.47E 10	2.24E 09	2.85E 10	8.67E 06	3.66E 05
160	959.8	1.06E 10	1.33E 09	1.77E 10	7.62E 06	2.64E 05
170	1052.3	8.07E 09	8.47E 08	1.18E 10	6.89E 06	2.01E 05
180	1127.2	6.39E 09	5.70E 08	8.29E 09	6.34E 06	1.60E 05
190	1188.3	5.20E 09	3.97E 08	6.01E 09	5.90E 06	1.30E 05
200	1238.3	4.31E 09	2.84E 08	4.46E 09	5.54E 06	1.09E 05
210	1279.6	3.62E 09	2.08E 08	3.38E 09	5.25E 06	9.24E 04
220	1313.8	3.08E 09	1.54E 08	2.59E 09	4.99E 06	7.97E 04
230	1342.2	2.64E 09	1.16E 08	2.01E 09	4.76E 06	6.95E 04
240	1366.0	2.28E 09	8.78E 07	1.58E 09	4.56E 06	6.13E 04
250	1386.0	1.98E 09	6.71E 07	1.24E 09	4.38E 06	5.46E 04
260	1402.8	1.73E 09	5.16E 07	9.87E 08	4.21E 06	4.91E 04
270	1416.9	1.51E 09	3.99E 07	7.88E 08	4.06E 06	4.45E 04
280	1428.9	1.33E 09	3.10E 07	6.31E 08	3.92E 06	4.07E 04
290	1439.1	1.17E 09	2.42E 07	5.08E 08	3.78E 06	3.74E 04
300	1447.8	1.03E 09	1.90E 07	4.09E 08	3.66E 06	3.46E 04
310	1455.2	9.10E 08	1.49E 07	3.31E 08	3.54E 06	3.22E 04
320	1461.6	8.06E 08	1.17E 07	2.68E 08	3.43E 06	3.01E 04
330	1467.0	7.14E 08	9.25E 06	2.18E 08	3.32E 06	2.84E 04
340	1471.7	6.34E 08	7.31E 06	1.77E 08	3.22E 06	2.68E 04
350	1475.8	5.64E 08	5.79E 06	1.45E 08	3.12E 06	2.54E 04
360	1479.3	5.01E 08	4.60E 06	1.18E 08	3.03E 06	2.42E 04
370	1482.3	4.46E 08	3.65E 06	9.66E 07	2.94E 06	2.32E 04
380	1485.0	3.98E 08	2.91E 06	7.91E 07	2.86E 06	2.22E 04
390	1487.3	3.55E 08	2.32E 06	6.48E 07	2.77E 06	2.14E 04
400	1489.3	3.17E 08	1.85E 06	5.31E 07	2.69E 06	2.06E 04
450	1496.2	1.81E 08	6.06E 05	2.00E 07	2.34E 06	1.79E 04
500	1499.9	1.05E 08	2.03E 05	7.69E 06	2.04E 06	1.62E 04
550	1501.9	6.11E 07	6.94E 04	3.01E 06	1.78E 06	1.51E 04
600	1503.1	3.60E 07	2.41E 04	1.19E 06	1.56E 06	1.42E 04
650	1503.7	2.14E 07	8.52E 03	4.80E 05	1.37E 06	1.36E 04
700	1504.1	1.28E 07	3.05E 03	1.96E 05	1.20E 06	1.30E 04
750	1504.4	7.73E 06	1.11E 03	8.07E 04	1.06E 06	1.25E 04
800	1504.5	4.70E 06	4.11E 02	3.38E 04	9.36E 05	1.21E 04
850	1504.6	2.87E 06	1.54E 02	1.43E 04	8.28E 05	1.17E 04
900	1504.7	1.77E 06	5.83E 01	6.12E 03	7.33E 05	1.13E 04
950	1504.7	1.10E 06	2.24E 01	2.65E 03	6.51E 05	1.10E 04
1000	1504.7	6.86E 05	8.74E 00	1.16E 03	5.78E 05	1.07E 04
1500	1504.7	8.56E 03		5.43E-01	1.93E 05	8.09E 03
2000	1504.7	1.81E 02			7.36E 04	6.34E 03
2500	1504.7	5.90E 00			3.13E 04	5.11E 03
3000	1504.7	2.77E-01			1.45E 04	4.22E 03

TABLE B4b *(continued)*

1500°K THERMOPAUSE

Temperature, Total Pressure, Pressure Scale Height, Total Concentration, and Total Density

Z (KM)	T (K)	P (TORR)	H (KM)	N (CM-3)	RHO (GM/CM3)
120	323.6	1.81E-05	10.9	5.40E 11	2.34E-11
130	527.9	9.02E-06	18.3	1.65E 11	6.95E-12
140	702.1	5.68E-06	25.0	7.81E 10	3.22E-12
150	844.9	3.97E-06	30.8	4.54E 10	1.83E-12
160	959.8	2.94E-06	35.7	2.96E 10	1.17E-12
170	1052.3	2.26E-06	40.0	2.08E 10	8.09E-13
180	1127.2	1.78E-06	43.7	1.53E 10	5.85E-13
190	1188.3	1.43E-06	46.9	1.16E 10	4.39E-13
200	1238.3	1.16E-06	49.8	9.06E 09	3.37E-13
210	1279.6	9.56E-07	52.4	7.22E 09	2.64E-13
220	1313.8	7.93E-07	54.8	5.83E 09	2.11E-13
230	1342.2	6.63E-07	57.0	4.77E 09	1.70E-13
240	1366.0	5.58E-07	59.0	3.95E 09	1.39E-13
250	1386.0	4.73E-07	60.9	3.29E 09	1.14E-13
260	1402.8	4.02E-07	62.6	2.77E 09	9.45E-14
270	1416.9	3.43E-07	64.3	2.34E 09	7.89E-14
280	1428.9	2.95E-07	65.9	1.99E 09	6.62E-14
290	1439.1	2.54E-07	67.4	1.70E 09	5.59E-14
300	1447.8	2.19E-07	68.8	1.46E 09	4.74E-14
310	1455.2	1.90E-07	70.2	1.26E 09	4.04E-14
320	1461.6	1.65E-07	71.5	1.09E 09	3.45E-14
330	1467.0	1.43E-07	72.8	9.45E 08	2.96E-14
340	1471.7	1.25E-07	74.1	8.22E 08	2.55E-14
350	1475.8	1.10E-07	75.2	7.17E 08	2.20E-14
360	1479.3	9.60E-08	76.4	6.27E 08	1.91E-14
370	1482.3	8.43E-08	77.5	5.50E 08	1.66E-14
380	1485.0	7.42E-08	78.5	4.83E 08	1.44E-14
390	1487.3	6.54E-08	79.6	4.25E 08	1.26E-14
400	1489.3	5.77E-08	80.6	3.74E 08	1.10E-14
450	1496.2	3.16E-08	85.1	2.04E 08	5.78E-15
500	1499.9	1.78E-08	89.0	1.15E 08	3.16E-15
550	1501.9	1.03E-08	92.5	6.60E 07	1.78E-15
600	1503.1	6.04E-09	96.0	3.88E 07	1.02E-15
650	1503.7	3.62E-09	99.6	2.33E 07	6.00E-16
700	1504.1	2.22E-09	103.7	1.42E 07	3.58E-16
750	1504.4	1.38E-09	108.7	8.89E 06	2.16E-16
800	1504.5	8.85E-10	114.9	5.68E 06	1.33E-16
850	1504.6	5.81E-10	122.9	3.73E 06	8.25E-17
900	1504.7	3.93E-10	133.2	2.52E 06	5.22E-17
950	1504.7	2.75E-10	146.6	1.76E 06	3.36E-17
1000	1504.7	1.99E-10	163.5	1.28E 06	2.21E-17
1500	1504.7	3.27E-11	445.1	2.10E 05	1.52E-18
2000	1504.7	1.25E-11	581.2	8.01E 04	5.04E-19
2500	1504.7	5.67E-12	690.9	3.64E 04	2.16E-19
3000	1504.7	2.92E-12	829.9	1.88E 04	1.04E-19

TABLE B4c (*continued*)

1500°K THERMOPAUSE

Temperature, Mean Molecular Mass, Pressure Scale Height, Pressure Scale Height Gradient, Density Scale Height, and Density Scale Height Gradient

Z (KM)	T (K)	M (AMU)	H (KM)	BETA	HRO (KM)	BETAR
120	323.6	26.1	10.9	0.808	6.1	0.539
130	527.9	25.4	18.4	0.710	10.8	0.461
140	702.2	24.8	25.1	0.625	15.5	0.478
150	844.9	24.3	30.9	0.534	20.2	0.466
160	959.8	23.9	35.8	0.456	24.8	0.437
170	1052.4	23.5	40.0	0.394	29.0	0.404
180	1127.3	23.1	43.7	0.345	32.8	0.370
190	1188.3	22.8	47.0	0.305	36.4	0.338
200	1238.4	22.4	49.9	0.273	39.6	0.310
210	1279.6	22.1	52.5	0.248	42.6	0.284
220	1313.8	21.7	54.8	0.227	45.3	0.261
230	1342.3	21.4	57.0	0.209	47.8	0.242
240	1366.1	21.1	59.0	0.195	50.2	0.225
250	1386.0	20.8	60.9	0.182	52.3	0.210
260	1402.8	20.6	62.7	0.172	54.4	0.197
270	1417.0	20.3	64.3	0.163	56.3	0.186
280	1429.0	20.0	65.9	0.155	58.1	0.177
290	1439.2	19.8	67.4	0.148	59.8	0.169
300	1447.9	19.5	68.9	0.141	61.5	0.162
310	1455.3	19.3	70.3	0.136	63.1	0.155
320	1461.6	19.1	71.6	0.130	64.6	0.149
330	1467.1	18.9	72.9	0.125	66.0	0.144
340	1471.8	18.7	74.1	0.121	67.5	0.139
350	1475.8	18.5	75.3	0.116	68.8	0.135
360	1479.3	18.3	76.4	0.112	70.2	0.131
370	1482.4	18.2	77.5	0.108	71.5	0.127
380	1485.0	18.0	78.6	0.104	72.7	0.123
390	1487.3	17.8	79.6	0.101	73.9	0.119
400	1489.3	17.7	80.6	0.097	75.1	0.116
450	1496.2	17.1	85.1	0.083	80.4	0.098
500	1499.9	16.6	89.0	0.074	85.0	0.083
550	1501.9	16.2	92.6	0.069	88.8	0.071
600	1503.1	15.9	96.0	0.070	92.1	0.062
650	1503.8	15.5	99.7	0.076	95.1	0.057
700	1504.2	15.1	103.8	0.089	97.9	0.056
750	1504.4	14.7	108.7	0.110	100.7	0.058
800	1504.6	14.1	114.9	0.140	103.8	0.064
850	1504.7	13.3	122.9	0.181	107.2	0.074
900	1504.7	12.5	133.2	0.234	111.3	0.090
950	1504.8	11.5	146.6	0.300	116.3	0.112
1000	1504.8	10.5	163.5	0.377	122.6	0.143
1500	1504.8	4.4	444.1	0.428	337.6	0.638
2000	1504.8	3.8	579.5	0.207	542.3	0.224
2500	1504.8	3.6	688.9	0.242	634.3	0.173
3000	1504.8	3.3	827.6	0.318	725.4	0.195

TABLE B5a

1750°K THERMOPAUSE

Temperature and Concentrations of Neutral Species

Z (KM)	T (K)	N(O) (CM-3)	N(O2) (CM-3)	N(N2) (CM-3)	N(HE) (CM-3)	N(H) (CM-3)
120	323.6	10.00E 10	4.00E 10	4.00E 11	2.00E 07	2.37E 06
130	571.3	3.75E 10	9.92E 09	1.10E 11	1.27E 07	9.52E 05
140	769.8	2.12E 10	4.29E 09	5.09E 10	9.85E 06	5.50E 05
150	930.0	1.42E 10	2.32E 09	2.90E 10	8.31E 06	3.70E 05
160	1059.6	1.04E 10	1.42E 09	1.86E 10	7.32E 06	2.70E 05
170	1165.5	8.06E 09	9.36E 08	1.27E 10	6.63E 06	2.07E 05
180	1252.8	6.47E 09	6.48E 08	9.16E 09	6.11E 06	1.65E 05
190	1325.4	5.32E 09	4.64E 08	6.80E 09	5.70E 06	1.35E 05
200	1386.1	4.47E 09	3.42E 08	5.17E 09	5.37E 06	1.12E 05
210	1437.3	3.80E 09	2.57E 08	4.00E 09	5.08E 06	9.49E 04
220	1480.6	3.27E 09	1.96E 08	3.14E 09	4.84E 06	8.14E 04
230	1517.4	2.84E 09	1.51E 08	2.50E 09	4.63E 06	7.05E 04
240	1548.8	2.48E 09	1.18E 08	2.00E 09	4.44E 06	6.16E 04
250	1575.7	2.18E 09	9.24E 07	1.62E 09	4.28E 06	5.43E 04
260	1598.8	1.92E 09	7.31E 07	1.32E 09	4.12E 06	4.83E 04
270	1618.7	1.70E 09	5.82E 07	1.08E 09	3.98E 06	4.32E 04
280	1635.9	1.52E 09	4.65E 07	8.84E 08	3.85E 06	3.88E 04
290	1650.8	1.35E 09	3.73E 07	7.29E 08	3.73E 06	3.51E 04
300	1663.7	1.21E 09	3.01E 07	6.03E 08	3.62E 06	3.20E 04
310	1674.9	1.08E 09	2.43E 07	5.00E 08	3.51E 06	2.92E 04
320	1684.7	9.73E 08	1.97E 07	4.16E 08	3.41E 06	2.68E 04
330	1693.3	8.75E 08	1.60E 07	3.47E 08	3.31E 06	2.48E 04
340	1700.8	7.88E 08	1.31E 07	2.90E 08	3.22E 06	2.29E 04
350	1707.3	7.11E 08	1.07E 07	2.42E 08	3.14E 06	2.13E 04
360	1713.1	6.42E 08	8.72E 06	2.03E 08	3.05E 06	1.99E 04
370	1718.2	5.80E 08	7.14E 06	1.70E 08	2.97E 06	1.86E 04
380	1722.7	5.24E 08	5.86E 06	1.43E 08	2.90E 06	1.76E 04
390	1726.6	4.75E 08	4.81E 06	1.21E 08	2.82E 06	1.66E 04
400	1730.1	4.30E 08	3.96E 06	1.02E 08	2.75E 06	1.57E 04
450	1742.6	2.65E 08	1.51E 06	4.38E 07	2.43E 06	1.25E 04
500	1749.8	1.65E 08	5.91E 05	1.92E 07	2.16E 06	1.05E 04
550	1754.0	1.04E 08	2.35E 05	8.59E 06	1.92E 06	9.24E 03
600	1756.5	6.62E 07	9.52E 04	3.89E 06	1.71E 06	8.42E 03
650	1758.1	4.24E 07	3.90E 04	1.78E 06	1.53E 06	7.82E 03
700	1759.1	2.73E 07	1.62E 04	8.27E 05	1.37E 06	7.38E 03
750	1759.8	1.77E 07	6.84E 03	3.88E 05	1.23E 06	7.04E 03
800	1760.2	1.16E 07	2.92E 03	1.84E 05	1.11E 06	6.76E 03
850	1760.5	7.61E 06	1.26E 03	8.84E 04	9.97E 05	6.52E 03
900	1760.7	5.03E 06	5.51E 02	4.28E 04	8.99E 05	6.31E 03
950	1760.8	3.34E 06	2.43E 02	2.10E 04	8.11E 05	6.13E 03
1000	1760.9	2.24E 06	1.09E 02	1.04E 04	7.34E 05	5.95E 03
1500	1761.1	5.28E 04		1.48E 01	2.87E 05	4.70E 03
2000	1761.1	1.96E 03			1.26E 05	3.82E 03
2500	1761.1	1.05E 02			6.06E 04	3.17E 03
3000	1761.1	7.71E 00			3.15E 04	2.69E 03

TABLE B5b (*continued*)

1750°K THERMOPAUSE

Temperature, Total Pressure, Pressure Scale Height, Total Concentration, and Total Density

Z (KM)	T (K)	P (TORR)	H (KM)	N (CM-3)	RHO (GM/CM3)
120	323.6	1.81E-05	10.9	5.40E 11	2.34E-11
130	571.3	9.31E-06	19.8	1.57E 11	6.64E-12
140	769.8	6.09E-06	27.3	7.64E 10	3.16E-12
150	930.0	4.39E-06	33.7	4.56E 10	1.85E-12
160	1059.6	3.34E-06	39.2	3.04E 10	1.22E-12
170	1165.5	2.62E-06	43.9	2.17E 10	8.56E-13
180	1252.8	2.11E-06	48.0	1.63E 10	6.32E-13
190	1325.4	1.73E-06	51.6	1.26E 10	4.82E-13
200	1386.1	1.43E-06	54.9	9.98E 09	3.77E-13
210	1437.3	1.20E-06	57.9	8.06E 09	3.01E-13
220	1480.6	1.01E-06	60.6	6.61E 09	2.43E-13
230	1517.4	8.62E-07	63.0	5.49E 09	1.99E-13
240	1548.8	7.38E-07	65.4	4.60E 09	1.65E-13
250	1575.7	6.35E-07	67.5	3.89E 09	1.38E-13
260	1598.8	5.49E-07	69.5	3.32E 09	1.16E-13
270	1618.7	4.76E-07	71.5	2.84E 09	9.84E-14
280	1635.9	4.15E-07	73.3	2.45E 09	8.39E-14
290	1650.8	3.63E-07	75.0	2.12E 09	7.18E-14
300	1663.7	3.18E-07	76.7	1.85E 09	6.18E-14
310	1674.9	2.79E-07	78.3	1.61E 09	5.34E-14
320	1684.7	2.46E-07	79.8	1.41E 09	4.63E-14
330	1693.3	2.18E-07	81.3	1.24E 09	4.02E-14
340	1700.8	1.93E-07	82.7	1.09E 09	3.51E-14
350	1707.3	1.71E-07	84.1	9.67E 08	3.07E-14
360	1713.1	1.52E-07	85.4	8.57E 08	2.70E-14
370	1718.2	1.35E-07	86.7	7.60E 08	2.37E-14
380	1722.7	1.21E-07	88.0	6.77E 08	2.09E-14
390	1726.6	1.08E-07	89.2	6.03E 08	1.85E-14
400	1730.1	9.64E-08	90.4	5.38E 08	1.64E-14
450	1742.6	5.64E-08	95.8	3.13E 08	9.17E-15
500	1749.8	3.39E-08	100.6	1.87E 08	5.33E-15
550	1754.0	2.09E-08	104.9	1.15E 08	3.19E-15
600	1756.5	1.31E-08	108.8	7.19E 07	1.96E-15
650	1758.1	8.33E-09	112.6	4.58E 07	1.22E-15
700	1759.1	5.38E-09	116.4	2.96E 07	7.74E-16
750	1759.8	3.53E-09	120.4	1.94E 07	4.98E-16
800	1760.2	2.35E-09	124.9	1.29E 07	3.24E-16
850	1760.5	1.59E-09	130.1	8.70E 06	2.13E-16
900	1760.7	1.09E-09	136.3	5.98E 06	1.42E-16
950	1760.8	7.62E-10	143.8	4.18E 06	9.52E-17
1000	1760.9	5.44E-10	153.0	2.99E 06	6.47E-17
1500	1761.1	6.29E-11	393.1	3.45E 05	3.32E-18
2000	1761.1	2.40E-11	630.1	1.32E 05	8.95E-19
2500	1761.1	1.16E-11	748.1	6.39E 04	4.11E-19
3000	1761.1	6.24E-12	857.9	3.42E 04	2.14E-19

TABLE B5c (*continued*)

1750°K THERMOPAUSE

Temperature, Mean Molecular Mass, Pressure Scale Height, Pressure Scale Height Gradient, Density Scale Height, and Density Scale Height Gradient

Z (KM)	T (K)	M (AMU)	H (KM)	BETA	HRO (KM)	BETAR
120	323.6	26.1	10.9	1.018	5.4	0.630
130	571.3	25.4	19.9	0.816	11.0	0.530
140	769.9	24.9	27.4	0.692	16.3	0.525
150	930.0	24.5	33.8	0.588	21.4	0.502
160	1059.6	24.1	39.2	0.504	26.3	0.471
170	1165.5	23.7	43.9	0.438	30.8	0.437
180	1252.9	23.4	48.0	0.386	35.0	0.404
190	1325.4	23.1	51.7	0.344	38.9	0.372
200	1386.2	22.8	54.9	0.310	42.5	0.344
210	1437.4	22.5	57.9	0.282	45.8	0.318
220	1480.7	22.2	60.6	0.259	48.9	0.295
230	1517.5	21.9	63.1	0.240	51.7	0.275
240	1548.9	21.6	65.4	0.223	54.4	0.257
250	1575.8	21.4	67.6	0.209	56.8	0.241
260	1598.9	21.1	69.6	0.197	59.2	0.226
270	1618.8	20.9	71.5	0.187	61.4	0.214
280	1636.0	20.6	73.3	0.178	63.5	0.203
290	1650.8	20.4	75.1	0.170	65.4	0.194
300	1663.7	20.2	76.7	0.163	67.3	0.185
310	1675.0	19.9	78.3	0.156	69.1	0.178
320	1684.8	19.7	79.9	0.151	70.9	0.171
330	1693.3	19.5	81.3	0.145	72.6	0.165
340	1700.8	19.3	82.8	0.140	74.2	0.160
350	1707.4	19.1	84.2	0.136	75.8	0.155
360	1713.1	19.0	85.5	0.132	77.3	0.150
370	1718.2	18.8	86.8	0.128	78.8	0.146
380	1722.7	18.6	88.0	0.124	80.2	0.142
390	1726.7	18.5	89.3	0.120	81.6	0.139
400	1730.2	18.3	90.5	0.117	83.0	0.135
450	1742.7	17.7	95.9	0.102	89.3	0.119
500	1749.8	17.1	100.7	0.090	94.9	0.105
550	1754.0	16.7	104.9	0.081	99.9	0.092
600	1756.6	16.4	108.9	0.076	104.2	0.081
650	1758.2	16.1	112.6	0.075	108.0	0.072
700	1759.2	15.8	116.4	0.078	111.5	0.066
750	1759.8	15.5	120.5	0.084	114.7	0.063
800	1760.3	15.1	125.0	0.096	117.8	0.062
850	1760.5	14.7	130.1	0.113	120.9	0.063
900	1760.7	14.3	136.3	0.136	124.1	0.067
950	1760.9	13.7	143.8	0.166	127.7	0.075
1000	1760.9	13.1	153.0	0.204	131.7	0.085
1500	1761.1	5.8	392.5	0.661	251.5	0.492
2000	1761.1	4.1	628.4	0.292	550.5	0.493
2500	1761.1	3.9	745.9	0.213	714.3	0.227
3000	1761.1	3.8	855.4	0.231	816.2	0.194

TABLE B6a

2000°K THERMOPAUSE

Temperature and Concentrations of Neutral Species

Z (KM)	T (K)	N(O) (CM-3)	N(O2) (CM-3)	N(N2) (CM-3)	N(HE) (CM-3)	N(H) (CM-3)
120	323.6	10.00E 10	4.00E 10	4.00E 11	2.00E 07	2.37E 06
130	590.9	3.65E 10	9.74E 09	1.08E 11	1.24E 07	9.44E 05
140	807.9	2.06E 10	4.24E 09	5.01E 10	9.60E 06	5.48E 05
150	985.5	1.38E 10	2.32E 09	2.89E 10	8.07E 06	3.70E 05
160	1131.4	1.02E 10	1.44E 09	1.87E 10	7.10E 06	2.72E 05
170	1252.4	7.89E 09	9.64E 08	1.30E 10	6.42E 06	2.10E 05
180	1353.7	6.37E 09	6.78E 08	9.44E 09	5.91E 06	1.68E 05
190	1439.2	5.27E 09	4.94E 08	7.10E 09	5.52E 06	1.38E 05
200	1512.0	4.45E 09	3.70E 08	5.48E 09	5.19E 06	1.15E 05
210	1574.2	3.81E 09	2.82E 08	4.30E 09	4.92E 06	9.77E 04
220	1627.6	3.30E 09	2.19E 08	3.43E 09	4.69E 06	8.40E 04
230	1673.8	2.88E 09	1.72E 08	2.77E 09	4.49E 06	7.29E 04
240	1713.8	2.54E 09	1.37E 08	2.26E 09	4.31E 06	6.38E 04
250	1748.7	2.25E 09	1.09E 08	1.85E 09	4.15E 06	5.62E 04
260	1779.0	2.00E 09	8.83E 07	1.53E 09	4.00E 06	4.99E 04
270	1805.6	1.79E 09	7.16E 07	1.27E 09	3.87E 06	4.46E 04
280	1828.9	1.61E 09	5.84E 07	1.06E 09	3.75E 06	4.00E 04
290	1849.4	1.45E 09	4.79E 07	8.93E 08	3.64E 06	3.61E 04
300	1867.5	1.31E 09	3.94E 07	7.52E 08	3.53E 06	3.27E 04
310	1883.4	1.18E 09	3.25E 07	6.35E 08	3.44E 06	2.97E 04
320	1897.5	1.07E 09	2.69E 07	5.38E 08	3.34E 06	2.71E 04
330	1910.0	9.73E 08	2.24E 07	4.57E 08	3.26E 06	2.49E 04
340	1921.1	8.85E 08	1.86E 07	3.89E 08	3.17E 06	2.29E 04
350	1930.9	8.07E 08	1.55E 07	3.32E 08	3.09E 06	2.11E 04
360	1939.7	7.36E 08	1.30E 07	2.83E 08	3.02E 06	1.95E 04
370	1947.6	6.72E 08	1.09E 07	2.42E 08	2.95E 06	1.81E 04
380	1954.6	6.14E 08	9.11E 06	2.08E 08	2.88E 06	1.69E 04
390	1960.8	5.62E 08	7.65E 06	1.78E 08	2.81E 06	1.58E 04
400	1966.5	5.15E 08	6.44E 06	1.53E 08	2.75E 06	1.47E 04
450	1987.1	3.35E 08	2.75E 06	7.27E 07	2.46E 06	1.10E 04
500	1999.6	2.21E 08	1.21E 06	3.53E 07	2.21E 06	8.71E 03
550	2007.4	1.47E 08	5.38E 05	1.74E 07	1.99E 06	7.23E 03
600	2012.3	9.90E 07	2.44E 05	8.70E 06	1.80E 06	6.26E 03
650	2015.6	6.70E 07	1.12E 05	4.40E 06	1.63E 06	5.58E 03
700	2017.7	4.57E 07	5.21E 04	2.25E 06	1.48E 06	5.10E 03
750	2019.2	3.13E 07	2.45E 04	1.17E 06	1.35E 06	4.75E 03
800	2020.2	2.16E 07	1.17E 04	6.08E 05	1.23E 06	4.49E 03
850	2020.9	1.50E 07	5.61E 03	3.21E 05	1.12E 06	4.28E 03
900	2021.4	1.04E 07	2.73E 03	1.71E 05	1.03E 06	4.11E 03
950	2021.8	7.32E 06	1.34E 03	9.15E 04	9.38E 05	3.96E 03
1000	2022.0	5.15E 06	6.64E 02	4.95E 04	8.59E 05	3.84E 03
1500	2022.8	1.98E 05	9.76E-01	1.65E 02	3.80E 05	3.11E 03
2000	2022.9	1.12E 04		1.08E 00	1.85E 05	2.60E 03
2500	2022.9	8.78E 02			9.80E 04	2.21E 03
3000	2022.9	9.04E 01			5.55E 04	1.92E 03

TABLE B6b (*continued*)

2000°K THERMOPAUSE

Temperature, Total Pressure, Pressure Scale Height, Total Concentration, and Total Density

Z (KM)	T (K)	P (TORR)	H (KM)	N (CM-3)	RHO (GM/CM3)
120	323.6	1.81E-05	10.9	5.40E 11	2.34E-11
130	590.9	9.42E-06	20.5	1.54E 11	6.50E-12
140	807.9	6.26E-06	28.7	7.49E 10	3.10E-12
150	985.5	4.59E-06	35.7	4.50E 10	1.83E-12
160	1131.4	3.55E-06	41.7	3.03E 10	1.21E-12
170	1252.4	2.83E-06	46.9	2.18E 10	8.64E-13
180	1353.7	2.31E-06	51.5	1.65E 10	6.44E-13
190	1439.2	1.92E-06	55.7	1.29E 10	4.96E-13
200	1512.0	1.61E-06	59.4	1.03E 10	3.92E-13
210	1574.2	1.37E-06	62.7	8.40E 09	3.16E-13
220	1627.6	1.17E-06	65.8	6.96E 09	2.59E-13
230	1673.8	1.01E-06	68.7	5.83E 09	2.15E-13
240	1713.8	8.76E-07	71.3	4.94E 09	1.80E-13
250	1748.7	7.63E-07	73.8	4.22E 09	1.52E-13
260	1779.0	6.68E-07	76.2	3.63E 09	1.29E-13
270	1805.6	5.87E-07	78.4	3.14E 09	1.11E-13
280	1828.9	5.18E-07	80.4	2.73E 09	9.53E-14
290	1849.4	4.58E-07	82.4	2.39E 09	8.25E-14
300	1867.5	4.06E-07	84.3	2.10E 09	7.18E-14
310	1883.4	3.61E-07	86.2	1.85E 09	6.27E-14
320	1897.5	3.22E-07	87.9	1.64E 09	5.49E-14
330	1910.0	2.88E-07	89.6	1.46E 09	4.83E-14
340	1921.1	2.58E-07	91.2	1.30E 09	4.26E-14
350	1930.9	2.31E-07	92.8	1.16E 09	3.77E-14
360	1939.7	2.08E-07	94.3	1.03E 09	3.34E-14
370	1947.6	1.87E-07	95.8	9.28E 08	2.97E-14
380	1954.6	1.69E-07	97.3	8.34E 08	2.65E-14
390	1960.8	1.52E-07	98.7	7.51E 08	2.36E-14
400	1966.5	1.38E-07	100.0	6.77E 08	2.11E-14
450	1987.1	8.49E-08	106.4	4.13E 08	1.24E-14
500	1999.6	5.37E-08	112.0	2.60E 08	7.59E-15
550	2007.4	3.47E-08	117.0	1.67E 08	4.76E-15
600	2012.3	2.29E-08	121.6	1.10E 08	3.06E-15
650	2015.6	1.53E-08	125.9	7.32E 07	2.00E-15
700	2017.7	1.03E-08	130.1	4.95E 07	1.33E-15
750	2019.2	7.08E-09	134.1	3.39E 07	8.97E-16
800	2020.2	4.91E-09	138.3	2.35E 07	6.11E-16
850	2020.9	3.44E-09	142.8	1.64E 07	4.21E-16
900	2021.4	2.44E-09	147.7	1.16E 07	2.92E-16
950	2021.8	1.75E-09	153.2	8.35E 06	2.05E-16
1000	2022.0	1.27E-09	159.5	6.07E 06	1.45E-16
1500	2022.8	1.22E-10	324.3	5.81E 05	7.78E-18
2000	2022.9	4.17E-11	638.8	1.99E 05	1.53E-18
2500	2022.9	2.12E-11	823.6	1.01E 05	6.78E-19
3000	2022.9	1.20E-11	947.3	5.75E 04	3.74E-19

TABLE B6c (*continued*)

2000°K THERMOPAUSE

Temperature, Mean Molecular Mass, Pressure Scale Height, Pressure Scale Height Gradient, Density Scale Height, and Density Scale Height Gradient

Z (KM)	T (K)	M (AMU)	H (KM)	BETA	HRO (KM)	BETAR
120	323.6	26.1	10.9	1.096	5.2	0.656
130	590.9	25.4	20.5	0.881	11.0	0.547
140	807.9	24.9	28.7	0.756	16.4	0.546
150	985.5	24.5	35.7	0.647	21.8	0.528
160	1131.5	24.2	41.7	0.560	27.0	0.500
170	1252.5	23.8	47.0	0.491	31.8	0.469
180	1353.8	23.5	51.6	0.435	36.3	0.438
190	1439.3	23.2	55.7	0.390	40.6	0.408
200	1512.0	22.9	59.4	0.353	44.5	0.380
210	1574.2	22.7	62.8	0.322	48.2	0.355
220	1627.7	22.4	65.9	0.297	51.6	0.332
230	1673.9	22.2	68.7	0.275	54.8	0.311
240	1713.9	21.9	71.4	0.256	57.8	0.292
250	1748.7	21.7	73.9	0.240	60.7	0.275
260	1779.1	21.4	76.2	0.226	63.3	0.259
270	1805.7	21.2	78.4	0.214	65.9	0.246
280	1829.0	21.0	80.5	0.204	68.2	0.233
290	1849.5	20.8	82.5	0.194	70.5	0.222
300	1867.5	20.6	84.4	0.186	72.7	0.212
310	1883.5	20.4	86.2	0.179	74.8	0.204
320	1897.5	20.2	88.0	0.172	76.8	0.196
330	1910.0	20.0	89.7	0.166	78.7	0.189
340	1921.1	19.8	91.3	0.161	80.5	0.182
350	1931.0	19.6	92.9	0.155	82.3	0.176
360	1939.8	19.4	94.4	0.151	84.1	0.171
370	1947.6	19.3	95.9	0.146	85.8	0.166
380	1954.6	19.1	97.3	0.142	87.4	0.162
390	1960.9	19.0	98.7	0.138	89.0	0.158
400	1966.5	18.8	100.1	0.135	90.6	0.154
450	1987.2	18.1	106.4	0.119	97.8	0.138
500	1999.7	17.6	112.0	0.106	104.4	0.124
550	2007.4	17.2	117.1	0.096	110.2	0.111
600	2012.4	16.8	121.7	0.089	115.5	0.100
650	2015.6	16.5	126.0	0.084	120.3	0.090
700	2017.8	16.2	130.1	0.082	124.5	0.082
750	2019.3	15.9	134.2	0.082	128.5	0.076
800	2020.3	15.7	138.4	0.086	132.1	0.071
850	2021.0	15.4	142.8	0.093	135.6	0.069
900	2021.5	15.1	147.7	0.103	139.0	0.068
950	2021.8	14.8	153.2	0.117	142.5	0.069
1000	2022.1	14.4	159.5	0.136	146.0	0.072
1500	2022.8	8.1	324.0	0.581	216.3	0.272
2000	2022.9	4.7	637.3	0.513	468.2	0.675
2500	2022.9	4.1	821.2	0.273	754.9	0.419
3000	2022.9	3.9	944.5	0.236	913.8	0.254

TABLE B7a

THERMOSPHERE TEMPERATURE MODELS

Z (KM)	600° T (K)	650° T (K)	700° T (K)	750° T (K)	800° T (K)	850° T (K)
120	323.6	323.6	323.6	323.6	323.6	323.6
122	342.4	342.2	341.8	343.1	342.7	346.7
124	360.7	360.5	359.8	362.4	361.7	369.6
126	378.1	378.3	377.5	381.4	380.3	391.9
128	394.7	395.6	395.0	400.1	398.9	413.9
130	410.4	412.3	412.1	418.6	417.4	435.7
132	425.2	428.4	429.0	436.8	435.7	457.0
134	439.1	443.8	445.4	454.6	453.9	477.9
136	452.1	458.4	461.3	471.9	471.8	498.1
138	464.1	472.3	476.5	488.6	489.3	517.6
140	475.2	485.3	491.1	504.6	506.4	536.4
142	485.5	497.4	505.0	519.9	523.0	554.3
144	495.0	508.8	518.1	534.5	539.0	571.4
146	503.7	519.4	530.5	548.3	554.4	587.6
148	511.7	529.3	542.1	561.3	569.0	603.0
150	519.1	538.4	553.0	573.5	582.9	617.5
152	525.8	546.8	563.2	585.0	596.1	631.3
154	532.0	554.7	572.7	595.8	608.6	644.2
156	537.7	561.9	581.6	605.9	620.4	656.4
158	542.8	568.6	589.8	615.3	631.4	667.8
160	547.5	574.7	597.5	624.2	641.8	678.6
162	551.9	580.4	604.7	632.4	651.6	688.7
164	555.8	585.7	611.3	640.1	660.8	698.2
166	559.4	590.5	617.5	647.3	669.4	707.1
168	562.8	595.0	623.2	654.0	677.4	715.5
170	565.8	599.1	628.5	660.2	684.9	723.3
172	568.5	602.9	633.4	666.0	692.0	730.7
174	571.1	606.4	638.0	671.5	698.6	737.6
176	573.4	609.6	642.3	676.5	704.8	744.1
178	575.5	612.6	646.2	681.2	710.5	750.2
180	577.5	615.3	649.8	685.6	716.0	755.9
182	579.2	617.8	653.2	689.7	721.0	761.3
184	580.9	620.1	656.4	693.5	725.7	766.3
186	582.3	622.3	659.3	697.1	730.2	771.1
188	583.7	624.3	662.0	700.4	734.3	775.5
190	585.0	626.1	664.5	703.5	738.2	779.7
192	586.1	627.8	666.9	706.4	741.8	783.6
194	587.2	629.4	669.1	709.1	745.2	787.3
196	588.1	630.8	671.1	711.6	748.4	790.8
198	589.0	632.2	673.0	714.0	751.4	794.1
200	589.9	633.4	674.7	716.2	754.2	797.1
202	590.6	634.5	676.3	718.2	756.8	800.0
204	591.3	635.6	677.9	720.1	759.3	802.7
206	591.9	636.6	679.3	721.9	761.6	805.3
208	592.5	637.5	680.6	723.6	763.8	807.7
210	593.1	638.3	681.8	725.2	765.8	810.0
212	593.6	639.1	682.9	726.7	767.7	812.1
214	594.0	639.8	684.0	728.0	769.5	814.1
216	594.4	640.5	685.0	729.3	771.2	816.0
218	594.8	641.1	685.9	730.5	772.8	817.8
220	595.2	641.7	686.8	731.6	774.3	819.5
222	595.5	642.3	687.6	732.7	775.7	821.1
224	595.8	642.8	688.3	733.7	777.0	822.5
226	596.1	643.2	689.0	734.6	778.2	824.0
228	596.4	643.7	689.7	735.5	779.4	825.3
230	596.6	644.1	690.3	736.3	780.5	826.6

TABLE B7b (*continued*)

THERMOSPHERE TEMPERATURE MODELS

Z (KM)	600° T (K)	650° T (K)	700° T (K)	750° T (K)	800° T (K)	850° T (K)
230	596.6	644.1	690.3	736.3	780.5	826.6
232	596.9	644.4	690.9	737.1	781.5	827.7
234	597.1	644.8	691.4	737.8	782.5	828.9
236	597.3	645.1	691.9	738.5	783.4	829.9
238	597.5	645.4	692.4	739.1	784.3	830.9
240	597.6	645.7	692.8	739.7	785.1	831.9
242	597.8	646.0	693.2	740.3	785.9	832.8
244	597.9	646.2	693.6	740.8	786.6	833.6
246	598.1	646.4	694.0	741.3	787.3	834.4
248	598.2	646.7	694.3	741.8	788.0	835.2
250	598.3	646.9	694.7	742.2	788.6	835.9
252	598.4	647.0	695.0	742.6	789.1	836.6
254	598.5	647.2	695.2	743.0	789.7	837.2
256	598.6	647.4	695.5	743.4	790.2	837.9
258	598.7	647.5	695.8	743.7	790.7	838.4
260	598.8	647.7	696.0	744.1	791.2	839.0
262	598.9	647.8	696.2	744.4	791.6	839.5
264	598.9	647.9	696.4	744.7	792.0	840.0
266	599.0	648.1	696.6	744.9	792.4	840.5
268	599.1	648.2	696.8	745.2	792.8	840.9
270	599.1	648.3	697.0	745.4	793.1	841.3
272	599.2	648.4	697.1	745.7	793.5	841.7
274	599.2	648.5	697.3	745.9	793.8	842.1
276	599.3	648.6	697.4	746.1	794.1	842.5
278	599.3	648.6	697.6	746.3	794.4	842.8
280	599.4	648.7	697.7	746.5	794.6	843.2
282	599.4	648.8	697.8	746.7	794.9	843.5
284	599.4	648.9	697.9	746.8	795.1	843.8
286	599.5	648.9	698.0	747.0	795.4	844.1
288	599.5	649.0	698.2	747.1	795.6	844.3
290	599.5	649.0	698.2	747.3	795.8	844.6
292	599.6	649.1	698.3	747.4	796.0	844.8
294	599.6	649.1	698.4	747.5	796.2	845.0
296	599.6	649.2	698.5	747.7	796.3	845.3
298	599.6	649.2	698.6	747.8	796.5	845.5
300	599.6	649.3	698.7	747.9	796.7	845.7
310	599.7	649.5	699.0	748.3	797.4	846.5
320	599.8	649.6	699.2	748.7	797.9	847.2
330	599.8	649.7	699.4	749.0	798.3	847.8
340	599.9	649.8	699.5	749.2	798.7	848.2
350	599.9	649.8	699.6	749.4	798.9	848.6
360	599.9	649.8	699.7	749.5	799.2	848.8
370	599.9	649.9	699.8	749.6	799.3	849.1
380	599.9	649.9	699.8	749.7	799.5	849.2
390	599.9	649.9	699.8	749.7	799.6	849.4
400	600.0	649.9	699.9	749.8	799.7	849.5
410	600.0	649.9	699.9	749.8	799.7	849.6
420	600.0	649.9	699.9	749.9	799.8	849.7
430	600.0	649.9	699.9	749.9	799.8	849.7
440	600.0	649.9	699.9	749.9	799.9	849.8
450	600.0	649.9	699.9	749.9	799.9	849.8
460	600.0	649.9	699.9	749.9	799.9	849.9
470	600.0	649.9	699.9	749.9	799.9	849.9
480	600.0	649.9	699.9	749.9	799.9	849.9
490	600.0	649.9	699.9	749.9	799.9	849.9
500	600.0	649.9	699.9	749.9	799.9	849.9

TABLE B8a

THERMOSPHERE TEMPERATURE MODELS

Z (KM)	900° T (K)	950° T (K)	1000° T (K)	1050° T (K)	1100° T (K)	1150° T (K)
120	323.6	323.6	323.6	323.6	323.6	323.6
122	349.1	350.5	355.3	358.1	357.5	359.2
124	374.2	377.1	386.3	391.6	390.6	393.9
126	398.7	403.0	416.0	423.6	422.4	427.2
128	422.8	428.4	444.8	454.4	453.3	459.5
130	446.5	453.4	472.7	484.1	483.4	491.0
132	469.6	477.8	499.6	512.6	512.5	521.3
134	492.1	501.6	525.5	540.0	540.7	550.6
136	513.8	524.6	550.2	566.0	567.7	578.8
138	534.8	546.8	573.9	590.9	593.5	605.8
140	554.8	568.1	596.4	614.5	618.3	631.6
142	574.0	588.4	617.7	636.9	641.8	656.2
144	592.2	607.8	638.0	658.2	664.3	679.6
146	609.5	626.3	657.2	678.3	685.6	701.9
148	625.9	643.8	675.4	697.4	705.9	723.1
150	641.4	660.4	692.5	715.4	725.2	743.3
152	656.1	676.1	708.8	732.5	743.4	762.4
154	669.9	690.9	724.1	748.6	760.8	780.6
156	682.9	704.9	738.6	763.9	777.2	797.9
158	695.2	718.2	752.3	778.3	792.8	814.3
160	706.8	730.7	765.2	791.9	807.5	829.8
162	717.7	742.5	777.4	804.9	821.5	844.6
164	727.9	753.6	788.9	817.1	834.8	858.7
166	737.6	764.1	799.8	828.6	847.4	872.0
168	746.6	774.1	810.1	839.6	859.4	884.7
170	755.2	783.4	819.8	849.9	870.7	896.7
172	763.2	792.2	829.0	859.7	881.5	908.2
174	770.8	800.6	837.7	869.0	891.7	919.1
176	777.9	808.4	845.9	877.8	901.4	929.4
178	784.6	815.8	853.7	886.1	910.6	939.3
180	790.9	822.8	861.0	894.0	919.3	948.6
182	796.8	829.4	867.9	901.5	927.6	957.5
184	802.4	835.7	874.5	908.6	935.5	966.0
186	807.7	841.6	880.7	915.3	943.0	974.1
188	812.7	847.1	886.6	921.7	950.1	981.8
190	817.3	852.4	892.2	927.7	956.9	989.1
192	821.7	857.3	897.4	933.5	963.3	996.1
194	825.9	862.0	902.4	938.9	969.4	1002.7
196	829.8	866.5	907.2	944.1	975.3	1009.0
198	833.5	870.7	911.6	949.0	980.8	1015.1
200	837.0	874.6	915.9	953.7	986.1	1020.8
202	840.3	878.4	919.9	958.1	991.1	1026.3
204	843.4	881.9	923.7	962.3	995.9	1031.5
206	846.3	885.3	927.3	966.3	1000.4	1036.5
208	849.0	888.4	930.8	970.1	1004.7	1041.3
210	851.6	891.5	934.0	973.7	1008.9	1045.8
212	854.1	894.3	937.1	977.1	1012.8	1050.1
214	856.4	897.0	940.1	980.4	1016.6	1054.3
216	858.6	899.6	942.8	983.5	1020.1	1058.2
218	860.7	902.0	945.5	986.5	1023.5	1062.0
220	862.7	904.3	948.0	989.3	1026.8	1065.6
222	864.5	906.4	950.4	992.0	1029.9	1069.0
224	866.3	908.5	952.6	994.5	1032.8	1072.3
226	867.9	910.5	954.8	996.9	1035.7	1075.5
228	869.5	912.3	956.8	999.2	1038.3	1078.5
230	871.0	914.1	958.8	1001.4	1040.9	1081.4

TABLE B8b (*continued*)

THERMOSPHERE TEMPERATURE MODELS

Z (KM)	900° T (K)	950° T (K)	1000° T (K)	1050° T (K)	1100° T (K)	1150° T (K)
230	871.0	914.1	958.8	1001.4	1040.9	1081.4
232	872.4	915.8	960.6	1003.5	1043.4	1084.1
234	873.8	917.3	962.4	1005.5	1045.7	1086.7
236	875.0	918.8	964.1	1007.5	1047.9	1089.3
238	876.2	920.3	965.7	1009.3	1050.1	1091.7
240	877.4	921.6	967.2	1011.0	1052.1	1094.0
242	878.4	922.9	968.6	1012.7	1054.1	1096.2
244	879.4	924.2	970.0	1014.2	1055.9	1098.3
246	880.4	925.3	971.3	1015.7	1057.7	1100.3
248	881.3	926.4	972.5	1017.2	1059.4	1102.2
250	882.2	927.5	973.7	1018.5	1061.0	1104.1
252	883.0	928.5	974.9	1019.8	1062.6	1105.9
254	883.8	929.4	975.9	1021.1	1064.1	1107.6
256	884.6	930.4	977.0	1022.3	1065.5	1109.2
258	885.3	931.2	978.0	1023.4	1066.9	1110.8
260	885.9	932.0	978.9	1024.5	1068.2	1112.2
262	886.6	932.8	979.8	1025.6	1069.4	1113.7
264	887.2	933.6	980.6	1026.5	1070.6	1115.1
266	887.8	934.3	981.4	1027.5	1071.8	1116.4
268	888.3	935.0	982.2	1028.4	1072.9	1117.6
270	888.8	935.6	983.0	1029.3	1073.9	1118.9
272	889.3	936.2	983.7	1030.1	1074.9	1120.0
274	889.8	936.8	984.3	1030.9	1075.9	1121.1
276	890.3	937.4	985.0	1031.7	1076.8	1122.2
278	890.7	937.9	985.6	1032.4	1077.7	1123.2
280	891.1	938.4	986.2	1033.1	1078.6	1124.2
282	891.5	938.9	986.8	1033.8	1079.4	1125.2
284	891.9	939.4	987.3	1034.4	1080.1	1126.1
286	892.2	939.8	987.8	1035.0	1080.9	1127.0
288	892.6	940.2	988.3	1035.6	1081.6	1127.8
290	892.9	940.6	988.8	1036.2	1082.3	1128.6
292	893.2	941.0	989.2	1036.7	1083.0	1129.4
294	893.5	941.4	989.7	1037.2	1083.6	1130.2
296	893.8	941.8	990.1	1037.7	1084.2	1130.9
298	894.0	942.1	990.5	1038.2	1084.8	1131.6
300	894.3	942.4	990.8	1038.6	1085.4	1132.2
310	895.4	943.8	992.5	1040.6	1087.9	1135.2
320	896.3	945.0	993.9	1042.3	1089.9	1137.7
330	897.0	945.9	995.0	1043.6	1091.6	1139.7
340	897.6	946.7	995.9	1044.7	1093.0	1141.4
350	898.0	947.3	996.6	1045.6	1094.2	1142.8
360	898.4	947.8	997.2	1046.4	1095.2	1144.0
370	898.7	948.2	997.7	1047.0	1096.0	1145.0
380	898.9	948.5	998.1	1047.5	1096.7	1145.8
390	899.1	948.8	998.5	1048.0	1097.3	1146.5
400	899.3	949.0	998.7	1048.3	1097.7	1147.1
410	899.4	949.2	999.0	1048.6	1098.2	1147.7
420	899.5	949.4	999.2	1048.9	1098.5	1148.1
430	899.6	949.5	999.3	1049.1	1098.8	1148.5
440	899.7	949.6	999.5	1049.3	1099.0	1148.8
450	899.8	949.7	999.6	1049.5	1099.3	1149.0
460	899.8	949.8	999.7	1049.6	1099.4	1149.3
470	899.9	949.8	999.8	1049.7	1099.6	1149.5
480	899.9	949.9	999.8	1049.8	1099.7	1149.7
490	899.9	949.9	999.9	1049.9	1099.8	1149.8
500	899.9	949.9	999.9	1049.9	1099.9	1149.9

TABLE B9a

THERMOSPHERE TEMPERATURE MODELS

Z (KM)	1200° T (K)	1250° T (K)	1300° T (K)	1350° T (K)	1400° T (K)	1450° T (K)
120	323.6	323.6	323.6	323.6	323.6	323.6
122	364.7	367.9	367.3	369.3	368.6	367.9
124	404.2	410.2	409.3	413.2	412.1	410.8
126	441.5	449.8	448.9	454.3	453.1	451.6
128	477.1	487.4	486.8	493.6	492.5	491.1
130	511.2	523.2	523.0	531.2	530.5	529.4
132	543.8	557.3	557.8	567.1	567.0	566.3
134	574.9	589.7	591.0	601.4	601.9	601.9
136	604.6	620.5	622.6	634.1	635.4	636.1
138	632.8	649.7	652.8	665.3	667.5	669.0
140	659.5	677.5	681.6	694.9	698.1	700.5
142	685.0	703.9	709.0	723.2	727.3	730.6
144	709.1	728.9	735.0	750.1	755.2	759.4
146	732.1	752.6	759.8	775.7	781.8	787.0
148	753.8	775.1	783.4	800.1	807.2	813.4
150	774.5	796.5	805.8	823.3	831.4	838.6
152	794.1	816.8	827.1	845.4	854.5	862.6
154	812.7	836.1	847.4	866.5	876.5	885.6
156	830.3	854.4	866.8	886.5	897.5	907.6
158	847.1	871.8	885.2	905.6	917.6	928.6
160	863.0	888.4	902.7	923.9	936.8	948.7
162	878.2	904.1	919.4	941.2	955.1	967.9
164	892.5	919.1	935.3	957.8	972.5	986.3
166	906.2	933.4	950.5	973.6	989.2	1003.9
168	919.2	946.9	964.9	988.7	1005.2	1020.7
170	931.6	959.9	978.7	1003.2	1020.5	1036.8
172	943.4	972.2	991.9	1016.9	1035.1	1052.2
174	954.6	983.9	1004.4	1030.1	1049.0	1067.0
176	965.2	995.1	1016.4	1042.7	1062.4	1081.2
178	975.4	1005.7	1027.9	1054.7	1075.2	1094.8
180	985.0	1015.9	1038.8	1066.2	1087.5	1107.8
182	994.2	1025.6	1049.3	1077.2	1099.2	1120.2
184	1003.0	1034.9	1059.3	1087.8	1110.5	1132.2
186	1011.4	1043.7	1068.8	1097.8	1121.2	1143.7
188	1019.4	1052.2	1078.0	1107.5	1131.6	1154.7
190	1027.0	1060.2	1086.7	1116.7	1141.5	1165.3
192	1034.2	1067.9	1095.0	1125.6	1151.0	1175.5
194	1041.1	1075.3	1103.0	1134.1	1160.1	1185.2
196	1047.8	1082.3	1110.7	1142.2	1168.9	1194.6
198	1054.1	1089.0	1118.0	1150.0	1177.3	1203.6
200	1060.1	1095.5	1125.0	1157.5	1185.3	1212.2
202	1065.8	1101.6	1131.7	1164.6	1193.1	1220.5
204	1071.3	1107.5	1138.2	1171.5	1200.5	1228.5
206	1076.6	1113.1	1144.3	1178.1	1207.6	1236.2
208	1081.6	1118.5	1150.3	1184.4	1214.5	1243.6
210	1086.4	1123.6	1155.9	1190.5	1221.1	1250.7
212	1091.0	1128.6	1161.3	1196.3	1227.4	1257.6
214	1095.3	1133.3	1166.6	1201.9	1233.5	1264.2
216	1099.5	1137.8	1171.5	1207.3	1239.3	1270.5
218	1103.5	1142.1	1176.3	1212.4	1245.0	1276.6
220	1107.4	1146.3	1180.9	1217.4	1250.4	1282.5
222	1111.0	1150.3	1185.3	1222.2	1255.6	1288.1
224	1114.5	1154.1	1189.6	1226.7	1260.6	1293.6
226	1117.9	1157.7	1193.6	1231.1	1265.4	1298.8
228	1121.1	1161.2	1197.5	1235.4	1270.0	1303.9
230	1124.2	1164.6	1201.3	1239.4	1274.5	1308.8

TABLE B9b (*continued*)

THERMOSPHERE TEMPERATURE MODELS

Z (KM)	1200° T (K)	1250° T (K)	1300° T (K)	1350° T (K)	1400° T (K)	1450° T (K)
230	1124.2	1164.6	1201.3	1239.4	1274.5	1308.8
232	1127.1	1167.8	1204.9	1243.3	1278.8	1313.5
234	1129.9	1170.9	1208.3	1247.1	1282.9	1318.0
236	1132.7	1173.8	1211.6	1250.7	1286.9	1322.3
238	1135.2	1176.7	1214.8	1254.2	1290.8	1326.6
240	1137.7	1179.4	1217.9	1257.5	1294.5	1330.6
242	1140.1	1182.0	1220.8	1260.7	1298.0	1334.5
244	1142.4	1184.5	1223.7	1263.8	1301.5	1338.3
246	1144.6	1186.9	1226.4	1266.8	1304.8	1341.9
248	1146.7	1189.2	1229.0	1269.7	1308.0	1345.5
250	1148.7	1191.5	1231.5	1272.4	1311.0	1348.8
252	1150.6	1193.6	1233.9	1275.1	1314.0	1352.1
254	1152.5	1195.7	1236.2	1277.7	1316.8	1355.3
256	1154.2	1197.6	1238.5	1280.1	1319.6	1358.3
258	1155.9	1199.5	1240.6	1282.5	1322.3	1361.3
260	1157.6	1201.3	1242.7	1284.8	1324.8	1364.1
262	1159.1	1203.1	1244.7	1287.0	1327.3	1366.9
264	1160.6	1204.8	1246.6	1289.1	1329.7	1369.5
266	1162.1	1206.4	1248.5	1291.2	1332.0	1372.1
268	1163.5	1207.9	1250.3	1293.2	1334.2	1374.6
270	1164.8	1209.4	1252.0	1295.1	1336.3	1376.9
272	1166.1	1210.9	1253.6	1296.9	1338.4	1379.3
274	1167.3	1212.2	1255.2	1298.7	1340.4	1381.5
276	1168.5	1213.6	1256.7	1300.4	1342.3	1383.6
278	1169.6	1214.9	1258.2	1302.0	1344.2	1385.7
280	1170.7	1216.1	1259.6	1303.6	1346.0	1387.8
282	1171.8	1217.3	1261.0	1305.2	1347.7	1389.7
284	1172.8	1218.4	1262.3	1306.6	1349.4	1391.6
286	1173.8	1219.5	1263.6	1308.1	1351.0	1393.4
288	1174.7	1220.6	1264.8	1309.4	1352.6	1395.2
290	1175.6	1221.6	1266.0	1310.8	1354.1	1396.9
292	1176.5	1222.6	1267.2	1312.1	1355.6	1398.5
294	1177.3	1223.5	1268.3	1313.3	1357.0	1400.1
296	1178.1	1224.4	1269.3	1314.5	1358.4	1401.7
298	1178.9	1225.3	1270.4	1315.7	1359.7	1403.2
300	1179.6	1226.2	1271.3	1316.8	1361.0	1404.6
310	1183.0	1230.0	1275.8	1321.8	1366.8	1411.2
320	1185.7	1233.1	1279.6	1326.1	1371.7	1416.8
330	1188.0	1235.8	1282.7	1329.7	1375.9	1421.6
340	1190.0	1238.0	1285.4	1332.8	1379.5	1425.8
350	1191.6	1239.9	1287.6	1335.4	1382.5	1429.3
360	1192.9	1241.5	1289.6	1337.6	1385.1	1432.3
370	1194.1	1242.9	1291.2	1339.5	1387.4	1435.0
380	1195.1	1244.0	1292.6	1341.2	1389.3	1437.3
390	1195.9	1245.0	1293.8	1342.6	1391.0	1439.2
400	1196.6	1245.9	1294.8	1343.8	1392.5	1441.0
410	1197.2	1246.6	1295.7	1344.9	1393.7	1442.5
420	1197.7	1247.2	1296.5	1345.8	1394.8	1443.8
430	1198.1	1247.7	1297.2	1346.6	1395.8	1444.9
440	1198.5	1248.2	1297.7	1347.3	1396.6	1445.9
450	1198.9	1248.6	1298.2	1347.9	1397.4	1446.8
460	1199.1	1248.9	1298.7	1348.4	1398.0	1447.6
470	1199.4	1249.2	1299.0	1348.8	1398.6	1448.3
480	1199.6	1249.5	1299.4	1349.2	1399.1	1448.9
490	1199.8	1249.7	1299.7	1349.6	1399.5	1449.4
500	1199.9	1249.9	1299.9	1349.9	1399.9	1449.9

TABLE B10a

THERMOSPHERE TEMPERATURE MODELS

Z (KM)	1500° T (K)	1550° T (K)	1600° T (K)	1650° T (K)	1700° T (K)	1750° T (K)
120	323.6	323.6	323.6	323.6	323.6	323.6
122	367.1	366.3	372.9	376.7	379.1	378.3
124	409.5	408.1	420.3	427.4	431.8	430.6
126	450.0	448.2	465.1	474.8	480.9	479.5
128	489.5	487.5	508.3	520.1	527.7	526.4
130	527.9	526.0	549.9	563.5	572.3	571.3
132	565.2	563.6	590.0	605.1	615.0	614.4
134	601.3	600.2	628.5	644.9	655.8	655.8
136	636.2	635.7	665.5	682.9	694.8	695.4
138	669.8	670.0	701.0	719.4	732.1	733.4
140	702.1	703.1	735.0	754.2	767.7	769.8
142	733.1	734.9	767.6	787.5	801.7	804.7
144	762.9	765.6	798.8	819.3	834.3	838.0
146	791.4	795.0	828.6	849.8	865.4	870.0
148	818.7	823.3	857.2	878.9	895.2	900.6
150	844.9	850.4	884.6	906.8	923.7	930.0
152	869.9	876.4	910.8	933.5	951.0	958.1
154	893.9	901.3	935.8	959.0	977.1	985.1
156	916.8	925.2	959.8	983.5	1002.2	1010.9
158	938.8	948.1	982.8	1006.9	1026.2	1035.8
160	959.8	970.1	1004.9	1029.4	1049.2	1059.6
162	979.9	991.1	1026.0	1051.0	1071.3	1082.5
164	999.2	1011.3	1046.3	1071.6	1092.5	1104.5
166	1017.7	1030.7	1065.7	1091.5	1112.9	1125.6
168	1035.4	1049.2	1084.3	1110.5	1132.5	1145.9
170	1052.3	1067.0	1102.2	1128.8	1151.3	1165.5
172	1068.6	1084.1	1119.4	1146.4	1169.3	1184.3
174	1084.2	1100.5	1135.9	1163.3	1186.7	1202.4
176	1099.1	1116.3	1151.8	1179.5	1203.5	1219.8
178	1113.5	1131.4	1167.0	1195.1	1219.6	1236.6
180	1127.2	1145.9	1181.7	1210.2	1235.1	1252.8
182	1140.4	1159.9	1195.8	1224.6	1250.0	1268.4
184	1153.1	1173.3	1209.3	1238.5	1264.4	1283.4
186	1165.3	1186.2	1222.3	1251.9	1278.2	1297.9
188	1177.0	1198.6	1234.9	1264.9	1291.6	1311.9
190	1188.3	1210.5	1247.0	1277.3	1304.5	1325.4
192	1199.1	1222.0	1258.6	1289.3	1316.9	1338.4
194	1209.5	1233.0	1269.8	1300.8	1328.9	1351.0
196	1219.5	1243.6	1280.6	1312.0	1340.4	1363.1
198	1229.1	1253.8	1291.0	1322.7	1351.6	1374.8
200	1238.3	1263.7	1301.0	1333.1	1362.4	1386.1
202	1247.2	1273.2	1310.6	1343.0	1372.7	1397.1
204	1255.8	1282.3	1319.9	1352.7	1382.8	1407.7
206	1264.0	1291.1	1328.9	1362.0	1392.5	1417.9
208	1271.9	1299.6	1337.6	1371.0	1401.9	1427.8
210	1279.6	1307.7	1345.9	1379.6	1410.9	1437.3
212	1286.9	1315.6	1354.0	1388.0	1419.7	1446.6
214	1294.0	1323.2	1361.8	1396.1	1428.1	1455.5
216	1300.9	1330.5	1369.3	1403.9	1436.3	1464.1
218	1307.4	1337.6	1376.5	1411.5	1444.2	1472.5
220	1313.8	1344.4	1383.5	1418.8	1451.9	1480.6
222	1319.9	1351.0	1390.3	1425.8	1459.3	1488.5
224	1325.8	1357.3	1396.8	1432.7	1466.4	1496.1
226	1331.5	1363.4	1403.1	1439.3	1473.3	1503.4
228	1337.0	1369.4	1409.2	1445.6	1480.0	1510.5
230	1342.2	1375.1	1415.1	1451.8	1486.5	1517.4

TABLE B10b (*continued*)

THERMOSPHERE TEMPERATURE MODELS

Z (KM)	1500° T (K)	1550° T (K)	1600° T (K)	1650° T (K)	1700° T (K)	1750° T (K)
230	1342.2	1375.1	1415.1	1451.8	1486.5	1517.4
232	1347.3	1380.6	1420.8	1457.8	1492.8	1524.1
234	1352.3	1385.9	1426.3	1463.5	1498.9	1530.6
236	1357.0	1391.0	1431.6	1469.1	1504.8	1536.9
238	1361.6	1396.0	1436.8	1474.5	1510.5	1542.9
240	1366.0	1400.8	1441.7	1479.7	1516.0	1548.8
242	1370.3	1405.4	1446.6	1484.8	1521.3	1554.6
244	1374.4	1409.9	1451.2	1489.7	1526.5	1560.1
246	1378.4	1414.2	1455.7	1494.4	1531.5	1565.5
248	1382.3	1418.4	1460.1	1499.0	1536.4	1570.7
250	1386.0	1422.5	1464.3	1503.5	1541.1	1575.7
252	1389.6	1426.4	1468.4	1507.8	1545.7	1580.6
254	1393.0	1430.2	1472.3	1512.0	1550.1	1585.4
256	1396.4	1433.8	1476.1	1516.0	1554.4	1590.0
258	1399.6	1437.4	1479.8	1519.9	1558.6	1594.5
260	1402.8	1440.8	1483.4	1523.7	1562.6	1598.8
262	1405.8	1444.1	1486.9	1527.4	1566.6	1603.0
264	1408.7	1447.3	1490.2	1531.0	1570.4	1607.1
266	1411.5	1450.4	1493.5	1534.4	1574.1	1611.1
268	1414.3	1453.4	1496.7	1537.8	1577.6	1615.0
270	1416.9	1456.4	1499.7	1541.0	1581.1	1618.7
272	1419.5	1459.2	1502.7	1544.2	1584.5	1622.4
274	1422.0	1461.9	1505.5	1547.2	1587.7	1625.9
276	1424.4	1464.5	1508.3	1550.2	1590.9	1629.3
278	1426.7	1467.1	1511.0	1553.1	1594.0	1632.7
280	1428.9	1469.6	1513.6	1555.9	1597.0	1635.9
282	1431.1	1472.0	1516.2	1558.6	1599.9	1639.1
284	1433.2	1474.3	1518.6	1561.2	1602.7	1642.1
286	1435.2	1476.6	1521.0	1563.8	1605.4	1645.1
288	1437.2	1478.7	1523.3	1566.2	1608.1	1648.0
290	1439.1	1480.9	1525.5	1568.6	1610.7	1650.8
292	1441.0	1482.9	1527.7	1571.0	1613.2	1653.5
294	1442.8	1484.9	1529.8	1573.2	1615.6	1656.2
296	1444.5	1486.8	1531.9	1575.4	1618.0	1658.7
298	1446.2	1488.7	1533.8	1577.5	1620.3	1661.3
300	1447.8	1490.5	1535.8	1579.6	1622.5	1663.7
310	1455.2	1498.8	1544.6	1589.1	1632.8	1674.9
320	1461.6	1505.9	1552.2	1597.3	1641.7	1684.7
330	1467.0	1512.1	1558.7	1604.4	1649.5	1693.3
340	1471.7	1517.4	1564.4	1610.6	1656.2	1700.8
350	1475.8	1522.0	1569.4	1616.0	1662.2	1707.3
360	1479.3	1526.0	1573.7	1620.8	1667.4	1713.1
370	1482.3	1529.4	1577.5	1624.9	1671.9	1718.2
380	1485.0	1532.5	1580.7	1628.5	1675.9	1722.7
390	1487.3	1535.1	1583.6	1631.7	1679.5	1726.6
400	1489.3	1537.4	1586.2	1634.5	1682.6	1730.1
410	1491.0	1539.5	1588.4	1637.0	1685.3	1733.2
420	1492.6	1541.3	1590.4	1639.2	1687.8	1736.0
430	1493.9	1542.8	1592.1	1641.1	1689.9	1738.5
440	1495.1	1544.2	1593.6	1642.8	1691.9	1740.7
450	1496.2	1545.5	1595.0	1644.3	1693.6	1742.6
460	1497.1	1546.6	1596.2	1645.7	1695.1	1744.4
470	1497.9	1547.5	1597.3	1646.9	1696.5	1746.0
480	1498.6	1548.4	1598.2	1648.0	1697.7	1747.4
490	1499.3	1549.2	1599.1	1648.9	1698.8	1748.6
500	1499.9	1549.8	1599.8	1649.8	1699.8	1749.8

TABLE B11a

THERMOSPHERE TEMPERATURE MODELS

Z (KM)	1800° T (K)	1850° T (K)	1900° T (K)	1950° T (K)	2000° T (K)
120	323.6	323.6	323.6	323.6	323.6
122	377.5	376.6	384.2	383.4	382.5
124	429.2	427.7	441.5	440.2	438.8
126	477.9	476.1	494.8	493.3	491.6
128	524.8	522.9	545.3	543.9	542.2
130	569.9	568.2	593.6	592.4	590.9
132	613.5	612.1	639.7	638.9	637.8
134	655.3	654.5	683.8	683.5	682.9
136	695.6	695.3	725.9	726.3	726.2
138	734.3	734.6	766.3	767.3	767.9
140	771.4	772.5	804.9	806.6	807.9
142	807.0	808.9	841.9	844.3	846.3
144	841.2	843.8	877.3	880.5	883.2
146	874.0	877.4	911.2	915.2	918.7
148	905.5	909.7	943.7	948.5	952.7
150	935.6	940.7	974.9	980.5	985.5
152	964.6	970.5	1004.8	1011.2	1017.0
154	992.4	999.1	1033.6	1040.7	1047.2
156	1019.1	1026.7	1061.2	1069.0	1076.4
158	1044.7	1053.1	1087.7	1096.3	1104.4
160	1069.4	1078.5	1113.2	1122.6	1131.4
162	1093.0	1103.0	1137.7	1147.8	1157.4
164	1115.8	1126.6	1161.3	1172.2	1182.5
166	1137.7	1149.2	1184.0	1195.6	1206.6
168	1158.8	1171.1	1205.9	1218.2	1229.9
170	1179.1	1192.1	1227.0	1240.0	1252.4
172	1198.6	1212.4	1247.3	1261.0	1274.1
174	1217.4	1231.9	1266.9	1281.3	1295.1
176	1235.6	1250.7	1285.9	1300.8	1315.3
178	1253.1	1268.9	1304.1	1319.7	1334.8
180	1269.9	1286.4	1321.7	1338.0	1353.7
182	1286.2	1303.3	1338.7	1355.6	1372.0
184	1301.8	1319.7	1355.1	1372.6	1389.6
186	1317.0	1335.4	1371.0	1389.1	1406.7
188	1331.6	1350.7	1386.3	1405.1	1423.3
190	1345.7	1365.4	1401.2	1420.5	1439.2
192	1359.3	1379.6	1415.5	1435.4	1454.7
194	1372.4	1393.3	1429.4	1449.8	1469.7
196	1385.2	1406.6	1442.8	1463.8	1484.3
198	1397.4	1419.5	1455.8	1477.3	1498.3
200	1409.3	1431.9	1468.4	1490.4	1512.0
202	1420.8	1443.9	1480.5	1503.1	1525.2
204	1431.9	1455.6	1492.3	1515.4	1538.0
206	1442.6	1466.8	1503.7	1527.3	1550.4
208	1453.0	1477.8	1514.8	1538.9	1562.5
210	1463.1	1488.3	1525.5	1550.1	1574.2
212	1472.8	1498.5	1535.9	1560.9	1585.5
214	1482.2	1508.5	1545.9	1571.5	1596.5
216	1491.4	1518.1	1555.7	1581.7	1607.2
218	1500.2	1527.4	1565.2	1591.6	1617.6
220	1508.8	1536.4	1574.3	1601.2	1627.6
222	1517.1	1545.1	1583.2	1610.6	1637.4
224	1525.1	1553.6	1591.9	1619.6	1646.9
226	1532.9	1561.8	1600.3	1628.4	1656.1
228	1540.4	1569.8	1608.4	1637.0	1665.1
230	1547.7	1577.5	1616.3	1645.3	1673.8

TABLE B11b *(continued)*

THERMOSPHERE TEMPERATURE MODELS

Z (KM)	1800° T (K)	1850° T (K)	1900° T (K)	1950° T (K)	2000° T (K)
230	1547.7	1577.5	1616.3	1645.3	1673.8
232	1554.8	1585.0	1623.9	1653.4	1682.3
234	1561.7	1592.3	1631.4	1661.2	1690.5
236	1568.4	1599.3	1638.6	1668.8	1698.5
238	1574.8	1606.2	1645.6	1676.2	1706.3
240	1581.1	1612.8	1652.4	1683.4	1713.8
242	1587.2	1619.3	1659.0	1690.4	1721.2
244	1593.1	1625.5	1665.5	1697.2	1728.4
246	1598.8	1631.6	1671.7	1703.8	1735.3
248	1604.4	1637.5	1677.8	1710.2	1742.1
250	1609.8	1643.3	1683.7	1716.4	1748.7
252	1615.0	1648.8	1689.4	1722.5	1755.1
254	1620.1	1654.3	1695.0	1728.4	1761.3
256	1625.0	1659.5	1700.4	1734.1	1767.4
258	1629.8	1664.6	1705.7	1739.7	1773.3
260	1634.5	1669.6	1710.8	1745.1	1779.0
262	1639.0	1674.4	1715.8	1750.4	1784.6
264	1643.4	1679.1	1720.6	1755.6	1790.1
266	1647.6	1683.7	1725.3	1760.6	1795.4
268	1651.8	1688.1	1729.9	1765.5	1800.6
270	1655.8	1692.4	1734.4	1770.2	1805.6
272	1659.7	1696.6	1738.7	1774.8	1810.5
274	1663.5	1700.7	1742.9	1779.3	1815.3
276	1667.2	1704.7	1747.0	1783.7	1820.0
278	1670.8	1708.5	1751.0	1788.0	1824.5
280	1674.3	1712.3	1754.9	1792.1	1828.9
282	1677.7	1715.9	1758.7	1796.2	1833.2
284	1681.0	1719.5	1762.4	1800.1	1837.4
286	1684.2	1722.9	1766.0	1804.0	1841.5
288	1687.4	1726.3	1769.5	1807.7	1845.5
290	1690.4	1729.6	1772.9	1811.4	1849.4
292	1693.4	1732.8	1776.2	1814.9	1853.2
294	1696.2	1735.9	1779.5	1818.4	1856.9
296	1699.0	1738.9	1782.6	1821.8	1860.5
298	1701.8	1741.8	1785.7	1825.0	1864.0
300	1704.4	1744.7	1788.6	1828.3	1867.5
310	1716.6	1757.9	1802.5	1843.1	1883.4
320	1727.3	1769.5	1814.6	1856.2	1897.5
330	1736.7	1779.7	1825.3	1867.8	1910.0
340	1744.9	1788.7	1834.8	1878.1	1921.1
350	1752.1	1796.7	1843.2	1887.2	1930.9
360	1758.5	1803.7	1850.6	1895.3	1939.7
370	1764.2	1809.9	1857.1	1902.5	1947.6
380	1769.2	1815.4	1863.0	1908.9	1954.6
390	1773.6	1820.3	1868.2	1914.6	1960.8
400	1777.5	1824.7	1872.9	1919.7	1966.5
410	1781.0	1828.6	1877.0	1924.3	1971.5
420	1784.1	1832.1	1880.7	1928.5	1976.0
430	1786.9	1835.2	1884.1	1932.2	1980.1
440	1789.4	1838.0	1887.0	1935.5	1983.8
450	1791.6	1840.5	1889.7	1938.5	1987.1
460	1793.6	1842.7	1892.1	1941.2	1990.1
470	1795.4	1844.7	1894.3	1943.6	1992.9
480	1797.0	1846.6	1896.3	1945.8	1995.3
490	1798.4	1848.2	1898.1	1947.8	1997.6
500	1799.7	1849.7	1899.7	1949.7	1999.6

Author Index for Part B

Numbers in parentheses are reference numbers and indicate that an author's work is referred to although his name is not cited in the text. Numbers in italics show the page on which the complete reference is listed.

A

Aamodt, R. E., 67(10), 71(10), *99*
Adams, G. W., 122(35), *123*
Aikin, A. C., 118(17), 119(17), 120(17), *122*, 125(7), 133(13), 135(7), 136 (7), 139(23), 140(23), 144(7), *150*
Alcayde, D., 5(11), *30*
Anderson, D. N., 191(8), *235*
Anderson, J. R., 119(18), *122*
Andrews, M. K., 220(59), 223(59), 225 (59), *236*
Angerami, J., 199(39), 225(80), *236, 237*
Aono, O., 245(21), *285*
Appleton, E. V., 101(1), *122*
Arnold, F., 125(8, 9), 133(8), 135(9), 136(8, 20), 137(9), 144(9), *150*
Axford, W. I., 162(9), *168*, 183(30), *190*, 196(32, 35), 197(35), 198(35, 37), 225(79), 226(37), 227(79), *236, 237*, 241(17), *285*, 298(49), *309*

B

Bailey, A. D., 133(14, 15), 134(14), 144 (14), *150*
Bailey, D. K., 117(15), *122*
Bailey, G. J., 6(27), *30*, 186(37), 188 (37), *190*
Banks, P. M., 20(48, 49), *31*, 166(10, 12), *168*, 183(26, 27, 30), 186(42, 43), 189(43), *190*, 196(34, 35), 197 (35), 198(35), 201(40), 215(51), 216(51, 52), 220(70), 223(70), 224, 225(52), 226(70), 227(34, 52), *236, 237*, 240(12, 13), 241(15), 247(13), 249(32), 252(32), 254(32), 257(32, 45), 259(32, 46), 261(32), 262(15), 263(52, 53), 265(54), 266(13), 267 (54), 273(54, 66), 274(12, 72), 279 (76), 281(76), *285, 286*, 288(7), 293(19), 295(7), 298(49, 51), 299 (51, 55), 300(51), 301(51, 55, 58, 59), 302(51), *308, 309*
Barat, J., 36(9), 38(14), *62*
Barbier, D., 302(60), 304(60), *309*
Barnett, M. A. F., 101(1), *122*
Barrington, R. E., 220(67), 223(67), *236*, 301(54), *309*
Barron, D. W., 169(1), 182(25), *189, 190*
Bartels, J., 160(7), *168*
Bates, D. R., 5(13), 16(13), 22(13), 25 (60), *30, 31*, 36(10), 46(32), 55 (10), 57(10), *62*, 191(5), 194(28), *235*
Bauer, E., 25(57), *31*
Bauer, P., 5(11), *30*, 215(50), *236*, 289 (11), 291(11), 289(48), *308, 309*
Bauer, S. J., 191(7, 11), 194(30, 31), 195(30), 223(77), 227(77), *235, 236, 237*
Belrose, J. S., 301(54), *309*
Bennett, R. T., 302(64), *309*
Bennett, W. H., 191(8), *235*
Bertaux, J-L., 95(26, 28), *100*

Beutler, A. E., 252(30), *285*, 288(6), 293(6, 16), 302(16), 303(16), *308*
Bhattacharya, K., 281(79), *286*
Bird, R. B., 2(2), 3(2), 5(2), 9(2), 12 (2), *30*, 38(19), 39(19), 41(19), *62*
Blake, D., 21(50), *31*
Blamont, J-E., 36(9), 38(14), *62*, 95(26, 28), *100*
Blum, P. W., 95(27), *100*
Boggess, R. L., 238(3), *284*, 293(20), *308*
Bonner, F. M., 220(64), *236*
Borst, W. L., 143(35), *151*
Bortner, M. H., 25(57), *31*
Bourdeau, R. E., 139(23), 140(23), 141 (25), *150*, 191(7), *235*, 293(35), *308*
Bowen, P. J., 191(10), 220(54), *235*, *236*, 293(31), *308*
Bowhill, S. A., 169(4), 171(4), 176(4), 183(29), *189*, *190*, 240(11), 257 (38, 44), *285*, *286*
Boyd, R. L. F., 191(10), 220(54), *235*, *236*, 293(31), *308*
Brace, L. H., 141(26), *151*, 191(9, 20), 202(20), 206(45), 208(45), 212 (45), *235*, *236*, 238(3), 239(5, 6, 9), *284*, *285*, 291(14), 293(14, 20, 21, 22, 24, 25, 30, 32, 33, 34), 297 (33), 298(47), 300(22), *308*, *309*
Bramley, E. N., 186(44), 187(44), 189 (44), *190*
Brandt, J. C., 150(44), *151*, 247(26), *285*
Breit, G., 101(2), *122*
Brinkmann, R. T., 49(40, 43), *62*, 69 (14), *99*
Brinton, H. C., 60(80), *63*, 139(24), 144 (24), *150*, 191(9, 18), 202(41, 43), 208(48), 212(48), 220(18, 61, 64, 65), 222(61), 225(18), *235*, *236*
Bruner, E. C., Jr., 54(62, 63), 57(63), *63*
Bryan, G. H., 65(5), *99*
Burgers, J. M., 152(2), 154(2), 155(2), *168*, 241(16), 244(16), 275(16), 276(16), *285*
Byram, E. T., 32(2, 5), 57(5), *61*, 64(1), *99*, 121(27), *122*

C

Cahn, J. H., 263(51), 281(79), *286*
Cairns, R. B., 121(22), *122*
Campbell, F. J., 49(38), *62*
Carignan G. R., 239(5, 6, 9), *285*, 293 (21, 22, 24, 25), 300(22), *308*
Carlson, H. C., Jr., 191(24), *235*, 293 (34), 302(61, 62, 63), *308*, *309*
Carpenter, D. L., 220(64, 65, 71, 72), 225(71, 72, 80), *236*, *237*
Carru, H., 5(8), *30*, 293(43), 302(43), *308*
Carruthers, G. R., 102(30), 121(30), *123*, 142(31), 150(31), *151*
Case, K. M., 67(10), 71(10), *99*
Catchpole, J. R., 257(41, 42), *285*
Cauffman, D. P., 186(47), 189(47), *190*
Chamberlain, J. W., 49(38, 39, 42), *62*, 67(11), 69(13), 70(11), 71(11), 91, *99*
Chandra, S., 186(45), 187(45), 189(45), *190*, 273(68), *286*, 293(35), 301 (57), *308*, *309*
Chapman, J. H., 220(69), *236*
Chapman, S., 2(1), 3(1), 5(1), 9(1), 12 (1), *30*, 33(6), 34(6), 38(6), 41 (6), 42(6), 49, *62*, 75(19), *100*, 102 (4), 107(2, 11), 109(2, 11, 12), *122*, 160(7), *168*, 275(73), 278(75), *286*
Chappell, C. R., 220(73), 221(73), 225 (73), *237*
Childs, G. E., 10(34), 12(34), *31*
Ching, B. K., 9(28), *30*
Christensen, A. B., 50(53), *63*
Chubb, T. A., 32(2, 5), 57(5), *61*, 64(1), *99*, 121(27), *122*
Cicerone, R. J., 257(44), *286*
Clarke, W. B., 50(54), *63*
Cohen, R., 290(13), 295(45), *308*, *309*
Cole, K. D., 20(46, 47), *31*, 186(41), 189(41), *190*, 241(14), 262(14), *285*, 305(68, 69), *309*
Colegrove, F. D., 34(7), 35(7), *62*
Colin, L., 220(62, 63), 223(62), *236*
Compton, D. M. J., 177(17), *190*
Cook, G. E., 49(48), *63*
Cook, S. R., 65(4), *99*
Cornwall, J. M., 305(70), *309*
Coroniti, F. V., 305(70), *309*

Cowling, T. G., 2(1), 3(1), 5(1), 9(1), 10(32), 12(1), *30, 31,* 33(6), 34(6), 38(6), 41(6), 42(6), *62,* 75(19), *100,* 278(75), *286*
Craig, H., 50(54), *63*
Craig, R. A., 23(55), *31*
Cummack, C. H., 5(18), *30*
Cunnold, D. M., 162(9), *168*
Curtiss, C. F., 2(2), 3(2), 5(2), 9(2), 12(2), *30,* 38(19), 39(19), 41(19), *62*

D

Dalgarno, A., 10(37), *31,* 92(21), *100,* 166(11, 13), *168,* 177(14, 15), 178 (20), 187(20), *190,* 245(19), 247 (19, 27), 252(19, 27, 33), 256(27), 266(19, 27), 268(55, 59), 269(62, 64), 270(27, 65), 273(67), *285, 286,* 287(1), 288(1), 289(8), 293(30), 295(1, 8), 301(56), *307, 308, 309*
da Rosa, A. V., 295(46), *309*
Daybilge, U., 274(70), 281(70), *286*
Deehr, C. S., 302(65), *309*
Degges, T. C., 269(64), *286*
Della Luca, L., 133(15), 136(15), *150*
Dessler, A. J., 223(78), 227(78), *237*
Dickinson, R. E., 5(22), 7(22), 9(29), *30, 31*
Doering, J. P., 254(34), *285*
Donahue, T. M., 54(66), 58(69), 60(77), *63,* 95(24), *100,* 121(23), *122,* 124 (2, 3), 135(3), 137(3), 141(3), 142 (29), 143(34, 35), 145(2, 3), *150, 151*
Donley, J. L., 139(23), 140(23), *150,* 191(7), 220(57), *235, 236,* 293(35), 307(76), *309*
Dougherty, J. P., 152(1), *168,* 169(2), *189*
Doupnik, J. R., 293(29), 294(29), 295 (29, 44), *308, 309*
Dowell, J. T., 269(63), *286*
Drukarev, G., 238(2), *284*
Duboin, M.-L., 254(35), *285,* 293(17), *308*
Dungey, J. W., 191(2), 192(2), 223(76), *235, 237*
Dunham, G. S., 191(20), 202(20), 206 (45), 208(45), 212(45), *235, 236,* 298(47), *309*

E

Eccles, D., 186(39, 40), 188(39, 40), *190*
Epstein, P. S., 37(12), *62*
Evans, J. V., 239(7), 257(43), *285, 286,* 288(3, 4, 5), 289(3, 5, 9, 12), 291(9, 12), 293(3, 4, 5, 9, 23, 26, 27), 296 (3), 298(50), 301(3), 304(50), *307, 308, 309*

F

Fahr, H. J., 49(41), *62,* 95(27), *100*
Faire, A. C., 38(18), 52(18), *62*
Farley, D. T., 191(25), *235,* 293(36), *308*
Fastie, W. G., 254(34), *285*
Fedder, J. A., 20(49), *31,* 186(43), 189 (43), *190,* 235(82), *237,* 241(15), 262(15), *285*
Fehsenfeld, F. C., 133(16, 17), 144(40), *150, 151*
Fejer, J. A., 156(6), 159(6), 160(6), 165 (6), *168*
Feldman, P. D., 22(53), *31,* 254(34), *285*
Ferguson, E. E., 124(5), 126(5), 132 (5), 133(16, 17), 134(5), 135(5), 136(5), 137(5, 21), 144(40), *150, 151*
Ferraro, V. C. A., 156(5), *168*
Findlay, J. A., 291(14), 293(14), 300 (14), 305(71), *308, 309*
Fish, R. A., 67, 70(12), 72(12), *99*
Fitzmaurice, J. A., 17(41), *31,* 107(8), *122*
Folkestad, K., 136(20), *150*
Fontheim, E. G., 215(50), *236,* 252(29, 30), *285,* 288(6), 293(6, 16), 298 (48), 302(16), 303(16), *308, 309*
Fournier, J. P., 252(29), *285*
Frank, L. A., 186(49), 189(49), *190*
Friedman, H., 32(2, 5), 57(5), *61,* 64 (1), *99,* 121(27, 29), *122*
Friedman, M. P., 5(5), *30*
Friedrich, M., 136(20), *150*

G

Gardner, M. E., 107(10), *122*
Geisler, J. E., 9(29), *31,* 183(29), 186

(34), 188(34), *190*, 206(46), 207 (46), 208(46), 209(46), *236*, 240 (11), 257(38), *285*
Gerson, N. C., 238(1), *284*
Gille, J. C., 23(55), *31*
Gleeson, L. J., 162(9), *168*, 241(17), *285*
Gliddon, J. E. C., 169(3, 6, 8), 171(3), 174(6), *189*
Goldberg, R. A., 125(7), 135(7), 136(7), 144(7), *150*
Goldstein, L., 281(77), *286*
Gordiets, B. F., 25(59), *31*
Gordon, W. E., 191(24), *235*
Gottlieb, B., 18(43), 19(43), 25(43), *31*, 38(16), 50(55), 52(55), *62, 63*
Gray, P., 10(32), *31*
Grebowsky, J. M., 206(47), 208(48), 212 (48), *236*
Green, A. E. S., 107(7), *122*
Green, J. L., 293(36), *308*
Grew, K. E., 42(24), *62*
Griggs, M., 107(7), *122*
Gupta, G. P., 11(39), 12(39), *31*
Gurnett, D. A., 186(47, 49), 189(47, 49), *190*, 223(74), *237*

H

Hageman, R., 54(59), *63*
Hagg, E. L., 220(56), *236*
Hake, R. D., 269(61), *286*
Hale, L. C., 191(8), *235*
Hall, L. A., 17(42), *31*
Hanley, H. J. M., 10(34), 12(34), *31*
Hanson, W. B., 34(7), 35(7), 60(76), *62, 63*, 94(23), *100*, 169(5), 183 (28), 186(28), *189, 190*, 191(6), 192(27), 206(44), 208(44), 212 (44), *235, 236*, 239(4, 10), *284, 285*, 289(10), 291(10, 14), 293(14, 15, 41), 300(14, 41), 301(10), *308*
Harm, R., 275(74), 276(74), 277(74), *286*
Harpold, D. N., 49(50), 52(50), *63*
Harris, I., 5(19, 20), 7(19, 20), 8(19), 26(19, 20, 65), *30, 31*
Harris, K. K., 220(73), 221(73), 225 (73), *237*
Hartmann, G., 50(52), *63*
Harwit, M., 22(52), *31*
Haskell, R. E., 153(3), *168*
Hays, P. B., 38(17), *62*, 245(20), *285*, 304(67), *309*
Hedin, A. E., 49(50), 52(50), *63*
Henderson, C. L., 293(31), *308*
Henry, R. J. W., 178(20, 21), 187(20), *190*, 268(59), *286*
Herman, J. R., 273(68), *286*, 301(57), *309*
Herndon, R. C., 281(78), *286*
Herring, J., 67(9), 71(9), 97(9), *99*
Heyborne, R. L., 220(64), *236*
Hines, C. O., 196(32), *236*
Hinteregger, H. E., 17(42), *31*
Hirschfelder, J. O., 2(2), 3(2), 5(2), 9(2), 12(2), *30*, 38(19), 39(19), 41(19), *62*
Hodges, R. R., Jr., 52(56), 60(56, 79), *63*
Hoegy, W. F., 252(29), *285*
Hoffman, J. H., 54(60, 61), 57(61), *63*, 191(12, 13, 21, 22), 196(21), 202 (21, 22), 203(21), 220(58, 68), 222 (68), 223(68), *235, 236*
Holmes, J. C., 54(61), 57(61), *63*, 102 (30), 121(30, 31, 32), *123*, 139(22), 141(22, 27), 142(22, 31, 32), 143 (33), 144(38), 149(22, 38), *150, 151*, 191(21), 196(21), 202(21), 203(21), *235*
Holt, E. H., 153(3), *168*
Holzer, T. E., 166(12), *168*, 183(26), *190*, 196(34), 215(51), 216(51, 52), 225(52), 227(34, 52), 235(82), *236, 237*
Horowitz, R., 49(50), 52(50), *63*
Houck, J. R., 22(52), *31*
Huffman, R. E., 121(22), *122*
Hulburt, E. O., 107(5), *122*
Hunt, D. C., 5(17), *30*
Hunten, D. M., 54(67), *63*, 121(20), *122*
Hynek, D. P., 239(8), *285*

I

Ibbs, T. L., 42(24), *62*
Istomin, V. G., 144(37), *151*, 191(26), *235*
Itikawa, Y., 245(21), 246(22), *285*
Izakov, M. N., 5(4), 18(44, 45), *30, 31*

J

Jacchia, L. G., 5(6), 26(61), *30, 31*
Jeans, J. H., 49, *62,* 75, *100*
Johannessen, A., 136(20), *150*
Johnson, C. Y., 54(61), 57(61), *63,* 102 (30), 121(30, 31, 32), *123,* 139 (22), 141(22, 27), 142(22, 31, 32), 143(33), 144(38), 149(22, 38), 150 (31, 32, 46), *150, 151,* 191(21, 23), 196(21), 202(21), 203(21), *235*
Johnson, F. S., 5(15), 16(15), 18(43), 19(43), 25(43), *30, 31,* 34(7), 35 (7), 38(16), 50(55), 52(55), 60 (79), *62, 63,* 67(12), 70(12), 72 (12, 16), 94(23), *99, 100,* 191(3), *235,* 239(4), *284*
Jones, R. A., 54(63), 57(63), *63,* 246 (24), 262(24), 276(24), *285,* 306 (75), *309*

K

Kamiyama, H., 133(18), 137(18), *150*
Kanal, M., 239(6), *285,* 293(22), 300 (22), *308*
Kasprzak, W. T., 50(51), *63*
Kato, S., 21(51), *31*
Keating, G. M., 49(47), *62*
Kendall, P. C., 169(3, 6), 171(3), 174 (6), *189*
Keneshea, T. J., 38(15), *62,* 127(10), 138(10), 142(10), *150*
Keyes, F. G., 9(30), 11(30), *31*
King, J. W., 6(26), *30,* 186, 187(32, 50), 188, 189, *190*
King-Hele, D. G., 30(69), *31*
Kissel, J., 125(8), 133(8), 136(8), *150*
Knudsen, W. C., 254(36), 255(36), 262 (36), *285,* 300(52, 53), 301(52, 53), 307(52, 53), *309*
Kockarts, G., 23(56), 29(67, 68), 30 (68), *31,* 36(11), 42(26), 43(26), 45(29), 46(11), 50(11), 54(11, 64, 65), 55(11, 64), 58(11, 68), *62,* 93(22), *100,* 199(38), *236*
Kohl, H., 6(26), *30,* 186(32, 33, 39), 187 (32), 188, *190*
Krankowsky, D., 125(8, 9), 133(8), 135 (9), 136(8, 20), 137(9), 144(9), *150*
Krishnamurthy, B. V., 191(11), *235*
Kruger, C., 274(70), 281(70), *286*
Kumer, J. B., 150(45), *151*
Kummler, R., 25(57), *31*
Kupperian, J. E., 32(5), 57(5), *61,* 64 (1), *99*
Kyle, L., 67(9), 71(9), 97(9), *99*

L

Lagos, C. P., 5(21, 22), 7(21, 22), 8 (21), *30*
Landau, L. D., 3(3), *30*
Lane, N. F., 269(62), *286*
Larrabee, J. C., 121(22), *122*
Lehmann, H. R., 144(39), *151*
Lejeune, G., 254(35), *285,* 289(11), 291 (11), 293(17), *308*
Lemaire, J., 235(83, 84), *237*
Lettau, H., 35(8), *62*
Lew, S. K., 49(34, 36), *62*
Lewak, G. J., 301(59), *309*
Lifshitz, E. M., 3(3), *30*
Lindenmeyer, C. S., 107(7), *122*
Lindzen, R. S., 21(50), *31*
Liwshitz, M., 49(35, 37), *62*
Lowan, A. N., 5(14), *30*
Lynn, N., 194(28), *235*

M

McAfee, J. R., 52(57), 60(77), *63*
McClure, J. P., 5(10), *30,* 293(36, 37), *308*
McDowell, M. R. C., 46(32), *62,* 166 (13), *168*
McElroy, M. B., 54(67), *63,* 121(20), *122,* 177(14, 15, 18), *190,* 245(19), 247(19, 26, 27, 28), 248(28), 252 (19, 27, 33), 256(27), 266(19, 27), 270(27), *285,* 287(1), 288(1), 289 (8), 295(1, 8), *307, 308*
McGowan, J. W., 201(40), *236*
McGuire, E. J., 178(22), *190*
McNutt, D. P., 22(53), *31*
Mahajan, K. K., 293(34), *308*
Mahoney, J. R., 5(21), 7(21), 8(21), *30*
Maier, E. J. R., 202(42), 220(55), *236,* 254(37), *285*
Mange, P., 32(1), 37(13), 38(13), 43

(27, 28), 58(71), *61, 62, 63,* 95 (25), *100,* 121(28), *122*
Mantas, G. P., 288(5), 289(5), 293(5), *308*
Markov, M. N., 25(58, 59), *31*
Marovich, E., 305(71), *309*
Marrero, T. R., 41(20), *62*
Marubashi, K., 227(81), *237*
Masley, A. J., 122(35), *123*
Mason, E. A., 41(20, 22), 42(25), *62*
Mata, L. A., 10(36), 12(36), 14(36), *31,* 41(23), *62*
Mathur, S., 10(33), *31*
Matsushita, S., 161(8), 162(8), *168,* 186 (46), *190*
Maynard, N. C., 186(48), 189(48), *190*
Mayr, H. G., 5(25), 21(25), *30,* 60 (80), *63,* 141(26), *151,* 191(20), 202(20, 43), 206(45, 47), 208(45, 48), 212(45, 48), *235, 236,* 293(32, 33, 36), 297(33), 298(47), *308, 309*
Meadows, E. B., 32(3), *61,* 143(33), *151*
Mechtley, E. A., 132(12), 133(12), *150*
Megill, L. R., 263(51), *286*
Meier, R. R., 58(71, 72), *63,* 95(25), *100,* 121(28), *122*
Mentzoni, M. H., 268(56, 57, 58), *286*
Michel, F. C., 223(78), 227(78), *237*
Milne, E. A., 49, *62*
Mironov, A. V., 49(45), *62*
Mitchner, M., 274(70), 281(70), *286*
Moffett, R. J., 6(27), *30,* 186(37), 188 (37), *190,* 245(19), 247(19), 252 (19), 266(19), *285,* 289(8), 295(8), *308*
Morozov, S. K., 18(45), *31*
Morton, K. W., 26(66), *31*
Muldrew, B. D., 223(75), *237*
Muller, D., 50(52), *63*
Mullins, J. A., 49(47), *62*
Munn, R. J., 42(25), *62*
Murphy, E. A., 38(18), 52(18), *62*

N

Nagy, A. F., 183(30), *190,* 196(35), 197(35), 198(35), 215(50), *236,* 239(6), 249(32), 252(30, 32), 254 (32), 257(32, 45), 259(32, 46), 261 (32), 263(50), *285, 286,* 288(6), 293(6, 16, 19, 22), 298(48, 49), 300(22), 302(16), 303(16), 304, *308, 309*
Narasinga Rao, K. V., 268(57), *286*
Narcisi, R. S., 127(10), 133(14, 15, 19), 134(14), 136(15), 138(10), 142 (10), 144(14), *150*
Nathan, K. V. S., 257(40), *285*
Neher, H. V., 119(18, 19), *122*
Nelms, G. L., 220(60, 69), *236,* 301 (54), *309*
Newell, R. E., 5(22), 7(22), *30*
Nicolet, M., 5(16), 16(16), 26(62), *30, 31,* 32(1), 36(11), 45(30), 46(11, 31), 49(46, 49), 50(11, 31), 54(11), 55(11), 58(11, 68, 74), *61, 63,* 79 (20), 93(22), *100,* 111(13), 116 (14), 118(14, 17), 119(17), 120 (17), *122,* 127(11), 133(13), 145 (11), *150,* 191(4), 199(38), *235, 236*
Nief, G., 54(59), *63*
Niemann, H., 239(9), *285,* 293(24), *308*
Nisbet, J. S., 5(9), *30,* 252(31), 257(31), 261(31), *285,* 293(18, 29), 304(18), *308*
Nishida, A., 196(33), 223(33), 226(33), *236*
Norton, R. B., 305(71), *309*

O

Öpik, E. J., 65(6), 67, 70(6, 8), 71, *99*
Ogawa, T., 121(25), *122,* 142(30), 150 (47), *151,* 247(25), *285*
Olivero, J. J., 38(17), *62*
Omholt, A., 177(16), *190*
Ortenburger, I. B., 192(27), *235*
Osterbrock, D. E., 179(19), *190*

P

Park, C. G., 183(31), *190,* 197(36), 220 (65), *236*
Parker, E. N., 219(53), *236*
Parkinson, T. D., 143(34), *151*
Patterson, N. P., 102(30), 121(30), *123,* 142(31), 150(31), *151*
Patterson, T. N. L., 36(10), 50(53), 55 (10), 57(10), 60(75, 76, 78), *62, 63,* 94(23), *100,* 169(5), 183(28), 186(28), *189, 190,* 191(5), 206 (44), 208(44), 212(44), *235, 236*
Paulsen, D. E., 121(22), *122*

Peetermans, W., 23(56), *31*
Petit, M., 5(8), *30*, 254(35), *285*, 289 (11), 291(11), 293(17, 43), 302 (43), *308*
Pharo, M. W., 139(24), 141(26), 144 (24), *150*, *151*, 202(43), 220(61), 222(61), *236*
Phelps, A. V., 269(61), *286*
Pickett, R. A., 202(41), *236*
Pineo, V. C., 239(8), *285*
Pokhunkov, A. A., 32(4), *61*
Prasad, S. S., 191(19), *235*, 293(38, 39), *308*
Priester, W., 5(7, 19, 20), 7(19, 20), 8 (19), 26(19, 20, 65), *30*, *31*
Prinz, D. K., 58(72), *63*
Prior, E. J., 49(47), *62*
Prokudina, V. S., 49(45), *62*

R

Rahman, N. K., 220(61), 222(61), *236*
Raitt, W. J., 191(10), 220(54), *235*, *236*
Rao, B. C. N., 254(37), *285*
Rao, P. B., 293(40), *308*
Rapp, D., 194(29), *236*
Ratcliffe, J. A., 101, 103, *122*, 124(1), *150*
Reber, C. A., 49(49, 50), 52(50), *63*
Reddy, B. M., 293(32, 33), 297(33), *308*
Rees, M. H., 122(33, 34), *123*, 143(36), *151*, 246(24), 247(27), 252(27), 256(27), 262(24, 47), 266(27), 270 (27, 65), 276(24), *285*, *286*, 287 (1), 288(1), 295(1), 306(73, 74, 75), *307*, *309*
Reid, G. C., 124(4), 132(4), 133(4), *150*
Rense, W. E., 54(63), 57(63), *63*
Richtmyer, R. D., 26(66), *31*
Riedler, W., 136(20), *150*
Rishbeth, H., 6(27), *30*, 150(43), *151*, 169(1, 7), 174(7, 11), 175(11, 12), 176(11), 182(25), 186(35, 36, 37), 188(35, 36, 37), *189*, *190*
Roble, R. G., 269(60), 270(60), *286*, 304(67), 305(71), *309*
Roemer, M., 5(7), 26(63, 64), *30*, *31*
Rostas, F., 281(79), *286*
Roth, E., 54(58, 59), *63*
Roth, W., 133(19), *150*
Rothwell, P., 186(40), 188(40), *190*
Row, R. V., 268(56), *286*
Rutherford, J. A., 177(17), *190*

S

Sanatani, S., 289(10), 291(10, 14), 293 (14, 41), 300(14, 41), 301(10), *308*
Sandler, S. I., 11(38), 12(38), *31*
Sato, T., 220(62, 63), 223(62), *236*
Saxena, S. C., 10(33), 11(39), 12(39), *31*
Saxena, V. K., 11(39), 12(39), *31*
Scherer, M., 235(83), *237*
Schulz, G. J., 269(63), *286*
Schunk, R. W., 167(14), *168*, 245(20), 246(23), *285*
Scott, L. R., 141(26), *151*
Seaton, M. J., 178(19), *190*
Sekiguchi, T., 281(77, 78), *286*
Serbu, G. P., 220(55), *236*
Sharp, G. W., 220(66, 73), 221(73), 225 (73), *236*, *237*, 300(52, 53), 301 (52, 53), 307(52, 53), *309*
Sharp, R. D., 247(28), 248(28), *285*
Shawhan, S. D., 223(74), *237*
Shea, M. F., 247(28), 248, *285*
Shefov, N. N., 49(45), *62*
Shelepin, L. A., 25(59), *31*
Shen, C. S., 70(15), *99*
Sherman, C., 133(15), 136(15), *150*
Shimazaki, T., 169(9), 171(9), *189*
Singer, S. F., 49(37), *62*, 65(6), 67, 70(6, 8), 71, *99*
Skovli, G., 136(20), *150*
Smith, C. R., 139(24), 144(24), *150*, 191(9, 18), 220(18), 225(18), *235*
Smith, F. J., 10(37), *31*, 42(25), *62*
Smith, G. R., 49(42), *62*, 69(13), *99*
Smith, J. M., 155(4), *168*, 244(18), *285*
Smith, L. G., 132(12), 133(12), *150*
Spencer, N. W., 238(3), 239(5, 9), *284*, *285*, 293(20, 21, 24, 25, 30), *308*
Spitzer, L., Jr., 5(12), *30*, 75, 78, *100*, 275(74), 276(74), 277(74), *286*
Sterling, D. L., 293(36), *308*
Stewart, A. I., 178(20), 187(20), *190*, 252(33), *285*
Stewart, R. W., 23(54), *31*
Stolarski, R. S., 263(50), *286*, 288(6), 293(6), 306(72), *308*, *309*
Stoney, G. J., 65(3), *99*
Storey, L. R. O., 191(1), *235*

Stubbe, P., 182(24), 186(24, 38, 45), 187(45), 188(38), 189(45), *190*, 273(69), *286*
Swider, W., Jr., 17(40), *31*, 107(9, 10), 117(16), 119, 120(16), 121(16, 24), *122*, 127(10, 11), 138(10), 142(10, 28), 144(41), 145(11), *150*, *151*

T

Taeusch, D. R., 239(9), *285*, 293(24), *308*
Takayangi, K., 246(22), *285*
Tanenbaum, B. S., 274(71), *286*
Taylor, H. A., 139(24), 141(26), 144(24), *150*, 191(9, 18), 202(41, 43), 206(47), 220(18, 61, 64, 65), 222(61), 225(18), *235*, *236*
Thomas, D. M., 133(15), 136(15), *150*
Thomas, G. E., 9(28), *30*, 58(73), *63*
Thomas, J. O., 199(39), 220(59), 223(59), 225(59), *236*
Thomas, L., 124(6), *150*
Thorne, R. M., 305(70), *309*
Timleck, P., 220(60), *236*
Tinsley, B. A., 50(53), 58(70), *63*
Tohmatsu, T., 121(25, 26), *122*, 142(30), 150(47), *151*, 247(25), *285*
Townsend, J. W., 32(3), *61*
Trans, E. V., 136(20), *150*
Tröim, J., 136(20), *150*
Troy, B. E., Jr., 293(35), *308*
Tsuruta, H., 247(25), *285*
Turner, B. R., 177(17), *190*
Tuve, M. A., 101(2), *122*

U

Utlaut, W. F., 295(45), *309*

V

Vanderslice, J. T., 41(22), *62*
Van Zandt, T. E., 5(17), *30*
Vasseur, G., 175(13), 176(13), *190*
Venkateswaran, S. V., 49(34, 36), *62*
Volland, H., 5(7, 23, 24, 25), 21(25), *30*

W

Wagner, C. U., 144(39), *151*
Waldteufel, P., 5(8, 11), *30*, 293(43), 302(43), *308*
Walker, E. L., 274(71), *286*
Walker, J. C. G., 122(34), *123*, 166(11), 167(14), *168*, 246(23, 24), 247(27), 252(27), 256(27), 262(24, 47, 48), 263(49, 50), 266(27), 270(27, 65), 273(67), 276(24), *285*, *286*, 287(1, 2), 288(1), 295(1), 301(56), 306(73, 74, 75), *307*, *309*
Walker, R. E., 10(35), *31*
Wallace, L., 177(18), *190*
Wand, R. H., 293(42), *308*
Watanabe, K., 121(21), *122*
Waterston, J. J., 65(2), *99*
Watt, T. M., 212(49), *236*
Weill, G. M., 254(35), *285*, 293(17), 302(63), *309*
Weissman, S., 41(21, 22), *62*
Weller, C. S., 121(32), *123*, 142(32), 150(32), *151*
Whipple, E. C., 191(7), *235*
Whitehead, J. D., 144, *151*
Whitten, R. C., 257(39), *285*
Wieder, H., 125(8, 9), 133(8), 135(9), 136(8), 137(9), 144(9), *150*
Wilke, C. R., 10(31), *31*
Wilkes, M. V., 107(6), *122*
Williams, A., 166(13), *168*
Willmore, A. P., 191(10), 220(54), *235*, *236*, 293(31), *308*
Wilson, T. E., 54(62), *63*
Wright, P. G., 10(32), *31*

Y

Yonezawa, T., 169(10), 171(10), 175(10), 181(23), 182(23), 185(23), *189*, *190*
Young, J. M., 54(61), 57(61), *63*, 102(30), 121(30, 31, 32), *123*, 139(22), 141(22, 27), 142(22, 31, 32), 144(38), 149(22, 38), *150*, *151*, 191(21), 196(21), 202(21), 203(21), *235*

Z

Zähringer, J., 125(8), 133(8), 136(8), *150*
Zimmerman, S. P., 38(15, 18), 52(18), *62*
Zipf, E. C., 143(34, 35), *151*

Subject Index for Parts A and B

The page numbers referring to Part A (Chapters 1 through Appendix A) are roman. The page numbers referring to Part B (Chapters 14 through Appendix B) are italic.

A

Absorption cross section, *see* Photoabsorption, Photoionization
Absorption of radiation, *103–107*
Airglow
  atmospheric bands, 245, 310–311
  first positive (N_2), 247
  green line (O), 63–64, 245–246, 295
  Herzberg system, 241, 244–245
  N emissions, 351
  NO emissions, 242, 246, 319–322, 345
  O infrared, *22–25*
  OH emissions, 250, 360–361, 370
  red line (O), *304–306*
  Schumann–Runge system, 241
Ambipolar diffusion, *156*, *164*, *170*, *215*
Ar
  abundance, 20, 22–24
  diffusion, 46–47
  ion reactions, 270–271, *see also* Appendix A, 401–403
  ionization thresholds, 108
  photoionization, 108–111
Atmosphere
  basic equations, *6–9*
  boundary conditions, 38, 45, 62–64, 68–75, 297, *5*
  column content, 18–19, 34, 39–44, 295, *97–99*
  composition, 18–20, 56–61, 75–77, *86*
  density, 6–10, 56–61, 69–77
  heat flow, 77, *16*
  heat production profile, *19*
  isotopic composition, 26–31
  Joule heating, *20–21*
  minor molecular constituents, 24–26
  models, *see* Model atmospheres
  noble gases, 20–24
  regions, 1–6
  temperature profile, 3, 9–11, 37–38, 57–61, 69
  thermal conductivity profile, *15*
Atmospheric cooling, *22–25*
Atmospheric heating, *15–21*
Atmospheric models, *see* Model atmospheres
Atom interchange, 249–252
Attachment, electron, 278–279

B

Ballistic particles, *66–67*, *71–72*, *86*
Bethe formula, 213–216
Black body emission, *see* Radiation
Boltzmann equation
  collision terms, *153–155*, *241–247*
  exosphere, *72–75*
Boundary conditions, *see* Atmosphere

C

CH_4
  abundance, 24–25, 362–363
  oxidation, 357–358
  photodissociation, 178, 357
  transport, 364–366

Chapman layer, *109–111*
Chappuis bands (O_3), 175, 304
Chemiluminescence, 243, 245, 247–248, 250, 320, 336, 370
Cluster positive ions, 272–277
CO
  abundance, 24–25
  ion reactions, 269–270, *see also* Appendix A), 401–409
CO_2
  abundance, 24–25
  ion reactions, 268–269, *see also* Appendix A, 401–409
  photoabsorption, 181
  photodissociation, 180–183
Collision cross section
  charge exchange, 219–222
  charged particles, 232–237
  differential, 189
  electron impact excitation, 198–206
  electron impact ionization, 206–217
  hard sphere, 186–187
  ion–neutral, 217–218
  momentum transfer, 189–191
  O^+—H charge exchange, 225–226
  thermal electron–neutral, 192–194
Collision frequency
  charge exchange, 222–224
  charged particles, 232–237
  definition, 186–192
  diffusion, 190–191, *155*
  electron–neutral, 192–198
  H^+—O charge exchange, 225–226
  hard sphere, 186–187
  ion–neutral, 218–220
  monoenergetic electrons, 191
  radiowave absorption, 191–192
  three-body, 187
Collision processes, 184–192
Collision time, 186–187
Column content, *see* Atmosphere
Conjugate region heating, *302–304*
Conductivity
  electrical, *159–160*
  thermal
    electron, *275–281*
    ion, *281–283*
    neutral, *12–15*
Conservation equations
  neutrals
    concentration, *2–3, 7*
    momentum, *3*
    energy, *3, 7*
  plasma
    concentration, *169–170*
    momentum, *153–155*
    energy, *241–247*
Critical level, *45, 64, 71–73, 75–80, 91*
Critical point, plasma, *216–217, 230*
Coriolis force, *6*
Current density, electric, *159–160, 215*

D

Debye length, 233–234
Density, *see* Atmosphere
Detachment, electron
  associative, 279–280, 282, 288
  collisional, 280
  photo, 280–281
Deuterium
  eddy diffusion effect, *56–57*
  vertical distribution, *54–57*
Diffusion coefficients
  ion, *164*
  neutral, *34, 38–41*
Diffusion equation
  ions, *see* Plasma transport
  neutrals, *33–38*
Diffusion time, *38*
Diffusive equilibrium, *see* Equilibrium
Dip angle, *157, 164*
Dissociative recombination, 253–256, 316, *110*
D-region
  electron density profiles, *133*
  ion densities, *125*
  ionic processes, *127*
  ionization, *132*
  negative ion reactions, *136*
  positive ion reactions, *134*
  time constant, *129*
Drift velocity, plasma, *170*
Dynamo theory, *159–160*

E

Eddy diffusion, 296, 350–351, 365–369, 384–385, *35, 38, 53*
Effusion velocity, *45–49*
Electric currents, *see* Current density, electric

Electric polarization, *see* Polarization
Electrical conductivity, *see* Conductivity, electrical
Electron collision frequency
  homosphere, 196–197, *see also* Collision frequency
  ion, 236
Electron concentration, *see* Ion composition
Electron cooling rates, *267–271*
Electron–electron energy transfer, *245*
Electron heating rates, *238, 240, 246, 251, 256, 262–263*
Electron impact cross sections, 198–217, 316
Electron production rates, *see* Ion production
Electron temperature profiles, *239, 288–290, 292–297*
Electron thermal conductivity, *see* Conductivity, thermal
Energy balance
  electron, *245–247, 256*
  ion, *240, 263–265*
  neutral, *5, 16–21*
Energy levels
  N, 205
  O, 203
Energy loss, energetic particles
  electron, 213–216
  ion, 226–232
Equation of motion, *see* Conservation equations
Equilibrium
  neutral gas
    diffusive, 47, 67–68, *35*
    hydrostatic, 6–7, 33–36, 67–68
    mixing, 67, *36*
    photochemical, 295, 297, 299–300, 348
  plasma
    chemical, *139–140, 145–147, 179, 192, 195*
    diffusive, *172, 199–206*
E-region
  effect of NO, *141, 143*
  ion densities, *102, 140, 142*
  ionic processes, *130*
  ionization, *138*
  nightsky radiation, *143*
  reaction, *138*
  time constant, *130*
  zenith angle, *141*
Escape
  flux, *79*
  probability, *77–79*
  time, *46*
  velocity, *68*
Excited atoms and molecules
  N, 200–202, 205–207, 254–255, 346–351
  N_2, 176, 200–202, 240–253
  O, 173, 200–204, 240–253, 304–313, 363–364, 387
  O_2, 200–202, 240–253, 304–313, 327, 333–334, *120–121*
Excited ions
  N_2^+, 121, 160, 206–217, *115*
  O^+, 95, 99–100, 159, 206–217, *114, 177–179*
  O_2^+, 115–116, 159, 206–217, *115*
Exosphere
  column content, *97–99*
  temperature, *95–97*
  trajectories, *65–68, 72–73*
  vertical distribution, 6, *68–75, 80, 90*
Exospheric temperature, *see* Thermopause

F

F_1-region
  effect of NO, *147*
  ion densities, *102, 146, 148–149*
  ionic processes, *131, 145*
  sunset effect, *148*
  time constant, *132*
  zenith angle, *147*
F_2-region, *see also* Topside ionosphere
  diffusive flow effect, *183*
  global dynamics, *186–189*
  ion densities, *180–185*
  ion excitation, *177–179*
  ionic processes, *131, 145, 180–186*
  neutral winds, *184–185*
  photoionization, *176–180*
  reactions, *175, 177*
  temperature effect, *181*
First negative bands (N_2), 119, 212–213
Forbidden transitions
  N, 204
  O, 202

Free path
altitude variation, *76*
photoelectron, *259*
polar wind, *234*
thermal particles, 186–187, *75–76*, *275*, *279*
vertical correction factor, *77–78*

G

Galactic cosmic rays, *see* Ionization, Cosmic rays
Geopotential height, 35
Gravitational acceleration, 9, 34
Gyrofrequency, *158*

H

H
abundance, 375–376, 390, 392
diffusion coefficient, *41*
diurnal variation, *60*
eddy diffusion effect, *58–59*
effusion velocity, *46*
escape, *46–47*
ions, *see* Topside ionosphere
maximum diffusion flow, *58*
photoionization, 155–158, 164
polar wind, *60–61*
principal reactions, 372, 389
reactions with nitrogen compounds, 336–339
sources, *58*
thermal conductivity, *12*
vertical distribution, *57–61*, *81–94*
viscosity, *11*
H_2
abundance, 24–25
dissociation, 358–359
principal reactions, 384
transport, 365, 367
Hartley bands (O_3), 123, 131, 304
He
abundance, 20
diffusion coefficient, *40*
eddy diffusion effect, *50–52*
effusion velocity, *46*
escape, 21, 27, *46*, *48–50*
global distribution, *48*, *52–53*
ions, *see* Topside ionosphere
ion reactions, 266–268, *see also* Appendix A, 403–405, 407
maximum diffusion flow, 46–47, *44*
photoionization, 156–158, 164
sources, 21–24, 27–28, *50*
thermal conductivity, *12*
vertical distribution, *49–53*, *81–90*
viscosity, *11*
Heat balance, *see* Energy balance
Heat conduction, temperature effects
electron, *283–284*, *288*
neutral, *15–16*
heat flux vector, *3–4*, *7*
Heat input, *see* Energy balance
Heating efficiency
photoelectrons, *247*, *250–251*, *256*, *289–292*
solar radiation, *17–19*
Herzberg system (O_2), 124, 168, 171
Heterosphere, 4–5, 11
High speed plasma flow, *see* Plasma transport
HNO, 337
HNO_2, 338–340
HNO_3, 338–340
HO_2
abundance, 339, 373–374, 392
loss, 337–338, 361
photodissociation, 361
principal reactions, 372, 386–387
production, 394
H_2O
abundance, 24–25, 362–363
cluster ions, 277
ion reactions, 272, *see also* Appendix A, 401–403, 405–409
oxidation, 356–357
photodissociation, 176–178, 355–356
principal reactions, 383, 388
transport, 365, 368–369
H_2O_2, 338, 340, 359–361, 388
Homosphere, 4–5, 18–31, 33–45
Huggins bands (O_3), 123, 175, 304
Hydrated ions, *see* Cluster ions
Hydrogen compounds, dissociation and oxidation, 354–361
Hydrostatic equation, *see* Equilibrium
Hyperbolic particles, *66–67*, *70*, *72–73*, *86*, *91–95*

I

Inert gases, *see* Noble gases
Infrared radiation (O), *22–25*
Ion–atom interchange, 256–257, 261–268
Ion composition
  D-region, 13–14, *125, 133*
  E-region, 13–14, *102, 140, 142*
  F-region, 13–14, *102, 146, 148–149, 176, 180–185*
  Topside, 13–14, *202–206, 222–223*
Ion diffusion, *see* Plasma transport
Ion diffusion coefficients, *166–168*
Ion drag, *184–189*
Ion energy loss rates, *271–274*
Ion heating rates, *263–265*
Ion–ion recombination, 289
Ion-neutral reactions, 256–272, *see also* Appendix A, 401–409
Ion production
  D-region, *108, 116–121*
  E-region, *108, 112–116*
  F-region, *108, 112–116*
  Topside, *192–196*
Ion temperature profiles, *298–302*
Ion thermal conductivity, *see* Conductivity, thermal
Ionization
  cosmic rays, *119–120*
  electrons
    cross sections, 206–217
    dissociation, 211–214
    ion ratios, *117*
  photons, *see* Photoionization rates
  protons, 226–232
  x rays, 83–84, 145, 147–148
Ionization potentials, 88, 91, 102, 108, 112, 118, 121
Ionizing efficiency, x rays, *see* x rays
Ionosphere, 12–17, *see also* D, E, F_1, F_2 regions, Topside ionosphere
Isopycnic level, 71
Isotopic composition, *see* Atmosphere

J

Joule heating
  neutral gas, *20–21*
  plasma, *243, 246, 262*

K

Kinetic temperature, exosphere, *see* Exosphere
Kr, 20, 23

L

Liouville's theorem, exosphere, *67*
Low speed plasma flow, *see* Plasma transport
Lyman-α, 127, 135, 160–162, 171, 177–178, 182, 356–357, 361, 393, *116–118, 121*
Lyman-β, 135, 153, 160–162, *117, 121*

M

Mach number, *216*
Magnetosphere, 14–17
Maximum transport velocity
  ion, *173–174, 209–210, 223*
  neutral, 364–367, *43–45*
Maxwellian velocity distribution, *68–72*
Mean free path, *see* Free path
Mean molecular mass, 11–12, *29*
Mesosphere
  definition, 2–3
  vertical transport, 364–369
Mixing distribution, 2, 46–47, 325, 384, *35*
Mixing ratio, *see* Atmosphere, composition
Model atmospheres
  exosphere, *81–90*
  heterosphere, *25–30, 310–338*
  homosphere, 36–45
  homosphere–heterosphere transition, 56–61

N

N
  abundance, 328, 331–336, 342–345, 347–349
  emissions, 205, 351
  energy levels, 205
  ion density, *202–203*
  ion reactions, 265, *see also* Appendix A, 401–409
  loss, 326–328, 332–334
  principal reactions, 344
  sources, 316–319, 340–346

N_2
abundance, 19
dissociation, 315–316
dissociative photoionization, 120
first negative system, 119
ion density, 13, *102*, *140–143*, *146*, *148–149*
ion diffusion coefficient, *166–168*
ion reactions, 263, *see also* Appendix A, 401–409
ionization thresholds, 118
neutral diffusion coefficient, *40*
photoabsorption, 116, 121
photodissociation, 176, 315, 317
photoionization, 120–121, 155–160, 164
potential energy diagram, 117, 247
thermal conductivity, *12*
viscosity, *10*
Ne, 20, 23
Negative ions, 278–279, *125*, *128–130*, *136–137*
Negative ion–electron ratio, *128–129*
Nightsky radiation, *121*
NO
abundance, 328, 331–336, 342–345, 347–349
cluster ions, 275–277
effective dissociation rate, 343
emissions, 242, 246, 319–322, 345
ion density, *102*, *125*, *140–143*, *146*, *148–149*
ion–ion recombination, 289
loss, 325–326
negative ion reactions, 289, *see also* Appendix A, 401–409
photodissociation, 178, 330–331
photoionization, 160–161
potential energy diagram, 242
principal reactions, 344
sources, 319–336, 340–346
transport, 350–351
NO_2
adundance, 24–25
loss, 340
negative ion reactions, 287, *see also* Appendix A, 402–409
photodissociation, 178–179, 323
NO_3
329–330
N_2O, 24–25
Noble gases, 20–24

O

O
abundance, 54–55, 69, 295–299, 311–313, 373–380
emissions, 63–64, 99, 245–246, 295, *22–25*, *304–306*
energy levels, 203
ion density, 13, *102*, *140–143*, *146*, *148–149*, *176*, *180–185*
ion diffusion coefficient, *166–168*
ionization thresholds, 91
lifetime, 53–55, 298, 376
negative ion reactions, 281, *see also* Appendix A, 401–409
neutral diffusion coefficient, *40*
photoabsorption, 90–100
photoionization, 154–159, 164
positive ion reactions, 257, *see also* Appendix A, 401–409
thermal conductivity, *12*
viscosity, *10*
O_2
abundance, 19
cluster ions, 273–274
dissociative photoionization, 113–115
ion density, 13, *102*, *140–143*, *146*, *148–149*
ion diffusion coefficient, *166–168*
ionization thresholds, 112
negative ion reactions, 279, *see also* Appendix A, 401–409
neutral diffusion coefficient, *40*
photoabsorption, 88–90, 112–116, 124–127, 303–304
photodissociation, 50, 167–174, 294–299, 308
photoionization, 114–116, 154–159, 161, 169
potential energy diagram, 113, 244
positive ion reactions, 262, *see also* Appendix A, 401–409
thermal conductivity, *12*
viscosity, *10*
O_3
abundance, 24–25, 53, 297–304, 311–313, 373–380
formation, 51–53

lifetime, 52, 300
loss, 298–300
negative ion reactions, 283, *see also* Appendix A, 401–409
photoabsorption, 122–124, 303–304
photodissociation, 50, 124, 174–176, 294–299, 304–306, 378–380
OH
abundance, 372–373, 390, 392
emissions, 250, 360–361, 370
loss, 334, 337–339
negative ion reactions, 288, *see also* Appendix A, 401–409
photodissociation, 361
positive ion reactions, 271–272, *see also* Appendix A, 401–409
principal reactions, 372, 386
production, 394
Optical depth
definition, *104*
optical depth factor, *17, 106–107*
Schumann–Runge, 303, 330–331, *18*
stratosphere, 302
unit value, 82–83, *105, 110*

P

Photoabsorption cross sections
ultraviolet
CO_2, 181
H, 155–158, 164
He, 156–158, 164
N, 101–104
N_2, 116–121
O, 90–100
O_2, 88–90, 112–116, 124–127, 303–304
O_3, 122–124, 303–304
x rays, *see* x rays
Photochemical equilibrium, *see* Equilibrium
Photodetachment, *see* Detachment
Photodissociation
CH_4, 178, 357
CO_2, 180–183
HO_2, 361
H_2O, 176–178, 355–356
H_2O_2, 388
N_2, 176, 315, 317
NO, 178, 330–331
NO_2, 178–179, 323
O_2, 167–174, 294–299, 308
O_3, 174–176, 294–299, 304–306, 378–380
OH, 361
Photoelectron
electron collisions, *245, 303*
energy spectrum, *249–252, 261–262*
escape altitude, *260*
escape flux, *259*
production, *247–248, 254–256*
transport, *257–260*
Photoionization cross sections
Ar, 108–111
H, 106–108
He, 105–106
N, 102–104
N_2, 120–121
O, 93–94, 96–99
O_2, 114–116
Photoionization rates
H, 155–158, 164
He, 156–158, 164
N_2, 155–160, 164
NO, 160–161
O, 154–159, 164, *176–180*
O_2, 154–159, 161, 164
$O_2(^1\Delta_g)$, 122, *120–121*
Plasmasphere, 15–17, *222–225*
Plasma temperature, *see* Temperature
Plasma transport
boundary conditions, *170–174, 208–209, 218–220*
collision terms, *153–155*
coordinate system, *157*
equations, *152, 157, 162–164*
high speed, *214–220*
low speed, *163–165, 206, 214*
minor ion, *165, 207*
multiple ion, *164*
single ion, *170–175*
Polar wind, 16, 27, *220–235*
Polarizability, neutral gas, 219
Polarization electric field, *155, 164–165, 173, 199–200*
Potential energy curves
NO, 242
N_2, 117, 247
O_2, 113, 244
Predissociation, 127, 176, 178, 318

Production, heat, *see* Energy balance
Production, ionization, *see* Ion production

Q

Quenching, 245, 310–311, 322

R

Radiation, solar
  black body, 134–136
  emission spectrum, 131–133, 135, 137–140, 152–153
  infrared, 138
  ultraviolet, 139–144, 151–160
  variation, 146–147, 162–164
  visible, 139
  x ray, 144–151
Rare gases, *see* Noble gases
Reaction rate, definition, 188
Reactions, *see* Appendix A, 401–409
Recombination
  ions
    dissociative, 253–256
    radiative, 252–253
  neutral
    radiative, 240–243
    three-body, 243–249
Red arc, *see* Subauroral red arc
Resonance charge exchange, 219–224

S

Satellite drag, 8–9
Satellite particles
  distribution, *72–86*
  formation and loss, *91–95*
Scale height
  density, *29*
  gradient, 35–36, 67–68, *29–30*
  plasma, *170*, *208*
  pressure, 9, 11, 34–36, 57–61, 67–69, *8*, *29*
Schumann Runge (O_2), 124–127, 169–173, 177, 330
Solar cycle variation, density, 8–9
Solar radiation spectrum, *see* Radiation
Solar radio emission, temperature correlation, *26*
Solar x rays, *see* x rays
Specific heats, *4*
Stratosphere
  definition, 1–2
  vertical transport, 364–369
Subauroral red arc, *304–306*
Supersonic flow, *see* Plasma transport

T

Temperature
  diurnal variation, *26–28*
  exosphere, *95–97*
  heterosphere, 67–68, *25–30*
  homosphere, 9–11, 37–38, 57–61, 67–68
  ionosphere, *see* Electron temperature profiles, Ion temperature profiles
Temperature gradient, 64, 66–67, *16*
Thermal balance, *see* Energy balance
Thermal conduction effects, *see* Heat conduction
Thermal conductivity, *see* Conductivity, thermal
Thermal diffusion, *4*, *33*, *35*, *41–43*
Thermal effects
  aurora, *306–307*
  polar wind, *307*
Thermoelectric effects, *275–277*
Thermosphere, 4, 45–47, *16*
Topside ionosphere
  chemical equilibrium, *192*, *195*
  chemical time constants, *194*, *196*
  diffusion equilibrium, *199–206*
  high speed flow, *214–220*
  inter-ion momentum transfer, *213–214*
  ion densities, *202–206*, *222–223*
  ion processes, *192–196*
  limiting flow, *209–210*, *223*
  low speed flow, *206–214*
  plasmasphere, 15–17, *222–225*
  polar wind, *220–235*
  temperature effect, *203–204*, *233*
  transport processes, *196–198*
Transport coefficients, *see* Conductivity, Diffusion coefficients, Viscosity
Troposphere, 1–2
Turbopause, 297, *36*

U

Ultraviolet radiation, *see* Radiation

V

Velocity
  average, *2*
  diffusion, *2, 7*
  effusion, *45–49*
  escape, *68*
  mass average, *2, 7*
  peculiar, *2*
  vertical, neutral gas, *8–9, 34–35, 44–45*
  vertical, plasma, *162, 164, 170*
Viscosity
  empirical expressions, *10–12*
  theory, *3, 9–10*
  vertical profile, *11*

W

Water vapor, *see* H_2O
Winds
  high latitudes, *20–21*
  homosphere, 36–37
  thermosphere, *184–185*

X

Xe, 20, 23
x rays
  absorption cross sections, 80–87
  ionization efficiency, 83–84, 147–148
  ion production, *118–120*
  solar emission, 144–151